1989

Electrochemical studies of the corrosion of painted and unpainted metals

G. W. Walter
University of Wollongong

ELECTROCHEMICAL STUDIES OF THE CORROSION OF PAINTED AND UNPAINTED METALS

A thesis submitted in fulfilment of the requirements
for the award of the degree of

DOCTOR OF PHILOSOPHY

from

THE UNIVERSITY OF WOLLONGONG

by

G.W. Walter, B.Sc. (Applied Chem), M.Phil (Chem)

Department of Metallurgy
and Materials Engineering
1989

CANDIDATE'S CERTIFICATE

This is to certify that the work presented in this thesis was carried out by the candidate in the Electrochemistry/Corrosion Laboratory at the Research and Technology Centre, BHP Steel International Group, Coated Products Division, Port Kembla and has not been submitted to any other university or institution for a higher degree.

In memory of my father and mother

John Henry Walter

Mary Winifred Walter

to whom this work is dedicated

ACKNOWLEDGEMENTS

The work described in this thesis has been carried out in the Electrochemical/Corrosion Laboratory, Organic Coatings Group, Research and Technology Centre, BHP Steel International Group, Coated Products Division, Port Kembla. The author wishes to express his sincere thanks to BHP, Dr Peter N. Richards and Dr Robert M. Hobbs for permission to initiate and proceed with this work, and to Mr Grahame J. Harvey and Dr Gordon W. Delamore for their supervision and encouragement given throughout.

During the course of this thesis, the author acknowledges the assistance of the following: Technical Officer, Mr Alan R. Richards for his part in the experimental programme, the drawing of graphs and assistance with flowcharting the computer programs; three trainees - Ms Danuta Obuchowski, Mr Gary Mortimer and Mr Bryan Shedden for their parts in the experimental program; Dr Ted M. Boge for helpful discussions on thesis preparation; Dr Malcolm Binns for discussions on paint formulations; Mr Ian Edgar for assistance with painting samples and Dulux Aust Ltd for supplying the special gloss formulations; Dr David J. Willis for discussions on metallography; Mr Wayne Renshaw for rolling the Zn-55% alloy; Ms Janelle Murada and Mr Rod W. Lucas for assistance with scanning electron microscope work; Mr John T. Flanagan for helpful discussions on statistics; Mr Mike Di Leva and Mr Larry Ciccarello for production of slides and photographs.

Finally, special thanks are due to Mrs Cecily M. Munro, without whose painstaking efforts in typing, this thesis would not have come to fruition.

PUBLICATION LIST

Part of the work reported in this thesis has been published. Details are as follows:

Publications

1. G.W. Walter, 'Comparison of single frequency and wide frequency range impedance tests for painted metals', Corros. Sci. accepted for publication, Aug (1989).
2. G.W. Walter, M.A.D. Madurasinghe, 'Corrosion rates from low polarization data calculated by a galvanostatic, non-linear curve fitting method', Corros. Sci. 29, 1039 (1989).
3. G.W. Walter, 'A review of impedance plot methods used for corrosion performance analysis of painted metals', Corros. Sci. 26, 681 (1986).
4. G.W. Walter, 'A critical review of dc electrochemical tests for painted metals', Corros. Sci. 26, 39 (1986).
5. G.W. Walter, 'A critical review of the protection of metals by paints', Corros. Sci. 26, 27 (1986).

Conference Papers

1. G.W. Walter, 'Painted metal/solution equilibria in chloride solutions', 1st Internat. Symp. Electrochem. Imped. Spectros., Bombannes, May (1989).
2. G.W. Walter, 'Use of electrochemical sensors for the measurement of corrosion characteristics of Zn and Zn-Al alloy coated steel under simulated atmospheric conditions', Galvatech 89, Tokyo, Sept (1989).
3. G.W. Walter, 'Corrosion rates of zinc based coatings from low polarization data calculated by a galvanostatic non-linear curve fitting method', Galvatech 89, Tokyo, Sept (1989).
4. G.W. Walter, 'Some electrochemical properties of immersed painted metals', 7th Aust. Electrochem. Conf., Sydney, Feb (1988).
5. G.W. Walter,' Surface coatings - measurements and mechanisms of degradation', 27th Aust. Corros. Assoc. Conf., Melb., Nov (1987).

ABSTRACT

An electrochemical test system of computer programs has been written that controls electrochemical instrumentation to carry out galvanic current, impedance and corrosion current tests, and processes the data. This test system has been applied to the study of corrosion mechanisms for painted and unpainted metals.

Laboratory simulated atmospheric conditions in a pollution gas box, PGB, have shown that mass loss of uncoupled steel increases markedly with increase in $[SO_2]$ up to 1 ppm, but that Zn, Al are relatively unaffected, whereas Zn-55%Al alloy shows a modest increase. Sacrificial protection of a steel substrate may therefore be difficult at the higher $[SO_2]$. However, ACM tests reveal the opposite is true when steel is galvanically coupled to Zn-55%Al alloy, which has difficulty providing sacrificial protection at zero and at low $[SO_2]$, and a mechanism is proposed. Corrosion of Fe, Zn-55%Al and Zn in the presence of up to 1 ppm $[SO_2]$ appears to be under mixed control, the first two because increases in $[SO_2]$ cause increases in corrosion brought about by depolarization of anodic and cathodic reactions. Random partial short circuits in Zn and Fe ACMs in third and fourth PGB cycles due to electron conducting corrosion products can make interpretation of data difficult. This has been modelled by the inclusion of an interfacial corrosion product resistance, R_{cp}, in the metal/solution equivalent circuit. Several methods are presented in order to determine the effect of R_{cp}. Mass losses for Fe, Zn-55%Al and Zn have been calculated from ACM galvanic current, impedance, and corrosion current data over the $[SO_2]$ range and compared with weighed mass loss.

The impedance test has been applied to study the permeation of chloride ions through paint films (painted Zn-55%Al coated steel), the rate of which appears to be rapid for the films tested, and about 50% complete within several

minutes. Solution uptake has been modelled by an equivalent circuit and paint film degradation is shown to occur predominantly at direct or D-type areas where the film resistance follows the resistance of the solution. Comparisons between free and attached film results, both here and below, provide evidence that the high frequency Nyquist semicircle contains paint film information and not metal substrate information.

Impedance tests have also been applied to study the effect of paint film flatting agent particles, which was found to be minimal, on solution uptake. Corrosion resistance of the substrate is controlled by the rate of degradation of the paint film, both of which decrease from the moment of sample immersion. Water initially enters the film but after a few hours this rate slows down and paint film degradation, probably resulting from hydrolysis of the silicone modified polyester top coat portion of the paint film, plus ingress of chloride ions, increase so that substrate corrosion also increases. Sample failure time decreases as solution chloride ion concentration increases, in agreement with outdoor exposure results. This is opposite to some other paint films where performance life is controlled by the solution osmotic pressure. Water uptake over the first few days is greater for attached than for free films, thought due to some special influence of the substrate. However, attached films perform better for a number of reasons. The capacitance method for calculating water uptake is more convenient experimentally but not as meaningful as the gravimetric method due to the superimposed effect of paint film degradation occurring after a few hours with these films. A comparison of single frequency and wide frequency range impedance methods indicates that the steeply rising, falling sections of 1 kHz resistive, capacitive/time trends can be simply explained by the rate of decline of paint film resistance.

TABLE OF CONTENTS

I. INTRODUCTION

I1 Primary Aim

The primary aim of this work is to demonstrate the applicability of electrochemical techniques to the investigation of corrosion problems. Three main electrochemical techniques have been utilized - impedance, galvanic current and corrosion current (or polarization resistance). However, others - namely potential/time and dc resistance, have also been used.

The corrosion problems investigated have been divided into two parts - unpainted and painted metals. Three problems have been studied, one in the first part and two in the second part.

I2 Development of a Computerized Electrochemical Test System

Modern electrochemical instrumentation is capable of being computer controlled such that experiments can be initiated from the computer keyboard and data, collected by the peripheral instruments, can be sent back to the computer for subsequent processing. Unfortunately, there is a lack of dedicated software available for this purpose and what is available is usually not specific enough for the tasks at hand. A computerized electrochemical test system of programs has, therefore, been written that not only controls instrumentation to carry out experiments using the above three electrochemical techniques, but also processes the data for graphical display, editing, sample number allocation, storage, retrieval and subsequent analysis.

I3 Corrosion of Unpainted Metals

1. Corrosion of ZINCALUME under acid rain conditions

The corrosion resistance and ability of Zn and Zn-55%Al alloy coatings to

sacrificially protect a steel substrate have been examined under laboratory simulated atmospheric conditions containing SO_2. The exposure conditions chosen attempt to simulate conditions where the performance of ZINCALUME coated steel, a Zn-55%Al alloy coating on a steel substrate, is unknown, an example being the corrosion performance of ZINCALUME under conditions of acid rain fallout.

Acid rain is a by-product of modern civilization and results predominantly from the release of sulphur and nitrogen oxides to the atmosphere from coal fired power stations and automobile exhausts. Acid rain is caused by the aerial conversion of these oxides to sulphurous and nitric acids in clouds and their subsequent precipitation as rain or fog, not necessarily in areas close to the source of emission. Acid rain is known to have devastating effects on fish life in lakes and on forests, but its effects on metals are less well established. In particular, the effect of acid rain on the corrosion resistance of ZINCALUME coated steel is not known. Although it is difficult to simulate in the laboratory, an attempt has been made to approximate acid rain conditions in a specially constructed box, called the Pollution Gas Box, PGB, where laboratory air containing sulphur dioxide as pollutant is passed through test chambers containing metal samples at elevated temperature and relative humidity. In this way the corrosion resistance and ability of ZINCALUME and galvanized coatings to sacrificially protect a steel substrate have been investigated.

I4 Corrosion Degradation of Painted Metals

Some electrochemical properties of immersed painted metals have been studied in order to clarify the mechanisms by which prepainted metal coated products degrade by corrosion.

1. Effect of large particles in paint films on corrosion performance

Large particles, usually silica flatting agents, are frequently observed in paint films. The diameter of these particles range up to 10 μm or even greater, which is a significant portion of the top coat thickness, usually 20 μm. It is expected that their presence increases the rate of permeation of water or solution into the paint film and this may affect performance life of the painted metal. An investigation was carried out to determine these aspects.

2. Effect of ionic permeation on corrosion performance

Atmospheric exposure results for typical production line painted ZINCALUME and painted galvanized steel on the east coast of Australia have established that corrosion performance is related to the distance from the ocean surf. The tendency towards paint film blistering and white corrosion product formation decreases as the distance increases. The permeation of chloride ions into typical line produced painted ZINCALUME coated steel has, therefore, been investigated in the laboratory. An attempt has been made to answer such questions as how quickly do solutions permeate through these paint films, or how reversible is the permeation process?

1. General

1.1 Principle of method

In impedance methods, small amplitude (a few millivolts) sine wave perturbations (current or voltage) are applied to a polarization cell containing the working electrode whose impedance characteristics are to be determined. The amplitude and phase of the working electrode's response (voltage or current) are compared with those of the perturbation in order to obtain the impedance at the measuring frequency. The experimental technique used in this thesis is the galvanostatic, so that a sine wave current is sent through the cell.

1.2 Linearity of polarization curve

In the galvanostatic technique, the sine wave current and the working electrode's voltage response should be restricted to within the linear range of the polarization curve. This means that the voltage response will also be sinusoidal and will have the same frequency as the current. Operating in the non-linear region causes complications such as faradaic distortion (the generation of a dc component)[1] which can be more troublesome on some instruments than on others but may also alter the outcome of the results by altering the system under test. The range of linearity varies from one system to another. For example, it has been shown[2] that the linear range is approximately 1.5 mV for unpainted zinc and galvanized steel and 3.0 mV for aluminium-killed steel in phthalate-buffered 0.1 M NaCl solution, pH 5.3. These values indicate a rather restricted linear range but extended linear ranges have also been reported (to 60 mV or more) in the literature[3].

The amplitude applied across the working electrode/solution interface may be larger at high frequencies, since most of the voltage is consumed by the solution resistance, R_s. For example, if R_s = 1 ohm.cm^2 and double layer capacitance, C_d = 20 μF.cm^{-2}, then at 8 kHz about half of the total voltage is applied across the interface and at 80 kHz it is only 10%[4]. With frequency response analyzers, see Section T1/1.3, the linear range is less important because harmonics due to non-linearity are totally rejected in the measurement by the correlation analysis. With painted metals, it is probably acceptable to somewhat exceed the linear range quoted for the unpainted metal because of the expected potential drop across the paint film.

1.3 Measuring equipment

Impedance measuring methods have been categorized by Macdonald and MacKubre[5] into frequency domain and time domain measurements. Frequency domain methods apply sinusoidal current (or voltage) excitation to the electrochemical cell under test, and measure the cell's sinusoidal voltage (or current) response in order to obtain the required electrode impedance.

The most common frequency domain method is correlation analysis using frequency response analyzers. The response to a sinusoidal excitation will consist of information at the reference frequency, corrupted by harmonics due to non-linear behaviour, and noise. The response signal is multiplied by, or correlated with, two reference signals, one the sine and the other the cosine of the reference frequency, and the results integrated over a number of cycles of the set frequency to obtain the resistive and reactive components of the response. The integration process ensures total rejection of any harmonic content other than the frequency of interest, plus most of the noise depending

on the time allowed for integration. Frequency response analyzers, also called transfer function analyzers, are examples of modern digital instrumentation which are capable of applying low level signals to an electrochemical system with or without the aid of a potentiostat, and can extract low level response signals from unwanted noise and system harmonic content, to obtain the system's impedance behaviour. Measurements, however, must be carried out at each frequency in a serial fashion which lengthens measurement time compared to techniques like fast Fourier transfer (FFT) spectrum analyzers. A frequency response analyzer has been used for the work in this thesis.

2. Single frequency impedance test

The single frequency impedance test measures the resistive, a, and reactive, b, (or capacitive, $c=1/2\pi fb$), components of impedance, Z. The impedance terms a and c are loosely referred to as resistance and capacitance, respectively.

One of the most thorough applications of the single frequency impedance test to painted metals was that by Wormwell and Brasher[6] who measured the resistance and capacitance of painted mild steel in artificial sea water. A test frequency of 1 kHz was chosen because it is commonly employed in measurements of electrolyte conductance. They showed that after a period of relatively steady values, the measured capacitance rose and the resistance fell sharply with immersion time. The relatively steady values of capacitance during the early stages of immersion gave information about the properties of the film such as paint thickness and water absorption. The sharp rise in capacitance or fall in resistance indicated breakdown of the paint and the onset of rusting. Capacitance/time curves prior to the onset of substrate rusting have been used to calculate the amount of water uptake in paint

films[7-12].

Attempts to explain the shape of typical resistance/time and capacitance/time curves have been made by a number of workers. Wormwell and Brasher[6] explained the decrease in resistance values with time, as an increase in the porosity of the paint film. The initial, steady and the latter sharply rising capacitance values were interpreted as water absorption and paint failure with onset of rusting, respectively. Brasher and Nurse[7] expanded on this by observing that in sea water, the rise indicated initial breakdown of the paint film and exposure of the bare substrate, whereas in other solutions the rise preceded visible breakdown. This led them to conclude that the capacitance rise did not indicate a sudden increase in water uptake but rather a reorientation in the mode of distribution of water. Leidheiser[8] believes that the large increase in capacitance is caused by accumulation of aqueous phase water at the metal/paint interphase. Smith[13] attributed the large capacitance rise to a change in the coating to a pore structure. Padget and Moreland[14] considered that capacitance measurements indicate water uptake by the film and resistance measurements indicate ion ingress into the film.

Figure T1/1 shows schematically, the typical shape of resistance/time and capacitance/time curves obtained for a 20 µm silicone modified polyester top coat on a 5 µm epoxy prime coat on a Zn/55%Al coated steel substrate immersed in 5% NaCl solution at room temperature. Values of resistance typically rise to a maximum value before declining sharply at times corresponding to the sharp rise in capacitance. Walter[15] initially thought that the rise in resistance to a maximum could be due to formation of a somewhat protective corrosion product resulting from corrosion of the substrate. Later[9], in a comparison between the single frequency and wide frequency range tests, he concluded that the rise was not due to

initiation of substrate corrosion, which was clearly shown to be preceding prior to the rise. Touhsaent and Leidheiser[12] obtained somewhat differently shaped resistance/time and capacitance/time curves for polybutadiene coatings on steel in 3% sodium chloride solution. The initial high resistance dropped sharply and the initial low capacitance rose sharply over the first day of immersion. Subsequently the resistance decreased and the capacitance increased more slowly at a linear rate over a period of weeks, dependent on the coating thickness, until the final sharp decline in resistance and rise in capacitance, signifying general corrosion of the steel. They proposed that the initial, small fall in resistance and rise in capacitance was due to fissures or capillaries present as defects in the coating filling with salt solution whilst the linear decrease in resistance and increase in capacitance was due to gradual penetration of the polymer by water.

Although the single frequency impedance test allows performance comparisons to be made on painted metal samples having different characteristics, it can only supply limited information on the mechanisms of paint degradation. This is because single frequency impedance information cannot be interpreted in terms of individual components of an equivalent electrical circuit representing the painted metal/solution interface. The resistive or capacitive contributions of impedance at a single frequency cannot be thought of as the resistance or capacitance of the paint film because they are frequency dependent terms containing both paint film resistance and capacitance components and other components of the equivalent electrical circuit. The difficulties in determining the individual components of an equivalent electrical circuit from the resistive and capacitive contributions of impedance at a single frequency is illustrated by Walter[16] in the simple case of just two resistors and one capacitor. The situation is even more complicated for painted metals due to

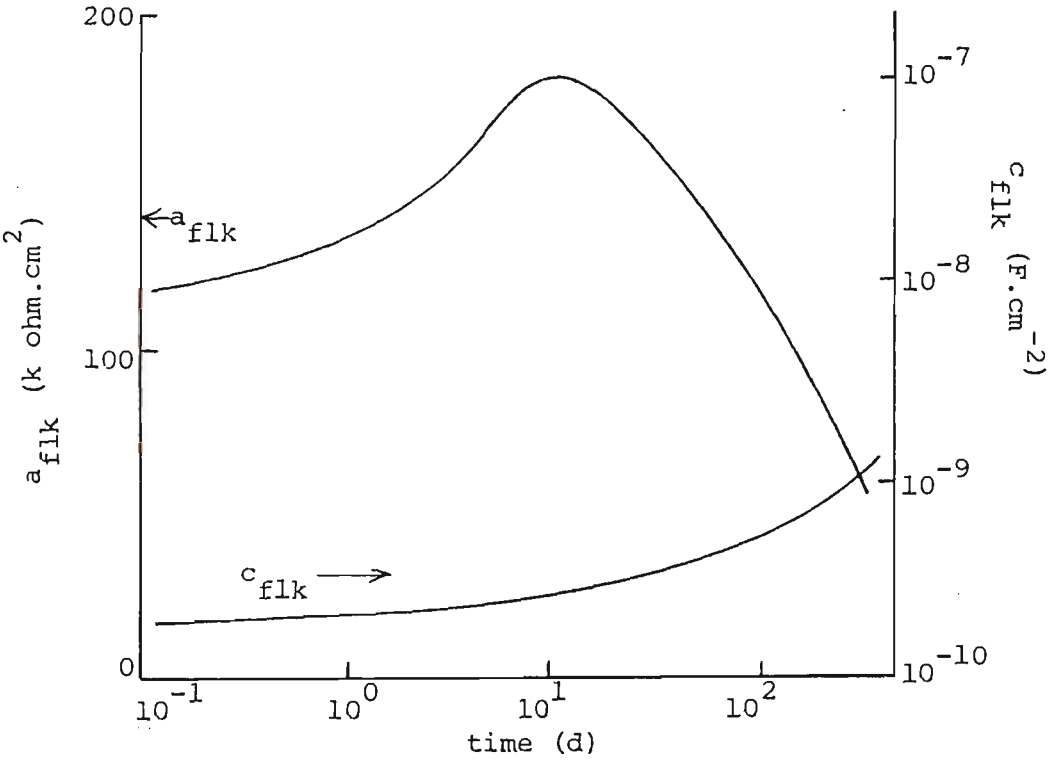

Figure T1/1. Typical shape of resistive, a_{flk}, and capacitive, c_{flk}, components of impedance versus immersion time in 5% NaCl solution at room temperature for a 20 µm silicone modified polyester top coat on a 5 µm epoxy primer on a ZINCALUME substrate.

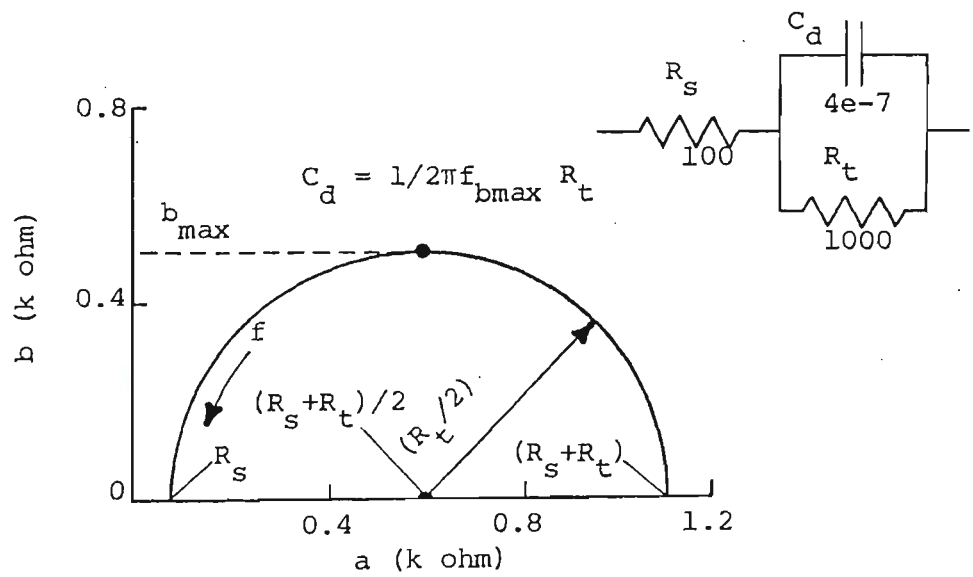

Figure T1/2. Nyquist complex plane plot of resistive, a, versus reactive, b, components of impedance for the equivalent circuit model indicated, and representing the metal/solution interface. R_s solution resistance; R_t charge-transfer resistance; C_d double-layer capacitance.

the inclusion of extra components in the equivalent electrical circuit.

The single frequency impedance test must therefore be empirically correlated with other measurements, such as visual observations of paint blistering or gravimetric water uptake measurements, in order to obtain mechanistic information on painted metal degradation. However, it is a useful method due to its simplicity and speed. It is, like the wide frequency range method, a relatively non-destructive test which can be repeated any number of times on the same sample to build up an immersion time history suitable for comparison with other samples. Sample deterioration can be detected at an earlier stage than visual observations, and give a clearer quantitative picture, considered[14] to be important advantages of the technique.

Additionally, the experimenter can always fall back on the single frequency method when the wide frequency range impedance method produces results that are too complex to interpret. The criterion of paint failure can easily be determined as the immersion time taken for the sample to produce a selected value of capacitance or resistance, a method which is free from the personal errors associated with visual observations, as pointed out by Wormwell and Brasher[6].

3. Wide frequency range impedance test

The wide frequency range method may overcome the problems of interpreting impedance suffered by the single frequency method because under the more ideal situations, individual component values of an equivalent electrical circuit representing the working electrode/solution interface can be derived by several established techniques. These components, such as paint film

resistance and capacitance, alter their values with immersion time as aggressive solution uptake occurs within the paint film resulting in corrosion of the metal substrate. The method is applicable to both painted and unpainted metals. The relative changes in the values of these components over the immersion time history of the sample can supply valuable information on the mechanisms involved in degradation and corrosion of the sample. Like the simpler, single frequency test, the wide frequency range test is simple to perform and is relatively non-destructive compared to the aggressive solutions in which the samples are immersed. This is important because the impedance test must be repeated a number of times on the same sample in order to build up patterns of performance behaviour.

Analysis of wide frequency range impedance is commonly carried out graphically with the aid of Nyquist complex plane plots or Bode plots. The Nyquist plot graphs the resistive, a, versus the reactive, b, components of impedance, Z, whilst the Bode plot graphs the logarithm of the modulus of impedance, r, and the phase angle, θ, versus the logarithm of frequency, f. The aim of these graphical methods is not only to predict the model, eg an equivalent circuit representing the working electrode/solution interface, but also the values of the individual components of the model at a given exposure or immersion time. A review of impedance plot methods has been published[17] recently by the author. The predominant mode of impedance analysis used in this thesis is the Nyquist plot.

Impedance methods, both single frequency and wide frequency range, are not without their limitations, as discussed elsewhere[17]. Analysis of full frequency range impedance data only leads to corrosion resistance - corrosion rates are not normally obtained. Area corrections for the actual corroding area may be

necessary. Applications have up to recently been generally limited to full immersion conditions. Painted samples must be visibly defect free because the failure criterion of a low impedance will result from any small scratch or defect that exposes metal substrate to the solution. Considerable variability is normal with painted metals, and often the results have to be treated statistically. Visual rating methods for painted metals do not suffer this disadvantage because larger samples are selected and an average blister rating is obtained. The plot shape can be distorted at high frequencies by the effect of stray capacitance across both the cell and the measuring/control resistor[16]. Finally, full frequency range impedance data may be too difficult to interpret in terms of an equivalent electrical circuit, even an approximate one[17].

4. Applications to unpainted metals

The equivalent electrical circuit model for an unpainted metal/solution interface without diffusion control is given by the simple Randles[18] type model shown in Figure T1/2, along with its Nyquist complex plane plot. The series component, R_s, represents the solution resistance between the working electrode and the tip of the Luggin probe for a 3-electrode type cell, or the solution resistance between working and auxiliary electrodes for a 2-electrode type cell, refer Section E1.2/1. The parallel components R_t and C_d represent the charge-transfer resistance and double layer capacitance, respectively. The shape of the complex plane plot not only gives information on the type of model and its component values, but also indicates the type of control for reactions occurring at the metal/solution interface. In this instance, the major control is caused by charge-transfer. For a corroding metal in the absence of diffusion, this can be thought of as the corrosion resistance of the

metal. The minor control is caused by IR_s drop across the solution resistance R_s. The lack of a diffusion tail at low frequencies would indicate that diffusion of reactants to and products from the metal/solution interface is much faster than the process of charge-transfer, which is more likely to be the case for reactive metals in dilute acids, eg iron in 1N H_2SO_4.

The impedance, Z, of the circuit in Figure T1/2 is given by Equation (T1/1).

$$\begin{aligned} Z &= R_s + R_t\,(1/j\omega C_d)/(R_t + 1/j\omega C_d) \\ &= R_s + (1/R_t)/(1/R_t^2 + \omega^2 C_d^2) - j\omega C_d/(1/R_t^2 + \omega^2 C_d^2) \end{aligned} \qquad (T1/1)$$

which is of the form

$$Z = a - jb$$

where

$$a = R_s + (1/R_t)/(1/R_t^2 + \omega^2 C_d^2) \qquad (T1/2)$$

$$b = \omega C_d/(1/R_t^2 + \omega^2 C_d^2) \qquad (T1/3)$$

The term $(1/R_t^2 + \omega^2 C_d^2)$ can be eliminated from Equations (T1/2) and (T1/3) to give $\omega = b/(a-R_s)\,R_t C_d$ which can be substituted into Equation (T1/2) and rearranged to give Equation (T1/4).

$$(a - R_s - R_t/2)^2 + b^2 = (R_t/2)^2 \qquad (T1/4)$$

This is the equation of a circle of radius $R_t/2$ and centre $(R_s + R_t/2)$ and explains the shape of the Nyquist complex plane semicircle of Figure T1/2 which results from the parallel combination of R_t and C_d.

The component values of the circuit of Figure T1/2 can be determined from the Nyquist plot or the corresponding Bode plot[17]. The series resistor R_s offsets the Nyquist complex plane semicircle along the resistive, a, axis by an

amount equal to R_s, obtained by intersection of the high frequency, LHS portion of the semicircle with the a-axis. The intersection of the low frequency, RHS portion of the semicircle with the a-axis gives the value (R_s+R_t), and the semicircle diameter is R_t. The value of C_d can be found by at least two complex plane plot methods. From Figure T1/2, C_d can be determined from the frequency, f_{bmax}, at which the reactive component, b, reaches a maximum value, b_{max}, and is given by $C_d = 1/2\pi f_{bmax} R_t$. However, it is not always possible to determine f_{bmax} accurately from a complex plane plot because the spacing of frequencies along the curve is non-linear, making interpolation between frequency points difficult. The effects of diffusion are discussed in Section T1/5.

5. Applications to painted metals

5.1 Equivalent electrical circuit model

An equivalent circuit model for the painted metal/solution interface requires inclusion of paint film parameters to the model of Figure T1/2. Mikhailovskii and co-workers[19] have proposed a model similar to that in Figure T1/3, which has since been used by other workers[20-23] or modified for the effects of Warburg diffusion impedance[16,22-24].

The resistor, R_{pf}, has been interpreted as the pore resistance due to electrolyte penetration[19,23] and at damaged areas of the film[19], or as areas where more rapid solution uptake occurs, namely, pre-existing holes or porous areas where inadequate cross-linking of the polymer is present[16]. A capacitor in parallel with R_{pf} and representing the capacitance of these areas is omitted in this simplified model. Corrosion of the substrate is assumed to occur via

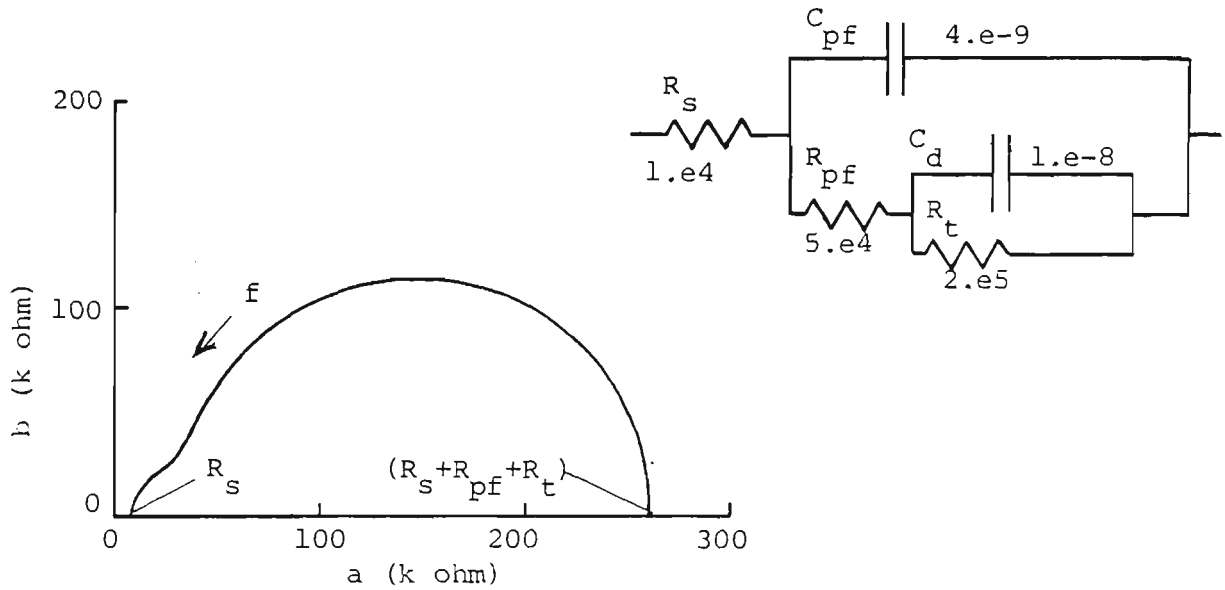

Figure T1/3. Equivalent circuit model for the painted metal/solution interface and corresponding Nyquist plot of resistive, a, versus reactive, b, components of impedance. R_s solution resistance, R_{pf},C_{pf} paint film resistance, capacitance, R_t,C_d metal charge-transfer resistance, double layer capacitance.

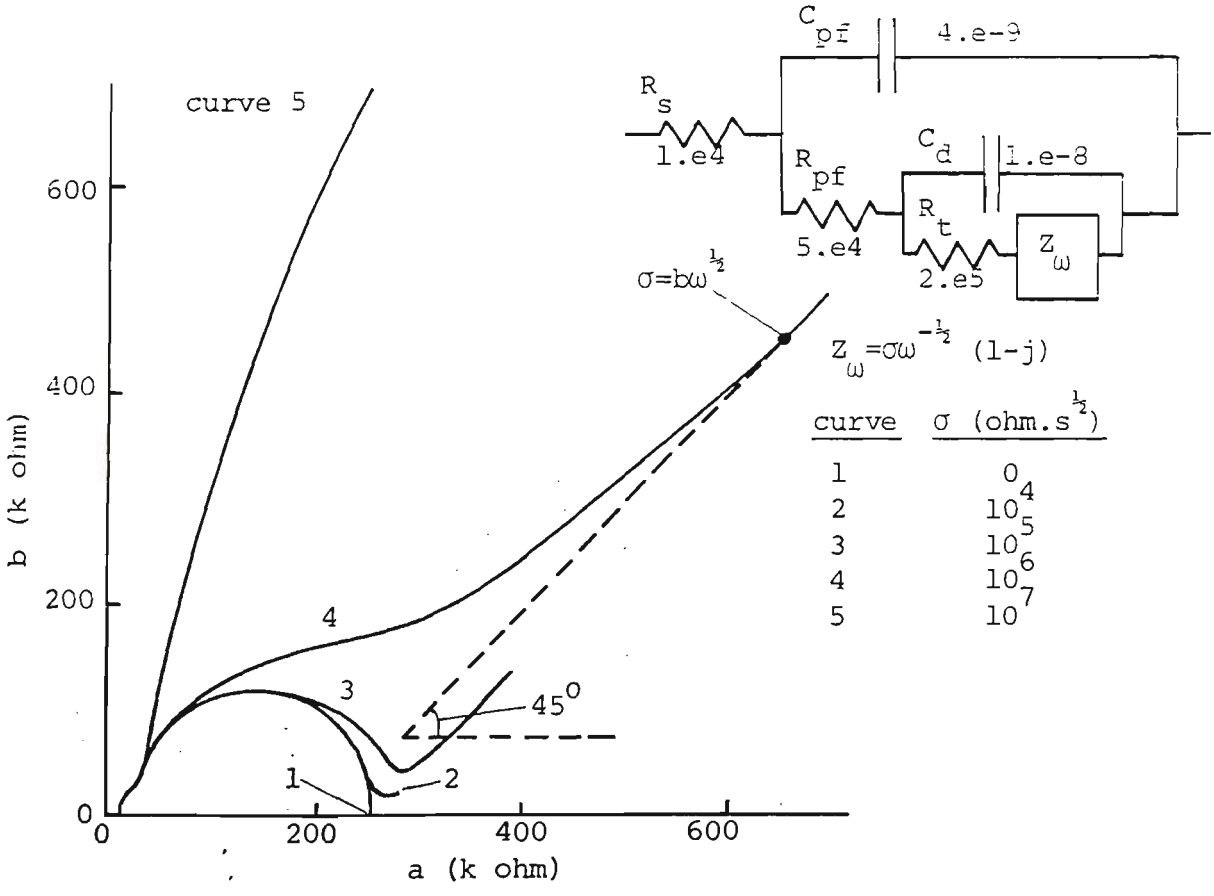

Figure T1/4. Equivalent circuit model identical to that above except for inclusion of Warburg diffusion impedance, Z_ω, and corresponding Nyquist complex plane plot. Symbols as per Fig. T1/3.

these areas, represented by the parallel combination of double layer capacitance, C_d, and charge-transfer resistance, R_t. The capacitor, C_{pf}, has been interpreted as the capacitance of the electric capacitor consisting of the metal and the electrolyte, with the paint film as dielectric[19]; or simply as the capacitance of the intact film[23], or as the capacitance of areas where rapid solution uptake does not occur[16]. A resistor in parallel with C_{pf}, representing the resistance of these latter areas, is omitted in this simplified model. Corrosion of the substrate is assumed to occur by the same mechanisms that occur on the unpainted substrate, but the kinetics will be restricted by the presence of the paint film. The interpretation taken for this thesis has been described previously in the literature[16].

The Nyquist complex plane plot in this case is made up of two semicircles with time constants (with units in seconds) for the paint film, τ_{pf}, and metal, τ_m, as given by Equation (T1/5)

$$\tau_{pf} = R_{pf}C_{pf}; \quad \tau_m = R_t C_d \qquad (T1/5)$$

The semicircle occurring at high frequencies will be caused by the paint film if $\tau_{pf}<\tau_m$, which is usually taken to be the case, although direct evidence has not been cited in the literature. The discussion in Sections R2.1/7 and R2.2/1.2 provides evidence that this interpretation is in fact correct. The shape of the plot will appear as two distinct semicircles if certain criteria[16] are met. Figure T1/3 is an example of indistinct separation into two semicircles where one of the criteria is not met. This subject has been discussed at length in the literature[17].

5.2 Inclusion of diffusion impedance

In many cases the equivalent circuit of Figure T1/2 for unpainted metals, or Figure T1/3 for painted metals will not be adequate as a model for the working electrode/solution interface. One modification takes into account diffusion processes - diffusion of reactants to and products from the interface. In the case of painted metals, diffusion processes occur within the paint film, presumably at areas of more rapid solution uptake, equivalent to R_{pf} in Figure T1/3. Diffusion is modelled by the inclusion of a Warburg impedance, Z_ω, placed in series with R_t in Figure T1/3, where Z_ω is defined by Equation (T1/6).

$$Z_\omega = \sigma\omega^{-1/2}(1-j) \qquad \text{(T1/6)}$$

where σ = Warburg impedance coefficient (ohm.$s^{1/2}$)

$\omega = 2\pi f$ (rad.s^{-1})

Figure T1/4 is identical to Figure T1/3 except for the inclusion of Z_ω and is a Nyquist complex plane plot for a painted metal/solution interface showing degradation of the paint film and corrosion of the substrate with diffusion, assumed to occur at areas of more rapid solution uptake, designated by resistor R_{pf}. Values of the Warburg coefficient, σ, vary from 0 to 10^7 ohm.$s^{1/2}$ in Figure T1/4. The Nyquist plot of curve 1 at σ=0 is identical to Figure T1/3, but at higher σ values (curve 2), a diffusion tail begins to appear at low frequencies attached to the second semicircle. When values of σ are about equal to R_t, this diffusion tail begins to overlap the second semicircle (curve 3) and subtends an angle of 45° to the a-axis in accord with Equation (T1/6). As σ increases still further (curve 4), this overlap becomes increasingly more severe, but the diffusion tail eventually becomes inclined at an angle of 45° to

the a-axis at sufficiently low frequencies. Finally, when σ is significantly greater than R_t (indicating that diffusion processes are occurring slower than the metal charge-transfer reaction), the diffusion tail completely distorts the semicircular shape (curve 5), being initially greater than 45° to the a-axis. This angle decreases as the frequency is lowered, eventually becoming 45° at much lower frequencies, not shown in Figure T1/4. The plot shapes in Figure T1/4 have been observed in experimental Nyquist plots on painted metals[14,16].

However, the appearance of diffusion tails which bend over towards the a-axis at low frequencies have been noted in the literature[14,16,25] and cannot be explained by Equation (T1/6). This equation assumes that the ac diffusion layer is much smaller than the dc Nernstian diffusion layer, but when both ac and dc diffusion layer thicknesses become comparable, a correction must be applied which accounts for both an increase above the 45° diffusion tail and finally a bending downwards towards the a-axis at very low frequency[4,16,17,25]. Under these circumstances, Equation (T1/6) is modified[16,25] to Equation (T1/7).

$$Z_\omega = \sigma\omega^{-1/2}(1-j)\tanh(\delta(j\omega/D)^{1/2}) \qquad \text{(T1/7)}$$

where δ = diffusion layer thickness (cm)

D = diffusion coefficient ($cm^2.s^{-1}$)

Depending on numerical values of $(\delta/D^{1/2})$, the tanh term can approximate to unity ($\delta/D^{1/2}>5$) at a frequency of 0.1 Hz, in which case Equation (T1/7) reverts to Equation (T1/6); or the tanh term can become increasingly significant as $(\delta/D^{1/2})$ decreases below 5. In this case, the 45° diffusion tail bends over towards the a-axis at low frequencies, and can give the appearance of a

skewed semicircle[16].

Values of σ and hence Z_ω (as well as C_d) can be calculated from any point on the equation for the 45° diffusion tail. This equation is derived from the full equation for the impedance of the painted metal equivalent circuit in Figure T1/4. For the case when frequencies are low enough to result in a straight line diffusion tail at 45°, the terms containing $\omega^{-1/2}$ are retained, but not terms containing ω to obtain Equation (T1/8).

$$Z = (R_s+R_{pf}+R_t+\sigma\omega^{-1/2}) + j(\sigma\omega^{-1/2}+2\sigma^2C_d) \quad \text{(T1/8)}$$

where $$a = R_s + R_{pf} + R_t + \sigma\omega^{-1/2} \quad \text{(T1/9)}$$

$$b = \sigma\omega^{-1/2} + 2\sigma^2 C_d \quad \text{(T1/10)}$$

The term containing $\omega^{-1/2}$ can be eliminated from the a and b values to give Equation (T1/11), the equation for the 45° diffusion tail.

$$b = a - R_s - R_{pf} - R_t + 2\sigma^2C_d \quad \text{(T1/11)}$$

According to this equation, a plot of b versus a is a straight line of slope = 1 (45° diffusion tails), and intercept on the a-axis of $(R_s+R_{pf}+R_t-2\sigma^2C_d)$. The value of σ can be calculated from this intercept[1], having previously calculated values of R_s, R_{pf}, R_t and C_d. This method compounds all the errors of these variables.

Walter[17] has indicated that Equation (T1/12) can be used to obtain estimates of σ.

$$b = \sigma\omega^{-1/2} \quad \text{(T1/12)}$$

This equation is approximate only, as it ignores the term $2\sigma^2 C_d$ in Equation (T1/10). This assumption can sometimes be justified, as discussed in Section R1.5/1. However, a better method is simply to take two data points (a_1,b_1), (a_2,b_2) at angular frequencies ω_1, ω_2 respectively, and calculate σ from either Equations (T1/9) or (T1/10) by subtraction of unwanted terms. This results in two new equations, Equations (T1/13) or (T1/14).

$$a_1 - a_2 = \sigma(\omega_1^{-1/2} - \omega_2^{-1/2}) \qquad (T1/13)$$

$$b_1 - b_2 = \sigma(\omega_1^{-1/2} - \omega_2^{-1/2}) \qquad (T1/14)$$

The right hand side of Equations (T1/13,14) are identical and therefore both these equations will give identical results for σ when the diffusion tail is inclined at 45°. However, as indicated in Section R1.5/2, the angle of the diffusion tail to the a-axis is not always 45°. For example, the diffusion tail may not only be governed by a bending over towards the a-axis at low frequencies according to Equation (T1/7). One additional cause of angles less than 45° for the diffusion tail is corrosion product resistance, R_{cp}, discussed in Section R1.8. In these cases, it is probably better to calculate σ from both Equations (T1/13,14) and to average the result. This is the basis of a computer program 'sigma' used to calculate σ values in Section R1.5/3 and described in Section A1/4.6.

5.3 Depressed Nyquist semicircles

It is frequently observed that Nyquist complex plane plots have semicircles with their centres depressed below the a-axis. This phenomenon, referred to as frequency dispersion, has been explained in a number of different ways[17] which take into account factors such as metal substrate surface roughness,

paint film heterogeneity, high resistance surface films, electrode geometry and variations in substrate/paint adhesion. The effects of frequency dispersion appear to decrease with increasing electrolyte concentration, being usually less than a few per cent in 1M solutions, but quite significant in 0.1M[4].

Nyquist plots showing frequency dispersion can be analyzed either by using the same equivalent circuit model, or a modified model. Using the same model, see Section A3/1, R_t can be calculated as the chord of the semicircle instead of the depressed diameter. This has been done using either a curve fitting routine[26] or by the modified tangential impedance technique[27]. Rammelt et al[28] modified the model by introducing frequency dependent resistors and capacitors to represent the frequency dispersion, although Cahan and Chen[29] consider this practice invalid.

5.4 Sample failure criteria

It is convenient to obtain a quantitative assessment of sample failure from impedance measurements. In the single frequency test, Walter[9] used two failure criteria based on the times, $t_{f,R}$ and $t_{f,C}$, taken for the resistive and capacitive components of impedance at a frequency of 1 kHz to fall, rise to 10 k ohm.cm^2 and 3 x 10^{-8} F.cm^{-2}, respectively. These values of impedance empirically correlated with either the initiation of blistering or obvious paint blistering and corrosion product formation for the particular samples used. In this thesis (Table R2/1 Section R2.2/1.1 and Section R2.2/3.1) the values of $t_{f,R}$ and $t_{f,C}$ were taken as the times for the resistive, a_{f1k}, and capacitive, c_{f1k}, components of impedance at a frequency of 1 kHz to fall, rise to 10^4 ohm.cm^2 and 10^{-8} F.cm^{-2}, respectively. A third failure criterion was used - an average failure time, $\overline{t_f}$, equal to the average of $t_{f,R}$ and $t_{f,C}$ according to

Equation (T1/15).

$$t_f = (t_{f,R} + t_{f,C})/2 \qquad (T1/15)$$

There does not appear to be any reference in the literature to failure criteria for the wide frequency range test. This is introduced in Sections R2.2/1.2,3.2.

6. Cell impedance corrections for identical working/auxiliary electrodes

In full immersion impedance experiments, a platinum mesh auxiliary electrode is used, Section E1.2/1.1, which has a low impedance compared with eg, a painted working electrode. The cell impedance in this case is essentially the impedance of the working electrode. This is not, however, the situation with impedance measurements on 3-electrode ACMs, Section E1.2/2, where the cell impedance consists of identical working and auxiliary plates (the reference plates are left unconnected). The measured impedance (R_t, C_d, Z_ω, etc) in this case relates to both working and auxiliary plates and a correction must be applied to obtain the impedance of just the working electrode. This situation was pointed out by Wormwell and Brasher[6] for two identical painted steel samples in artificial sea water. They considered that $R=R_m/2$, $C = 2C_m$ where R, C represent resistance, capacitance of one electrode and R_m, C_m represent measured resistance, capacitance respectively. The relationships were assumed correct if the solution resistance between electrodes was negligible and breakdown of the electrodes was equal.

A similar result applies to measured impedance on ACMs as given by Equations (T1/16-19). These equations are derived in Section A3/2 for n identical working and auxiliary plates having total areas A_W, A_A respectively.

$$R_t = R_t^m A_W/2 \quad (T1/16)$$
$$(ohm.cm^2) \quad (ohm)(cm^2)$$

$$C_d = 2C_d^m/A_W \quad (T1/17)$$
$$(F.cm^{-2}) \quad (F)\ (cm^2)$$

$$\sigma = \sigma^m A_W/2 \quad (T1/18)$$
$$(ohm.cm^2.s^{1/2}) = (ohm.s^{1/2})(cm^2)$$

$$R_s = R_s^m A_W \quad (T1/19)$$
$$(ohm.cm^2) \quad (ohm)(cm^2)$$

where m refers to measured cell value and R_t, C_d, σ refer to charge-transfer resistance, double layer capacitance, diffusion coefficient of the working electrode, respectively.

Equations (T1/16-19) have been applied to all ACM impedance calculations in Sections T1/7, R1.5 and R1.7.

7. Mass loss calculations from R_t

The method of calculating mass loss, ΔM_{Rt}, from charge-transfer resistance, R_t, is essentially the same as described in Section T3/7 for mass loss calculations from R_p, and is given by Equation (T1/20).

$$\Delta M_{Rt} = Eq.(B/2.303) \int^{tdry} (1/R_t).dt \quad (T1/20)$$
$$(g) \quad (coulomb.g.equiv)^{-1}\ (V)\ (ohm^{-1})$$

where Eq. = electrochemical equivalent ($coul.g.equiv^{-1}$)

$B = [1/b_a + 1/b_c]^{-1}$ = mixed Tafel slope constant

The main difference between the R_p and R_t methods is the fact that the measured values of R_p relate to the working plates of the ACMs, whereas the measured values of R_t relate to both the working and auxiliary plates of the ACMs, and a correction is necessary. This has been discussed at length in Section A3/2, where the measured values, R_t^m, were corrected to R_t for the working electrode only using Equation (T1/16). Substituting Equation (T1/16) into Equation (T1/20) gives Equation (T1/21).

$$\Delta M_{Rt} = \text{Eq. } (2/A_W)(B/2.303) \int^{tdry} (1/R_t^m).dt \qquad \text{(T1/21)}$$

$$(g.m^{-2})\ (coul.g.equiv^{-1})\ (m^{-2})\ (V)\ (ohm^{-1})$$

Note that the working electrode area, A_W, is in units of m^2.

Equation (T1/21) has been applied to calculate mass loss of ACMs from R_t/time trends in Section R1.5/3. Refer also to Sections R1.7/1,4.

1. Definition

A potential difference usually exists between two dissimilar metals or alloys when they are immersed in a conductive solution. If these metals are placed in contact (or otherwise electrically connected), this potential difference produces electron flow between them, called the galvanic current, I_g. Corrosion of the less corrosion resistant metal (more active) is usually increased while that of the more resistant (more noble) metal is decreased, compared with the behaviour of these metals prior to contact. The more active metal becomes anodic and the more noble metal becomes cathodic. Usually, but not always, the cathodic metal corrodes very little or not at all in this type of couple. The driving force for galvanic current flow is the potential difference developed between the two dissimilar metals prior to being connected.

Dissimilar metal couples can exist as a result of mechanical, economic reasons; as a result of poor design or they can be deliberately designed into a system. An example of the latter is galvanized steel sheet in which zinc will protect the steel substrate by acting as a barrier coating. However, at any spots where the steel substrate is exposed (sheared edges, scratches, pinholes), to an aggressive environment, the steel will be sacrificially protected by the surrounding zinc. Zinc becomes anode of the dissimilar metal couple and corrodes at a faster rate, whilst the exposed steel becomes cathode and corrodes at a slower rate.

2. Electrochemical principles

Fontana and Greene[30] applied the mixed potential theory of Wagner and

Traud[31] to galvanically coupled, corroding metals. They considered the effect of galvanically coupling zinc to platinum in an air-free acid solution, where only the zinc corroded, and the more general situation where two dissimilar metals in contact both corroded by activation controlled cathodic hydrogen ion reduction. They made use of Evans (E/log I) diagrams to show how corrosion of the more active metal increased on coupling to the more noble metal. Figure T2/1 is an Evans diagram of E versus log I for two coupled, corroding dissimilar metals (A is more active and corrodes faster than B) where activation controlled hydrogen ion reduction occurs on both metals at different rates determined by the difference in exchange currents, $I^{A}_{o,H}$ and $I^{B}_{o,H}$. The normal uncoupled corrosion rates of metals A and B are I^{A}_{k} and I^{B}_{k} at respective corrosion potentials E^{A}_{k} and E^{B}_{k}. The galvanic potential, Eg of the couple lies between E^{A}_{k} and E^{B}_{k} at the intersection of the two dashed lines representing the total oxidation and total reduction rate, equivalent to I_t according to Equation (T2/1).

$$[I_t]_{Eg} = [I^{A}_{a}]_{Eg} + [I^{B}_{a}]_{Eg} = | [I^{A}_{c}]_{Eg} + [I^{B}_{c}] |_{Eg} \qquad (T2/1)$$

At Eg, the dissolution rate, I^{A}_{a}, of metal A is greater than the uncoupled corrosion rate, I^{A}_{k}, but the dissolution rate, I^{B}_{a}, of metal B is less than the uncoupled corrosion rate, I^{B}_{k}. The galvanic current, I_g is defined by Equation (T2/2).

$$I_g = [I^{A}_{a}]_{Eg} - [I^{A}_{c}]_{Eg} = | [I^{B}_{c}]_{Eg} - [I^{B}_{a}] |_{Eg} \qquad (T2/2)$$

Mansfeld[32,33] has done much to put galvanic corrosion theory on a quantitative basis, and has shown that the magnitude of galvanic corrosion depends not only on the potential difference between dissimilar metals prior to

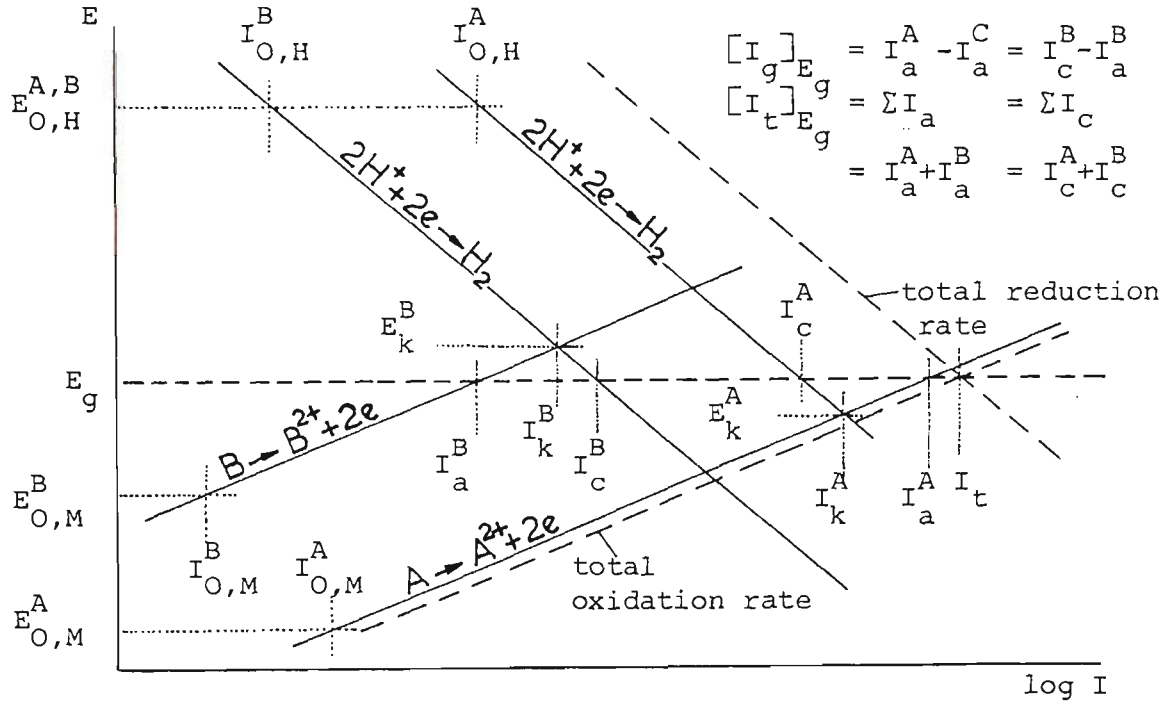

Figure T2/1. Evans diagram for 2 coupled dissimilar metals A and B both corroding by activation controlled hydrogen ion reduction. E_k, I_k corrosion potential, current of uncoupled metal; E_g, I_g galvanic potential, current of couple; I_a, I_c anodic, cathodic partial currents; I_t total dissolution current; $E_{o,M}$, $I_{o,M}$ metal equilibrium potential, exchange current; $E_{o,H}$, $I_{o,H}$ hydrogen ion equilibrium potential, exchange current.

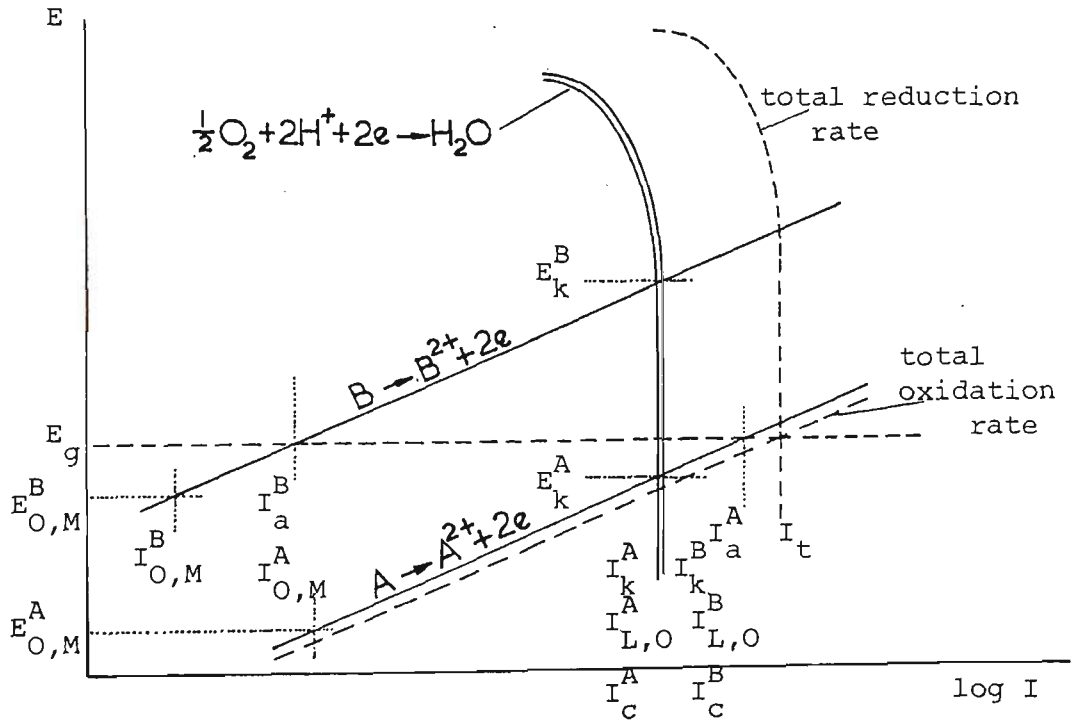

Figure T2/2. Evans diagram for 2 coupled dissimilar metals A and B both corroding by diffusion controlled reduction of oxygen. Symbols as per Figure T2/1.

contact, but also on kinetic parameters such as corrosion rates, exchange currents, Tafel slopes and area ratios[34].

The case of galvanic corrosion under diffusion control of the cathodic reaction, where it is assumed that the only reaction occurring on the cathode at the galvanic potential, Eg, is the reduction of oxygen, is relevant to this thesis. Theoretical considerations for this case have been detailed by Mansfeld and Kenkel[34,35]. Figure T2/2 is an Evans diagram for two coupled dissimilar metals (A is more active than B) where it is assumed that the only reaction occurring on the cathode B at Eg is the reduction of oxygen, that is, $[I_a^B]_{Eg}$ is negligible compared to $[I_a^A]_{Eg}$. In the uncoupled state, A and B are assumed to have corrosion potentials, E_k^A, E_k^B and corrosion rates I_k^A, I_k^B, equivalent to the limiting currents, $I_{L,O}^A$, $I_{L,O}^B$, respectively. The galvanic potential, Eg, of the couple lies between E_k^A and E_k^B at the intersection of the two dashed lines representing the total oxidation and total reduction rate, also given by Equation (T2/1) except that $[I_a^B]_{Eg}$ is negligible. At Eg, the dissolution rate, I_a^A, of metal A is greater than I_k^A, but the dissolution rate, I_a^B, of metal B, is less than I_k^B. Galvanic current, Ig, is also given by Equation (T2/2) except that $[I_a^B]_{Eg}$ is negligible. Equation (T2/2) can be written in this case in terms of current densities, and areas A^A, A^B of anode and cathode respectively, according to Equation (T2/3).

$$i_g^A A^A = i_a^A A^A - i_c^A A^A = i_c^B A^B \qquad \text{(T2/3)}$$

Assuming that Eg is in the region where the cathodic reaction on both metals is entirely diffusion controlled, as is shown in Figure T2/2, then $i_c^A = i_c^B = i_{L,O}$. Combining with Equation (T2/3) leads to Equation (T2/4).

$$i_g^A = i_a^A - i_{L,O} = i_{L,O}(A^B/A^A) \qquad (T2/4)$$

But, for diffusion control $i_{L,O} = i_k^A$, and therefore it follows that

$$i_g^A = i_a^A - i_k^A = i_k^A(A^B/A^A) \qquad (T2/5)$$

or $$i_a^A = i_k^A + i_g^A$$

According to Equation (T2/5), the galvanic current density, i_g^A, is the difference between the anodic dissolution current density, i_a^A, due to galvanic coupling and the normal uncoupled corrosion current density, i_k^A. Alternatively, the anodic dissolution current density, i_a^A, is the sum of the uncoupled corrosion current density, i_k^A, and the galvanic current density, i_g^A, at metal A. It should also be noted from Equation (T2/5) for the special case where the area of anode and cathode are equal, ie $A^A = A^B$, then $i_g^A = i_k^A$. Under these conditions the galvanic current can be used to directly calculate the corrosion rate of the uncoupled metal A despite the fact that metal A is coupled to metal B in the galvanic couple[36]. Use is made of this fact and Equation (T2/5) in Section T2/4.

Equation (T2/4) can be rearranged to give Equation (T2/6).

$$i_a^A = i_{L,O}(1 + A^B/A^A) \qquad (T2/6)$$

This is the catchment area principle originally proposed by Whitman and Russell[37], according to which the dissolution current density of the anode in a galvanic couple is proportional to the area ratio, A^B/A^A, of cathode/anode[34].

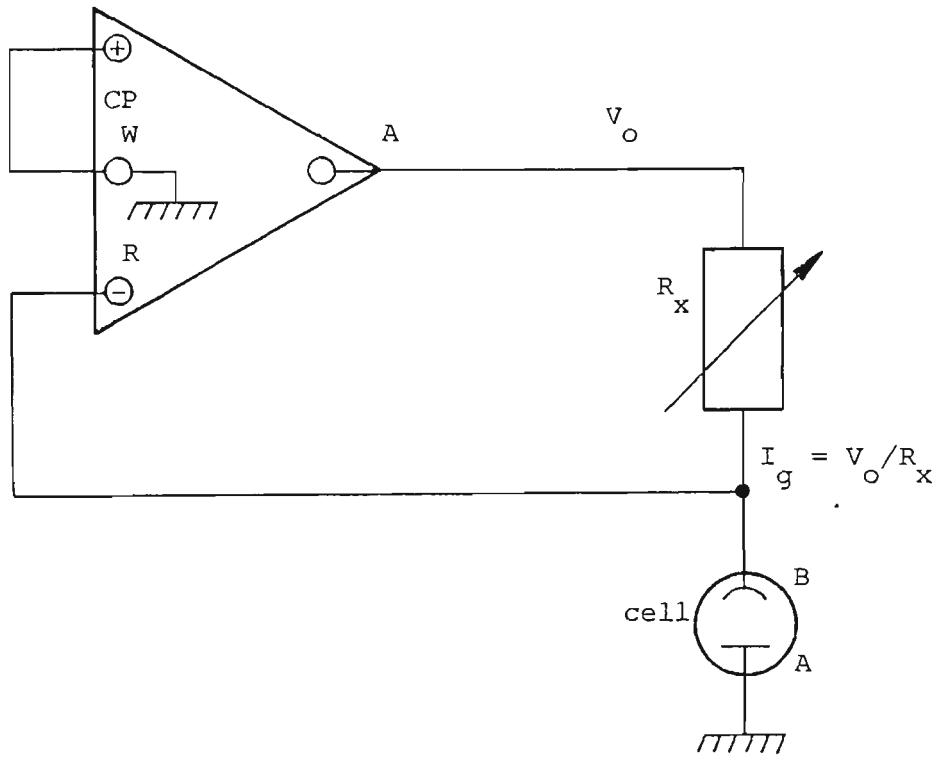

Figure T2/3. Schematic for either a potentiostat or an operational emplifier wired as a zero resistance ammeter for the measurement of galvanic current, I_g. W, R, A working, reference, auxiliary inputs of potentiostat or earth, inverting input and output of operational amplifier. CP control potential input of potentiostat (CP=0) or non-inverting input of operational amplifier; R_x current sensing resistor; cell A, B dissimilar metals of galvanic cell.

3. Measurement of galvanic current

The method of using a potentiostat for measurement of galvanic corrosion currents was first described by Devay, Lenyel and Meszaros[38]. This was followed in 1970 by an article by Lauer and Mansfeld[39]. Figure T2/3 applies equally to a potentiostat or an operational amplifier[40]. The two metals, A and B, of the galvanic cell are connected directly across the differential input of the inverting operational amplifier or between the reference, R, and working, W, electrode inputs of the potentiostat with the control potential, CP, set to zero. Under these conditions, the inverting input of the operational amplifier (or R input of the potentiostat) is at virtual earth (zero volts), and the output voltage, V_o, of the operational amplifier (or the auxiliary, A, input of the potentiostat) is related to the galvanic current, Ig, flow by Equation (T2/7), where R_x is the current measuring resistor. Operating a potentiostat or operational amplifier in this manner is equivalent to a zero resistance ammeter, ZRA.

$$I_g = V_o/R_x \qquad \text{(T2/7)}$$

4. Mass loss calculations from Ig

The method of calculating mass loss, ΔM_{Ig}, from galvanic current, Ig, is essentially the area under the Ig/time curve multiplied by an electrochemical equivalent, Eq, and divided by the exposed cathode area. This is based on the following derivation. Rearranging Equation (T2/5) in Section T2/2 gives Equation (T2/8).

$$i_k^A = i_g^A A^A/A^B \qquad \text{where } i_k^A = I_k^A/A^A;\ i_g^A = I_g^A/A^A$$

$$\text{or} \quad I_k^A = I_g^A A^A/A^B$$

$$\text{Now } \Delta M_{Ig} = Eq \int I_k^A \, dt \quad (g)$$

$$\therefore \quad \Delta M_{Ig}/A^A = (Eq/A^B) \int_o^{tdry} I_g^A \, dt \quad (g.m^{-2}) \qquad \text{(T2/8)}$$

This equation has been applied in Section R1.4/1 to determine mass loss calculated from Ig/time curves obtained from pollution gas box experiments using atmospheric corrosion monitor, ACM, cells. Values taken for Eq for the various ACMs are discussed in Sections R1.4/1, T3/7. The assumptions made for Equation (T2/5) in Section T2/2 will also apply to the calculated values of ΔM_{Ig}.

1. History

In 1938, Wagner and Traud[31] formulated the concept of mixed potential theory which explained corrosion reactions occurring at the metal/solution interface as composed of partial reactions for the anodic dissolution of the metal and the reduction of cathodic reactants. Bonhoeffer and Jena[41] in 1951 introduced the concept of polarization resistance, defined as the slope of the polarization curve at the corrosion potential. They demonstrated that corrosion rate decreased as polarization resistance increased, for a series of 11 steels in sulphuric acid solution. In 1957, Stern and Geary[42] derived an equation relating the slope of the linear region of the polarization curve to the corrosion rate and Tafel slopes. This equation was based on the kinetics of electrochemical reactions and the concept of mixed potential theory as proposed by Wagner and Traud[31]. Stern and Geary pointed out that since measurements were carried out close to the corrosion potential, any surface changes which may result from high polarizations are eliminated. Stern and Weisert[43] commented that corrosion rates could be estimated to within a factor of two without knowledge of Tafel slope values by a simple measurement of the current required to polarize a few millivolts, that is, by knowledge of the polarization resistance. An excellent review by Mansfeld[44] exists on the historical development of the polarization resistance technique.

Developments have been made to the technique since the early papers described above. Hoar[45] commented that polarization resistance measurements were superfluous to the electrical determination of corrosion rates because Tafel slopes are required to convert polarization resistance to corrosion rate. If these are derived from the Tafel region of polarization curves, then back-extrapolation to the corrosion potential can yield corrosion

current, making it unnecessary to convert polarization resistance. To overcome this criticism, more recent research has been concerned with determination of Tafel slopes from low polarization data, such as the two- and three-point methods of Barnartt[46], the graphical curve fitting method of Mansfeld[47,48] and the method of Reeve and Bech-Nielsen[49]. The Tafel slope constants have also been determined by Makrides[50] as a lumped constant by calibration using mass loss data. In the last few years, iterative curve-fitting methods using a computer have taken over from these simpler methods, and determine corrosion current and Tafel slopes from low polarization data. These methods are discussed further in Section T3/5. Such methods, referred to in this thesis as corrosion current methods, make the determination of polarization resistance superfluous, as corrosion current can be derived from the general current/voltage equation, Equation (T3/1), in Section T3/2, without knowledge of polarization resistance. Other developments of the polarization resistance technique are discussed in Section T3/5.

2. Definitions

According to the mixed potential theory of Wagner and Traud[31], the polarization curve relationship between current and voltage for a metal corroding by charge-transfer control of both the anodic and cathodic reactions is given by Equation (T3/1).

$$I = I_k[\exp(2.3\epsilon/b_{a,M}) - \exp(-2.3\epsilon/b_{c,X})] \qquad (T3/1)$$

where I is current; I_k is corrosion current; ϵ ($=E-E_k$) is polarization value or voltage; $b_{a,M}$ is the Tafel slope for anodic dissolution of the metal; $b_{c,X}$ is the Tafel slope for the cathodic reduction reaction involving reactant X, a

common example being the evolution of hydrogen from hydrogen ions; E is potential at current, I; E_k is corrosion potential. In the derivation of Equation (T3/1), the corrosion potential is assumed to be far removed from the equilibrium potentials of the anodic and cathodic reactions. In the example given, these are the metal equilibrium potential, $E_{o,M}$, and the X-reaction equilibrium potential, $E_{o,X}$, eg the hydrogen equilibrium potential, $E_{o,H}$.

Differentiating Equation (T3/1) with respect to ε gives the slope ($dI/d\varepsilon$) of the polarization curve at any value of ε. The slope of the polarization curve of I versus ε at the corrosion potential is the slope $(dI/d\varepsilon)_{\varepsilon\to 0}$. The inverse of this slope, that is, the slope of the polarization curve of ε versus I, defines polarization resistance, R_p, and its relationship to I_k according to Equation (T3/2), which has become known as the Stern-Geary equation[42].

$$(d\varepsilon/dI)_{\varepsilon\to 0} = R_p = B/2.3I_k \qquad (T3/2)$$

where $B = [1/b_{a,M} + 1/b_{c,X}]^{-1}$ and is a constant containing Tafel slope information, sometimes referred to as the lumped, or mixed, Tafel slope constant.

The polarization curve of ε versus I, and its slope $(d\varepsilon dI)_{\varepsilon\to 0} = R_p$ are shown in Figure T3/1a where only small polarizations, ε, are shown. Data obtained for such plots are referred to as low polarization data. The polarization curve is also shown plotted in the Evans diagram form of E versus log I in Figure T3/1b where currents extend to higher polarizations. The partial reaction lines for anodic dissolution of the metal and reduction of the cathodic reactant, X, (in this case hydrogen ions) are shown dotted. The slope of these lines are the Tafel slopes $b_{a,M}$ and $b_{c,X}$ respectively. Back-extrapolation of the slopes

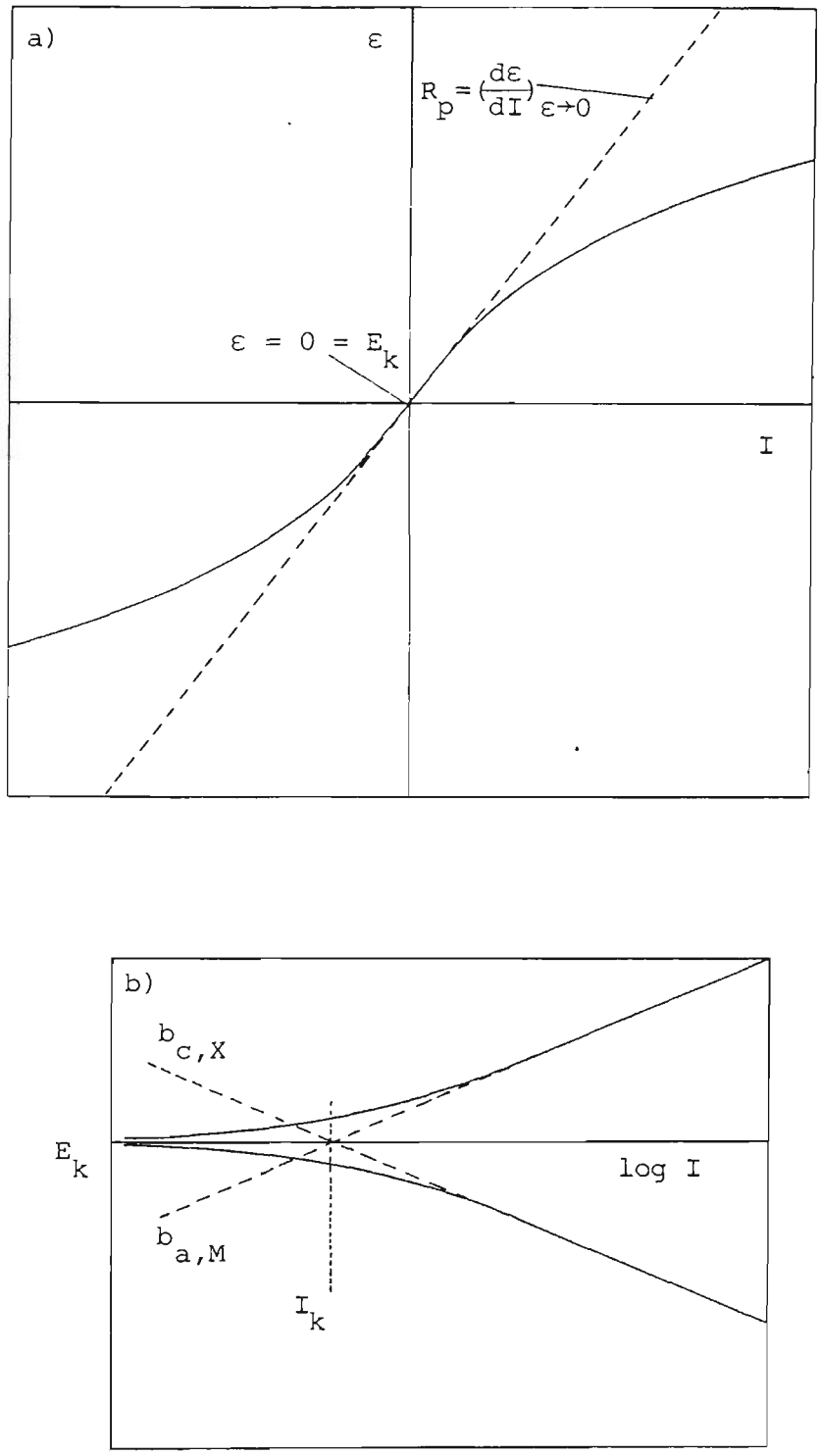

Figure T3/1. Polarization curve of polarization $\varepsilon(=E-E_k)$, versus applied current, I, (Fig. T3/1a), and the corresponding Evans diagram form of ε versus log I (Fig. T3/1b) for the case of charge-transfer control of both anodic and cathodic reactions. Back extrapolation of Tafel slopes $b_{a,M}$ or $b_{c,X}$ to the corrosion potential, E_k, yield a value for corrosion current, I_k.

$b_{a,M}$ or $b_{c,X}$ in Figure T3/1b to E_k yield a value of I_k. This method is referred to as the back-extrapolation method from high polarization data.

For the special case when the cathodic reaction is limited by the rate of mass transfer of cathodic reactant, eg hydrogen ions to the metal surface, $b_{c,X}$ approaches an infinite value, and Equations (T3/1,2) are altered to Equations (T3/3,4) respectively. The equation of the polarization curve for a metal corroding by mass transfer control of the cathodic reaction is given by Equation (T3/3). The corresponding polarization curve slope at the corrosion potential, given by Equation (T3/4), enables corrosion current to be calculated from R_p and $b_{a,M}$.

$$I = I_k[\exp(2.3\varepsilon/b_{a,M}) - 1] \qquad (T3/3)$$

$$(d\varepsilon/dI)_{\varepsilon \to 0} = R_p = (b_{a,M})/(2.3I_k) \qquad (T3/4)$$

Both Equations (T3/2,4) show that polarization resistance is inversely related to corrosion current, so that a high value of R_p means a low value of I_k, and vice versa. Plots corresponding to Figures T3/1a,b but for the case of mass transfer or diffusion limited control of the cathodic reaction are shown in Figures T3/2a,b respectively. A common example of this situation is near neutral aerated solutions where the rate of arrival of the cathodic reactant, oxygen, at the metal surface is limited by the rate at which it can diffuse across the diffusion layer. This rate is shown by $I_{L,O}$ in Figure T3/2b which is known as the limiting current for oxygen diffusion, and is equal to I_k. Back-extrapolation of the slope, $b_{a,M}$, in Figure T3/2b yields a value of I_k.

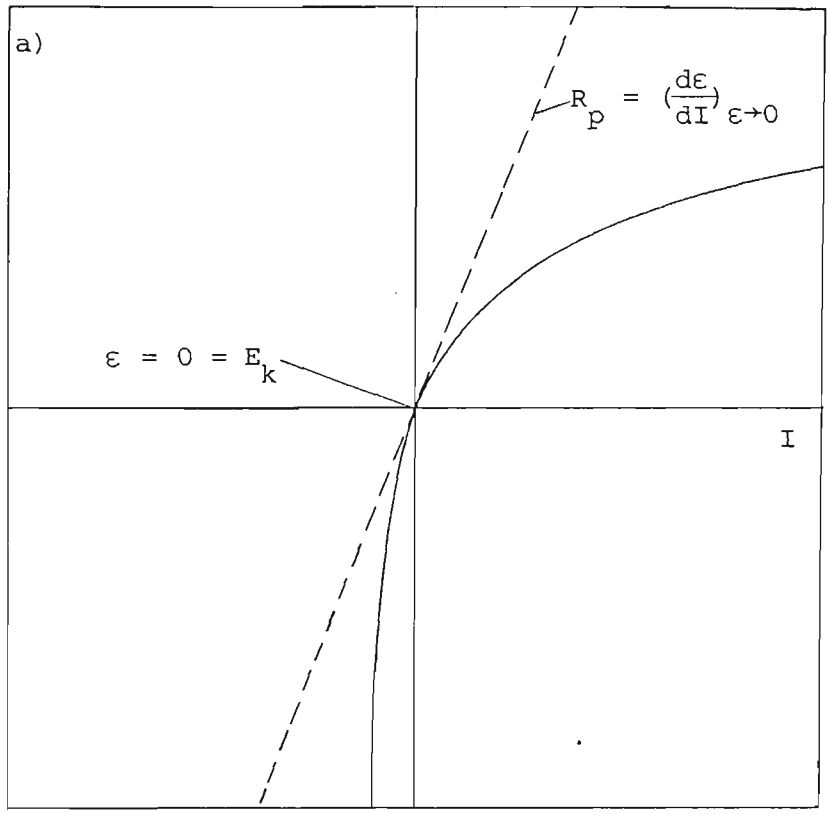

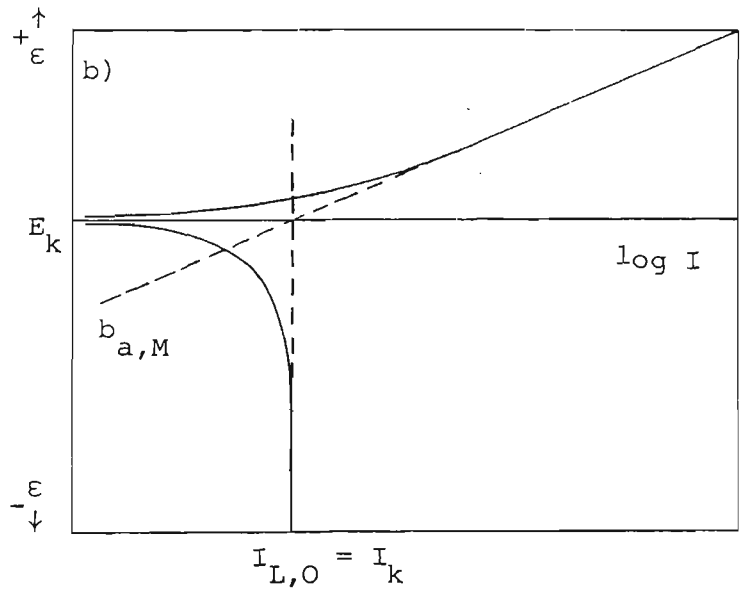

Figure T3/2. Polarization curve of polarization, $\varepsilon(=E-E_k)$, versus applied current, I, (Fig. T3/2a), and the corresponding Evans diagram form of ε versus log I (Fig. T3/2b) for the case of charge-transfer control of the anodic reaction and diffusion control of the cathodic reaction. $I_{L,O}$ limiting current for diffusion of oxygen; other symbols as per Fig. T3/1.

3. Principle of method

The polarization resistance and corrosion current methods are fast, sensitive and relatively non-destructive tests for the evaluation of instantaneous corrosion rate. The test procedure leaves the corroding metal relatively undisturbed so that repeated measurements can be made on the same sample[51]. Experimental time for one measurement lasts no more than several minutes so that corrosion rates can be regarded as essentially instantaneous. Patterns of corrosion behaviour can therefore be built up over short periods of time allowing the effect of system variables on corrosion rate to be evaluated rapidly. Examples of system variables are the introduction of inhibitors to a corrosion fluid, or the deterioration of passivation films applied to metal surfaces.

There are several ways of obtaining low polarization data using a potentiostat. The control mode can be either potentiostatic (potential between working and reference electrodes is controlled and current response measured) or galvanostatic (current applied to the electrochemical cell is controlled and voltage response of the working electrode with respect to the reference electrode is measured). The way in which the controlled voltage or current is altered can be either a scan, a sequence of steps (staircase), or a series of pulses. The scan method is usually referred to as potentiodynamic or galvanodynamic, whereas the step and pulse methods are usually described as potentiostatic or galvanostatic.

In this thesis, the galvanostatic single pulse method has been employed. The merits of this method have been described previously[52,53], and a brief discussion is given in Section T3/4.1. Experimental technique is described in

Section E1.2/4 but brief details are as follows. Current (dc) is applied to the cell in the form of a series of increasing single pulses which last normally about 7 s (but can sometimes be >30 s) and the working/reference electrode voltage response, E, is monitored. The current is then switched off and the potential is allowed to drift back to near the corrosion potential, E_k, prior to application of the next pulse. Normally, an anodic pulse is followed by a cathodic pulse to prevent movement of E_k in one direction or the other over the series of anodic and cathodic pulses. A train of such pulses, and their corresponding voltage responses are shown in Figure T3/3 and typical I,ε plots are shown in Figures T3/1a,2a.

The shape of the voltage response/time curve follows an experimental growth pattern, equivalent to the charging of a capacitor via a parallel resistor which obeys the relationship given in Equation (T3/5).

$$E = IR_t [1-\exp(-tR_tC_d)] \qquad (T3/5)$$

This equation assumes the metal/solution interface to be represented by a simple equivalent electrical circuit consisting of the double layer capacitance, C_d, and charge-transfer resistance, R_t.

The voltage response is read at the time, t_{ss}, corresponding to E reaching a steady stat situation, where $t_{ss} \approx 4R_tC_d$. For example, when C_d = 20 $\mu F.cm^{-2}$ and R_t = 10,000 $ohm.cm^2$, the steady state time will be approximately 200 ms. High values of R_t and C_d caused by low corrosion rates or pseudo-capacitance will increase t_{ss}. However, experimental times to steady state found in the experimental work for this thesis are usually longer than 200 ms. This subject has been referred to previously[52] and will be

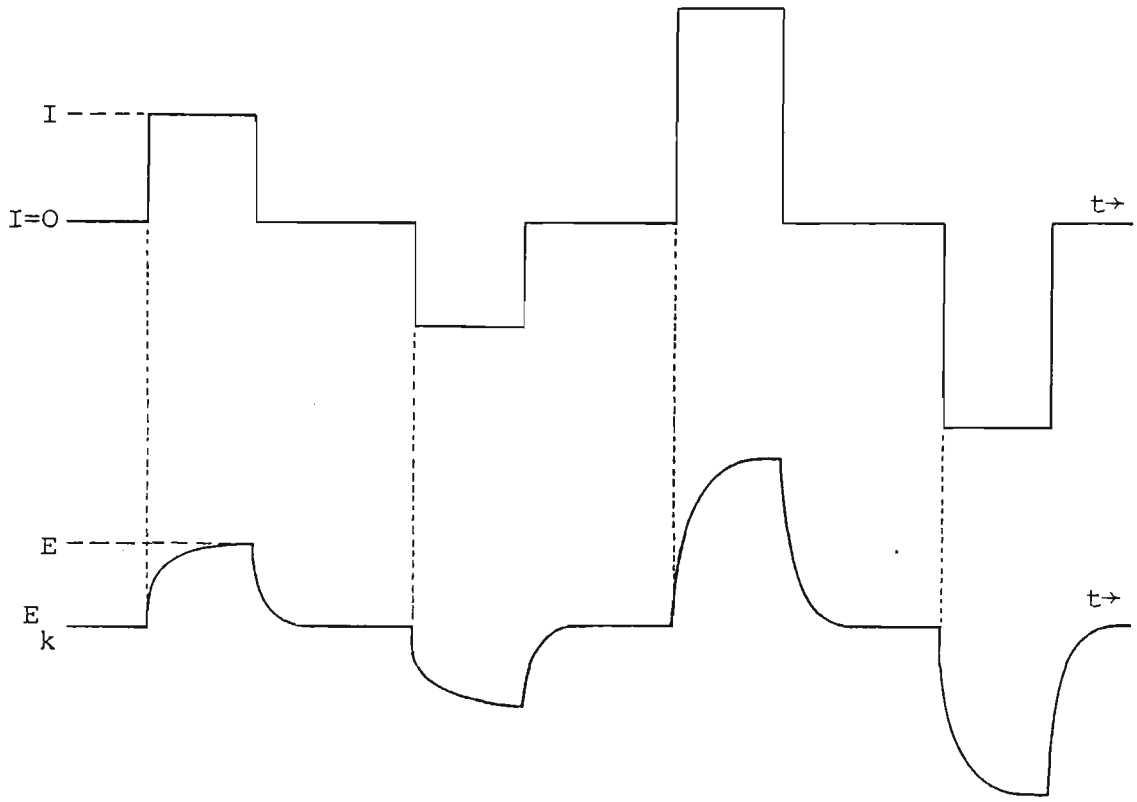

Figure T3/3. The galvanostatic single pulse method. Current, I, is applied in the form of a series of single pulses, and the working/reference electrode potential, E, monitored with time, t. The current is switched off between pulses to enable the corrosion potential, E_k, to stabilize prior to the next pulse.

further discussed in Section T3/4.

4. Errors in the method

Four of the main sources of error in the calculation of corrosion currents from polarization resistance are discussed in the following sections. These are time dependence of the voltage response, curvature in polarization curves near the corrosion potential, corrosion potential close to equilibrium potentials and resistance polarization (IR_s drop). These discussions are not intended to be thorough reviews as this has been adequately accomplished by Mansfeld[44], Walter[51] and Callow et al[54]. A further source of error - namely, bad data points, is discussed in Section R1.6/2. At the end of each of the following sections a brief comment on the relevance of the particular source of error to this thesis is given.

4.1 Time dependence of voltage response

The galvanostatic current pulse method is considered the most convenient method of obtaining low polarization data for the calculation of corrosion rates. Useful information concerning the kinetics of the corrosion process can be obtained from the time dependency of the voltage response which will assist in obtaining accurate polarization data. For example, it is possible to detect and eliminate from the measurement resistance polarization (IR_s drop) or diffusion polarization. These are not considered in the derivation of polarization resistance or corrosion current and should not be included in the measurement if Equation (T3/1) is to be used[55]. It is more difficult to treat the galvanostatic staircase step method[52] or the Transient Linear Polarization method of Jones and Greene[52,56] in this manner. The R_p or I_k results

obtained from these methods, or from the galvanodynamic scan method, can become dependent on scan rate when the voltage response includes a slow-rise portion attributed to diffusion polarization[52]. Walter[55] pointed out that the Stern-Geary Equation (T3/2) was not completely applicable to his experimental conditions (zinc in near-neutral chloride solutions) and that new equations were necessary to take these more complex conditions into account.

Some attempts have since been made to address the problem of measuring corrosion current under conditions of mixed charge-transfer and mass transport control notably by Britz and Hougaard[57], Hougaard and Britz[58], and Allan and Cherry[59]. Katoh and Koyama[60] suggest a method of obtaining the steady-state potential from non-steady state data based on a theoretical transient equation. Azzerri[61,62] considered the case in near neutral solution where the dissolving metal surface is covered by corrosion product layers and the electrode capacitance becomes very large, giving rise to a shift in the corrosion potential upon application of a galvanostatic step. He derived an equation similar to Equation (T3/5), Section T3/3. Gonzalez et al[63] use a potentiostatic technique for measurement of the slow corrosion of steel embedded in concrete where the kinetics are mixed charge-transfer and diffusion. They showed that the potentiostatic technique achieved a steady-state time orders of magnitude less than that with the galvanostatic technique because the time constant depended on the solution resistance, and not the polarization resistance, as it did for the galvanostatic technique.

In this thesis, the kinetics are shown to be mixed charge-transfer and diffusion control in near-neutral, stagnant environments. The Equations (T3/1-4) in Section T3/2 do not take partial diffusion control into account, as has been discussed above. A steady state situation which includes diffusion will be

inappropriate for calculation of corrosion rates using these equations. Yet to eliminate the diffusion portion from the measurement and use the Stern-Geary equations is also inappropriate. The best solution is to develop modifications of the Stern-Geary theory that takes partial diffusion control into account, as already stated. This, however, is considered to be outside the scope of this thesis. The method adopted here is to use a standard voltage response reading time of 6 s, except where this is obviously unsatisfactory, and to compare corrosion rates with those calculated from other methods. This is discussed further in Section R1.6/2.

4.2 Curvature in polarization curves near the corrosion potential

Stern and Geary[42] originally described a region in the vicinity of the corrosion potential where a linear dependence of potential on applied current existed for a corroding electrode. Their equation (T3/2) related the slope of this linear region to the corrosion rate and the method became known as Linear Polarization Resistance. The extent of linearity was shown[64] to be dependent upon Tafel slope values, as shown in Figure T3/6,7. Walter[2] showed that this could be small and around 1.5 mV for zinc and galvanized coatings and 3.0 mV for steel in aerated buffered chloride solutions. Barnartt[3], on the other hand, found extended ranges of linearity of 60 mV or more for iron in 1N HBr and 1N H_2SO_4. The practice of obtaining data in excess of the linear range and/or on one side only of the corrosion potential and determining the slope of the line of best fit can lead to inaccurate corrosion rates. Oldham and Mansfeld[65] pointed out that the gradient at the corrosion potential could be employed to determine corrosion current whether or not the polarization curve was linear at the corrosion potential. This statement has meant that in recent usage the word 'linear' has been largely dropped from the name, because the criterion

of linearity is not required for the determination of polarization resistance.

In this thesis, corrosion current, I_k was calculated using the computer program IK_CALC8, Section A1/5.2, but R_p was not required in order to obtain I_k. It was, however, calculated from Equation (T3/2) after determination of I_k, $b_{a,M}$ and $b_{c,X}$.

4.3 Corrosion potential close to equilibrium potentials

Equations (T3/1-4) were derived assuming the corrosion potential, E_k, was far removed from the equilibrium potentials of the anodic, $E_{o,M}$, and cathodic, $E_{o,X}$, reactions. As E_k approaches either $E_{o,M}$ or $E_{o,X}$, the error in calculating corrosion current using Equation (T3/1) rises sharply due to neglect of the metal ion deposition reaction and the anodic reaction of the species X, termed the 'reverse' reactions. An exact equation has been derived by Mansfeld and Oldham[66]. Use of this exact equation requires $E_{o,M}$ and $E_{o,X}$ which are often unknown. The exact equation has been applied by Walter[2] to the corrosion of zinc, galvanized coatings and steel in stagnant phthalate-buffered chloride solutions of pH 5.3 and 5.9 which resulted in a lowering of the calculated mass loss towards that calculated from solution analysis but the error associated with ignoring the reversing reactions was calculated to be less than 20% at most.

In this thesis no attempt has been made to correct for the influence of the reverse reactions. Calculations of corrosion current have been based on the simpler Equation (T3/1) where the reverse reactions are ignored and the assumption is implied that the corrosion potential is far removed from either of the equilibrium potentials.

4.4 Resistance polarization

Resistance polarization, or IR_s drop as it is commonly called, refers to the voltage error introduced between the corroding working electrode and the tip of the Luggin-probe leading to the reference electrode when a current is flowing between working and auxiliary electrodes. The voltage error is caused by uncompensated solution and/or surface film resistance, R_s, between these two points. This is known to be a problem in poorly conducting solutions, but is very often overlooked as a potentially large source of error in R_p measurements. Mansfeld[67] pointed out that errors due to neglect of IR_s-drop could be severe even in solutions of moderate conductivity, if corrosion rates are high (R_p low). This is because the ratio R_s/R_p, and not the magnitude of R_s, determines the error in R_p. Walter[55] found that neglect of IR_s drop had the effect of increasing values of R_p, which by itself would be expected to make calculated corrosion rates too low. However, calculated corrosion rates can be too high due to neglect of IR_s drop in cases where both R_p and $b_{a,M}$ are calculated ($b_{c,X}$ was assumed infinite for the experimental conditions), because there is a greater positive error in calculated values of $b_{a,M}$ than in R_p.

In this thesis, IR_s drop has not been compensated instrumentally by techniques like positive feedback, but has been measured using a Wheatstone bridge method[55]. For ACMs, values of R_s were found to be negligible and therefore correction of IR_s drop was not required, refer Section R1.6/8.

5. Analysis methods

A number of numerical analysis methods have recently appeared which use

Equation (T3/1), Section T3/2, to determine the three unknowns I_k, $b_{a,M}$ and $b_{c,X}$. For simplicity, this can be written in the equivalent form of Equation (T3/6).

$$I = I_k[\exp(\varepsilon/b_a)-\exp(-\varepsilon/b_c)] \qquad (T3/6)$$

where $b_a = b_{a,M}/2.303$

$b_c = b_{c,X}/2.303$

The numerical analysis methods can be either iterative or non-iterative, and curve fit Equation (T3/6) to the experimental (I_i, ε_i) data. The determination of R_p then becomes no longer necessary to the determination of I_k, except perhaps to obtain first guess values of the three unknowns, I_k, b_a and b_c.

The conventional method of numerical analysis is to minimize the sum of squares, S, of the difference between the curve fit value of I and the individual data point value, I_i, according to Equation (T3/7).

$$S = \sum(I-I_i)^2 \qquad (T3/7)$$

Equation (T3/7) assumes all experimental error is in I_i and none in ε_i, which is appropriate for potentiostatic experiments where potential is controlled at a known value and current is measured. Equation (T3/7) is used with Equation (T3/6) in one way or another by different authors. Walter and Madurasinghe[53] have recently discussed several of these authors' methods and the choice of experimental technique - either potentiostatic or galvanostatic.

This laboratory has preferred the galvanostatic technique for many years. With this technique, experimental errors are predominantly in voltage

response, not current, and this leads to significantly greater errors in estimating I_k, b_a and b_c if Equation (T3/7) is used as the basis of the analysis routine. To solve this problem Walter and Madurasinghe[53] wrote analysis routines, IK_CALC8 and IK_CALC9, Section A1/5.2, based on the sum of squares of the voltage differences, according to Equation (T3/8).

$$S = \sum(\varepsilon-\varepsilon_i)^2 \qquad (T3/8)$$

These analysis routines were evaluated using program THEO_IK, Section A1/5.3, and shown to lead to reduced errors in I_k, b_a and b_c. They concluded that if the galvanostatic method is to be used experimentally, where errors are predominantly in measured voltage, then a galvanostatic analysis routine should be used to analyze the data, that is, a method based on minimization of voltage residuals, according to Equation (T3/8).

6. Effect of I_k, b_a b_c values on plot shape

The shape of the (I,ε) polarization curve can provide information on the anodic and cathodic Tafel slope values b_a and b_c, respectively, which assists in the understanding of the kinetics controlling the corrosion process. Furthermore, the analysis routines return more accurate values of I_k, b_a, b_c with lower standard deviations if there is a degree of curvature in the polarization curve. It is therefore useful to know what controls this degree of curvature.

At least three basic polarization curve shapes are possible depending on the values of b_a and b_c in Equation (T3/6). These are illustrated in Figure T3/4 which was produced using program THEO_IK, Section A1/5.3. In Figure T3/4a, values of b_a, b_c were chosen to be low and equal (60 mV decade) and indicative

of activation or charge-transfer control of the anodic and cathodic reactions. This plot has a point of inflection[68] (where the slope of the curve reaches a maximum) near the origin (ε=0). In Figure T3/4b, b_a=60, b_c=3000 mV/decade and an inflection point is not observed. The curve on the cathodic side becomes very steep, with current values changing markedly for only a small increase in voltage response. This shape is caused by the high b_c value and indicates substantial polarization of the cathodic reaction towards a limiting current value as illustrated in Figure T3/2b for diffusion limited control of the oxygen reduction reaction. In Figure T3/4c, b_a=3000, b_c=60 mV/decade. Again, an inflection point is not observed. The curve on the anodic side becomes very steep, with current values changing markedly for only a small increase in voltage response. This shape is caused by the high b_a value and indicates substantial polarization of the anodic reaction typical of, for example, passivation of the metal surface or severe concentration polarization (mass transfer control) of the anodic reaction.

Figure T3/5 demonstrates the effect of varying I_k on polarization curve shape. The basic curve shape is an inflection point near the origin (ε=0) caused by equal values of b_a and b_c. As the value of I_k increases, the main effect is to decrease the value of polarization resistance, R_p (slope at the origin). The shape of the anodic and cathodic sides of the polarization curve is equally affected. The curve bends over towards the current axis more, such that the value of I is higher for a given value of ε, but the change in I is not as marked as it is when b_a or b_c are altered.

Figure T3/6 demonstrates the effect of varying b_a on polarization curve shape. The basic curve shape still shows an inflection point near the origin but is asymmetric when $b_a \neq b_c$. As the value of b_a increases, R_p increases, but not

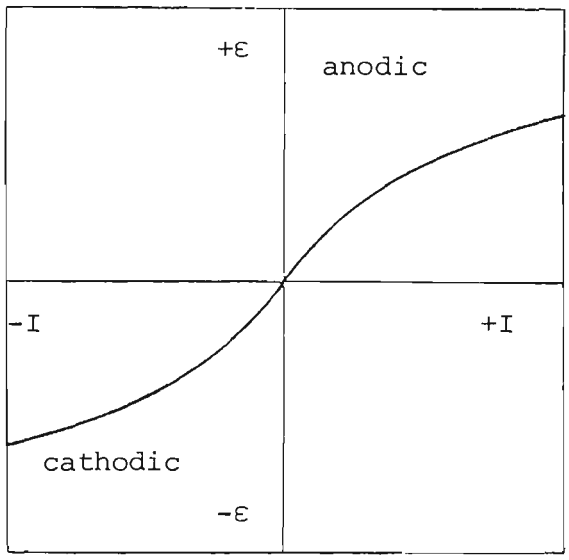

Figure T3/4. Three polarization curve shapes are possible, depending on the values of b_a and b_c.

a) b_a 60 mV/decade
b_c 60 mV/decade

Note the inflection point at the origin

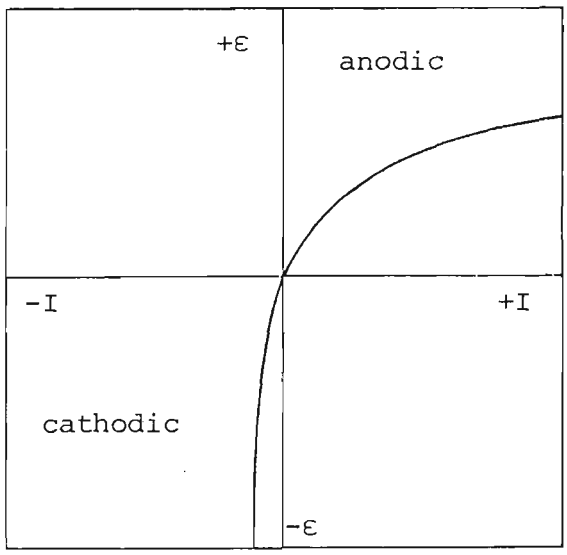

b) b_a 60 mV/decade
b_c 3000 mV/decade

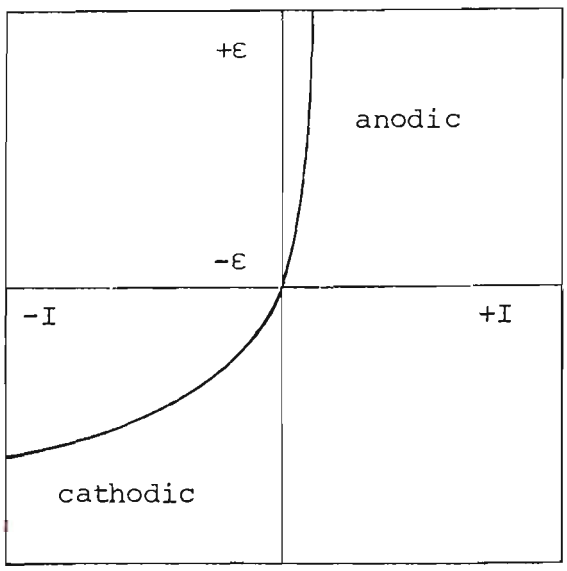

c) b_a 3000 mV/decade
b_c 60 mV/decade

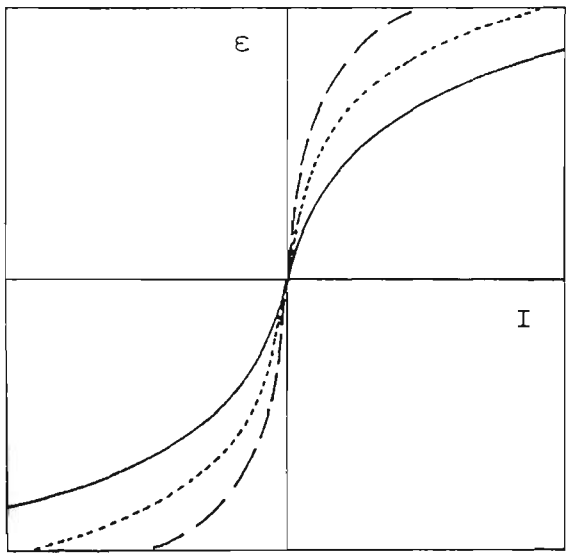

Figure T3/5. Effect of I_k on polarization curve shape

code	I_k (μA)
– – –	50
------	100
———	200
b_a	60 mV/decade
b_c	60 mV/decade

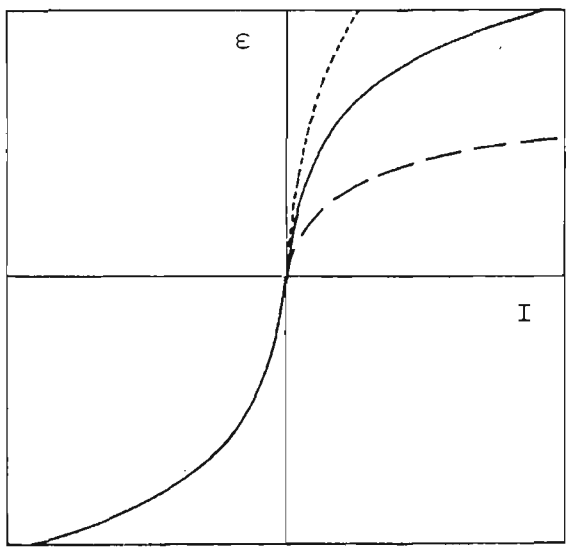

Figure T3/6. Effect of b_a on polarization curve shape

code	b_a (mV/decade)
– – –	30
———	60
------	90
I_k	100 μA
b_c	60 mV/decade

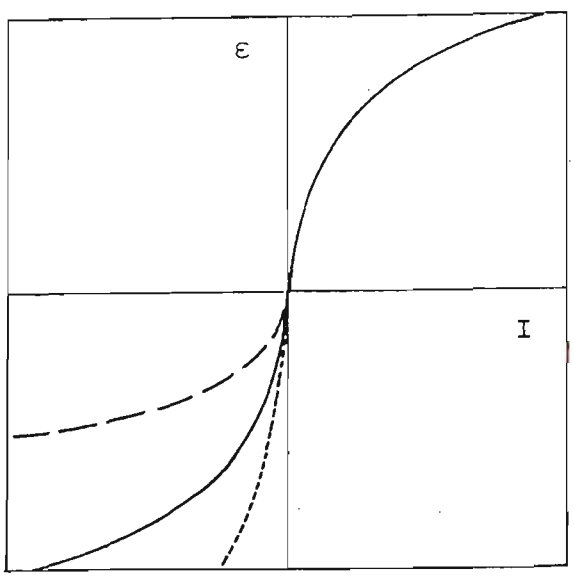

Figure T3/7. Effect of b_c on polarization curve shape

code	b_c (mV/decade)
– – –	30
———	60
-------	90
I_k	100 μA
b_a	60 mV/decade

as markedly as it does when I_k is increased. The main effect occurs on the anodic side where the curve straightens such that the value of I is lower for a given value of ε and the linear range extends as b_a increases. Altering b_a has very little effect on the cathodic side of the polarization curve.

Figure T3/7 demonstrates the effect of varying b_c on polarization curve shape. The basic curve shape still shows an inflection point near the origin but is asymmetric when $b_a \neq b_c$. As the value of b_c increases, R_p increases, but like b_a, not as markedly as it does when I_k is increased. The main effect occurs on the cathodic side where the curve straightens such that the absolute value of I is lower for a given value of ε and the linear range extends as b_c increases. Altering b_c has very little effect on the anodic side of the polarization curve.

Summarizing, the main effect of increasing I_k is to decrease R_p, the slope of the polarization curve at the origin. Altering b_a mainly affects the shape of the anodic side of the polarization curve, whilst altering b_c mainly affects the cathodic side.

7. Mass loss calculations from I_k and R_p

The method of calculating mass loss, ΔM_{Ik}, from corrosion current I_k, is essentially the area under the I_k/time curve multiplied by an electrochemical equivalent, E_q, and divided by the exposed area of the working electrode, A_w, according to Equation (T3/9).

$$\Delta M_{Ik} = E_q/A_w \int_o^{tdry} I_k \, dt \qquad \text{(T3/9)}$$

where tdry = time for water film to evaporate (min)

E_q = electrochemical equivalent = A/Fz (coulomb.g. equiv^{-1})

A = atomic weight

F = Faraday (96,500 coulomb.equiv^{-1})

z = valency (number of electrons involved)

E_q = 3.387×10^{-4} for ACM3 (Zn)

= 2.894×10^{-4} for ACM8 (Fe)

= 3.387×10^{-4} for ACM4 (rolled Zn-55%Al)

ΔM_{Ik} = mass loss (g.m^{-2})

A_w = working electrode area (m^{-2})

The value of E_q for ACM4 (rolled Zn-55%Al) is not known and was taken to be the value for Zn. This is based on the assumption that Zn-55%Al coatings corrode preferentially from zinc-rich areas as discussed in Section R1.4/1. The value of E_q chosen will be too high if Al is involved in the corrosion mechanism, and as a result, mass losses will be calculated somewhat too high.

The method of calculating mass loss, ΔM_{Rp}, from polarization resistance, R_p, is obtained from Equation (T3/9) by substituting $I_k = B/2.303\ R_p$ from Equation (T3/2) to give Equation (T3/10).

$$\Delta M_{Rp} = Eq.B/2.303\ A_w \int^{tdry} 1/R_p\ dt \qquad (T3/10)$$

where $B = [1/b_a + 1/b_c]^{-1}$ and is the mixed Tafel slope constant. The values of other variables were the same as those used for mass loss calculated from I_k in Equation (T3/9). Values of b_a were fixed at 35, 69, 35 mV/decade, whilst values of b_c were fixed at 10,000 mV/decade for ACM3 (Zn), ACM8 (Fe) and ACM4 (rolled Zn-55%Al alloy). These values of b_a correspond to that previously measured[2] for zinc, galvanized coatings and steel fully immersed

in near neutral buffered chloride solution. The value of b_a for ACM4 (rolled Zn-55%Al) was assumed to be the same as that for ACM3 (Zn). The cathodic reaction was assumed to be diffusion limited oxygen reduction and therefore a very high b_c value was used. The b_a, b_c values chosen were not important because these results were used to compare with mass losses calculated from R_t in Section R1.7/4 and the same b_a, b_c values were used in both cases.

These calculation methods have been applied to calculate mass loss of ACMs from I_k/time trends in Section R1.6/3 and from R_p/time trends in Section R1.6/7. Refer also to Sections R1.6/4 and R1.7.

1. Atmospheric SO_2 pollution and acid rain

Atmospheric pollutants can be classified[69,70] as either particulate (eg dust, smoke, ash, aerosol, lead, sulphates, nitrates) or gaseous (eg SO_2, H_2S, NO_2, NO, hydrocarbons, HF). Of the gases, SO_2 has been identified as a major pollutant, and comes almost exclusively from man made sources, particularly from coal fired power stations. The aqueous chemistry of sulphur-containing species plays an important role in the phenomenon of acid precipitation, commonly referred to as acid rain. Sulphur dioxide is absorbed by clouds and raindrops where it can be oxidized to sulphate. The hydrogen ions liberated during this process contribute to the acidity of the droplets[71]. A wide variety of mechanisms has been proposed to account for the SO_2 oxidation process - O_3 and H_2O_2 are currently accepted as the most important of the oxidants, but NaCl particles[72], Fe(III)[71] and Mn(II)[70,73] appear to act as catalysts. Clarke and Radojevic[71] found that pH and Fe(III) concentration of rainwater samples were important in affecting the oxidation rate but there was poor correlation between this rate and Mn, Cu and Zn concentrations. Mason[74] discusses the oxidation of SO_2 to H_2SO_4 in cloud droplets. However, the sulphate content of rainwater could not be accounted for in this way, and he attributed this to the presence of ammonia, which is found to catalyse the conversion of SO_2 to SO_4^{2-}.

The level of SO_2 in the atmosphere can vary from hour to hour; day to night; winter to summer; and it depends on the distance from the source and wind velocity/direction[70]. With implementation of air pollution control schemes, levels have fallen over the past decades. Hudson and Stanners[75] in 1953 reported levels in England ranging from slight pollution ($\leqq$0.02 ppm SO_2) through to severe pollution (0.13 ppm SO_2). Sydney's industrial areas

annual average concentrations have been around 0.016 ppm since about 1975. However, maximum hourly values above 0.4 ppm still exist in about 100 US locations[76]. Funke and Haagan[77] quote characteristic SO_2 levels in West Germany of small to large towns of 0.04 to 0.15 ppm but 1.28 ppm maximum in an industrial area (Ruhr). Duncan and Spedding[78] state that $[SO_2]$ is around 0.2 ppm in heavily polluted areas.

The oxidation of SO_2 in the atmosphere causes acidification of rainfall. Acid rain loosely refers to rainwater with a pH value lower than 5.6, the lowest pH which may result from saturation of CO_2. In Europe[70], pH values of 4.0-4.5 have been recorded in many regions, and also in North America, particularly SE Canada and NE United States[79]. Holbrow[80] in 1962 stated that the pH of rain at Manchester could be as low as 2.6-2.8 in winter and 4.0 in summer. Sydney's rain had an average of about 4.5 over the period 1980-82. A sample collected at Epping gave the most acidic reading (pH 3.6)[81].

2. SO_2 corrosion of metals

Schikorr[82] summarised the known facts of rusting of iron by moist air containing SO_2. One molecule of SO_2 will convert 15 to 20 atoms of iron to rust in the winter, and 30 to 40 atoms in the summer; but since in winter four times as much SO_2 is present in the air as in summer, the rusting is twice as fast. Two theories[83], the acid regeneration cycle and the electrochemical cycle, exist that explain the corrosion of iron by SO_2. In the acid regeneration cycle, adsorption of SO_2 occurs on pre-existing rust, followed by oxidation of SO_2 to $FeSO_4$ in the presence of Fe and O_2. Oxidation hydrolysis of the $FeSO_4$ to rust then occurs with liberation of H_2SO_4 which then attacks more Fe, producing fresh $FeSO_4$, hence more H_2SO_4 and so on. This cycle can

continue many times until the SO_4^{2-} is removed as ferric sulphate. In the electrochemical cycle, FeOOH is reduced to Fe_3O_4 at cathodic sites, whilst Fe dissolves as Fe^{2+} ions at anodic sites. Evans and Taylor[84] concluded that both cycles take place, but once rust and $FeSO_4$ are present, the electrochemical cycle proceeds much faster than the acid regeneration cycle.

Ericsson and Sydberger[85] concluded that at SO_2 supply rates normally occurring in outdoor urban and industrial atmospheres and at relative humidities, rh, around 90%, SO_2 molecules reaching a rusty steel surface would be quantitatively adsorbed. The atmospheric concentration of SO_2 during the initial exposure does not only determine the corrosion rate during this period, but will also affect the long term corrosion by determining the density and distribution of anodic sites, referred to as sulphate nests. This explained why steel samples exposed in winter when $[SO_2]$ was high continued to corrode at a high rate over more than one year compared to samples exposed in summer. Adsorption of SO_2 onto an Fe surface occurs at discrete areas rather than uniformly[86]. Little correlation has been found to exist between uptake sites and surface properties of Fe, but uptake is consistently higher at regions where visible rust is present. The atmospheric corrosion of steel is mainly governed by the temperature, the relative humidity, and the deposition of SO_2, the latter being determined by $[SO_2]$ in the air and the deposition rate. Above about 90% rh, the deposition rate was found so high that the deposition per unit time was the product of gas velocity and $[SO_2]$[87]. Walton, Johnson and Wood also found that the amount of SO_2 presented to iron specimens was a more important corrosion parameter than its atmospheric concentration at >90% rh[88]. They found that the corrosion mechanism depended on the catalytic promotion of sulphate formation from SO_2 by inorganic species such as Fe^{2+} and Mn^{2+} ions[89].

The effect of SO_2 on Zn has also been studied extensively but much of the early work used SO_2 concentrations that were much higher than found in the atmosphere. The relevance of conclusions reached must therefore be questioned. Vernon[90] showed that the presence of 0.01% SO_2 in the air caused a marked increase in corrosion when the relative humidity exceeded a critical value. In a 3-day test in which 13.5 $mg.L^{-1}$ $[SO_2]$ was added to the humidified air, Schikorr[91] found that the weight of Zn corroded was about equivalent to the SO_2 content of the corrosion products up to about 85% rh. The following three reactions were suggested.

$$Zn + SO_2 + O_2 \rightarrow Zn\,SO_4 \qquad (T4/1)$$

$$2\,Zn + 2\,SO_2 + O_2 \rightarrow 2\,Zn\,SO_3 \qquad (T4/2)$$

$$3\,Zn + SO_2 \rightarrow ZnS + 2\,ZnO \qquad (T4/3)$$

Barton and Beranek[92] showed that at 95-100% rh, increasing $[SO_2]$ from 0.01-0.5 volume per cent markedly increased the corrosion of Zn. Haynie and Upham[93] found excellent correlation between the corrosion of zinc and atmospheric $[SO_2]$ for eight US cities at sites with high humidity, and showed that Zn corrosion increased as $[SO_2]$ increased. In a 3-year test at Berlin-Dahlem, Schikorr[91] showed that corrosion increased with $[SO_2]$ and relative humidity, and was higher in the winter months. Hudson and Stanners[75] found that corrosion of Zn increased as $[SO_2]$ increased at 16 sites in England where atmospheric pollution varied from slight to severe. Edney et al[94] thought that it was likely that SO_2-induced corrosion of galvanized steel was initiated by H_2SO_3 and H_2SO_4 acids generated in the dew; H_2SO_4 will react with either the metal or protective corrosion products, $ZnCO_3$ or $Zn(OH)_2$, to produce soluble $ZnSO_4$ with limited protective properties. In a later paper[95], they concluded that a 1:1 relationship existed between the

number of SO_2 molecules deposited onto the surface and the number of Zn molecules that dissolve into the dew. Eijnsbergen[96] found that reactions of SO_2 on zinc surfaces were comparable with those on steel, but ZnO, contrary to Fe_3O_4 is not electroconductive. Therefore reactions proceed at a slower rate in spite of the fact that Zn is less noble than Fe. A discussion of the role played by electron conductive Fe_3O_4 is given by Evans[83]. Adsorption of SO_2 occurs at discrete areas on an Fe surface, but general uptake occurs all over the surface on Zn, enhanced at areas of bulk corrosion product growth[78]. Skerry et al[97] agree, also stating that SO_2 (3.5 ppm at 85% rh) has a very serious corrosion enhancement effect on Zn, irrespective of surface finish, being about 20 times that in control air. They concluded that corrosion mechanisms for Zn in SO_2-containing atmospheres appear quite different from those on Fe, where pitting is more prevalent. This contrasts with the conclusions of Eijnsbergen[96] stated above.

The effect of SO_2 on Al is not as well documented as with Fe and Zn. Schikorr[98] found that Al takes up less SO_2 than most other metals. Spedding[99] found that gas phase SO_2 was adsorbed onto an Al surface, the amount taken up being strongly dependent on rh and also on the partial pressure of SO_2 in the gas phase. The SO_2 in the aqueous phase may then be oxidised to sulphate which produces free protons. This acidic solution attacks the protective layer on the Al to produce corrosion product, presumably $Al_2(SO_4)_3.18\,H_2O$.

1. History

Atmospheric corrosion of metals using electrochemical cells has been investigated for many years dating back at least to the late fifties. Most of the early work was with dissimilar metal galvanic cells, notably by the Russian school represented by Tomashov and his colleagues[100-103] and also by Sereda[104,105] in Canada. The Russians used galvanic cells of Fe/Cu, Fe/Zn, Fe/Al, Cu/Al with most of the work being with Fe/Cu. The authors believed that their method was suitable for the fast determination of the corrosivity of the atmosphere. The cells were also used to study time-of-wetness due to moisture films formed as a result of rain, snow, fog or dew. It was found that corrosion was approximately proportional to the period of wetness of the metal surface[103]. Sereda[104,105] in 1960 used galvanic cells of Fe/Pt and Zn/Pt to determine the total period of wetness, and an instrument was developed that recorded the period the voltage across a 100 M ohm resistor connected to the cell exceeds 0.1 V. This corresponded to relative humidities in excess of about 85%. This early work has been summarized by Kucera and Mattsson[106].

Other researchers have developed electrochemical techniques for studying atmospheric corrosion in thin electrolyte layers. Rosenfeld[107] in 1962 concluded that, in the case of many industrial metals (Fe, Zn, Mg) the anodic reaction of metal ionization proceeded very slowly in thin layers, but that the oxygen depolarization rate increased markedly during the course of electrolyte evaporation from the metal surface. Gladkikh et al[108] in 1970 studied the corrosion kinetics of Zn and Fe under thin films and concluded that for zinc, each subsequent wetting of the surface was accompanied by a decrease in corrosion. For Fe, the corrosion rate under an evaporating film was governed

primarily by the oxygen diffusion rate. Fishman and Crowe[109] in 1977 applied potentiostatic polarization techniques to study the thin film corrosion of iron in a specially constructed cell. They obtained polarization curves similar to those in bulk electrolytes and determined corrosion currents by the back-extrapolation method, see Section T3/2.

In 1974, Kucera et al[106] attempted to measure the instantaneous rate of atmospheric corrosion of metals. They used two types of cells - a galvanic cell and three electrolytic cells. The galvanic cell consisted of alternate plates of Fe and Cu identical in principle to galvanic cells used earlier by Tomashov[100,110]. The electrolytic cells used plates of only one metal (Fe, Zn or Cu) to which an external voltage (100 mV) was applied and the cell current measured. This current was shown to vary widely with different climatic conditions such as time of wetness, relative humidity and SO_2 content of the atmosphere. These changes were at least in qualitative agreement with variations in the atmospheric corrosion rate as reported by other authors. They concluded that their technique was useful for studies of atmospheric corrosion in the laboratory as well as on atmospheric test sites.

The term, Atmospheric Corrosion Monitor or ACM, seems to have been named by Mansfeld et al[111] in 1976 who used galvanic cells of Zn/Cu or Fe/Cu encapsulated in epoxy resin, but similar to earlier cells used by Tomashov[110] and later by Kucera et al[106]. They measured galvanic currents by connecting their ACMs to a zero resistance ammeter, see Section T2/3, and showed that they could be useful not only to measure time-of-wetness, but also the corrosivity of the test environment.

Gonzalez[112] in 1978 used ACM single-metal (steel) multilayer plate cells

and imposed a polarization $\epsilon = \pm 10$ mV in order to measure the resulting current, I. He calculated corrosion current, I_k, from Equation (T5/1)

$$I_k = 2BI/\epsilon = kI \qquad (T5/1)$$

where B is the lumped Tafel constant. This equation is similar to the Stern-Geary Equation (T3/2) in Section T3/2 except that it is modified for twin, identical electrodes. A constant value of B was assumed as B was not measured. Electrochemical and gravimetric calculated corrosion rates were claimed to be in good agreement and practically coincided if the B value was doubled. However, inspection of the actual data reveals this to be somewhat over-optimistic.

In 1980, Mansfeld and Tsai[113] used both the galvanic cell (Fe/Cu, Zn/Cu) and single-metal (Fe or Zn) type of ACM, and compared electrochemical and gravimetric calculated mass loss. The Fe/Cu ACM followed the same trends as mass loss data but only accounted for about 20% of the corrosion rate estimated from mass loss. The Zn/Cu ACM showed too much scatter to make a comparison. Equation (T5/1) was used to obtain corrosion rates from single metal ACMs, but the results were considered doubtful because B was not known.

Mansfeld et al[114] in 1982 carried out a statistically designed experiment using 15 galvanic cell ACMs (Fe/Cu) and 15 single-metal ACMs (Fe). They wanted to evaluate the reproducibility of ACM data and the effects of cell design on time-of-wetness and cell efficiency. A cell efficiency of about 20% was found for the Fe/Cu ACMs and about 7% for the single-metal (Fe) ACMs. This low cell factor was considered to be due mainly to local cell action on

individual plates and to uncompensated ohmic drop in the electrolyte.

Haagenrud, Kucera and Gullman[115] in 1982 attempted to find an empirical relationship between the cell current of single-metal (Fe) ACMs and atmospheric corrosion rate. They used the term cell factor, CF, according to Equation (T5/2).

$$CF = \frac{\text{electrochemical mass loss from cell current}}{\text{gravimetric mass loss}} \qquad (T5/2)$$

They showed that the cell current diminished linearly with increase in the insulator thickness between steel plates from 100 to 400 μm; the cell current increased by 50 and 100% for increases in the impressed voltage of 100 to 200 mV and 100 to 300 mV, respectively; and the cell current diminishes by about 30% when the steel plate thickness increased from 0.5 to 0.9 mm.

In 1982 Mansfeld[36] introduced the 3-electrode ACM which is discussed in Section T5/2. With this type of ACM, Mansfeld was able to obtain anodic and cathodic polarization curves for a type 4130 steel ACM under thin layers of electrolyte which assisted in the interpretation of thin film atmospheric corrosion mechanisms.

Gonzalez et al[116] in 1984 used a very similar 3-electrode ACM, also discussed in Section T5/2. Polarization curves were obtained for ACMs made of Al, Cu, Fe and Zn covered with 400 μm electrolyte layers. They also determined Nyquist impedance plots for Fe and Zn ACMs. Electrochemical mass losses calculated using Equation (T5/1) with a fixed value of B, were compared with mass losses obtained gravimetrically. Cell factors, although not stated, can

can be calculated from their Figure 9. They were lowest for the Al ACM (0.13-0.34); the Cu ACM gave 0.55-2.25; the Fe ACM gave 0.47-1.0; and the Zn ACM gave 0.45-1.5. They used an insulator thickness between adjacent plates which was 170 μm. Although the authors claim good agreement between electrochemical and gravimetric mass loss, the above cell factor calculations show that this is not always the case.

In 1984/85 Feliu, Bastidas and Morcillo[117,118] described a multi-layer sandwich cell, discussed in Section T5/2, which was painted. They used the wide frequency impedance technique to study, using Nyquist complex plane plots, the electrochemical activity taking place under the paint films. Mansfeld et al[119] in 1986 applied essentially the same methods to a single metal (steel) ACM painted with a 20 μm epoxy coating. They used Bode impedance diagrams, refer Section T1/3, to study the reactions taking place above and below the paint film.

Metikos-Hukovic and Zevnik[120] in 1984 made an ACM of SnPb deposited onto copper using printed circuit technology. (This was not a new idea because this technique has been used earlier[121] with Zn/Cu or Cu/Au sensors for the measurement of time-of-wetness.) They used the polarization resistance technique based on Equation (T5/1) to evaluate this ACM in the salt spray test and in hot steam with/without SO_2. Mansfeld et al[122] also used the Sereda[121] concept of printed circuitry to produce what they described as a new atmospheric corrosion rate monitor, ACRM, using solid Zn instead of Zn plated onto Cu. A Zn/Zn sensor was tested using the polarization resistance technique based on Equation (T5/1), to determine atmospheric corrosion rates in the presence of atmospheric pollutants (SO_2, O_3, NO_2). A Zn/Zn and a Ni/Ni sensor of this type has been used to study the effects of acid rain/acid

fog over 15 months exposure at Long Beach, Southern California[123].

2. Construction

Kucera and Mattson[106] described their method of ACM construction for both galvanic cells and single-metal cells. Each cell consisted of 20 plates (65 x 10 x 0.5 mm) standing on end and insulated from each other by 100 μm polycarbonate or Teflon foil. The whole plate assembly was then encapsulated in epoxy resin and the cross-sections of all plates polished flat so as to expose an area of 6.5 cm^2. The galvanic cell consisted of 10 steel plates and 10 copper plates, the plates in each set being connected in parallel. The single-metal cell consisted of 20 plates of the same metal, ie Fe, Zn or Cu with 10 alternate plates connected in parallel to one terminal, and the other 10 plates connected in parallel to the other terminal. Both terminals were then connected to an external voltage. Gonzalez[112] constructed a similar type of single-metal (steel) cell but showed more design features in a schematic diagram. The plates were in the form of a rectangle with part of each plate cut away at the end to produce a metal tab. The plate assembly was bolted together. All the cathode plates (that is, each alternate plate) had their metal tabs protruding from one end of the plate assembly, whilst all the anode plates had their tabs protruding from the other end. The insulation thickness between plates was 170 μm, but no details for insulating the bolts were given. Mansfeld and Kenkel[111] showed a photograph of their galvanic cell type ACM. The insulator thickness between plates was 60 μm. Mansfeld[36] described his 3-electrode single-metal ACM. This consisted of 10 identical metal plates connected such that the two inner plates served as reference electrodes, the outer four plates served as auxiliary electrode, and the four plates between reference and auxiliary served as working electrode.

This simple arrangement located all three electrodes of the ACM in the same plane. The insulator thickness between adjacent plates was 60 μm. No other details of construction are available. Gonzalez et al[116] showed more design details for a similar type of 3-electrode cell, which consisted of only one central reference plate, followed on either side by repeated working/auxiliary electrode pairs of plates. The insulator thickness between adjacent plates was 170 μm. Details for insulating the plate assembly bolts were shown. Feliu et al[117] designed a 'segmented test piece' cell which they later[118] referred to as a multi-layer sandwich cell. This consisted of six relatively large mild steel test pieces (55 x 15 x 8 mm) insulated from each other with 170 μm plastic foil, polished to achieve a flat surface and painted with vinyl paint or acrylic lacquer. The printed circuit type of ACM is described in Section T5/1.

3. Cell Factor

This is adequately covered in Sections T5/1,4.

4. Advantages/Disadvantages

The aim of this section is to assess the advantages/disadvantages of using atmospheric corrosion monitors, ACM, to study the corrosion rates and mechanisms of metals under laboratory simulated atmospheric corrosion in a polluted SO_2 environment.

The obvious advantage of ACMs is that they are electrochemical cells that allow the study of thin film atmospheric corrosion in the laboratory[36,111-114,116,118,120,122] and to characterize the corrosivity of outdoor exposure sites[36,106,115,116,118,123-125]. Studies of reactions

occurring above and below paint films have also been made using ACMs[117-119]. The cells are of two types - 2-electrode dissimilar metal type, used for the measurement of galvanic corrosion, Ig, and 3-electrode single-metal type, used to measure corrosion currents, Ik, and impedance, Z. Both of these cell types present a flat surface to allow thin moisture films to form between working and auxiliary electrodes without complications of electrode shape which is a problem in assessing dissimilar metal corrosion in the atmosphere[126]. The printed circuit type is easier to manufacture, smaller in size[123] and has a faster response[122] than the more bulky metal plate assemblies set in epoxy resin.

These advantages come at the expense of certain disadvantages. They are difficult and tedious to manufacture[116]. In order to make an electrochemical cell that presents a flat surface to the environment, the individual plates that make up the cell have to be placed parallel with one another but on edge. This arrangement is impossible for metallic coatings on steel such as galvanized and ZINCALUME because such samples on edge are themselves dissimilar metal couple 'sandwiches' consisting of two coatings separated by a steel substrate. In order to study the atmospheric corrosion of such metallic coatings using ACMs, one has to resort to casting, rolling or slicing zinc or zinc-aluminium alloys and using these plates on edge rather than galvanized or ZINCALUME coated steel. This then poses the problem as to whether the ACM cell simulating the metallic coating's corrosion behaviour is typical of the metallic coating itself. This is the case in this thesis attempting to simulate the atmospheric corrosion behaviour of ZINCALUME using cast and rolled Zn-55%Al alloys.

The width of ACM plates and the insulator thickness separating them is a

further problem. The ACM cell current diminishes with increases in both plate thickness and insulator thickness[115], as discussed in Section T5/1. Both these factors result in reduced cell factor, CF. Thick insulation lowers CF. Decreasing the insulator thickness will raise CF, thus potentially giving better correlation with gravimetric mass loss, but this may give rise to partial shorts as discussed below. Another difficulty is the influence of the surface state of the metal at the start of the test. ACMs polished with diamond paste offer considerable resistance to coverage by electrolyte films[112]. The printed circuit type of ACM cannot be repolished in order to be reused. A new ACM must be employed for each new experiment. The multiple plate assemblies cast in epoxy can be repolished and used many times.

Mansfeld and Tsai[113] obtained cell factors, CF, for their polarization resistance method using Equation (T5/1) in Section T5/1 of 0.18 for a single-metal (Fe) ACM at different relative humidities, and CF ranging from 0.10 to 0.37 for a single-metal (Zn) ACM in similar experiments. They considered that these ACM measurements can only be used as a qualitative measure of corrosion rates. If, however, constant CF values are found experimentally as they were for the Fe ACM, the electrochemical ACM data can be converted into meaningful corrosion rates[106]. The cell factor has been found to vary from exposure site to exposure site, depending to some extent on the degree of pollution. A CF of approximately 0.36 was obtained after exposing a single-metal (Zn) ACM at Birkenes in Southern Norway for a period of one year[24].

The polarization resistance method using Equation (T5/1) in Section T5/1 to determine corrosion rates of ACMs has the limitation that the value of the lumped Tafel slope constant, B, is unknown. This, alone, can lead to

inaccuracies[112,116]. Mansfeld and Tsai[113] considered that the possible range of B values (6.5-52 mV) was large enough to prevent calculation of corrosion rates by this method. Furthermore, the time-of-wetness, which is required for conversion of ACM data to mass loss, is difficult to estimate[116].

Finally there is the problem of partial short circuits in ACMs. This is considered due to bridging between adjacent plates by electron-conducting corrosion products formed under a strongly acid, sulphur polluted surface film[124]. The risk of this occurring increases when the insulator between plates is made thinner[106]. This problem has been encountered with ACMs made of Fe, Zn and to some extent Cu, but not Al. An insulation thickness of 400 μm for Fe; 300 μm for Zn; 200-300 μm for Cu; and 100 μm for Al has been recommended[115]. Partial shorts are frequently found for Fe ACMs, and sometimes with Zn ACMs[116].

1. General

A review of the protection of metals by paints has been written recently by the author, and published[127]. Only brief details are reproduced here.

The evaluation of the corrosion performance of painted metals has received considerable attention over the years but recently there has been an upsurge of interest in electrochemical testing. The aims of such tests have been to find accelerated laboratory tests which can evaluate new paint systems much quicker than by atmospheric exposure trials, and/or to provide a better understanding of how a paint film protects a metal substrate. The mechanisms involved in the protection of metals by paint films have been the subject of controversy for many years. This is hardly surprising considering not only the complexity of corrosion processes through paint films but also that paint films vary widely in thickness and type with different mechanisms applicable.

2. Metal substrate

The type of metal substrate can influence the overall rate of degradation of the painted metal. Tomashov et al[128], working on very thin (1-4 μm) insulating films on platinum, copper and iron stated that the electrochemical nature of the metal is one of the deciding factors determining the initial deterioration of the insulating film. They indicated that the rate of the corrosion process on filmed metals increases as the metal's electrode potential becomes more negative in the order - platinum, copper and iron, zinc and aluminium. This is not completely in accord with expected behaviour. Walter[9] studied 25 μm paint films on steel, galvanized steel, Zn/55%Al coated steel and aluminium immersed in 5% NaCl solution at 50°C. He concluded

that the corrosion performance of these painted metals, as measured by their failure time (the immersion time taken for the resistive and capacitive components of sample impedance to reach selected values) was directly related to the corrosion resistance of the unpainted substrate, as assessed by polarization resistance, shown in Figure T6/1.

3. Water, oxygen permeability

The reactants necessary for corrosion to proceed in normal environments are water and oxygen. Aggressive ions, for example, chloride, can also influence the rate of corrosion by forming soluble corrosion products and reducing the electrolyte resistance between cathodic and anodic sites. As the corrosion process can not proceed faster than the slowest mechanistic step, limiting the rate of arrival of one of the reactants will slow the overall corrosion process. The concept of the paint film as an impermeable membrane has been largely discredited by permeability data for water and oxygen. In many paint systems[129-134], water permeability is faster than that required for corrosion of the bare substrate[129-139], indicating that the rate determining step is not uptake of water. Likewise, it has been concluded that the weight of oxygen which could pass through a number of paint films varies from one tenth to a value greater than that consumed by an unpainted steel specimen. Since exposed painted specimens do not corrode at these rates, unless the film has been degraded, the rate of oxygen diffusion cannot be the rate controlling factor[140] in these cases.

4. Ionic resistance

Paint films which cannot inhibit corrosion by preventing water, water vapour

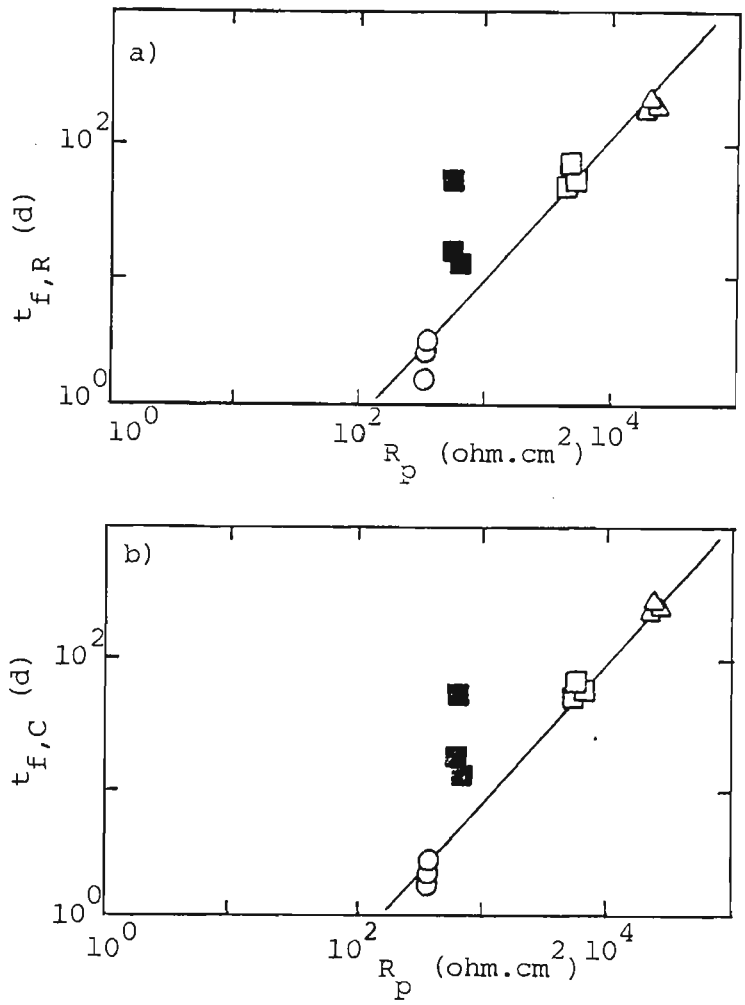

Figure T6/1. Sample failure time a) $t_{f,R}$ and b) $t_{f,C}$ for 25 μm painted substrates versus polarization resistance, R_p, of unpainted substrate immersed in 5% NaCl solution at 50°C. $t_{f,R}$, $t_{f,C}$ times taken for resistive, capacitive components of impedance at 1 kHz to fall, rise to 10^4 ohm.cm^2 and 10^{-7} F.cm^{-2} respectively. Substrates tested ○ steel; ■ galvanized steel; □ Zn-55% Al coated steel; △ Al.

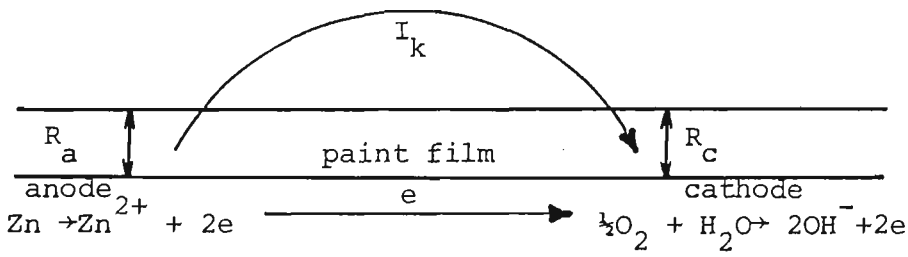

Figure T6/2. The process of corrosion involves a flow of electrons from anode to cathode through the metal, accompanied by an ionic current flow that passes through the paint film twice in going from anode to cathode. R_a, R_c resistance of anode, cathode.

and oxygen from reaching the substrate metal cannot inhibit the cathodic oxygen reduction reaction. It has been pointed out by Mayne[141] that although certain pigments (metallic, soluble or basic) may modify the anodic reaction of metal corrosion, there are many types of paint not containing inhibitive pigments which have given very satisfactory service. Such paints appear to protect by virtue of their high electrolytic resistance[132,140,142], which impedes the movement of ions as the rate controlling step.

The relationship between the ionic resistance of a coating and its protective ability has been discussed by Sykes[143] and Wolstenholme[144]. The process of corrosion involves a flow of electrons from anode to cathode sites through the metal, accompanied by an ionic current flow that passes through the paint film twice in going from anode to cathode, see Figure T6/2. The potential drop between anode and cathode dissipates most of the electrochemical driving force for the corrosion reaction, and the corrosion current is small. This causes the anodic and cathodic reactions to operate close to their reversible potentials and the measured potential of the sample has a value somewhere between that of the anodes and cathodes. The anodic areas will initially constitute the larger proportion of the total ionic resistance because the area of active anodes will initially be extremely small[145]. Current passes to the cathodes through a much larger area of the coating, as deduced from the high measured potential of samples in the early stages of immersion.

Studies have been made of the factors which control film resistance and the mechanism by which ions flow through the polymer film. Kittleberger and Elm[146] found a linear relationship between the rate of diffusion of ions and the reciprocal of the film resistance. Mayne[141] concluded that when the dc resistance of detached varnish films was high, it was controlled by the uptake

of water, but when low the resistance of the film followed the resistance of the solution in which it was immersed. Maitland and Mayne[147] showed that the resistance depended on two factors - uptake of water which is fast, and an ion exchange process which is slow. The latter process may bring about a fall in resistance, along with structural changes in the film which slowly destroy its protective properties. Mayne[132] determined that the amount of chloride ions which could pass through a 100 μm polystyrene film was several thousand times smaller than the quantity of water which could pass through and concluded that a polystyrene film is almost impermeable to chloride ions, interposing a high ionic resistance between anodic and cathodic sites on the metal surface. He proposed the following mechanism for corrosion of steel under an unpigmented polystyrene film immersed in sea water. Water is first taken up by the film, causing its resistance to fall. At first, corrosion would be very slight due to iron corroding in the presence of water and oxygen. Chloride ions would be excluded at this stage due to the negative charge on the film. Corrosion of the steel would continue because the film is permeable to positive ions - iron ions moving outwards at the anode and sodium ions moving inwards at the cathodes. Only at a later stage would chloride ions migrate into the film causing a further decrease in ionic resistance, slowly reaching the metal surface to form soluble corrosion products. In this way, steady breakdown of the resistance of the film will occur causing corrosion to progressively increase.

5. Osmotic pressure

Morrell[148] pointed out that the presence of salts in solution in water inhibited the uptake of water by varnishes, and the stronger the salt solution, the less is the amount of water absorbed. Brasher and Nurse[7] observed that paint

blistering is more usual in fresh water than in sea water, whilst corrosion of the substrate metal with accompanying paint breakdown is accelerated by the presence of chloride ions in the solution. By capacitance measurements, they confirmed previous conclusions of Kittleberger and Elm[149], arrived at by gravimetric methods, that water uptake by the paint in the early stages of immersion depends only on the osmotic pressure of the solution. Brasher and Nurse[7] showed that water uptake in painted steel panels in sucrose solutions increased with both time of immersion up to equilibrium values, and with decreasing osmotic pressure. The influence of osmotic pressure extends to nearly 200 atmospheres. However water uptake is most sensitive to changes in solution osmotic pressure in the low range below about 50 atmospheres. In solutions of sodium chloride of various concentrations, paint breakdown occurred more quickly the more dilute the solution, as shown in Figure T6/3 from capacitance/time curves. This led Brasher and Nurse[7] to conclude that the primary controlling factor in the life of the paint (the time to reach paint breakdown) was the amount of water taken up. Ionic concentration was a secondary controlling factor. In a series of mixed sucrose-NaCl solutions of constant osmotic pressure, paint breakdown occurred more quickly, the higher the chloride ion concentration.

However, Walter[127] has shown that the time to breakdown (assessed from both resistive and capacitive components of impedance at a frequency of 1 kHz) of 25 μm painted Zn-55%Al coated steel at 50°C is inversely related to the sodium chloride concentration, a fact which agrees with outdoor exposure results that are related to distance from the ocean surf. This is opposite to the results of Brasher and Nurse[7] shown in Figure T6/3 which show a direct relationship between time to breakdown and sodium chloride concentration. Both sets of results are shown replotted in Figure T6/4, which illustrates their

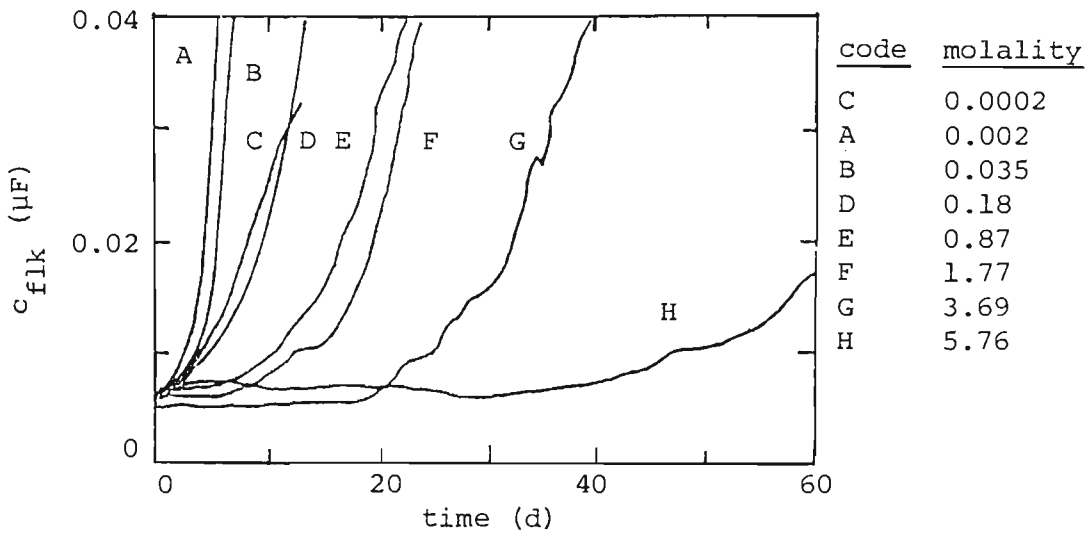

Figure T6/3. Capacitive component of impedance at 1 kHz versus time in NaCl solutions at room temperature, from a paper by Brasher and Nurse [7].

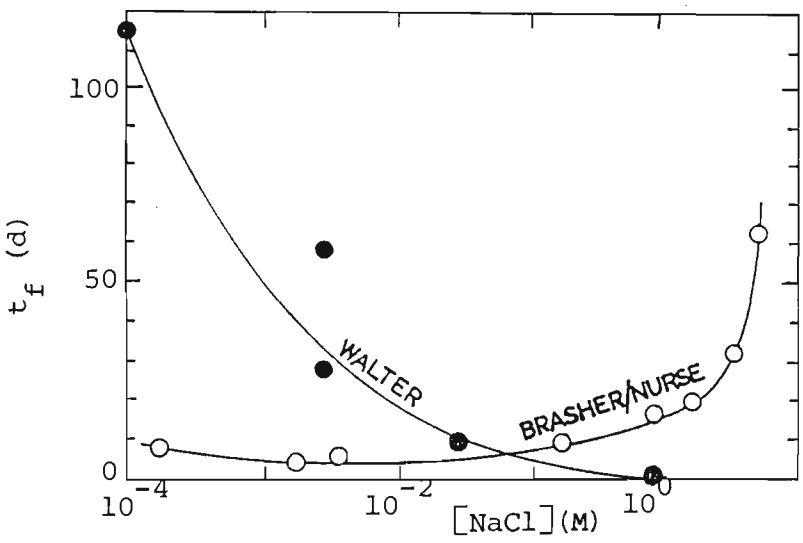

Figure T6/4. Calculated time to breakdown, t_f, of two painted metal systems as a function of solution NaCl concentration: o painted steel from a paper by Brasher and Nurse [7]; ● 25 um painted Zn-55% Al coated steel from a paper by Walter [127]. t_f calculated as time to reach a capacitance of 0.02 uF from Fig. T6/3 (Brasher/Nurse) or 1 $nF.cm^{-2}$ (Walter); point for distilled water arbitrarily plotted at a concentration of 10^{-4} M.

striking differences. Note that whilst the trends in time to breakdown can be compared, their absolute values cannot be compared between the two sets of data due to the different methods of calculation. Whereas the primary factor controlling the life of the paint film was determined by Brasher and Nurse to be the amount of water taken up in the painted steel samples, this does not appear to be the case with the painted Zn-55%Al samples tested by Walter. It is more likely that transport of ions is the rate controlling factor in this different paint system. The different trends shown in Figure T6/4 suggest that it can be sometimes misleading to extrapolate the results of one painted metal system to another.

6. Degradation mechanisms

Studies have been carried out on how water, water vapour, gases and ions permeate through polymer films. Much of this work has been on whether pores or capillaries exist or not, and has been summarized in several literature references[150-152] The distribution of water within paint films has been investigated by comparing water uptake/time curves obtained by gravimetric and capacitance methods[153] to distinguish between water in pores normal to the surface, in layers parallel to the surface, or randomly distributed. Phase-contrast microscopy has been used to visually detect the distribution of water[141], which is shown to be different for different paint film types. The formation of a boundary layer, also termed aqueous phase water or water-rich layer, at the paint film/substrate interface is thought to be the destructive form of water causing corrosion of the substrate[141] and a decrease in paint film adhesion[154]. High frequency dielectric measurements have been used to identify this water-rich layer[8], and combined with a calorimetric technique to distinguish microscopic water filled cavities, termed clusters, in

polyethylene[155]. D'Alkaine et al[156] have shown that the amount of water absorbed, see Figure T6/5, in attached films is quite different from unattached films not only as a consequence of water accumulation at the film/substrate interphase, but thought also due to some special influence of the metal itself. These findings have led them to cast doubts on the extrapolation of unattached film results to films attached to metals in actual practice. One explanation of the influence of the substrate has been given by Kresse[157]. The primary action of water diffusing through the paint film causes anodic corrosion of the substrate and cathodic oxygen reduction resulting in the formation of hydroxyl ions. As a secondary effect, these hydroxyl ions can have a hydrolyzing effect on the paint binder, making the binder more permeable to water in the case of easily hydrolyzing binders. It should be noted that cathodic oxygen reduction resulting in the formation of hydroxyl ions can only occur if another cation, such as the sodium ion, is present at the paint/metal interface to balance the charge locally.

A number of cross-linked polymer films (alkyd, tung oil, epoxy, polyurethane, urethane alkyd has been shown to be heterogeneous in structure, containing small areas, termed D-type areas, which have a vastly lower ionic resistance than the rest of the film, called I-type areas[158], as illustrated in Figure T6/6. With direct or D-type conduction in paint films, the dc resistance of the film follows that of the solution in which it is immersed, whereas with inverse or I-type conduction, the film resistance increases with increasing concentration of electrolyte. Differences between D- and I-type areas have been connected with differences in cross-linking density within the polymer film[140]. Breakdown of the painted metal has been shown to occur at D-type areas of low resistance where polymer cross-linking density is presumably lower, leading to corrosion of the substrate[159].

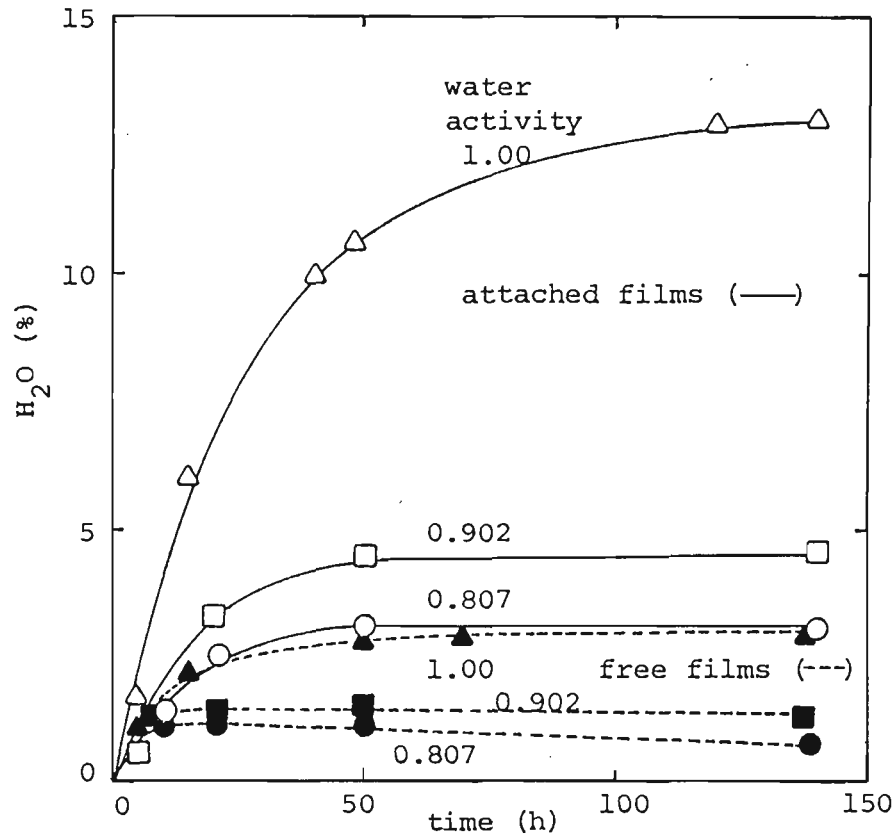

Figure T6/5. Absorption of water in epoxy chromate paint films versus time at 20°C for various water activities with free films and films attached to a steel substrate, from a paper by D'Alkaine et al[156].

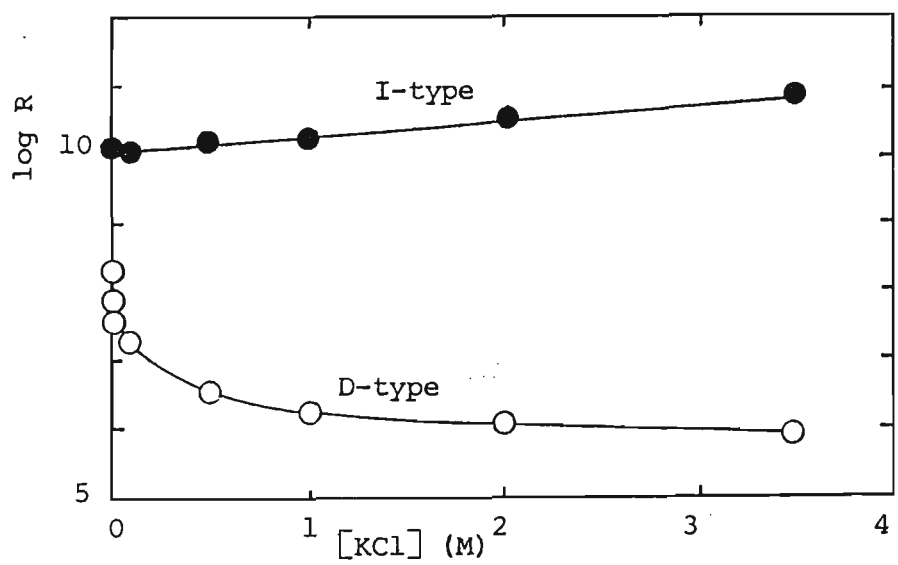

Figure T6/6. Effect of KCl concentration on the dc resistance, R, of clear alkyd D- and I-type films, from a paper by Mills and Mayne[158].

Funke[160] considered that differences in corrosion performance of various coating systems could be explained by primary parameters of wet adhesion, oxygen and water permeability. Padget and Moreland[14] consider that the reduction in water permeability is particularly important. They considered that even when water permeation is directly prevented, the conductivity and resistance of the coating is highly dependent upon the water content of the coating because it strongly influences solubilization of ions and the ionic diffusion characteristics of the film.

7. Choice of testing method

In order to measure the overall rate of corrosion degradation of a painted metal in a given environment, a simple, repetitive, relatively non-destructive test is desirable. A critical review of dc electrochemical tests for painted metals has been published recently by the author[161]. The dc tests discussed are potential/time, dc resistance, polarization curve, polarization resistance and galvanic current tests, of which the potential/time and polarization resistance methods are regarded as the most appropriate dc methods for a laboratory corrosion performance test. However, it was concluded that none of the dc methods were ideally suitable as a corrosion rating test for painted metals.

The impedance technique is discussed at length in Section T1, both as a single frequency test (Section T1/2) and a wide frequency range test (Section T1/3), and its applications to painted metals in Section T1/5. Both single and wide frequency range impedance methods can be performed in low conductivity media where conventional dc methods are difficult, and both give a quantitative estimation of sample failure. Their limitations are discussed in

Section T1/3. As long as the sinewave signal is maintained around the sample's linear range (Section T1/1.2), these tests are relatively non-destructive, repetitive and simple to operate, especially the single frequency test, with modern instrumentation such as frequency response analyzers (Section T1/1.3).

It is concluded that impedance methods are suitable for rapid laboratory assessment of corrosion performance of painted metals and possess advantages over dc electrochemical methods.

8. Water uptake calculations

Water uptake by the paint film can be calculated using the Brasher and Kingsbury formula[153] according to Equation (T6/1):

$$X_V = [100 \log (C_{m,t}/C_{m,o})]/\log 80 \qquad \text{(T6/1)}$$

where X_V = water uptake in paint film (% v/v)

$C_{m,t}, C_{m,o}$ = measured values of 1 kHz capacitance at time, t, and at zero time, respectively

80 = dielectric constant of absorbed water

The value of $C_{m,o}$ can be calculated by extrapolating readings of $C_{m,t}$ taken in the first 20 minutes of sample immersion back to zero time.

Other equations have been used to calculate water uptake from impedance measurements, but the empirical Equation (T6/1) of Brasher and Kingsbury gave better agreement with gravimetric results[162].

SECTION E1 EXPERIMENTAL - GENERAL

SECTION E2 EXPERIMENTAL - UNPAINTED METALS

E1.1 Electrochemical Test System

1. Instrumentation

Two sets of instruments, digital and analogue, were used.

Figure E1/1 shows the main digital instruments and how they were connected to the computer. The computer used was a Hewlett-Packard Model 217H containing a built-in HPIB interface, an analogue-to-digital card, Model HP 98640A, a floating point maths card, Model HP 98635A, to speed calculations, and 1.25 M byte of RAM. Connection to most of the peripheral instruments was achieved via HPIB interfacing cables. Mass storage was a combined double-sided 3.5 in flexible disc/15 M byte hard disc, Model HP 9133D. A printer, Model HP 2225AK Thinkjet, and a plotter, Model HP 7475A were connected to obtain hard copies of graphs and tables.

A Solartron Model 1286 Electrochemical Interface was used for corrosion current, polarization resistance and low polarization data experiments. Impedance experiments were performed using the Electrochemical Interface in conjunction with a Solartron Model 1250 Frequency Response Analyzer. Galvanic currents were measured on an operational amplifier box which could be switched to operate as either potentiostat, galvanostat or zero resistance ammeter, the latter mode being used for galvanic currents. Voltages proportional to the galvanic current were sent via a shielded cable to the computer's analogue-to-digital card for storage, plotting or tabulation. Most tests were performed using the above digital based instrumentation.

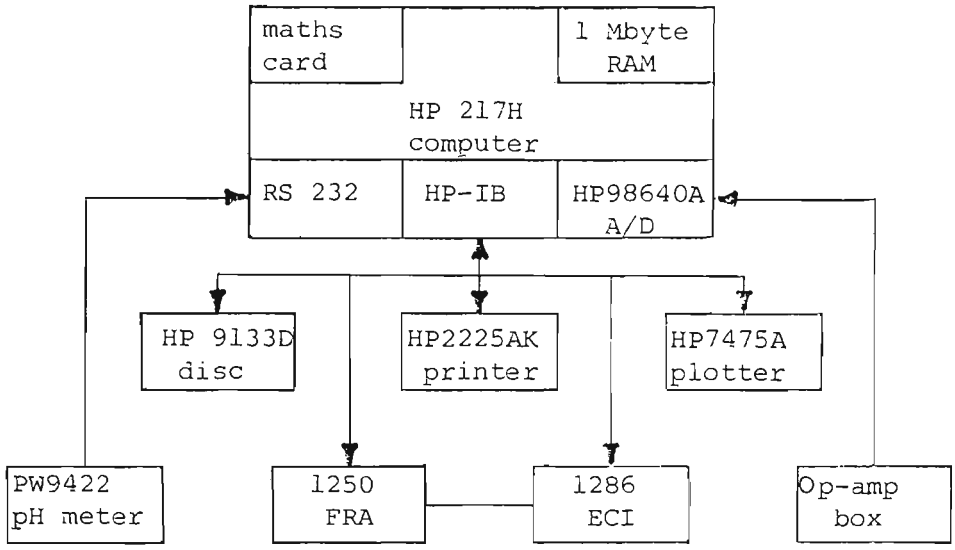

Figure E1/1. Digital instrumentation used in the electrochemical test system. FRA Frequency Response Analyzer; ECI Electrochemical Interface; A/D analogue-to-digital. Refer Section E1/1.

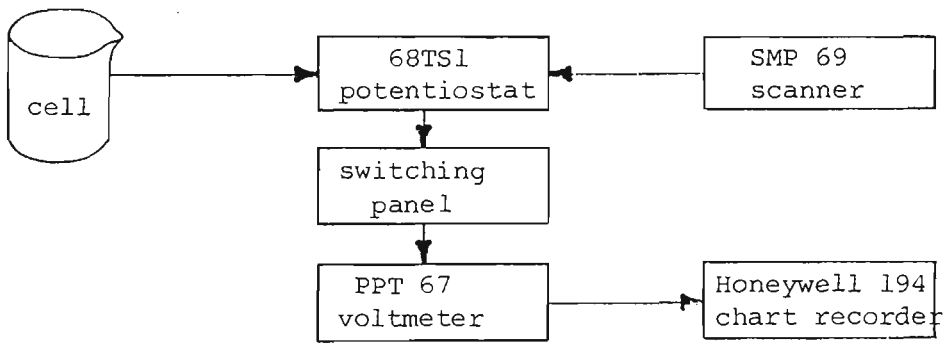

Figure E1/2. Analogue instrumentation used in the electrochemical test system. Refer Section E1/1.

The analogue instrumentation is shown in Figure E1/2. The central instrument was a Wenking Model 68TS1 potentiostat. With the aid of the external switching panel, this could be wired as either potentiostat, galvanostat or zero resistance ammeter. A Wenking Model SMP 69 Scanning Potentiometer could be used to superimpose a potential on the potentiostat's potential and thus serve to obtain potentiodynamic or galvanodynamic polarization curves. A Wenking Model PPT 67 Precision Potential Meter was capable of measuring working/reference potentials and served as both a very high impedance voltage follower (preventing polarization of small commercial saturated calomel reference electrodes) and as a means of backing off the unwanted portion of the voltage and thereby raising the measurement sensitivity. A Honeywell Model Electronik 194 Lab Y/t recorder was used to record results from polarization resistance and polarization curve tests.

2. Electrochemical test system computer programs - overview

A series of programs has been written in HP BASIC 5.0 (a powerful Fortran-like operating system supplied by Hewlett-Packard), to form an electrochemical test system. The test system comprises one main controlling program, CONTROL, which allows the operator to select a number of subprograms. These subprograms are either related to one of three electrochemical test methods (impedance, galvanic current, corrosion current) or are concerned with general computer tasks such as plotting, sample number allocation or data storage and retrieval.

The three test method subprograms control instruments dedicated to the collection of electrochemical data. Each instrument can be set up in a specified manner by the computer under program control so that

experiments on electrochemical cells are initiated and data collected. This data is then either tabulated, plotted, stored on disc or further analyzed. Details of each program, together with a flowchart, appear in Section A1. A typical sequence of events for an experiment by either of the three test methods would be:

1. allocation of sample numbers
2. enter sample immersion time
3. perform electrochemical test
4. store data results
5. plot data
6. further analysis of data

3. Sample number allocation

Samples were identified by a number code using program SAMPLE_NUM, see Section A1/6.2. These codes, plus associated information, were stored on the computer's hard disc. A number of samples, called a series, were usually tested for each experiment and the series was given a title. A sample series could be further divided into groups, each group representing a different parameter, eg primer thickness, to be evaluated. Each group contained a number (from 1 to 5) of identical samples, and was given a distinct title. Sample details such as sample area and initial immersion time were recorded to assist in the later calculation of results, eg conversion of corrosion rates to unit area, or calculation of immersion time interval. All this information could be retrieved from disc by an operator upon entering the sample code.

4. Computer-controlled electrochemical tests

Three standard electrochemical tests were controlled by computer programs.

The impedance test was performed by subprogram FRA_EXPT, Section A1/4.1, which controlled the Solartron Model 1250 Frequency Response Analyzer and the Solartron Model 1286 Electrochemical Interface operating in galvanostatic mode, Section E1/1. Either a single frequency (1 kHz) or a wide frequency range (65 kHz - 0.1 Hz) test could be performed, see Section E1.2/2.

The galvanic current test was performed by program CONTROL, see Section A1/2.1,2.2. This program made periodic calls to subprogram ADC, Section A1/3.1, which used the analogue-to-digital card in the computer, see Figure E1/1 and Section E1/1. The analogue-to-digital card measured the voltage drop across a current measuring resistor, R_x, in the operational amplifier box, switched to operate as a zero resistance ammeter, see Section E1.2/3.

The corrosion current test was performed by subprogram RP_EXPT, Section A1/5.1, which controlled the Solartron Model 1286 Electrochemical Interface, Section E1/1, selected to operate in galvanostatic mode. The size and sign of current steps could be selected by the operator. These current steps were sent to the test cell and the voltage response of the working electrode recorded for data analysis, see Sections E1.1/5, E1.2/4.

5. Computer program experimental data analysis

Only minimal analysis of experimental impedance data is performed in subprogram FRA_EXPT. No data analysis was involved in the single frequency impedance test. Data was obtained in cartesian form (a+jb) from the Solartron Model 1250 Frequency Response Analyzer and stored on computer disc in this form using a coded format as described in Section A1/6.3. The wide frequency range test initially plotted data to the VDU screen as Nyquist plots, but data

could be recalculated in cartesian form as Nyquist plots of b versus a or in polar form (r,Θ) as Bode plots of either log r versus log f or Θ versus log f, see Section T1/3, and thence replotted in these forms using subprogram PLOT8, refer Section A1/7.1. Data is stored on hard disc in cartesian form using a coded format. Further analysis of all impedance plots, whether Nyquist or Bode, was carried out manually, see Sections T1/4,5.

Galvanic current/time data, obtained from subprogram ADC, Section A1/3.1, can either be converted to coulombs and mass loss in subprogram MASS_LOSS, Section A1/3.2, and stored in coded format on hard disc, or plotted using subprogram PLOT8, Section A1/7.1.

The corrosion current test performed experiments to obtain voltage/current/time data (E,I,t), using subprogram RP_EXPT, Section A1/5.1. This data was stored in coded format on hard disc. In order to calculate corrosion currents and Tafel slopes from this data, the polarization, ε, value at the steady state time must be calculated for each current step, I. Figure E1/3 indicates how this was done. The ε value can be accurately obtained even in the presence of steady, slow upward or downward drifts in corrosion potential, E_k. The value of E_k at the operator chosen voltage reading time, t_v, is calculated by extrapolating the voltage readings before the current step to t_v. The value of ε is then the difference between the voltage response, E, at t_v and the extrapolated value of E_k, that is $\varepsilon=E-[E_k]_{tv}$. The set of (I,ε) values so obtained are plotted as data points on an (I,ε) graph. Values of corrosion current, I_k, anodic and cathodic Tafel slopes, b_a and b_c are then calculated using the non-linear iterative analysis routines described in Section A1/5.2, and a curve is plotted through the data points.

6. Data Storage and Retrieval

Experimental data for each of the three experiment types were stored on disc as coded integers using subprogram STORE_DATA, Section A1/6.3. Each data set is identified by a specific sample number code and a run number, the latter indicating the particular experimental run carried out and stored for that sample. For the impedance test, frequency, f, a and b are stored. Coulombs, q, mass loss, M, and Ig/time data are stored for galvanic current tests. The corrosion current test stores the set current, the number of readings for each current step and voltage/current/time readings. Experimental run time is also stored for each experiment type.

Experimental data are retrieved from disc and decoded using subprogram EDIT_DISC, Section A1/6.4. Retrieval of data is used for listing/printing data sets, plotting or further data analysis. Besides listing a particular experimental data set, information about the data can also be accessed. This includes series and group titles, sample area, initial immersion time, experiment run time, immersion time interval and sample/run numbers.

7. Plotting

Both the impedance and galvanic current tests make calls to subprogram PLOT8, Section A1/7.1. Corrosion current tests make use of specific plotting and curve fitting routines in subprogram THEO_IK, Section A1/5.3, which have autoscaling but are otherwise inflexible. Subprogram PLOT8 is a general purpose plotting routine that can operate independently or be called from within another program, which can pass a set of defaults that select various plotting options in PLOT8 such as plot type, plot title, plot position, axis

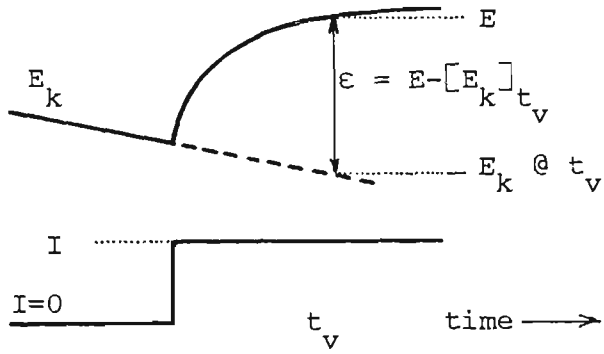

Figure E1/3. Method of determining the polarization value, $\varepsilon(=E-E_k)$, from a voltage response to an applied current step, I, in the presence of slow downward or upward drifts in corrosion potential, E_k. E_k before current step is extrapolated to the voltage reading time, t_v.

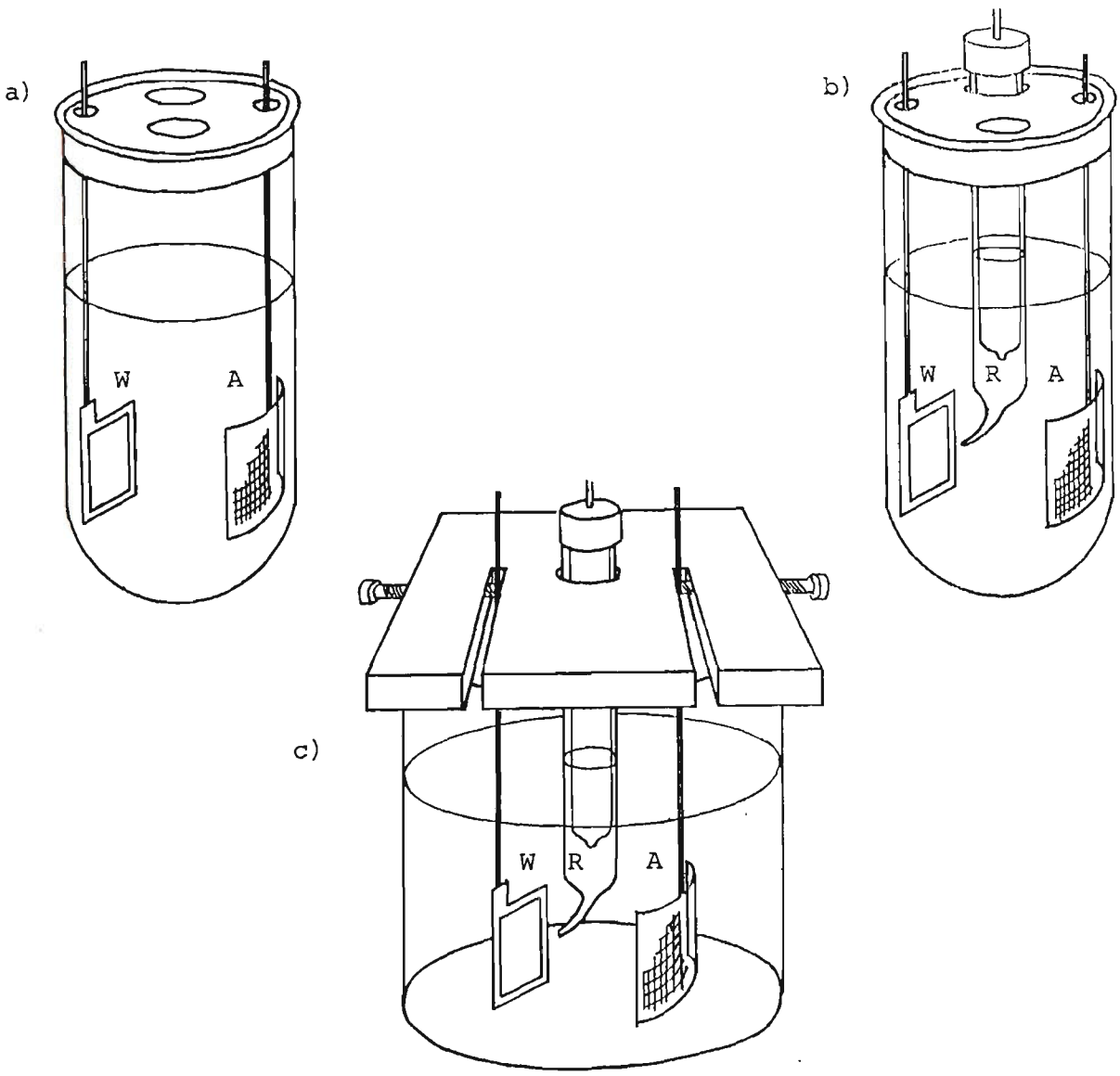

Figure E1/4. Types of electrochemical cells used in the electrochemical test system containing working, W, reference, R, and auxiliary, A, electrodes. a) 2-electrode 50C cell; b) 3-electrode 50C cell; c) 3-electrode room temperature cell.

labels, autoscaled or fixed axes, pen colour, etc. Within PLOT8, the operator can alter existing plotting options for axis range, pen choice, symbol on/off, symbol type, graph extension, plot title, output device, axis/grid choice.

E1.2 Electrochemical Techniques

1. Electrochemical cells

Two types of electrochemical cells were used - full immersion type and simulated atmospheric ACM type, both being made in 2-electrode and 3-electrode configurations, see Figure E1/4. Painted metal studies in Section E3 used the full immersion type cell, while both full immersion and ACM type cells were used in the simulated atmospheric corrosion studies in Section E2.

1.1 Full immersion type cell

The full immersion 2-electrode and 3-electrode types were similar - both consisted of a working and an auxiliary electrode. The 3-electrode configuration had an additional reference electrode. The auxiliary electrode was a large (25 cm^2) fine mesh platinum electrode, (19 holes/cm, wire diameter 0.015 cm). The working electrode was either a painted or an unpainted metal.

Impedance studies on painted metals, Section E3, employed the 2-electrode cell configuration for tests at 50°C, see Figure E1/4a. The painted metal working electrodes usually had an exposed area of 6 cm^2. The reverse face, edges and lacquered copper lead out wire were coated with Ciba-Geigy kit K273 Araldite epoxy resin. Tests showed that samples completely coated with

this resin had a much higher impedance than the impedance of painted metals under test, and therefore their contribution could be neglected. Likewise, tests showed that the impedance of the platinum auxiliary electrodes was negligible compared to the impedance of the painted metals. Therefore the impedance of the 2-electrode cell was essentially equal to the impedance of the painted metal/solution interface.

The electrodes were mounted in different cell assemblies depending on whether experiments were performed at 50°C or room temperature. For experiments at 50°C (2- or 3-electrode configuration in Figure E1/4a,b), the electrodes were mounted in stoppers cast from Dow Corning RTV 734 Silastic self-levelling silicone rubber sealant. These stoppers had four holes bored through them with a cork borer - two small holes for working and auxiliary electrodes and two large holes - one for the Luggin probe/reference electrode (for the 3-electrode cell configuration) and one (diameter 1 cm) for air access to the cell. The stopper assemblies containing the electrodes were pushed into the top of large (5 cm diameter) glass test tubes which contained 150 mL of test solution. The glass test tubes were immersed in a thermostatted (Braun Thermomix Model 1441 heater/stirrer) oil bath (Esso Marcol 82 mineral oil) at 50°C. This cell type is illustrated in Figure E1/4a. For experiments at room temperature (3-electrode configuration), the electrodes were clamped into perspex or Formica rectangular cell tops with slots cut for working and auxiliary electrodes, which were held in place by nylon bolts threaded into the cell top. A hole was drilled for the Luggin probe/reference assembly. These cell tops were placed on top of glass beakers of various sizes depending on the experiment (600 mL or 1 L). This cell type is illustrated in Figure E1/4c. Unpainted metal working electrodes had the reverse face, edges and top of the sample coated with Canning Fortolac stop-off lacquer so as to expose 6 cm^2

to the electrolyte.

The 3-electrode cell configuration for tests at 50°C is shown in Figure E1/4b and differs from the 2-electrode configuration in Figure E1/4a only by the inclusion of Luggin probe/reference electrode assembly. As shown in Figure E1/4b,c, the Luggin probe is simply a smaller test tube containing a commercial saturated calomel reference electrode that sits in the larger test tube cell. A capillary protrudes from the bottom of the smaller test tube and is bent around towards the working electrode, fronting up to within about 1 mm of the surface and having an internal/external diameter of about 1,2 mm. The Luggin probe test tube assembly minimizes the solution IR_s drop between working and auxiliary electrodes by minimizing the distance between working electrode and probe tip. This distance is a compromise which attempts to minimize the distance whilst not introducing an excessive amount of shielding of the working electrode by the Luggin probe[163]. The Luggin/reference probe assembly for the 3-electrode cell for room temperature tests is identical to that described above, see Figure E1/4c.

1.2 Simulated atmospheric ACM type cell

Both 2-electrode and 3-electrode cells were made in order to simulate atmospheric behaviour in the laboratory. These cells have been termed Atmospheric Corrosion Monitors, ACMs, also known as thin water film wafer cells. These are described in detail in Section E2.4 and shown in Figure E2/6. The 2-electrode configuration was used to measure galvanic currents flowing between dissimilar metals (eg zinc and steel) of the wafer cell, representing working and auxiliary electrodes. Three types of 2-electrode cells were made - zinc/steel, cast and rolled Zn-55%Al alloy/steel. The 3-electrode

configuration was used to measure polarization resistance, corrosion currents, Tafel slopes of the working electrode or impedance of the cell. It consisted of working, reference and auxiliary electrodes, all of identical material. Three types of 3-electrode cells were made - zinc, steel, and rolled Zn-55%Al alloy.

2. Impedance test

Both single frequency (1 kHz) and wide frequency range impedance tests were carried out. The single frequency test was used only for painted metal studies in Section E3, whilst the wide frequency range test was used for both painted (Section E3) and unpainted metal (Section E2) studies. Impedance tests were performed using 2-electrode cell configuration, Section E1.2/1.1, for full immersion painted metal studies in Section E3, and 3-electrode ACMs (in which the lead out wire from the reference plates was left unconnected) for simulated atmospheric ACM type cells, Section E2.6/4.

2.1 Single frequency (1 kHz) test

The single frequency test is performed using the same instrumentation and technique as the wide frequency range test, as per Section E1.2/2.2, except that a frequency sweep is not performed. A frequency of 1 kHz is selected, sent through the test cell and a measurement of impedance, $Z=a + jb$ is made. Repeat measurements can be made as often as desired, or the frequency can be switched off. Measurement intervals are indicated in Section E3.2/4.2 for attached paint films, and Section E3.2/4.4 for free paint films.

2.2 Wide frequency range test

A sine wave frequency sweep is initiated, starting at the maximum frequency (65 kHz) of the Solartron Model 1250 Frequency Response Analyser, FRA, and finishing at a frequency selected by the operator (usually 0.1 or 1 Hz). The FRA generates a sine wave voltage, e_g, which is converted into a sine wave current, i_{cell}, by the Solartron Model 1286 Electrochemical Interface, ECI, see Figures E1/1, E1/5, operating in galvanostatic mode, and sent through the 2-electrode cell configuration, Section E1.2/1. The sine wave voltage response from the cell, e_{cell}, is compared with the generated sine wave current in the analyzer section of the FRA. By selecting a [channel 2/channel 1] ratio measurement, and a divide by factor of 1/Rx (Rx = current control resistor selected in ECI), in the set-up of the FRA, as controlled by program FRA_EXPT, see Section A1/4.1, the resistive, a, and reactive, b, components of impedance, Z, are displayed on the FRA according to Equations (E1-E2).

$$Z = e_{cell}/i_{cell}$$

$$= (e_{cell}/e_{x}.)\, Rx$$

$$Z = Ch2/Ch1.Rx \qquad (E1)$$

$$= a + jb \qquad (E2)$$

A downward frequency sweep direction is preferable to an upward sweep because it has been found that low frequencies (around 1 Hz and less) temporarily change the impedance of the immersed painted metal more so than high frequencies. The impedance data will be more accurately obtained from a downward sweep.

The galvanostatic method (sine wave currents) rather than the potentiostatic

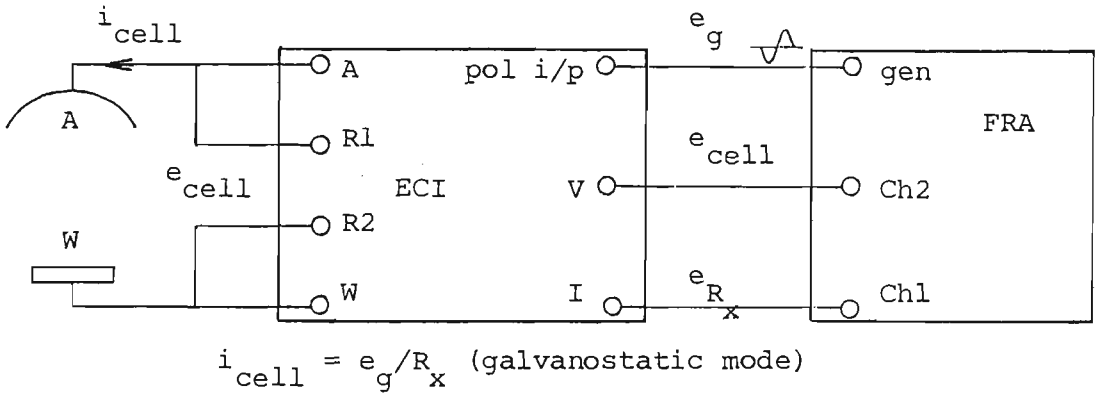

Figure E1/5. The wide frequency range test. Frequency Response Analyzer, FRA, generates a sinewave voltage, e_g. This is converted into a sinewave current, i_{cell}, by the Electrochemical Interface, ECI, using its nternal current control resistor, R_x, and sent through the 2-electrode cell. W, A working, auxiliary electrodes of cell; also refers to working, auxiliary electrodes of cell; also refers to working, auxiliary inputs to ECI; R1, R2 reference inputs to ECI; gen FRA generator output; pol i/p polarization (external) input of ECI.

method (sine wave voltages) was preferred because the potential of paint films is not very stable with immersion time, which would require continual adjustment of the potentiostat's control potential to ensure that the dc current is zero. The galvanostatic method does not require a reference electrode for impedance measurements, and is therefore simpler to use. Although the painted metal impedance is in the control circuit of the galvanostat with the galvanostatic mode, it has been possible to measure the impedance of paint films having resistances in excess of 30 M ohm. Stray cell capacitance can alter the shape of the Nyquist impedance plot at high frequencies and particularly the intercept on the a-axis, commonly interpreted as solution resistance. This has been discussed elsewhere[16] along with methods of compensation for stray capacitance. No compensation for stray capacitance was made for any of the results presented in this thesis.

3. Galvanic current test

Galvanic current tests, Section E2.6/2, were performed on 2-electrode ACM cell configurations, Section E1.2/1.2. Galvanic currents were measured by connecting the lead out wires from anode and cathode dissimilar metal plates of the ACM wafer cell up to a 'home-made' operational amplifier box switched to operate in zero-resistance ammeter mode, see Section E1.1/4. After switching the box on, a shorting link between the two dissimilar metals of the ACM was removed and the galvanic current measured as the voltage drop, V_g, across a current measuring resistor, R_x, see Figure T2/3 in Section T2/3. Periodically, and automatically, measurements of Vg were made using the computer's analogue-to-digital card, see Section A1/3.1.

4. Corrosion current tests

Corrosion current tests were performed on simulated atmospheric ACM type cells, Section E2.6/5. Tests were conducted using the computer controlled Solartron Model 1286 Electrochemical Interface, ECI, in galvanostatic mode for corrosion current tests, Sections E1.1/4 and E2.6/5. When the working electrode's corrosion potential, E_k, had become reasonably steady with time, a series of current steps were sent through the electrochemical cell, and the voltage response of the working electrode was monitored on computer screen. Between each current step the current was switched off after about 10 seconds, and the corrosion potential monitored until a reasonably steady value was again reached. Figure T3/3, Section T3/3 schematically illustrates a series of current steps and voltage responses obtained in a typical experiment. The current steps differ in magnitude and sign so as to produce a polarization curve either side (anodic and cathodic) of E_k, see Section T3/3. The order of obtaining the current steps was either a series of anodic steps followed by a series of cathodic steps or an anodic step followed by a cathodic step. The latter method is probably better because small changes (pH or metal ions) produced by the anodic step would be minimized by the cathodic step, which may possibly result in better curve fitting of the (I,ε) data.

Slow steady upward or downward drifts in E_k prior to the current step could be tolerated because the value of E_k was extrapolated to the voltage response reading time in computer program, RP_EXPT, see Figure E1/3, Section E1.1/5. The times for reading the voltage response approximate the times to a steady state situation and are given in Section E2.6/5 for ACM tests. The frequency of performing the corrosion current test is also given.

E2.1 Phthalate-buffered 0.1 M NaCl, pH 5.3 (refer Section E2.2/1.4)

Phthalate-buffered 0.1 M NaCl solution, pH 5.3, was made by adding potassium hydrogen phthalate solution (500 mL, 0.1 M $KHC_8H_4O_4$) to sodium hydroxide solution (315 mL, 0.1 M NaOH), sodium chloride (5.845 g NaCl) and diluting to 1 litre. The pH was adjusted to pH 5.3 with 0.1 M NaOH solution.

E2.2 Metals/Alloys

1. ACM tests (refer Section E2.6)

1.1 Steel

capped steel sheet, coils 4277, 1452 abraded to #600 grade.

dimensions (mm):	Coil -	75(l) x 35(w) x 0.53 av (thick)	ACM1
	Coil 4277	67(l) x 35(w) x 0.86 av (thick)	ACM2,5,9
	Coil 1452	67(l) x 35(w) x 0.68 av (thick)	ACM6,7

analysis: (%): Coil 4277

C	P	Mn	Si	S	Ni	Cr	Mo	Cu	Al	Sn
.04	.01	.24	.000	.01	.02	.01	.002	.01	.004	.000
	Ti	Nb	N	O						
	.002	.004	.003	.06						

1.2 Zinc

soft Titan zinc rolled sheet abraded to #600 grade.

dimensions: 67(l) x 35 (w) x 0.65 (thick) ACM2,3,7

analysis: (%)

Zn	Ti	Cd	Cu
>99.97	<0.02	0.004	0.004

1.3 Cast Zn-55%Al alloy

cast Zn-55%Al alloy, water quenched abraded to #600 grade.

dimensions (mm): 60(l) x 35 (w) x 2.36 av (thick) ACM1

analysis (%):

	Zn	Al	Fe	Si
cast Zn-55%Al alloy	41.6	56.6	0.90	1.05
typical ZINCALUME coating	42.8	55.2	1.02	1.02

The Zn-55%Al alloy was cast by pouring molten alloy, taken from the ZINCALUME production line bath, into a preheated steel mould, followed by water quenching after the alloy had solidified. Alloy plates, approximately

90 x 90 x 2 mm were produced by this procedure and cut with a hacksaw to the required plate size (2.36 av x 70 x 25 mm) for manufacturing ACMs, approximately 70 x 25 x 2.36 av mm for working and auxiliary plates, see Section E2.4/2.

The corrosion characteristics of cast Zn-55%Al alloy were evaluated and compared with rolled/heat treated Zn-55%Al alloy and a typical ZINCALUME coating, Section E2.2/1.4. Results are discussed in Section R1.2/3.

1.4 Rolled Zn-55%Al alloy

rolled Zn-55%Al alloy, heat treated 400°C for 0.5 hour, furnace cooled to 260°C and held for 24 hours, furnace cooled, abraded to #600 grade.

dimensions (mm): 67 (l) x 35 (w) x 0.82 (thick) ACM4,5,9

analysis (%):

	Zn	Al	Fe	Si
cast Zn-55%Al alloy	41.5	56.9	0.57	1.01
typical ZINCALUME coating	42.8	55.2	1.02	1.02

The Zn-55%Al alloy was cast by pouring molten alloy, taken from the ZINCALUME production line bath, into a preheated mould and allowed to cool in air. Alloy rectangular bars, approximately 20 x 50 x 175 mm were produced. These were rolled over about five passes in an experimental rolling mill at 350°C, which resulted in about a 25% reduction. A further pass split the bar down the middle. After air cooling, one half of the bar was cold rolled by 50-60% and annealed for 60 hours at 260°C. Further passes of cold rolling and annealing were performed to achieve the desired thickness of approximately 1 mm.

A number of final annealing cycles were attempted in order to produce a microstructure as close to the ZINCALUME coating structure as possible. The main aim of the anneal cycle was to coarsen the β-phase particles. The anneal

cycle chosen as being the best approach was to heat at 400°C for 0.5 hour, furnace cool to 260°C and hold for 24 hours, followed by furnace cooling to room temperature. Rolled alloy strip, about 500 x 70 x 0.9 mm was produced by this procedure and cut to the required plate sizes for manufacturing ACMs, approximately 62 x 35 x 0.9 mm for working and auxiliary plates, and 67 x 35 x 0.9 mm for reference plates, see Section E2.4/2.

The corrosion characteristics of the rolled (and cast, Section E2.2/1.3) Zn-55%Al alloy were compared against that of a typical ZINCALUME coating, see Section E2.2/1.5, by immersion in phthalate-buffered 0.1 M NaCl solution, pH 5.3 at room temperature, Section E2.1, over 38 days. This solution was chosen because the corrosion characteristics of ZINCALUME coated steel had previously been determined in it[164]. The slightly acidic buffer solution resulted in soluble corrosion products of zinc, and the total life of the coating (Zn-rich and Al-rich phases) could be evaluated in a period of weeks. The corrosion potential, E_k, was measured as a function of immersion time using the analogue potential meter, Section E1.1/1, and an electrochemical 3-electrode full immersion type cell, Section E1.2/1.1. The exposed area of the working electrodes was 3.5 cm^2. Results are discussed in Section R1.2/3.

1.5 Unpassivated ZINCALUME coated steel (refer Section E2.2/1.4, E2.6/3)

AZ150 (75 $g.m^{-2}$ Zn-55%Al coating per side) ZINCALUME coated steel sheet, coil X0525, oiled, unpassivated production line feed from paint line. Material degreased with MEK prior to use.

2. Pollution Gas Box, PGB, weighed mass loss tests (refer Sections E2.5)

2.1 Steel sheet. Same as ACM tests (Coil 4277), Section E2.2/1.1.

dimensions (mm)	exposed area (mm^2)	expt no.
70 (l) x 30 (w) x 0.86 (thick)	1500	(PGB99-112)
35 (l) x 30 (w) x 0.86 (thick)	750	(PGB113-139)
35 (l) x 30 (w) x 0.86 (thick)	530	(PGB140)
35 (l) x 30 (w) x 0.86 (thick)	338	(PGB145-147)
30 (l) x 22 (2) x 0.86 (thick)	338	(PGB148-158)

2.2 Zinc sheet. Same as for ACM tests, Section E2.2/1.2

35 (l) x 30 (w) x 0.58 (thick)	750	(PGB117-128)
35 (l) x 30 (w) x 0.58 (thick)	530	(PGB144)
35 (l) x 30 (w) x 0.58 (thick)	338	(PGB145-147)

2.3 Galvanized steel sheet

A. Z300 passivated galvanized steel sheet, 16/3/84, Coil No. A81307

dimensions (mm)	exposed area (mm^2)	expt no.
35 (l) x 30 (w) x 0.80 (thick)	750	(PGB113-116)

coating mass ($g.m^{-2}.side^{-1}$)	150 (side A)	200 (side B)
total chromium ($mg.m^{-2}$ surface)	13	13

B. Z300 unpassivated galvanized steel sheet

dimensions (mm)	exposed area (mm^2)	expt no.
35 (l) x 30 (w) x 0.64 (thick)	750	(PGB129-139)
35 (l) x 30 (w) x 0.64 (thick)	530	(PGB140)

2.4 ZINCALUME coated steel sheet

A. AZ150 passivated ZINCALUME coated steel sheet Coil No. 3615-20

35 (l) x 30 (w) x 0.49 (thick)	750	(PGB113-116)
total chromium ($mg.m^{-2}$ surface)	33 (side A)	28 (side B)

B. AZ150 unpassivated ZINCALUME coated steel sheet Coil No. 0525

35 (l) x 30 (w) x 0.52 (thick)	750	(PGB129-139)
35 (l) x 30 (w) x 0.52 (thick)	530	(PGB140)

2.5 Cast Zn-55%Al alloy plates. same as ACM tests, Section E2.2/1.3

dimensions (mm)	exposed area (mm^2)	expt no.
70 (l) x 30 (w) x 4 (thick)	1500	(PGB99-112) (PGB117-128)

2.6 Rolled Zn-55%Al alloy plates. Same as for ACM tests, Section E2.2/1.4

dimensions (mm)	exposed area (mm^2)	expt no.
35 (l) x 30 (w) x 0.63 (thick)	530	(PGB144)
30 (l) x 27 (w) x 0.63 (thick)	338	(PGB145-147)

2.7 Aluminium sheet

35 (l) x 25 (w) x 0.65 (thick)	530	(PGB144)
35 (l) x 25 (w) x 0.65 (thick)	338	(PGB145-147)

E2.3 Pollution Gas Box, PGB

1. Design

Figure E2/1 is a flowchart of the pollution gas box, PGB, system which is based on apparatus used by Spedding[165] and Johnson and Bromley[166]. Essentially, this is a constant temperature environment containing three test chambers through which humidified laboratory air, which can be mixed with a pollutant gas, flows. Test samples are exposed to the air stream in the test chambers.

2. Air pump

Laboratory air (6 $L.min^{-1}$) is first passed through a Drechsel bottle containing glass wool and acting as a dust filter, and thence through a flowmeter (Gilmont No. 13 200-12 500 $mL.min^{-1}$). The air stream is pushed through the PGB system by an air pump (Iwaki diaphragm air pump Model AP 115A, maximum capacity 15 $L.min^{-1}$).

3. Relative humidity control stage

Following the pump is a relative humidity control stage, Figure E2/2. This

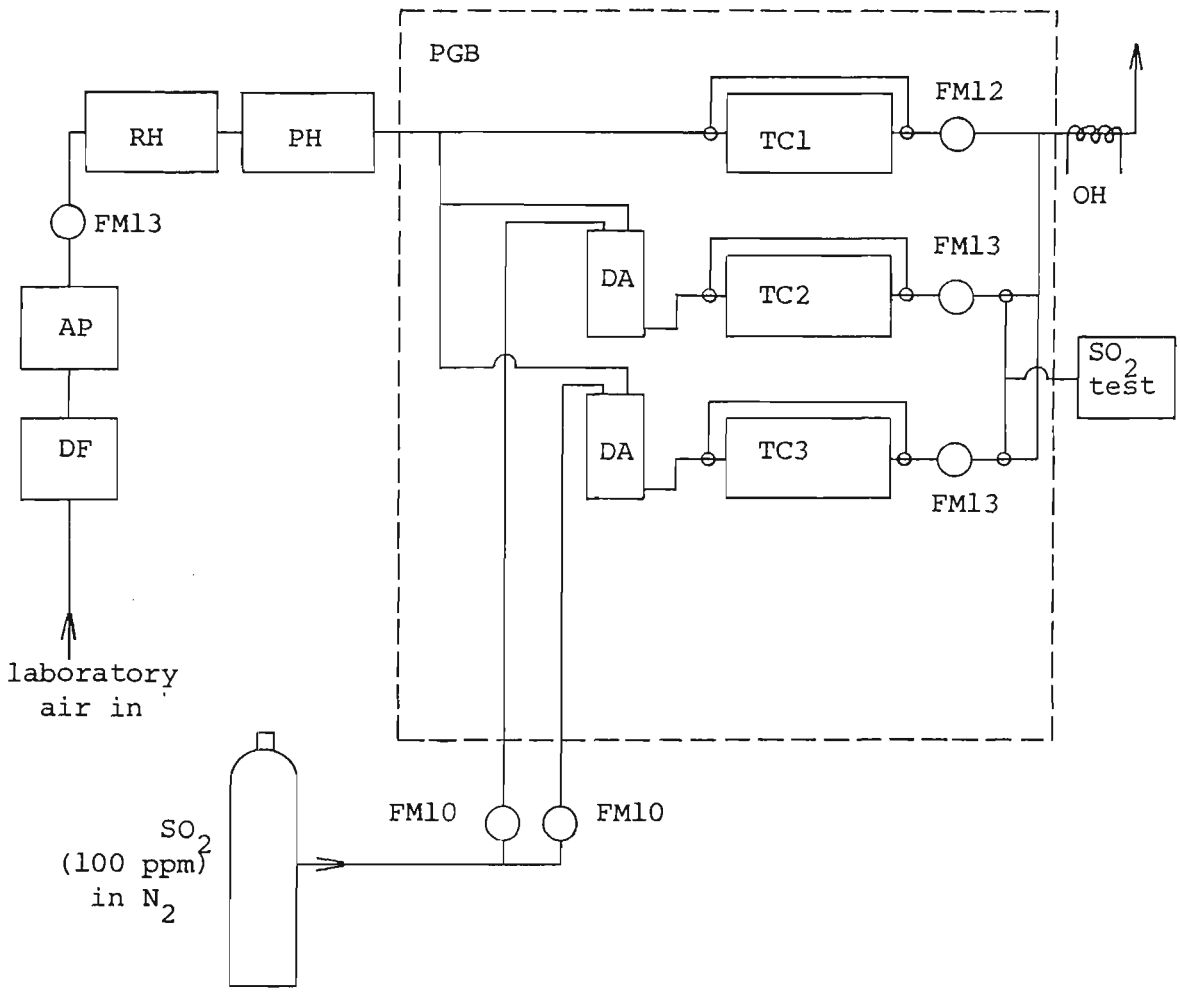

Figure E2/1. Flowchart of pollution gas box, PGB. DF dust filter; AP air pump; RH relative humidity controller; PH preheater; DA dilution apparatus; TC test chamber; OH outlet heater; FM flow meter (FM10,12,13 Gilmont No. 10,12,13).

Figure E2/2

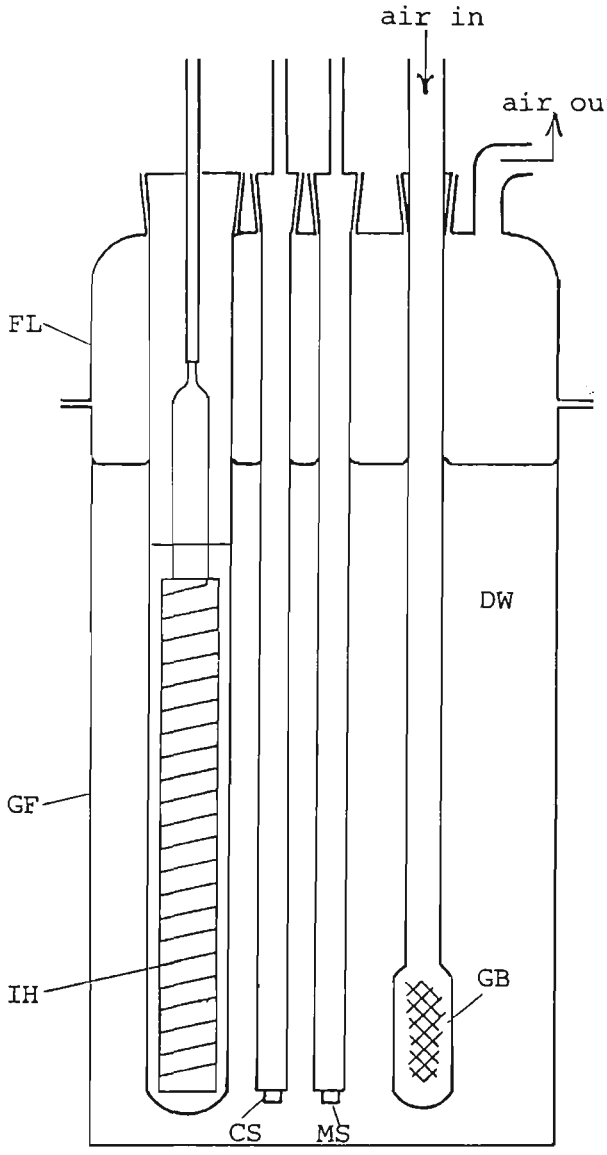

Figure E2/3

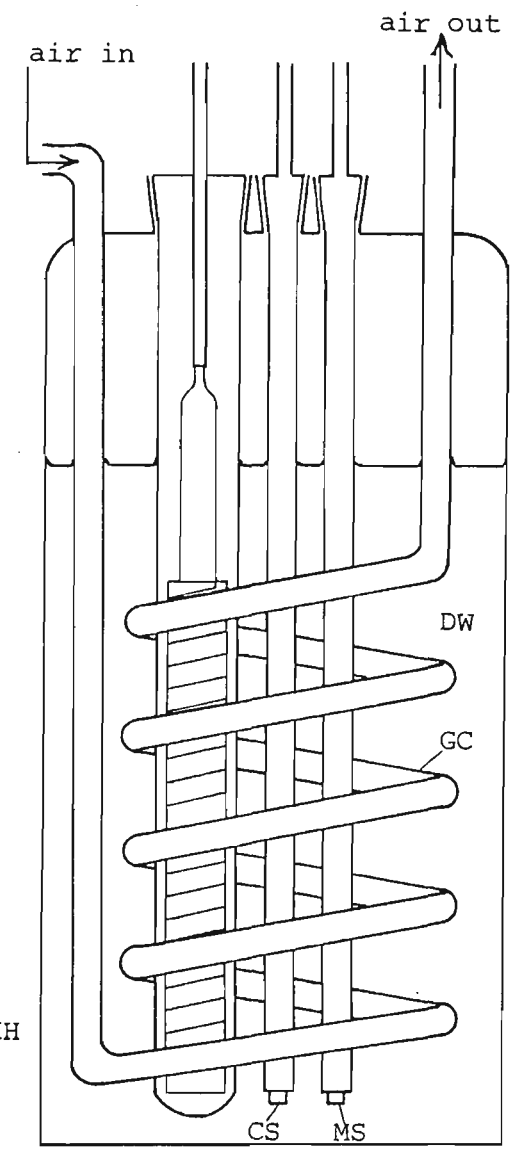

Figures E2/2,3. Relative humidity control stage (Fig. E2/2), and preheater (Fig. E2/3) in pollution gas box, refer Fig. E2/1. GF glass flask; FL flanged lid; GB gas bubbler; DW distilled water; IH immersion heater; CS control sensor; MS temperature measuring sensor; GC glass coil.

consists of a large (1 L capacity) cylindrical glass flask with a flanged lid. The flask is filled with distilled water. The air stream is passed via a coned glass joint (B19/26) in the flanged lid through a gas bubbler (zero porosity glass frit) which is immersed in the water. The gas stream is thereby broken up into a fine stream of bubbles and will become 100% saturated at the temperature of the water. The water temperature is controlled by a thermoregular operating a fish tank heater (150 W) and is sensed by a transistorized sensor. The heater is immersed in oil contained in a glass finger which is itself immersed in the water. The sensor is fixed with sealant (Silastic RTV 732 silicone rubber) at the bottom of a long, thin glass tube and makes intimate contact with the water. The water temperature is measured by a separate integrated circuit sensor, fixed in the same manner as the thermoregular's sensor. All three glass fingers are attached to the flanged glass lid. The relative humidity of the air stream was calculated[167] knowing the temperatures of the water (the wet temperature) and the test chambers (the dry temperature).

4. Preheater

After the relative humidity control stage, the air stream is passed through a preheater and then into the PGB itself. The preheater, see Figure E2/3, warms the air stream up to the temperature of the PGB and thus lowers its relative humidity towards that required in the test chambers. The preheater is a cylindrical glass water jacket containing a glass helical coil immersed in water, through which the air stream flows. The water jacket has inlets for a fish tank heater, a thermoregulator sensor and a measuring sensor, as described in Section 2.3/3.

5. Pollution gas box housing

The PGB housing is a perspex box (710 w x 520 h x 410 d mm) which contains three test chamber flowmeters (Gilmont 1x No. 12 20-2100, 2 x No. 13 200-12 500 $mL.min^{-1}$), three test chambers and two gas dilution chambers, through which the air stream flows. The temperature of the PGB housing was controlled at 35°C by a thermoregular operated by a sensor and a fish tank heater, see Section E2.3/3. An air fan (Dick Smith rotary fan model Y-8500) circulated hot air surrounding the heater around the entire PGB housing.

6. Test chambers

Three glass test chambers are contained in the PGB housing. These contain test samples to be evaluated. Two of the test chambers can operate at varying levels of pollutant gas which is bled into the gas stream via gas dilution chambers, Section E2.3/7. The test chambers, see Figure E2/4, are glass cylinders (diameter 100 mm ID, approx 250 mm high) with a flanged glass lid at the top which is clamped to the test chamber with clamps (8 x 32 mm fold back clamps). The air flow enters via a tap (Interflon teflon tap) and a coned glass joint (B19/26) at the top of the flanged lid and exits via a similar tap at the bottom of the test chamber. These taps are used to bypass the air stream around the test chamber when samples are being placed in it. The test samples are located on a glass grid near the bottom of the test chamber. Thus the air stream must impinge on the sample surface as it travels through the test chamber. The flanged lid has inlets for a temperature sensor (via a B19/26 coned glass joint), see Section E2.3/3, and a pressure gauge (via a B34/35 coned glass joint). The pressure gauge (Dobbie Instruments 0-40 kPa) measures the pressure in the test chamber, which is normally 20 kPa above

Figure E2/4

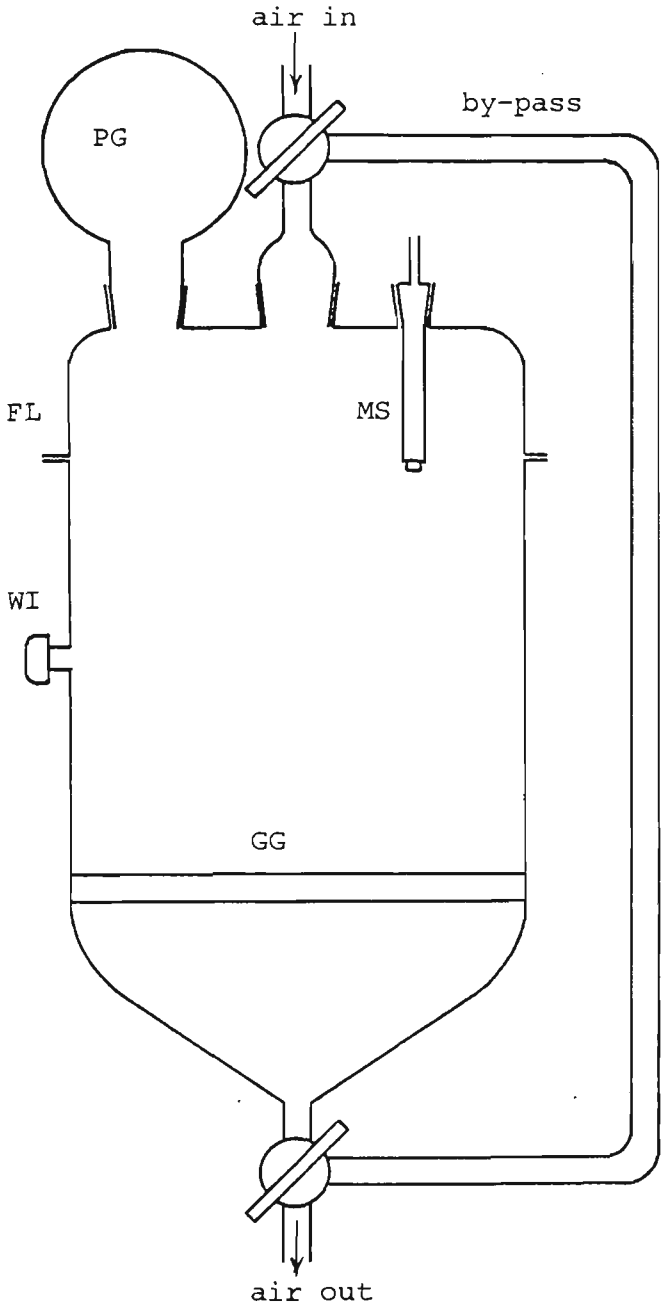

Figure E2/5

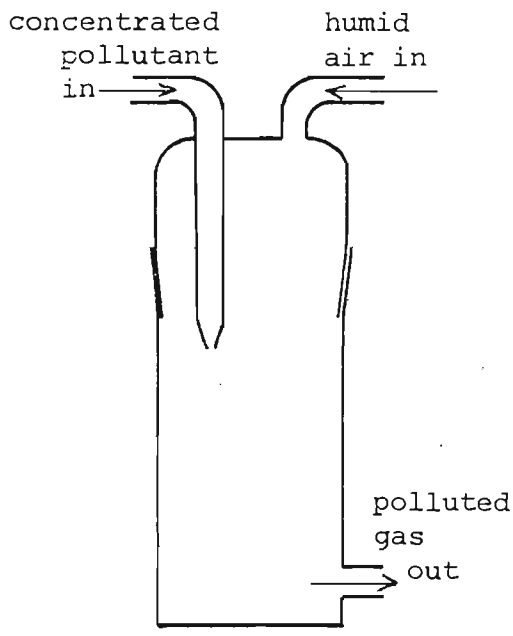

Figures E2/4,5. Pollution gas box test chamber (Fig. E2/4) and gas dilution apparatus (Fig. E2/5). FL flanged lid; GG glass grid for test samples. MS temperature measurement sensor; PG pressure gauge; WI lead out wire inlet.

atmospheric pressure. This pressure build-up is caused by the flow rate (2 $L.min^{-1}$ in each test chamber) and the resistance to air flow due to taps, tubing, flowmeters, etc. Three lead out wires allow ACM samples to be connected to the PGB electrical control box and thence to a potentiostat. These wires enter the side of the test chamber near the bottom via a plastic screw on thread and a plastic seal plus sealant (Silastic RTV 732 silicone rubber).

7. Gas dilution chambers

Immediately prior to test chambers 2 and 3, see Figure E2/1, are two gas dilution chambers, which allow pollutant gas to be bled into the humidified air stream via a glass coned joint (B40/38), see Figure E2/5. Humidified air enters the gas dilution chamber at the top via a second inlet and the flow of air (2 $L.min^{-1}$) mixes with the much lower volume of pollutant gas (9-20 $mL.min^{-1}$) prior to exit near the bottom of the gas dilution chamber, and thence into the test chamber.

8. Inlet/outlet tubing

All inlet tubing from the cylinder of pollutant gas to both flowmeters and gas dilution chambers, plus all outlet tubing from the PGB was stainless steel (type 316, 6 mm OD, 1 mm wall), connected together with stainless steel unions. All tubing internal to the PGB housing was glass.

The outlet tubing was wired with a heating coil and controlled by a thermoregulator operating at 40°C. This was necessary to prevent condensation in the tubing. Inlet tubing between preheater and PGB housing

was polyvinyl chloride tubing lagged with a thermal insulating tape.

9. Pollutant gas

The pollutant gas was provided from a cylinder of sulphur dioxide in nitrogen (CIG Spectra-seal 100 ±2 ppm SO_2 in N_2, calibrated by CIG).

The concentration of SO_2 in test chambers 2 and 3 was controlled by two flowmeters (Gilmont No. 10 0.2-90 mL.min^{-1}). For example, a concentration of 0.1 ppm SO_2 in the test chamber could be achieved by setting a flow rate of 2 mL.min^{-1} of the pollutant gas for an air flow rate of 2 L.min^{-1}. Tests covered the range 0-1.0 ppm SO_2.

10. Calibration procedures

10.1 Flowmeters

The flowmeters, refer Figure E2/1, were calibrated using a bubble flowmeter (HP model number 0101-0113) as the time taken for a bubble to travel between 0 and 1 mL calibration points; by displacement of water in an inverted gas bottle; and by an LPG flowmeter (Aichi Tokei Model ED22). All methods gave calibration results which were within the limit of setting of the particular flowmeter, typically 2% low. No attempt was made to correct the readings obtained directly from the flowmeters.

10.2 Temperature sensors

The temperatures of the humidity control stage, preheater and test chambers are all measured using LM334 current generator integrated circuit

temperature sensors which produce an output current which increases linearly with temperature. These sensors are connected to a digital thermometer (Electronics Australia kit). The sensors were all calibrated together at 35°C to within 0.10°C in a thermoregulated fish tank, by comparing with a glass thermometer (Emil gold line).

E2.4 Atmospheric Corrosion Monitor, ACM, Construction

1. Description

The Atmospheric Corrosion Monitors, ACM, were manufactured of metal plates standing on end, each plate separated from its neighbour by a thin mylar insulator. The plates were set in epoxy resin and the surface machined down to a smooth finish onto which a thin water film was placed. Two types of ACMs were made - a 2-electrode type and a 3-electrode type.

The 2-electrode type consisted of alternative plates of two dissimilar metals, such as zinc and steel. This type was used to measure the corrosion resistance of the more anodic metal (in this case zinc), and also to give a measure of its ability to sacrificially protect the more cathodic metal (in this case steel) plates. Galvanic current was measured between the dissimilar metal plates, by connection to a potentiostat wired as a zero resistance ammeter.

The 3-electrode type was made of only one type of metal in a similar manner to the 2-electrode type. Each third plate was connected together, see Section E2.4/2, so that there were essentially three electrodes - working, reference and auxiliary which were connected to a potentiostat. This type was used to measure electrochemical parameters such as impedance, corrosion current,

and Tafel slopes. This was useful in determining the way in which corrosion resistance changes with time of wetness or pollutant level, and was especially useful for samples with low corrosion rates which could not easily be measured by mass loss techniques. Sections T2/2 and T5 gives details on the theory of ACMs.

2. Construction method

The following method of ACM construction is an improved method based on other authors' designs, see Section T5/2.

Details of the materials used and initial plate dimensions are given in Section E2.2/1. Final plate sizes are shown in Figure E2/6a (working and auxiliary plates for both 2- and 3-electrode type ACMs) and in Figure E2/6b (reference plates for 3-electrode type ACMs). The order of assembling the metal plates for a 2-electrode type ACM was different to that of a 3-electrode type. In a 2-electrode type ACM, alternate pairs of dissimilar metals were used, repeated a number of times. Thus the order of assembly was:

W A W A W A W A ....W

where W represents the working electrode (eg zinc) and A represents the auxiliary elecgrode (eg steel). Either end was terminated in a working electrode plate to ensure that each auxiliary electrode plate was properly sacrificially protected on either side. Figure E2/6c is a schematic of the method of assembly of 2-electrode type ACM plates. In a 3-electrode type ACM, all plates were of the same material, but each third plate was connected together. The order of assembly was:

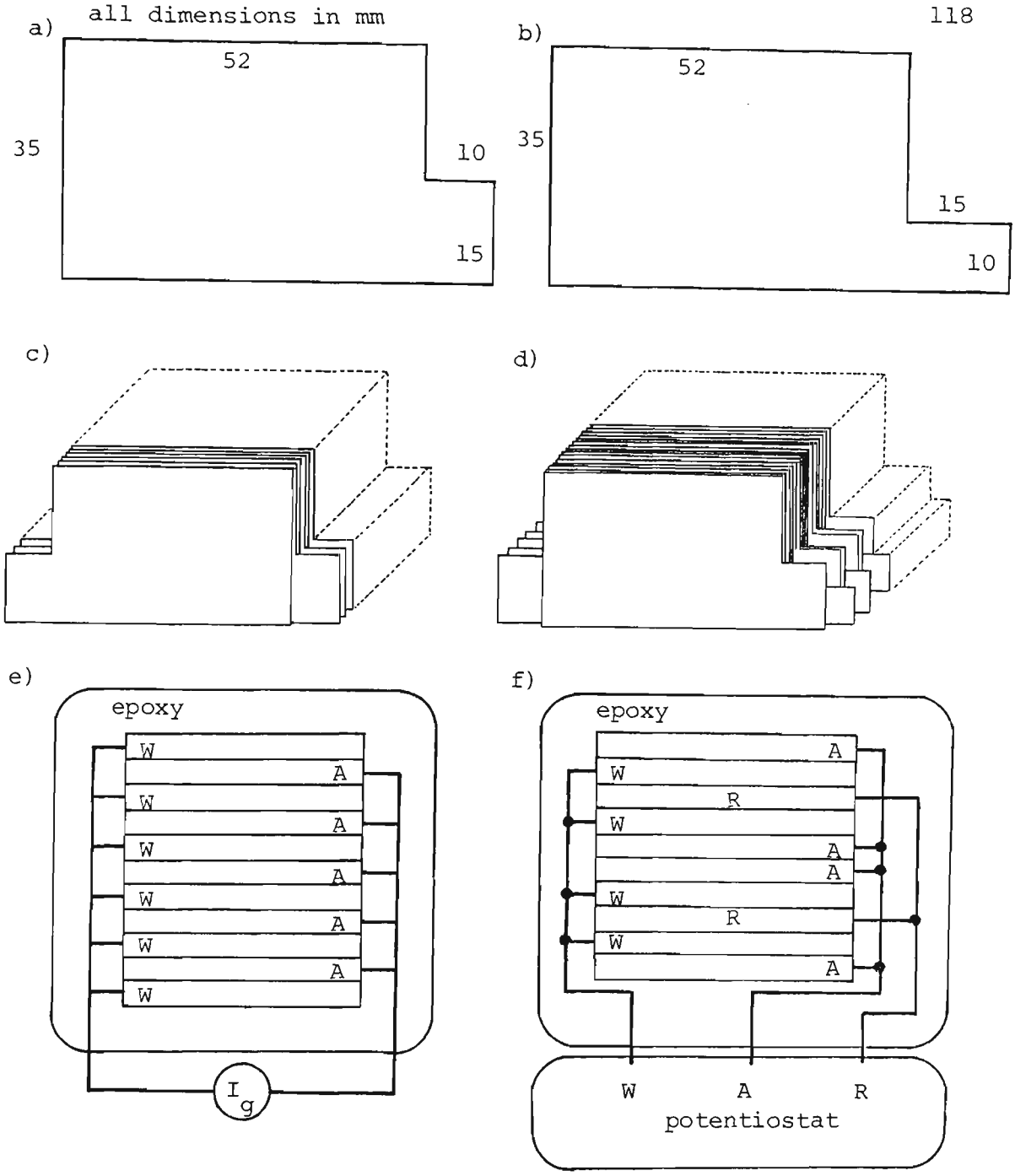

Figure E2/6. Design of atmospheric corrosion monitors, ACM. a) working, auxiliary plate dimensions for 2- and 3-electrode ACMs; b) reference plate dimensions for 3-electrode ACMs; c),d) schematic of method of assembly of 2-electrode, 3-electrode ACMs, respectively; e),f) method of connection of lead out wires for 2- and 3-electrode ACMs, respectively. W,R,A working, reference, auxiliary electrode; Ig galvanic current.

A W R W A A W R W A A W R W A .....

where W, A have the meaning given above and R represents a reference electrode plate. Figure E2/6d is a schematic of the method of assembly of 3-electrode type ACM plates.

All plates were ground to #600 grade finish with silicon carbide paper to make them sufficiently flat, and burrs were abraded off the edges. Pairs of plates, each separated by a thin mylar insulator (23 μm, corona discharge treated one side), were glued together using epoxy (Ciba Geigy LC191 Araldite epoxy resin; HY951 hardener in the ratio of 8:1), which were pressed together and held with weights whilst drying. After setting, pairs of plates were glued to plate pairs in the same manner to make a 4-plate combination. Then 4-plate combinations were glued to 4-plate combinations to make 8-plate combinations, and so on. This method ensured that a thin, uniform layer of epoxy was sandwiched either side of each plate and mylar insulator section which prevented leakage of water down between adjacent plates during experiments. The entire ACM was held together with epoxy and thus circumvented the need for bolts to clamp the plates together. Experience showed that the latter method frequently resulted in unwanted short-circuits between plates during experiments and that extreme care was necessary in deburring all the holes drilled in each plate.

The final combination of plates had lead-out wires soldered to the plate ends, as shown in Figure E2/6e,f, which also connected all plates of each type together, eg all working electrode plates. The plate assembly was then encased in the same epoxy and abraded flat to a #600 grade finish to reveal a smooth surface consisting of metal plate ends with mylar and epoxy

sandwiched in between.

3. Table of ACM details

Table E2/1 shows the various types of 2-electrode and 3-electrode ACMs that were made, along with plate dimensions and exposed areas. Although ACM plate areas were different for different ACMs, a constant area was exposed for a 0.5 mm wafer film from PGB runs 238 onwards, by masking off the remaining area of each ACM with wax Chinagraph pencil, see column 17. The working electrode (cast Zn-55%Al alloy) of ACM1 was much thicker than the auxiliary electrode (Fe) as a result of the casting method. Other ACMs had reasonably equal plate thicknesses for working, auxiliary and reference plates (the latter for 3-electrode type only).

E2.5 Pollution Gas Box, PGB, Weighed Mass Loss Tests

The materials used for samples, their analysis, dimensions and exposed areas are described in Section E2.2/2. Samples of steel, zinc, cast Zn-55%Al alloy, rolled Zn-55%Al alloy, passivated/unpassivated ZINCALUME, passivated/unpassivated galvanized and aluminium were weighed then edges, reverse face stopped off with lacquer (Peel-off). They were then placed in test chambers 1-3 in the PGB, described in Section E2.3/6, which was controlled at 35 $\pm$0.05°C. Due to the flow through of air, the test chamber temperatures were 34.2 $\pm$0.1°C. The samples were carefully positioned on the glass grid platform using a small level gauge. Distilled water containing wetting agent (1 drop Teric/200 mL) was pipetted onto the samples through the coned glass joint in the test chamber cell tops. The volume of water was calculated to produce a 0.5 mm thick film on the exposed sample surface.

Table E2/1 Table of ACM Details

1 ACM code	2 working electrode type	3 N_W [1]	4 plate dimensions length (mm)	5 thick (mm)	6 A_W [1] (cm^2)	7 auxiliary electrode type	8 N_A [1]	9 plate dimensions length (mm)	10 thick (mm)	11 A_A [2] (cm^2)	12 reference electrode type	13 N_R [1]	14 plate dimensions length (mm)	15 thick (mm)	16 A_R [2] (cm^2)	17 ACM area A_T [2] (cm^2)	18 V [4] (mL)	19 Comments PGB [3] run numbers
A. 2-electrode type ACMs																		
1	CZA [5]	9	60	2.35av	12.7	Fe	9	60	0.53	2.9						16.0	0.8	PGB 1-161
2	Zn	21	52	0.65	7.1	Fe	20	52	0.86	8.8						15.9	0.795	PGB 129-185 failed; replaced by ACM7
5	RZA [5]	21	54	0.86	9.8	Fe	20	54	0.85	9.2						19.0	0.95	PGB 186 only failed
7	Zn	21	52.4	0.64	7.0	Fe	20	52.7	0.68	7.2						14.4	0.72	PGB 213-234
9	RZA [5]	21	54	0.81	6.8	Fe	20	54	0.83	6.7						14.0	0.70	PGB 238-304
B. 3-electrode type ACMs																		
3	Zn	16	52	0.65	5.4	Zn	16	52	0.65	5.4	Zn	8	52	0.65	2.7	16.0 13.5 14.0	0.80 0.675 0.70	PGB 132,133 PGB 134-239 PGB 241-315
4	RZA [5]	12	54	0.82av	5.2	RZA [5]	12	54	0.83av	5.2	RZA [5]	6	54	0.77av	2.4	14.0	0.7	PGB 266-327
6	Fe	16	55	0.63	5.5	Fe	16	55	0.63	5.5	Fe	8	55	0.63	2.8	13.8	0.69	PGB 187-194 failed; remade as ACM8
8	Fe	16	52.4	0.68	5.5	Fe	16	52.4	0.68	5.5	Fe	8	52.4	0.68	2.75	14.0	0.70	PGB 244-321

Notes:

1 N_W, N_A, N_R number of working, N_W, auxiliary, N_A, and reference, N_R, plates
2 A_W, A_A, A_R, A_T exposed ACM area of working, A_W, auxiliary, A_A, reference, A_R, plates, and total ACM area, A_T, which includes metal plates and gaps in between plates due to mylar insulators and epoxy
3 PGB Pollution Gas Box
4 V solution volume to give 0.5 mm water film
5 RZA, CZA rolled, cast Zn-55%Al alloy

This water was allowed to evaporate to dryness in the air stream flowing through the test chambers. Pollutant gas (SO_2) was metered into test chambers 2 and 3 as appropriate. The range of [SO_2] covered was 0-1 ppm. This cycle was repeated a total of four times, as corrosion products built up, whereafter the samples were removed, stripped of the stop-off lacquer, cleaned and reweighed to obtain a mass loss. The cleaning procedure removed corrosion products and was different depending on the sample type. Steel was cleaned by a 2 minute immersion in Rhodine inhibited (1 g/L) hydrochloric acid (2.5N), followed by a hot wash in alcohol, a hot dry using a hair dryer, and a scrub with a toothbrush. The sample was then given a further 30 s pickle, hot wash, hot dry and was weighed. The aluminium, cast/rolled Zn-55%Al alloy and ZINCALUME samples were cleaned in 10% CrO_3/5% H_3PO_4 solution at 75°C for 10 min followed by hot wash, hot dry and weigh. Zinc and galvanized samples were cleaned by a 10 min immersion in 10% CrO_3 solution followed by hot wash, hot dry and weigh.

E2.6 Electrochemical Tests - ACM Type

1. Method

The method of carrying out electrochemical tests on various ACMs in the pollution gas box, PGB, is generally the same as described in Section E2.5, using standard conditions, see Section R1.1. A PGB experiment consisted of four cycles of applying 0.5 mm thick distilled water films (unless otherwise stated), to the ACM surface and evaporating to dryness at 70% relative humidity. Two cycles were performed per day, each lasting between two and four hours. Corrosion products built up from cycle to cycle. The [SO_2] in the air stream flowing through the PGB test chambers was varied over the range

0-1 ppm. Galvanic current, impedance and corrosion current tests were carried out as appropriate. Details are given in Sections E2.6/2,4,5.

2. Galvanic current tests

Galvanic current/time tests were carried out, using the method indicated in Section E2.6/1, on the following 2-electrode type ACMs, refer Table E2/1 Section E2.4/3 - ACM1 (cast Zn-55%Al/Fe), ACM9 (rolled Zn-55%Al/Fe) and ACM2 (Zn/Fe). Two series of tests investigated the anode mass loss of these ACMs and its sacrificial protection ability to the cathodic steel plates. The first of these used 0.5 mm thick distilled water films containing surfactant and $[SO_2]$ in the PGB test chamber air stream was varied over the range 0-1 ppm. In the second test series, 0.5 mm thick water films containing various levels of sodium chloride (distilled water, 10^0,10^1,10^2,10^3 $mg.L^{-1}$ $[Cl^-]$ plus surfactant in the first PGB cycle) were applied to the surface of ACM9 (rolled Zn-55%Al/Fe) with zero $[SO_2]$ in the air stream. Distilled water was applied in cycles 2-4. Section E1.1 describes the electrochemical test system used to carry out galvanic current/time tests, and the storage/retrieval of data on hard disc along with sample information. Briefly, an operational amplifier box, wired as a zero resistance ammeter, was used to collect galvanic current/time data which was sent to the computer via an analogue-to-digital card. Acquisition of data was controlled by a galvanic current subroutine in program CONTROL, which made periodic calls to subprogram ADC, see Sections A1/2.1,3.1.

3. Sacrificial protection ability of ZINCALUME coating versus $[SO_2]$

Discs (65 mm diameter) of unpassivated ZINCALUME coated steel, refer

Section E2.2/1.5, had two 1 mm circular grooves cut through the coating with a lathe so as to just reveal the steel substrate. The inner, outer circular grooves had diameters of 18, 27 mm, respectively, and the total area of steel exposed was 142 mm^2. A circular wax pencil line was drawn around the outer groove at a diameter of 42.2 mm, so as to expose a total area of 1440 mm^2. A distilled water film (0.7 mL) was applied to the sample in the PGB test chamber, so that a 0.5 mm thick water film was produced. The water film was then evaporated to dryness at 34.2°C and 70% relative humidity over 4 cycles in the same manner as the ACM tests, see Section E2.6/1. The range of $[SO_2]$ was 0-1 ppm. At the end of the 4-cycle test, the per cent red rust in the two grooves was measured.

4. Impedance tests

Impedance tests were carried out 3-5 times (runs) for each of 4 cycles in the PGB, using the method indicated in Section E2.6/1. The following 3-electrode type ACMs, refer Table E2/1, Section E2.4/3, were used - ACM3 (Zn), ACM4 (rolled Zn-55%Al alloy), ACM8 (Fe). The lead out wire from the reference plates was left unconnected, whilst the lead out wires from the working and auxiliary plates were connected to the working and auxiliary inputs of the potentiostat operating in galvanostatic mode. The wide frequency range impedance method, Section E1.2/2.2, was used. The resistive, a, and reactive, b, components of impedance, Z, where Z = a+jb, were collected over the range 65 kHz to 1 Hz for each run of the 4 PGB cycles. This data was stored on hard disc along with sample numbers, series/group titles and sample information and could be recalled for later analysis, see Section E1.1/3. Briefly, impedance data was collected by the Solartron Model 1250 Frequency Response Analyzer and Solartron Model 1286 Electrochemical Interface (in

galvanostatic mode). These instruments were controlled by the computer's subprogram FRA_EXPT, see Section A1/4.1. The amplitude of the sinewave currents applied to the cell generally ranged from 0.9 μA up to 900 μA rms, equivalent to a sinewave voltage of 9 mV rms across a control resistor ranging in decade steps from 10^4 to 10^1 ohm. The size of the control resistor was determined by the impedance of the cell to be measured, a low cell impedance requiring a low control resistance (or a higher sinewave current).

5. Corrosion current tests

Corrosion current tests were carried out 3-5 times (runs) for each of 4 cycles in the PGB, using the method indicated in Section E2.6/1. The following 3-electrode type ACMs, refer Table E2/1, Section E2.4/3, were used - ACM3 (Zn), ACM4 (rolled Zn-55%Al), ACM8 (Fe). Lead out wires from the working, reference and auxiliary plates of the ACM were connected to working, reference and auxiliary inputs of the potentiostat operating in galvanostatic mode. An experimental run consisted of applying a number of current steps to the ACM during the evaporation cycle with the aid of the Solartron Model 1286 Electrochemical Interface, Section E1.1/1, and the computer's subprogram RP_EXPT, Section A1/5.1. The technique is described in Section E1.2/4. The voltage response between the working and reference plates of the ACM was measured as a function of time before and during application of the current step. Generally, the voltage response reading time was 6 s after application of the current step, although this time depended on achieving an approximate steady-state situation. For example, ACM8 (Fe) showed very slow attainment of a steady state voltage response for early PGB cycles at low or zero [SO_2] as a result of a low corrosion rate. In these cases, the voltage response reading time was extended to 10 or even 30 s as appropriate to the

attainment of an approximate steady state situation. Corrosion current, anodic and cathodic Tafel slopes were all calculated automatically from the current/voltage data by subprogram RP_EXPT and a current/voltage plot produced. The current steps were applied so as to produce a significant degree of curvature in the I/ε polarization curve. The degree of curvature is related to the Tafel slope values, as discussed in Section T3/6. Thus the voltage range varied from run to run to take changing Tafel slope values into account. For example, the voltage range may have been ±15 mV for one run but ±300 mV for another. The current steps applied varied over a wide range, depending on conditions. This could be as low as ±1 μA or up to ±70 mA.

SECTION E3 - EXPERIMENTAL - PAINTED METALS

E3.1 Painted Metal/Solution Equilibria in Chloride Solutions

1. Attached films (paint films attached to a substrate metal)

A large panel of ZINCALUME coated steel, primed with Dulux EX90038-D epoxy primer and painted with Bronze Olive Dulux silicone modified polyester, SMP, top coat was obtained from No. 1 Paint Line, Port Kembla. The primer and top coat thickness was measured, see Section E3.2/3, as 4 μm and 18 μm respectively.

Three small flag shaped test samples, see Section E3.2/2.1 for details, were cut from this panel, a lacquered copper lead out wire was soldered to the stem of each sample, and the edges, rear face and soldered joint were all masked off with a wax mixture (50% paraffin, 50% Tervan 2530) so as to expose 6 cm^2 of the sample surface. Sample code numbers 405/85 to 407/85 were allocated.

These test samples were immersed in 150 mL of 5% NaCl solution at 50°C in a 2-electrode 50°C type cell, see Figure E1/4a, Section E1.2/1, which was immersed in a thermostat oil bath. The test samples 'lived' in 5% NaCl 'test' solution (30 500 mg.L^{-1} [Cl^-]) over at least 41 days, but were periodically transferred to 'measurement' solutions of various chloride ion concentrations and an impedance test carried out. The chloride ion concentration range was 10^0,10^1,10^2,10^3,10^4 and 3.05 x 10^4 (5% NaCl) mg.L^{-1}, all as NaCl solutions. The order in which the samples were transferred was not always the same. The wide frequency range test, see Section E1.2/2.2, was carried in each of the measurement solutions and in the 5% NaCl test solution in which the samples 'lived'.

2. Free films (paint films only)

Free films were prepared according to the method given in Section E3.2/2.2. Table E3/1 shows the type of paint films, either single or dual top coats, with or without a primer, that were produced as free films in this manner. Paint film thickness was determined by the method in Section E3.2/3 for free films.

Table E3/1 Free Film Characteristics

System[1]	Primer[2] Film thickness (µm) nominal	actual	Top Coat[3] Film thickness (µm) nominal	actual
SMP/P/SMP	5	5	20/20	29/22
SMP			20	27
SMP/SMP			10/10	27 (total)

1. P, SMP primer, silicone modified polyester top coat in different combinations
2. primer is Dulux Dualprime Mk II laboratory applied using a #0015 spreader bar, stoved at 280°C and cured for 65 s
3. top coat is Armorsil 500 SMP (Bronze Olive), laboratory applied with a #0032 spreader bar, stoved at 280°C and cured for 65 s.

A free film sample was mounted between two perspex holders with a circular hole cut out of the middle so as to expose an area of 10.75 cm^2. The perspex holders were then clamped between two arms of a glass U-cell so as to make a leakproof cell. Large platinum grid electrodes (25 cm^2, 20 holes/cm) were inserted into both arms of the U-cell to measure the cell impedance. The U-cell was filled with 10 000 $mg.L^{-1}$ $[Cl^-]$ (NaCl) solution at room temperature. The wide frequency range impedance test was carried out after approximately 1 hour immersion. The solution was then emptied, the U-cell carefully rinsed with distilled water with the free film still clamped in place, and filled with 1000 $mg.L^{-1}$ $[Cl^-]$ (NaCl) solution, and also repeated for 100 $mg.L^{-1}$ $[Cl^-]$ (NaCl). The above procedure was then repeated for all the free film samples listed in Table 3/1.

E3.2 Effect of Paint Film Flatting Agents on Solution Uptake

1. Paint formulations with differing flatting agent levels

A series of three special paint formulations containing different levels of flatting agent particles was supplied by Dulux Australia. They were classified as follows:

Table E3/2 Paint Formulations Containing Differing Flatting Agent Levels

Code	Name	Colour	Type	Gloss Level (%)
377/R/980	Armorsil 500	Bronze Olive	SMP	85
377/R/981	Armorsil 500	Bronze Olive	SMP	50
377/R/982	Armorsil 500	Bronze Olive	SMP	25

The formulations were prepared from a common base (Code 377/R/980) having no flatting agent particles. For identification purposes, these were known as 85, 50 and 25% gloss level, where the maximum gloss level contains no added flatting agent and the minimum gloss level contains maximum flatting agent, equivalent to normal production line levels.

2. Preparation of test samples

2.1 Attached films (paint films attached to a substrate metal)

Panels approximately 150 x 300 mm, of production line Dulux EX900-D epoxy primed ZINCALUME® coated steel, pretreated with Parker Bonderite B1310 chromate based pretreatment, were laboratory painted with the above three top coat paint formulations. A #0032 spreader bar, known to give a paint film thickness of approximately 20 µm, was used to apply the liquid paint to these panels, which were then cured for 75 seconds to reach a peak metal temperature, PMT, of 232°C, see Table E3/3.

Table E3/3 Gloss Series Attached Film Types on a ZINCALUME Coated Steel Substrate

System	Primer[1] Film thick (µm)	Code	Top Coat[2] Film thick (µm)
85% gloss	2	377/R/980	29
50% gloss	2	377/R/981	27
25% gloss	2	377/R/982	23
85% gloss	4	377/R/980	25
50% gloss	4	377/R/981	25
25% gloss	5	377/R/982	24

Notes

1. primer is Dulux Armorprime 440 HCR4 produced on-line at 241°C
2. top coats are experimental Dulux formulations (Bronze Olive), laboratory applied using #0032 spreader bar and stoved at 232°C and cured for 75 s.

From each painted panel, five small test samples, 26 x 56 mm, were cut. The perimeter of each panel was generally not used for test samples, but was used for determining paint film thickness. Using a nibbling tool, a small rectangle, 20 x 20 mm, was cut out of each sample to give the sample a shape like a flag, see Figure E3/1. A heavy lacquered copper lead out wire was soldered to the stem of each sample. The edges, rear face and soldered joint were all masked with Ciba-Geigy Araldite epoxy resin with polyamine adduct hardener, kit K273, so as to leave an exposed front face of 20 x 30 mm.

2.2 Free films (paint films only)

Dow silicone non-stick coating was applied with a #0015 spreader bar, to give approximately 10 µm coating, to a ZINCALUME coated steel substrate and stoved for 180 seconds at 280°C. This produced a surface upon which primers and/or top coats could be applied, but could readily be peeled off to produce free films, that is, paint films not attached to a substrate. Table E3/4 shows the type of paint films and their characteristics that were produced as free films in this manner.

Table E3/4 Free Film Types, Stoving Conditions, Film Thickness

			Top Coat				
System	Maker	Code	Colour	Spreader bar	Film thick (µm)	Cure time (s)	Cure temp (°C)
TC/TC 85% gloss	Dulux	377/R/980 Armorsil 500	Bronze Olive	#0015	27	75	232
TC/TC 50% gloss	Dulux	377/R/981 Armorsil 500 SMP	Bronze Olive	#0015	27	75	232
TC/TC 25% gloss	Dulux	377/R/982 Armorsil 500 SMP	Bronze Olive	#0015	27	75	232

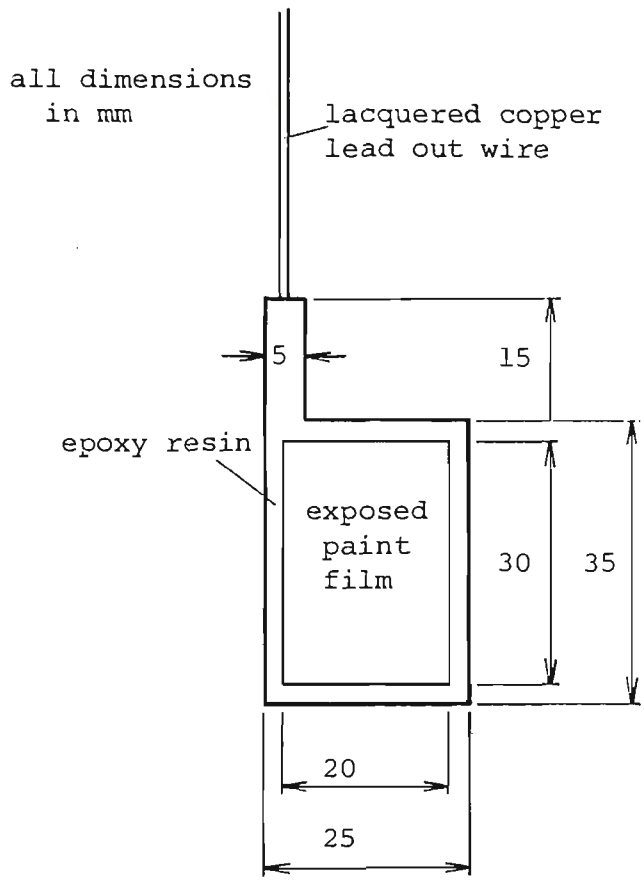

Figure E3/1. Flag type working electrode used for painted metal studies.

3. Paint film thickness measurements

Attached film thickness was measured by assembling a small sample of each panel in a metallurgical mount and determining the primer and top coat thickness under the microscope with a graticule eye piece. This method resulted in some uncertainty in the primer thickness estimation because the primer/top coat interface was not always clearly defined. An alternative check was to measure panel thickness at the top of each panel in three places - before the primer started, before the top coat started and after the top coat had started. The difference between the first two gave the primer thickness while the third minus the first two measurements gave the top coat thickness. Free film thickness was measured directly on the test sample by micrometer. The thickness of primer/top coat combination samples was measured by peeling off from the non-stick coating small areas of primer (or top coat) at the top of each panel before the top coat (or primer) film had started. The difference between this measurement and the total thickness of the combination sample gave the individual primer or top coat thickness. Paint thickness measurements for both attached and free film samples are shown in Tables E3/3,4. The level of confidence was generally ± 1 µm.

4. Test conditions

4.1 Solutions

Three solutions were chosen - 100, 1000, 30 500 (5% NaCl) $mg.L^{-1}$ $[Cl^-]$ (NaCl). The solution conductivity was measured as a check on the chloride ion concentration. Tests were carried out at 50°C by placing samples in 2-electrode 50°C type cells, see Figure E1/4a, Section E1.2/1.1 containing 150 mL of the respective solution which were contained in a thermostat oil bath.

4.2 Attached films - impedance samples

Generally, five small flag type samples, Section E3.2/2.1 and Table E3/3, were tested for each parameter investigated, making a total of 42 samples. Of these samples, 10 were used for only the wide frequency range impedance test, 27 samples were used for only the 1 kHz frequency test and the remaining 5 samples were used for both the wide frequency range test and the single frequency test. Table E3/5 gives details of these samples. Tests were carried out frequently at low immersion times, but at longer intervals as immersion time proceeded so as to produce approximately equally spaced data points on a logarithmic time axis. Tests were continued until the failure criterion was met, see Section T1/5.4.

Table E3/5 Details of Gloss Series Attached Film Impedance Samples

Solution mg/L $[Cl^-]$ (NaCl)	gloss level (%)	Sample number[1]							
30,500 (5% NaCl)	25	1	2*	3	33**	34**			
	50	4*	5	35**	36**				
	85	6*	7	8	9	10	37**	38**	
1000	25	11	12	13	14	15	16	17	39**
	50	18	19	20	40**				
	85	21	22	41**					
100	25	23*	24	25	26	27			
	50	28	29	30	31*	32			
	85	42**							

Notes:

1. sample codes marked with one asterisk (*) were samples that had both wide frequency range tests and single frequency tests; two asterisks (**) were samples that had only the wide frequency range test.

The parameters investigated were the effect of paint film gloss level (25, 50, 85%) to determine the influence of flatting agent and the effect of solution

chloride ion concentration (100, 1000, 30 500 (5% NaCl) mg/L^{-1} [Cl^-] as NaCl) as per Section E3.2/4.1.

4.3 Attached films - gravimetric samples

The parameters investigated were the effect of paint film gloss level (25, 50, 85%), to determine the influence of flatting agent, refer Table E3/3, Section E3.2/2.1 and the effect of solution chloride ion concentration (100, 1000, 30 500 (5% NaCl) mg/L^{-1} [Cl^-] as NaCl). Three small rectangular samples, each 50 x 25 mm, were tested for each parameter evaluated, making a total of 27 samples. A number of tests were repeated. The primer and top coat thickness of each sample was determined after testing by sectioning and metallographic examination. The primer thickness was 5 µm and the top coat thickness was 21-23 µm for all the samples. A wax mixture (50% paraffin, 50% Tervan 2530) was applied to sample edges and reverse face, exposing approximately 8.2 cm^2 of the sample surface. Samples were exposed to the three chloride ion solutions, refer Section E3.2/4.1, for up to 10 days. Samples were weighed before/after immersion and also after one day in a desiccator. After immersion and before reweighing, samples were pressed lightly between blotting paper, so as to dry off excess water but not to desorb water in the paint film. Solutions were analyzed for Zn, Al ion concentration by atomic absorption spectroscopy after the immersion period. A blank sample, completely covered in wax, was immersed for three days to check on the degree of water absorption by the wax.

4.4 Free films - impedance samples

A free film sample of Dulux Armorsil 500 SMP 25% gloss, see Section E3.2/2.2

and Table E3/4, was mounted in the U-cell described in Section E3.1/2. The U-cell was filled with 30 500 mg.L^{-1} [Cl$^-$] (5% NaCl) solution and the whole cell placed in a thermostatted oil bath at 50°C. Both the 1 kHz frequency test, Section E1.2/2.1, and the wide frequency range impedance test, Section E1.2/2.2, were carried out as a function of time so as to produce approximately equally spaced data points on a logarithmic time axis. This experimental procedure was repeated using identical free film samples in 100 and 1000 mg.L^{-1} [Cl$^-$] (NaCl) solution until severe degradation of the film occurred.

4.5 Free films - gravimetric samples

Free film samples of Dulux Armorsil 500 SMP 25% gloss, see Section E3.2/2.2 and Table E3/4, having an area of 8.3 cm^2, were held between plastic drinking straws split up the middle to hold a sample. These samples were immersed in 150 mL of 30 500 mg.L^{-1} [Cl$^-$] (5% NaCl) solution contained in large test tubes which were held at 50°C in a thermostatted oil bath. The period of immersion was 1, 2, 10, 38 days. This procedure was repeated on identical samples in 100, 1000 mg.L^{-1} [Cl$^-$] (NaCl) solution. The free film samples were weighed before/after immersion and after one day in a desiccator. The sample drying procedure was identical to that used in Section E3.2/4.3. A further series of 12 samples was repeated at 0.3, 1, 2 and 3 d in each solution to support evidence obtained in the first series.

Section Topic Page

Preliminary testing with Atmospheric Corrosion Monitors, ACM, was carried out to determine whether galvanic current, corrosion current, and impedance tests could satisfactorily be performed using thin (0.5 mm) water films on ACM surfaces. Preliminary tests were also carried out using the galvanic current test to determine suitable standard conditions for ACM tests. The effects of reproducibility, water film thickness, area of surface wet, relative humidity and the effect of corrosion product build-up were investigated. These results are not reported here but they are in agreement with similar studies[36,112,114,116-120,122,125] published since this work was started. The standard conditions chosen were as follows.

Standard conditions

number of cycles	:	4 per test
water film	:	distilled water + Terric (1 drop/200 mL) preheated to PGB temperature
water film thickness (mm)	:	0.5*
water film volume (mL)	:	0.7*
$[SO_2]$ (ppm)	:	variable
relative humidity (%)	:	70
ACM surface	:	cycle 1 - abraded, clean surface cycles 2-4 - allow corrosion product build-up use level gauge to set up ACM in test chamber
test chamber temp (%)	:	34.2 $\pm$0.1

* A wax pencil was drawn as a rectangle to surround ACM plates. This kept the water film from spreading to a wider surface area over the resin portion of the ACM. This wax pancil was removed with naphtha prior to repolishing the ACM surface for a subsequent experiment.

Galvanic currents can satisfactorily be measured between dissimilar metal plates of 2-electrode type ACMs as a function of the time the ACM surface is wet. The shape of the I_g/t plot is essentially a decrease of I_g with time thought to be caused by corrosion product formation and eventually also a decreasing wet surface area. The important parameters appear to be the area, q, under the I_g/t curve, and the dry-out time, t_{dry}. Reproducibility under

identical test conditions on a clean surface for one cycle is reasonable. The above standard conditions allow a build-up of corrosion products which can absorb pollutants over four cycles of applying water films to the ACM surface, starting from a clean, abraded surface.

Impedance and corrosion current tests could all be satisfactorily performed on 3-electrode ACMs using the above standard conditions.

R1.2 Cast, Rolled Zn-55%Al Alloy Evaluation

1. Zn-Al phase equilibrium diagram

The Zn-Al phase diagram[168] is shown in Figure R1/1. The main phases are L (liquid), α (Al-rich fcc phase) and β (Zn-rich hcp phase). The γ and α' are similar to α and are not always shown as separate phases in some diagrams. Important features of the Al-Zn phase equilibrium diagram are the eutectic point which occurs at 390°C and 95% Zn; the eutectoid point which occurs at 275°C and 78% Zn; the large (α+L) region of the diagram and the large variation in solid solubility of Zn in α between the eutectoid temperature and room temperature. Liquid of the eutectic composition undergoes the eutectic reaction $L \rightarrow \gamma + \beta$ on cooling below the eutectic temperature. Likewise solid γ of the eutectoid composition undergoes the eutectoid reaction $\gamma \rightarrow \alpha + \beta$ on cooling below the eutectic composition.

2. Microstructure

Figure R1/2 compares the cast Zn-55%Al alloy microstructure, Figure R1/2a, with that of a rolled Zn-55%Al alloy, Figure R1/2b, and also a typical

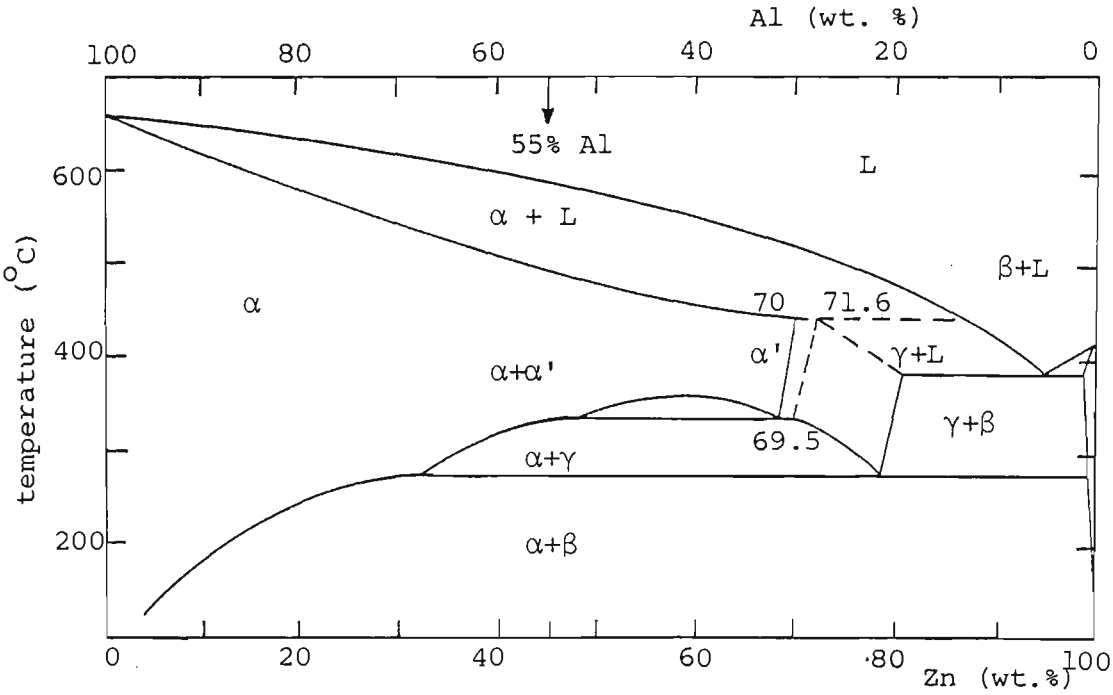

Figure R1/1. Zn-Al phase diagram showing the approximate composition of the ZINCALUME coating (55%Al) showing the main phases - L liquid; α (Al-rich fcc); β (Zn-rich hcp) and γ.

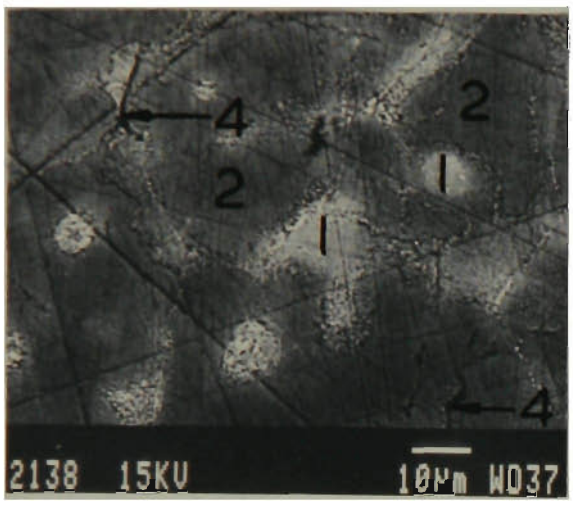

a) cast Zn-55%Al alloy

micro no. 3249
neg no. 2138

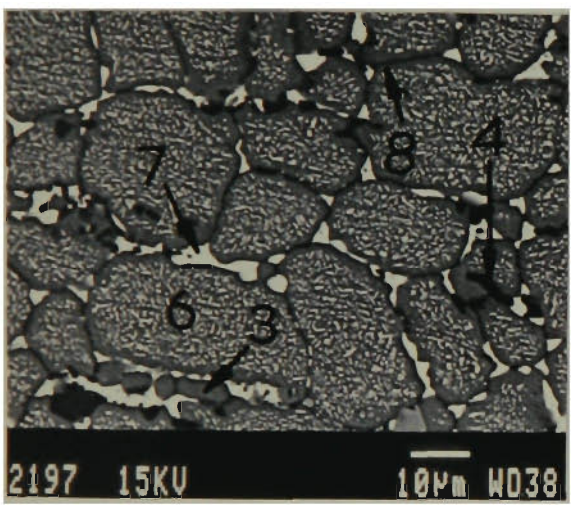

b) rolled Zn-55%Al alloy

micro no. 3842
neg no. 2197

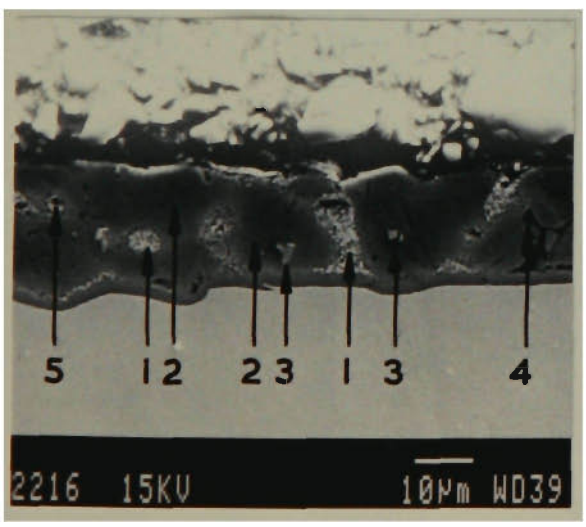

c) production line ZINCALUME

micro no. 6611
neg no. 2216

Figure R1/2. Typical microstructure of a) cast Zn-55%Al alloy, b) rolled Zn-55%Al alloy and c) normal production line ZINCALUME coating. 1. Zn-rich areas; 2. Al-rich areas; 3. dross inclusions; 4. silicon particles; 5. voids; 6. Al-rich grains containing small Zn-rich precipitates; 7. large Zn-rich precipitates; 8. narrow precipitate free zone. Magnification x1000.

production line ZINCALUME coating, Figure R1/2c. All three samples were examined unetched. Micros were photographed at typical regions using secondary electron images on a JEOL Model JSM 840 scanning electron microscope. Average composition of each region in the micros was obtained by averaging line scans through typical regions obtained using energy dispersive spectroscopy, and results are shown in Table R1/1.

Table R1/1 Average Zn, Al Compositions of Zn-rich and Al-rich Regions of Zn-55% Al Alloy Coatings

Alloy	Zn-rich regions[1]		Al-rich regions[1]	
	Zn (%)	Al (%)	Zn (%)	Al (%)
cast Zn-55% Al	65.1 ±1.05 (n=9)	32.4 ±9.8 (n=9)	43.3 ±4.6 (n=20)	56.7 ±4.2 (n=20)
rolled Zn-55% Al	95.8 ±4.6 (n=3)	3.8 ±4.7 (n=3)	41.3 ±7.4 (n=30)	58.0 ±7.2 (n=30)
typical ZINCALUME coating (ZL)	72.8 ±9.0 (n=7)	25.7 ±9.0 (n=7)	35.5 ±3.8 (n=20)	62.9 ±3.8 (n=20)

Al-rich areas: Al (%) cast < = rolled <ZL; Zn (%) cast > = rolled >ZL
Zn-rich areas: Al (%) rolled <<ZL <cast; Zn (%) rolled >> ZL >cast

Notes:

1 Zn, Al concentrations are quoted as a mean ±1 standard deviation

2.1 ZINCALUME coating

The ZINCALUME coating consists of 43.5% Zn, 55% Al and 1.5% Si. The coating is formed by rapid cooling in air from the molten hot dip bath temperature; is not in equilibrium; and is essentially a cored, dendritic structure[169]. In terms of the phase diagram, which relates to equilibrium conditions, the first phase to freeze out from the liquid is the α-phase, starting to separate at about 590°, and containing about 20% Zn in solid solution, refer to the (α+L) phase in Figure R1/1. These alpha dendrites will

continue to grow and separate as the temperature decreases with an increasing proportion of Zn in the outer layers, since solid state diffusion is not rapid enough to maintain the equilibrium composition of α throughout the dendrite.

As the α-phase grows, Zn-rich liquid will be rejected between the dendrites, and the last liquid to solidify will have about the eutectic composition of 95% Zn. Other solid state reactions are possible as the solidified coating cools down; β precipitation will occur from the α (or γ) phase during cooling at a temperature dependent upon the local α composition. At low Zn concentrations (in the middle of α dendrites), β precipitation cannot occur until the temperature is below about 250-275°C, and even then it is precluded for kinetic reasons. Above about 30% Zn, eutectoid decomposition of γ can occur, giving a mixture of α and β. In the interdendritic regions, eutectic decomposition, forming α and β phases, can again be followed by the eutectoid decomposition reaction. The final coating will therefore contain β precipitates of varying distribution, size and morphology. About 80% of the coating consists of α dendrites with optically visible β precipitates, and 20% consists of Zn-rich interdendritic regions which are a mixture of α and β.

The ZINCALUME coating microstructure, Figure R1/2c, consists of Zn-rich, labelled 1, and Al-rich, labelled 2, regions. The regions have higher Zn levels in the Zn-rich regions, and higher Al levels in the Al-rich regions than the cast alloy, as shown in Table R1/1, Section R1.2/2. The dendrite arm spacing (estimated from the distance between adjacent Al-rich regions) is also similar for the two samples, suggesting similar cooling rates. Also present in the coating are quaternary (Fe-Zn-Al-Si) dross inclusions, labelled 3, Si particles, labelled 4, and voids, labelled 5.

2.2 Cast Zn-55%Al alloy

As-cast Zn-55%Al alloy gives a similar microstructure to the ZINCALUME coating, compare Figures R1/2a,c. The same sequence of cored dendritic formation and solid state β precipitation occurs[170]. The only difference is that the cooling rate is not identical to that of the coating. However, the similar dendrite arm spacing indicates that the cooling rate was not too different.

The as-cast microstructure, Figure R1/2a, consists of Zn-rich regions, labelled 1, having Zn precipitates of various sizes, and Al-rich dendrites, labelled 2, having no visible precipitates of Zn. The cast material also contains Fe (0.1%) and Si (0.4) - Si needles are labelled 4.

2.3 Rolled Zn-55%Al alloy

The rolled Zn-55%Al alloy produced ACM plates of approximately the same thickness as the steel plates, refer Table E2/1, Section E2.4/3. This was important for mass loss calculations in Section T2/4 but was achieved at the expense of producing a microstructure which was further removed from the ZINCALUME coating microstructure than the cast material. Figure R1/2b in Section R1.2/2 shows the microstructure resulting from the thermomechanical treatment described in Section E2.2/1.4. The heat treatment at 400°C completely removed the dendritic microstructure. At temperature, the rolled strip would have consisted of an as-recrystallized grain structure of single phase α of uniform composition. On cooling below 340°C, γ precipitates would be formed at the grain boundaries, and below 275°C, these would be replaced by β precipitates. The hold at 260°C resulted in a coarsening of these grain

boundary precipitates. Furnace cooling to room temperature resulted in a large decrease in the solubility of Zn in α and, consequently, a further precipitation of β onto the existing grain boundary β plus smaller precipitates throughout the grain interior. There is also a precipitate free zone, PFZ, surrounding the grain boundaries resulting from diffusion of Zn in these regions to the existing grain boundary precipitate rather than nucleation of new precipitates. As in the case of the ZINCALUME coating, the microstructure consists of three regions - the large β particles, the regions of fine β precipitation and the Al-rich regions (PFZ and interior of dendrites). The distribution of these regions is obviously different but electrochemically the overall corrosion behaviour would be expected to be similar. This is discussed at length in Section R1.2/3.

The rolled coating microstructure in Figure R1/2b consists of α-phase (Al-rich) grains containing small β-phase (Zn-rich) precipitates, labelled 6, large Zn-rich precipitates at the grain boundaries, labelled 7, and a narrow precipitate free zone around the grain perimeter, labelled 8. As seen in Table R1/1, the large Zn-rich precipitates are high in Zn, and the small Zn-rich precipitates are likely to have a similar composition.

The average composition of the Al-rich grain interior is slightly lower in Zn but higher in Al than the cast alloy. Quaternary (Fe-Zn-Al-Si) dross, labelled 3, and Si particles, labelled 4, are broken up and aligned in the rolling direction. Some smaller Si particles are also present at the grain boundaries. The grain size is approximately the same as the dendrite arm spacing in both the cast alloy and the ZINCALUME coating microstructures.

Table R1/1 indicates that both cast and rolled alloys have more Zn in Al-rich

regions than the ZINCALUME coating sample. In the Zn-rich regions, the rolled alloy sample has significantly more Zn than the ZINCALUME sample which has more Zn than the cast alloy. These differences are likely to affect the corrosion behaviour, which is discussed in Section R1.2/3.

3. Corrosion testing

The aim of this section is to compare the corrosion performance of the cast and rolled Zn-55%Al alloys, Sections E2.2/1.3,1.4, with that of a typical ZINCALUME coated steel sample under corrosive conditions that produce well known behaviour of the latter. The cast and rolled Zn-55% Al alloys were necessary because it was not possible to use ZINCALUME coated steel samples in the construction of Atmospheric Corrosion Monitors, ACMs, see Section E2.4, due to the exposed steel edge. The rolled alloy was made as well as the cast alloy because the cast alloy plates were rather thick (average 2.36 mm), for use in ACMs, and rolling was capable of producing thinner alloy plates.

Figure R1/3 shows that all three working electrodes (cast, rolled Zn-55% Al alloy and a sample taken to be typical of ZINCALUME coated steel) give a marked rise in corrosion potential, E_k (over 150 mV) in the first few days of immersion in phthalate-buffered 0.1 M NaCl solution, pH 5.3, refer Section E2.2/1.4. The initial E_k values are close to that expected for zinc (around -1100 mV/SCE), whilst the final plateau values are thought to be characteristic of oxide covered Al-rich areas. Initially, corrosion of a ZINCALUME coating in this environment is by preferential dissolution of Zn-rich areas. The Al-rich areas are thought to be covered by a protective oxide film in this solution, and so the Zn-rich phase will be anodic to the Al-rich phase and preferentially corrode. The steep rise in E_k corresponds to a cessation of corrosion at these regions and the initiation of corrosion of Al and Zn from Al-rich areas[164]. The fact that the cast and rolled alloys

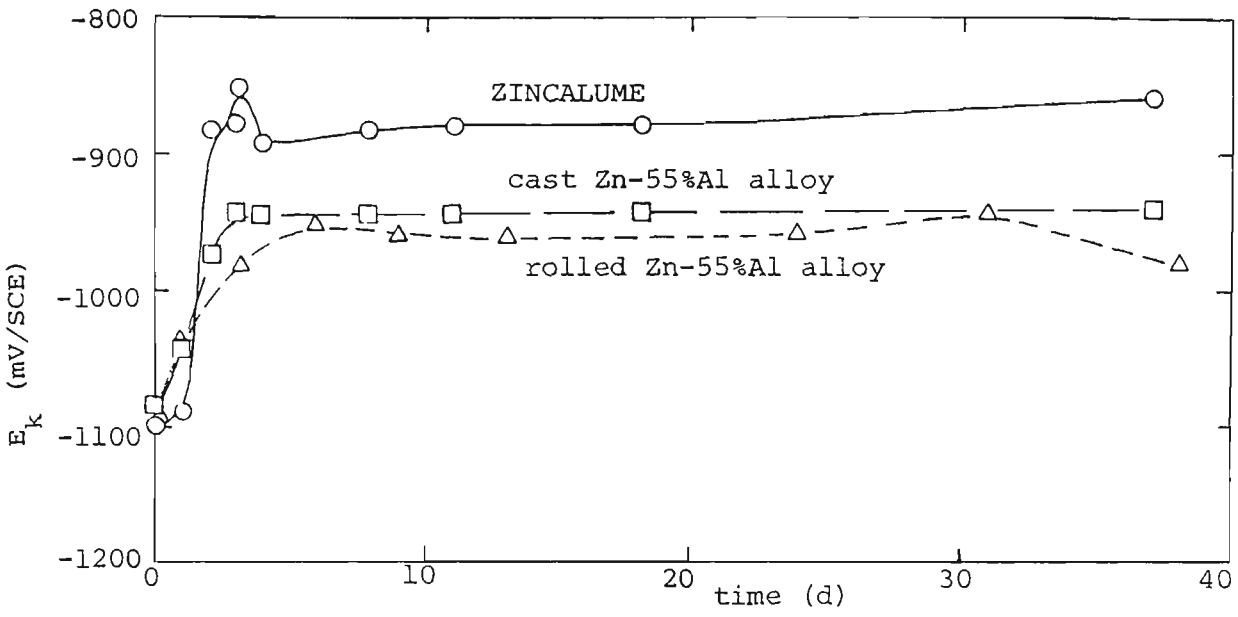

Figure R1/3. Effect of immersion time in phthalate-buffered 0.1 M NaCl solution, pH 5.3, at room temperature on corrosion potential, E_k, of ZINCALUME, cast and rolled Zn-55%Al alloys.

show marked initial rises in E_k similar to the ZINCALUME coating sample suggests that initial corrosion of cast and rolled alloy is also by preferential dissolution of Zn-rich regions.

However, the steep rise in E_k occurs at different rates for the three samples. This behaviour is thought to be due to the amount of available Zn in the Zn-rich regions of each sample. The ZINCALUME coating sample has an E_k value that remains low for the longest time (about 1 day), thought to indicate that this sample has the most Zn in Zn-rich regions available for corrosion. After about 1 day, E_k values rise at the fastest rate. The cast and rolled alloy samples have E_k values that rise at slower rates, but the rise starts soon after immersion, suggesting that there is less Zn available from Zn-rich areas for these samples. The steep rise in E_k at around 2 d for the rolled alloy sample is slower than that for the cast alloy which more closely resembles the behaviour of the ZINCALUME coating sample. This suggests that the rolled alloy sample does not run out of available Zn from Zn-rich areas as quickly as the other two samples.

The final plateau values of E_k are different for each of the samples, which is thought due to small differences in the Al/Zn ratio of the Al-rich areas. As discussed in Section R1.2/2.1, the Al-rich regions of the ZINCALUME coating sample are higher in Al than those in either the cast or rolled alloy samples. The potential of the Al-rich regions would therefore be expected to be higher, and this is indeed the case for the final plateau E_k values in Figure R1/3. The ZINCALUME coating sample is therefore expected to be less electrochemically active than the other samples at times corresponding to corrosion from Al-rich regions. The final plateau E_k values are lowest for the rolled alloy sample, but are close to those for the cast alloy sample. Using the same reasoning as above, it would be expected that the rolled alloy sample

would have a lower Al in Al-rich regions than the cast alloy sample. However, Table R1/1 Section R1.2/2 shows that this is not the case. This discrepancy may possibly be explained by the distribution of Zn-rich precipitates in the Al-rich regions of the rolled sample shown in Figure R1/2b, which may cause the Al-rich regions of the rolled alloy sample to be more electrochemically active than that of the cast alloy sample.

Although differences exist between the cast, rolled Zn-55%Al alloy and a ZINCALUME coating, the essential electrochemical behaviour is thought to be similar in terms of corrosion and sacrificial protection ability. Corrosion occurs preferentially at Zn-rich areas, and subsequently at Al-rich areas. As E_k for steel is around -680 mV/SCE in this solution, E_k values for the Zn-rich portions (around -1100 mV) and the Al-rich portions (<-860 mV), Figure R1/3, suggest that all three samples will maintain sacrificial protection at all times in this solution. The use of cast and rolled Zn-55%Al alloy in the construction of ACMs is therefore expected to reasonably simulate the behaviour of ZINCALUME coated steel which cannot be used.

R1.3 PGB Weighed Mass Loss Tests

The aim of this section is to compare mass losses, obtained by weighing, of steel; zinc; aluminium; passivated and unpassivated galvanized and ZINCALUME; cast Zn-55%Al alloy and rolled Zn-55%Al alloy. The unpassivated materials were necessary for a direct comparison with the cast, rolled alloys. The passivated materials were added because these are the normal production line products. These mass losses were obtained from simulated atmospheric exposures over four cycles at 34.2°C in the pollution

gas box, PGB, for the pollutant gas concentration range 0-1 ppm [SO_2], see Section E2.5.

Figures R1/4,5 show weighed mass loss as a function of [SO_2] for the various metals/alloys listed above. They are presented as two separate sets because the exposed sample area per test chamber was different. Results in Figure R1/4 are for a total of 3000 mm^2 exposed surface area, made up of either four samples, each 750 mm^2, or two samples each 750 mm^2 plus one sample (cast Zn-55%Al alloy) of 1500 mm^2. Results in Figure R1/5 are for a total of 1352 mm^2 exposed surface area, made up of four samples, each 338 mm^2. Samples in Figure R1/4 are not strictly comparable with those in Figure R1/5 because it is possible to show from the statistical analysis in Appendix A4/2.1 and Figures R1/4,5, that for steel and zinc, there is a tendency for mass loss to be higher as exposed sample area increases. This can also be observed by comparing curves 1, 2 in Figures R1/48,49, Section R1.7/2. This effect is likely to be caused by an increased time of wetness as exposed sample area per test chamber increases. Lines shown in Figures R1/4,5 are regression lines, see Appendix A4/2.1.

From Figures R1/4,5 it appears that steel has about the same mass loss as zinc and unpassivated galvanized at zero [SO_2]. Light white corrosion products developed on zinc and unpassivated galvanized after 4 PGB cycles and the steel sample was stained with red rust at some half dozen sites. Individual sample mass losses for steel are fairly scattered at zero SO_2 pollutant.

As [SO_2] increases up to 1 ppm, a distinct difference emerges between steel and zinc/unpassivated galvanized. The mass loss of steel increases markedly, whereas those for zinc and unpassivated galvanized remain relatively constant

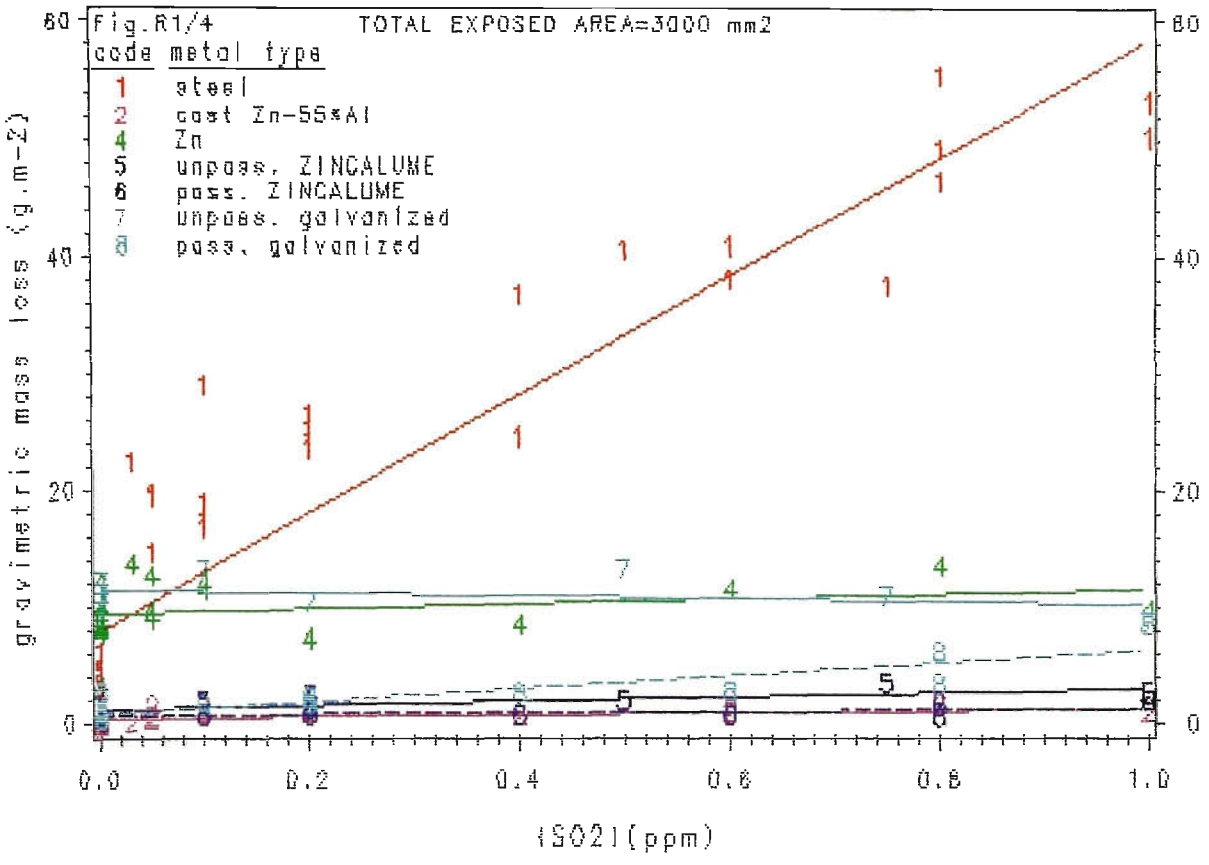

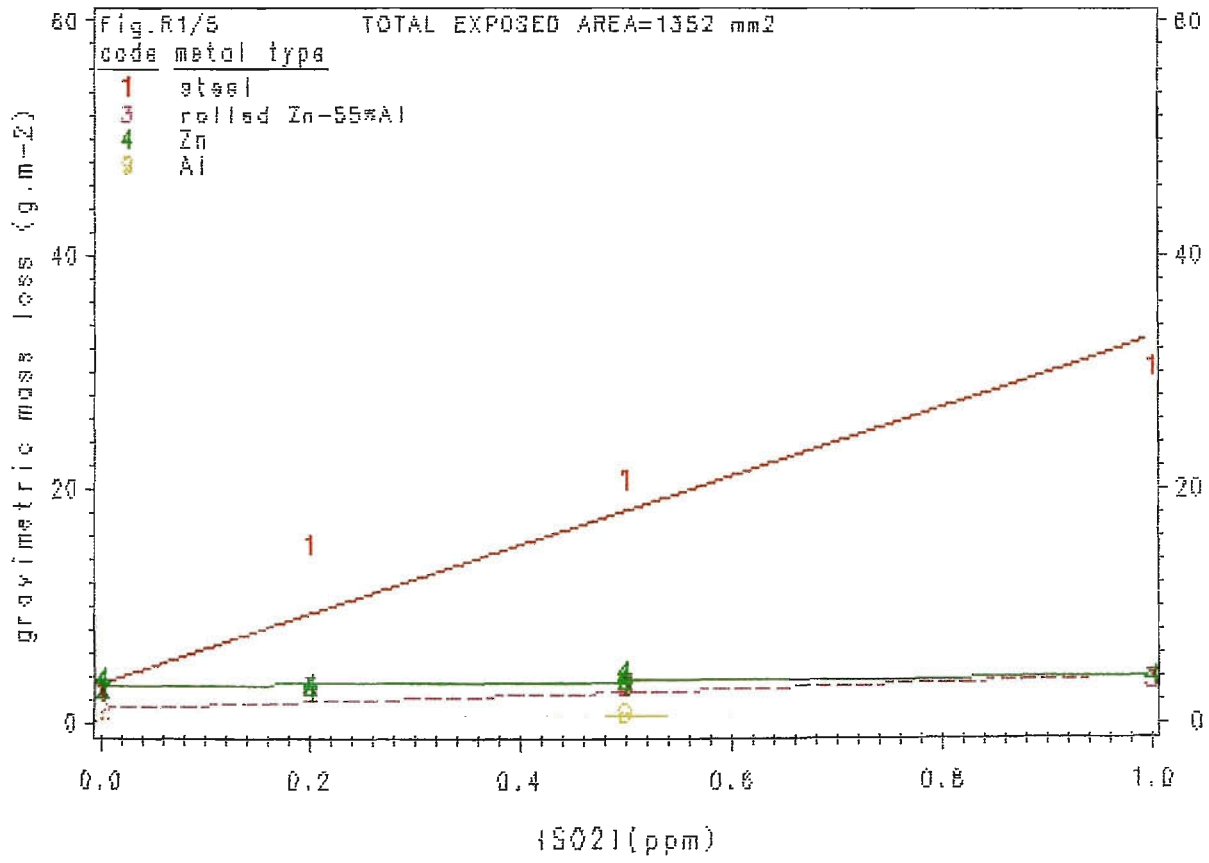

Figures R1/4,5. Effect of {SO2} concentration on weighed mass loss for total exposed sample area in PGB of 3000 mm2 (Fig.R1/4), 1352 mm2 (Fig.R1/5), respectively. Numbers on plots indicate data points; lines are linear regression lines.

(no significant trends were detected in the statistical analysis). These results agree with those of Mansfeld and Tsai[113] who carried out similar thin water film experiments over a wide relative humidity range and found that [SO_2] accelerates the corrosion of steel but does not change or even inhibit the corrosion of zinc.

The weighed mass losses for zinc in Figures R1/4,5 are compared with other methods of calculating Zn mass loss in Figure R1/48, Section R1.7/2. It can be seen that the lack of a significant trend in weighed mass loss (curves 1,2 are replots of Figures R1/4,5 for Zn) is also apparent for galvanic current calculated mass loss (curve 3) and corrosion current calculated mass loss (curve 4). However, the evidence presented in Section T4/2 indicates that Zn corrosion in the atmosphere is markedly increased by SO_2, which is contrary to the above findings based on laboratory experiments. The increasing weighed mass loss trends for Fe with [SO_2] is in agreement with literature findings in Section T4/2. The laboratory results for Zn must therefore be questioned. Two possibilities exist that may explain this discrepancy. Firstly, other particulate and/or gaseous pollutants, see Section T4/1, exist in the atmosphere which were not considered in the simple laboratory simulation. It is possible that these may have some synergistic effect with SO_2 to enhance atmospheric corrosion[70] of Zn. Secondly, Section T4/1 indicates that SO_2 is oxidised to sulphate in the atmosphere and the reaction is catalysed by O_3, H_2O_2 or Fe(II). Experimental evidence[70] has shown that unless the pH of rain droplets is unusually high, excessively long lead times are necessary for the effective oxidation of SO_2 in the absence of catalysts or oxidants. This oxidation may be a necessary prerequisite for the subsequent corrosion of metals. In the laboratory simulation, SO_2 is not oxidised in the gaseous state. This may readily happen on an Fe surface catalysed by the presence of Fe(II),

but may be more difficult on a Zn surface, see Section T4/1. The fact that rolled Zn-55% Al alloy also shows a modest increase in mass loss as [SO_2] increases, refer Figure R1/5 and Figure R1/50 in Section R1.7/2, may be due to the dross inclusions in the alloy which are high in Fe, and which may be responsible for catalysing the oxidation of SO_2 to sulphate.

The mass loss of steel in Figures R1/4,5 at 1 ppm [SO_2] is 7.5, and 10 times higher than at zero [SO_2] respectively. Steel samples showed more red rust initiating sites as the [SO_2] increased. This is in line with the observations of Duncan et al[86] that SO_2 adsorbs at discrete areas on an iron or steel surface, whereas general uptake occurs all over a zinc surface, but is enhanced at areas of bulk corrosion product growth[78].

Mass loss of aluminium, passivated ZINCALUME and cast Zn-55% Al alloy showed no significant trends with [SO_2] in the statistical analysis and have the lowest mass losses, refer Figures R1/4,5. Aluminium is reported to take up SO_2 at discrete areas of the surface[171], but this could not be detected visually because of the very low mass losses involved over the range of [SO_2]. It would appear from these mass loss experiments that cast Zn-55%Al alloy and passivated ZINCALUME show a similar behaviour to aluminium. As actual mass losses were very low (Al 0.1-0.3 mg; rolled Zn-55%Al 0.2-1.2 mg; cast Zn-55%Al 0-2.3 mg; passivated ZINCALUME 0-1.3 mg), it is possible that a sizeable error (max 0.4 mg) may exist.

Unpassivated ZINCALUME shows a slightly higher mass loss, Figure R1/4, which rises slightly with [SO_2], although the trends are only significant at the 95% level of confidence. By comparison with passivated ZINCALUME, it would appear that the passivation film suppresses the adsorption of SO_2 and

hence lowers the mass loss, compared with unpassivated ZINCALUME. Mass losses of passivated galvanized, Figure R1/4, and rolled Zn-55%Al alloy, Figure R1/5, are low at low [SO_2] and similar to those of passivated ZINCALUME, cast Zn-55%Al alloy and aluminium. As [SO_2] rises, mass loss increases, and approaches towards those of zinc and unpassivated galvanized at 1.0 ppm SO_2. The passivation film on galvanized would therefore appear to be somewhat effective at suppressing adsorption by SO_2 at low [SO_2], but is not so effective at higher [SO_2]. The passivation film on galvanized is thus not as effective against the suppression of SO_2 type corrosion as is the passivation film on ZINCALUME. Rolled Zn-55%Al alloy in Figure R1/5 is similar to cast Zn-55% Al alloy at low [SO_2], but there is an increase in mass loss at higher [SO_2].

The significantly higher mass losses for steel at high [SO_2] are of concern because they imply that it will be more difficult to sacrificially protect a steel substrate under these conditions. It is anticipated that it will be more difficult for Zn-55%Al based coatings to sacrificially protect a steel substrate than zinc and galvanized coatings, due to their generally lower mass losses. Normally, urban concentrations of SO_2 are well below 0.1 ppm, but situations arise in highly industrial areas or in localised pockets where concentrations rise above this level, refer Section T4/1, which would increase the corrosion of unprotected steel structures.

The relationship between mass loss of steel and [SO_2] in Figures R1/4,5 may not be strictly linear and may curve over at higher [SO_2]. However, only a simple, linear regression model was used in the statistical analysis and this gave a highly significant correlation between mass loss and [SO_2]. A more complex model was therefore not attempted.

1. Aims, method of calculation

The aim of this section is to compare the mass loss and sacrificial protection ability of the anode electrode of 2-electrode ACMs during 4-cycle PGB test chamber tests at 34.2°C in which the SO_2 concentration was varied over the range 0-1 ppm, Section E2.6/1,2. ACMs investigated were ACM1 (cast Zn-55%Al/Fe), ACM9 (rolled Zn-55%Al/Fe) and ACM2 (Zn/Fe), where the anode electrode is the first mentioned in each pair.

The method of calculating mass loss is given in Equation (T2/8) Section T2/4, and is essentially the area under the I_g/time curve multiplied by an electrochemical equivalent, E_q, and divided by the cathode exposed area. The value of E_q was taken to be that for Zn (3.387×10^{-4} coulombs.g.equiv^{-1}) for all 2-electrode ACMs. This will be approximately correct for the Zn-55%Al alloy ACMs at least in the initial stages of corrosion because the zinc-rich regions corrode preferentially to the aluminium-rich regions[164] during atmospheric exposure. These calculations will overestimate mass loss from Zn-55%Al alloy ACMs if there is any appreciable dissolution of aluminium because E_q will be too high (E_q for Al 0.932×10^{-4} coulombs.g.equiv^{-1}).

2. ACM anode mass loss versus [SO_2]

The shape of I_g/t plots varied considerably but the overall trend was for the area under the curve (and hence the anode mass loss) to decrease from cycle to cycle as corrosion products built up. This can be observed in the statistical tables in Section A4/2.2. The general pattern was for I_g to rise slowly to a broad maximum in the first cycle and then decline rapidly as the water film evaporated to dryness. This was always observed for the ACM2 (Zn/Fe) but

less frequently with cast and rolled Zn-55%Al/Fe (ACM 1,9 respectively). Subsequent cycles reduced the maximum I_g value and flattened the broad maximum for ACM2 (Zn/Fe), but this was rarely observed in the cast and rolled Zn-55%Al/Fe ACMs where the general trend was an initial rapid decline in I_g followed by a plateau for most of the cycle, thence a more rapid decline as the water film evaporated to dryness.

Tables of anode mass loss calculated from I_g/t curves as a function of $[SO_2]$ in the PGB air stream are listed in Appendix A4/2.2 along with the results of statistical analysis. Figure R1/6 is a plot of the regression equations obtained from this analysis, plus the data points for anode mass loss versus $[SO_2]$. The exposed areas were different for each ACM, as shown in Figure R1/6 and the tables in Section A4/2.2, which causes complications when attempting to compare one ACM with another. However, the areas are similar enough and the mass losses different enough to make reasonably valid comparisons. Furthermore, the results are supported by weighed mass loss results in Figures R1/4,5, Section R1.3.

Zinc in ACM2 (Zn/Fe) has the highest mass loss, than either rolled Zn-55%Al alloy in ACM9 (rolled Zn-55%Al/Fe) or cast Zn-55%Al alloy in ACM1 (cast Zn-55%Al/Fe). The correlation between mass loss of zinc in ACM2 and $[SO_2]$, was not significant although the regression line is still plotted in Figure R1/6. This indicates that the mass loss of zinc is relatively unaffected by SO_2 pollutant in the air stream over the range 0-1 ppm as was found for Zn weighed mass losses in Section R1.3. There was a significant positive correlation between mass loss of rolled Zn-55%Al alloy in ACM9 (rolled Zn-55%Al/Fe) and $[SO_2]$ indicating that there is a moderate increase in mass loss as $[SO_2]$ is increased. There is no significant correlation between mass

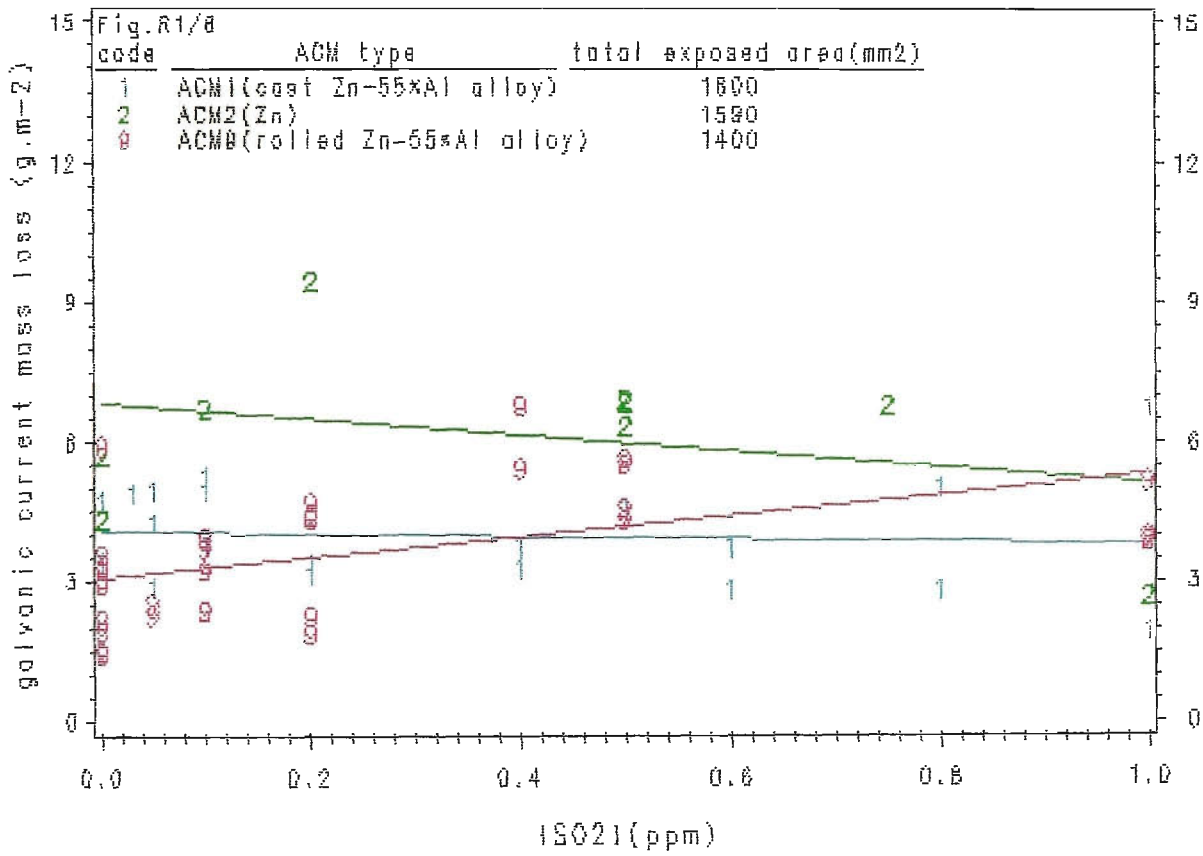

Figure R1/6. Effect of [SO2] concentration on ACM mass loss derived from galvanic current/time data for various 2-electrode ACMs. Numbers on plot indicate data points ; lines are linear regression lines.

loss of cast Zn-55%Al alloy in ACM1 (cast Zn-55%Al/Fe) and [SO_2]. A similar situation exists for weighed mass loss/[SO_2] trends in Section R1.3. Mass loss/[SO_2] trends are reasonably similar for cast and rolled Zn-55%Al/Fe ACMs and this indicates the following. Firstly, the corrosion behaviour of cast and rolled Zn-55%Al alloy is reasonably similar as would be expected. Secondly, the method of calculation, Equation (T2/8), Section T2/4, appears to be justified because areas of anode and cathode plates are very different in ACM1 (cast Zn-55%Al/Fe) but quite similar in ACM9 (rolled Zn-55%Al/Fe), see Table E2/1, Section E2.4/3.

3. ACM sacrificial protection ability versus [SO_2]

The zinc in ACM2 (Zn/Fe) sacrificially protected the steel plates for the entire 4-cycles at all [SO_2] over the 0-1 ppm range. A slight amount of red rust (less than 0.1% of the total steel area), was occasionally observed at the end of the fourth PGB cycle as indicated in Table A4/13, Section A4/2.2. However, white corrosion products precipitated mainly over the steel plates, leaving the zinc plates appearing dark grey. Photographs, typical of the [SO_2] range are shown in Figure R1/7a,b for 0 and 0.5 ppm [SO_2].

The mechanism of sacrificial protection of the steel plates in ACM2 (Zn/Fe) is depicted in Figures R1/8. This is essentially a dual mechanism in which the steel cathode plates are protected by the normal sacrificial mechanism of the zinc plates, plus an added benefit of precipitation of corrosion products on the steel plates. The normal sacrificial protection mechanism is explained in Section T2/1,2. The corrosion product precipitation mechanism is as follows. Zinc ions from corrosion of the zinc plates migrate towards the cathodic steel plates. Hydroxyl ions formed by reduction of oxygen, Equation (R1/1), migrate

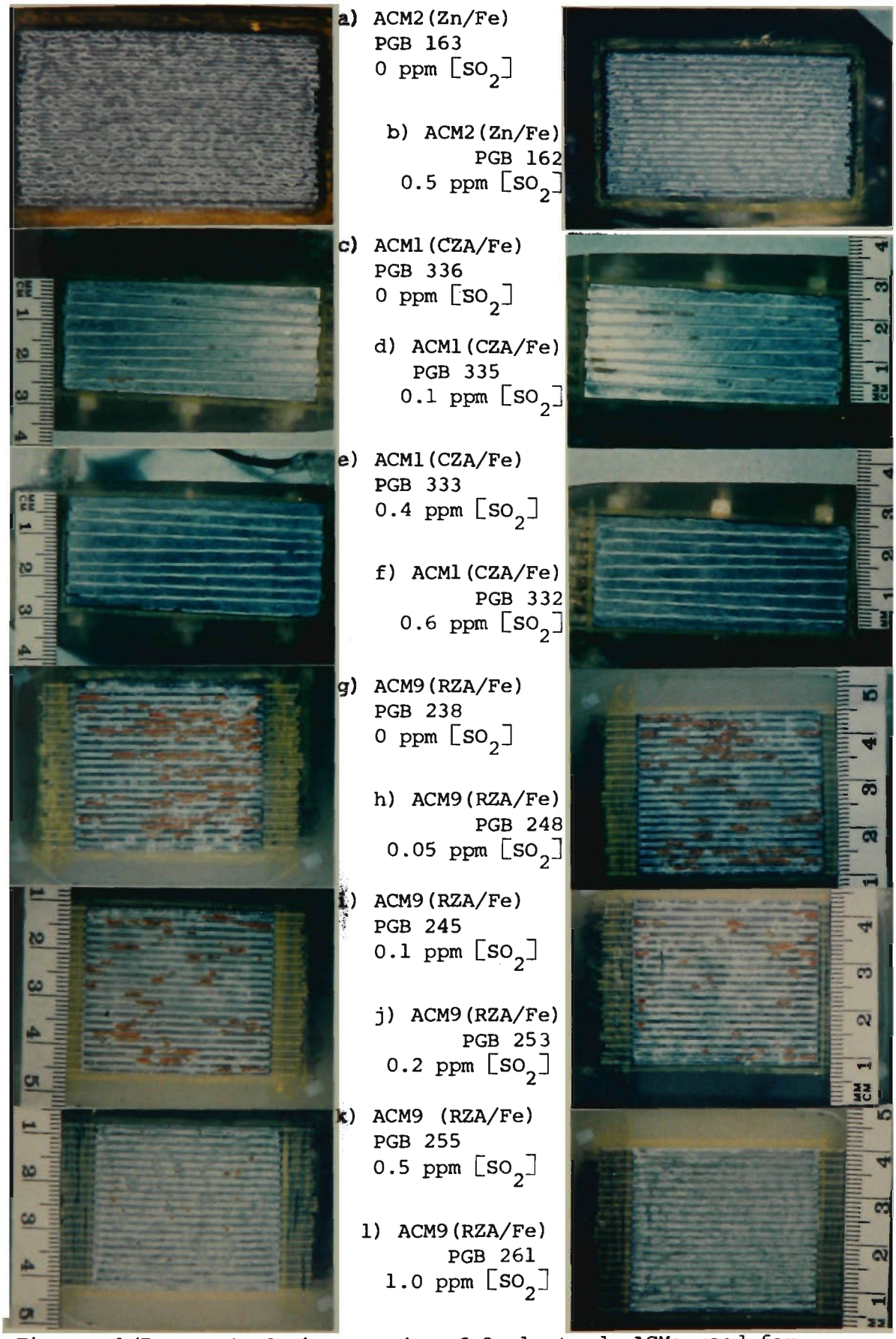

Figure R1/7. Typical photographs of 2-electrode ACMs used for galvanic current tests after 4 PGB cycles at various [SO_2] showing corrosion product build-up and red rusting of steel cathode plates. ACM2(Zn/Fe) (Fig. R1/7a,b);ACM1(CZA/Fe)(Fig. R1/7c-f);ACM9(RZA/Fe) (Fig. R1/7g-l); CZA,RZA cast, rolled Zn-55%Al alloy.

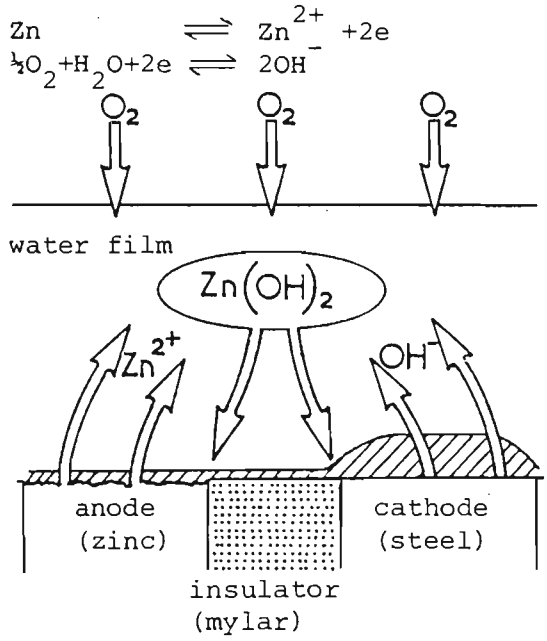

Figure R1/8. Schematic diagram showing mechanism of sacrificial protection of steel plates in ACM2 (Zn/Fe). This is a dual mechanism of normal sacrificial protection by the zinc anode plates, plus precipitation of zinc corrosion products predominantly onto the steel cathode plates.

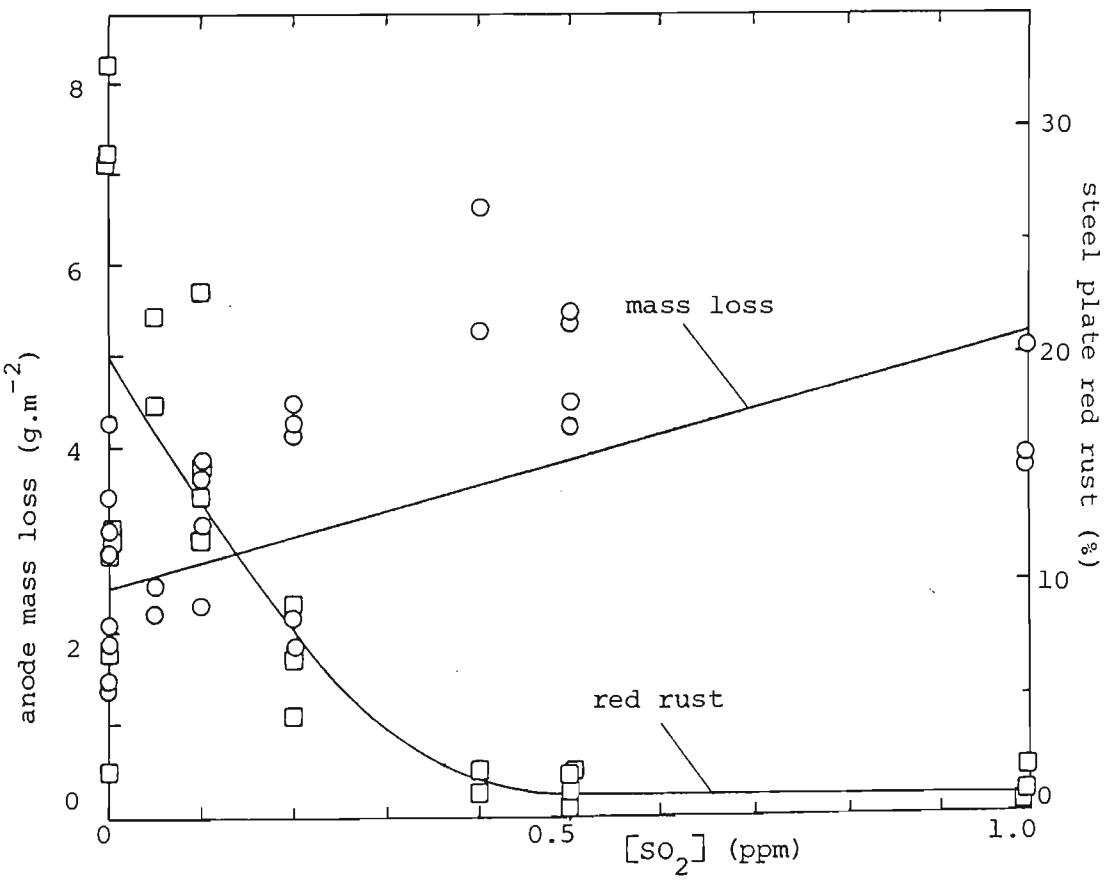

Figure R1/9. Effect of $[SO_2]$ on anode mass loss and steel cathode red rust for ACM9 (rolled Zn-55%Al/Fe) after 4 PGB cycles. Mass loss line is regression line based on a linear model; red rust line is curve of best fit by eye through the data points.

towards the anode zinc plates, but cause the solution adjacent to the steel plates to become alkaline. After sufficient build-up of zinc ions and hydroxyl ions, the solubility product[167], K_{sp}, Equations (R1/2,3), is exceeded, and precipitation of insoluble zinc hydroxide occurs predominantly in the alkaline regions adjacent to the steel plates.

$$\tfrac{1}{2}O_2 + H_2O + 2e \Leftrightarrow 2OH^- \qquad (R1/1)$$

$$Zn^{2+} + 2OH^- \Leftrightarrow Zn(OH)_2 \downarrow \qquad (R1/2)$$

$$K_{sp} = [Zn^{2+}][OH^-]^2 \qquad (R1/3)$$

$$= 1.8 \times 10^{-14} \text{ at } 18\text{-}20°C$$

This precipitation is likely to have two effects - the efficiency of the steel cathode plates to oxygen reduction, Equation (R1/1), will be reduced, and the anodic zinc plates will achieve some inhibition. This is evidenced by the fact that the area under the I_g/t curves decreases from PCB cycle 1 to cycle 4, indicating reduced zinc corrosion, see Section R1.4/2.

Red rust was observed on steel plates of both ACM1 (cast Zn-55%Al/Fe) and ACM9 (rolled Zn-55%Al/Fe). Typical photographs after 4 PCB cycles are shown in Figure R1/7c-1 at different $[SO_2]$. These indicate that both the cast Zn-55%Al alloy and the rolled Zn-55%Al alloy do not sacrificially protect their respective steel plates as effectively as the zinc in the Zn/Fe (ACM2) ACM, due no doubt, to their lower mass loss, Figure R1/6.

Not as much red rust appears to have formed on the steel plates of ACM1 (cast Zn-55%Al/Fe) as on those of ACM9 (rolled Zn-55%Al/Fe) and the amount of red rust did not show a clear decreasing trend with increasing $[SO_2]$ as did ACM9. However, this may be connected with the cathode/anode area,

which was 0.22 for ACM1 and 0.99 for ACM9, see Table E2/1, Section E2.4/3.

Figure R1/9 shows the extent of red rust formation of the steel plates of ACM9 (rolled Zn-55%Al/Fe) as a function of $[SO_2]$. The regression line for anode mass loss (rolled Zn-55%Al) is also shown replotted from Figure R1/6, see below. Although there is a large amount of scatter in results at zero and low $[SO_2]$, the general trend is for an exponential decrease in the extent of red rust and a moderate increase in anode mass loss as $[SO_2]$ increases. These results indicate that the rolled Zn-55%Al alloy plates have difficulty in sacrificially protecting the exposed steel plates at zero and low $[SO_2]$. This conclusion is quite opposite to that suggested from the analysis of weighed mass loss trends in Figures R1/4,5, Section R1.3, and illustrates the problem of attempting to extrapolate results from one type of measurement (mass loss on uncoupled metals) to another (sacrificial protection ability using coupled dissimilar metals). Although Figures R1/4,5 suggest that steel at high $[SO_2]$ will have markedly increased corrosion rates and this will mean that the low corrosion rates for Zn-55%Al alloys will have difficulty in sacrificially protecting the steel, it is apparent from Figure R1/9 that this is not the case. It is hypothesized that when steel is coupled to rolled Zn-55%Al alloy plates in ACM9, the degree of sacrificial protection rises as the $[SO_2]$ rises. This is attributed mainly to an increase in the conductivity of the water film on the ACM surface, caused by oxidation of SO_2 to sulphate, see Section T4/2. This increased solution conductivity causes a modest increase in mass loss of the rolled Zn-55%Al alloy plates, as shown in Figure R1/9, which is sufficient to protect the steel plates at the higher SO_2 levels. White corrosion products from corrosion of rolled Zn-55%Al alloy plates are observed to form over most of the steel plates, leaving the rolled Zn-55%Al alloy appearing dark grey. Therefore it is likely that zinc and aluminium ions released by corrosion from

rolled Zn-55%Al alloy plates precipitate onto adjacent steel plates as a result of zinc and aluminium hydroxide formation caused by increased alkalinity at the cathodic steel plates where oxygen reduction predominantly occurs. This is a similar mechanism to that discussed earlier in this section for the Zn/Fe ACMs which also protects the steel plates.

4. ACM9 mass loss/sacrificial protection ability versus $[Cl^-]$

The hypothesis, expounded in Section R1.4/3, that rolled Zn-55%Al alloy plates in ACM9 (rolled Zn-55%Al/Fe) sacrificially protect the steel plates even at high $[SO_2]$ because of an increase in conductivity of the water film, has been supported by a further test series. In this series, described in Section E2.6/2, water films containing a range of NaCl concentrations from distilled water to 1000 $mg.L^{-1}$ $[Cl^-]$, were applied in the first PGB cycle only, thence distilled water in cycles 2-4, to the surface of ACM9 at zero $[SO_2]$ in the air stream. Typical photographs of ACM9 after 4 PGB cycles are shown in Figure R1/10, which indicate that the extent of red rust on the steel plates decreases as $[Cl^-]$ increases.

Figure R1/12 shows curves of best fit by eye for anode mass loss/$[Cl^-]$ and per cent red rust/$[Cl^-]$. Data for distilled water has been arbitrarily plotted at 10^{-3} $mg.L^{-1}$ $[Cl^-]$. It is seen from the curve of best fit that there is a marked increase in mass loss with increase in $[Cl^-]$ concentration at 10^1 $mg.L^{-1}$ $[Cl^-]$ and above. There is also a marked decrease in per cent red rust as $[Cl^-]$ increases, at 10^1 $mg.L^{-1}$ $[Cl^-]$ and above.

Solution conductivity increases with increasing chloride ion concentration[167]. This experiment therefore demonstrates that an increase in anode mass loss,

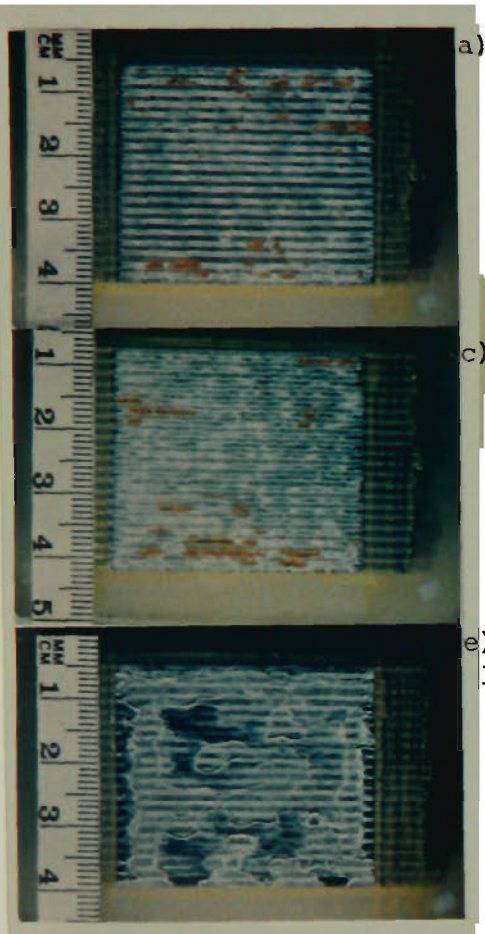

a) PGB 278
distilled water

b) PGB 281
1 mg.L^{-1} [Cl^-]

c) PGB 285
10 mg.L^{-1} [Cl^-]

d) PGB 286
100 mg.L^{-1} [Cl^-]

e) PGB 272
1000 mg.L^{-1} [Cl^-]

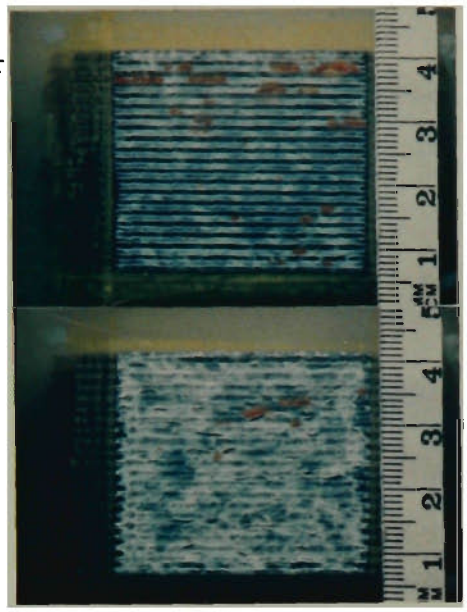

Figure R1/10. Typical photographs of ACM9 (rolled Zn-55%Al/Fe) after 4 PGB cycles over a range of [Cl^-] showing corrosion product build-up and red rusting of steel cathode plates.

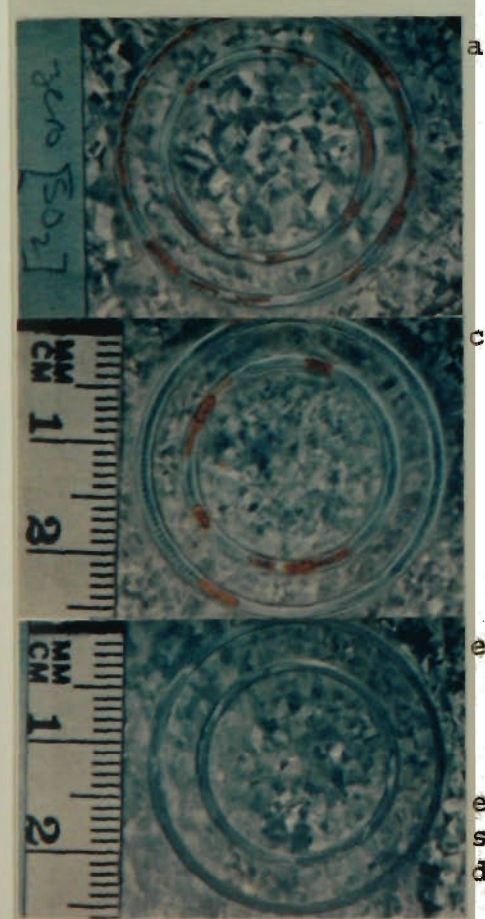

a) PGB 309
0 ppm [SO_2]

b) PGB 309
0.05 ppm [SO_2]

c) PGB 308
0.1 ppm [SO_2]

d) PGB 308
0.4 ppm [SO_2]

e) PGB 309
1.0 ppm [SO_2]

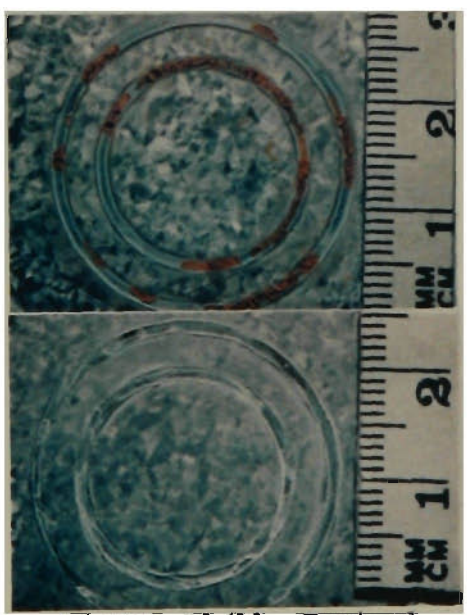

Figure R1/11. Typical photographs of grooved ZINCALUME after 4 PGB cycles over a range of [SO_2] showing that the extent of red rust of the exposed steel substrate in the grooves increases as [SO_2] decreases.

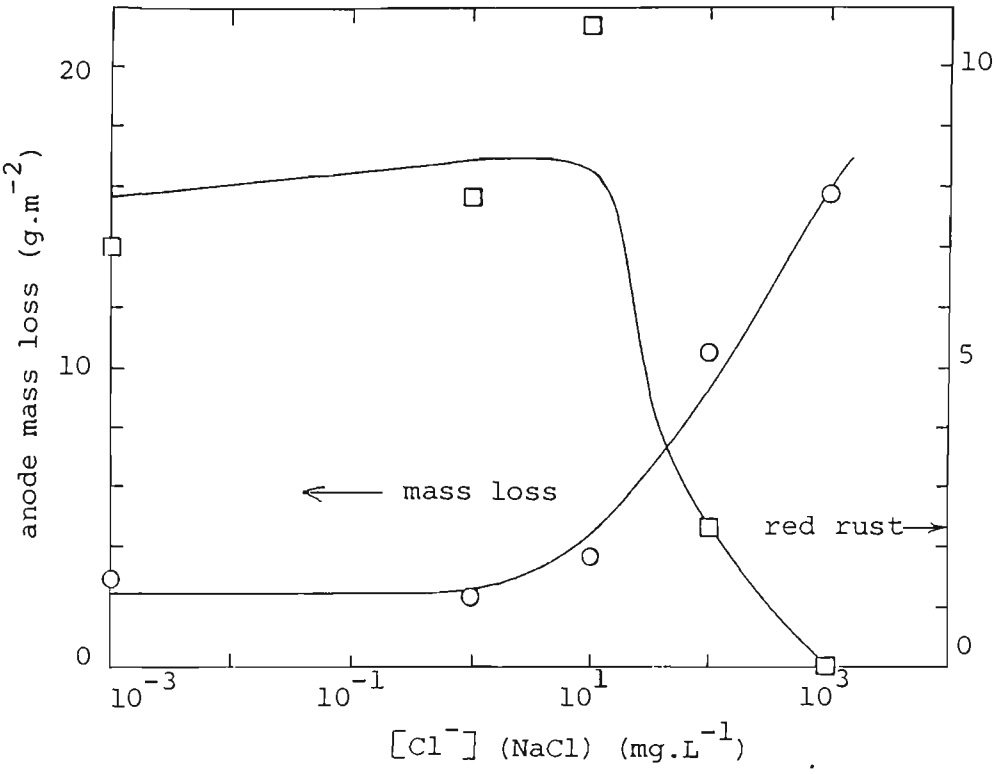

Figure R1/12. Effect of $[Cl^-]$ on anode mass loss and steel cathode red rust for ACM9 (rolled Zn-55%Al/Fe) after 4 PGB cycles showing that mass loss increases and red rust decreases as solution $[Cl^-]$ increases above 10 $mg.L^{-1}$. Data for distilled water arbitrarily plotted at 10^{-3} $mg.L^{-1}$ $[Cl^-]$.

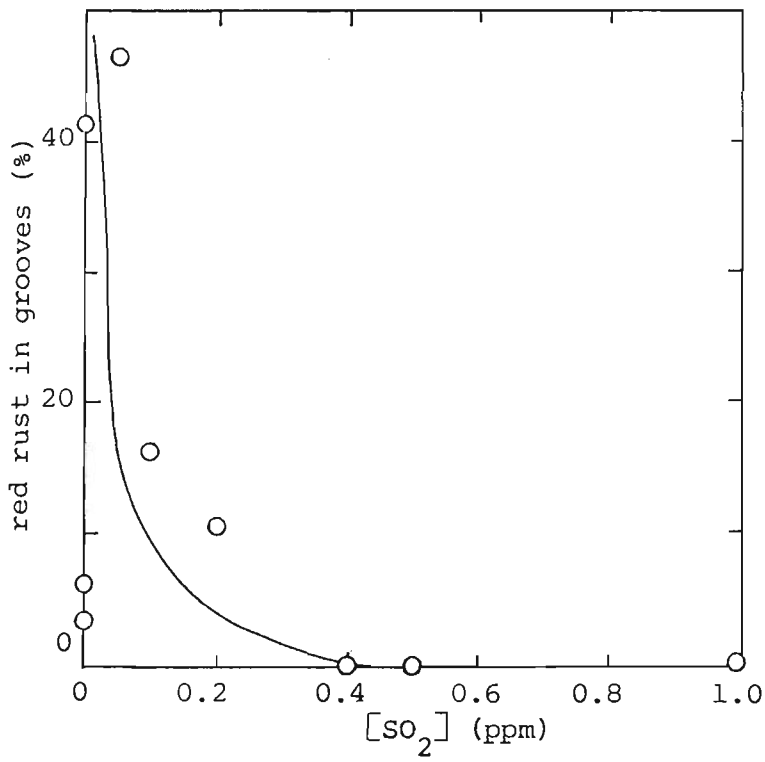

Figure R1/13. Extent of red rust in circular grooves on unpassivated ZINCALUME disc samples after 4 PGB cycles as a function of $[SO_2]$ in the air stream. Refer Section E2.6/3 for details.

brought about by an increasing solution conductivity, results in a decrease in the amount of red rust on the steel plates of ACM9 (Zn-55%Al/Fe), and hence an increase in the level of sacrificial protection of the steel by the rolled Zn-55%Al alloy plates. This conclusion supports the conclusion in Section R1.4/3 regarding the reduction in red rust at higher [SO_2] thought to result in a higher solution conductivity brought about by oxidation of SO_2 to sulphate.

5. Sacrificial protection ability of ZINCALUME coating versus [SO_2]

The results in Sections R1.4/3,4 show that the ability of rolled Zn-55%Al alloy to sacrificially protect the steel plates in ACM9 increases as the conductivity of pure water films increases, either by small additions of chloride ions or sulphate ions, the latter thought to result from the oxidation of SO_2 from the air. This section attempts to show that an unpassivated ZINCALUME coating acts in a similar way to its exposed steel substrate. Discs of unpassivated ZINCALUME coated steel, with grooves cut in them so as to just expose the steel substrate, were exposed in the PGB test chambers to water films which were allowed to evaporate to dryness over 4 PGB cycles in an air stream containing different concentrations of SO_2 pollutant, as described in Section E2.6/3.

The general pattern was for red rust to occur in the grooves to differing degrees depending on the [SO_2], and for white corrosion products from corrosion of the ZINCALUME coating to spread across the coating/groove interface and into the groove itself. Typical photographs of grooved ZINCALUME discs after 4 cycles at various [SO_2] are shown in Figure R1/11, illustrating the extent of red rust in the steel groove areas decreases as [SO_2] increases.

Figure R1/13 is a plot of the extent of red rust in the exposed steel grooves as a function of [SO_2] in the air stream. A fair degree of scatter exists in the results at zero and low [SO_2] as was observed in Figure R1/9, Section R1.4/3. However, the general trend is for an exponential decrease in the extent of red rust as [SO_2] increases, indicating that sacrificial protection ability of the ZINCALUME coating increases as [SO_2] increases. The same mechanism, as discussed in Section R1.4/3, is thought to occur here, that is, a dual mechanism of sacrificial protection by the ZINCALUME coating aided by precipitation of corrosion products on the steel. There is a fair degree of similarity in this plot and Figure R1/9, for red rust on steel plates of ACM9. This suggests that the degree of sacrificial protection afforded by the rolled Zn-55%Al alloy plates in Figure R1/9 is similar to that afforded by the unpassivated ZINCALUME coating, despite differences in microstructure and corrosion behaviour discussed in Section R1.2/2.

R1.5 PGB Impedance Tests on 3-Electrode ACMs

1. Aims, method of calculation

The aim of this section is to compare the impedance behaviour of the various 3-electrode ACMs during 4-cycle PGB test chamber tests at 34.2°C in which the [SO_2] was varied over the range 0-1 ppm, see Section E2.6/1. The ACMs investigated were ACM3 (Zn), ACM4 (rolled Zn-55%Al alloy) and ACM8 (Fe).

The wide frequency range impedance method was used to collect impedance data for each ACM, as discussed in Section E2.6/4. For each run within a PGB cycle, this data was analyzed manually by first plotting a Nyquist plot (reactive, b, versus resistive, a, components of impedance, Z, where Z = a + jb)

and a Bode (log modulus of impedance, r, and phase angle, θ, versus log frequency, f) plot on the digital plotter. Parameter values of an equivalent circuit model representing the metal/solution interface were then calculated from these plots. The model chosen to best suit the impedance data was the normal charge-transfer resistance, R_t, in series with a Warburg diffusion resistance, Z_ω, both in parallel with the double layer capacitance, C_d. A solution resistance, R_s, was also included. This model is described partly in Section T1/4, Figure T1/2, and partly in Section T1/5, Figure T1/4. Nyquist plots were preferred to Bode plots for obtaining parameter values R_s, R_t, C_d and σ (Warburg diffusion coefficient), but in certain cases difficulty was experienced in analyzing Nyquist plots and Bode plot values were obtained instead. Because these values were manually calculated, a larger degree of error would be included compared to values calculated by an iterative computer program method, which is at present under development. Manual calculation methods for R_s, R_t, C_d are described in Section T1/4, for σ in Section T1/5.2 and also in reference 17. Cell impedance corrections for identical working/auxiliary electrodes have been applied to the results discussed in Sections R1.5/3-5. These correction methods are described in Section T1/6. Values of σ were calculated by two methods as described in Section T1/5.2. The first method is an approximate one using Equation (T1/12). The second method, using program 'sigma' in Section A1/4.6 is more accurate and uses Equations (T1/13,14). However, both methods gave very similar results for these ACM calculations.

2. Nyquist plot shapes

Some 411 Nyquist and 411 Bode plots were obtained but only example plots of each ACM are shown in Figures R1/14-16 (Nyquist) and R1/17-19 (Bode). The

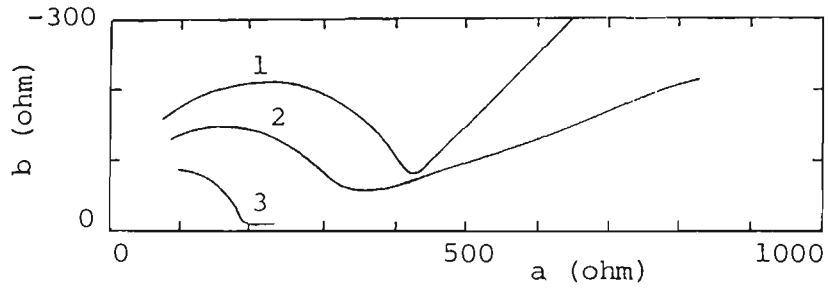

Figure R1/14. Nyquist complex plane plots of resistive, a, versus reactive, b, components of impedance for ACM3 (Zn) at 1.0 ppm [SO_2].

code	PGB cycle	run	time (mm)
1	290/1	1	10
2	290/3	1	10
3	290/4	1	10

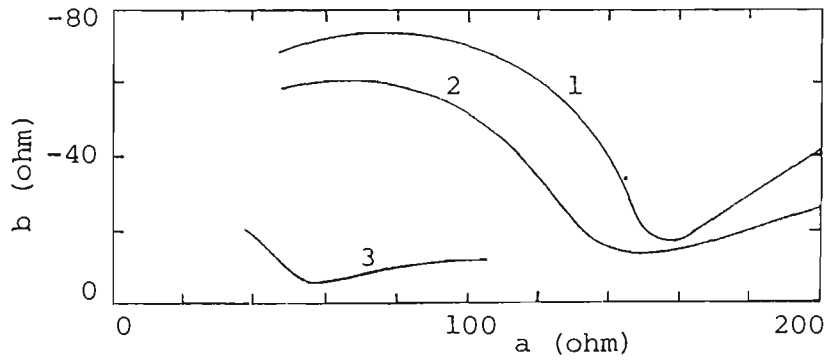

Figure R1/15. Nyquist complex plane plots of resistive, a, versus reactive, b, components of impedance for ACM8 (Fe) at 1.0 ppm [SO_2].

code	PGB cycle	run	time (min)
1	262/1	1	10
2	262/1	4	160
3	262/2	4	160

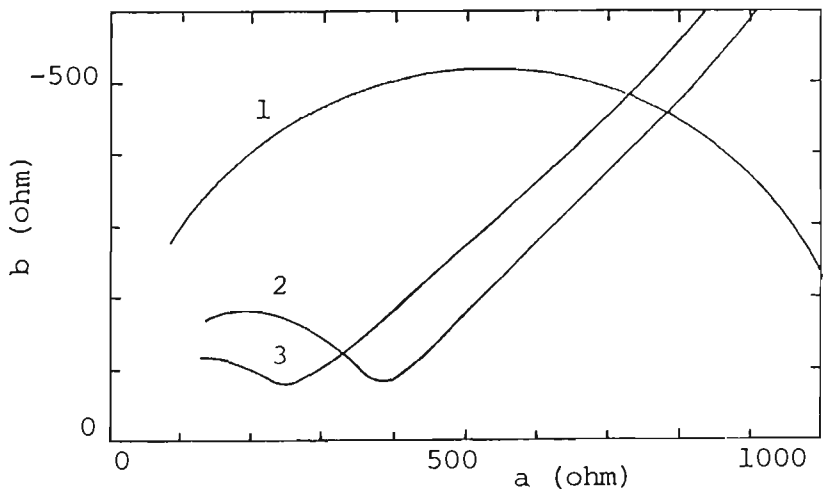

Figure R1/16. Nyquist complex plane plots of resistive, a, versus reactive, b, components of impedance for ACM4 (rolled Zn-55%Al) at 1.0 ppm [SO_2].

code	PGB cycle	run	time (min)
1	294/1	1	10
2	294/2	3	81
3	294/4	3	120

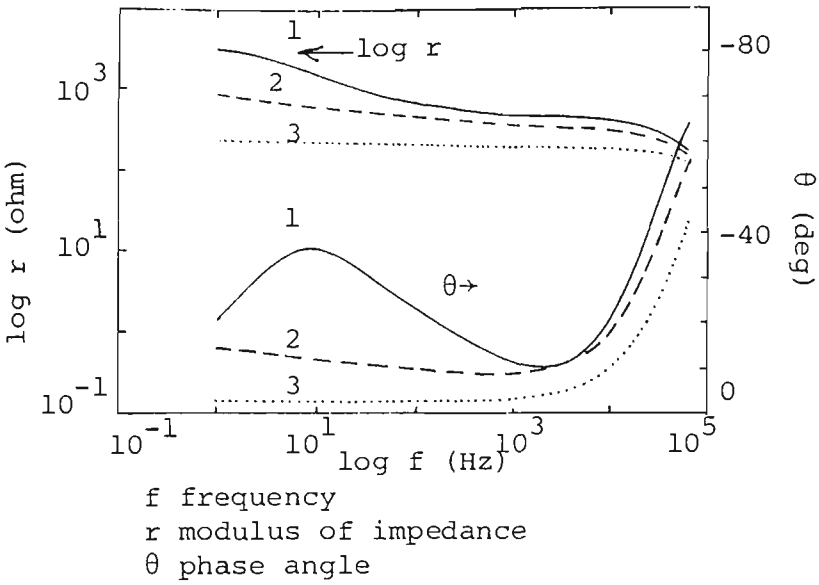

f frequency
r modulus of impedance
θ phase angle

Figure R1/17. Bode plot of log f versus log r and θ for ACM3 (Zn) at 1.0 ppm [SO_2], PGB 290.

code	cycle/run	time
1	1/1	10
2	3/1	10
3	4/1	10

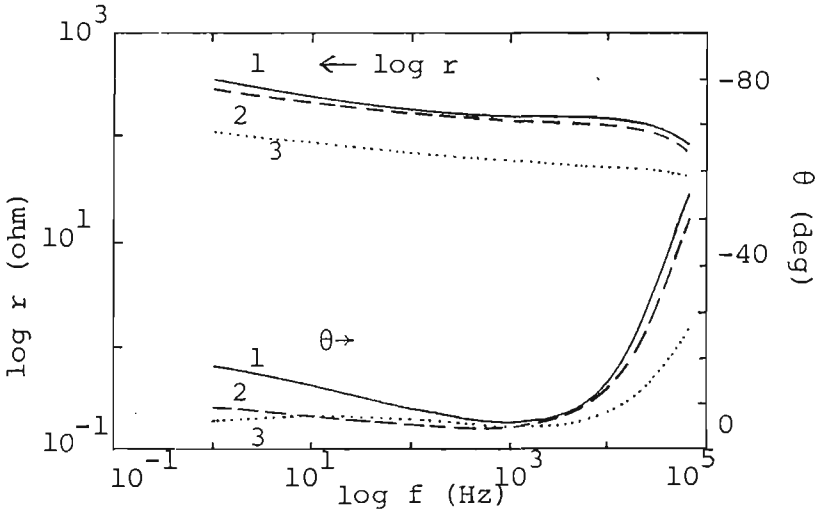

Figure R1/18. Bode plot of. log f versus log r and θ for ACM8 (Fe) at 1.0 ppm [SO_2], PGB 262.

code	cycle/run	time
1	1/1	10
2	1/4	160
3	2/4	160

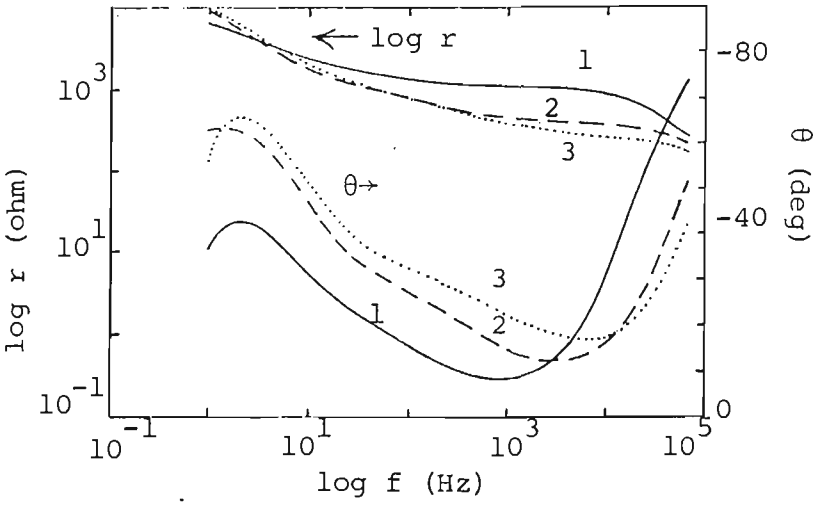

Figure R1/19. Bode plot of log f versus log r and θ for ACM4 (rolled Zn-55%Al) at 1.0 ppm [SO_2], PGB 294.

code	cycle/run	time
1	1/1	10
2	2/3	81
3	4/3	120

general Nyquist plot shape was a semicircular arc at higher frequencies, plus a diffusion tail at lower frequencies, interpreted as R_t plus Z_ω in parallel with C_d. The shape of the plot indicates the type of corrosion control, which here is a combination of charge-transfer and diffusion. There was a general trend for the semicircular shape to decrease from cycle to cycle, indicating decreased values of R_t, but there were exceptions, notably with ACM4 (rolled Zn-55%Al).

Difficulties were experienced in analyzing all the Nyquist or Bode plots in two general cases. Firstly, the semicircular arc was sometimes only partly formed, with the highest frequency portion missing. The severity of this problem depended on the ACM type and the build-up of corrosion products, gradually getting worse from cycle to cycle in the PGB and degrading in the order from left to right: ACM4 (rolled Zn-55%Al) < ACM3 (Zn) < ACM8 (Fe).

This problem was a result of the frequency response analyzer being limited to an upper frequency of only 65 kHz. It was caused by the time constant $\tau_m = R_t\ C_d$ being too low, and mainly by R_t being too low, because C_d was relatively constant, see Section R1.5/4. This can be readily explained because the frequency, f_{bmax}, at the maximum b value on a Nyquist plot is given by Equation (R1/4).

$$f_{bmax} = 1/2\pi R_t\ C_d = 1/2\pi\ \tau_m \qquad \text{(R1/4)}$$

If R_t is low with C_d relatively constant, then f_{bmax} will be high and all other frequencies will be high, compared to the case where R_t is high. As can be seen by the results in Section R1.5/3, R_t values for ACM8 (Fe) are lowest and

ACM4 (rolled Zn-55%Al alloy) highest, so that the semicircle will be less complete for ACM8 (Fe) and give rise to difficulties in obtaining R_t and especially C_d. Secondly, the angle of the diffusion tail to the a-axis declined from a value close to the theoretical 45° to almost horizontal to the a-axis, making it extremely difficult to estimate diffusion coefficient, σ, values. Section T1/5.2 describes how program sigma was used to obtain an average σ value in these cases. The severity of this problem depended on ACM type and build-up of corrosion products, gradually getting worse from cycle to cycle in the PGB and degrading in the same order as before. This problem was obviously related to the build-up of corrosion products and is discussed further in Sections R1.8/1,3. The angle of the diffusion tail actually increased above 45° at the lowest tested frequencies at zero $[SO_2]$ for ACM8 (Fe) and ACM4 (rolled Zn-55%Al), Section R1.5/3.3, but a linear diffusion tail inclined close to 45° was observed at higher frequencies and no difficulties were experienced in determining values of σ in this case. These two general problems are illustrated in the Nyquist plots of Figures R1/14-16.

3. R_t and σ trends versus time and $[SO_2]$

Figures R1/20-22 shows R_t as a function of time for each run within a PGB cycle, and from cycle to cycle at each SO_2 concentration for ACM3 (Zn), ACM8 (Fe) and ACM (rolled Zn-55%Al). Similar plots for σ are shown in Figures R1/23-25.

3.1 Trends within a cycle

The last data point in a cycle is sometimes higher for R_t and σ than previous points in the same cycle for each of the 3 ACMs. This was caused by the

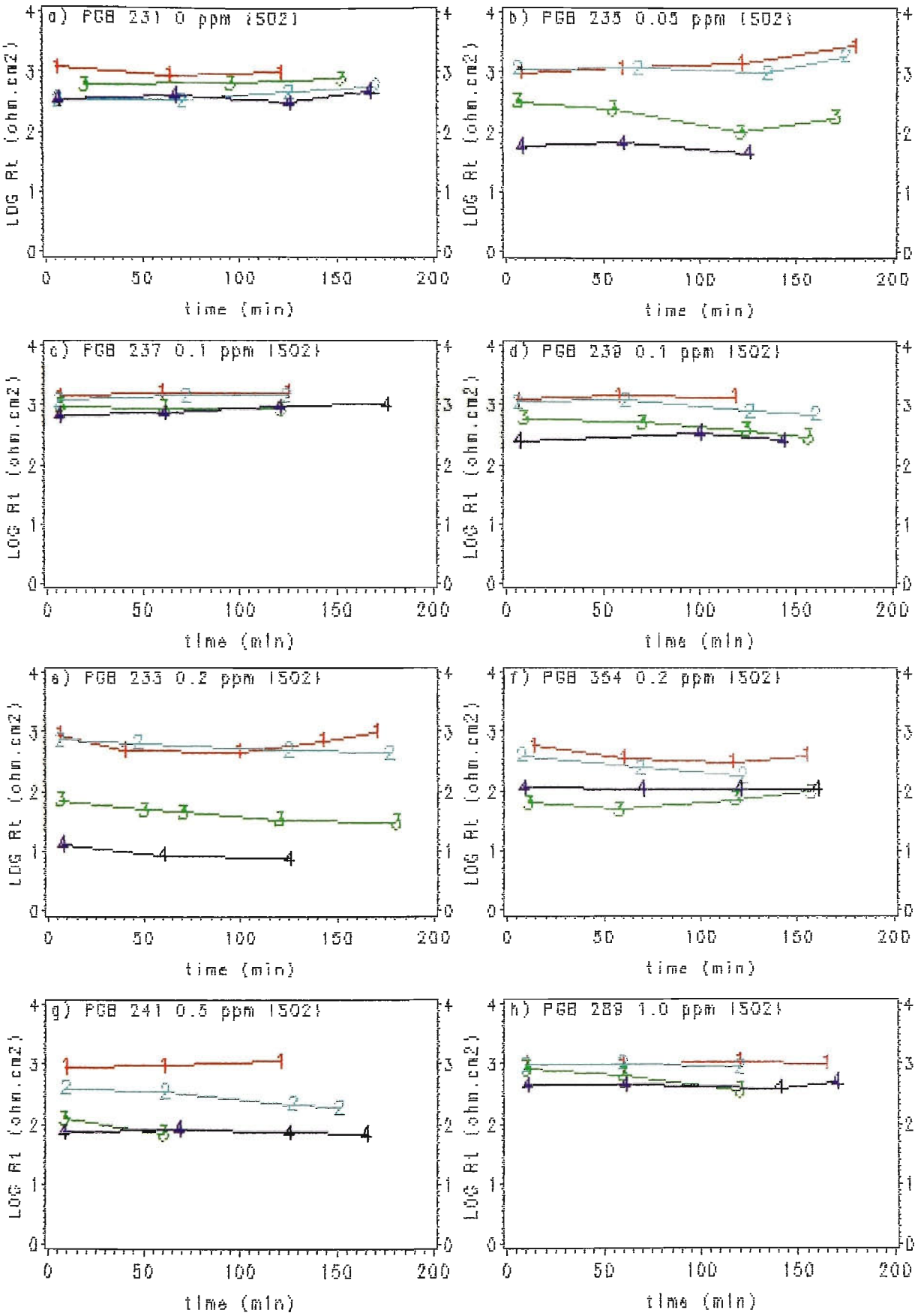

Figure R1/20. Effect of time on charge-transfer resistance, Rt, from run to run within a cycle; from cycle to cycle; and from (SO2) to (SO2) for ACM3(Zn). Numbers on plots are run data points for cycles 1-4 respectively.

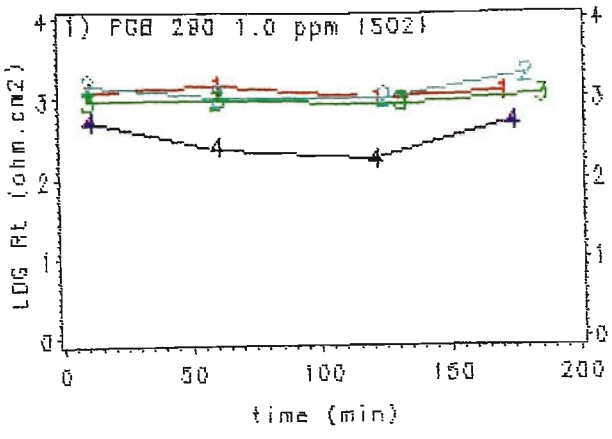

Figure R1/20.(cont.)

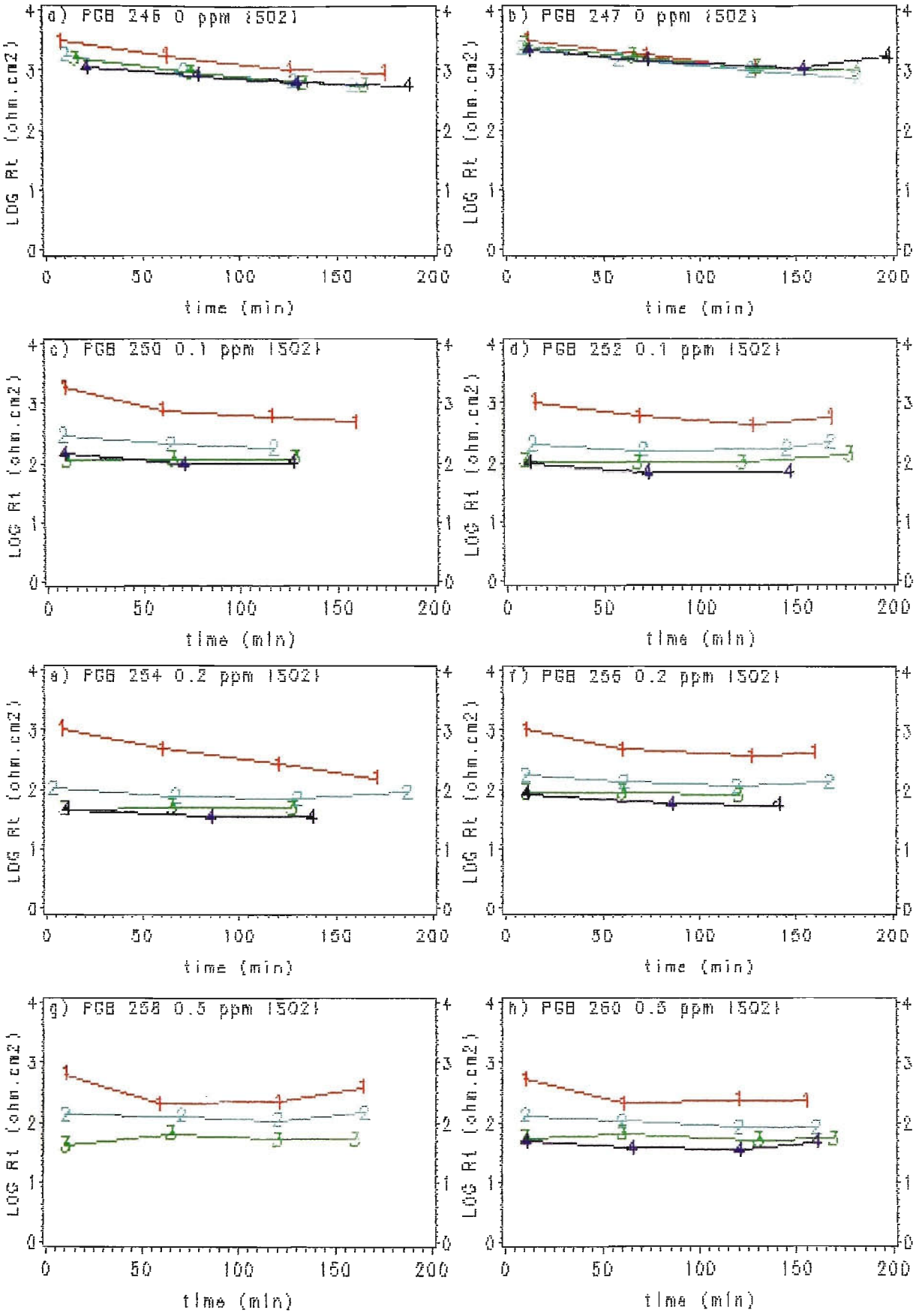

Figure R1/21. Effect of time on charge-transfer resistance, Rt, from run to run within a cycle; from cycle to cycle; and from (SO2) to (SO2) for ACM8(Fe). Numbers on plots are run data points for cycles 1-4 respectively.

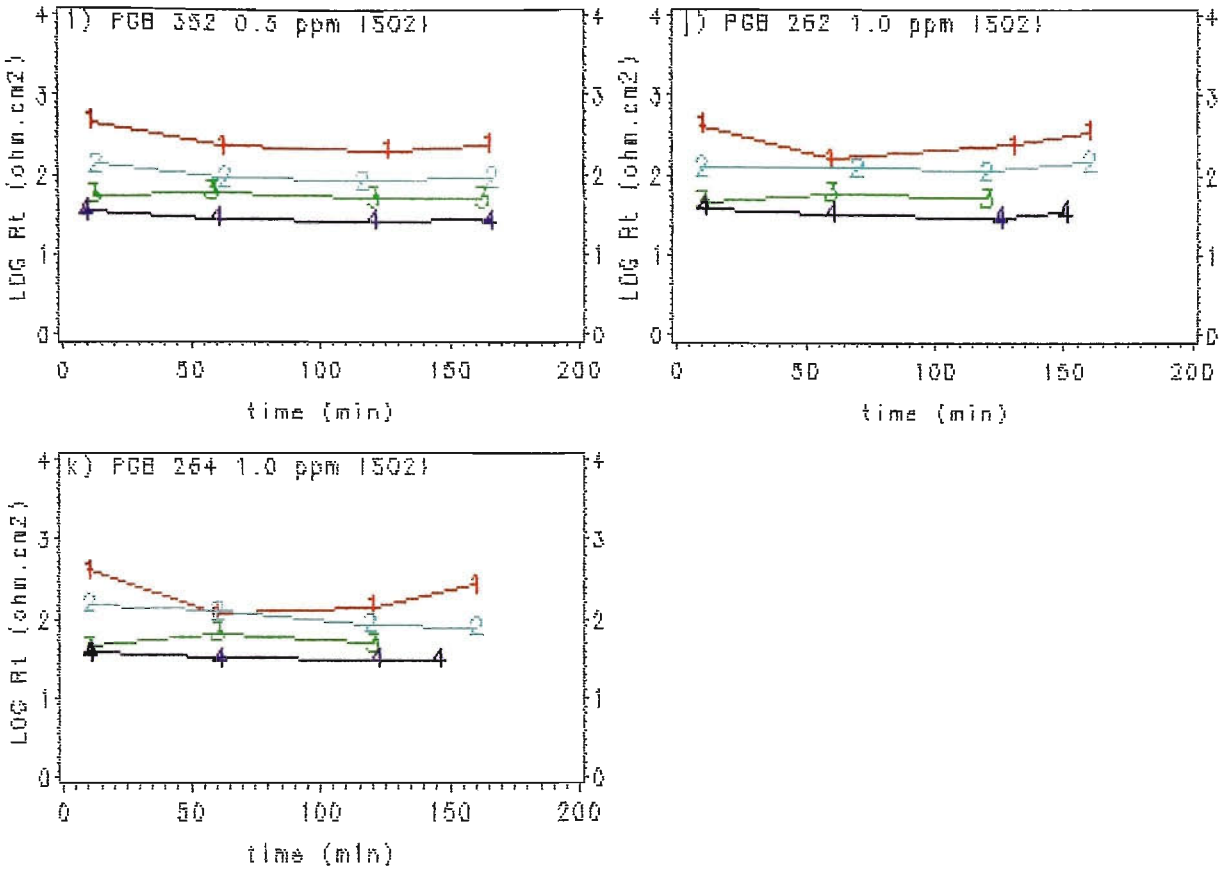

Figure R1/21.(cont.)

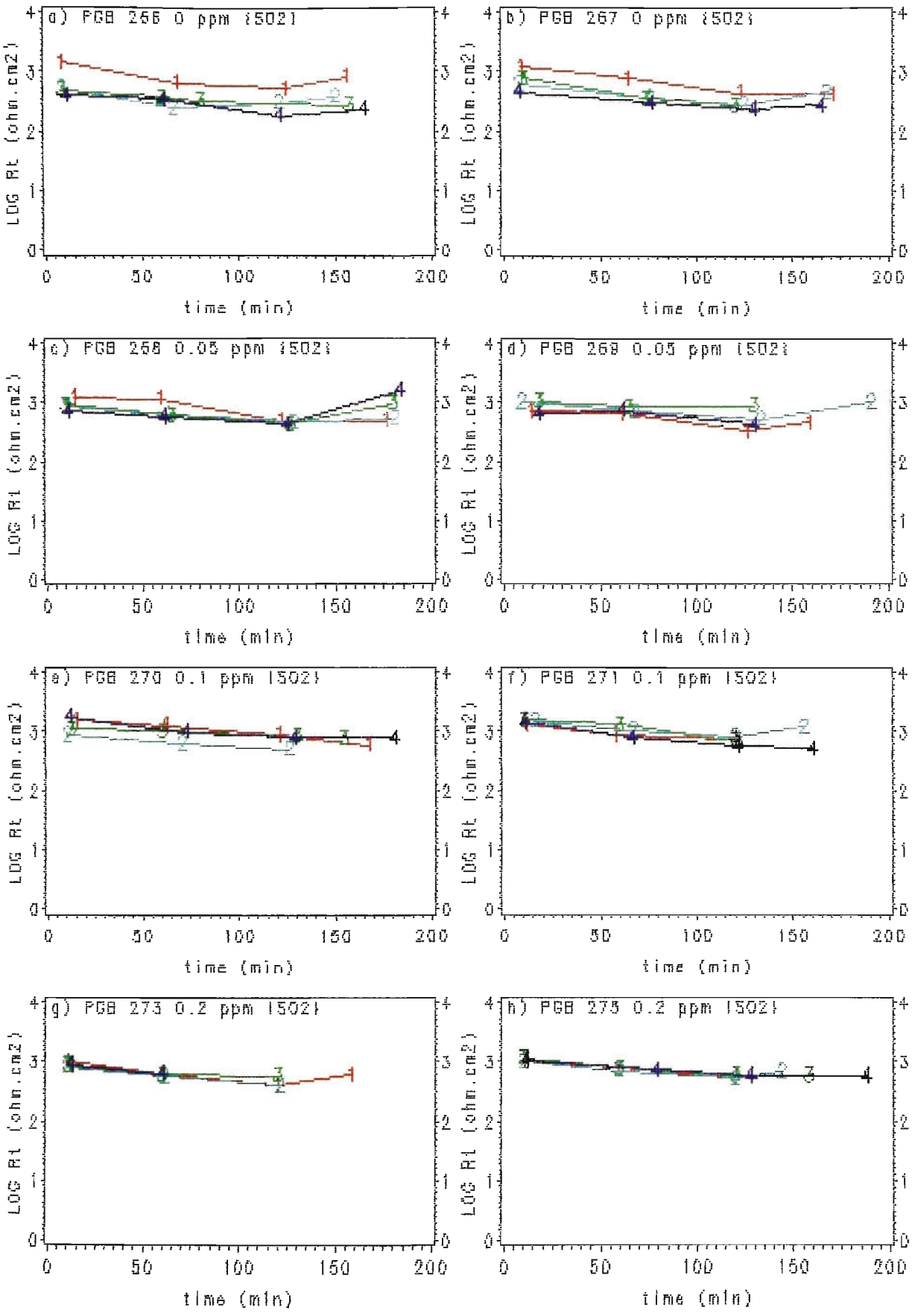

Figure R1/22. Effect of time on charge-transfer resistance, Rt, from run to run within a cycle; from cycle to cycle; and from (SO2) to (SO2) for ACM4(rolled Zn-55%Al). Numbers on plots are run data points for cycles 1-4 respectively.

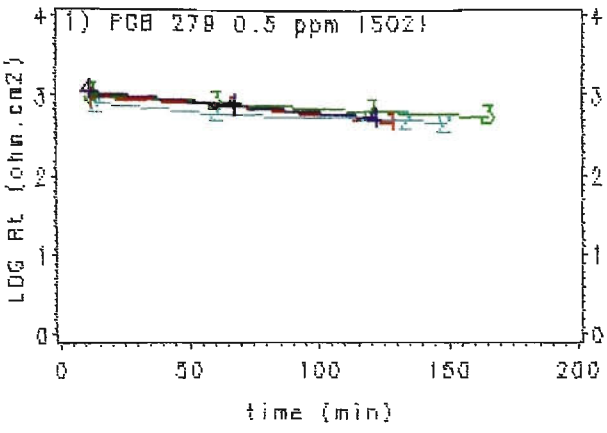

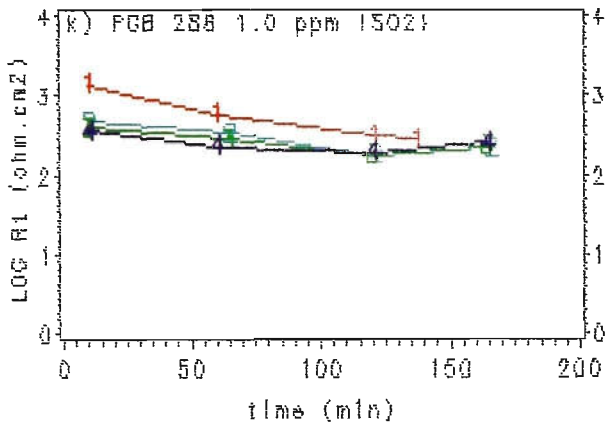

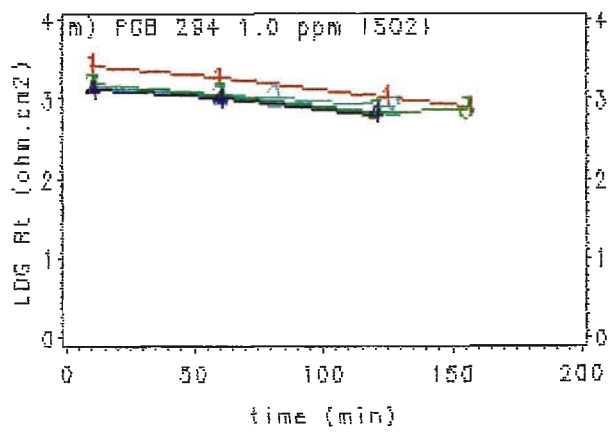

Figure R1/22.(cont.)

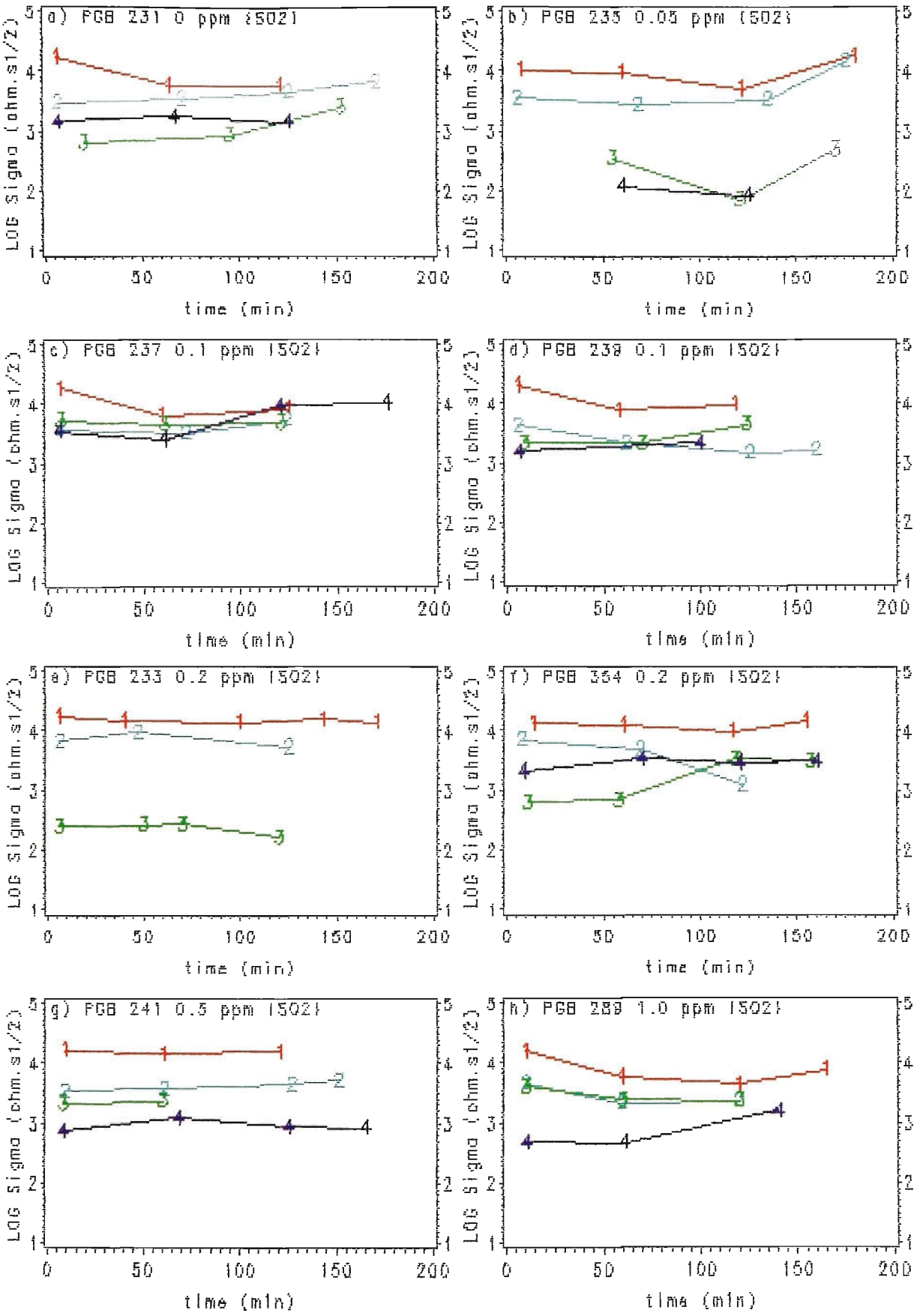

Figure R1/23. Effect of time on Warburg diffusion coefficient, Sigma, from run to run within a cycle; from cycle to cycle; and from (SO2) to (SO2) for ACM3(Zn). Numbers on plots are run data points for cycles 1-4 respectively.

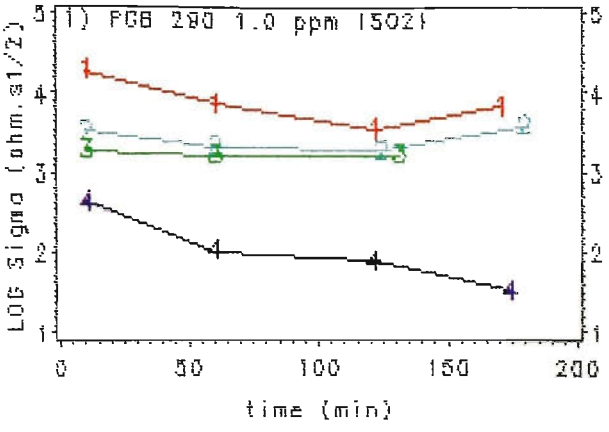

Figure R1/23.(cont.)

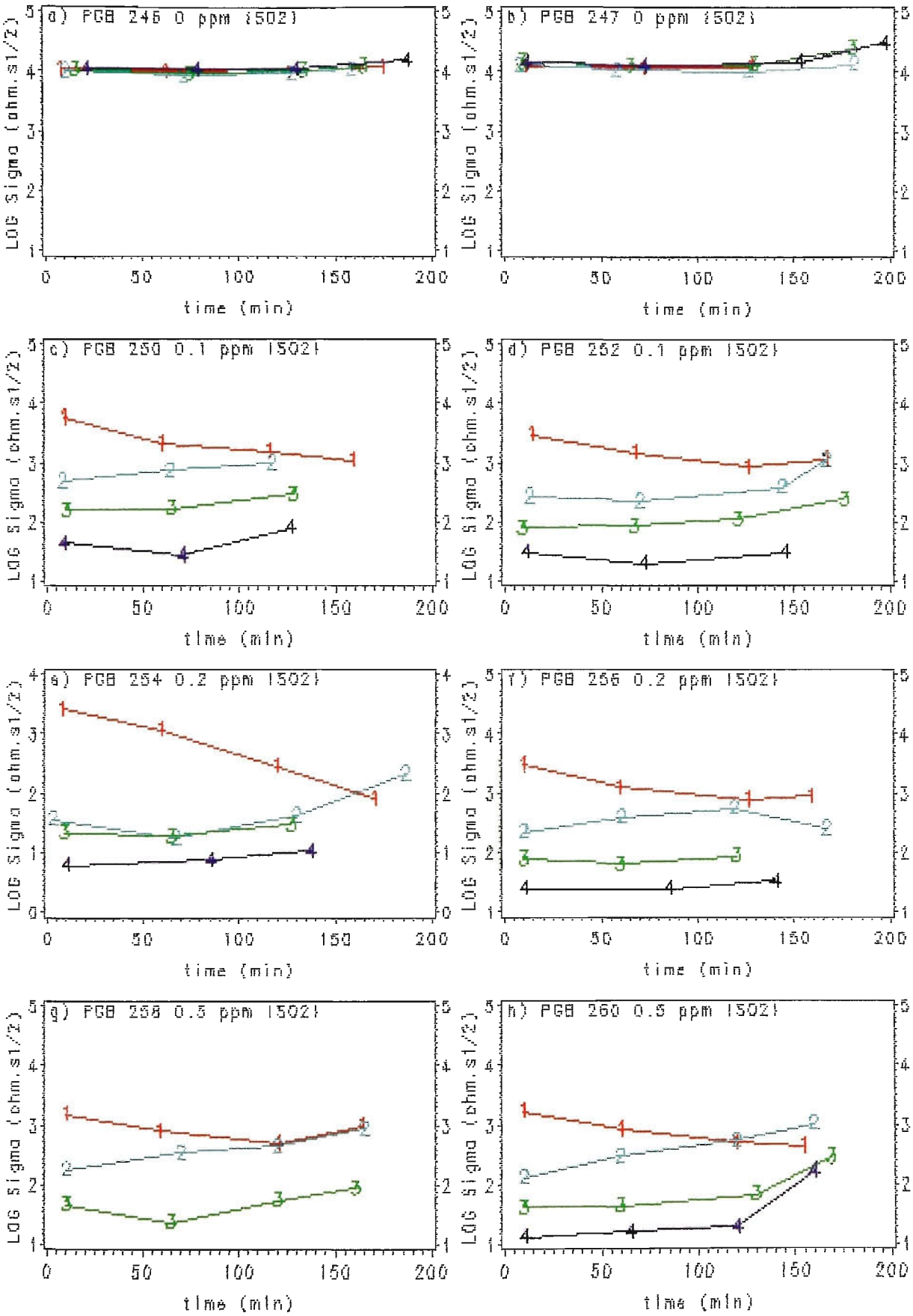

Figure R1/24. Effect of time on Warburg diffusion coefficient, Sigma, from run to run within a cycle; from cycle to cycle; and from (SO2) to (SO2) for ACMB(Fe). Numbers on plots are run data points for cycles 1-4 respectively.

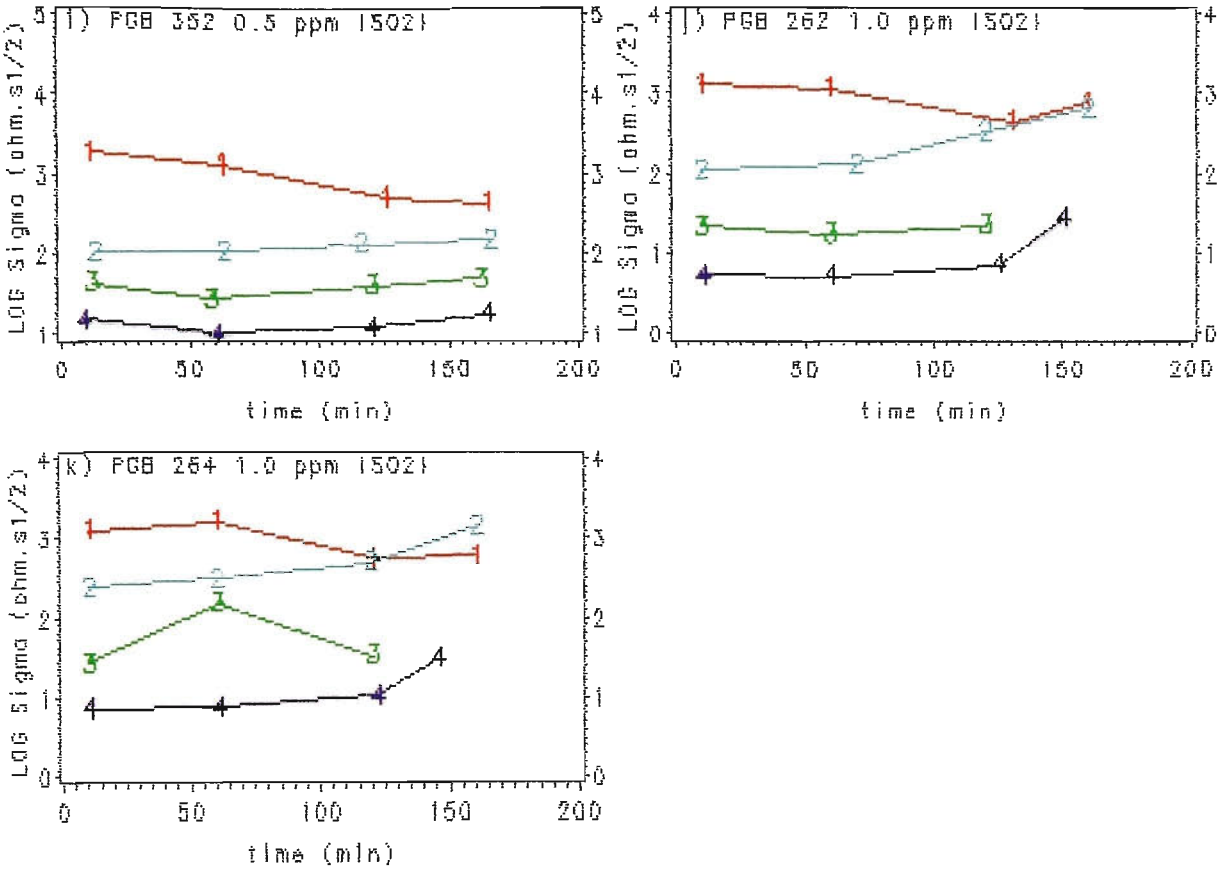

Figure R1/24.(cont.)

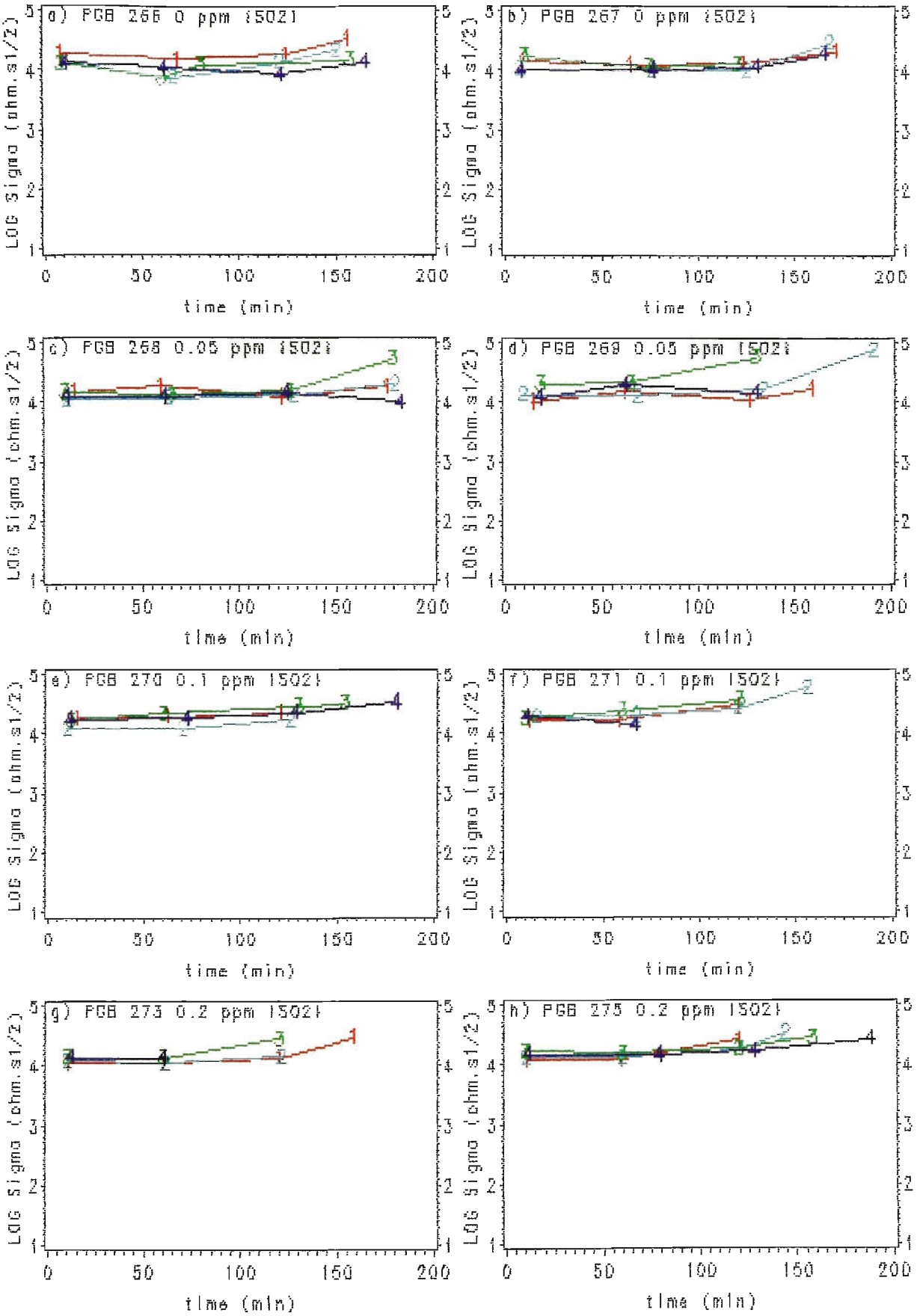

Figure R1/25. Effect of time on Warburg diffusion coefficient, Sigma, from run to run within a cycle; from cycle to cycle; and from (SO2) to (SO2) for ACM4(rolled Zn-55%Al). Numbers on plots are run data points for cycles 1-4 respectively.

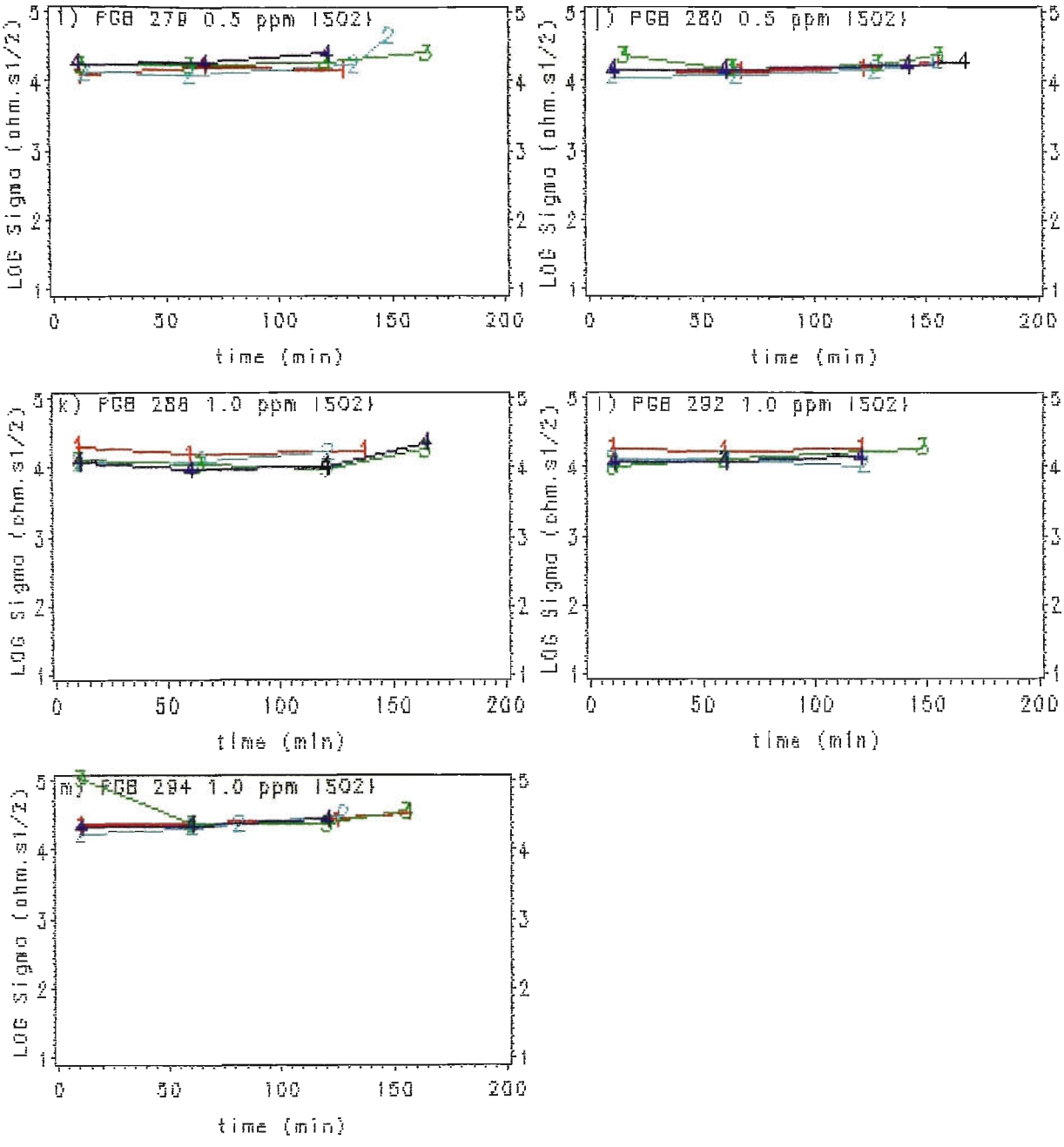

Figure R1/25.(cont.)

water film drying out so that the ACM surface was either <100% wet or only a very thin film existed. This rise does not necessarily mean that charge-transfer and diffusion rates decrease, but may simply be due to a reduced area of corrosion.

For ACM3 (Zn), R_t and σ trends within a cycle are similar in behaviour. Values of R_t, Figure R1/20, and σ (Figure R1/23) do not show the tendency to decrease within a PGB cycle as is shown with ACM8 (Fe) in Figures R1/21,24. In some cycles, R_t and σ drop, in others they rise and in others still they remain relatively constant with time. These results suggest that corrosion of the Zn plates and diffusion processes to/from the ACM surface remain relatively constant within a given cycle, but with some exceptions.

For ACM8 (Fe), R_t values, Figure R1/21, decrease within a cycle for all four PGB cycles at zero [SO_2]. When SO_2 is present, there is still a decrease in the first cycle, but the decrease is not as marked in later cycles. In Figure R1/24, σ values are relatively constant within a cycle for all four cycles at zero [SO_2], but a decrease is noted in cycle 1 when SO_2 is present. This decrease becomes less marked for PGB cycles 2-4. These results suggest that charge-transfer rates increase at zero [SO_2] within a PGB cycle, but diffusion processes remain unaltered. When SO_2 is present, both charge-transfer and diffusion processes increase.

For ACM4 (rolled Zn-55%Al), R_t values, Figure R1/22, decrease within a cycle over the entire [SO_2] range in a similar manner and degree to ACM8 (Fe), and more marked than ACM3 (Zn). In Figure R1/25, σ values are relatively constant within a cycle. These results indicate that charge-transfer processes decrease within a PGB cycle, but that diffusion processes remain unaltered.

3.2 Trends from cycle to cycle

For ACM3 (Zn), R_t values, Figure R1/20, generally decrease from cycle to cycle over the entire [SO_2] range, although there are exceptions. The drop from cycle to cycle was relatively small at 0,0.1,0.2 (PGB 354) and 1 ppm [SO_2], but was quite marked at 0.05,0.2 (PGB 233) and 0.5 ppm [SO_2]. This variable behaviour is also reflected in the σ trends from cycle to cycle in Figure R1/23 but to a less noticeable extent. It is therefore difficult to conclude that decreases in R_t and σ from cycle to cycle indicate faster rates of charge-transfer and diffusion. An explanation is discussed in Section R1.8/1 where this variability is thought to be caused by random partial short circuits between alternate ACM plates. The pattern for σ to decrease from cycle to cycle over the entire [SO_2] range is similar, but less pronounced than that for ACM8 (Fe) in Figure R1/24. Values of σ are generally an order of magnitude higher than R_t values at the same [SO_2], cycle and run time, as can be ascertained by comparing Figures R1/20,23. This suggests that a combination of charge-transfer and diffusion control governs the corrosion rate, with the possibility that diffusion control may even predominate, a finding that is supported by the discussion in Appendix A5/2. This is reasonable for corrosion under thin, stagnant water films.

For ACM8 (Fe), R_t values, Figure R1/21, and σ values, Figure R1/24, are close together from cycle to cycle at zero [SO_2], indicating little change in the rates of charge-transfer and diffusion processes. There is a marked lowering of both R_t and σ values from cycle to cycle when SO_2 is present, normally indicating much faster corrosion rates and/or corroding area, and diffusion processes that speed up markedly. It is also possible that partial shorts are involved, refer to Section R1.8. This is summarized in Figures R1/26,27 for R_t

and σ values taken at about 10 min test time (results taken from Figures R1/21,24 respectively). Values of σ are generally higher than corresponding R_t values, but there is not as great a difference as was found for ACM3 (Zn). This may indicate that diffusion may not be as controlling as it was for ACM3 (Zn). In cycle 1, the drop in R_t and σ as $[SO_2]$ is increased suggests that there is a rapid equilibrium of SO_2 in the water film on the freshly abraded ACM surface. This pattern is reflected in cycles 2-4 which also indicates a rapid uptake of SO_2 in the water film and/or the corrosion products.

For ACM4 (rolled Zn-55%Al), R_t values, Figure R1/22, and σ values, Figure R1/25, are remarkably constant from cycle to cycle at all $[SO_2]$, indicating little change in the rates of charge-transfer and diffusion processes.

3.3 Trends with $[SO_2]$

For ACM3 (Zn), it is difficult to summarise the effect of $[SO_2]$ on R_t and σ value from Figures R1/20,23 because of the variability at 0.05,0.2 (PGB 233), 0.5 ppm $[SO_2]$ as previously mentioned in Section R1.5/3.2, and assumed to be caused by partial short circuits, refer Section R1.8/1. However, typical photographs at 0,0.2,1.0 ppm $[SO_2]$ in Figure R1/28a-c show white corrosion product build-up over the entire ACM surface after four cycles, but there does not appear to be any essential difference in the amount of build-up at the different SO_2 levels. This is supported by the weighed mass losses in Figures 4,5, Section R1.3; the galvanic current calculated mass losses in Figure R1/6, Section R1.4/2; and the corrosion current calculated mass losses in Figure 1/35, Section R1.6/4; all of which show no significant trends with $[SO_2]$. Figure R1/48, Section R1.7/2 summarises the effect of $[SO_2]$ on Zn mass loss for each of these test methods.

For ACM8 (Fe), Figures R1/26,27 are summary plots for R_t and σ taken after about 10 minutes duration of each cycle from Figures R1/21,24 respectively. The R_t and σ results at zero [SO_2] are both higher in value and closer together from cycle to cycle, indicating lower corrosion and diffusion rates with little change from cycle to cycle, compared with results in the presence of [SO_2]. The corresponding Nyquist plots show a very large diffusion tail relative to the semicircle diameter, suggesting that diffusion processes are rate determining. The angle of the diffusion tail is <45° at around 100 Hz but increases to >45° at lower frequencies. This is also observed with ACM4 (rolled Zn-55%Al) and may indicate some adsorption processes. Visual inspection, see Figure R1/28d-i, indicated that only a small number of red rust 'nests' had formed at zero[SO_2] after four cycles, Figure R1/28d,e, but the number of 'nests' initiating on the surface in the first cycle increased markedly as [SO_2] in the air stream increased, and the ACM surface was heavily covered with red rust at 1.0 ppm [SO_2] after four cycles, Figure R1/28f-i. Visual inspection therefore supports the R_t/time results. Values of R_t at zero [SO_2] are higher than for ACM3 (Zn) or ACM4 (rolled Zn-55%Al alloy), suggesting a lower corrosion rate. However, as [SO_2] increases, R_t values decrease markedly and more so than ACM3 (Zn) or ACM4 (rolled Zn-55%Al alloy), normally indicating a greater increase in corrosion rate in the presence of [SO_2].

X-ray examination of the red rust after four cycles at 0.5 ppm [SO_2] for PGB 260 indicated the presence of mainly Fe_3O_4, magnetite, together with δFeO(OH), lepidocrocite, and αFeO(OH), goethite. Reaction products of SO_2, such as sulphates, could not be detected. Two steel samples were placed in the PGB for one and two cycles at 0.5 ppm [SO_2] and subsequently analyzed by energy dispersive spectroscopy, EDS. To roughly measure the presence of sulphur products in the red rust, a number of cellotape strips were applied to

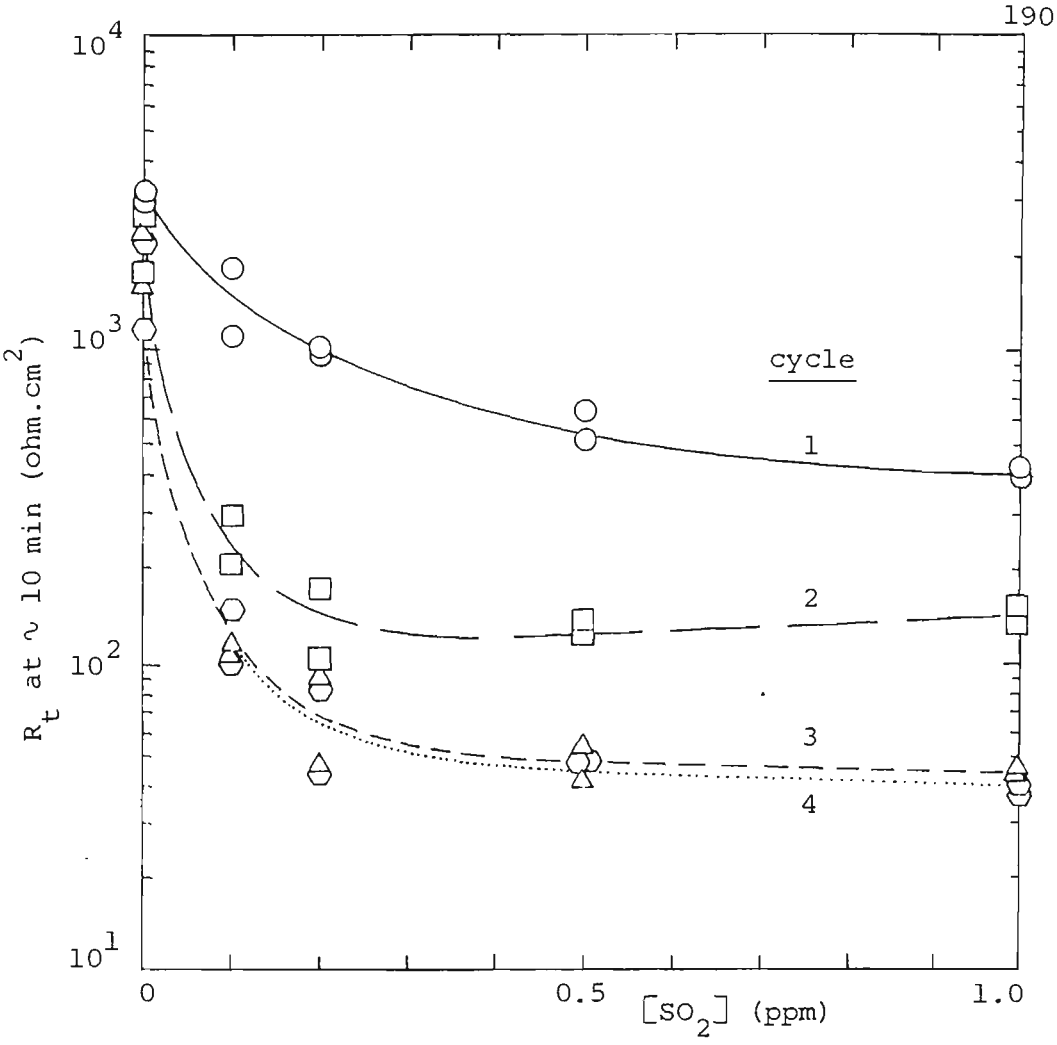

Figure R1/26. Summary plot of the effect of [SO_2] on charge-transfer resistance, R_t, obtained after about 10 minutes duration of each cycle for ACM8 (Fe) from Figure R1/21.

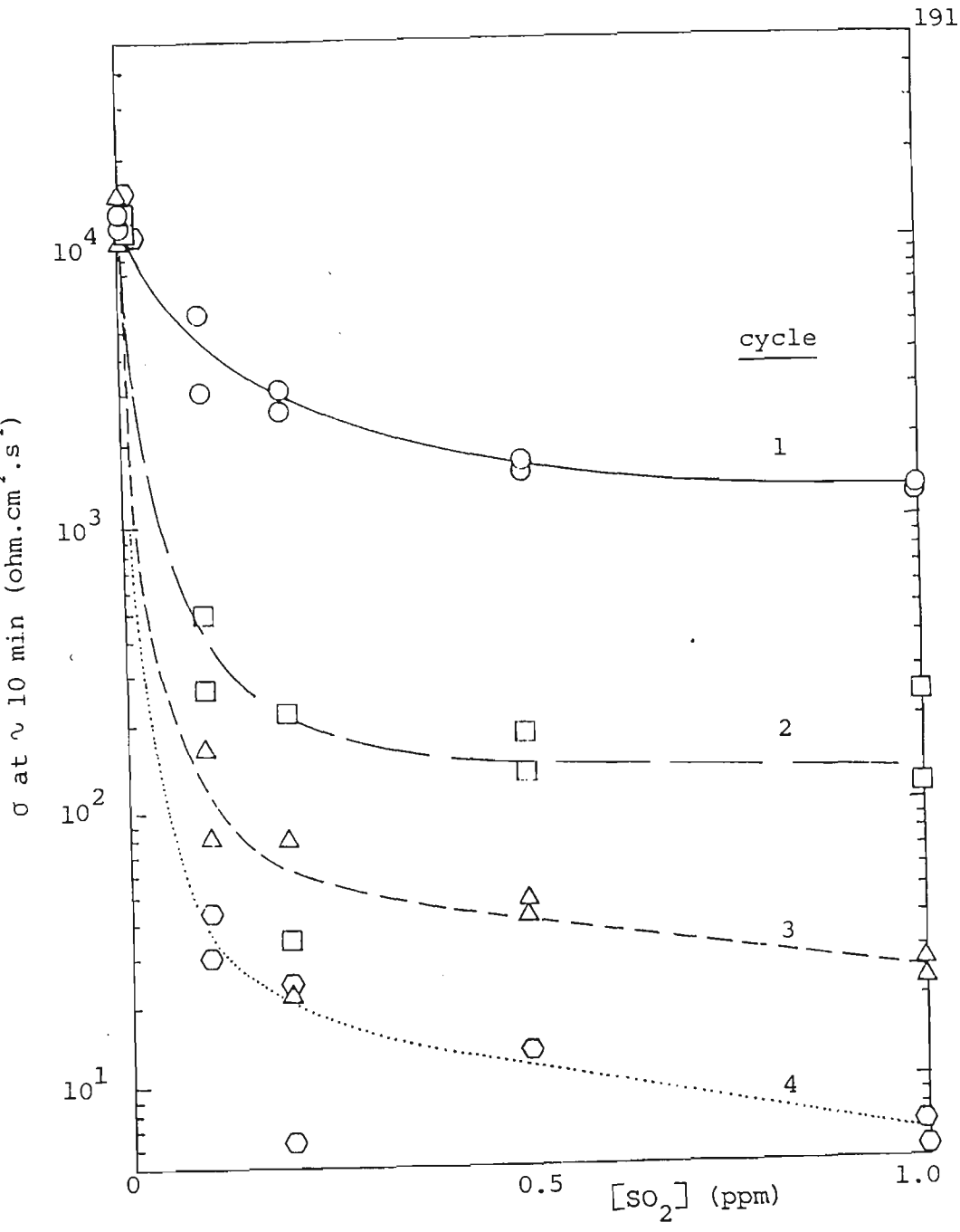

Figure R1/27. Summary plot of the effect of [SO_2] on Warburg diffusion coefficient, σ, obtained after about 10 minutes duration of each cycle for ACM8 (Fe) from Figure R1/24.

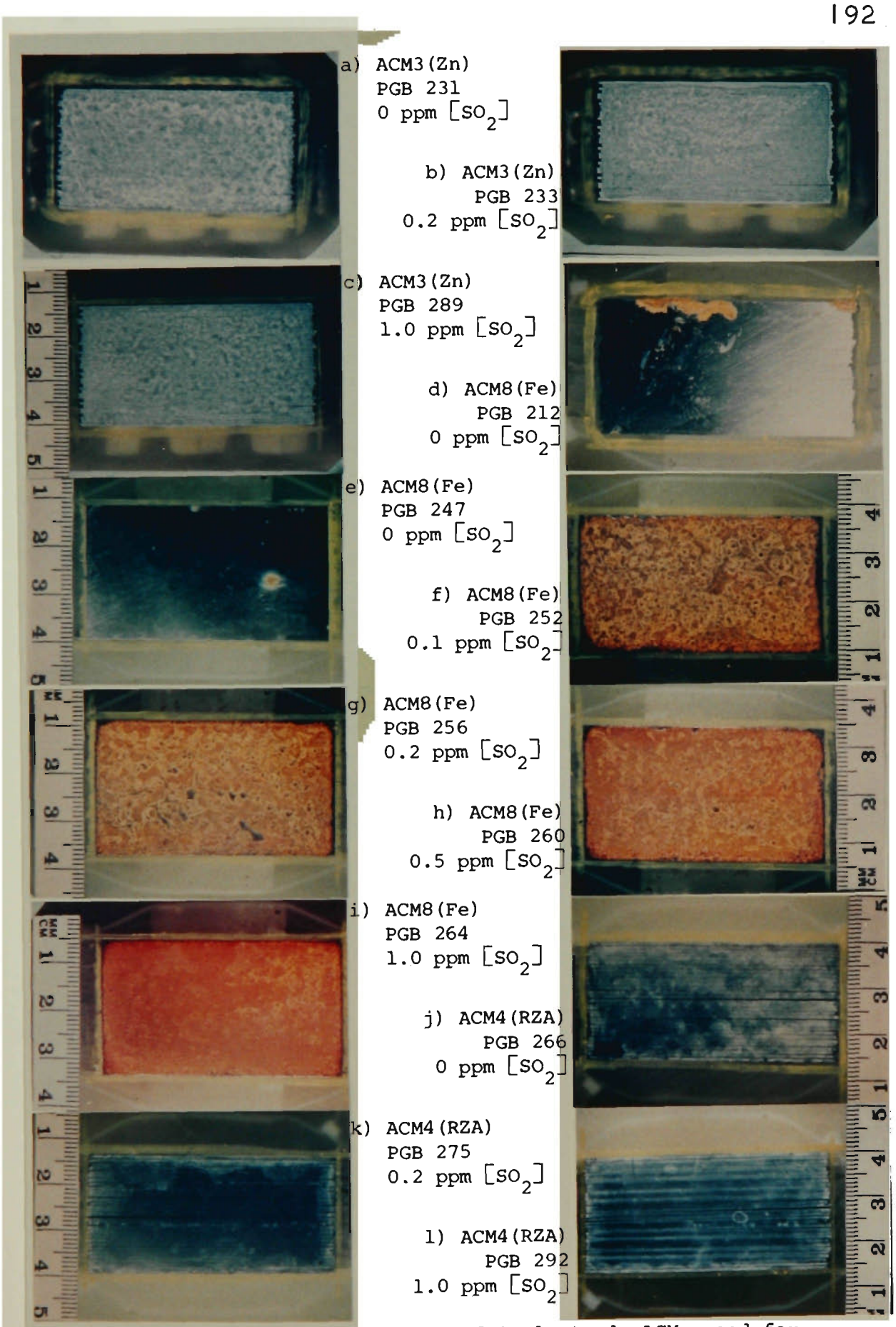

Figure R1/28. Typical photographs of 3-electrode ACMs used for impedance tests after 4 PGB cycles at various [SO_2], showing corrosion product build-up. ACM3(Zn)(Fig. R1/28a-c);ACM8(Fe) (Fig. R1/28d-i);ACM4(RZA)(Fig. R1/28j-l);RZA rolled Zn-55%Al alloy.

the surface with increasing pressure and then analyzed using EDS in a JEOL Model JSM 840 scanning electron microscope. The spectra obtained (not shown) clearly showed S peaks, with the concentration in the range of 1-4%, indicating the presence of sulphur based products.

For ACM4 (rolled Zn-55%Al), close inspection of Figures R1/22,25 indicate that there is a small decrease in R_t as $[SO_2]$ increases, but that σ values are relatively constant, suggesting a small increase in charge-transfer processes but a relatively constant diffusion process. This is more clearly shown in mass loss/$[SO_2]$ curves in Figure R1/50, Section R1.7/2. Typical photographs at 0,0.2,1.0 ppm $[SO_2]$ are shown in Figure R1/28j-l, which show only a small amount of corrosion product after four cycles compared to ACM3 (Zn) and ACM8 (Fe).

4. $\underline{C_d/\text{time}, C_d/[SO_2] \text{ trends}}$

Double layer capacitance, C_d, trends versus time are not shown because values were relatively constant with time, with $[SO_2]$ and with ACM type. Values range from 4-7 $nF.cm^{-2}$ for ACM3 (Zn), ACM4 (rolled Zn-55%Al alloy) and 9-10 $nF.cm^{-2}$ for ACM8 (Fe) and are several orders of magnitude lower than expected for the double layer capacitance (20 $\mu F.cm^{-2}$), under fully immersed conditions. The double layer capacitance is effectively in parallel with the capacitance of the mylar insulator and hence their capacitance should add. On this basis, the expected measured capacitance should be quite high. Mansfeld[36] has observed capacitances (~5 nF), of the same order as measured here on ACMs that have become dry and considers that it is due to the capacitance of the mylar film. This is a reasonable assumption but why the capacitance remains around these values when a water film is applied is not

known.

5. R_s values

Solution resistance, R_s, between working and auxiliary plates of an ACM was obtained or estimated from Nyquist plots as per the method outlined in Section T1/4 and Figure T1/2. Values are not tabulated but Figures R1/14-16, Section R1.5/2 are typical Nyquist plots that indicate R_s had to be always less than 1/10 of charge-transfer resistance, R_t, suggesting that R_s was not significant compared to R_t. This supports the conclusions found from square-wave tests using a bridge circuit to estimate R_s discussed in Section R1.6/8.

However, the values of R_s obtained from ac impedance (Nyquist plots) are consistently higher than that measured in Section R1.6/8 from bridge measurements. This is probably because the intercept on the a-axis of a Nyquist plot at high frequencies, which determines the value of R_s, can be effected by stray cell capacitance in galvanostatic impedance experiments, resulting in higher R_s values than in the absence of stray capacitance[16].

Mansfeld[36,125,172] performed potentiostatic impedance experiments (which do not produce large R_s values as a result of stray capacitance), on steel/steel and Cu/steel ACMs in 0.01 N NaCl and Na_2SO_4 solutions and also concluded that R_s was much lower than R_t. Gonzales et al[116] came to the same conclusion for 3-electrode ACMs made with Al, Cu, Fe and Zn plates for invisible adsorbed moisture layers in a moisture-saturated atmosphere, although the values quoted for R_s were much higher (110-3800 ohm) than values measured here (range 0-10 ohm) or reported by Mansfeld (range 8-50 ohm)[125,172].

R1.6 PGB Corrosion Current Tests on 3-Electrode ACMs

1. Aims, method of calculation

The aim of this section is to compare the corrosion rate behaviour of the various 3-electrode ACMs during 4-cycle PGB test chamber tests at 34.2°C in which the [SO_2] was varied over the range 0-1 ppm, see Section E2.6/1. The ACMs investigated were ACM3 (Zn), ACM4 (rolled Zn-55%Al alloy) and ACM8 (Fe).

The method used to collect corrosion rate information (corrosion current, I_k, anodic and cathodic Tafel slopes, b_a and b_c respectively) is given in Sections E2.6/5, E1.2/4. Values of I_k, b_a and b_c are calculated automatically in subprogram RP_EXPT, as discussed in Section A1/5.1. A plot of experimental current, I, versus voltage response, $\varepsilon(=E-E_k)$, along with the curve fitted line through these data points is also produced. An example plot is shown in Figure R1/51, Section R1.7/3.3.

2. Current/voltage response plots and analysis problems

Some 288 (I/ε) polarization curve plots were obtained corresponding to four runs per cycle over four cycles at six [SO_2] levels for three ACMs.

The shape of the (I/ε) plots depended on the Tafel slope, b_a and b_c, values, and the corrosion current, I_k, as discussed in Section T3/6 and shown in Figure T3/4. All three basic curve shapes were observed - the curve indicating relatively low b_a and b_c values (like Figure T3/4a); the curve indicating low b_a and high b_c (like Figure T3/4b); and the curve indicating high b_a and low b_c

(like Figure T3/4c).

Some difficulties were experienced in analyzing all the plots. Large b_c values caused the analysis routine IK_CALC8, Section A1/5.2, to diverge and no parameter values were returned. In this case the data was re-analyzed using analysis routine IK_CALC9, which is programmed to return parameter values if b_c reaches a maximum of around 10 000 mV/decade. Values of this magnitude indicate diffusion control of the cathodic reaction and a b_c value of infinity.

Lack of sufficient curvature in some (I,ε) plots results in a large uncertainty (high standard deviations) in the parameter values I_k, b_a and b_c. This lack of curvature can occur on the cathodic side, anodic side, or both sides, of the polarization curve. It has previously been referred to[3] as an extended range of linearity which results from moderately high Tafel slope values. The plot shape, and hence the amount of curvature, is shown in Figure T3/6,7, Section T3/6 to be determined by the values of I_k, b_a and b_c. In cases where there is a lack of curvature, the voltage response range must be increased by the application of higher currents so that a greater degree of curvature will result. However, it is difficult to assess whether a sufficient degree of curvature in the polarization curve has been attained when the (I,ε) data is being collected. One bad (I,ε) data point can made a considerable difference to calculated I_k, b_a, b_c values when there is little curvature in the polarization curve. Subprogram RP_EXPT, Section A1/5.1, has an operator selectable option to delete data points prior to analysis to overcome this sort of problem.

The shape of the ε/time voltage response was not always ideally an exponential growth to an easily detectable steady state as shown by type 1 in Figure R1/29, representing the charging of the double layer capacitance, C_d,

via the parallel charge-transfer resistance, R_t. Sometimes superpolarization (an initial peak followed by a decay as shown by type 2 in Figure R1/29) was observed either in anodic, cathodic or both the voltage responses but more often with anodic voltage responses. This usually became more pronounced at the higher voltage responses (anodic or cathodic). It was frequently observed with ACM3 (Zn), less frequently and the superpolarization peaks were of lesser magnitude for ACM4 (rolled Zn-55%Al alloy) and only occasionally observed with ACM8 (Fe).

Superpolarization effects have been observed previously[2,173] for zinc, galvanized steel and steel under full immersion conditions and their interpretation has been widely discussed in the literature, particularly with reference to iron[174-178]. Drazic et al[178] has summarized the attempts made by other authors to explain superpolarization effects as due to the reaction mechanism, local pH changes, surface morphology changes, desorption of absorbed hydrogen. They concluded that superpolarization effects on iron in sulphuric acid solutions were due to partial blockages of the surface with adsorbed hydroxo particles at high coverages which block the surface for the main reaction. Bockris et al[174] suggest that the superpolarization peak may be caused by a change in the pseudocapacitance as the voltage response changes in magnitude. They explain the pseudocapacitance in terms of adsorption of a species on the electrode.

For the simpler case of superpolarization without other complications, as illustrated by type 2 in Figure R1/29, the peak in the voltage response lasted only up to several seconds depending on the size of the current step. Voltage responses read at 6 s were reasonably steady state values in this case, and did not contain the effects of the voltage peak.

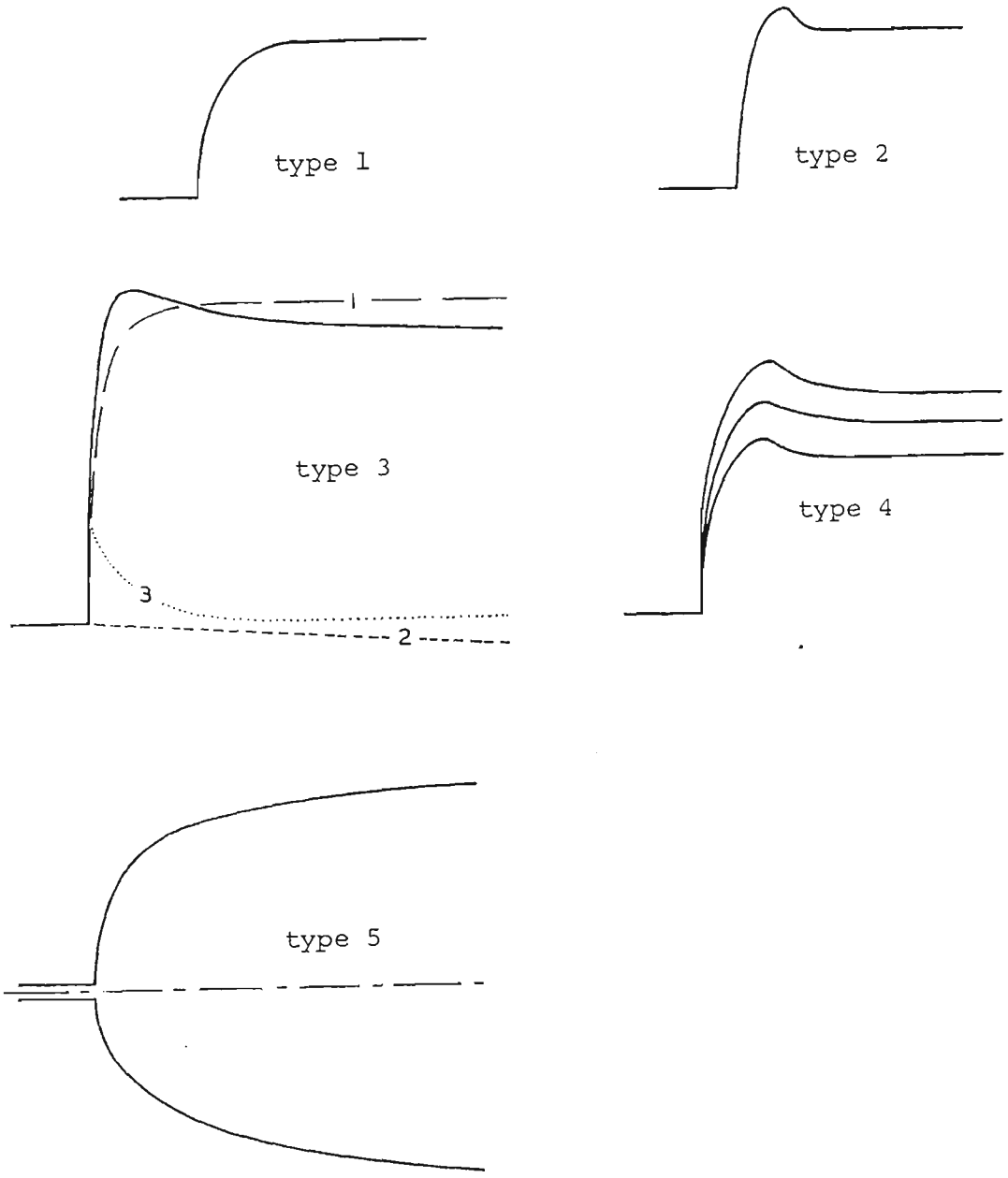

Figure R1/29. Typical shapes of polarization, ε, $(=E-E_k)$,time/voltage responses following a galvanostatic applied current step, I. Normal response (type 1); response with superpolarization (type 2); superpolarization response with slow decay is caused by the sum of three effects - normal double-layer charging (curve 1); downward shift in corrosion potential, E_k, due to I (curve 2); and superpolarization effect (curve 3); anodic responses appear to be limited in magnitude (type 4); voltage responses slow to attain steady state (type 5).

However, there was a complicating situation where the decay of the superpolarization peak took longer than the normal voltage response reading time of 6 s, as illustrated by type 3 in Figure R1/29. This was observed at higher applied currents for both ACM3 (Zn) and ACM4 (rolled Zn-55%Al alloy) to a lesser extent. Barnartt[176] considered this type of voltage transient to be the sum of three effects, and these are shown dotted for type 3 in Figure R1/29 for the anodic pulse only. Curve 1 is due to charging of the double layer capacitance, C_d, via the parallel charge-transfer resistance, R_t; curve 2 is due to an (unexplained) slow downward drift in the corrosion potential caused by the applied current; curve 3 is due to the superpolarization effect. Reading the voltage response prior to the steady state situation so as to include a portion of the superpolarization peak will cause the voltage responses to be larger than those measured at the true steady state. This will result in higher calculated values of b_a and b_c, if the calculated I_k value remains approximately constant, as is shown in Section T3/6. No attempt was made to correct this situation. All voltage responses for ACM3 (Zn) and ACM4 (rolled Zn-55%Al alloy) were read at 6 s and most voltage response data was collected for only about 7.5 s. It was considered that there was some merit in keeping the voltage response reading time constant.

The size of anodic voltage responses on ACM4 (rolled Zn-55%Al alloy) sometimes appeared to be limited after the superpolarization peak, as shown by type 4 in Figure R1/29 for three voltage responses at increasing applied currents. This problem was somewhat overcome by restricting the range of applied currents on the anodic side to smaller values, but such an effect resulted in low calculated values of b_a compared to b_c values. The cathodic voltage responses also tended to limit, but only when the voltage response was much larger in magnitude.

Anodic and cathodic voltage responses were frequently slow to rise to a steady state situation, sometimes taking up to 30 s to achieve steady state, but more usually reaching a steady state in less than the usual voltage reading time of 6 s. Figure R1/29 shows a typical type 5 anodic and cathodic voltage response in which the cathodic voltage response is slower to achieve a steady state situation than the anodic voltage response which was the usual situation with type 5 voltage responses. This slower cathodic response was probably due to the applied currents nearing the oxygen diffusion limiting current. The slow voltage response rise (anodic or cathodic) was observed less frequently on ACM4 (rolled Zn-55%Al alloy) than either ACM3 (Zn) or ACM8 (Fe). Its occurrence was generally associated with low values of I_k and high values of R_p, indicating its cause as simply the slow charging of the double layer capacitance via a high polarization resistance as discussed in Section T3/3. However, the slow rise usually was more pronounced at higher absolute values of applied current, suggesting that diffusion of anodic reaction products away from the working electrode played a role. This subject has been referred to previously as mass transfer effects[2,51,52], or as a slow upward drift in the corrosion potential due to the applied current when the dissolving metal is covered by corrosion product layers causing a large pseudocapacitance [61,62], and is discussed in Section T3/4.1. The slow upward drift was not observed in cases exhibiting the superpolarization peak.

These slow voltage response rises were combated in either of two ways. When the voltage response indicated simply a low I_k or high R_p value, applied currents were extended up to about 30 s, and the respective voltage responses analyzed at different reading times. This occurred at 0, 0.05 ppm [SO_2] for ACM8 (Fe) and in cycles 3 and 4 for ACM4 (rolled Zn-55%Al alloy) at low [SO_2]. The case of the slow rise being due to mass transfer effects was mainly

associated with ACM8 (Fe) at higher I_k or lower R_p values. In this case, voltage responses were read at the standard time of 6 s, which was a good compromise allowing completion of double layer charging but excluding the majority of the slow upward drift due to E_k shifts.

Figure R1/30 is an example (ACM4 PGB 325 cycle 3 run 1 at 0.2 ppm [SO_2]) of the effect of voltage response reading time on calculated corrosion parameter values for the case of low corrosion rates. The voltage responses are shown in Figure R1/30a and the effect of voltage response reading time, t_v, on calculated values of I_k, b_a and b_c are shown in Figures R1/30b-d respectively. This demonstrates the seriousness of neglecting the effect of reading time in calculating corrosion parameter values, as there is a large decrease in calculated values of I_k, b_a and b_c as t_v is increased. If galvanodynamic scans were employed instead of galvanostatic steps, then scan rate would be the important variable rather than t_v. Double layer charging has not been completed at 2 s, as can be observed in Figure R1/30a, nor even at 6 s. Therefore, these times are not really applicable for analysis in this case. However, the 10 s voltage response readings cause the calculated values of I_k, b_a and b_c to be respectively 40, 23 and 2% higher than the 30 s readings and this rises to 105, 51 and 19% if the 6 s readings are taken instead of the 30 s readings. The charging curve method of Jones and Greene[56] is available to calculate corrosion rate parameter values from non-steady state data, but was not used in this thesis.

In certain instances the fitted polarization curve through the (I,ε) data points was not a good fit, and this resulted in large standard deviations for I_k, b_a and b_c and a high percentage error (equivalent to the sum of the squares of the differences between fitted ε-value and ε data point at a given I). Although

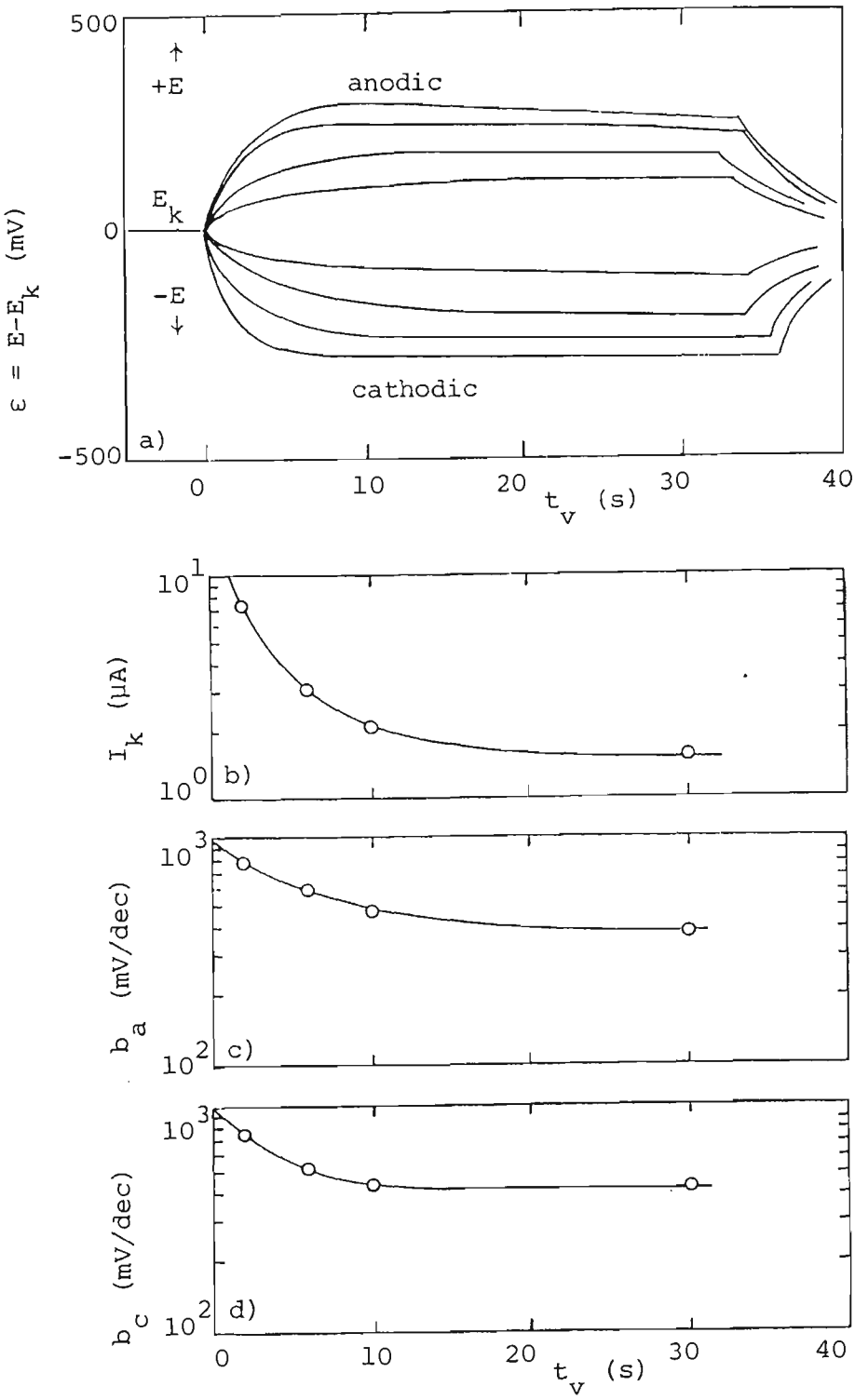

Figure R1/30. Effect of voltage response reading time, t_v, on calculated values of I_k, b_a, b_c for ACM4 (rolled Zn-55%Al) PGB 325 cycle 3 run 1 0.2 ppm [SO_2]. Voltage responses for applied current steps of $\pm$2,4,7,10 μA, respectively (Fig. R1/30a); effect of t_v on I_k (Fig. R1/30b), b_a (Fig. R1/30c), b_c (Fig. R1/30d).

the 'delete a data point' routine in subprogram RP_EXPT, Section A1/5.1, improved this situation, there were instances where curve fits could not be improved sufficiently, eg Figure R1/51, Section R1.7/3.3. These cases were likely to be caused by a change in corrosion rate characteristics during collection of the voltage responses, or because the data did not properly fit the model equation.

The analysis problems mentioned in this section help to explain the wide variation in calculated corrosion parameter values observed in Sections R1.6/3-6.

3. i_k/time trends

3.1 ACM3 (Zn)

Figure R1/31 shows corrosion current density, i_k, as a function of time for each run within a PGB cycle, and from cycle to cycle at each $[SO_2]$.

Starting from a freshly abraded surface in cycle 1, i_k generally increased with time at all $[SO_2]$ levels and then levelled off, finally dropping somewhat just prior to the ACM surface drying out. This suggests that the corrosion rate and/or area (the number of corrosion initiating sites) increases with time within this first cycle. There also appeared to be some suggestion that subsequent cycles gave lower i_k values, except for 0.2 ppm $[SO_2]$, suggesting that the build-up of corrosion products had a somewhat inhibiting effect as would be expected. There did not seem to be any particular trend with time in cycles 2-4. The values of i_k at 0.5 ppm $[SO_2]$ were closer together from cycle to cycle and lower than at other $[SO_2]$ levels, suggesting lower corrosion rates. This is confirmed by Figure R1/32e which shows white corrosion

product build-up after four cycles was minimal at 0.5 ppm [SO_2] compared to other [SO_2] levels, Figures R1/32a-d,f. Apart from the 0.5 ppm [SO_2] case, there did not appear to be any particular trend with [SO_2], within the variation observed in the i_k results from cycle to cycle. This suggests that the corrosion rate of zinc may well be relatively constant with variation in [SO_2] over the range 0-1 ppm, except for 0.5 ppm [SO_2]. Refer also to Section R1.6/4.

3.2 ACM8 (Fe)

Figure R1/33 shows i_k as a function of time for each run within a PGB cycle, and from cycle to cycle at each SO_2 concentration.

No particular trends with time were observed, i_k/time trends either increasing, steady or decreasing within a given cycle. There was a marked increase in the magnitude of i_k from cycle to cycle at all [SO_2], suggesting that increased corrosion occurs when water is reapplied in the next cycle. The number of red rust 'nests' initiating on the ACM surface grew with time and from cycle to cycle. This increased corrosion from cycle to cycle is quite different from ACM3 (Zn) where the opposite trend occurred but to a lesser degree. Generally, there was a marked increase in the magnitude of i_k as [SO_2] was increased, except at 0.05 ppm [SO_2]. The corrosion rate of ACM8 (Fe) is less than that of ACM3 (Zn) at zero and 0.05 ppm [SO_2], but increases markedly with increasing [SO_2] becoming significantly higher than ACM3 (Zn) at 0.1 ppm [SO_2] and above.

3.3 ACM4 (rolled Zn-55%Al alloy)

Figure R1/34 shows i_k as a function of time for each run within a PGB cycle,

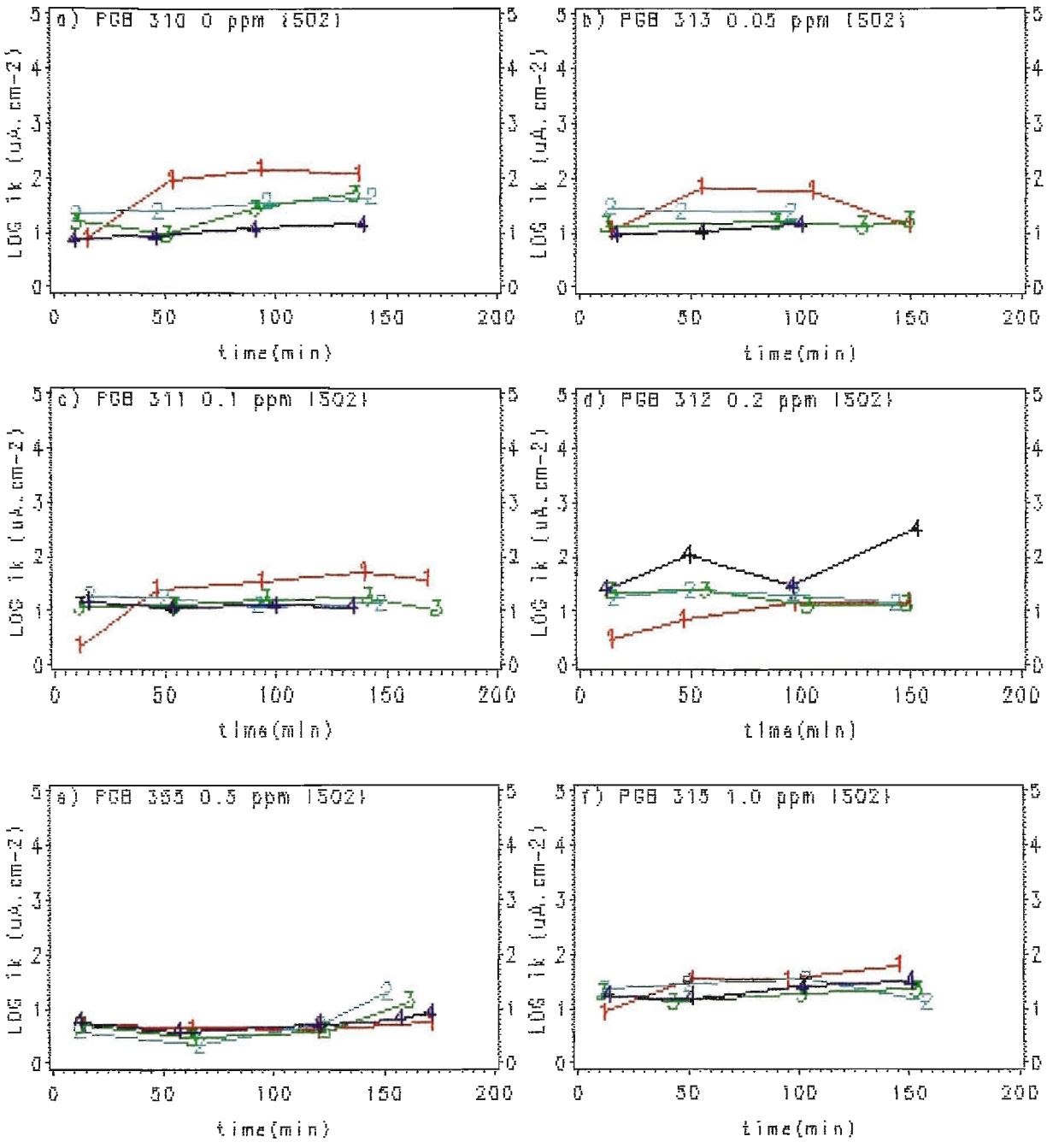

Figure R1/31. Effect of time on corrosion current density, ik, from run to run within a cycle; from cycle to cycle; and from (SO2) to (SO2) for ACM3(Zn). Numbers on plots are run data points for cycles 1-4 respectively.

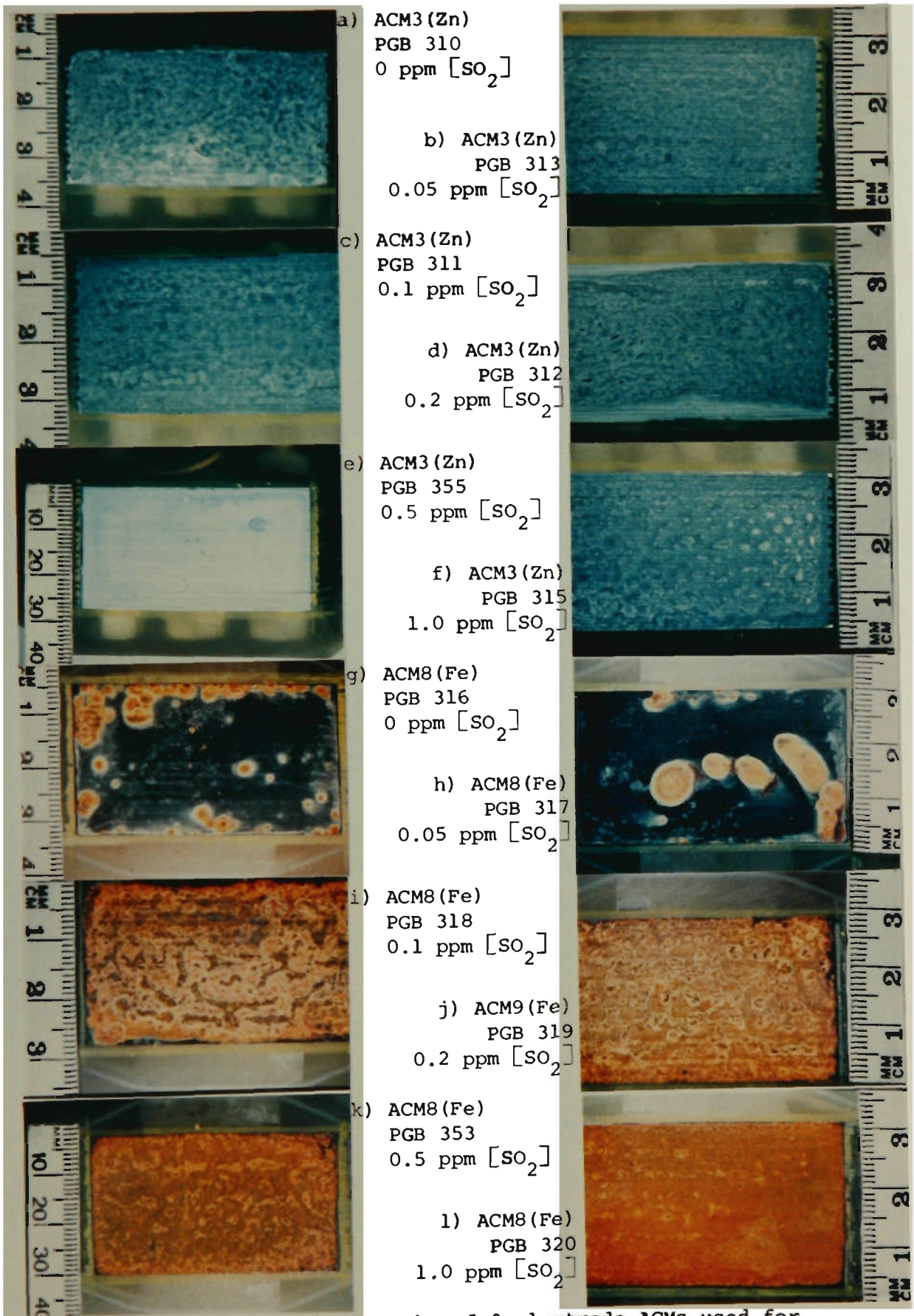

Figure R1/32. Typical photographs of 3-electrode ACMs used for corrosion current tests after 4 PGB cycles at various [SO_2], showing corrosion product build-up. ACM3(Zn)(Fig. R1/32a-f); ACM8(Fe)(Fig. R1/32g-l); ACM4(RZA)(Fig. R1/32m-r); RZA rolled Zn-55%Al.

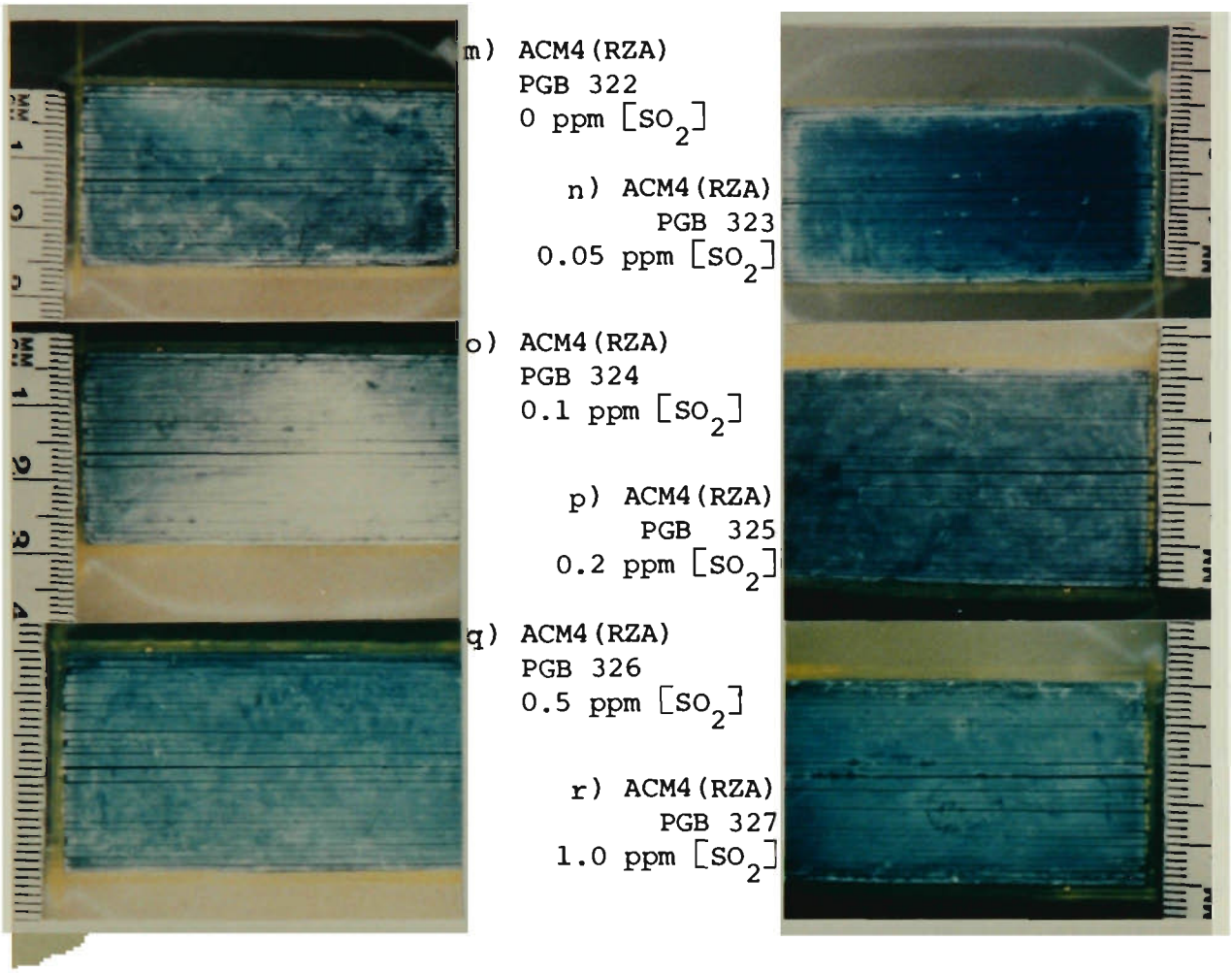

m) ACM4(RZA)
PGB 322
0 ppm [SO_2]

n) ACM4(RZA)
PGB 323
0.05 ppm [SO_2]

o) ACM4(RZA)
PGB 324
0.1 ppm [SO_2]

p) ACM4(RZA)
PGB 325
0.2 ppm [SO_2]

q) ACM4(RZA)
PGB 326
0.5 ppm [SO_2]

r) ACM4(RZA)
PGB 327
1.0 ppm [SO_2]

Figure R1/32 (cont.)

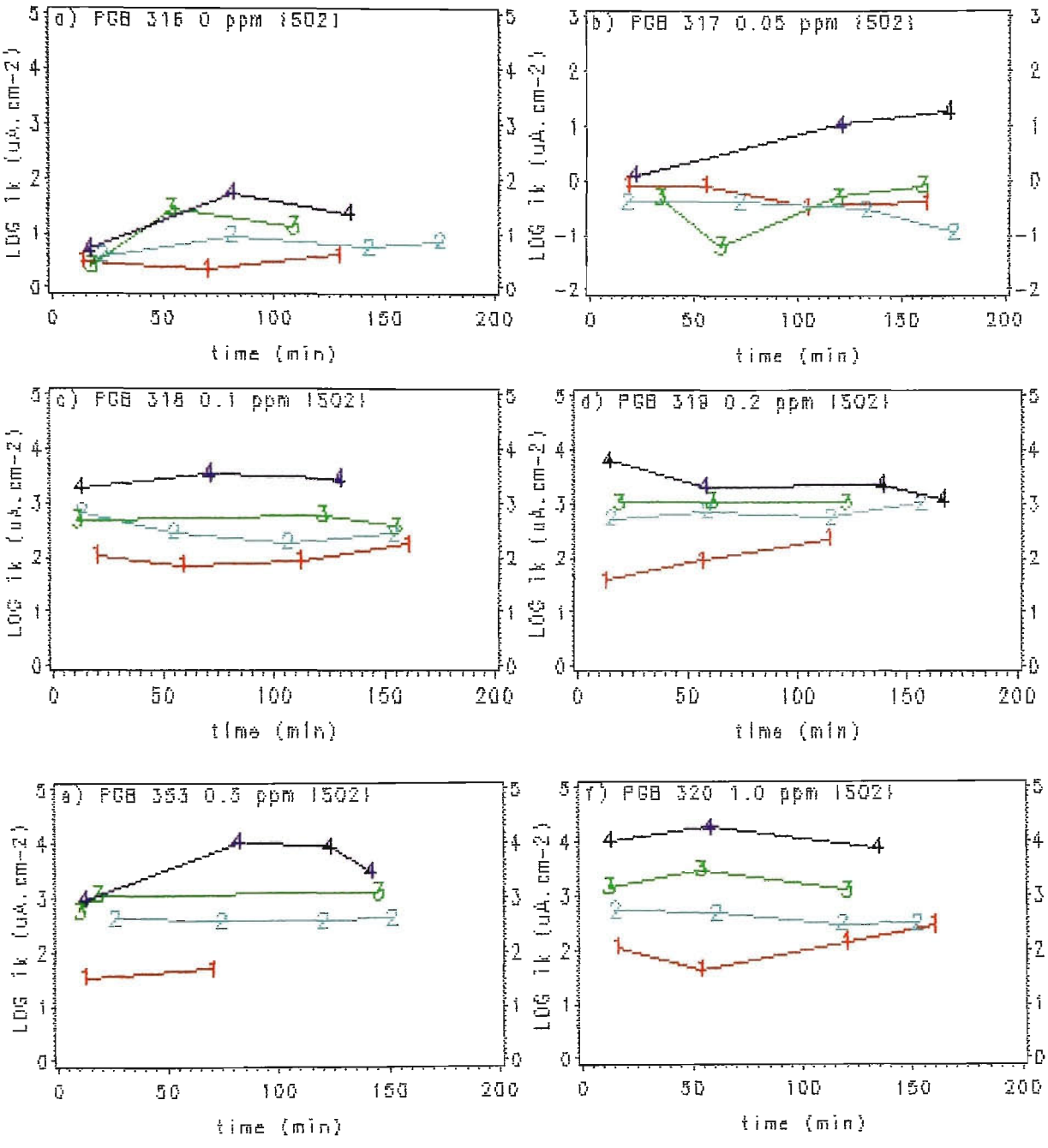

Figure R1/33. Effect of time on corrosion current density, ik, from run to run within a cycle; from cycle to cycle; and from (SO2) to (SO2) for ACM8(Fe). Numbers on plots are run data points for cycles 1-4 respectively.

and from cycle to cycle at each SO_2 concentration.

There was a downward trend in i_k from run to run within a cycle for zero and 0.05 ppm [SO_2], suggesting decreasing corrosion rates as thin films of corrosion product build up on the ACM surface. This trend did not generally hold for cycles 2-4 at higher [SO_2]. This suggests that the SO_2 reaction products may absorb into the thin corrosion product layers during cycle 1 and counteract the protective effect of corrosion product films. From cycle to cycle, the magnitude of i_k decreased in a more clearly defined manner than with ACM3 (Zn). This occurred at all [SO_2] and must be attributed to the build-up of thin but somewhat protective corrosion products as was concluded in the case of ACM3 (Zn). This is reasonable, because Zn-55%Al alloy is expected to corrode by preferential dissolution at zinc-rich areas and behave, at least in the initial stages, like zinc. This situation is opposite to that for ACM8 (Fe) where corrosion rates appear to increase from cycle to cycle at all [SO_2] levels. As [SO_2] is increased, there is first a small drop in i_k values as [SO_2] increases from zero to 0.05 ppm, then a modest increase as [SO_2] is further increased. Thus the situation is different to ACM3 (Zn), Section R1.6/3.1, where it was concluded that the corrosion rate of zinc could be relatively constant with variation in [SO_2] over the 0-1 ppm range, except for 0.5 ppm [SO_2].

By comparison of Figure R1/34 with Figures R1/31,33, it can readily be ascertained that the corrosion rate of rolled Zn-55%Al alloy in ACM4 is less than that of zinc in ACM3 and markedly less than that of steel in ACM8 over the [SO_2] range, 0-1 ppm. This is also confirmed in Section R1.6/4.

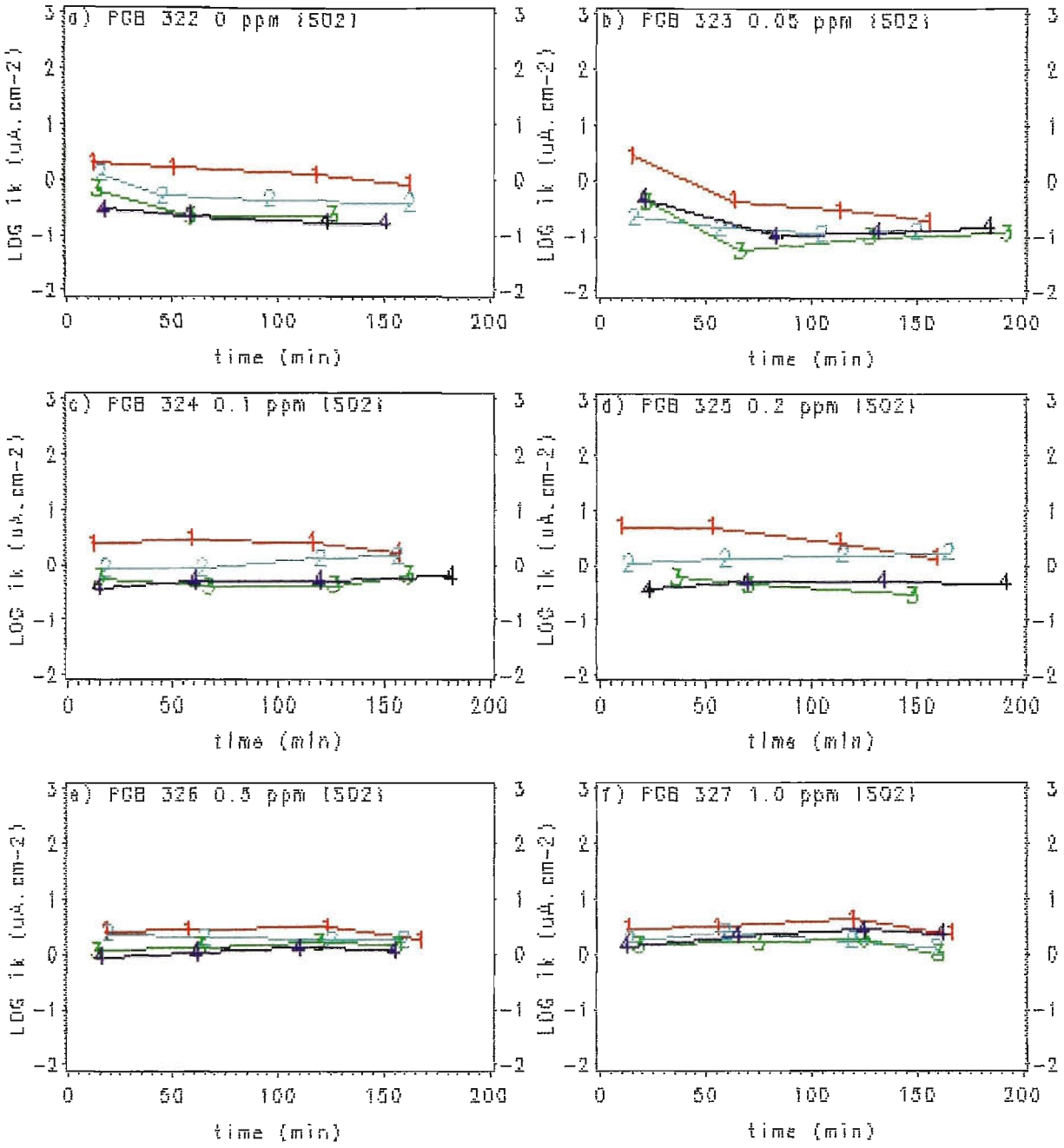

Figure R1/34. Effect of time on corrosion current density, ik, from run to run within a cycle; from cycle to cycle; and from (SO2) to (SO2) for ACM4(rolled Zn-55%Al). Numbers on plots are run data points for cycles 1-4 respectively.

4. Calculated mass loss versus $[SO_2]$

Mass losses were calculated from i_k/time trends by the method outlined in Section T3/7, essentially being the area under the i_k/time curves shown in Figures R1/31,33,34 multiplied by the electrochemical equivalent for the respective metal. Mass losses were calculated for the working electrodes of ACM3 (Zn), ACM8 (Fe) and ACM4 (rolled Zn-55%Al alloy), and are shown in Figure R1/35 as a function of $[SO_2]$.

At zero and 0.05 ppm $[SO_2]$, the calculated mass loss of rolled Zn-55%Al alloy in ACM4 is lowest, followed by steel in ACM8, then zinc in ACM3. However, the mass loss of steel shows a general marked increase as the level of $[SO_2]$ increases, so that at 0.1 ppm $[SO_2]$, steel has a higher mass loss than zinc. The mass loss of zinc appears relatively independent of $[SO_2]$ over the range 0-1 ppm, except at 0.5 ppm which appears anomalous. An explanation for this anomaly is suggested in Section R1.6/6.1 regarding spasmodic initiation of corrosion. The mass loss of rolled Zn-55%Al alloy in ACM4 increases modestly with $[SO_2]$. For steel, the fourth cycle had the highest i_k values and contributed more to the overall mass loss than any other cycle, as can be verified in Figure R1/33. The first cycle generally had the highest i_k for Zn in ACM3 and rolled Zn-55%Al alloy in ACM4, and hence contributed more to the overall mass loss than any other cycle, refer Figures R1/31,34 respectively. This illustrates the different corrosion behaviour of zinc and rolled Zn-55%Al alloy compared to steel.

For steel, the magnitude of mass loss at each $[SO_2]$ level in Figure R1/35 is in complete agreement with the extent of red rust formation shown from Figure R1/32g-l. This comparison is more difficult with zinc (compare Figures

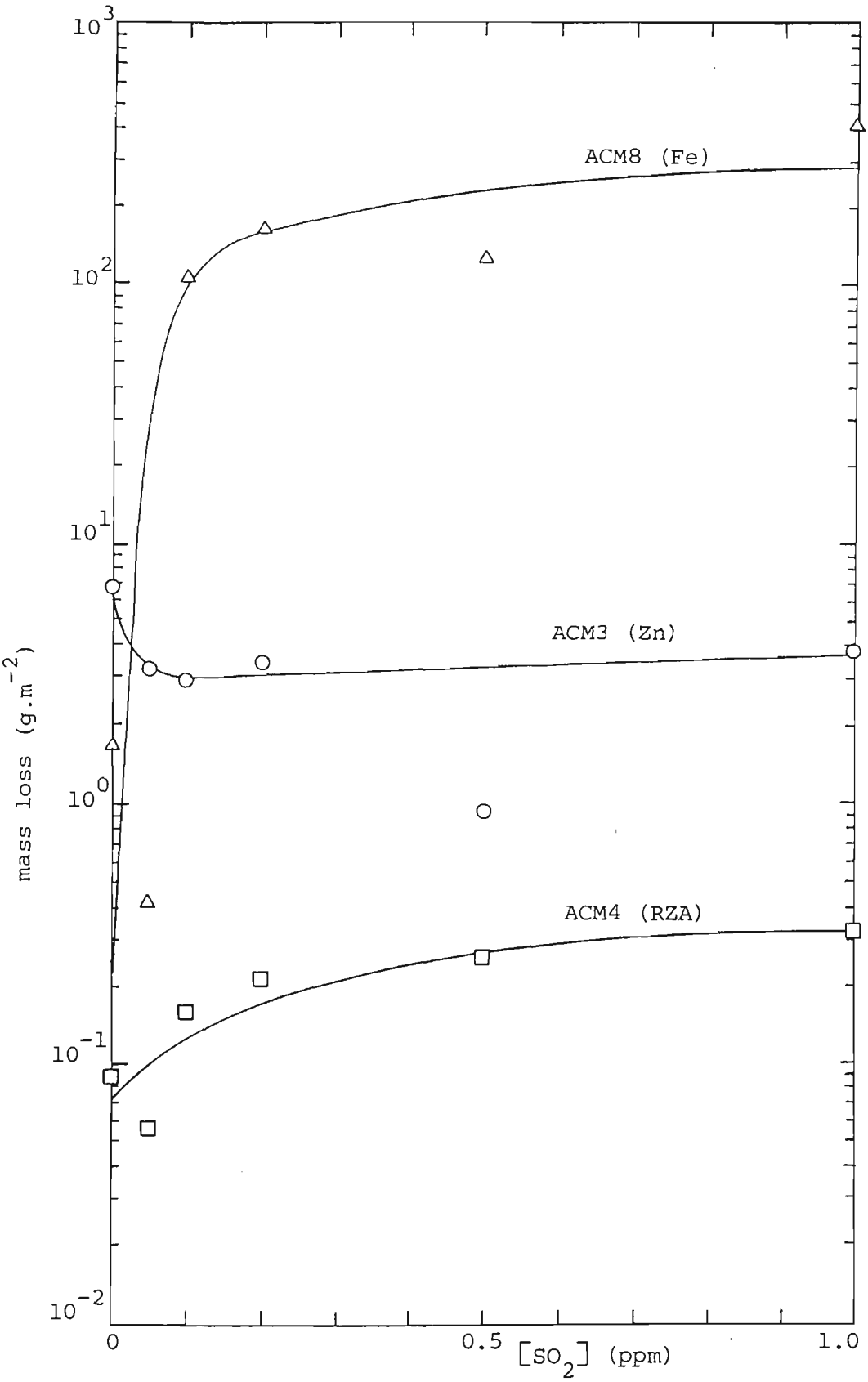

Figure R1/35. Mass loss, calculated from i_k/time trends in Figures R1/31,33,44, as a function of [SO_2] for each of the 3-electrode ACMs. RZA rolled Zn-55%Al.

R1/35,32a-f) but the lower mass loss at 0.5 ppm [SO_2] certainly corresponds to less white corrosion product. The comparison (Figures R1/35,32m-r) for rolled Zn-55%Al alloy is also more difficult because of the much lower corrosion rates, but there does appear to be an increase in the amount of corrosion product formation as [SO_2] increases, in agreement with the corresponding increase in calculated mass loss.

Such comparisons are most worthwhile because they establish credence in the mass losses calculated from i_k/time trends. As i_k is in turn calculated from Tafel slopes b_a and b_c, this also establishes confidence in b_a/time and b_c/time trends in Sections R1.6/5,6.

5. b_a/time trends

5.1 ACM3 (Zn)

Figure R1/36 shows anodic Tafel slope for the metal, b_a, as a function of time for each run within a PGB cycle, and from cycle to cycle at each [SO_2].

There does not appear to be any marked trend from run to run within a PGB cycle. However, there is a suggestion that b_a values generally increased at zero [SO_2], whereas they generally decreased, at least for cycles 2 and 3, for experiments with [SO_2], indicating that [SO_2] may have a depolarizing effect on zinc at least on the anodic reaction.

This is more marked from cycle to cycle at each [SO_2], where the general tendency is for b_a values to decline, except at 0.5 ppm [SO_2] where b_a values do not change much from cycle to cycle. The fall in b_a from cycle 1 to cycle

4 can be quite marked as at 0.05, 0.1 and 1.0 ppm [SO_2], where values fall from well over 100 to around 30 at 0.05 and 1.0 ppm [SO_2], but to around 16 at 0.1 ppm [SO_2]. As this does not happen at zero [SO_2], it is possible that SO_2 reaction products equilibrate in the zinc corrosion product build-up from cycle to cycle to depolarize the anodic reaction of zinc dissolution. Partial short circuits may also be involved, see Sections R1.8/1, A5/2.

Figure R1/37 shows b_a results taken from Figure R1/36 for the first run (around 10 min) in cycle 1 for ACM3 (Zn) which helps to summarize the trends in b_a with variation in [SO_2] level. There is no real trend with [SO_2] except for the low value at 0.5 ppm [SO_2], which corresponds in Figure R1/32e to less corrosion than at other [SO_2] and is clearly an anomaly. The apparent lack of a trend in b_a with [SO_2] is consistent with the curve for ACM3 (Zn) in Figure R1/35 which shows no real trend in mass loss with [SO_2].

The wide range of b_a in Figure R1/36 values is quite surprising and can range from over 500 mV/decade for cycle 3 run 1 at zero [SO_2] down to around 15 mV/decade at 0.2 ppm [SO_2]. The higher values normally indicate significant polarization of the anodic metal dissolution reaction, and hence lower corrosion rates would be predicted from this cause, whilst the lower values normally indicate substantial depolarization, and higher corrosion rates would be predicted. These predictions are not borne out in Figure R1/35 where zinc mass loss in ACM3 is approximately constant with increase in [SO_2], except at 0.5 ppm, and indicate other factors are also important in controlling the corrosion rate. This subject is discussed further in Section R1.6/8.

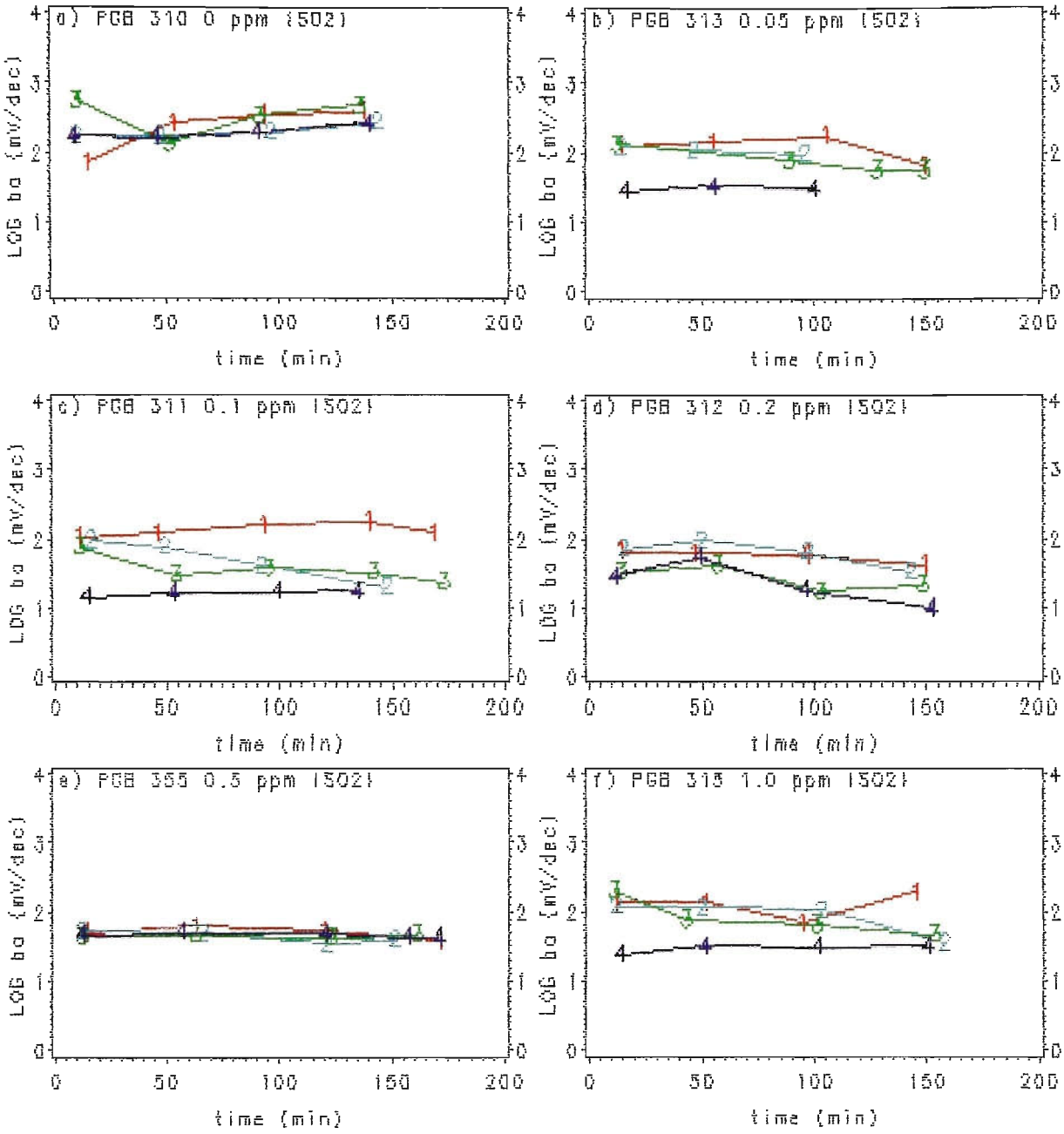

Figure R1/36. Effect of time on anodic Tafel slope for the metal,ba, from run to run within a cycle; from cycle to cycle and from (SO2) to (SO2) for ACM3(Zn). Numbers on plots are run data points for cycles 1-4 respectively.

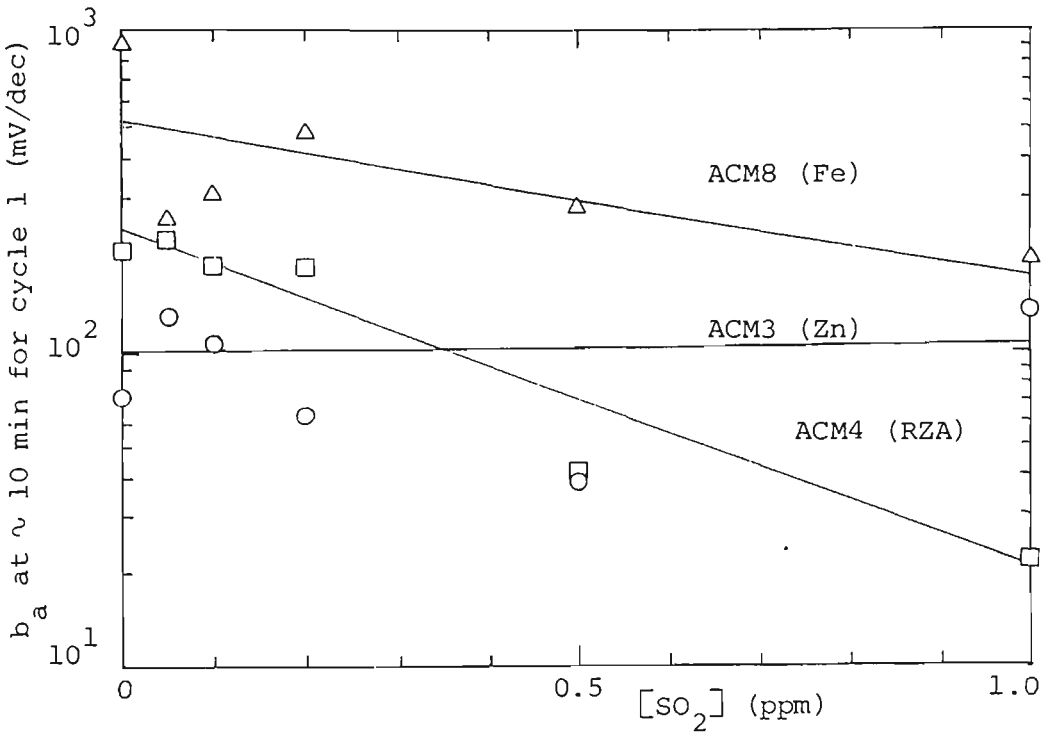

Figure R1/37. Summary plot of the effect of $[SO_2]$ on the anodic Tafel slope for the metal, b_a, obtained after about 10 minutes duration of cycle 1 for ACM3 (Zn) taken from Figure R1/36; for ACM8 (Fe) taken from Figure R1/38; and for ACM4 (RZA) taken from Figure R1/39. RZA rolled Zn-55%Al.

5.2 ACM8 (Fe)

Figure R1/38 shows b_a as a function of time for each run within a PGB cycle, and from cycle to cycle at each SO_2 concentration.

Generally, there is a marked downward trend in b_a from run to run within a cycle, indicating depolarization of the anodic metal dissolution reaction. This occurs also at zero [SO_2], so that the drop in b_a can not only be attributed to the presence of SO_2 but rather to an increase in the number of corrosion initiating sites on the ACM surface.

There also appears to be a drop in b_a values from cycle to cycle, although this trend is not so marked and exceptions occur. The first run value of b_a in the next cycle is generally higher than the final run value in the previous cycle, but subsequent run values drop below this previous final run value. A possible explanation is that the decrease from run to run within a cycle is caused by concentration of soluble reaction products as the water film evaporates. When water is re-applied in the next cycle, the dilution of these soluble 'salts' causes a partial re-establishment of the previous conditions, but further concentration of salts occurs as this new water film evaporates, causing a further lowering of b_a.

Figure R1/37 shows b_a results taken from Figure R1/38 for the first run (around 10 min) in cycle 1 for ACM8 (Fe) which helps to summarize the trends in b_a with variation in [SO_2]. There appears to be a general decrease in b_a as [SO_2] is increased, which corresponds to an increase in mass loss for ACM8 (Fe) in Figure R1/35. This trend is not so clearly defined for other cycles in Figure R1/38, but it does suggest that increased corrosion rates as [SO_2] is

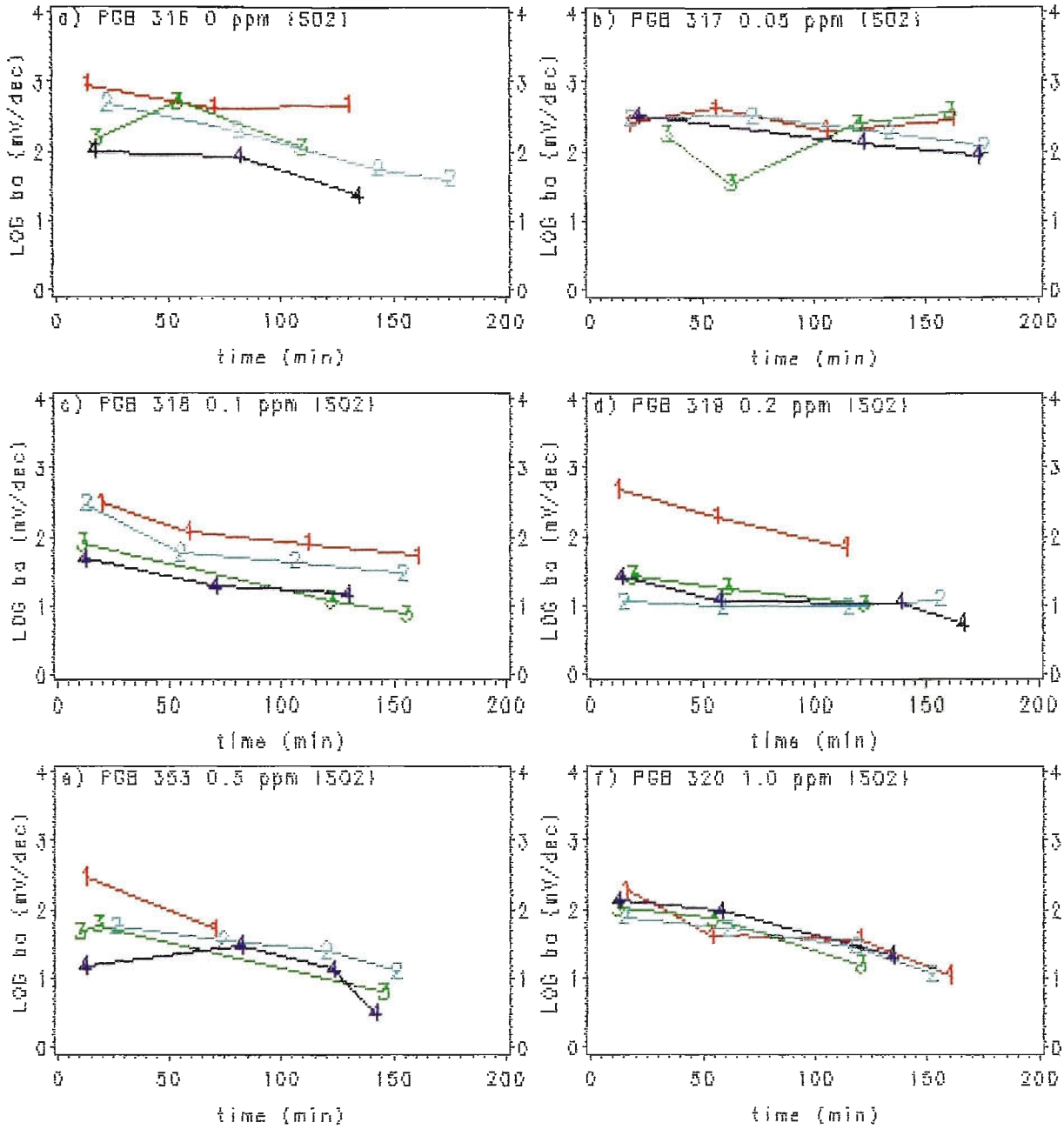

Figure R1/38. Effect of time on anodic Tafel slope for the metal, ba, from run to run within a cycle; from cycle to cycle and from (SO2) to (SO2) for ACM8(Fe). Numbers on plots are run data points for cycles 1-4 respectively.

increased is caused, at least in part, by depolarization of the anodic metal dissolution reaction. This is discussed further in Section R1.6/8.

The wide range of b_a values for steel in ACM8 is quite surprising, and can range from around 900 mV/decade in cycle 1 run at zero [SO_2] down to around 5 mV/decade in cycle 4 run 4 at 0.2 ppm [SO_2]. A similar situation occurred with the ACM3 (Zn) b_a results in Section R1.6/5.1. The importance of b_a in controlling corrosion rate is discussed in Section R1.6/8.

5.3 ACM4 (rolled Zn-55%Al alloy)

Figure R1/39 shows b_a as a function of time for each run within a PGB cycle, and from cycle to cycle at each SO_2 concentration.

Generally, there is a downward trend in b_a values from run to run within a PGB cycle at all [SO_2] levels, which is more marked than ACM3 (Zn) but less marked than ACM8 (Fe). This normally indicates depolarization of the anodic metal dissolution reaction. As it also occurs at zero [SO_2], as it did with ACM8 (Fe) but not with ACM3 (Zn), it can not only be attributed to the presence of SO_2 but possibly to an increase in the number of corrosion initiating sites on the ACM surface.

There is no general tendency for b_a values to decline from cycle to cycle as they do for ACM3 (Zn) and ACM8 (Fe). Rather, there are some instances, notably 0, 0.1, 0.2 ppm [SO_2] where the opposite effect, that is, a small increase in b_a, occurs from cycle to cycle. Such a trend would normally indicate polarization of the anodic dissolution reaction and would predict lower corrosion rates from cycle to cycle in these instances, all other

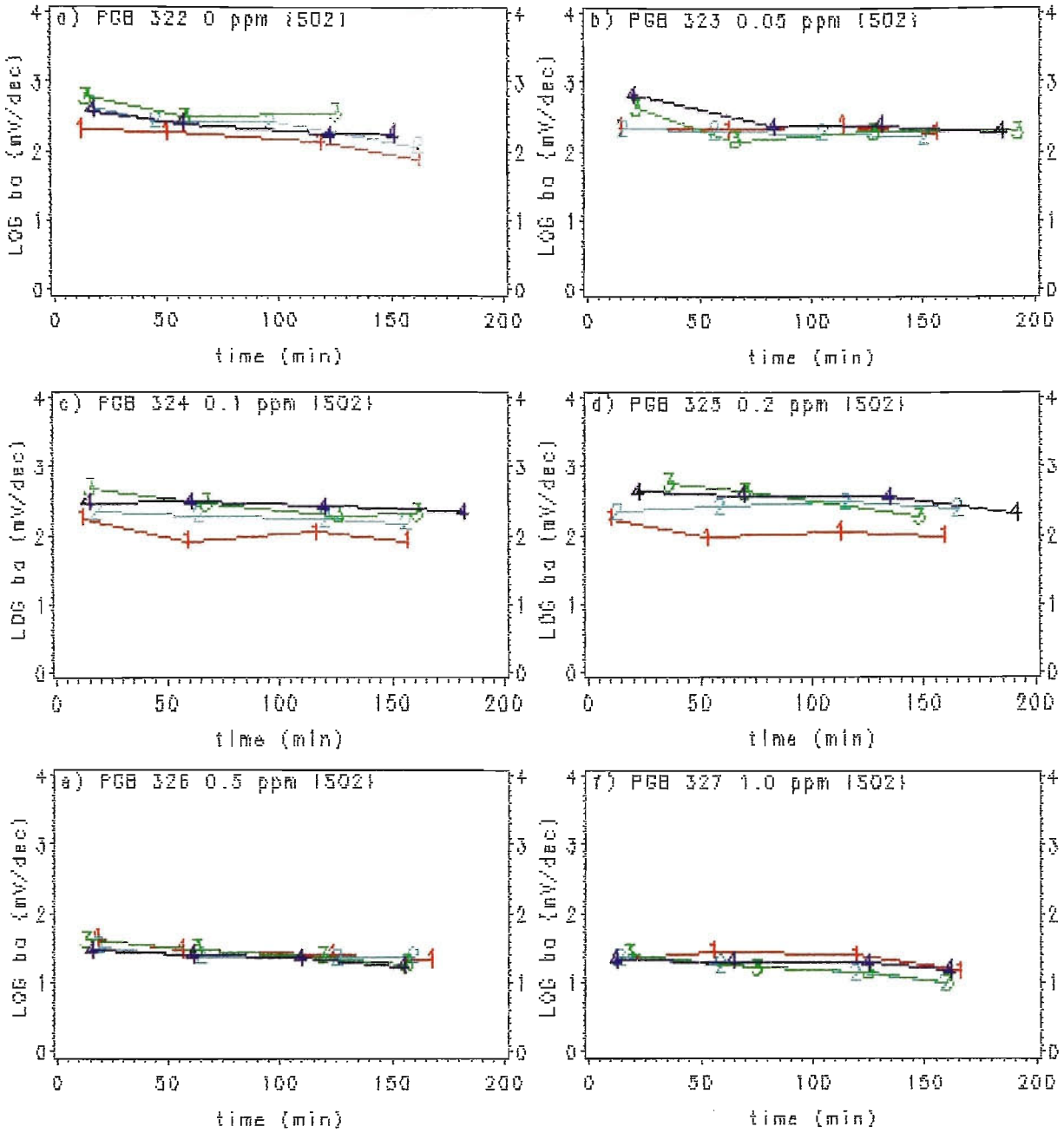

Figure R1/39. Effect of time on anodic Tafel slope for the metal,ba, from run to run within a cycle; from cycle to cycle; and from (SO2) to (SO2) for ACM4(rolled Zn-55%Al). Numbers on plots are run data points for cycles 1-4 respectively.

variables being constant, probably as the result of protective corrosion product build-up.

There appears to be a trend towards decreasing b_a values as $[SO_2]$ is increased. This is especially noticeable at 0.5, 1.0 ppm $[SO_2]$ where a large drop in b_a occurs compared to lower $[SO_2]$ levels. Figure R1/37 shows b_a results taken from Figure R1/39 for the first run (around 10 min) in cycle 1 for ACM4 (rolled Zn-55%Al) which helps to summarize the trends in b_a with variation in $[SO_2]$ level. This general decrease can readily be observed in this case. Such a decrease would normally indicate depolarization of the anodic dissolution reaction; and predict increased corrosion rates, as a result of the presence of SO_2. This does seem to be the case, because the mass loss of rolled Zn-55%Al alloy in ACM4 shows a modest increase in mass loss as $[SO_2]$ is increased, refer Figure R1/35. Because of this downward trend in b_a values, they tend to be higher or equal at zero and low $[SO_2]$ levels, (0, 0.05, 0.1, 0.2 ppm) but lower at high $[SO_2]$, (0.5, 1.0 ppm), than ACM3 (Zn) and ACM8 (Fe).

As was found with ACM3 (Zn) and ACM8 (Fe), the range of b_a values is surprisingly large, ranging from about 600 mV/decade at low $[SO_2]$, (zero ppm/cycle 3/run 1, 0.05 ppm/cycle 4/run 1), to around 10 mV/decade at 1.0 ppm $[SO_2]$, (cycles 2,3/run 4). In this case, solution resistance, R_s, is not likely to be a problem, refer discussion in Section R1.6/8, because the applied currents only ranged up to 0.3 mA maximum, whereas they were 3 mA max for ACM3 (Zn) and 70 mA max for ACM8 (Fe). If IR_s drop is not a problem for ACM4 (rolled Zn-55%Al) and a wide range of b_a values still occurs, then it suggests that the wide range of b_a values also observed for ACM3 (Zn) and ACM8 (Fe) may not be due solely to errors caused by IR_s drop not being eliminated from the voltage response.

6. b_c/time trends

6.1 ACM3 (Zn)

Figure R1/40 shows the Tafel slope for the cathodic reduction reaction, b_c, as a function of time for each run within a PGB cycle, and from cycle to cycle at each SO_2 concentration.

No general trend from run to run within a given PGB cycle could be detected. However, there was a suggestion that b_c values generally increased at zero [SO_2], whereas they generally decreased (cycle 1 sometimes an exception) for experiments with [SO_2]. A similar conclusion was reached for ACM3 (Zn) b_a values in Section R1.6/5.1. The presence of [SO_2] may therefore have a depolarizing effect on the cathodic reduction reaction. This is to be expected if a second cathodic reduction reaction involving SO_2 occurs on the ACM surface, along with the cathodic reduction of oxygen.

The very high b_c values (>1000 mV/decade) in cycles 1, 3 at zero [SO_2] simply mean that the cathodic reduction reaction is diffusion limited. The analysis routine is not capable of resolving b_c values higher than about 1000 using experimental data because slight errors in the (I/ε) data points can alter the calculated b_c value significantly. Such high b_c values cause divergence in the analysis routine IK_CALC8 and data must be re-analyzed using routine IK CALC9, as discussed in Section R1.6/2.

There is quite a marked drop in b_c values from cycle to cycle at each [SO_2] level, except 0.5 ppm where b_c values do not change much from cycle to cycle. A drop in b_c values normally indicates depolarization of the cathodic

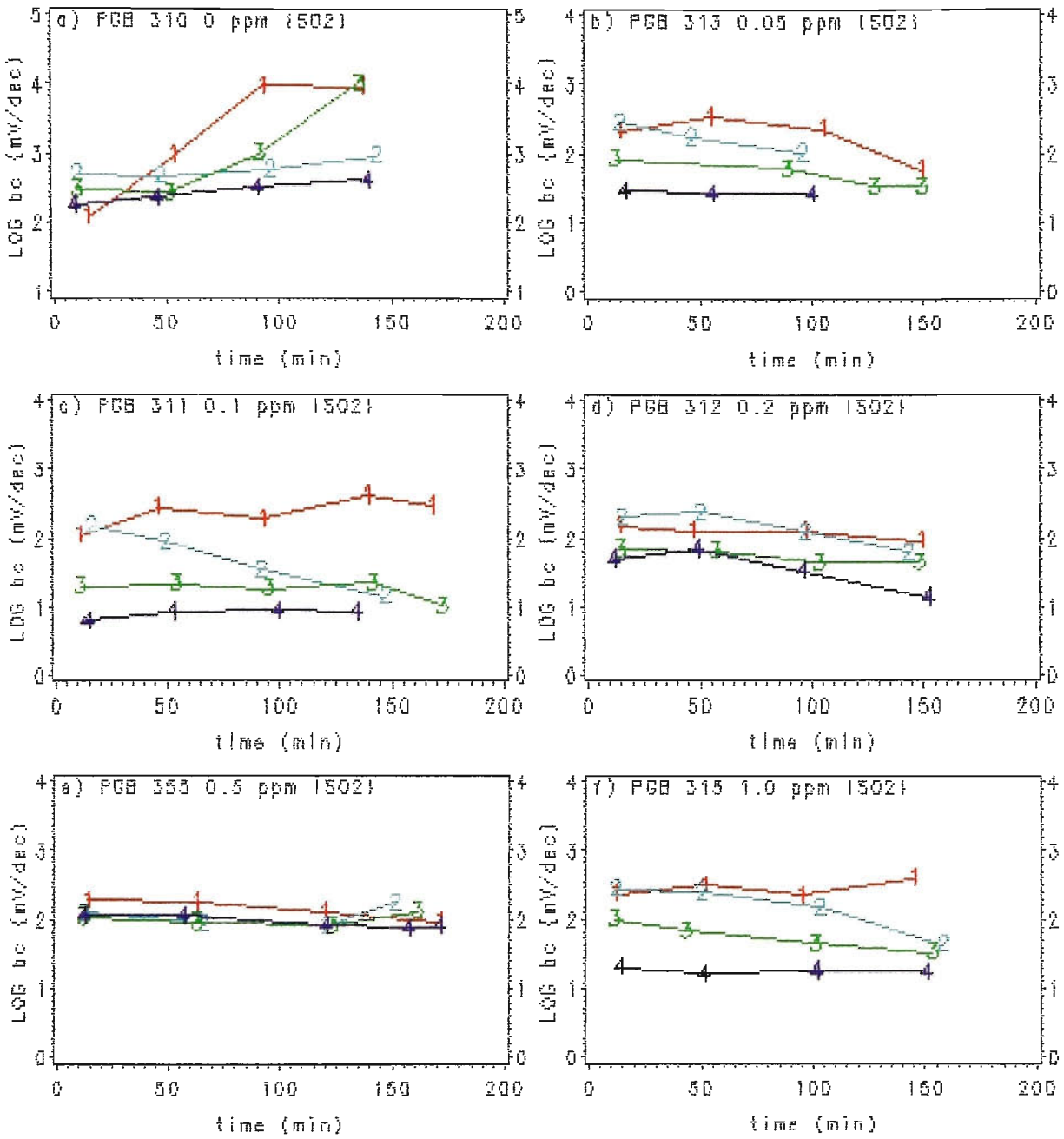

Figure R1/40. Effect of time on cathodic Tafel slope for the metal,bc, from run to run within a cycle; from cycle to cycle and from (SO2) to (SO2) for ACM3(Zn). Numbers on plots are run data points for cycles 1-4 respectively.

reduction reaction, and would predict higher corrosion rates if all other conditions were constant. This depolarization has been explained above as due to the presence of a second cathodic reduction reaction involving SO_2. It appears that the decrease in b_c values from cycle to cycle is more dependent on the particular conditions of corrosion initiation and corrosion product formation, rather than directly related to $[SO_2]$ level. It is possible that corrosion initiates in a spasmodic way on the ACM surface. The number of corrosion sites initiating on the ACM surface will depend on the surface energy at particular sites, which in turn would be expected to depend on the level of abrasion of the surface (nominally to #600 grade using silicon carbide paper), and the concentration of adsorbed impurities which may inhibit initiation.

There is no overall trend in b_c with $[SO_2]$ although b_c values are significantly higher at zero $[SO_2]$, as explained.

6.2 ACM8 (Fe)

Figure R1/41 shows b_c as a function of time for each run within a PGB cycle, and from cycle to cycle at each SO_2 concentration.

There was some evidence of a downward trend in b_c from run to run within a given PGB cycle. This was particularly noticeable at 0.1 ppm $[SO_2]$ for all cycles. A similar downward trend was observed in b_a values for ACM8 (Fe) in Section R1.6/5.2. The downward trend in b_c values may indicate depolarization of the cathodic reduction reaction, but as this also occurs at zero $[SO_2]$, it can not only be due to the presence of SO_2, but rather may be due to an increase in the number of corrosion sites initiating on the ACM

surface and/or thinning of the water film. Mansfeld[36] found that b_c values changed markedly from around infinity (indicating diffusion control of the cathodic reaction) at the beginning of a 3-electrode ACM experiment on 4130 steel, to between 40 and 120 mV/decade (indicating charge-transfer control) as a 1N NaCl electrolyte layer evaporated. (The $[SO_2]$ level was not stated and was presumably zero.)

There was some evidence that b_c values decrease from cycle to cycle, particularly at zero and 0.1 ppm $[SO_2]$, but also at other $[SO_2]$ levels for some of the cycles. This decrease can also be explained by depolarization of the cathodic reduction reaction, as discussed above. At 0.1 ppm $[SO_2]$, b_c values fall from very high values in cycle 1 to much lower values, suggesting a change from complete diffusion limiting control in cycle 1 to activation control in subsequent cycles.

The situation is more complex with variation in $[SO_2]$ level. There does not appear to be any general trend as $[SO_2]$ increases, and because mass loss of steel in ACM8 is strongly related to $[SO_2]$, see Figure R1/35, this suggests that the corrosion rate is not controlled solely by the cathodic reaction. The explanation regarding corrosion initiation in Section R1.6/6.1 is relevant here. Once corrosion has initiated, it is accelerated by the presence of SO_2, causing large changes in I_k, b_a and b_c from cycle to cycle, for example, at 0.1 ppm $[SO_2]$, refer Figures R1/33c,38c,41c. If the corrosion rate of steel is controlled by the cathodic reduction reaction, then it would be expected that b_c values at 1.0 ppm $[SO_2]$ would be significantly lower than those at zero or 0.05 ppm $[SO_2]$, but they are not very different. This evidence supports the comment made above that the corrosion rate is not solely controlled by the cathodic reduction reaction.

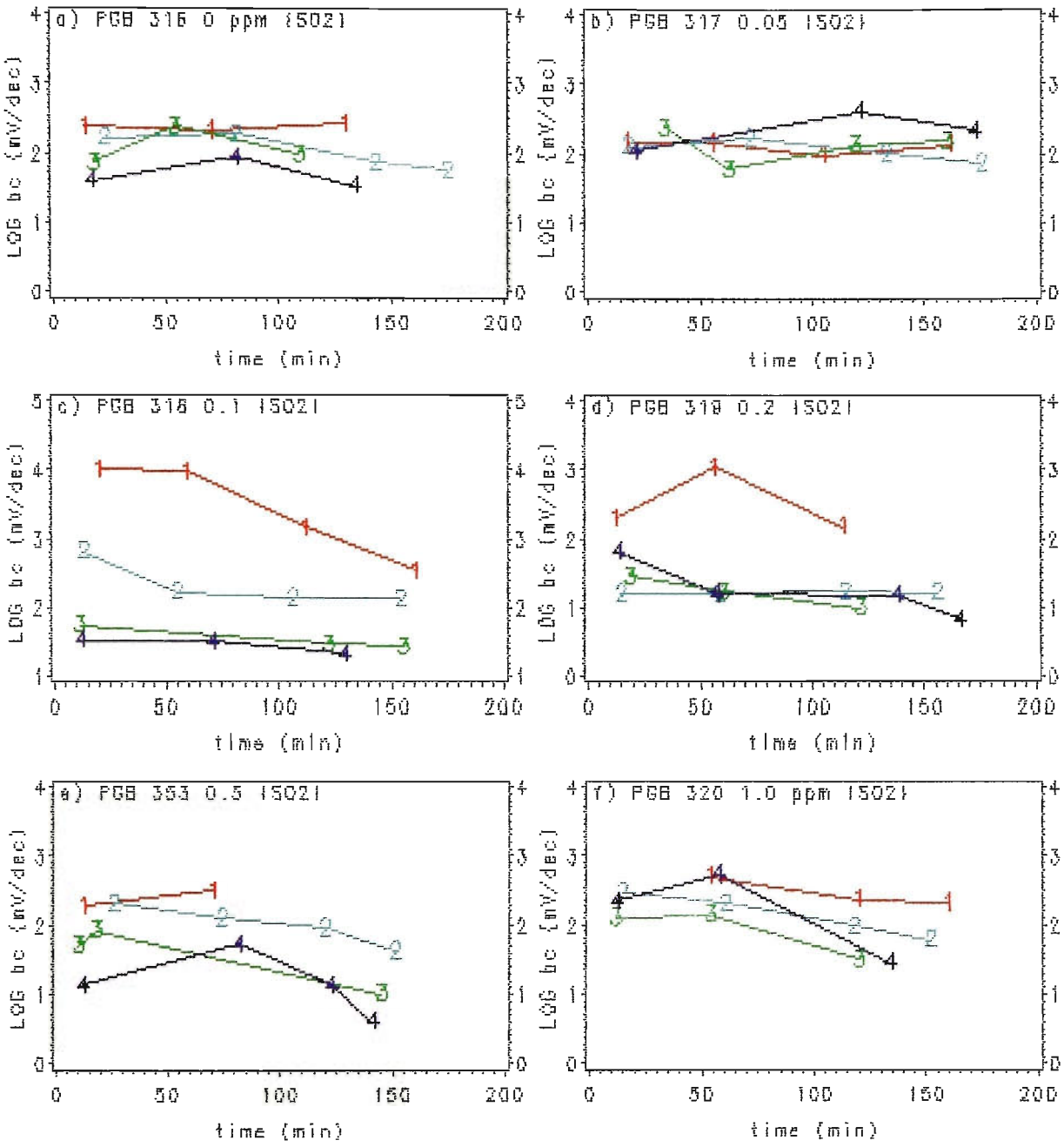

Figure R1/41. Effect of time on cathodic Tafel slope for the metal,bc, from run to run within a cycle; from cycle to cycle and from (SO2) to (SO2) for ACM8(Fe). Numbers on plots are run data points for cycles 1-4 respectively.

6.3 ACM4 (rolled Zn-55%Al alloy)

Figure R1/42 shows b_c as a function of time for each run within a PGB cycle, and from cycle to cycle at each SO_2 concentration.

Values of b_c are relatively constant from run to run within a given cycle although there is some evidence of a downward trend with time. Similar downward trends were observed for b_a values in Section R1.6/5.3. Such downward trends normally suggest depolarization of the cathodic reduction reaction, but can not only be attributed to the presence of SO_2, because this can also occur at zero [SO_2]. It has previously been explained as being due to an increase in the number of corrosion sites initiating on the ACM surface.

There is no general trend for b_c values to drop from cycle to cycle as they do for some [SO_2] levels for ACM3 (Zn) and ACM8 (Fe) in Figures R1/40,41. A similar conclusion was drawn for b_a values in Section R1.6/5.3. Values of b_c from cycle to cycle are bunched close together and this closeness must be indicative of relatively constant corrosion rates.

Up to 0.2 ppm [SO_2], b_c values remain essentially constant, but at 0.5, 1.0 ppm [SO_2], b_c values are significantly lower. A similar situation occurred with b_a trends in Figure R1/39 with some decrease in b_a apparent at other [SO_2] levels. The drop in b_c at 0.5, 1.0 ppm [SO_2] may indicate depolarization of the cathodic reduction reaction due to the presence of SO_2. The corrosion rate can not completely be controlled by the cathodic reduction reaction because mass loss increased from zero to 0.2 ppm [SO_2], refer Figure R1/35, whereas the above b_c trends are relatively constant over this range. However, these results do indicate at least partial control by the cathodic reaction at the

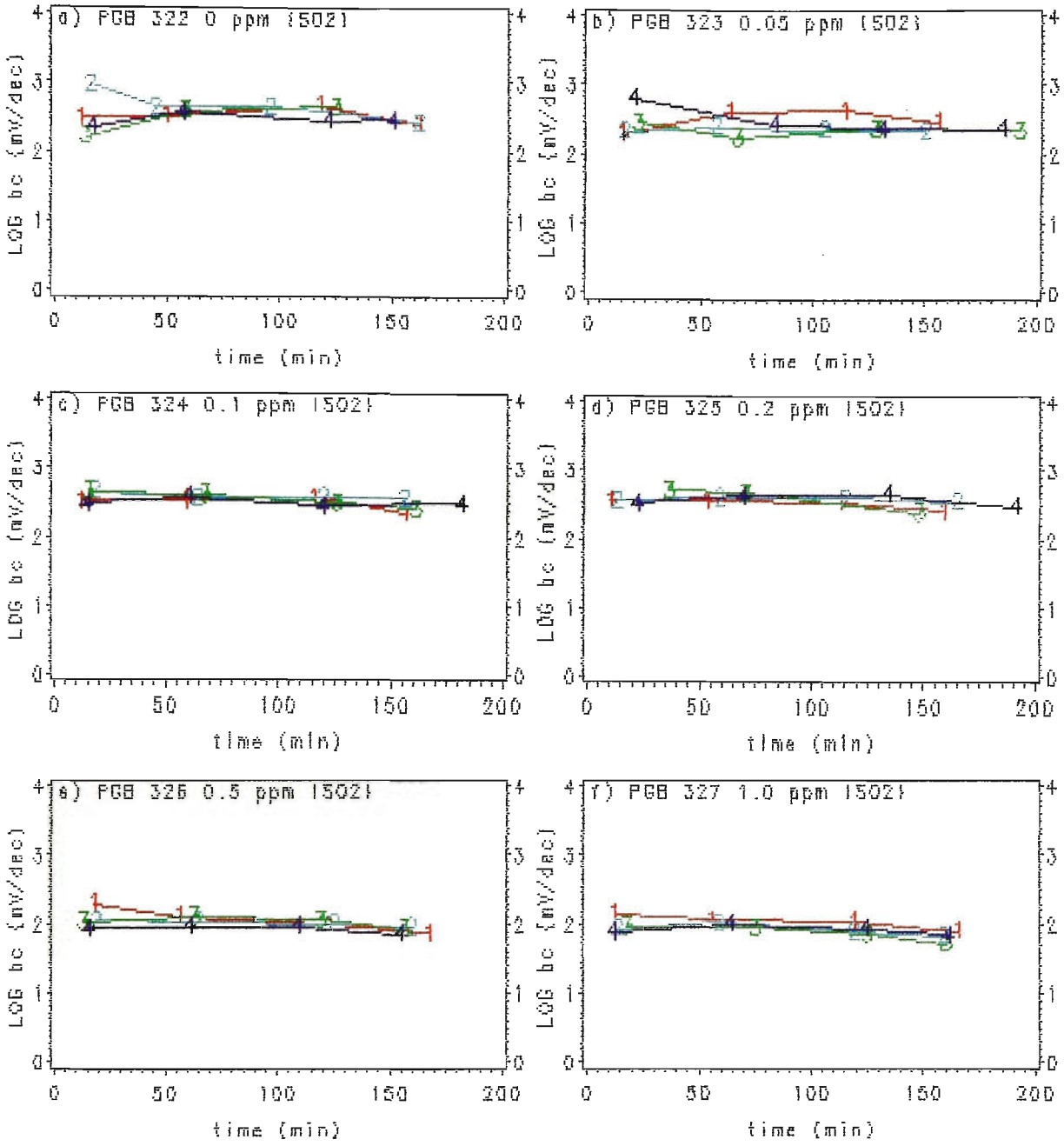

Figure R1/42. Effect of time on cathodic Tafel slope for the metal,bc, from run to run within a cycle; from cycle to cycle and from (SO2) to (SO2) for ACM4(rolled Zn-55%Al). Numbers on plots are run data points for cycles 1-4 respectively.

higher [SO_2] levels, together with partial control by the anodic metal dissolution reaction as discussed in Section R1.6/5.3.

7. r_p/time trends

Figure R1/43 shows polarization resistance, r_p, as a function of time for each run within a PGB cycle, and from cycle to cycle at each [SO_2] for ACM3 (Zn).

If Tafel slopes b_a and b_c are held relatively constant, an inverse relationship should exist between i_k and r_p. It is apparent from Figures R1/36,40 that b_a and b_c are not always constant and therefore an inverse relationship between i_k and r_p may not necessarily be expected. This is in fact the case. Comparisons between r_p and i_k in Figure R1/31,43 reveal that an inverse relationship holds in certain instances from cycle to cycle, but there are many exceptions, with cycles appearing in a different order and upward trends in i_k with time not being mirrored by downward trends in r_p. At 0.5 ppm [SO_2], all four cycles have low i_k values compared with other SO_2 concentrations, and these are mirrored by high r_p values. In this instance, the inverse relationship holds because b_a/time and b_c/time trends are relatively constant for all four cycles, refer Figures R1/36e,40e. However, at 0.1 ppm [SO_2], where b_a and b_c vary considerably from cycle to cycle, i_k trends are not mirrored by r_p trends and the inverse relationship does not hold.

The importance of this is that evaluation of corrosion rate characteristics using polarization resistance will result in predictions that are not as accurate as using corrosion current in cases where the anodic and cathodic Tafel slopes vary. Unless Tafel slopes are measured, there will always remain the uncertainty that they could vary and affect evaluations based on polarization

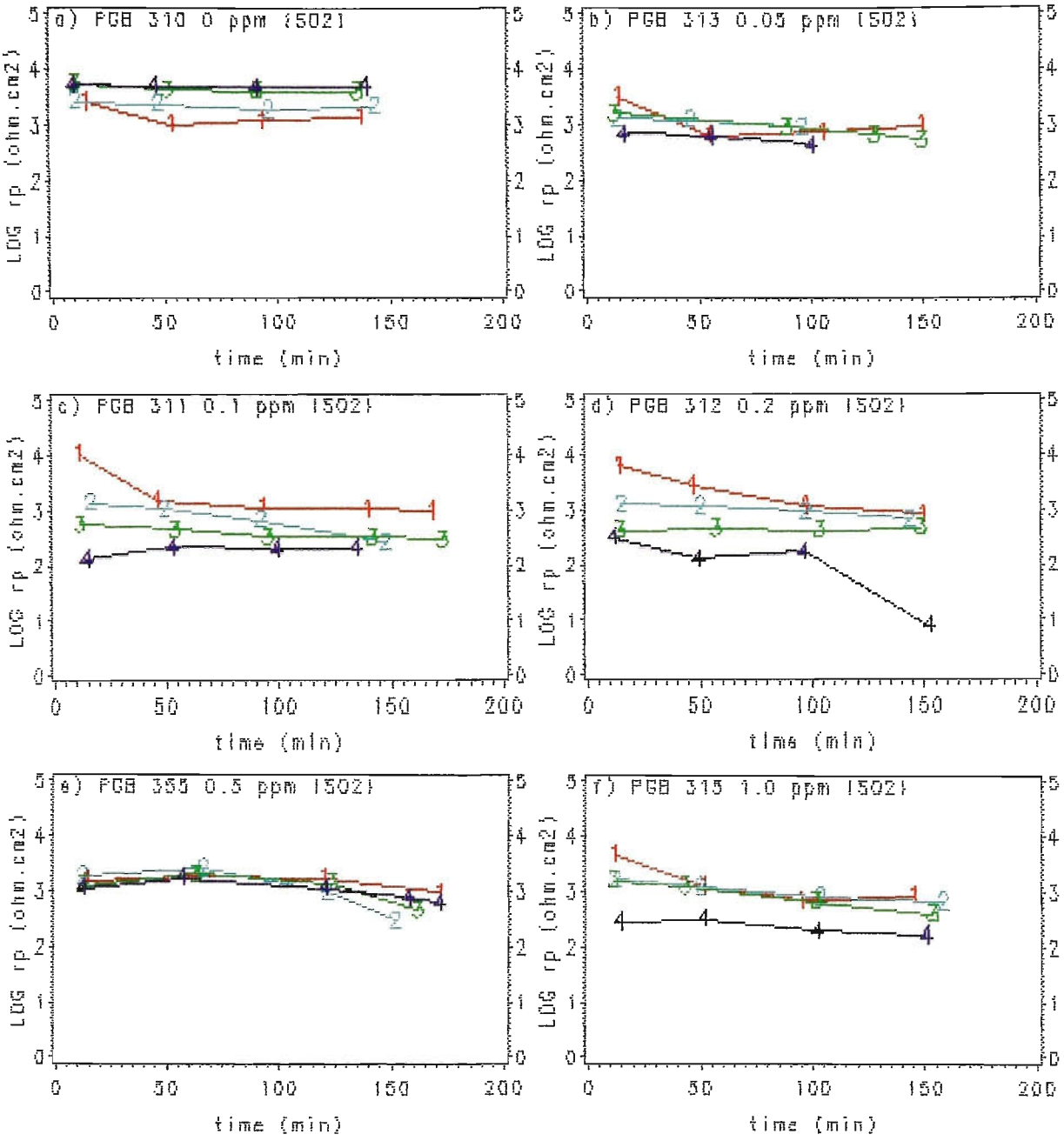

Figure R1/43. Effect of time on polorization resistance, rp, from run to run within a cycle; from cycle to cycle and from (SO2) to (SO2) for ACM3(Zn). Numbers on plots are run data points for cycles 1-4 respectively.

resistance. Of course, if Tafel slopes are measured, polarization resistance as an evaluation tool becomes redundant, because corrosion current can be calculated and used more effectively instead.

Figures R1/44,45 show r_p as a function of time for each run within a PGB cycle, and from cycle to cycle at each $[SO_2]$ for ACM8 (Fe) and ACM4 (rolled Zn-55%Al alloy), respectively.

By comparing r_p/time and i_k/time graphs (Figures R1/44,33 and R1/45,34), it is seen that there is a better inverse relationship between i_k and r_p for ACM4 (rolled Zn-55%Al) and ACM8 (Fe) than for ACM3 (Zn). With ACM4 (rolled Zn-55%Al) this is because the Tafel slope values are reasonably close together, Figures R1/39,42. The explanation for ACM8 (Fe) is not so straightforward because b_a and b_c values vary considerably, Figures R1/38,41.

The overall relationship between i_k and r_p for the three ACMs can be observed in Figure R1/46 to be a respectable inverse relationship. The correlation coefficient between log i_k and log r_p is -0.944 for 278 observations, which is highly significant at the 99% level of confidence, and indicates a very strong inverse relationship. However, exceptions can clearly be observed.

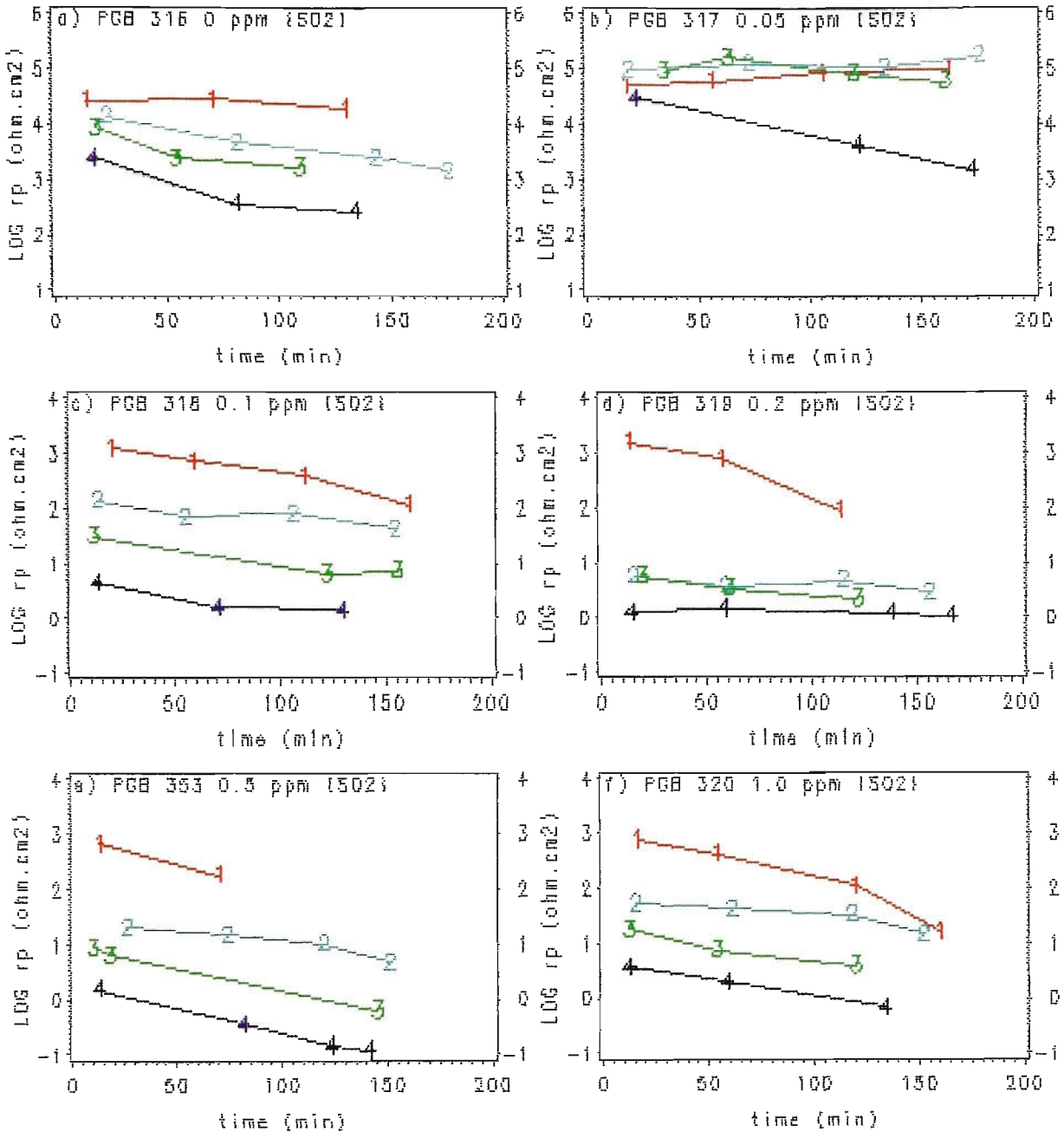

Figure R1/44. Effect of time on polarization resistance, rp, from run to run within a cycle; from cycle to cycle and from (SO2) to (SO2) for ACM8(Fe). Numbers on plots are run data points for cycles 1-4 respectively.

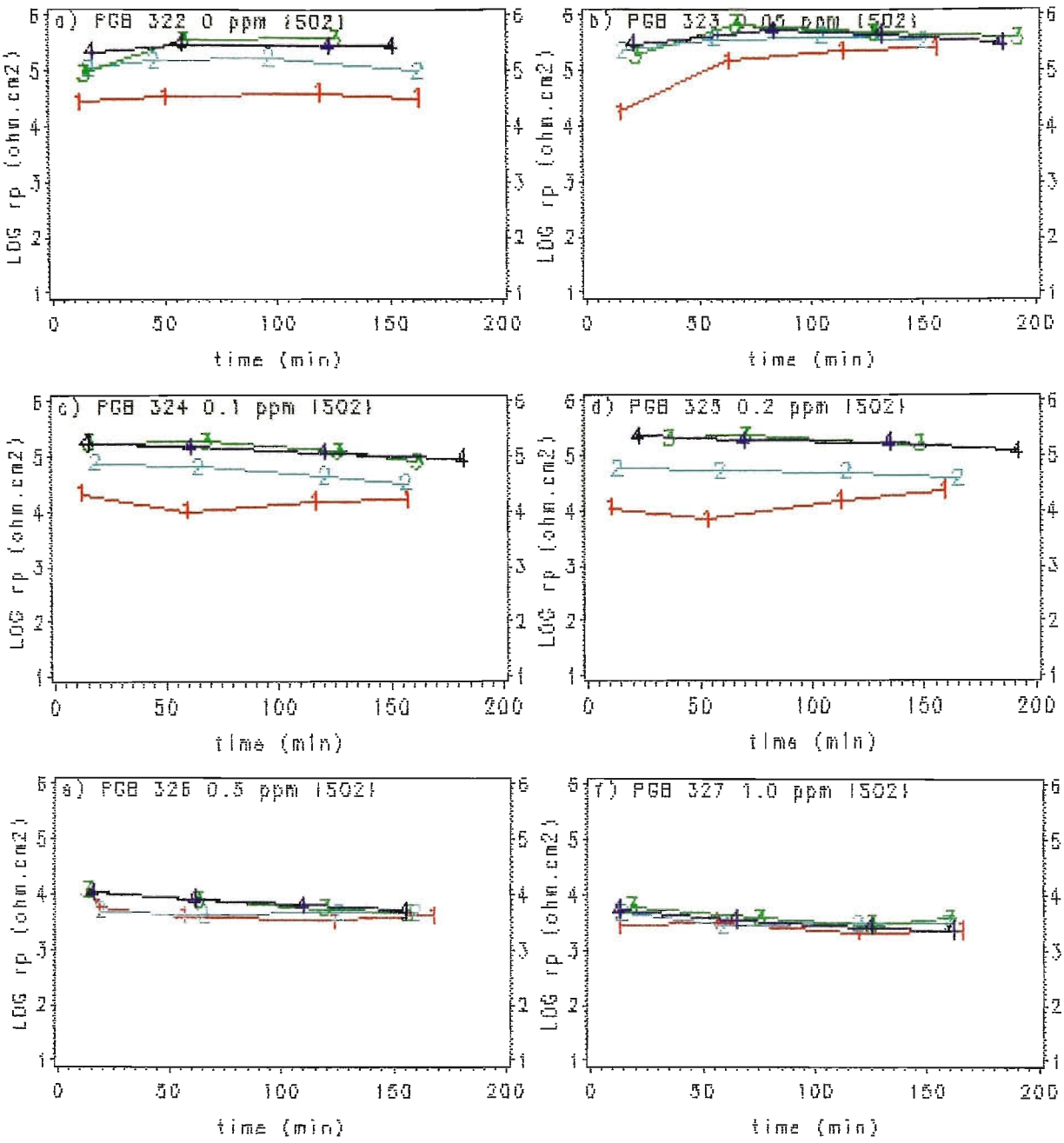

Figure R1/45. Effect of time on polorization resistance, rp, from run to run within a cycle; from cycle to cycle and from (SO2) to (SO2) for ACM4(rolled Zn-55%Al). Numbers on plots are run data points for cycles 1-4 respectively.

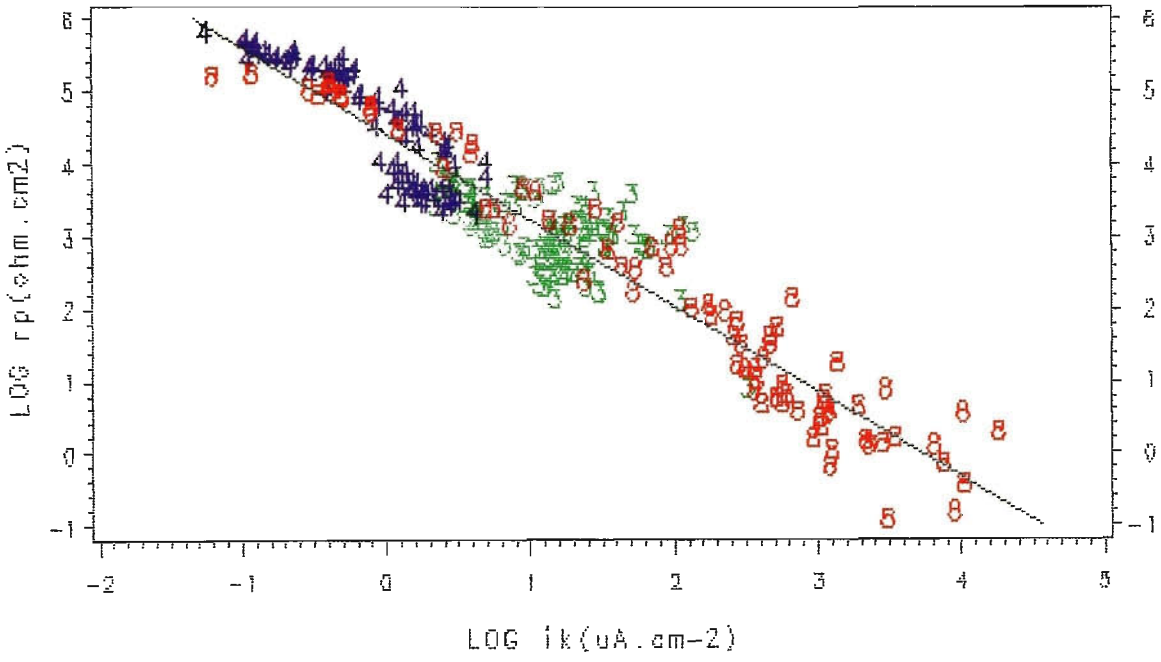

Figure R1/46. LOG ik vs. LOG rp for ACMs in PGB experiments over the range 0-1.0 ppm (SO2). Numbers on plot indicate data points for each ACM type.
code: ACM3(Zn) ACM8(Fe) ACM4(RZA) RZA rolled Zn-55%Al alloy

8. Corrosion rate control

The aim of this section is to determine, by re-examining all the ACM data in Sections R1.6/3-7, what factors control the corrosion rate of ACMs under thin water films and in the presence of SO_2 containing atmospheres.

The task of determining whether corrosion rate control is cathodic, anodic or mixed is more difficult with ACMs because a corrosion potential, E_k, measurement is unavailable. This is because corrosion products build up on the reference plates to the same extent as working and auxiliary plates, as all plates are essentially equal. It is therefore not possible to determine whether E_k increases, decreases or remains constant as corrosion current density, i_k, increases, corresponding to cathodic, anodic or mixed control, respectively.

A further problem is the presence of partial short circuits between working and auxiliary plates, which is discussed extensively in Section R1.8. It is suspected, refer Sections R1.8/1,5.2, that these shorts may exist to some degree and appear to occur at random in cycles 3, 4 of the impedance test for ACM3 (Zn) and perhaps ACM8 (Fe), but not for ACM4 (rolled Zn-55%Al). They would therefore be expected to occur in the corrosion current test in a similar and perhaps worse manner than in the impedance test.

One factor which may exert an influence on corrosion rate control is resistance polarization due to a high solution resistance, R_s, in the thin water films on the ACM surface. The solution resistance between reference and working electrode plates was not compensated for in these results. Its value

would be expected to be small because of the thin water film and the very small distance involved (insulator thickness between plates 23 μm). Solution resistance would be expected to decrease from run to run and cycle to cycle, especially when [SO_2] was present, as the soluble reaction products and ions from adsorption of SO_2 build up in the water film. The high values of b_a, b_c and the fact that they decrease markedly, could be in part attributed to this cause and an IR_s drop error could be incorporated into the voltage responses, leading to incorrect calculation of b_a values. However, this does not appear to be the case because ACM4 (rolled Zn-55%Al alloy) in Section R1.6/5.3, also shows a wide variation in b_a values, and this is not likely to be attributed to errors caused by inclusion of IR_s drop because of the much lower currents applied.

Solution resistance, R_s, was measured on ACM3 (Zn) and ACM8 (Fe) after completion of four cycles in the PGB, that is, after PGB 315 for ACM3 (Zn), and PGB 321 for ACM8 (Fe). This coincided with heavy white corrosion product build-up of ACM3 (Zn) and light red rust spots on ACM8 (Fe). A film of distilled water was re-applied to the ACM surface and R_s measured by the square-wave bridge method used previously in this laboratory[55]. Values of R_s in both instances were less than 0.1 ohm, being the minimum resistance measurable using this technique. This value would include the resistance of corrosion products as well as solution resistance between working and reference plates on the ACM. It is concluded that R_s values are negligible after four PGB cycles and voltage responses do not require correction for IR_s drop. This is supported by the discussion in Section R1.5/5 on R_s measurements from ac impedance tests.

In order to obtain insight into corrosion rate control in PGB ACM experiments, all the i_k, b_a, b_c/time plots at each $[SO_2]$ were re-examined. The situation was not straightforward because correlations between i_k and b_a or b_c that were apparent in one cycle at a given $[SO_2]$, were not necessarily apparent in the next cycle. Therefore all the i_k, r_p, b_a, b_c data was treated statistically for all $[SO_2]$ levels and for each ACM. The details appear in Appendix A4/2.3, and indicate the following:

(i) an inverse relationship exists between log i_k and log r_p for each of the three ACMs. A similar conclusion was reached in Figure R1/46 and Section R1.6/7 for all ACM data lumped together;

(ii) a direct relationship exists between log i_k and log b_a and between log i_k and log b_c for ACM3 (Zn);

(iii) an inverse relationship exists between log i_k and log b_a for both ACM4 (rolled Zn-55%Al) and ACM8 (Fe);

(iv) an inverse relationship exists between log i_k and log b_c for both ACM4 (rolled Zn-55%Al) and ACM8 (Fe).

The fact that there is a relationship between log i_k and both log b_a and log b_c suggests mixed control by both the cathodic and anodic reactions. This applies to all three ACMs. However, there appears to be two distinct types of mixed control - one type for ACM3 (Zn) and a different type for both ACM4 (rolled Zn-55%Al) and ACM8 (Fe). These types of mixed control are depicted in the Evans E/log I diagrams in Figure R1/47.

For ACM4 (rolled Zn-55%Al) and ACM8 (Fe) in Figure R1/47a, an increase in corrosion current, I_k, from position 1 to position 2 corresponds to a decrease in both b_a and b_c, without requiring changes to the exchange currents, $I_{o,M}$, $I_{o,X}$. This is the normal situation where depolarization of both anodic and cathodic reactions causes an increase in corrosion rate. As both Fe and rolled Zn-55%Al show increases in mass loss with [SO_2], refer Figures R1/49,50 Section R1.7/2, it is reasonable to conclude that depolarization of anodic and cathodic reactions is caused by increased levels of SO_2. This has also been suggested in Sections R1.6/5.2,5.3 for b_a/time trends, and in Sections R1.6/6.2,6.3 for b_c trends, but the evidence was not clear cut. Zinc shows a more constant mass loss over the [SO_2] range, refer Figure R1/48 Section R1.7/2, and hence it is not surprising that the type of corrosion rate control is different. For ACM3 (Zn) in Figure R1/47b, an increase in I_k from position 1 to position 2 corresponds to an increase in both b_a and b_c. This requires an increase in both exchange currents, $I_{o,M}$, $I_{o,X}$. It represents a more unusual situation where increases in corrosion rate are caused by increases in the

respective exchange currents. The secondary effect of increasing Tafel slopes (polarization of both anodic and cathodic reactions), will inhibit the increase in I_k caused by increasing exchange currents.

These explanations are idealised and represent the overall situation when all $[SO_2]$ levels are considered together.

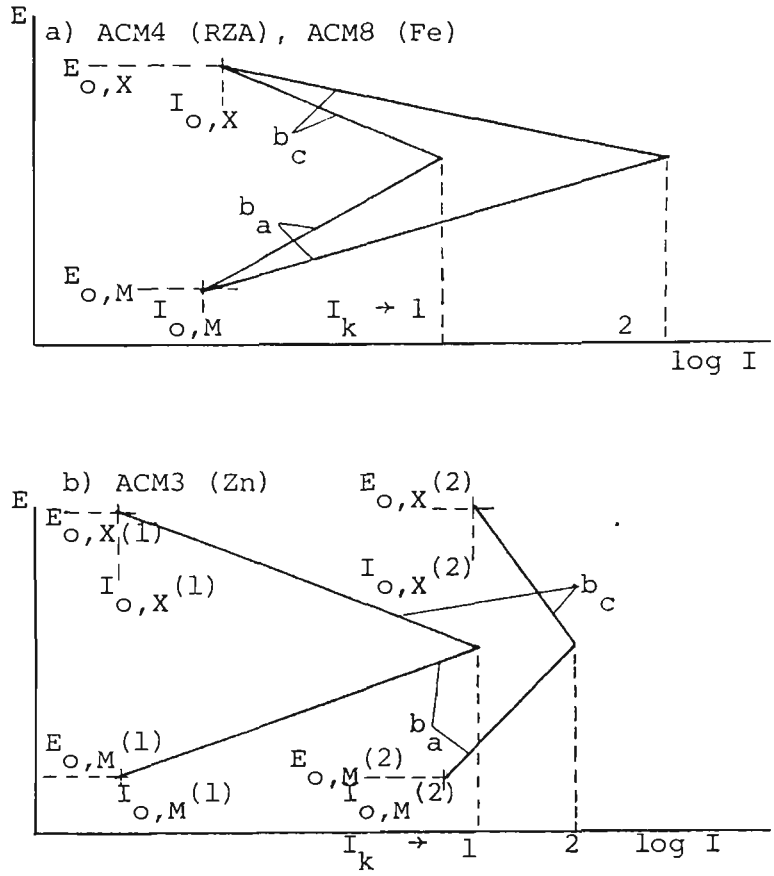

Figure R1/47. Idealized Evans diagrams of potential, E, versus log current, I, showing that a) depolarization of both anodic and cathodic partial reactions lead to an increase in corrosion current, I_k (from position 1 to 2) without requiring a change in exchange currents, $I_{o,M}$, $I_{o,X}$; and b) polarization of both anodic and cathodic partial reactions lead to an increase in I_k but only if $I_{o,M}$, $I_{o,X}$ increase. Case a) appears typical of ACM4 (RZA) and ACM8 (Fe) behaviour and is the more usual situation; case b) appears typical of ACM3 (Zn) behaviour. RZA rolled Zn-55%Al.

1. Method of calculation

Figures R1/48-50 are mass losses, obtained either by weighing or calculated, for zinc, steel and cast or rolled Zn-55%Al alloy over the range 0-1 ppm [SO_2]. Weighed mass losses are discussed in Section R1.3 and shown previously in Figures R1/4,5. The method of calculation of mass loss obtained from ACM galvanic current, I_g/time measurements is discussed in Section R1.4/1 and mass losses shown in Figures R1/6,9. Mass losses calculated from ACM corrosion current, i_k/time measurements are discussed in Sections T3/7, R1.6/4 and shown in Figure R1/35. Mass losses were also calculated from ACM polarization resistance, r_p/time measurements and from ACM charge-transfer resistance, R_t/time measurements. The r_p and R_t results are discussed in Sections R1.6/7 and R1.5/3, respectively. The method of mass loss calculation from r_p is discussed in Section T3/7. Essentially the same method was used for the calculation of mass losses from R_t, except that the impedance technique measures the impedance of both working and auxiliary electrodes of an ACM and a correction must be applied. This is discussed in Section T1/6.

2. Weighed versus galvanic current calculated mass loss

The comparison between galvanic current calculated mass loss, ΔM_{Ig}, and weighed mass loss, ΔM_w, was only available for zinc and rolled Zn-55%Al alloy. No such comparison was possible for steel because an ACM in which steel was anode, eg Fe/Cu, was not manufactured.

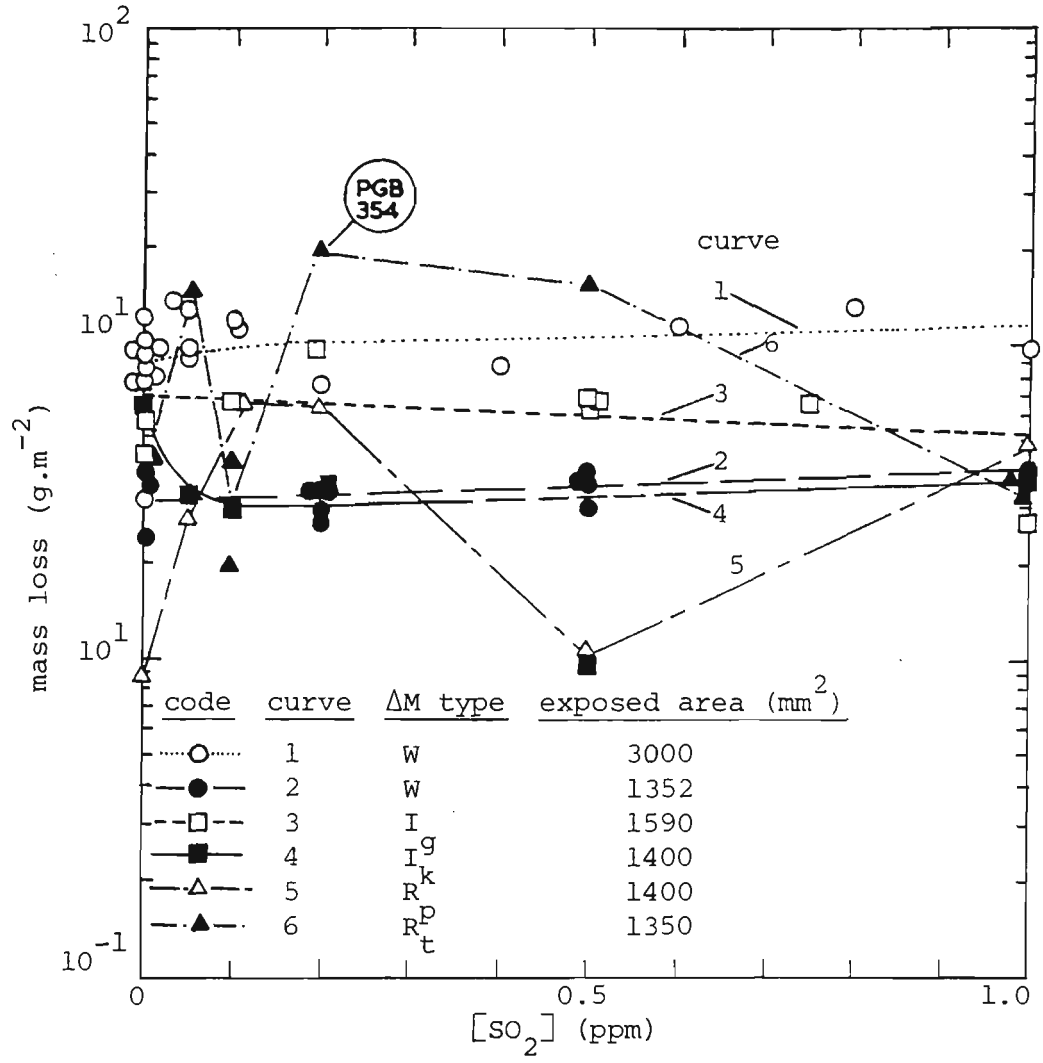

Figure R1/48. Summary plot to show the effect of [SO_2] on mass loss of zinc calculated from direct weighing, ΔM_W; from galvanic currents using ACM2 (Zn/Fe), ΔM_{Ig}; from corrosion currents using ACM3 (Zn), ΔM_{Ik}; from polarization resistance using ACM3 (Zn), ΔM_{Rp}; and from charge-transfer resistance using ACM3 (Zn), ΔM_{Rt}.

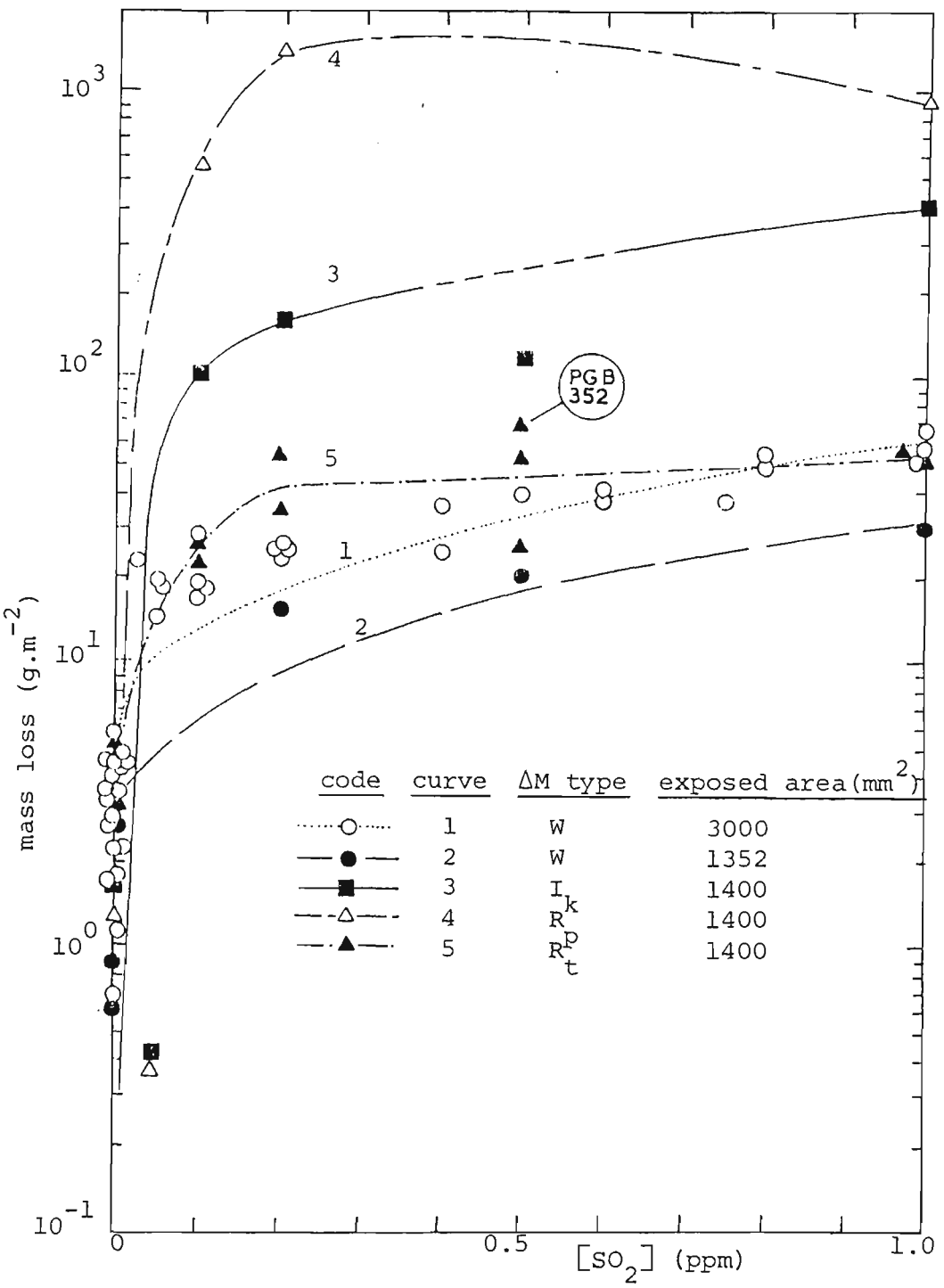

Figure R1/49. Summary plot of the effect of [SO_2] on mass loss of steel calculated from direct weighing, ΔM_W; from corrosion currents using ACM8 (Fe), ΔM_{Ik}; from polarization resistance using ACM8 (Fe), ΔM_{Rp}; and from charge-transfer resistance using ACM8 (Fe), ΔM_{Rt}.

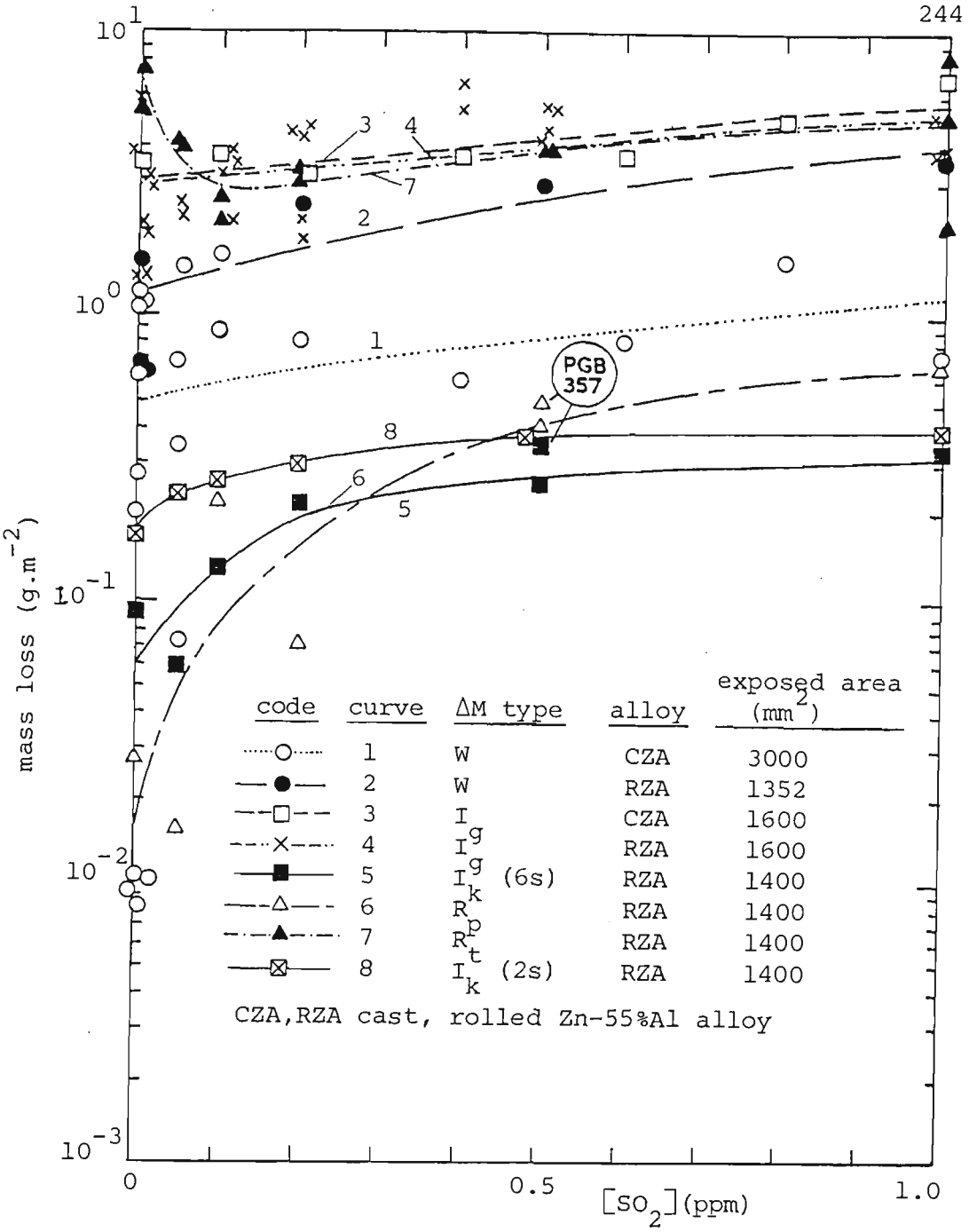

Figure R1/50. Summary plot to show the effect of [SO_2] on mass loss of cast and rolled Zn-55%Al alloy from direct weighing, ΔM_W; from galvanic currents using ACM1 (CZA/Fe), ACM9 (RZA/Fe), ΔM_{Ig}; from corrosion currents using ACM4 (RZA), ΔM_{Ik}; from polarization resistance using ACM4 (RZA), ΔM_{Rp}; and from charge-transfer resistance using ACM4 (RZA), ΔM_{Rt}. 2 s, 6 s voltage response reading time for I_k test.

2.1 ACM2 (Zn/Fe)

Figure R1/48 shows the comparison for zinc. The $\Delta M_{Ig}/[SO_2]$ trend, curve 3, falls between the two $\Delta M_w/[SO_2]$ trends obtained at 1352, 3000 mm^2 total exposed area/test chamber, curves 1 and 2 respectively. The total exposed area exposed/test chamber for the galvanic current tests using ACM2 (Zn/Fe) was 1590 mm^2. The effect of total exposed area/test chamber was discussed in Section R1.3 where it was pointed out that mass loss was higher at higher total exposed area. Therefore, the $\Delta M_{Ig}/[SO_2]$ trend for the regression line in curve 3 is more directly comparable to the $\Delta M_w/[SO_2]$ trend in curve 2, both having similar total exposed areas, rather than to curve 1. Such a comparison indicates that ΔM_{Ig} is about twice ΔM_w and not very dependent on $[SO_2]$ concentration. The slight negative slope with increasing $[SO_2]$ is due mainly to the low data point at 1.0 ppm $[SO_2]$.

The ratio of calculated/measured mass loss (given above as $CF = \Delta M_{Ig}/\Delta M_w \approx 2$), has become known as the cell factor, CF, originally proposed by Kucera and Mattsson[179] to convert ACM data into corrosion rates. Mansfeld and Tsai[113] carried out galvanic current experiments using 2-electrode ACMs made of Zn/Cu plates with thin films of 0.01 N Na_2SO_4 solution at different relative humidities. They obtained cell factors of between 0.47 to 0.96 (average 0.72, standard deviation 0.20) and explained the low cell efficiency as probably due to corrosion occurring on single cell plates without electrolyte bridging adjacent cells. Low cell factors are more likely to occur as insulator thickness between adjacent plates, and/or plate thickness increases[115,180]. Although not stated in the Mansfeld and Tsai[113] paper, the mylar insulator thickness is probably 60 μm[111] which is considerably thicker than used in this thesis (23 μm). Thus the lower cell factor obtained by Mansfeld and Tsai may be

explained by an increased mylar insulator thickness. However, there are other differences between their work and that reported here. They used a 2-electrode Zn/Cu ACM, thin electrolyte layers of 0.01 N Na_2SO_4 and relative humidities between 30 and 75%, whereas the present work employed a Zn/Fe ACM with thin distilled water layers in air containing a range of $[SO_2]$ (0-1 ppm), at a fixed relative humidity of 70%. It is possible that these differences also contributed to a difference in cell factor.

The reason why the cell factor, CF, is approximately 2 for the present results, that is, the galvanic current calculated mass loss is about twice that for the mass loss samples with a total exposed area of 1352 mm^2, is not entirely clear. As CF is also greater than unity for the two other galvanic current ACMs (ACM1 (cast Zn-55%Al/Fe) and ACM9 (rolled Zn-55%Al/Fe), see Section R1.7/2.2), it appears to be a reproducible phenomenon. It cannot be due to corrosion occurring on single cell plates without electrolyte bridging adjacent cells, as explained by Mansfeld and Tsai[113] results, because this leads to CF values less than unity. Neither can it be due to partial short circuits between plates, refer Section R1.8, because Table A4/13 in Section A4/2.2 show that the q value (area under the I_g/t curve) generally decreases from cycle to cycle. The existence of partial short circuits would be expected to increase the q value from cycle to cycle.

The most likely explanation is that the experimental conditions did not ideally conform to the Equation (T2/8) in Section T2/4 used to calculate mass loss from galvanic current data. These equations assume that the galvanic current density, i_g, is equal to the corrosion current density, i_k, for equal anode and cathode plate areas, and that the cathodic reaction is under diffusion control. Likely errors in each of these assumptions are discussed below.

Firstly, white corrosion products from corrosion of the zinc plates deposit on the steel plates, refer Section R1.4/3, which could reduce the effective cathode plate area, A^B. According to Equation (T2/5), Section T2/2, this will result in a lower galvanic current density, i_g, and hence I_g. According to Equation (T2/8), calculated mass loss will depend on the ratio I_g/A^B, both of which have been reduced. It is therefore difficult to tell whether mass losses increase, decrease or remain the same. Secondly, Figure R1/40, Section R1.6/6.1 shows that b_c values are not always high and indicative of the cathodic reaction being under diffusion control as they are in cycles 1, 3 at zero $[SO_2]$. Values of b_c generally fall from cycle to cycle in the presence of $[SO_2]$ and indicate a change away from diffusion limiting control towards charge-transfer control of the cathodic reaction. Therefore Equation (T2/8) in Section T2/4 may not always be entirely appropriate for the calculation of mass loss because it assumes b_c is very high.

2.2 ACM1 (cast Zn-55%Al/Fe); ACM9 (rolled Zn-55%Al/Fe)

Figure R1/50 shows the comparison between ΔM_{Ig} and ΔM_w for cast and rolled Zn-55%Al alloy. The $\Delta M_{Ig}/[SO_2]$ trend for both ACM1 (cast Zn-55%Al/Fe), curve 3, and ACM9 (rolled Zn-55%Al/Fe), curve 4, are both similar in magnitude, both show a moderate increase in mass loss as $[SO_2]$ increases, and both are higher than the $\Delta M_w/[SO_2]$ trends for mass losses obtained by weighing for cast Zn-55%Al alloy, curve 1, and rolled Zn-55%Al alloy, curve 2. The weighed mass loss trends for cast Zn-55%Al, curve 1, are surprisingly low, especially considering that the exposed area/test chamber was 3000 mm^2. Correction of mass losses so as to compare with other trends obtained at a lower exposed area, as discussed in Section R1.3, would tend to lower these mass losses even further. Results in curves 2-4 were all obtained

at similar exposed areas and may be compared directly with each other. If the correction for exposed area for curve 1 is neglected, some idea of cell factor, CF, can be obtained, using points on the lines of best fit, rather than actual data points. The values of CF for rolled Zn-55%Al alloy are 1.8, 1.9, 1.1 at 0, 0.5, 1.0 ppm [SO_2] respectively, whilst CF values for cast Zn-55%Al alloy are 7.6, 4.3, 5.8 at the same [SO_2]. The CF values for the rolled material are similar to those obtained for zinc in Section R1.7/2.1. The higher values for the cast material are probably caused by rather low weighed mass loss results. The actual mass loss involved, before area correction, is very small (range 0.2-1.2 mg), and it is possible that a sizeable error (max 0.4 mg) may exist. The discussion in Section R1.7/2.1 on reasons for CF values for Zn being greater than unity is also relevant here.

3. Weighed versus corrosion current calculated mass loss

3.1 ACM3 (Zn)

The comparison for zinc is shown in Figure R1/48. As discussed in Section R1.7/2.1, the weighed mass loss trends obtained at an exposed area/test chamber of 1352 mm^2, curve 2, are more relevant for comparison with ΔM_{Ik} trends obtained at 1400 mm^2 exposed area, curve 4, than the weighed mass loss trends obtained at 3000 mm^2 exposed area, curve 1. The ΔM_{Ik} trend, curve 4, virtually overlaps the ΔM_w trend, curve 2, with the exception at 0.5 ppm [SO_2] for ΔM_{Ik} which did not initiate corrosion in the normal manner and which is discussed in Section R1.6/3.1. This curve overlap indicates a cell factor, CF, very close to unity. Mass losses calculated from corrosion current data are therefore quite similar to those obtained by weighing, for experiments at a similar exposed area/test chamber.

3.2 ACM8 (Fe)

Figure R1/49 shows the comparison between ΔM_{Ik} and ΔM_w for steel over the range 0-1 ppm [SO_2]. There are two curves for weighed steel mass loss at 3000, 1352 mm^2 total exposed area/test chamber, curves 1, 2 respectively. Curve 2 at 1352 mm^2 exposed area is more relevant for comparison with ΔM_{Ik} data obtained at 1400 mm^2 exposed area, curve 3. It is seen that the $\Delta M_{Ik}/[SO_2]$ trend, curve 3, is significantly higher than the $\Delta M_w[SO_2]$ trend, curve 1. Using the curves of best fit, rather than the data points, some idea of cell factor, CF, can be obtained. The values for CF for steel are 1.9, 13.9, 12.1 at 0, 0.5, 1.0 ppm [SO_2] respectively. Although the value at 0 [SO_2] is acceptable, these results indicate a severe problem in the accurate measurement of mass loss by corrosion current technique using 3-electrode steel ACMs in the presence of SO_2.

The very high calculated steel mass losses are a result of very high calculated values of I_k in the presence of [SO_2], particularly in the third and fourth cycles, see Figure R1/33, Section R1.6/3.2. It is difficult to compare the extent of red rust after four cycles over the [SO_2] range in the corrosion current test, Figure R1/32g-l, with that in the impedance test, Figure R1/28d-i, and with weighed mass loss samples (not shown) due to the heavy build-up of red rust. Such a comparison, however, does not reveal any gross differences in the extent of red rust formation at the respective [SO_2]. This suggests that the discrepancy between I_k calculated and weighed mass loss is more likely to be a calculation or measurement error than a real difference in the extent of corrosion. Calculation problems are discussed in Section R1.6/2. The most likely measurement error is partial short circuits due to partially electronically conducting corrosion products between adjacent ACM

plates, refer Section R1.8/1. This would explain the very high calculated I_k values at 0.1-1.0 ppm [SO_2] especially in the third and fourth cycles. However, if this reasoning is accepted, it is necessary to explain why the impedance tests using the same ACM (at different experimental times) result in significantly lower calculated mass loss values. Corrosion current, I_k = B/2.3 R_p according to Equation (T3/2) Section T3/2. ΔM_{Ik} trends in Figure R1/49, curve 3, are calculated using variable B (b_a and b_c) values, whereas R_p calculated mass loss, ΔM_{Rp}, in curve 4 uses fixed B values but is calculated from the same (I,ε) data set, refer Section R1.7/4. The higher mass loss values for ΔM_{Ik} in curve 3 cannot be explained by high (variable) B values because ΔM_{Rp}, trend in curve 4, which is very high, uses the same (fixed) B values as the ΔM_{Rt} trend in curve 5, which is significantly lower. It is suggested that ACM8 (Fe) is more prone to partial short circuits in the corrosion current tests than in the impedance tests because the impedance test was a more non-destructive test under these conditions in the presence of SO_2. Large dc currents, up to ±70 mA at 1.0 ppm [SO_2] were applied to the ACM in order to measure a suitable voltage response in the I_k test. By comparison, the impedance test applied sinewave currents up to 900 µA rms, equivalent to a sinewave voltage of 9 mV rms across a control resistor of 10 ohm. Thus the actual impedance measurement was considerably less destructive because it applied much lower currents and these were ac currents rather than dc currents. This would imply that the corrosion current test may produce more corrosion products bridging working to auxiliary plates at high dc applied currents, although this could not be ascertained by visual inspection as stated above. The subject of partial short circuits is discussed further in Section R1.8.

3.3 ACM4 (rolled Zn-55%Al)

Figure R1/50 shows the comparison between ΔM_{Ik} and ΔM_{w} for rolled Zn-55%Al alloy for the range 0-1 ppm $[SO_2]$. The total exposed area/test chamber is very similar for the $\Delta M_{w}/[SO_2]$ trend in curve 2, (1352 mm^2), and $\Delta M_{Ik}/[SO_2]$ trend in curve 5, (1400 mm^2), and therefore these trends may be directly compared. The $\Delta M_{Ik}/[SO_2]$ trend, curve 5, is significantly lower than the $\Delta M_{w}/[SO_2]$ trend, curve 2. Using the curves of best fit rather than the data points, some idea of the cell factor, CF, can be obtained. The values of CF for rolled Zn-55%Al alloy are 0.05, 0.11, 0.09 at 0, 0.5, 1.0 ppm $[SO_2]$ respectively, which are very low.

The large discrepancy may, in some part, be due to the weighed mass losses because the actual mass losses were very small (maximum 1.2 mg). A constant error could be involved because no correction was applied to correct the mass loss of 'blank' samples (samples not tested but immersed in the cleaning solution) in the case of rolled Zn-55%Al alloy due to the low mass loss. However, any attempt at lowering weighed mass losses would only increase the cell factor for the galvanic current calculated mass loss trend in curve 3.

It has already been pointed out in Section T3/7 that the value of the electrochemical equivalent, E_q, for rolled Zn-55%Al alloy is unknown and the value for Zn was used. Although this may introduce an error to mass loss calculated from corrosion currents, ΔM_{Ik}, it will introduce the same errors for ΔM_{Ig} (curves 3,4), ΔM_{Rp} (curve 6) and ΔM_{Rt} (curve 7). Therefore this does not explain the low trends for ΔM_{Ik} in curve 5.

Low cell factors have previously been explained[113] as corrosion occurring on

single cell plates without electrolyte bridging. Although this is possible for ACM4 (rolled Zn-55%Al), it is not considered likely to be a major contribution because the mylar insulator thickness was only 23 μm compared to 60-400 μm used by other workers, as discussed in Section T5/1,2.

Section R1.6/2 describes two problems encountered in the analysis of current/voltage data for ACM4 (rolled Zn-55%Al). These are superpolarization peaks and anodic (sometimes cathodic as well) voltage responses that appeared to limit as shown in Figure R1/29, Section R1.6/2, types 3 and 4. Voltage responses were read at 6 s, at which time the superpolarization peak had virtually ended, but a steady state was not always achieved because the voltage response continued to sag. This produced anodic voltage responses which tended to limit, that is, did not increase as expected when a high current step was applied. The mechanistic interpretation of such an effect is unknown, but may be due to a downward shift in the corrosion potential due to the applied current[176]. Some data was analyzed at a voltage reading time of 2 s which produced higher values of I_k. The increase in I_k was greatest at zero $[SO_2]$, and decreased as the $[SO_2]$ increased. The $\Delta M_{Ik}/[SO_2]$ trend in curve 5, Figure R1/50, was corrected to take into account the 2 s voltage reading time, and is shown in curve 8. The increase in I_k for the 2 s voltage responses was considerable, ranging from -7.3% to 378% with an average of 76.1%, standard deviation 82.3 for a sample size of 76. However, the corrected curve 8 is still significantly lower than the $\Delta M_w/[SO_2]$ trend in curve 2.

Choosing a voltage reading time corresponding to the maximum of the superpolarization peak may increase calculated values of I_k even further, thus increasing the $\Delta M_{Ik}/[SO_2]$ trend even further and also the cell factor.

However, as there is no satisfactory theoretical explanation of the superpolarization peak, refer Section R1.6/2, such a choice of voltage reading time cannot be justified. The voltage response reading time was taken at 6 s where the response is sagging with time, but this is not entirely theoretically justifiable. This illustrates one of the limitations inherent in the corrosion current method - the correct choice of voltage response reading time, and the subject has been discussed at length in Section T3/4.1. The second analysis problem, of anodic (and sometimes cathodic) voltage responses that tended to limit, caused the computer calculated curve to be a poor fit through the experimental current/voltage data points. An example is shown in Figure R1/51. This means that the model, Equation T3/6 Section T3/5, used to calculate corrosion rate parameters is not wholly suitable to the system under test in this case. It is therefore not surprising that significant differences exist between weighed and calculated mass loss. It has been known for many years in this laboratory that Zn-55%Al alloy coatings give rise to difficult low polarization data, and this has been attributed to corrosion of the two-phase coating structure, where both Zn and Al dissolve. This is described more fully in Section R1.2/3. As the corrosion characteristics of these two metals are quite different (number of electrons involved, stability of corrosion products), it is not surprising that the electrochemical data is not as straightforward as that for a single metal.

4. R_t versus R_p calculated mass loss

Figures R1/48-50 show the comparison between mass loss, ΔM_{Rt}, calculated from charge-transfer resistance, R_t, and mass loss, ΔM_{Rp}, calculated from polarization resistance, R_p, over the range 0-1 ppm [SO_2]. The R_t values were calculated from impedance data in Section R1.5/3, whilst the R_p values were

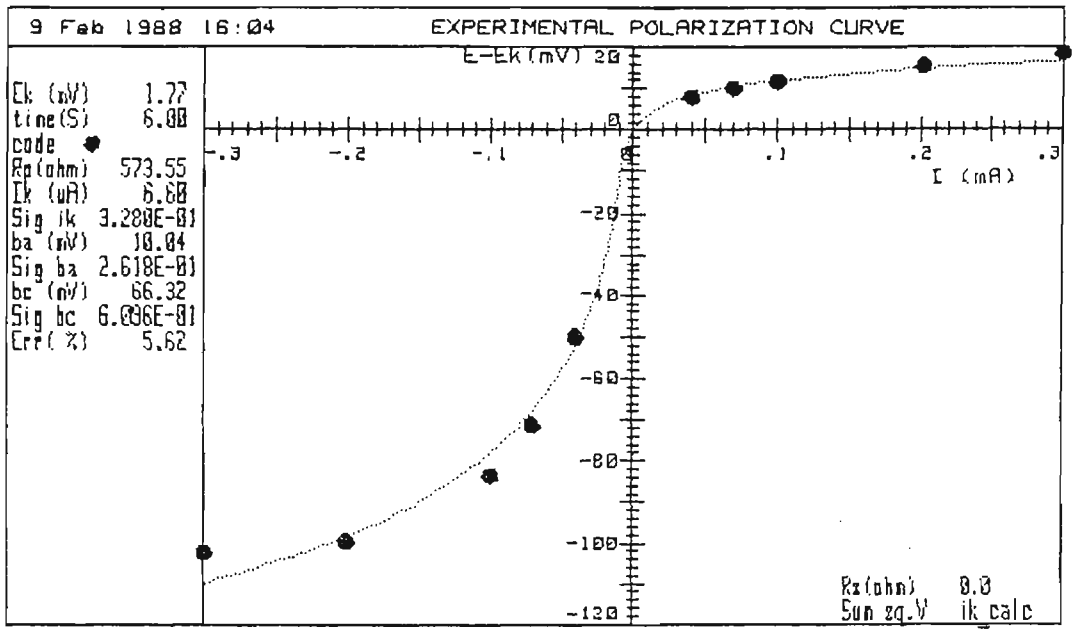

Figure R1/51. Example of polarization curve of polarization, ε, versus applied current, I, for ACM4 (rolled Zn-55%Al) where the anodic voltage responses tended to limit, as shown in type 4 pulses, Figure R1/29. The resulting computer curve is a poor fit through the data.

calculated from corrosion current data in Section R1.6/7. The method of calculation of mass loss from R_t and R_p is outlined in Section R1.7/1.

4.1 ACM3 (Zn)

Figure R1/48 shows the comparison between ΔM_{Rt}, curve 6, and ΔM_{Rp}, curve 5, for ACM3 (Zn). There appears to be no correlation between trends in $\Delta M_{Rt}/[SO_2]$ and $\Delta M_{Rp}/[SO_2]$. The $\Delta M_{Rp}/[SO_2]$ trends in curve 5 are widely scattered about the $\Delta M_{Ik}/[SO_2]$ trend in curve 4, which is relatively constant versus $[SO_2]$ in agreement with the weighed mass loss, $\Delta M_w/[SO_2]$ trends in curves 1 and 2. The $\Delta M_{Rp}/[SO_2]$ trends in curve 5 dramatically illustrate the problem of calculating mass loss from just polarization resistance data without taking the trends in Tafel slopes b_a and b_c into account (constant values of b_a, b_c were used in these calculations, refer Sections R1.7/1,T3/7). The difference between $\Delta M_{Rp}/[SO_2]$, curve 5, with $\Delta M_{Ik}/[SO_2]$, curve 4, is simply that the latter uses the calculated values of b_a, b_c and a sensible trend with $[SO_2]$ is achieved. Although an overall inverse relationship exists between I_k and R_p, as discussed in Section R1.6/7 and shown in Figure R1/46, it is not good practice to rely on trends in R_p or in mass losses calculated from R_p. The same conclusions apply to the $\Delta M_{Rt}/[SO_2]$ in curve 6. These trends also used constant Tafel slope values and show a wide scatter around the straight line $\Delta M_w/[SO_2]$ trend in curve 1.

4.2 ACM8 (Fe)

Figure R1/49 shows the comparison between ΔM_{Rt}, curve 5, and ΔM_{Rp}, curve 4, for ACM8 (Fe). The same basic curve shape exists, but $\Delta M_{Rp}/[SO_2]$ trends in curve 4 are much higher than $\Delta M_{Rt}/[SO_2]$ trends in curve 5. This is

attributed to the existence of partial shorts between adjacent ACM plates as explained in Section R1.7/3.2, which are thought to be more prone to forming in the dc corrosion current tests than in the ac impedance tests. The effect of these partial short circuits in this case is that R_p values are calculated too low, so that the resulting mass losses are calculated too high.

The $\Delta M_{Rt}/[SO_2]$ trends in curve 5 are also calculated somewhat high compared to $\Delta M_w/[SO_2]$ trends in curve 2 obtained at a similar total exposed area per test chamber. The mass losses, although high, only result in cell factors of 1.4, 2.1, 1.7 for 0, 0.5, 1.0 ppm $[SO_2]$ respectively, which are reasonable values that suggest mass loss for steel can be reasonably calculated using R_t values. However, the discussion in Section R1.8/5.1 suggests that partial shorts were involved to some degree even in curve 5.

Mass losses calculated from R_t therefore appear to be more reliable than those calculated from R_p for steel. The reasons are different to those proposed by Epelboin et a[181] for iron who showed that R_t was a better predictor than R_p to use in the Stern-Geary equation, Equation (T3/2) in Section T3/2. Their reasoning was based on the fact that R_p values were less than R_t because of an inductive loop at low frequencies. In Figure R1/49, the reason why R_t is a better predictor than R_p is thought to be due to the fact that ACM8 (Fe) is more prone to partial short circuits in the dc corrosion current measurements than in the ac impedance measurements, as discussed above.

Figure R1/49 also shows that using constant values of the Tafel slopes b_a, b_c instead of actual measured values results in calculated losses, ΔM_{Rp}, curve 4, that are too high. The $\Delta M_{Rp}/[SO_2]$ trends in curve 4 are even higher than the

high results for $\Delta M_{Ik}/[SO_2]$ in curve 3 which use actual measured b_a, b_c values. This comparison supports the conclusions made for ACM3 (Zn) in Section R1.7/4.1, that it is not good practice to rely on trends in R_p or in mass loss calculated from R_p, where Tafel slopes are not measured along with R_p or I_k. Trends in curve 5 are also calculated high compared to $\Delta M_w/[SO_2]$ trends in curve 2 obtained at a similar total exposed area/test chamber. The high mass losses here result in cell factors of 1.4, 2.1, 1.7 for 0, 0.5, 1.0 ppm $[SO_2]$ respectively, which are reasonable values that suggest mass losses for steel can be reasonably calculated using R_t values.

4.3 ACM4 (rolled Zn-55% Al)

Figure R1/50 shows the comparison between ΔM_{Rt}, curve 7, and ΔM_{Rp}, curve 6, for ACM4 (rolled Zn-55%Al). Apart from the low $[SO_2]$ range (0-0.1 ppm), there is an increase in mass loss as $[SO_2]$ increases in both cases. However, the $\Delta M_{Rp}/[SO_2]$ trends in curve 6 are much lower than $\Delta M_{Rt}/[SO_2]$ trends in curve 7. This is the opposite order to ACM8 (Fe) in Section R1.7/4.2 and has been attributed in Section R1.7/3.3 to voltage reading time errors and curve fitting errors as a result of more difficult low polarization data for Zn-55%Al alloys. This causes R_p values to be calculated too high (I_k too low) and hence mass losses are calculated too low. The $\Delta M_{Rp}/[SO_2]$ trends in curve 6 give lower values than the $\Delta M_{Ik}/[SO_2]$ trends in curve 5 at low $[SO_2]$, but higher values at higher $[SO_2]$. Thus the trend for mass loss to increase with $[SO_2]$is more exaggerated for ΔM_{Rp} than for ΔM_{Ik} and also more exaggerated than ΔM_w in curve 2. As was stated in Sections R1.7/4.1,4.2, it is not good practice to rely on trends in R_p or in mass loss calculated from R_p, where Tafel slopes are not measured.

The $\Delta M_{Rt}/[SO_2]$ trends in curve 7 are calculated somewhat high compared to $\Delta M_w/[SO_2]$ trends in curve 2 and result in cell factors of 5.8, 1.5, 1.25 at 0, 0.5, 1.0 ppm $[SO_2]$ respectively. With the exception of 0 $[SO_2]$, these values are quite reasonable. The cell factor at 0 $[SO_2]$ is higher because the $\Delta M_{Rt}/[SO_2]$ trend shows a decrease in mass loss in the range 0-0.1 ppm $[SO_2]$ which does not appear typical, and may be the result of neglecting measured Tafel slopes in the calculation. Taking the $\Delta M_{Rt}/[SO_2]$ trend in curve 7 as a whole and comparing with the $\Delta M_w/[SO_2]$ trend in curve 2 suggests that mass loss for Zn-55%Al alloy can be reasonably calculated using R_t values.

Mass losses calculated from R_t therefore appear to be more reliable than those calculated from R_p. The reasons are different to those proposed by Epelboin et al[181] for iron as discussed in Section R1.7/4.2. In Figure R1/50, the reason why R_t is a better predictor than R_p is due to difficulties with voltage response reading time and curve fitting in calculating R_p, as discussed in Section R1.7/3.3.

R1.8 Validity of ACM Measurements

The aim of this section is to look critically at the problems encountered with the measurement of electrochemical parameters using ACMs, and to determine the reliability of ACMs in this role.

1. Evidence for corrosion product partial short circuits

Two sets of measurements shown in Figures R1/48-50 give abnormally high calculated values of mass loss - $\Delta M_{Rt}/[SO_2]$ trend in curve 6, Figure R1/48 for ACM3 (Zn), and $\Delta M_{Ik}/[SO_2]$ trend in curve 3, Figure R1/49 for ACM8 (Fe).

With the $\Delta M_{Rt}/[SO_2]$ trend for ACM3 (Zn), high values of mass loss occur at 0.05, 0.2 and 0.5 ppm $[SO_2]$, and these correspond to significant falls in R_t from cycle to cycle, see Figure R1/20, Section R1.5/3.1. With the $\Delta M_{Ik}/[SO_2]$ trend for ACM8 (Fe), high values of mass loss occur at 0.1-1.0 ppm $[SO_2]$, and these correspond to significant rises in I_k from cycle to cycle to rather high values, or falls in R_p from cycle to cycle to rather low values, see Figure R1/33, Section R1.6/3.2 and Figure R1/44, Section R1.6/7.

Further evidence of abnormal impedance behaviour is given by the shape of the Nyquist plots corresponding to cycles where R_t and σ values show a large drop, eg cycles 3,4 at 0.05,0.2,0.5 ppm $[SO_2]$ for ACM3 (Zn). The Nyquist plots in these cases show large decreases in the semicircle diameter ($=R_t$), plus a diffusion tail at low frequencies that declines from an angle close to the theoretical 45° to almost horizontal to the a-axis, as described in Section R1.5/2. Examples of this sort of Nyquist plot shape are shown in curves 2,3, Figure R1/14 for ACM3 (Zn) during cycles 3,4 respectively. This sort of behaviour has also been observed with ACM8 (Fe), especially in cycles 3,4. An example is shown in Figure R1/15 curve 2, where it is just starting to occur, and in curve 3 at a more advanced stage. By comparison, this behaviour was never observed for ACM4 (rolled Zn-55%Al), the Nyquist plots in Figure R1/16 being quite typical of the whole $[SO_2]$ range. Furthermore, ACM4 (rolled Zn-55%Al) did not show large decreases in R_t and σ values from cycle to cycle, all values being remarkably close together over the whole $[SO_2]$ range.

Haagenrud[124] exposed similar zinc ACMs in southern Norway and found that the cell performed well for almost the whole of the measurement period except for periods where the ACM appeared to short circuit. He explained this as being caused by electron conductive corrosion products formed under

an SO_2 polluted surface film and stated that the problem of short circuits between zinc plates could be solved by increasing the insulator thickness between plates from 100 to 300 μm. Gonzales et al[116] stated that short circuits take place, frequently with Fe monitors, and sometimes with Zn monitors, when the corrosion products are bulky and have a certain electronic conductivity. They used 170 μm thick insulating sheet. In the case of ACM3 (Zn), the insulator thickness is only 23 μm, see Section E2.4/2, and corrosion products built up over four cycles, so that this explanation of at least partial short circuits between adjacent working and auxiliary plates seems likely.

It has been suggested in Sections R1.5/3.2, R1.7/3.2,4.2, that partial short circuits due to the formation of electron conductive corrosion products between working and adjacent auxiliary plates may be responsible for the above abnormal behaviour. It has also been suggested in Section R1.7/3.2 that ACM8 (Fe) is more prone to partial short circuits in the dc corrosion current test than in the ac impedance test. Yet for ACM3 (Zn), the reverse situation existed, that is, the dc corrosion current test appeared to produce good results, with the $\Delta M_{Ik}/[SO_2]$ trend producing a cell factor close to unity, see Section R1.7/3.1, but the existence of partial shorts were suspected for the ac impedance test in cycles 3, 4 at 0.05, 0.2, 0.5 ppm $[SO_2]$, see Section R1.5/3.2. Much lower currents were applied (maximum $\pm$20 mA but only in PGB 312 run 4 cycle 4, otherwise maximum $\pm$3 mA, typically less than $\pm$0.5 mA) in the dc corrosion current test for ACM3 (Zn) than for ACM8 (Fe) (maximum $\pm$70 mA). Thus the corrosion current test would be expected to be significantly less destructive for ACM3 (Zn) than for ACM8 (Fe). The ac impedance test used ac currents up to 9000 μA rms for ACM3 (Zn) which gave problems, but only up to 900 μA rms for ACM8 (Fe), which did not. Therefore the magnitude of the applied current may be at least partly responsible for

encouraging the formation of partial short circuits in ACMs. However, it can not be totally responsible because higher currents (ac or dc) were only applied in order to measure low cell resistances or impedances. The build up of bulky corrosion products of Zn, Fe must first lead to the lower resistance or impedance values. Not all cycles showing increasing corrosion rate trends lead to abnormally high mass losses, for example, compare Figures R1/21 with Figure R1/49 curve 5 for ACM8 (Fe). This suggests that these trends from cycle to cycle are a real effect. The detection of partial shorts by inspection of these trends from cycle to cycle is therefore not a simple matter. High applied currents may accelerate the formation of these corrosion products and hence be somewhat destructive to the sample. The above explanation leads to the conclusion that increasing corrosion rate trends observed from cycle to cycle may very well be real effects caused by corrosion of the ACM plates, but that the increases may be excessive due to the formation of partial shorts and lead to calculated mass losses than are too large in certain cases. Partial shorts do not appear to be prevalent with ACM4 (rolled Zn-55%Al). Although ACM4 is thought to corrode by preferential dissolution of Zn-rich areas, see Section R1.2/3, and will therefore produce Zn-based corrosion products, the lack of partial short circuits is attributed to the lower corrosion and minimal build-up of corrosion products, see Figure R1/28j-l.

2. Measurement of cell resistance

Some proof of the existence of these partial shorts has been obtained by additional impedance and corrosion current tests at 0.2 ppm [SO_2] on ACM3 (Zn), and at 0.5 ppm [SO_2] on ACM8 (Fe), and ACM4 (rolled Zn-55%Al). After each cycle, when the ACM surface was nominally dry, multimeter readings of the resistance between working and auxiliary plates were taken as a function

of time as the corrosion products dried out further. A satisfactory ACM will show a resistance greater than 20 M ohm between working and auxiliary plates after final abrasion and prior to applying the water film for cycle 1. Corrosion products build up over the first cycle and continue to build up in subsequent cycles. Figure R1/52 shows some typical multimeter resistance readings taken as a function of time after the ACM surface was visually dry for each of four PGB cycles for ACM3 (Zn), ACM8 (Fe) and ACM4 (rolled Zn-55%Al). The resistance rises markedly with time in most cycles, probably due to further drying of the corrosion product. It is observed that the resistance at a given time (say 1 hour) usually drops from cycle to cycle due to further build-up of corrosion products. Resistance values for a given cycle are significantly lower for ACM8 (Fe) than for ACM3 (Zn) or ACM4 (rolled Zn-55%Al). These resistance readings demonstrate that there is partial shorting of the ACM cell between working and auxiliary electrodes due to the build-up of corrosion products. This becomes worse from cycle to cycle and is more severe with ACM8 (Fe). Further interpretation is given in Sections R1.8/3,4.

3. Modelling of partial short circuits

The exact interpretation of the multimeter resistance readings is unclear but the following discussion may provide at least a partial explanation. If the corrosion product simply bridges across working to auxiliary electrodes, this will just reduce the value of solution resistance, R_s, in the ACM equivalent circuit shown in Section A3/2, Figure A3/3a. It will not, however, correctly model the experimental conditions where Nyquist plot diffusion tails at low frequencies decline from an angle close to 45° on a freshly abraded surface to angles almost horizontal to the a-axis, as described in Section R1.8/1 and shown in Figure R1/14,15, Section R1.5/2 for typical experimental Nyquist

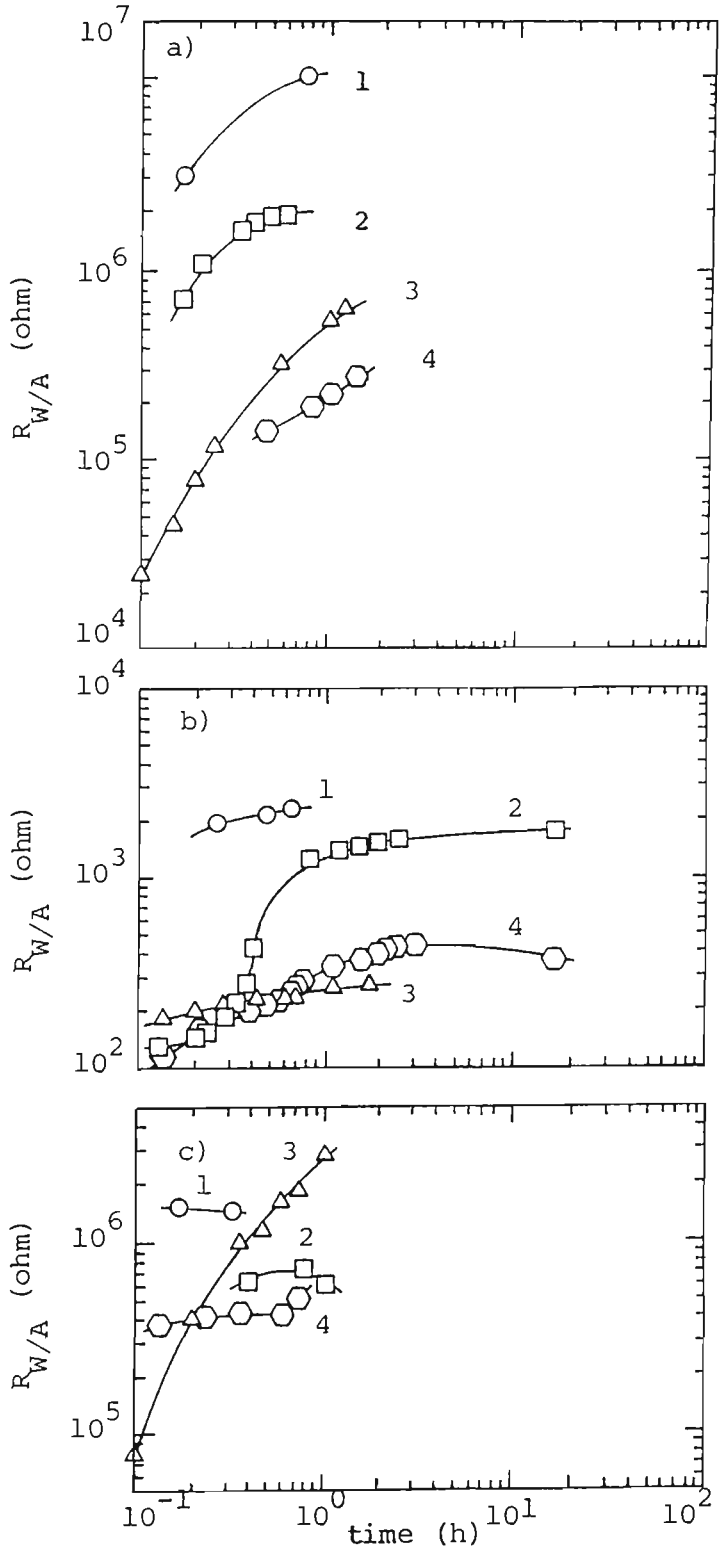

Figure R1/52. Working to auxiliary plate multimeter resistance, $R_{W/A}$, as a function of time as corrosion products on the surface dried out for a) ACM3 (Zn), PGB 354 at 0.2 ppm [SO_2]; b) ACM8 (Fe), PGB 353 at 0.5 ppm [SO_2] and c) ACM4 (rolled Zn-55%Al), PGB 357 at 0.5 ppm [SO_2]. Numbers on plots indicate PGB cycles.

plots on ACM3 (Zn) an ACM8 (Fe). This sort of behaviour did not occur with ACM4 (rolled Zn-55%Al), shown in Figure R1/16. Although R_s may be lowered by build-up of electron conductive corrosion products, some other factor is involved. A resistor, R_{cp}, nominally termed corrosion product resistance, placed in parallel with (R_t+Z_ω) in the ACM equivalent circuit very satisfactorily models the type of experimental Nyquist impedance plot seen for ACM3 (Zn), ACM8 (Fe) in cycles 3,4. This resistor has the effect of partially shorting out the interfacial region as would be expected from electron conductive corrosion products. Figure R1/53 shows the modified equivalent circuit and demonstrates the effect of varying R_{cp} on Nyquist plot shape for constant values of R_t, C_d, σ. The semicircle diameter becomes smaller and the diffusion tail bends over horizontally towards the a-axis as R_{cp} is reduced. These plots were obtained using program equiv_crt, described in Appendix A1/4.5, which demonstrate that similar plot shapes to the experimental Nyquist plots can be obtained, indicating that the inclusion of R_{cp} in the model is valid. Values of R_t, C_d, σ have been calculated from these theoretical Nyquist plots just like they would be calculated from experimental plots, and calculated values compared to their original starting values. Figure R1/54b-d shows the effect of R_{cp} on the errors in calculating R_t, C_d, σ for the different sets of σ values (R_t, C_d constant) when R_{cp} is included in the equivalent circuit of Figure R1/54a. There is not much effect on C_d, Figure R1/54c and the scatter in the points results from estimating C_d from the frequency where b is a maximum, which may not be known with sufficient accuracy.

Calculated values of R_t, Figure R1/54b, reduce to 46-49% of the theoretical value (depending on the chosen σ value) when R_{cp} equals R_t ($=10^4$ ohm). The effect on σ, Figure R1/54d, is even more severe, with calculated values of σ

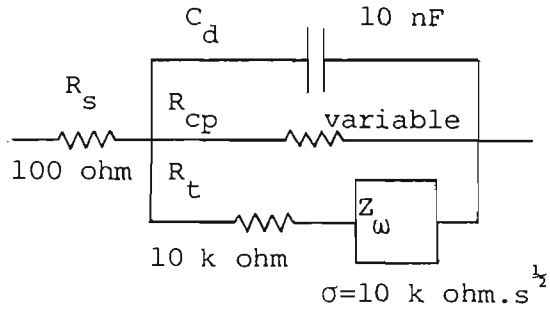

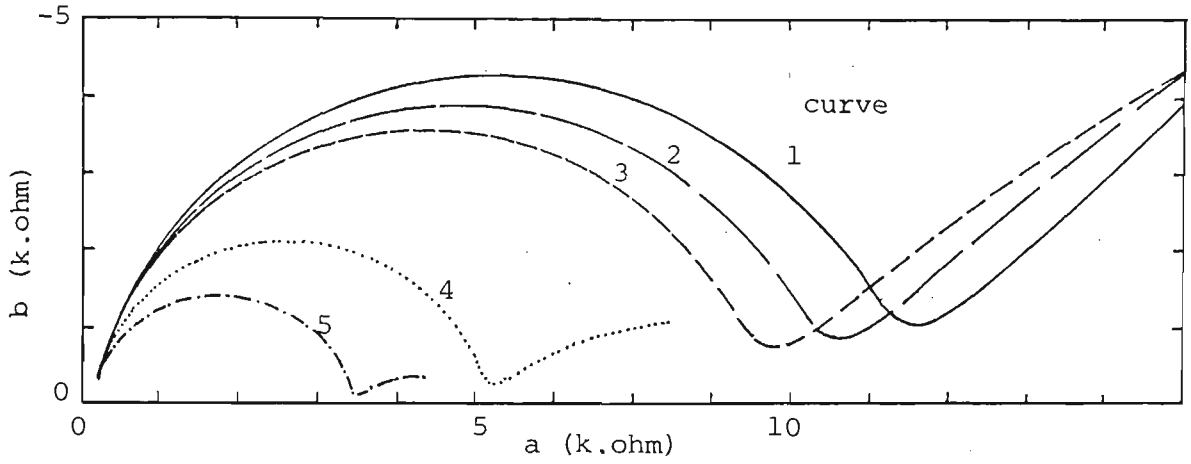

Figure R1/53. Theoretical Nyquist complex plane plots of resistive, a, versus reactive, b, components of ACM working to auxiliary cell impedance modelled by the above equivalent circuit, showing the effect of varying R_{cp}. R_s solution resistance; R_t charge-transfer resistance; R_{cp} interfacial corrosion product resistance; C_d double layer capacitance; Z_ω Warburg diffusion impedance; σ Warburg diffusion coefficient. Values of R_{cp} (ohm) are 10^{99} (curve 1); 10^5 (curve 2); 5×10^4 (curve 3); 10^4 (curve 4); 5×10^3 (curve 5).

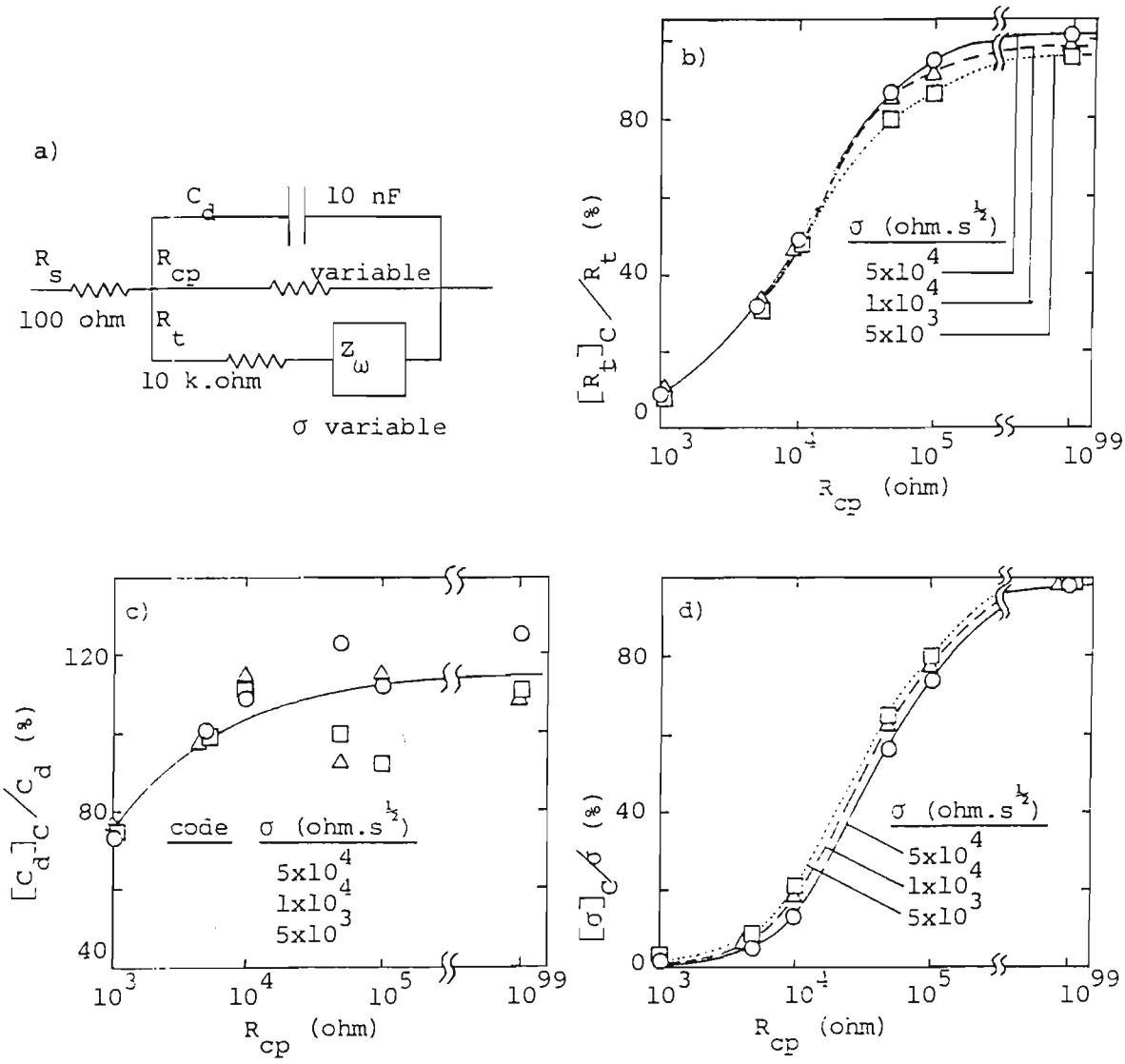

Figure R1/54. Effect of corrosion product resistance, R_{cp}, on error in b) R_t; c) C_d; d) σ for equivalent circuit of Fig. R1/54a. $[R_t]_C$, $[C_d]_C$, $[\sigma]_C$ calculated values of R_t, C_d, σ from theoretical Nyquist plots of the model in Figure R1/54a. Other symbols have meanings as per Figure R1/53.

reducing to 13-21% of the theoretical value (depending on the chosen σ value) when R_{cp} equals σ. It is therefore difficult to conclude that decreasing R_t and σ trends from cycle to cycle in Figures R1/20,23 indicate increasing rates of corrosion and diffusion. However, these findings do not exclude this possibility. It is probable that the rates of corrosion and diffusion increase from cycle to cycle as well as R_{cp} decreasing due to the build-up of somewhat electron conductive corrosion products at some $[SO_2]$ levels.

The semicircle diameter for the theoretical Nyquist plots in Figure R1/53 becomes large relative to the bent over diffusion tail as R_{cp} decreases to values equal to, or less than R_t. (All plots are obtained over the same frequency range.) In this plot, R_t and σ remain constant. This suggests a rudimentary method of determining the severity of partial short circuits. The method assumes that, in the absence of partial shorts, when R_t lowers then σ lowers to a similar extent thus preserving a similar basic Nyquist plot shape. In the author's experience, this assumption is valid. Figure R1/14, curve 3, Section 1.5/2, is an example of an experimental plot for ACM3 (Zn) where the semicircle becomes large compared to the diffusion tail, suggesting in this case that R_{cp} has become equal to, or less than, R_t. The calculated R_t value may therefore be substantially in error. Figure R1/15, curve 3 is an example of an experimental plot for ACM8 (Fe) where the semicircle diameter remains about the same size as the diffusion tail, suggesting that R_{cp} has not fallen to values $\leqq R_t$. The calculated R_t value will probably be reasonably accurate in this case.

4. Methods to calculate error in R_t

An attempt has been made to determine a method, similar to that shown in

Figure R1/54b-d, that can estimate the likely errors in calculating parameters R_t, C_d, σ from experimental Nyquist plots whose shape is affected by partial shorts. The method in Figure R1/54b-d cannot itself be used because neither the true parameter values nor R_{cp} are known. Two methods are presented to estimate the error in R_t. The first method is difficult to obtain reliable estimates of the parameter errors because the ratio of R_t/σ is not known for experimental plots. The second method uses a crude estimate for R_{cp} from working to reference plate resistance measured with a multimeter, but cannot be used with the existing data sets because such a measurement was not made.

In the first method, referred to as the $[R_t/\sigma]_C$ method, a plot of $[R_t]_C/R_t$, (representing the error in calculating R_t), versus $[R_t/\sigma]_C$, where C refers to calculated value, is obtained from theoretical Nyquist plots like those in Figure R1/53 at different values of R_{cp}. This method is based on the assumption that the ratio R_t/σ will not change significantly over the exposure interval unless R_{cp} becomes significant compared to R_t. Then the change in the ratio $[R_t/\sigma]_C$ can give an estimate of the error in calculating R_t. Figure R1/55 shows such a plot for six parameter sets where R_t, C_d are held constant at 10 k ohm and 10 nF respectively and σ varies from 0.5 R_t to 50 R_t. This shows, for example, that a ratio = $[R_t/\sigma]_C$ = 2.2 for the σ=R_t = 10^4 (dashed line) set will cause the calculated value of R_t to fall to 50% of the true value. The ratio $[R_t/\sigma]_C$ can be calculated from experimental Nyquists plot to obtain a value of $[R_t]_C/R_t$ using the theoretical plot in Figure R1/55. The problem with this method is that the actual values R_t, σ are not known, and therefore it is difficult to read off the ratio $[R_t]_C/R_t$. For example, an experimental Nyquist plot may look as if partial shorts are a problem (large semicircle, small diffusion tail nearly horizontal to the a-axis) and calculation of the ratio

$[R_t/\sigma]_C$ from this plot may give a value 2.2. However, without knowledge of R_t, σ, it is not possible to obtain an accurate estimate of the ratio $[R_t]_C/R_t$ from Figure R1/55, as the calculated value of R_t can lie between 14% and 86% (dashed lines) of the true value within the range σ = 50 R_t to 0.5 R_t. It is not possible to estimate R_t, σ from the Nyquist plot shape because the shape is also a function of R_{cp}. If the assumption is made that the factor R_t/σ does not change significantly from run to run or cycle to cycle, then an estimate of the error in $[R_t]_C$ can be obtained. This assumption appears to be valid most of the time because the ratio $[R_t/\sigma]_C$ for cycle 1/run 1 (where partial shorts are not likely to be present) remains relatively constant over the entire four PGB cycles for a given ACM, see column 6 in Tables A5/2, 3, Section A5/2. Firstly, it is assumed that PGB cycle 1 run 1 is relatively free of partial shorts, because corrosion product has not built up sufficiently. Therefore the calculated $[R_t]_C$, $[\sigma]_C$ values will give a good indication of the true ratio R_t/σ which is assumed to apply to all cycles/runs at a given $[SO_2]$. This ratio is then used to find the correct curve to use in Figure R1/55 in order to calculate the error in R_t from the ratio $[R_t/\sigma]_C$ calculated from experimental Nyquist plots. A modification of this is to construct a graph of $[R_t/\sigma]_C$ versus R_t/σ at various errors in R_t from the whole family of six curves in Figure R1/55. This graph is shown in Figure R1/56, and like Figure R1/55, is obtained completely from theoretical Nyquist plots using program equiv_crt. The error in R_t is depicted in Figure R1/56 as the calculated value that R_t falls to expressed as a percentage of the true value. For example, when $[R_t/\sigma]_C$ = 2.2 at R_t/σ=1 (dashed lines), then $[R_t]_C$ will be 50% of the true value, R_t. This method is reasonable enough and will allow at least a relative estimate of the error in R_t from run to run or cycle to cycle when no better method is available. This method is therefore applicable to most of the existing ACM data sets because the second method is not possible. It has been applied to ACM data in Section

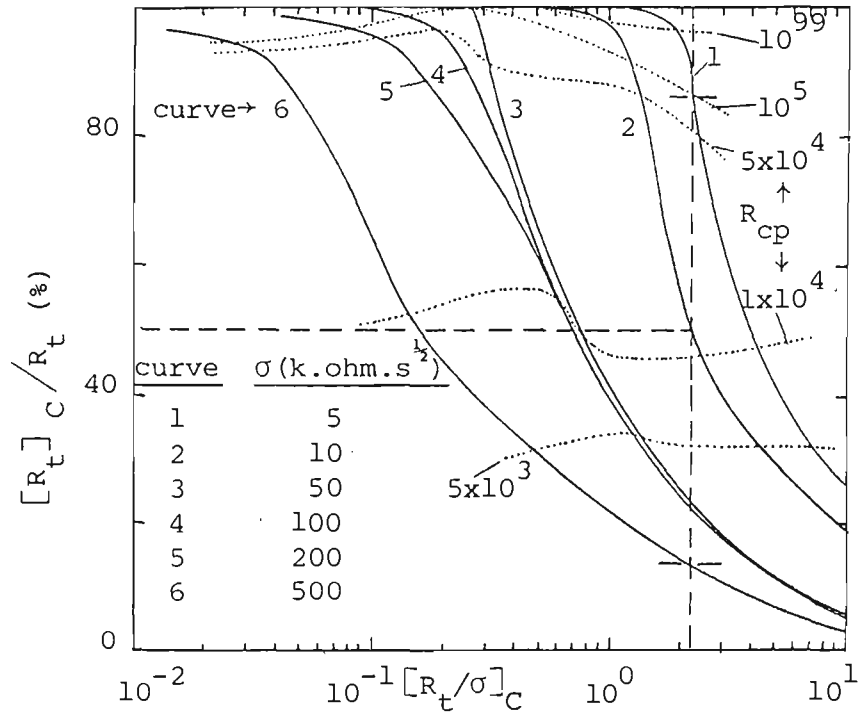

Figure R1/55. Error, $[R_t]_C/R_t$, in calculating R_t as a function of the ratio $[R_t/\sigma]_C$, where C refers to calculated value, obtained from Nyquist plots at different values of R_{cp} (shown dotted). The six curves are for different values of σ. R_t, C_d held constant at 10 k ohm, 10 nF respectively. Equivalent circuit as per Figure R1/54a.

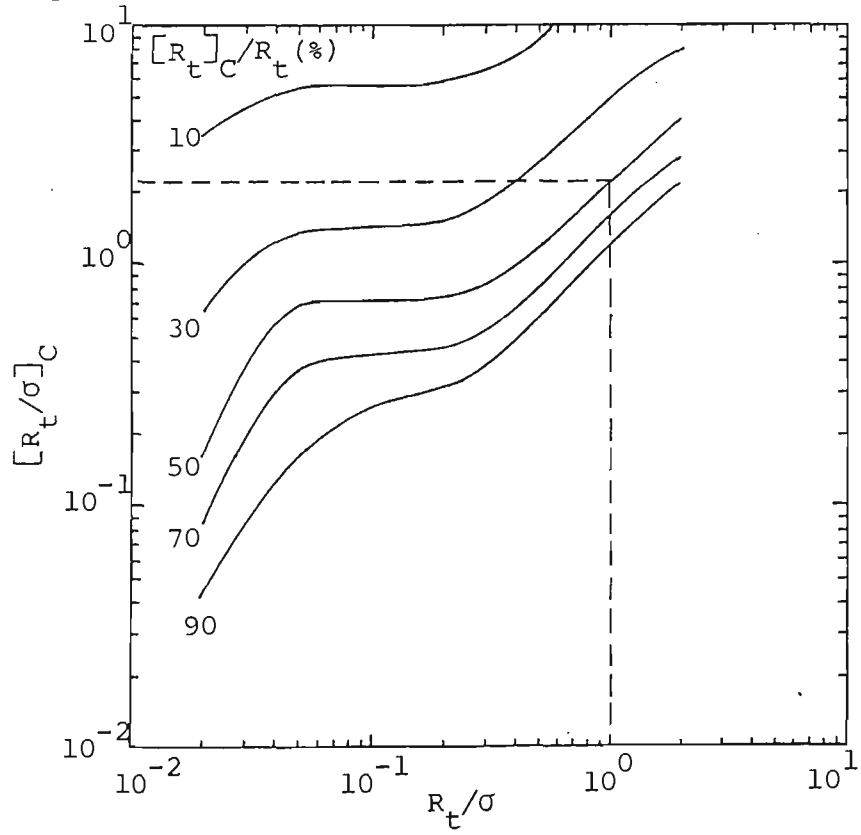

Figure R1/56. Error, $[R_t]_C/R_t$, in calculating R_t, obtained from a plot of the calculated ratio, $[R_t/\sigma]_C$ versus the true ratio, R_t/σ. Values of R_t/σ are estimated from Nyquist plots for PGB cycle 1 run 1 assuming negligible partial shorts. $[R_t/\sigma]_C$ values are calculated from any PGB cycle.

R1.8/5.2.

The second method, referred to as the $R_{cp}/[R_t]_C$ method, will be applicable when an estimate of R_{cp} is available. A crude method can be derived from the ACM working to auxiliary plate cell resistance measured with a multimeter after the ACM surface is nominally dry, as discussed in Section R1.8/2. This method is only applicable to a few ACM data sets because the multimeter cell resistance measurements were only carried out on a few additional experiments. It is assumed that corrosion product build-up was uniform over the entire ACM surface and that the corrosion product resistance, R_{cp}, occurring on the working electrode plates could be calculated from this cell resistance simply by an area correction factor equal to the (total insulator area/total working electrode area), as given by Equation (R1/5).

$$R_{cp}(\text{ohm}) = R_{WA} \times A_I/A_W \qquad \text{(R1/5)}$$

where R_{WA} = cell resistance (ohm) across nominally dry working, W, to auxiliary, A, plates of ACM

A_I = total insulator area (cm^2)

= $2.3 \times 10^{-3} \times 5.0 \times n$ (cm^2)

where n = number of working electrode plates

A_W = total exposed working electrode area (cm^2)

= 5.4 cm^2 ACM3 (Zn) for n = 16

5.5 cm^2 ACM8 (Fe) for n = 16

5.2 cm^2 ACM4 (rolled Zn-55%Al) for n = 12

(refer Table E2/1, Section E2.4/3)

A theoretical plot can be obtained that calculates the error in R_t from the

ratio $R_{cp}/[R_t]_C$ using the theoretical data sets calculated from program equiv_crt as described in Section R1.8/3. Note that R_{cp} and $[R_t]_C$ are theoretical values in this instance, $[R_t]_C$ being calculated from the theoretical Nyquist plots as shown in Figure R1/53. This theoretical plot, shown in Figure R1/57, is then used with experimental values of the ratio $R_{cp}/[R_t]_C$ to determine the error in R_t due to partial short circuits. This method has been applied to ACM data in Section R1.8/5.1.

5. Application of methods

The two methods described in Section R1.8/4 to calculate errors in R_t due to the presence of partial shorts have each been applied to experimental ACM data, as described below.

5.1 $R_{cp}/[R_t]_C$ method

The second method, based on the ratio $R_{cp}/[R_t]_C$, has been applied to a PGB 4-cycle impedance test for each of three ACMs. Table A5/1 in Section A5/1 shows that partial shorts were not a problem for a repeat test on ACM3 (Zn), PGB 354, at 0.2 ppm $[SO_2]$, because R_t was calculated to be >90% of the true value. Inspection of the relevant Nyquist plots revealed that the angle of the diffusion tail became less than 45° after the second PGB cycle. However, even after four cycles, a reasonable semicircle and diffusion tail was observed. There was no sign of the Nyquist plot shape indicating substantial partial short circuits, that is, a large semicircle diameter relative to a small nearly horizontal diffusion tail. The mass loss calculated from R_t for PGB 354 is shown plotted at 0.2 ppm $[SO_2]$ in Figure R1/48 curve 6, Section R1.7/2. Partial shorts did become a problem for a repeat test on ACM8 (Fe), PGB 352,

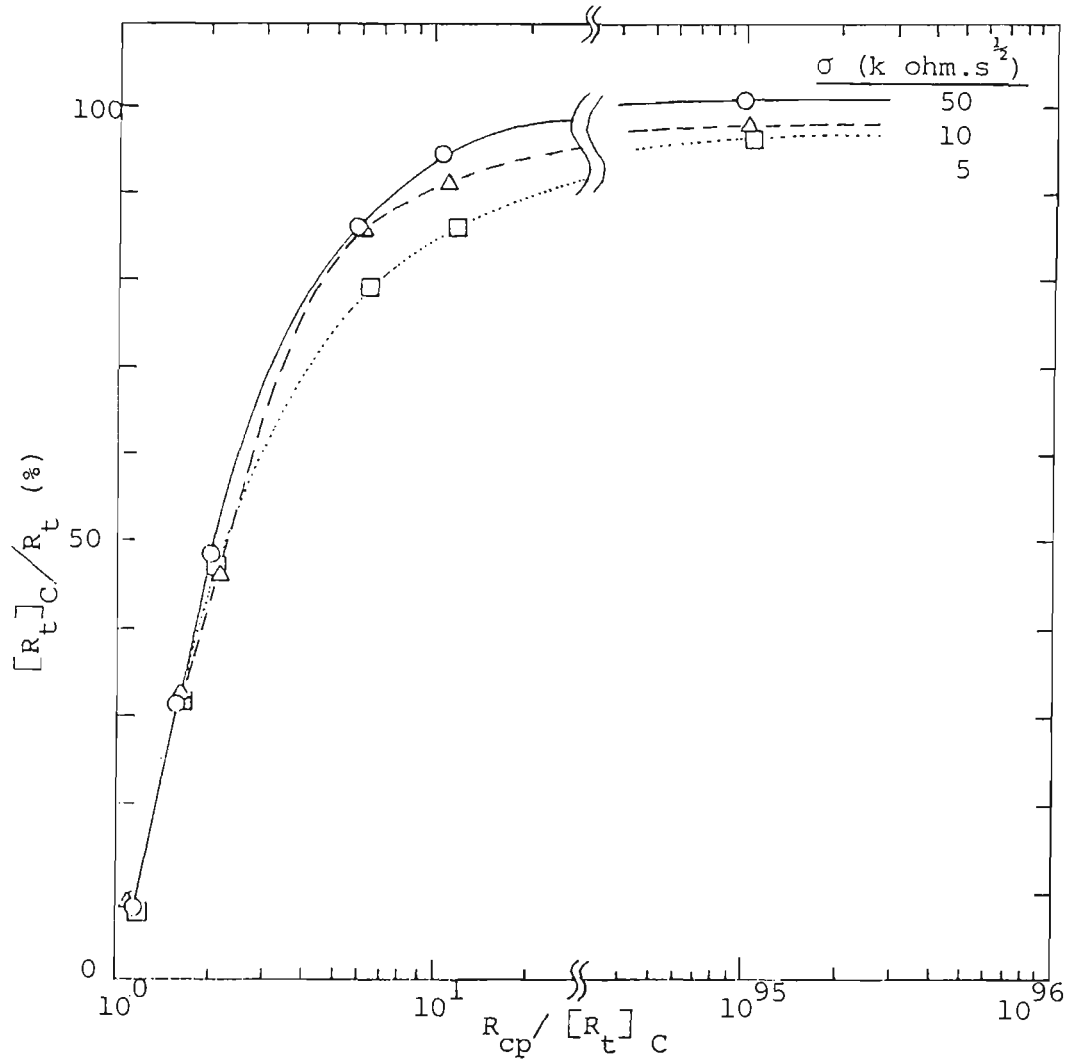

Figure R1/57. Error, $[R_t/]_C/R_t$, in calculating R_t versus the ratio $R_{cp}/[R_t]_C$ for 3 values of σ, obtained from Nyquist plots. Equivalent circuit as per Figure R1/54a.

at 0.5 ppm $[SO_2]$. Values of R_t were calculated to be only 48, 47, 23% of the true values at the end of PGB cycles 2, 3, 4 respectively. Inspection of the relevant Nyquist plots showed the shape to be satisfactory for runs in cycle 1, but thereafter there was a shrinking of the diffusion tail in size and the angle gradually drops towards horizontal from run to run. The diffusion tail was also small in size relative to the semicircle diameter. These are signs of the formation of significant partial short circuits due to R_{cp}, and indicate errors are to be expected in calculating R_t as discussed in Section R1.8/3. The mass loss calculated from R_t for PGB 352 is shown plotted at 0.5 ppm $[SO_2]$ in Figure R1/49 curve 5 in Section R1.7/2. The high value for PGB 352 probably explains why the $\Delta M_{Rt}/[SO_2]$ plot in curve 5 is higher than the $\Delta M_w/[SO_2]$ plot at 1352 mm^2 total exposed area in curve 2. No impedance tests which included R_{cp} measurements are available for ACM4 (rolled Zn-55%Al). A repeat corrosion current test, PGB 357, see Section A5/1 Table A5/1, showed that R_{cp} values were high and not likely to cause partial shorts. This is confirmed by Figure R1/28j-l Section R1.5/3.3 which shows that very little corrosion product has formed on ACM4 (rolled Zn-55%Al), and by inspection of other Nyquist plots, eg Figure R1/16, Section R1.5/2, which shows no evidence of abnormal plot shape attributed to partial short circuits. The mass losses calculated from I_k and R_p for PGB 357 are shown plotted at 0.5 ppm $[SO_2]$ in Figure R1/50 curves 5, 6 respectively in Section R1.7/2, and fall in line with existing values, all of which are low compared to weighed mass losses in curve 2.

5.2 $[R_t/\sigma]_C$ method

The first method referred to in Section R1.8/4, based on the ratio $[R_t/\sigma]_C$, has been applied to all the ACM data in Section R1.5/3. Tables A5/2,3 in

Appendix A5/2 show the calculations for estimating the error in R_t due to partial shorts based on this method. Table A5/2 are results for ACM3 (Zn), whilst Table A5/3 are results for ACM8 (Fe). As partial shorts were not a problem with ACM4 (rolled Zn-55%Al), see Section R1.8/1, no calculations are given.

A summary of the discussion in Appendix A5/2 is as follows.

1. The relative rates of charge transfer and diffusion remain approximately the same over the $[SO_2]$ range, at least for cycle 1 run 1, thus allowing the ratio $[R_t/\sigma]_C$ for cycle 1 run 1 to be used as the true ratio, R_t/σ. This assumption allows calculation of the error in R_t due to partial short circuits and applies to both ACM3 (Zn) and ACM8 (Fe).
2. The assumption made in item 1 is not strictly correct for ACM8 (Fe) in later cycles because charge-transfer processes speed up whereas diffusion processes remain relatively constant. Other problems are apparent for ACM3 (Zn). Nyquist plot shape can sometimes indicate partial shorts yet calculated errors in R_t remain small. Sometimes the σ value is difficult to determine and this leads to over-correction of R_t values. These problems indicate weaknesses in the method such that the calculated errors in R_t can only be taken as an approximate guide.
3. Diffusion is more rate determining than charge-transfer for ACM3 (Zn) than it is for ACM8 (Fe), a finding that supports the discussion in Sections R1.5/3.2.
4. The formation of corrosion products that give rise to partial shorts appear to occur at random and may or may not occur for apparently identical tests.

5. The partial shorts can be substantially minimized by terminating the PGB test after 1 or 2 cycles, rather than 3 or 4.
6. Correction of R_t/time plots for the effect of R_{cp} for ACM3 (Zn), ACM8 (Fe) in Figures R1/20,21 respectively, have indicated that the existing trends are in the majority of cases real, especially for cycles 1,2.

5.3 Comparison of both R_t methods

Because of the suspected random nature of partial short formation, as summarized above in item 4, and discussed in Section A5/2, it is not feasible to compare the $R_{cp}/[R_t]_C$ and $[R_t/\sigma]_C$ methods using different PGB experiments, even at the same $[SO_2]$, eg PGB 233 and 354 at 0.2 ppm $[SO_2]$ in Figure R1/20 suggest partial shorts formed to different extents in apparently identical tests. It is, however, possible to compare both methods using the same PGB experiment. This has been done for both ACM3 (Zn) with PGB 354 and ACM8 (Fe) with PGB 352, compare Table A5/1 with Tables A5/2,3. There is satisfactory agreement in the error in R_t, shown in column 7 of each table, for both R_t methods, indicating that both R_t methods estimate partial short circuits to a similar extent.

6. Interpretation of I_k, b_a, b_c trends

The increasing I_k trends, decreasing b_a, b_c trends observed for ACM8 (Fe) within a cycle, and from cycle to cycle, can be interpreted as follows. These changes normally indicate an increase in the number and/or area of corrosion sites or an increase in corrosion rate brought about by depolarization of anodic and cathodic reactions in the presence of SO_2 pollutant. In certain cases the electronic conductivity of the resulting corrosion products interfere with the

measurement, especially in cycles 3 and 4, by producing partial short circuits between adjacent working and auxiliary plates of the ACM. This can lead to abnormally high values of both I_k and calculated mass loss. These partial shorts do not completely invalidate the measurements because comparison of test results and photographs of the corroded ACMs after four cycles, as discussed in Section R1.6/4, establish credence in the calculated mass losses and in I_k, b_a, b_c trends. Even with the partial short problems for ACM8 (Fe), the mass loss/[SO_2] trends calculated from corrosion currents, Figure R1/35, Section R1/6.4, still show similar results to the weighed mass loss/[SO_2] trends in Figures R1/4,5, Section R1.3.

The ΔM_{Ik}/[SO_2] trends for ACM3 (Zn) in curve 4, Figure R1/48, Section R1.7/2; the ΔM_{Rt}/[SO_2] trends for ACM8 (Fe) in curve 5, Figure R1/49 and for ACM4 (rolled Zn-55%Al) in curve 7, Figure R1/50 give reasonable cell factors as previously discussed in Sections R1.7/3.1,4.2,4.3, respectively. The ΔM_{Ig}/[SO_2] trends for ACM2 (Zn/Fe), ACM2 (cast Zn-55%Al/Fe), ACM9 (rolled Zn-55%Al/Fe), discussed in Section R1.7/2.1,2.2, also give reasonable cell factors. Therefore this group of tests show that ACMs give satisfactory mass losses when compared to weighed mass losses, which themselves may be subject to some uncertainty due to the actual mass losses (before area correction) being small, as discussed in Sections R1.3,R1.7/2.2.

The low cell factors for ACM4 (rolled Zn-55%Al) in the ΔM_{Ik}/[SO_2] trends, Figure R1/50, Section R1.7/2, curve 5, are a problem thought to be caused by more difficult low polarization data, resulting in voltage response reading time difficulties and curve fits to (I,ε) data that are not always optimum.

7. Summary

Summarizing, ACM tests are a useful method of studying thin moisture film atmospheric behaviour in the presence of an SO_2 polluted atmosphere which can be simulated in the laboratory. A large portion of the test results appears to be valid, but ACMs are not without problems. They are difficult and tedious to manufacture. Care is needed to avoid applying excessive currents (ac or dc) to the ACM during testing. The polluted atmosphere appears to sometimes cause partial short circuits in 3-electrode Zn and Fe ACMs due to bulky corrosion product build-up that possesses some electron conducting ability. Care is needed in the analysis of results to detect this situation, and comparisons with weighed mass loss are required for confirmation of electrochemical results using these ACMs.

8. Comparison with previous work

However, the scope of what has been attempted with these ACMs is, to the author's knowledge, much wider than previous work in the literature using ACMs. A new method of manufacture, Section E2.4/2, which does not use bolts to clamp the ACM plates together, has been devised and implemented. The choice of thin mylar insulation (23 μm) has been a deliberate step to attempt to obtain results with cell factors closer to unity, rather than the very low cell factors reported[115,180] using 100-400 μm mylar. Corrosion currents have been calculated directly from ACM (I,ε) low polarization data which simultaneously calculates I_k, b_a and b_c. Previous corrosion current tests on ACMs reported in the literature[36,106,112-116,120,124,172,180] have applied a constant potential difference, ΔE, (eg 10 mV[112,116], 30 mV[36,113,114,172] or 100 mV[106,115,124,180]) and measured the resulting current, eg I_{30} for ΔE=30

mV. The corrosion current is then calculated from Equation (T5/1), Section T5/1. There are two problems with this method. Firstly, if ΔE is outside the linear range of the system under test, refer Section T3/4.2, then polarization resistance, $R_p=(\Delta E/\Delta I)_{\Delta E \to 0}$, will not be correctly calculated, and this will lead to inaccurate values of calculated corrosion rate. Secondly, Equation (T5/1) uses the lumped Tafel constant, B, and previous use of this equation in the literature has employed fixed values of b_a, b_c to obtain B, rather than actual measured values obtained simultaneously, as has been done in this thesis. Therefore, the corrosion current method employed here is more sophisticated than used previously with ACM experiments. Finally, this thesis has attempted a much wider correlation of electrochemically calculated mass loss with weighed mass loss than has previously been published in the literature. Previously, correlations between both galvanic current derived mass loss[36,114,172] and corrosion current derived mass loss[36,112-114,116,124,172], with weighed mass loss have been obtained. This thesis attempts correlations with weighed mass loss of not only galvanic current and corrosion current calculated mass loss, but also impedance (charge-transfer resistance) and polarization resistance calculated mass loss as well.

The samples (405/85-407/85) referred to are described in Section E3.1/1. Each sample was periodically transferred from the 5% NaCl solution, referred to as the test solution, to solutions of differing chloride ion concentration, referred to as measurement solutions, and its impedance measured. It was then transferred back to the 5% NaCl test solution in which the sample 'lived'. All three samples were tested for at least 41 days. It was not realised until the results were thoroughly analysed at the end of the test period that samples 405/85 and 406/85 had failed prematurely (less than 5 days). Refer to Section T1/5.4 for a discussion on failure criteria. The single frequency (1 kHz) test results (not shown) gave similar patterns for all three samples as they were transferred to different measurement solutions at times over their immersion history. However, the two samples showing early failure gave impedance results that decreased faster than sample 407/85. Therefore, although only one sample's results were analysed, it is believed that the results are a consistent set of results that is typical behaviour for this material.

1. Painted metal/solution interface equivalent circuit model

Figure R2/1 is a wide frequency range Nyquist impedance plot of the resistive, a, versus reactive, b, components of impedance for sample 407/85 in 10 g/L $[Cl^-]$ (NaCl) measurement solution after 8.9 d in 5% NaCl test solution, both at 50°C. Although the plot shape varied considerably with both immersion time and solution chloride ion concentration and was often difficult to analyse, this plot is reasonably typical and consists of two interacting semicircles plus a low frequency tail. This shape has been interpreted according to the equivalent circuit model for painted metals as discussed in Section T1/5. Thus the high frequency semicircle is considered to contain paint film information (R_{pf}, C_{pf} paint film resistance, capacitance), whilst the semicircle at lower

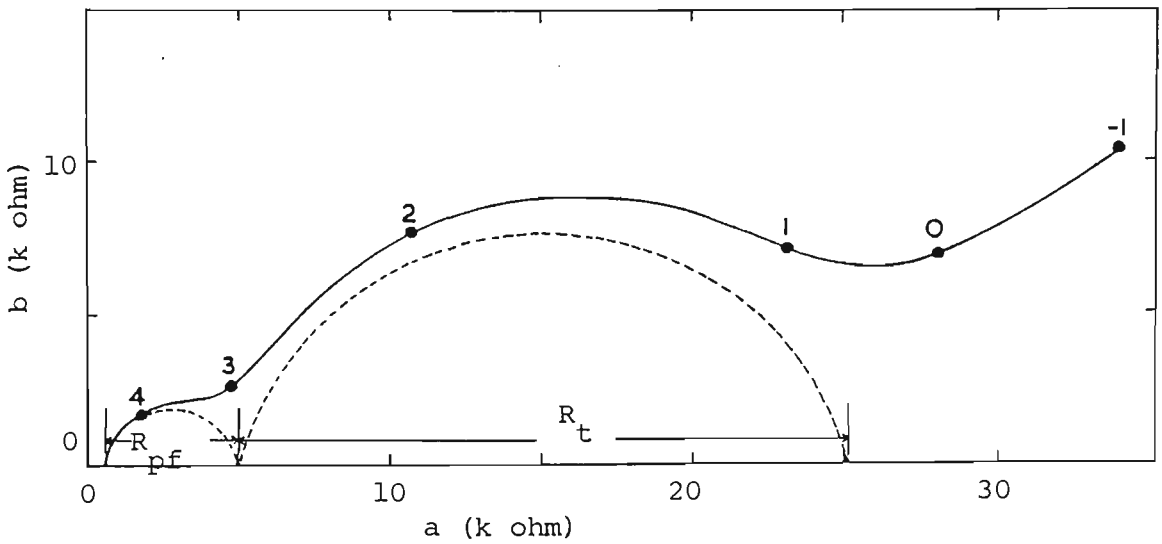

Figure R2/1. Nyquist impedance plot of resistive, a, versus reactive, b, components of impedance for sample 407/85 in 10 g/L [Cl^-] measurement solution after 8.9 d in 5% NaCl test solution, both at 50°C. Numbers on plot indicate frequencies, eg $0=10^0$ Hz, $1=10^1$ Hz ... R_{pf} paint film resistance, R_t metal charge-transfer resistance.

frequencies is thought to contain metal substrate information (R_t, C_d metal's charge-transfer resistance, double layer capacitance). The low frequency tail gives information about the diffusion of reactants (water, oxygen, ions) and products (metal ions from substrate corrosion) into and out of the paint film and is termed a pseudo-Warburg diffusion impedance, Z_ω. In most cases, the low frequency tail was difficult to analyse according to the equivalent circuit model in Section T1/5, being inclined at angles less than 45°. Therefore no attempt has been made to obtain Z_ω values in this case.

Figures R2/2-5 summarize the results obtained for R_{pf}, R_t, C_{pf}, C_d respectively, as a function of chloride ion concentration of the measurement solution.

Values of R_{pf} and R_t, Figures R2/2,3, decrease with both measurement solution chloride ion concentration after a given immersion time in 5% NaCl test solution, and also with immersion time, R_{pf} values being lower than R_t. By comparison, values of C_{pf} and C_d, Figures R2/4,5, are relatively constant with both changes in chloride ion concentration at a given immersion time, and with immersion time.

At any given immersion time, transferring sample 407/85 from one chloride ion solution to another quickly (within several minutes), gave impedance values (R_{pf}, R_t, C_{pf}, C_d) that were characteristic of the measurement solution and the state of degradation of the paint film, as can be observed from Figures R2/2-5. This demonstrates the relative ease with which the solution in the paint film comes into equilibrium with the surrounding solution, and is in line with results of other researchers[7,141].

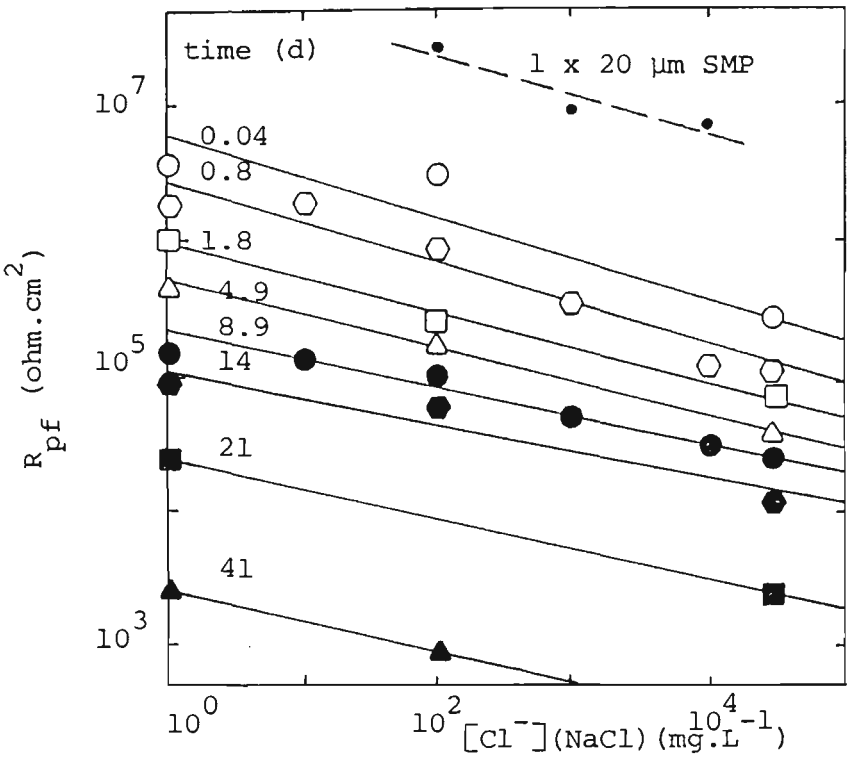

Figure R2/2. Paint film resistance, R_{pf}, versus chloride concentration of the measurement solution for attached film sample 407/85 (full lines) after various times in 5% NaCl test solution at 50°C, compared to 1 x 20 µm SMP top coat free film (dashed line).

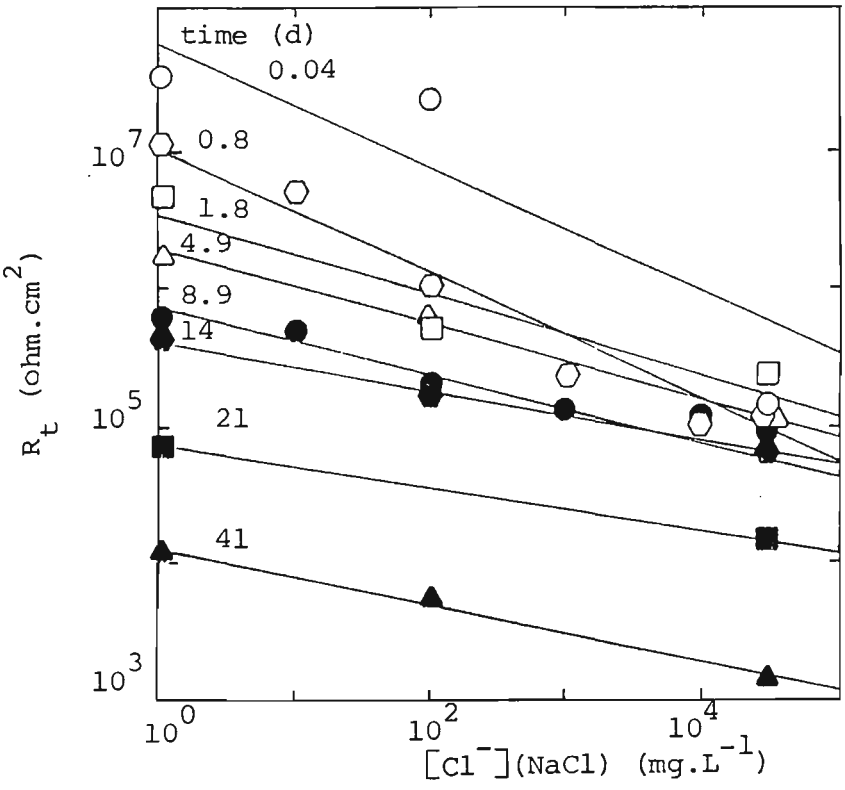

Figure R2/3. Metal's charge-transfer resistance, R_t, versus chloride ion concentration of the measurement solution for sample 407/85 after various times in 5% NaCl test solution at 50C.

Figure R2/4

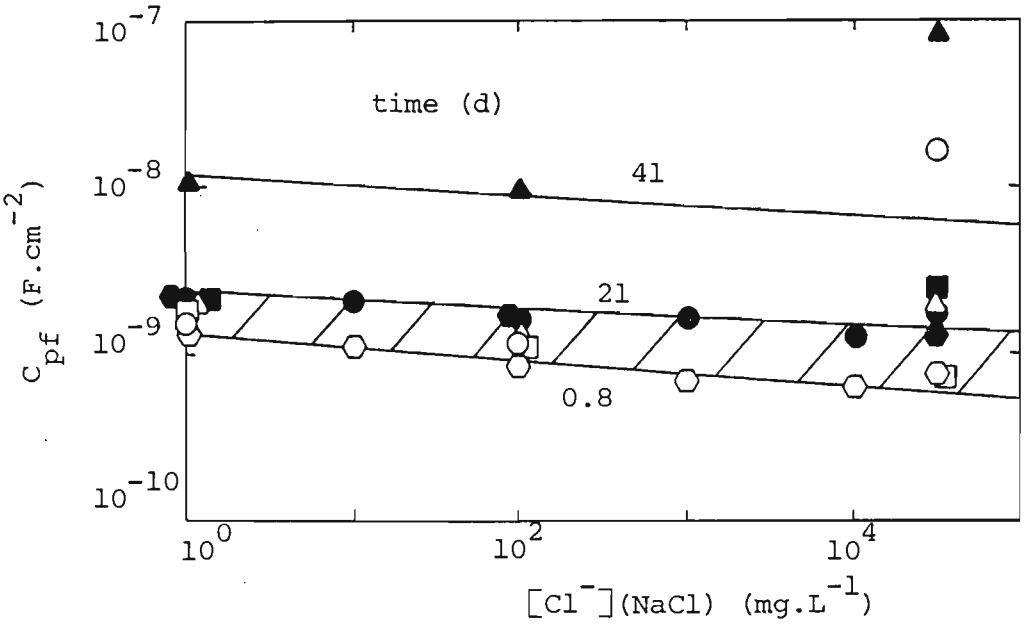

Figure R2/5

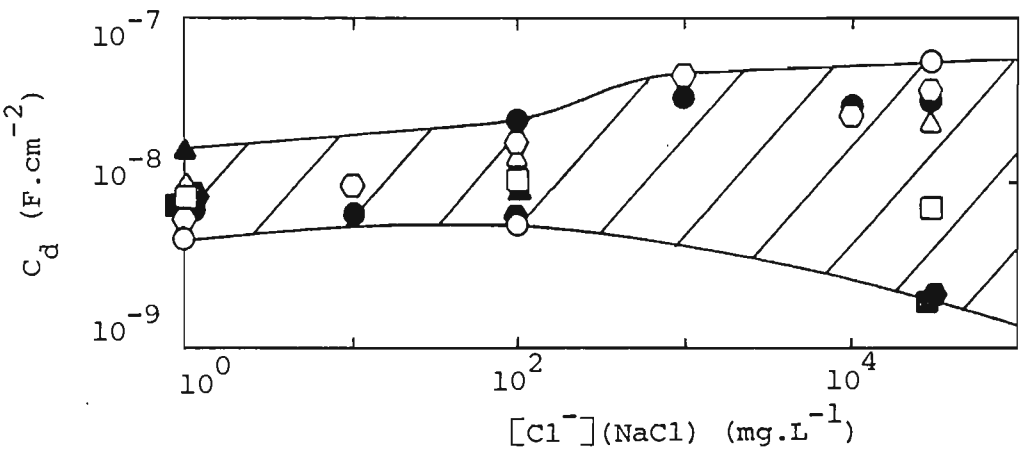

Figures R2/4,5. Paint film capacitance, C_{pf}, (Figure R2/4) and metal's double layer capacitance, C_d, (Figure R2/5) versus chloride ion concentration of the measurement solution for sample 407/85 after various times in 5% NaCl test solution at 50°C. Symbol codes are the same as in Figures R2/2,3.

2. Paint film resistance, R_{pf} trends

Figure R2/2 shows that the paint film resistance, R_{pf}, decreases as the chloride ion concentration of the measurement solution increases for any given immersion time by about 0.3 decades per decade increase in chloride ion. In other words, the resistance of the paint film directly follows the resistance of the solution. This indicates that R_{pf} is controlled by the penetration of the paint film by ions[141]. Mills and Mayne[158] observed that the dc resistance of free paint films, classified as direct or D-type films (because they followed the resistance of the solution, refer Section T6/6), fell about two orders of magnitude when transferred from 0.001 M KCl to 3.5 M KCl solution at 25°C, which is a similar drop to that found in the above R_{pf} trends. It is concluded that the performance of sample 407/85 paint film is controlled predominantly by direct or D-type areas. Other evidence supports this conclusion, see Sections R2.1/7, R2.2/1.2. D-type film behaviour has been ascribed to areas of lower resistance where polymer cross-linking density is presumably lower[158,182], see Figure R2/6, and where breakdown of the painted metal has been shown to occur[159]. However, Cherry and Wright[183], working with thicker 200 μm free film epoxy resins have stated that the hydrophobic nature of the curing agent, and not necessarily the cross-linking density, is the most important factor governing the electrical resistance of the polymer.

The marked drop off in R_{pf} values with immersion time in 5% NaCl solution, see Figure R2/2, is believed to be indicative of the state of degradation of the paint film caused by ingress of the solution. It is difficult to say whether this degradation is randomly induced by solution ingress, or whether pathways (thought of more generally as areas of greater solution uptake rather than more specifically as pores or capillaries), open up in a perpendicular fashion to

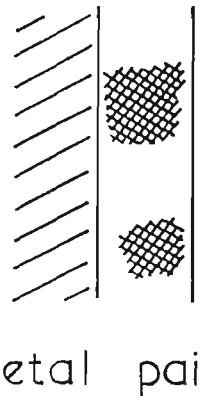

Figure R2/6. Schematic of a paint film on a metal substrate. Hatched areas are areas of lower paint film resistance where more rapid solution uptake occurs[16] and breakdown of the painted metal[159].

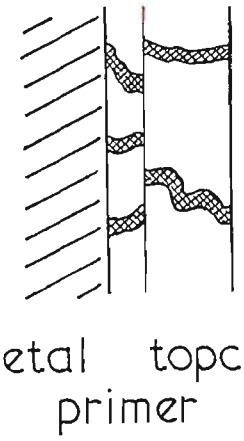

Figure R2/7. Schematic of a primer + top coat paint system on a metal substrate showing pathways (areas of greater solution uptake) in the paint film.

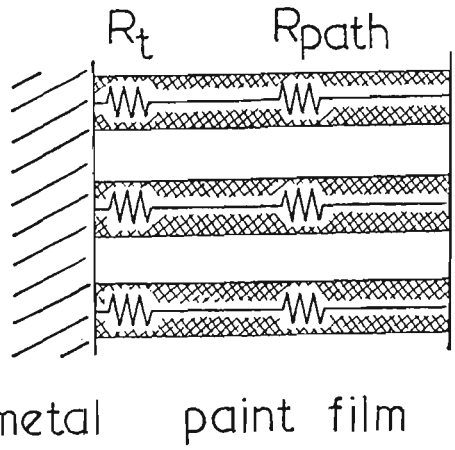

Figure R2/8. Schematic of a paint film on a metal substrate in terms of a simple equivalent electrical circuit for the metal's charge-transfer resistance, R_t, in series with the resistance of a paint film pathway, R_{path}, for three such pathways.

the surface, see Figure R2/7. The latter is thought more likely because breakdown (blistering with the formation of white corrosion products) mostly occurs locally. Mayne[141] has discussed the existence or otherwise of paint film pores, stating that extensive electron microscope examinations by other workers have shown that paint films are free of pores. However, he correctly points out that it is possible for paint films to be free of capillaries when dry (as they must be when examined under vacuum), and only develop them owing to the take-up of water. Mayne and Scantlebury[182] concluded that D-type conduction cannot be attributed to the presence of pores, unless of molecular dimensions, because portions of the films having D properties were distributed over an appreciable area and not confined to a single area, as would be the case if the sample contained a single pore.

The present evidence of R_{pf} decreasing with time in Figure R2/2 suggests that solution ingress permanently damages the paint film and that this damage increases with time. It is believed that this damage is caused by solution penetrating the film locally at discrete pathways. In the initial stages of immersion, it is only necessary for a minimum of one pathway to open up through the paint film to the substrate to be able to measure a potential which is typical of the bare substrate. As time proceeds, the number of pathways increase, and may even overlap or intersect due to the cross-sectional area of each pathway increasing, so that the state of degradation of the paint film, and hence the value of R_{pf}, will then depend on the total summed area of these pathways. The situation is more complicated than this, and Lindquist[162] has discussed this in some detail. He points out that water can be randomly distributed; in clusters; as a coating on the surface of pigment particles; in voids; in pores; as interfacial water at the paint/metal solution interface; in blisters or below the paint in corrosion products at the substrate surface.

Figure R2/8 depicts a very simple model for the resistance of the paint film, R_{pf}, showing the existence of three such pathways. No distinction between primer and top coat is made in this model. Solution uptake is assumed to be predominantly via these pathways, the remainder of the film taking only a minor role because of its presumed much higher resistance. In the following discussion, the conductivity of the pathways is taken to be that of the bulk solution, and the average distance of the pathways is taken as the thickness of the paint film. As the immersion time in 5% NaCl solution increases, the number of pathways increases, and hence the total paint film resistance, made up of all the individual parallel pathway resistances, will decrease, according to Equations (R2/1,2).

$$1/R_{pf} = 1/R_{path1} + 1/R_{path2} + ... = \sum^{n} 1/R_{path} \qquad (R2/1)$$

$$R_{pf} = R_{path}/n = \ell/nAk \qquad (R2/2)$$

where n = number of pathways

ℓ = average distance of pathways $\approx$ paint film thickness (25 μm)

k = conductivity of pathway $(\text{ohm cm})^{-1}$

A = average cross-sectional area of pathway (m^2)

Likewise, as the chloride ion concentration of the measurement solution increases, and hence the conductivity of the paint film pathways, the value of R_{pf} will decrease, in accord with Equation (R2/2). Values of R_{pf} from Figure R2/2 have been used to calculate nA, equivalent to the total summed area of the pathways in the paint film, using Equation (R2/2). Results for nA versus measurement solution concentration were calculated only at one immersion time (0.5-1.5 h $\approx$ 0.04d) in 5% NaCl test solution. Results for nA versus time

in the 5% NaCl test solution were calculated only at one chloride ion measurement concentration (5% NaCl = 3.05×10^4 mg.L^{-1} [Cl^-]). Figure R2/9 shows that nA increases with immersion time in 5% NaCl test solution and with decreasing chloride ion concentration of the measurement solution. The increase with immersion time is expected because the number and possibly the area of pathways should increase as the extent of paint degradation increases. The increase in nA with decreasing chloride is unexpected. It would be anticipated that nA should be constant and independent of the measuring solution. Appendix 2 shows that nA is related to the concentration of the measuring solution, C, by Equation (R2/3).

$$nA = [\ell/k^{o}R^{o}_{pf}C_{o}^{-(1+m)}]\, C^{-(1+m)} \qquad (R2/3)$$

As ℓ, k^{o}, R^{o}_{pf} and C_{o} are all constants, nA will increase as concentration decreases if m, the slope in Figure R2/2, is greater than -1. This condition is met because m = -0.3 for the 0.5-1.5 h line in Figure R2/2. If the assumptions made in deriving Equation (R2/3) are correct, the variation of nA with concentration is a real effect.

It can be argued that the value of nA is determined by the immersion time interval in 5% NaCl test solution and remains constant and independent of the measuring solution. Then R_{pf} values in 5% NaCl test solution can be used to calculate nA values. These nA values can then be used to calculate what R_{pf} would be if the bulk solution conductivity is equal to the pathway conductivity. This is shown plotted for three immersion times in Figure R2/10, along with measured values of R_{pf} taken from Figure R2/2. It can be seen that the calculated value of R_{pf} becomes higher than the measured value as the concentration of the measurement solution decreases. One or more of

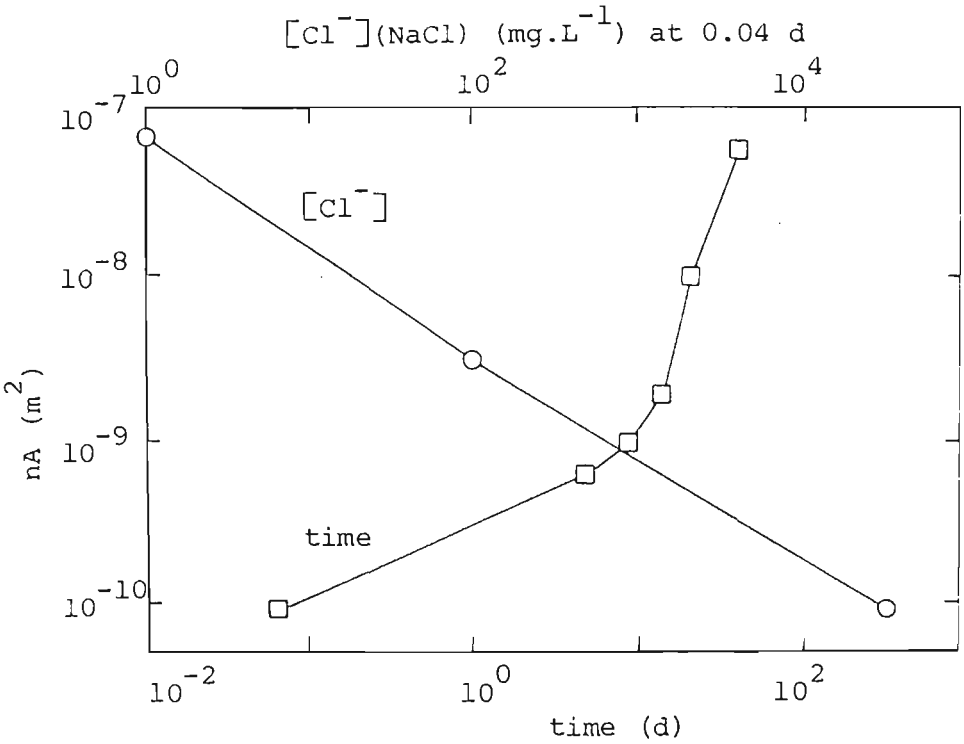

Figure R2/9. Total summed area of paint film pathways, nA, versus both time in 5% NaCl test solution and chloride ion concentration of the measurement solution after 0.5-1.5 h (0.04 d) in the test solution. Values of nA calculated from R_{pf} values in Figure R2/2 and Equation (R2/2).

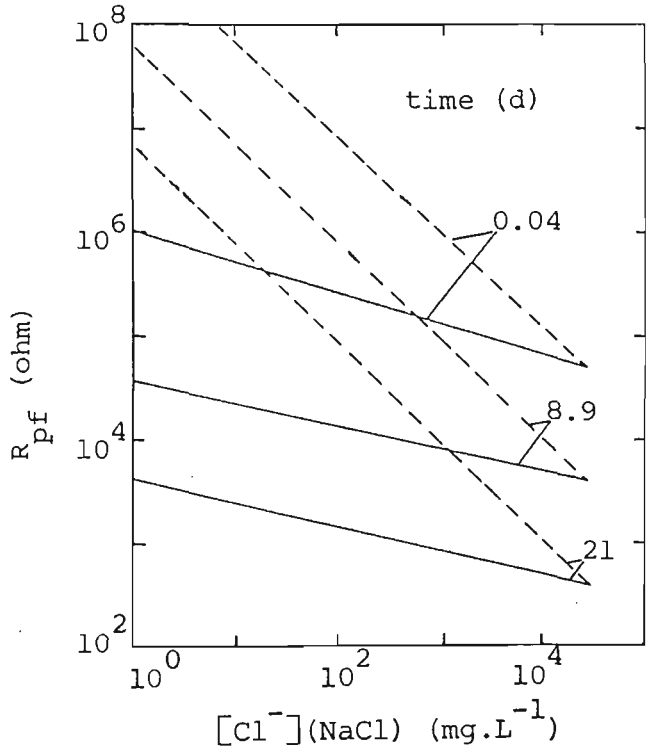

Figure R2/10. Measured (full lines) and calculated (dashed) paint film resistance, R_{pf}, values versus measurement solution chloride ion concentration after various times in 5% NaCl test solution.

the following statements must be true to account for these facts.

1. Areas surrounding D-type pathways may be inverse or I-type areas, whose resistance rise with increasing concentration[158]. The measured values of R_{pf} may be affected by these areas because they have the opposite trend with concentration to the D-type pathways (resistance of D-type areas decreases, resistance of I-type areas increases with increasing concentration).

2. Solution conductivity in the pathways is greater than the bulk solution conductivity. This would be true if equilibrium between paint film and bulk solution was not completely attained at the time of transfer to the next measurement solution.

3. Size and/or number of the pathways increases with decreasing chloride ion concentration.

Regarding point 1, if, as Mills and Mayne[158] show, I-type areas are at least two orders of magnitude higher in resistance than D-type areas over the concentration range, see Figure T6/6, Section T6/6, then the effect of I-type areas on the paint film resistance, R_{pf}, will be negligible. If, on the other hand, I-type areas are comparable with, or lower, in resistance at low solution concentrations than D-type areas, as shown in Figure 1 of ref 184, then the surrounding I-type areas will affect R_{pf} values and nA will be incorrectly calculated. However, values of R_{pf} will more closely represent D-type pathway resistance at higher solution concentrations than at lower concentrations because the resistance of I-type areas has been shown to increase with concentration whilst the resistance of D-type areas decrease

with concentration[158]. The differences between calculated and measured R_{pf} values shown in Figure R2/10 can be explained by this reasoning.

Regarding point 2, a repeat experiment was carried out to check how quickly equilibrium was attained between paint film and bulk solution. A 25% gloss painted sample, see Section E3.2/2.1, which had been in 5% NaCl solution at 50°C for four days, was transferred to 100 mg.L^{-1} [Cl^-] (NaCl) solution. Wide frequency impedance tests were performed in 5% NaCl solution just prior to transferring; in the 100 mg.L^{-1} [Cl^-] (NaCl) solution over a period of one day; and then after transferring back to 5% NaCl solution. The results, see Figure R2/11, indicate that equilibrium is not wholly complete within three minutes of transferring to the new solution (with R_{pf}, rising from 27.0 k ohm.cm^2 in 5% NaCl to 64.2 k ohm.cm^2 in 100 mg.L^{-1} [Cl^-] solution), because R_{pf} rises slowly to 120 k ohm.cm^2 after one day. Three minutes after transferring the sample back to 5% NaCl solution, R_{pf} falls to 40.8 k ohm.cm^2. This experiment confirms that a rapid exchange between paint film and bulk solution occurs on transferring a sample from one solution to another. However, the results show that, whilst the new equilibrium situation is about 50% complete within a three minute period, there is a much slower attainment of a more complete equilibrium at longer times. This suggests that the conductivity of the solution in the paint film pathways would be somewhat higher than the bulk solution conductivity for the results shown in Figure R2/2. Therefore, according to Equation (R2/2), the measured value of R_{pf} at this time would be lower than that calculated assuming the pathway solution conductivity was equal to the bulk solution conductivity. This reasoning is also sufficient to explain why measured R_{pf} values are lower than calculated values, as shown in Figure R2/10.

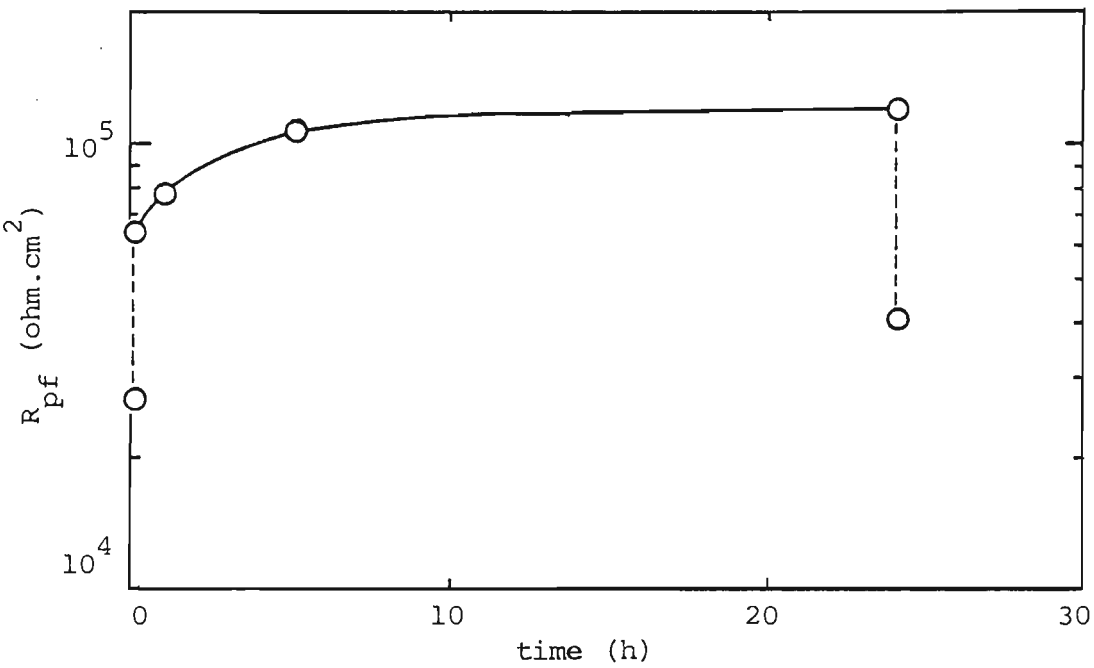

Figure R2/11. Effect of time in 100 mg.L^{-1} [Cl$^-$] (NaCl) measurement solution on paint film resistance. R_{pf}, for a 25% gloss painted sample after 4 d in 5% NaCl test solution at 50°C. The points at 0,24 h below the two dashed lines are R_{pf} values in 5% NaCl test solution before, after transferring to the measurement solution, respectively.

Regarding point 3, it is considered unlikely that the size and/or number of pathways would increase with decreasing concentration of the measurement solution. A measurement solution of lower chloride concentration would encourage the outward diffusion of Na^+ and Cl^- ions into the bulk solution. The reverse process, that of inward diffusion of water, would only be possible if the area of the pathways increased, that is, the pathways swelled. This may occur at long times, but is considered highly unlikely at times as short as several minutes.

Therefore, it may be concluded that the variation of nA with concentration of the measuring solution is not a real effect and may be explained either by areas adjacent to the pathways contributing to the measured paint film resistance, or the solution in the pathways having a higher concentration than the bulk solution after transferring to a solution of lower concentration or by both these processes. It is more likely that nA is constant and independent of the concentration of the measurement solution, and determined only by the immersion time interval in 5% NaCl solution.

The simple model for the resistance of the paint film, depicted in Figure R2/8, has been shown to adequately explain the results of Figure R2/2. However, the abovementioned complications indicate that the model is oversimplified. This is easy to demonstrate because the value of R_{pf} for the repeat experiment in Figure R2/11 did not change sufficiently to be satisfied by Equation (R2/2) when the sample was transferred from 5% NaCl test solution to 100 $mg.L^{-1}$ $[Cl^-]$ measurement solution. Equation (R2/4) is derived from Equation (R2/2) and shows that the ratio of R_{pf} values at two solution concentrations is equal to the inverse of the solution conductivities.

$$(R_{pf})_1/(R_{pf})_2 = k_2/k_1 \qquad (R2/4)$$

From Equation (R2/4), the calculated value of R_{pf} in 100 $mg.L^{-1}$ $[Cl^-]$ measurement solution should have been 4.99 M $ohm.cm^2$ instead of the measured value of 120 k $ohm.cm^2$ after one day shown in Figure R2/11. The ratio of $(R_{pf})_{calc}/(R_{pf})_{meas}$ = 41.5 which clearly shows that the simple model does not explain the results sufficiently.

An attempt has been made to quantify the effects on the measured paint film resistance, R_{pf}, of the resistance of I-type areas, and also of the paint film pathway solution concentration being different to that in the bulk solution.

Let it be assumed that the pathway solution conductivity is equal to the bulk solution conductivity for the 5% NaCl solution in which the sample lived, and that the D-type pathways are effectively in parallel with the rest of the film (assumed to be I-type areas). Then:

$$\begin{aligned} R_{pf} &= R_I.R_D/(R_I+R_D) \\ &= F.R_D \\ &= F\ell/nAk \qquad (R2/5) \end{aligned}$$

where $F = R_I/(R_I+R_D)$

The factor, F, is the fraction of the total measured paint film resistance caused by the resistance of I-type areas. When F=1, the value R_I is significantly higher than R_D so that R_{pf} equals R_D, the resistance of the pathways. This is equivalent to the situation assumed for Equation (R2/2). If R_I in 5% NaCl solution is not significantly higher than R_D, then F will be less than unity and therefore calculated values of nA will be less than those

calculated from Equation (R2/2).

When the sample is transferred to a solution of lower chloride ion concentration and R_{pf} measured within an interval of three minutes, the situation is further complicated. Firstly, the factor F will change for the measurement solution, becoming lower as the chloride ion concentration decreases. Secondly, a factor, G, is also needed to take into account the fact that the pathway conductivity will be higher than the bulk solution conductivity, according to Equation (R2/6).

$$k_{path} = G\, k_{bulk} \qquad \text{(R2/6)}$$

The factor, G, will be greater than unity when both the measurement solution is more dilute than the test solution and the pathway conductivity is higher than that of the bulk solution. For 5% NaCl test solution, the factor G is unity because it is assumed that the sample was equilibrated in this test solution.

The corrected value of paint film resistance, $(R_{pf})_{corr}$, will then be according to Equation (R2/7).

$$(R_{pf})_{corr} = [F]_{Cl}.\ell/nA[G]_{Cl,t,x}.k \qquad \text{(R2/7)}$$

The factor F is a function of the solution chloride ion concentration and the extent of degradation of the paint film. The factor G is a function of solution chloride ion concentration, time, t, and distance, x, within the paint film. The value of nA is that calculated by Equation (R2/5) for the 5% NaCl test solution. All three factors are unknowns in Equation (R2/7). This equation calculates better estimates of R_{pf} than were calculated by Equation (R2/2) and shown in Figure R2/10. An exact solution of this equation is a complex mathematical modelling problem and has not been attempted.

However, some idea of the effectiveness of these corrections can be estimated for the case where sample 407/85, after 8.9 d in 5% NaCl test solution, was transferred to 100 mg.L^{-1} [Cl^-] measurement solution. Reasonable values for factor F would be 0.9 (based on R_I = 10 R_D) in the 5% NaCl test solution and 0.5 (based on R_I=R_D) in the 100 mg.L [Cl^-] measurement solution. From Figure R2/11, the factor G for 100 mg.L^{-1} [Cl^-] solution is estimated at 2 (R_{pf} rises from 64.2 k ohm.cm^2 at 2 min to 120 k ohm.cm^2 at 1 day after transferring the sample to 100 mg.L^{-1} [Cl^-] solution). The value of nA was calculated to be 9.38 x 10^{-4} cm^2 using Equation (R2/7) with G=1 (pathway conductivity assumed equal to bulk conductivity after 8.9 d in 5% NaCl test solution); F=0.9; and R_{pf}=4.0 x 10^{-3} ohm, obtained from Figure R2/2 after suitable area correction. Equation (R2/7) can then be used with these values to calculate $(R_{pf})_{corr}$ = 205 k ohm for the corrected paint film resistance several minutes after transferring from the 5% NaCl test solution to the 100 mg.L^{-1} [Cl^-] measurement solution. This is considerably lower than the calculated value of $(R_{pf})_{calc}$ = 740 k ohm, using Equation (R2/2) and shown (8.9 d dashed line at 100 mg.L^{-1} [Cl^-]) in Figure R2/10. However, this corrected value of 205 k ohm is still some 11.7 times higher than the measured value of 17.5 k ohm (8.9 d full line at 100 mg.L^{-1} [Cl^-] in Figure 2/10. It is seen that, even with these corrections, the modified simple model for the paint film resistance is still oversimplified.

Two explanations can be suggested. The value of G calculated above could be in error by a factor of 11.7 times if the pathway conductivity was not equal to the bulk solution conductivity at 1 day after transferring the sample to 100 mg.L^{-1} [Cl^-] solution. Although there is a small upward slope at 1 day in Figure R2/11, suggesting that outward diffusion of chloride ions from pathways continues for longer times, this would mean that R_{pf} in Figure

R2/11 would have to rise still further from 64.2 k ohm.cm^2 at 1 day to 752 k ohm.cm^2 which is estimated to take well in excess of 100 days. If equilibrium between paint film pathway and bulk solution occurs by outward diffusion of Na^+ and Cl^- ions, it will theoretically take an infinite time to reach equilibrium. This explanation is thought to be possible but unlikely. The second explanation is that equations based on Equation (R2/2) are too simple to predict the resistance of the paint film pathways, and this is thought to be more likely. Perhaps that, if fixed ion groups exist in the walls of the pathways, then the application of a Donnan membrane phenomena will lead to a smaller increase in ionic concentration inside the pathways as the external concentration increases. This could then explain the smaller increase in conductivity with external concentration than expected from the simple pathway model[191].

3. Performance evaluation test

As already stated in Section R2.1/2, the value of R_{pf} at any given immersion time is related only to the state of degradation of the paint film and the measurement solution chloride ion concentration. This is based on the simple model for paint film resistance without complicating factors. It follows that samples previously exposed to another environment, such as the salt spray cabinet or at a severe marine site, can be evaluated for their extent of degradation by impedance testing in a standard chloride ion solution. Because of the relatively rapid exchange between paint film and bulk solution, at least initially, it may even be possible for samples so tested to be re-exposed to their original environment for further degradation. Thus a quantitative measure of a sample's degradation should be possible by repeated exposure in one environment and evaluation in another. Such a procedure would show up degradation patterns when they were not visibly detectable.

4. Metal substrate charge-transfer resistance, R_t, trends

The decreasing values of R_t with immersion time for sample 407/85 in 5% NaCl solution, shown in Figure R2/3, initially suggest that the corrosion resistance of the substrate drops from the moment of initial immersion in a similar manner to trends in R_{pf} shown in Figure R2/2. Although this may be true to some extent, such a simple explanation does not take into account the actual substrate area exposed to the solution at a given time. Walter[17], commenting on limitations of impedance plot methods, has discussed the effect of the actual corroding area and methods available for its measurement. An increase in corroding area probably explains why the low frequency Nyquist semicircle diameter has been observed to decrease with time, implying an increased corrosion rate. Such behaviour is opposite to that expected for uncoated metals.

The simple pathway model, described in Section R2.1/2, can also be used to explain why R_t values decrease with time. The value of R_t at any given time will then depend on the total summed area of the paint film pathways, nA, as depicted in Figure R2/8. As more pathways open up with increasing time, more of the substrate becomes exposed to the solution. This may eventually form a boundary layer, also termed aqueous phase water or water-rich layer, at the paint film/substrate interface, as described by several authors and summarised recently by Walter[127].

An attempt has been made to separate out the effects of increased corroding area and increased magnitude of corrosion, both of which are expected to lower measured R_t values as immersion time proceeds. It was thought that a plot of of R_t versus total summed pathway area, nA, might show the same linear slope as R_{pf} values if only the substrate area, and not the magnitude of corrosion, was increasing. Divergence from this slope may then be indicative of a change in the magnitude of corrosion, which would not be

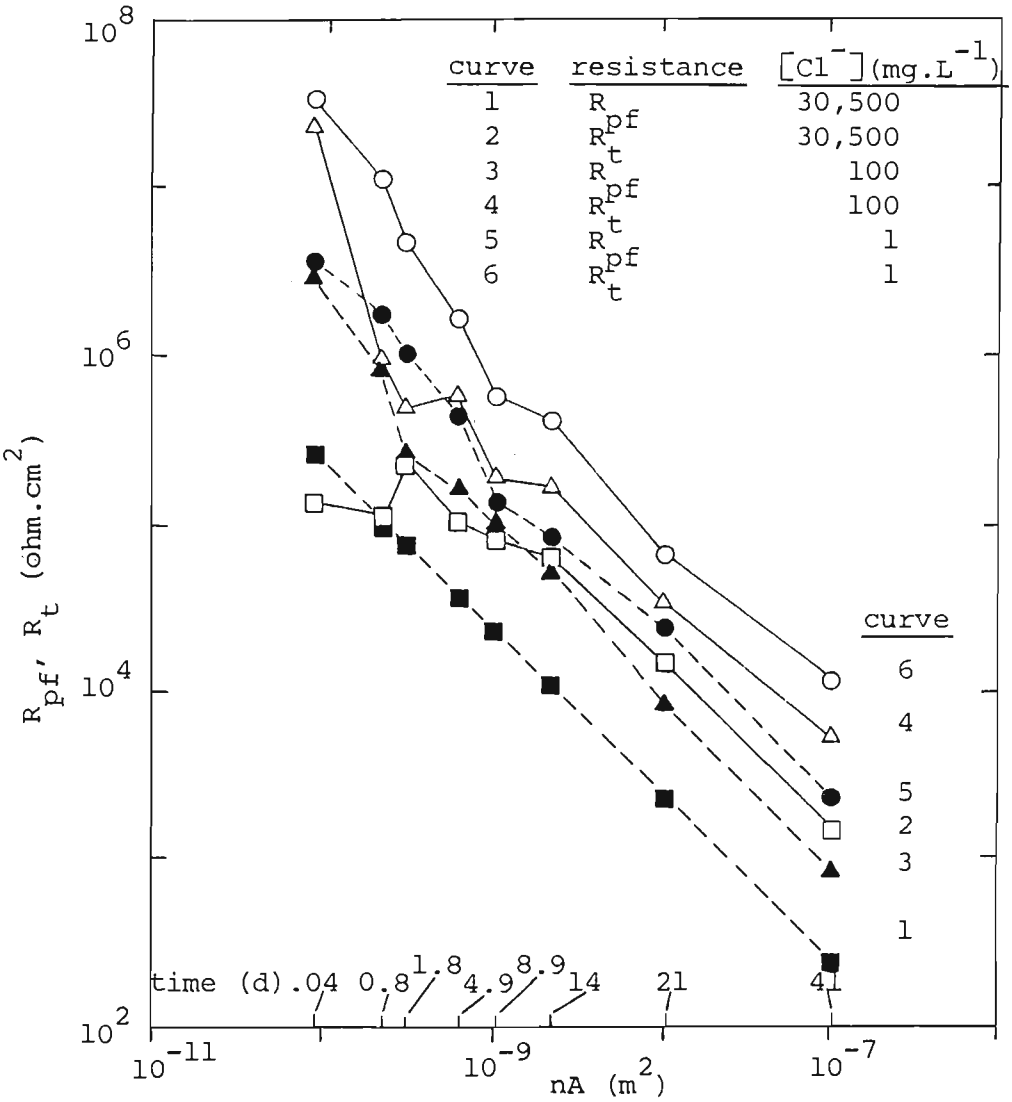

Figure R2/12. Paint film resistance, R_{pf}, (dashed lines, filled symbols) and metal charge-transfer resistance, R_t, (full lines, open symbols) for sample 407/85 in 3 measurement solutions, versus total summed pathway area, nA, corresponding to different immersion periods in 30,500 mg.L^{-1} [Cl^-] (5% NaCl) test solution.

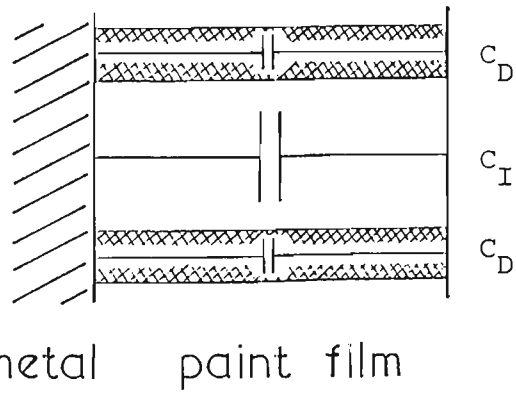

Figure R2/13. Schematic of a paint film on a metal substrate in terms of a simple equivalent electrical circuit for the paint film capacitance. C_D direct or D-type pathway areas where more rapid solution uptake occurs; C_I inverse or I-type areas for remainder of film.

expected to be linearly related to nA. A plot of R_{pf} versus nA for 5% NaCl, curve 1 of Figure R2/12, was perfectly linear. Note that the order of increasing nA values corresponds to increasing immersion times in 5% NaCl test solution, as indicated above the nA-axis. However, a plot of R_t versus nA for 5% NaCl (30 500 $mg.L^{-1}$ $[Cl^-]$) showed the same slope at high nA values, corresponding to longer immersion times, but lower slopes as nA decreased, ie at shorter immersion times, cf, curve 1 and 2. This could be due to either scatter in the results, or a real effect. Curves 3 and 4 show the R_{pf}/nA and R_t/nA plots for the 10^2 $mg.L^{-1}$ $[Cl^-]$ measurement solution, whilst curves 5 and 6 show the corresponding plots for the 1 $mg.L^{-1}$ $[Cl^-]$ solution. It can be seen that the R_t/nA plot for both these cases (curves 4 and 6), but especially for the latter solution (curve 6), has approximately the same slope as the corresponding R_{pf}/nA plot (curves 3 and 5). There is no obvious reason why the R_t/nA plot for the 5% NaCl solution (curve 2) should have a different slope at low nA to its corresponding R_{pf}/nA plot, so that the curvature in curve 2 is thought to be due to scatter in the data. If this is correct then it appears that only the substrate area increases over the immersion period in 5% NaCl and not the corrosion rate of the substrate.

5. Paint film capacitance, C_{pf}, trends

The relatively constant values of C_{pf}, except at 41 d, in Figure R2/4 suggest that the paint film capacitance is determined solely by the characteristics of the film (permittivity, thickness, cross-sectional area) and not by the solution itself or the state of degradation of the paint film.

Figure R2/13 is an extension of the very simple model of Figure R2/8, showing only the influence of paint film capacitance. Here, the small capacitor represents the capacitance of the paint film pathways, C_D, which are assumed to be direct or D-type areas of the paint film where more rapid solution

uptake occurs, according to the discussion in Section R2.1/2. The large capacitor represents the capacitance of the remainder of the paint film, C_I, assumed to be inverse or I-type areas where solution uptake has not occurred to the same extent as in D-type areas. The measured paint film capacitance, C_{pf}, will simply be given by Equation (R2/8), based on two capacitors in parallel.

$$C_{pf} = C_I + C_D \qquad \text{(R2/8)}$$

Now the capacitance of a paint film can be expressed[162] according to Equation (R2/9).

$$C = \varepsilon \varepsilon_o A/d \text{ (Farad)} \qquad \text{(R2/9)}$$

where ε = relative dielectric constant of paint film

ε_o = dielectric constant of a vacuum (8.85×10^{-12} F.m^{-1})

A = cross-sectional area of exposed sample (m^2)

d = thickness of paint film (m)

The dielectric constant at 25°C and a frequency of 1 kHz for polyesters and epoxy resins is given[185] as 3.22-4.30 and 3.63-3.67 respectively. No dielectric constant data was available for polyesters or epoxies at 50°C. A sample of ZINCALUME coated steel painted with an epoxy primer and a silicone modified polyester top coat (similar material to sample 407/85) was clamped between two brass plates, placed in a test tube containing no solution, and the test tube was immersed in a thermostatted oil bath at 50°C. A Nyquist plot was obtained which showed that the impedance of this sample in air was predominantly capacitive (curve nearly parallel to the b-axis, curving over slightly towards the a-axis at low frequencies). The value of C_{pf} was

calculated[17] from the 1 kHz value of b using $C_{pf} = 1/2\pi fb$, and the dielectric constant, ε, calculated using Equation (R2/9) to be 4.7. This is close to the above literature values and was used in subsequent calculations. The dielectric constant for water was 78.3 at 25°C and 69.9 at 50°C. Assuming solution, rather than water, is taken up by the paint film, the dielectric constant at 25°C is estimated from literature data[186] to be around 68, instead of 78.3, for 5% NaCl solution.

Using the above values, C_D and C_I can be calculated from Equation (R2/9) as follows.

$$C_I = 4.7 \times 8.85 \times 10^{-12} \times 6 \times 10^{-4}/2.5e{-}5 \quad F$$
$$= 9.98 \times 10^{-10} \text{ F for a 6 cm}^2 \text{ sample}$$
$$= 1.66 \times 10^{-10} \text{ F.cm}^{-2}$$

This value represents the capacitance of the paint film having no pathways or no solution uptake within I-type areas, and compares favourably with the value of 6×10^{-10} F.cm^{-2} obtained from Figure R2/4 for C_{pf} after 0.8 days in 5% NaCl test solution. Two values of C_D are calculated for minimum and maximum summed area of pathways, nA, taking values of nA from Figure R2/9.

$$C_{D(min)} = 68 \times 8.85 \times 10^{-12} \times 10^{-10}/2.5 \times 10^{-5} \quad F$$
$$= 2.4 \times 10^{-15} \text{ F for a 6 cm}^2 \text{ sample}$$
$$= 4.0 \times 10^{-16} \text{ F.cm}^{-2}$$
$$C_{D(max)} = 68 \times 8.85 \times 10^{-12} \times 5.63 \times 10^{-8}/2.5 \times 10^{-5} \quad F$$
$$= 1.4 \times 10^{-12} \text{ F for a 6 cm}^2 \text{ sample}$$
$$= 2.3 \times 10^{-13} \text{ F.cm}^{-2}$$

Both of these values are very small - $C_{D(min)}$ is predicted at low immersion times in 5% NaCl solution; $C_{D(max)}$ is predicted after 41 days in 5% NaCl solution. From Equation (R2/8) it is easily seen that the measured value of paint film capacitance, C_{pf}, would not be expected to be influenced by changes in nA over the immersion time history of sample 407/85 because C_D is much less than C_I. Thus the simple capacitance model of Figure R2/13 is seen to be substantially correct because it explains the relatively constant values of C_{pf} over the immersion period in 5% NaCl solution.

Again, it is easy to demonstrate that this model is oversimplified. Although the above calculations predict an increase in C_D as the number of paint film pathways increase, values of C_{pf} are calculated by Equation (R2/8) to remain unaffected as already stated. However, Figure R2/4 does show a small increase in C_{pf} values with immersion time in 5% NaCl test solution up to 21 days, and then a relatively large increase at 41 days. Examination of sample 407/85 after 41 days immersion in 5% NaCl test solution revealed that failure (see Section T1/5.4 for a discussion on failure criteria), resulted from a single paint blister which was perforated by white corrosion products. The size of this blister was about 4 mm in diameter, and thus had an area of about 1.26×10^{-5} m^2. If this value is used for nA in Equation (R2/9), C_D is calculated to be 3.0×10^{-10} F for a 6 cm^2 or 5.1×10^{-11} $F.cm^{-2}$. From Equation (R2/8), using the value of C_I calculated above, it is seen that even this value of C_D cannot explain the large increase in C_{pf} from 21 to 41 days immersion. It is more likely that the increase in C_{pf}, especially that which occurs between 21 and 41 days, is due to the influence of solution uptake in I-type areas of the paint film, which would be expected to increase the dielectric constant and hence the value of C_I. Mayne[141] indicates that the dielectric constant will rise from 4 to 18 when the paint film takes up an equal weight of water. From

Figure R2/4, C_{pf} values increase by a factor of between 1.7 and 2.3 for immersion times up to 21 days in 5% NaCl and by a factor of between 8.6 and 10.2 (using lines of best fit) after 41 days. If this increase is solely due to an increase in the dielectric constant, then the dielectric constant would have risen to between 8.0 and 10.8 for times up to 21 days, and between 40.4 and 47.9 at 41 days. These values for increase in the dielectric constant are perfectly reasonable compared to the above calculations by Mayne[141], and thus, could indicate that solution is taken up by areas of the paint film other than the D-type pathways.

The small upward slope in C_{pf} as chloride ion concentration decreased for the $C_{pf}/[Cl^-]$ plot in Figure R2/4, and the higher values of C_{pf} in 5% NaCl solution, cannot be explained.

6. Metal substrate double layer capacitance, C_d, trends

From Figure R2/5 there do not appear to be any apparent trends of C_d with immersion time in 5% NaCl test solution or with concentration of the measurement solution. This is somewhat surprising, firstly because the comparable set of results for the gloss sample series in Section R2.2/1.2 show a rise with immersion time, and secondly, if the number of paint film pathways, nA, increase with immersion time in 5% NaCl solution, then more of the substrate area becomes exposed to the solution via the pathways, see Section R2.1/4. As the capacitance of a bare substrate is something of the order of 20 $\mu F.cm^{-2}$, the value of C_d would be expected to increase towards this value as more of the substrate area becomes exposed. Perhaps scatter in the data shields a small rising trend with time.

7. Attached/free film comparisons

The free film samples referred to are described in Table E3/1 Section E3.1/2. These were free films made up of different combinations of primer and top coat. A description of the U-cell used for the full frequency range tests is given, along with the solutions used in Section E3.1/2.

The aims of this section were:

1. to see if the Nyquist or Bode impedance plots could distinguish the primer from the top coat, or identify the cause of frequency dispersion so often seen with immersed painted metals
2. to determine whether free film combinations of primer and top coat were predominantly D- or I-type films
3. to compare the impedance results of free films with those for attached films.

It was observed that single top coat films would sometimes have uncharacteristically low impedance values on testing in the U-cell. This was found due to the existence of small pinholes (holidays) in the films, observed by the naked eye by holding the film up to the light. The samples discussed below had no pinholes visible to the naked eye.

Two-coat combinations of primer and top coat would be expected to have a much lower probability for the existence of pinholes and were therefore used as much as possible, rather than single primer (which could not be cast) or single top coat samples. For example, a 2 x 10 μm dual top coat sample was preferable to a 1 x 20 μm single top coat sample. Nyquist plots of a versus b

were always close to either a semicircle or the arc of a semicircle, depending on whether the frequency scan had proceeded to sufficiently low frequencies to complete the semicircle. The angle of depression of the semicircle, α, was always less than 6°. There was no essential difference in Nyquist plot shape between a top coat/primer free film and just a top coat free film. This indicates that the shape of a Nyquist plot can not distinguish features of a primer from those of a top coat. Although angle α is fairly small compared to that typically obtained for attached film samples, no special significance can be made regarding the cause of frequency dispersion because other free film samples, eg 25% gloss 2 x 10 μm SMP in Section R2.2/3.2 gave α values up to 18°.

The Nyquist semicircles were analyzed by the methods outlined in Section T1/5 to give paint film resistance, R_{pf}, and capacitance, C_{pf} for the three chloride ion solutions. The effect of solution concentration on these parameters after about 1 hour immersion is shown in Figure R2/14 for three free film types. The general trend is for R_{pf} values to decrease with increasing chloride ion concentration. This was attributed in Section R2.1/2 to the existence of D-type areas in the paint film or areas of lower resistance where more rapid solution uptake occur.

The values of C_{pf} in Figure R2/14b are relatively constant with solution chloride ion concentration. This was explained for attached films in Section R2.1/5, but is summarized here for free films. The area of the D-type pathways in the film are very small compared to the remaining areas of the film, and do not greatly contribute to the overall measured capacitance, C_{pf}, even though the dielectric constant in these pathways would be expected to change with solution concentration, thus affecting the capacitance of the

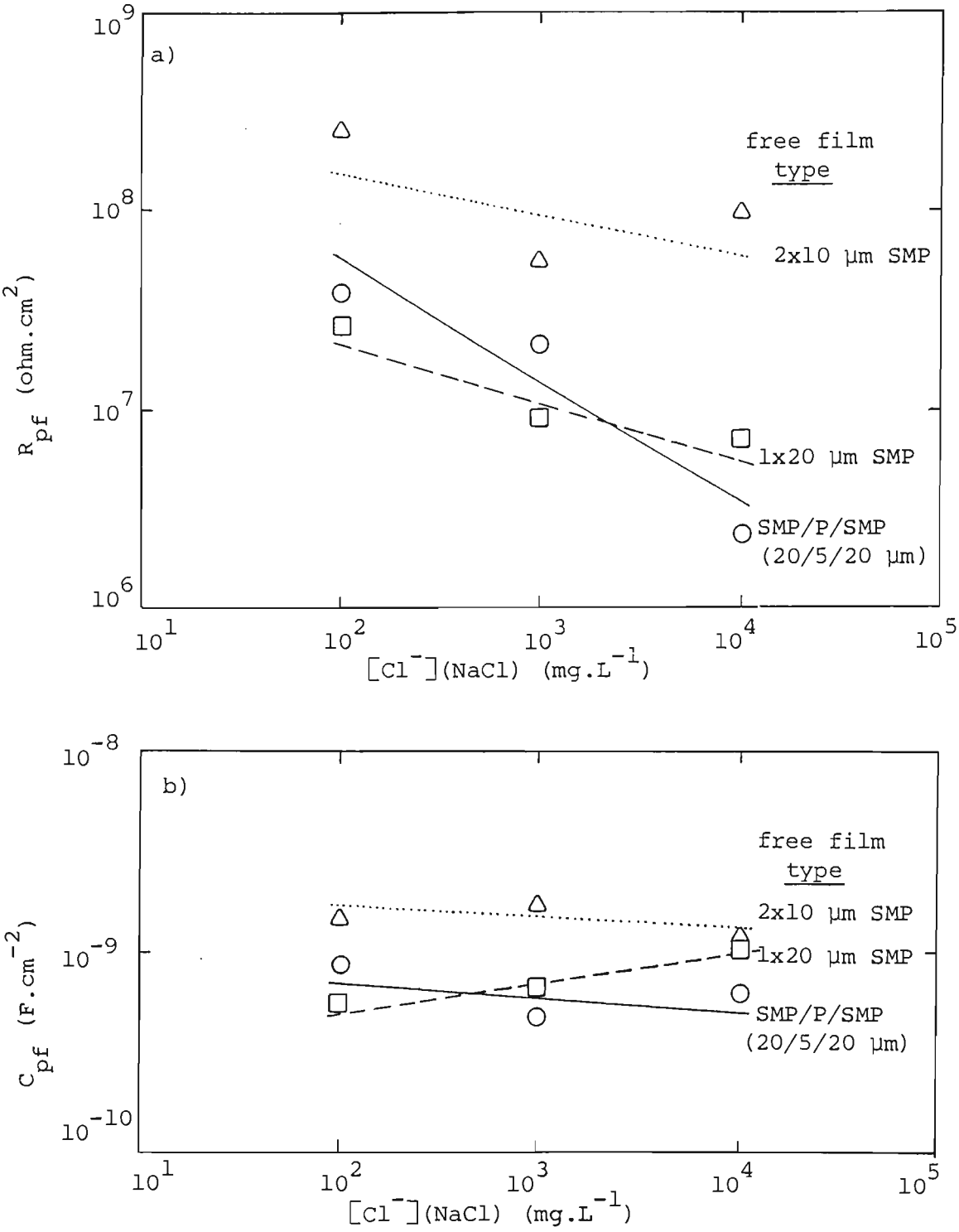

Figure R2/14. Effect of solution chloride ion concentration on paint film resistance, R_{pf}, (Figure R2/14a), and capacitance, C_{pf}, (Figure R2/14b), for various combinations of free films after 1 h immersion. SMP silicone modified polyester top coat; P primer, nominal film thicknesses shown.

pathways themselves.

It is worthwhile comparing the attached film results obtained in Sections R2.1/2,4-6 with the above free film measurements.

Firstly, the value of C_{pf} in Figure R2/14b is about 1 $nF.cm^{-2}$ for each free film type, which is about the same as values of C_{pf} obtained on attached films in Figure R2/4 Section R2.1/1. This is significant, because the values of the metal's double layer capacitance, C_d, are an order of magnitude higher in Figure R2/5 Section R2.1/1. This provides evidence, see also Section R2.2/1.2, that the interpretation of the equivalent circuit model in Section R2.1/1 is correct, that is, the high frequency Nyquist semicircle, eg in Figure R2/1, contains paint film information (and not metal substrate information).

Secondly, Figure R2/2 shows the effect of measurement solution chloride ion concentration on R_{pf} values for a single top coat 20 μm SMP free film (dashed line) compared to attached film results (full lines), previously discussed in Section R2.1/2. The free film sample shows approximately the same downward slope in R_{pf} with increasing solution concentration, indicative of the presence of D-type film areas, as already discussed above.

1. Attached films - impedance results

The paint formulations referred to are described in Section E3.2/1. The painted metal samples refer to Section E3.2/2.1. Solutions used, and test conditions for, these samples are described in Sections E3.2/4.1,4.2 respectively.

The two main aims of this section were to investigate the effects of different amounts of flatting agent in the paint film top coat (as indicated by gloss level, refer Section E3.2/1), and different solution chloride ion concentrations.

1.1 Single frequency test

Because of the large number of samples (32), it is not convenient to reproduce graphs of the effect of immersion time on the resistive, a_{flk}, and capacitive, c_{flk} ($=1/2\pi f b_{flk}$), components of impedance for each paint film gloss level in each chloride ion solution. Instead, Figure R2/15 is a typical example of a_{flk} and c_{flk} versus immersion time for the three solutions. From such graphs, the following information was obtained for each sample-performance life, assessed by the failure times, $t_{f,R}$ and $t_{f,C}$ and their average, t_f, see Section T1/5.4 on failure criterion; initial 1 kHz capacitance extrapolated to zero time, $C_{m,0}$; and the 1 kHz capacitance, $C_{m,2h}$ and $C_{m,1d}$, at immersion times of 2 h and 1 d respectively. This data is tabulated in Table R2/1. Using the Brasher and Kingsbury formula[153], see Section T6/8, the percentage volume of water taken up by the paint film, $X_{v,2h}$ and $X_{v,1d}$, was calculated at 2 h and 1 d respectively, and is also shown in Table R2/1. The data in this table was subjected to statistical analysis, and is reported in two parts - effects on water uptake, and effects on time to sample failure.

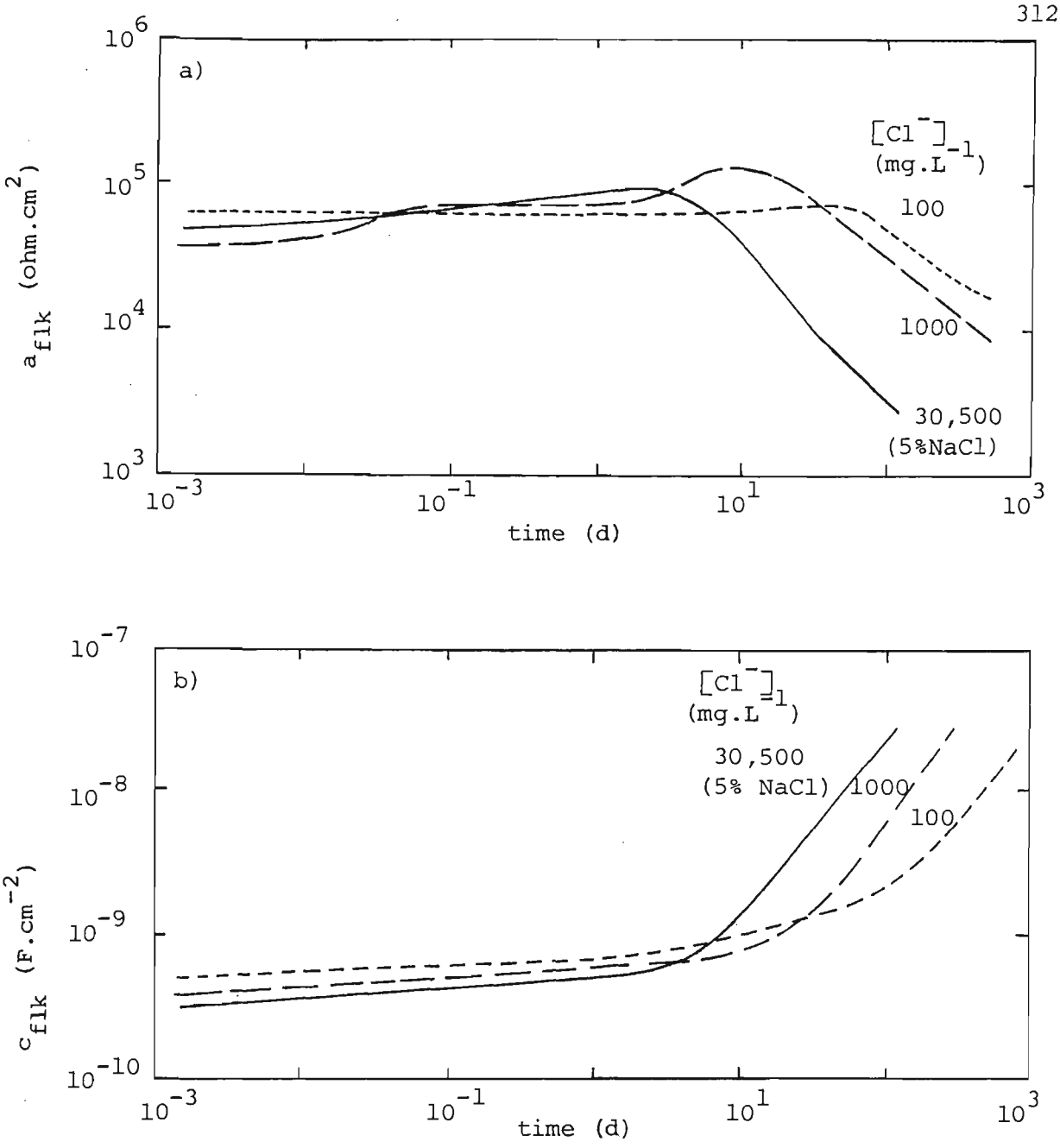

Figure R2/15. Effect of immersion time in different chloride ion solutions at 50C on resistive, a_{flk}, (Figure R2/15a), and capacitive, c_{flk}, (Figure R2/15b), components of impedance for a 25% gloss SMP/ZINCALUME sample.

Table R2/1 Gloss Series Attached Films – Single Frequency Impedance Test Results

Sample number	Solution mg.L^{-1} [Cl$^-$]	Gloss level	Pthk (um)	$C_{m,0}$ (nF.cm^{-2})	$C_{m,2h}$ (nF.cm^{-2})	$C_{m,1d}$ (nF.cm^{-2})	$X_{v,2h}$ (% v/v)	$X_{v,1d}$ (% v/v)	$t_{f,R}$ [3] (d)	$t_{f,C}$ [3] (d)	$\overline{t_f}$ [3] (d)
1	30,500	25	5	.379	.429	.547	2.83	8.37	65	10.8	37.9
2[4]	(5% NaCl)	25	5	.353	.405	.537	3.14	9.57	29	10	19.5
3		25	5	.377	.445	.551	3.78	8.66	33	10	21.5
4[4]		50	2	.452	.584	.878	5.85	15.15	89	41	65
5		50	2	.428	.545	.870	5.51	16.19	160	52	106
6[4]		85	4	.337	.393	.533	3.51	10.46	51	8.7	29.9
7		85	4	.337	.383	.839	2.92	20.82	53	11.0	32
8		85	4	.334	.382	.755	3.06	18.61	26	3.3	14.7
9		85	4	.354	.420	.522	3.90	8.86	57	8.7	32.9
10		85	2	.433	.56 [1]	1.10	5.87	21.28	104	12	58
11	1000	25	2	.490	.636	.782	5.95	10.67	370 [6]	260 [6]	315 [6]
12		25	2	.480	.618	.684	5.77	8.08	450 [6]	410 [6]	430 [6]
13[4]		25	5	.394	.499	.615	5.39	10.16	280 [6]	220 [6]	250 [6]
14		25	5	.430	.540	.658	5.20	9.71	310 [6]	250 [6]	280 [6]
15		25	5	.343	.420	.527	4.62	9.80	240 [6]	230 [6]	235 [6]
16		25	5	.395	.49 [1]	.591	4.92	9.20	320 [6]	330 [6]	325 [6]
17		25	5	.343	.433	.515	5.32	9.28	295 [6]	300 [6]	297 [6]
18		50	2	.430	.54 [1]	.655	5.20	9.60	270 [6]	330 [6]	300 [6]
19		50	2	.410	.528	.644	5.77	10.30	440 [6]	360 [6]	400 [6]
20		50	2	.470	.600	.725	5.57	9.89	370 [6]	340 [6]	355 [6]
21		85	2	.440	.548	.668	5.01	9.53	200 [6]	300 [6]	300 [6]
22		85	2	.440	.575	.693	6.11	10.37	300 [6]	320 [6]	310 [6]
23[4]	100	25	2	.422	.561	.623	6.50	8.89	430 [6]	420 [6]	425 [6]
24		25	2	.494	.623	.762	5.29	9.89	350 [6]	540 [6]	445 [6]
25		25	2	.508	.65 [1]	.739	5.63	8.55	380 [6]	450 [6]	415 [6]
26		25	2	.476	.606	.687	5.51	8.37	350 [6]	450 [6]	400 [6]
27		25	2	.470	.603	.684	5.69	8.56	290 [6]	500 [6]	395 [6]
28		50	2	.445	.561	.65 [1]	5.30	8.60[2]	280 [6]	410 [6]	345 [6]
29		50	2	.434	.562	.64 [1]	5.90	8.86[2]	300 [6]	400 [6]	350 [6]
30		50	2	.430	.536	.63 [1]	5.03	8.72[2]	310 [6]	450 [6]	380 [6]
31[4]		50	2	.400	.490	.55 [1]	4.63	7.27[2]	310 [6]	500 [6]	405 [6]
32		50	2	.454	.621	.86 [1]	7.15	14.58[2]	3 [5]	3 [5]	3 [5]

Notes:

1 values are not data points but are obtained by extrapolation
2 calculated values based on some approximation and may not be accurate
3 failure criterion, $t_{f,R}$, $t_{f,C}$, taken as time for a_{f1k}, c_{f1k} to fall, rise to 10^4 ohm.cm^2, 10 nF.cm^{-2} respectively
4 indicates both 1 kHz and wide frequency range tests carried out on sample
5 sample failed prematurely
6 sample fail time estimated (not yet failed)

Explanation of Symbols

pthk	primer thickness
$C_{m,0}$	1 kHz capacitance extrapolated back to zero time from readings of $C_{m,2h}$ or $C_{m,1d}$ taken in first 15 or 20 minutes of immersion
$C_{m,2h}$,$C_{m,1d}$	1 kHz capacitance measured after 2 h, 1 d sample immersion, respectively
$X_{v,2h}$,$X_{v,2d}$	water uptake (% v/v) calculated using the Brasher and Kingsbury[153] equation for samples immersed 2 h, 1 d, respectively
$t_{f,R}$,$t_{f,C}$	sample fail time (d) based on 1 kHz resistance, capacitance failure criteria, respectively – see note 3
$\overline{t_f}$	average sample fail time (d) [$\overline{t_f} = (t_{f,R} + t_{f,C})/2$]

1.1.1 Effect of [Cl^-] on water uptake

A negative correlation, ($r = -0.62$), was obtained between calculated water uptake at 2 h, $X_{v,2h}$, and the logarithm of the solution chloride ion concentration, which was significant at the 99% level of confidence. A positive correlation, ($r = 0.52$), was obtained for the water uptake at 1 d case, $X_{v,1d}$, which was also significant at the 99% level of confidence. These results show that water uptake after 2 h is high at low solution chloride ion concentration, but that water uptake after 1 d is high at high chloride concentration. Clearly, a discrepancy exists. A thorough examination of all the capacitance/time curves revealed that in certain cases for the 5% NaCl solution, the capacitance at 1 d was at the start of the sharply rising portion of the curve, see Figure R2/15b for a typical curve shape. This did not occur for the 1000 or 100 $mg.L^{-1}$ [Cl^-] solutions. Brasher and Nurse[7] consider the sharp capacitance rise is caused by a reorientation in the mode of distribution of water within the paint film, probably by a linking together of water droplets, which in certain cases can precede visible breakdown of the paint film. The sharp capacitance rise in sea water has also been attributed to the much larger values of capacitance of bare substrate areas exposed to solution during paint breakdown[6,7,187]. However, such rises also occur in U-cell free film tests at 50°C, see Section R2.2/3.1, where an alternative explanation is discussed - that of degradation of the paint film. In any case, it is inappropriate to calculate water uptake using Equation (T6/1) in Section T6/8 from a portion of the capacitance/time curve where more than just random water uptake by the paint film is occurring. The positive correlation between 1 d water uptake and solution concentration must therefore be carefully interpreted. This subject is further discussed in Section R2.2/6.

The effect of primer thickness was also analyzed statistically using ten data points at 5% NaCl solution (sample numbers 1-10). Negative correlations (r = -0.77, -0.91) were obtained for $C_{m,0}$/primer thickness and $X_{v,2h}$/primer thickness respectively, which were significant at the 99% level of confidence. This suggests firstly, that initial capacitance is inversely related to primer thickness, which would be expected from Equation (R2/9) in Section R2.1/5, and secondly, that water uptake after 2 h is inversely related to primer thickness. No correlation could be found between $C_{m,0}$ and either top coat thickness or total thickness. This suggests that increases in primer thickness is more important for reducing water uptake than increases in top coat thickness.

The data set in Table R2/1 was also analyzed using the general linear model procedure, which is described along with the statistical results, in Section A4/3.1. The results obtained were not entirely satisfactory because of an accidental correlation between independent variables log chloride/primer thickness and also log chloride/gloss. However, the strong correlation noted above was again obvious between 2 h water uptake and primer thickness. A correlation between 2 h water uptake and gloss could not be resolved and the coefficients in the general linear Equation (A4/28) were not sufficiently accurate. Eliminating all samples with a primer thickness other than 2 µm (to eliminate the effect of primer thickness) did not show any significant correlations with water uptake. Eliminating gloss as a variable from the data set was more satisfactory, and is justified on the basis that no correlation could be found. All samples in the data set were therefore treated as if they had the same gloss level. A general linear model equation was obtained in this case with coefficients that were significantly different from zero, see Equation (A4/29), which is reproduced below.

$$X_v = 7.24 - 0.374 \log \text{chloride} - 0.355 \text{ primer thickness} \quad \text{(A4/29)}$$

where X_v = 2 h water uptake (% v/v)

The confidence limits on the coefficients in Equation (A4/29) were satisfactory for the intercept but were of the same order as the coefficient itself for log chloride and primer thickness so the fit of this equation to the data set was not good. This equation predicts that 2 h water uptake will increase as solution chloride ion concentration and primer thickness decrease, and is shown plotted as water uptake at 2 hours versus solution chloride ion concentration in curve 2 of Figure R2/45, Section R2.2/5.1.2. The effect with chloride is in agreement with the results of Brasher and Nurse[7] for a different paint system; in agreement with the gravimetric results on attached films in Section R2.2/2; and in agreement with the gravimetric results on free films in Section R2.2/4.

1.1.2 Effect of $[Cl^-]$ on sample failure

The 32 sample data set from Table R2/1 was statistically analyzed using the general linear model procedure described in Appendix A4/1.1. The statistical results for sample failure times appear in Tables A4/20-22, Section A4/3.2.

The discussion in Section A4/3.2 indicates a strong negative correlation between all three sample failure time estimates, $t_{f,R}$, $t_{f,C}$, $\overline{t_f}$ and log solution chloride, indicating that fail times increase as log chloride decreases. This is expected behaviour in agreement with previous results[127], also shown in Figure T6/4, Section T6/5, and with outdoor exposure tests which show time to degradation is related to distance from the ocean surf, as discussed in Section T6/5. Results for the wide frequency range test in Figure R2/31 Section

R2.2/1.2 also support the above conclusions. Plots of $t_{f,R}$, $t_{f,C}$, $\overline{t_f}$ versus $[Cl^-]$ appear in Figure R2/16a-c. Both data points and regression lines, Equations (A4/30-32), Section A4/3.2, are shown. The general linear model Equation (A4/31), representing the $t_{f,C}$ data in Table R2/1 and relating $t_{f,C}$ to log chloride is shown plotted in curve 1, Figure R2/47, Section R2.2/5.2.

The fact that both 2 h water uptake, $X_{v,2h}$, refer Section R2.2/1.1.1, and also curve 2, Figure R2/45 in Section R2.2/5.1.2), and failure times, $t_{f,R}$, $t_{f,C}$, $\overline{t_f}$ are negatively correlated with log chloride, Table A4/20, Section A4/3.2, is interesting. This indicates that initial 2 h water uptake is lowest for the strongest chloride solutions in which attached film samples break down the fastest, an apparent paradox. The following explanation is offered. Water is initially taken up faster for solutions low in chloride. However in strong chloride solutions other processes, such as reorientation of the mode of water uptake and/or degradation of the paint film occur, as discussed in Sections R2.2/1.1.1 and R2.2/3.1.1. Evidence for these other processes is the finding in Section R2.2/1.1.1 that calculated water uptake at 2 h is negatively correlated with solution chloride, but water uptake at 1 d is positively correlated. This is discussed further in Section R2.2/6.

1.2 Wide frequency range test

Fifteen of the 42 samples listed in Table E3/5, Section E3.2/4.2, had wide frequency range tests performed over their immersion period. These samples are indicated by note 4 next to the sample number in Table R2/1, or are indicated by 1 or 2 asterisks in Table E3/5. This has resulted in over 150 Nyquist plots of resistive, a, versus reactive, b, components of the painted metal/solution interface. This is too much data to present as Nyquist plots,

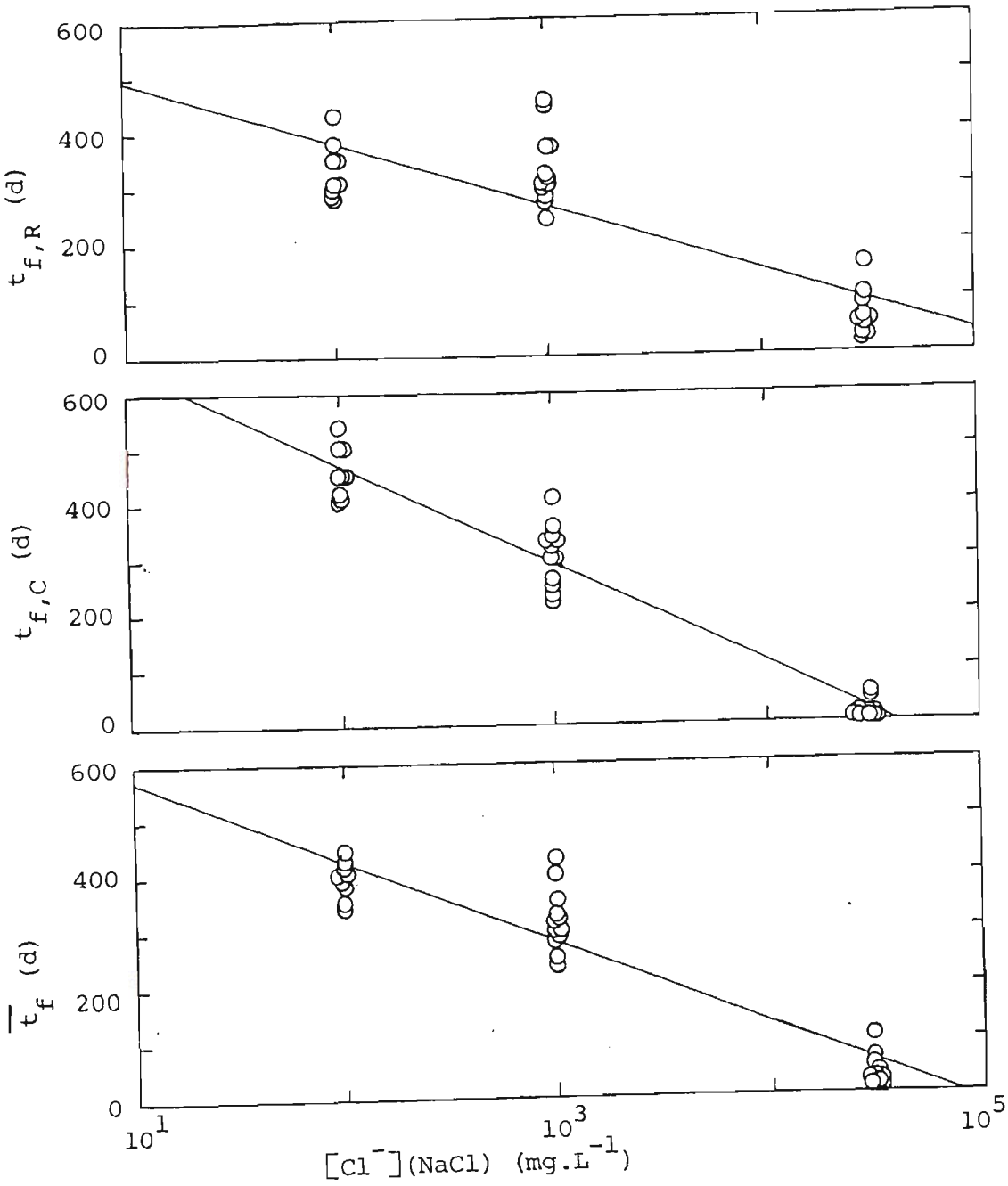

Figure R2/16. Effect of solution chloride ion concentration on sample failure time for gloss/flatting agent series tested by the single frequency method. $t_{f,R}$, $t_{f,C}$ sample fail times based on 1 kHz resistance, capacitance to fall, rise to 10^4 ohm.cm^2, 10 nF.cm^{-2}, respectively. t_f is average of $t_{f,R}$ and $t_{f,C}$.

and only the results from these plots will be presented. Figure R2/1 from Section R2.1/1 is reasonably typical of this series, but the plot shape altered considerably with both immersion time and solution chloride ion concentration. For a description of this Nyquist plot see Sections R2.1/1 and T1/4,5. The low frequency tail, giving information about the diffusion of species within the paint film, was not very well developed at the lowest measured frequency of 1 Hz for the present series, and no attempt has been made to obtain diffusion parameters. Analysis of the Nyquist plots was not always straightforward, as it was sometimes difficult to fit two semicircular arcs, corresponding to paint film and metal substrate information. Especially at longer immersion times, the two well defined Nyquist semicircles merged into one making it difficult to separate R_{pf} and R_t, as discussed in Section T1/5.1. Calculation of C_{pf}, C_d at these times could not be made under these circumstances. This has inevitably led to a large degree of scatter in some of the equivalent circuit parameter values.

Plots of R_{pf}, R_t, C_{pf} and C_d versus time are shown in Figures R2/17-28, for each of the three gloss levels and three solutions. It is obvious from these plots that no effect of gloss level can be detected in any of the parameters R_{pf}, R_t, C_{pf} or C_d, indicating that different levels of flatting agent in the paint film top coat has little, if any, effect. It is also clear that the shape of each plot is similar in all three solutions, but the position of the curve may alter as solution chloride ion concentration changes. For example, the position of the R_{pf}/t curves shifts to lower values of R_{pf} as solution concentration increases.

A summary graph (mean line estimated by eye from Figures R2/17-20 and plotted up to 60 days) of the effect of immersion time, plotted on a linear

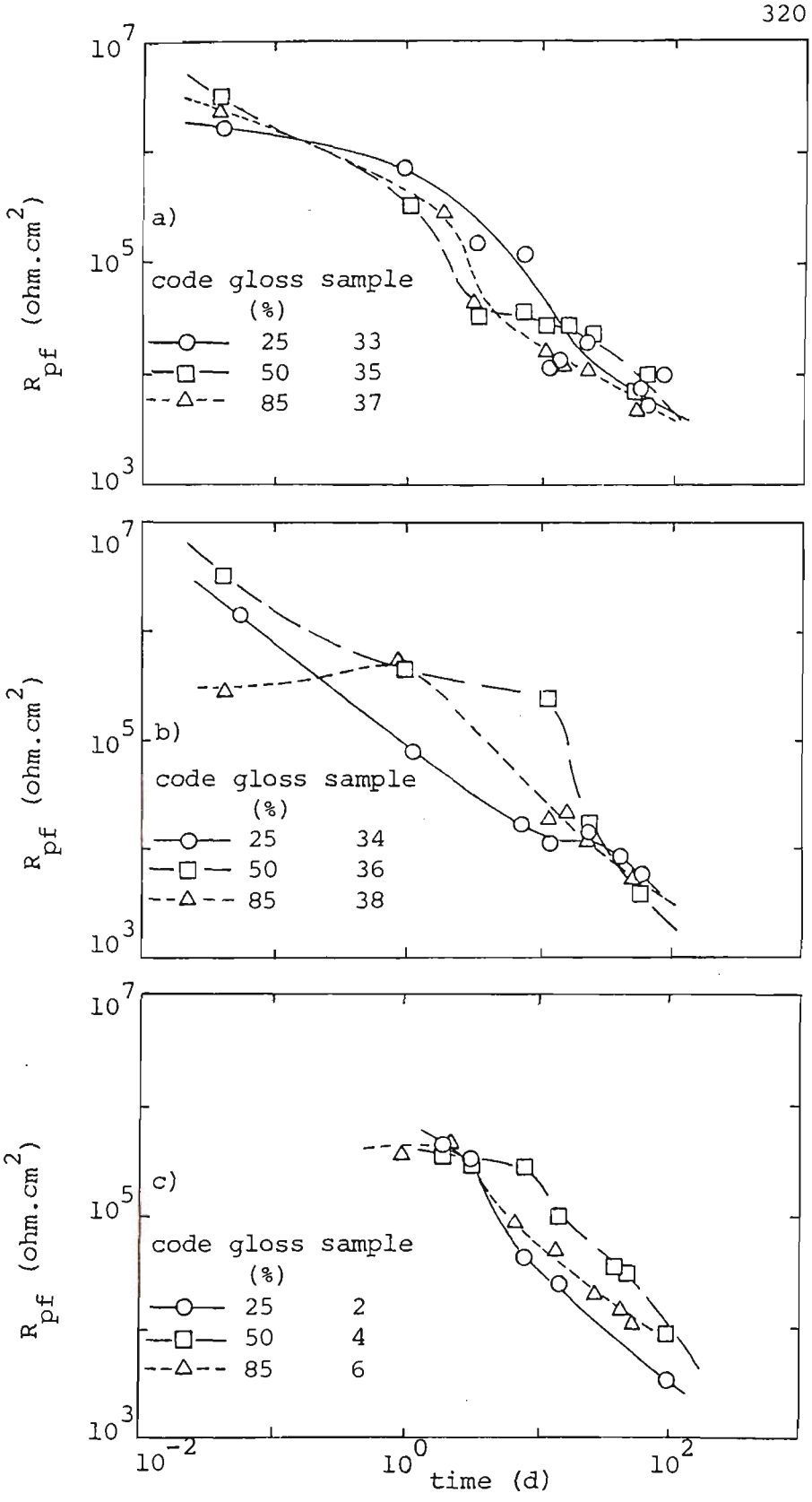

Figure R2/17. Effect of immersion time in 5% NaCl solution at 50°C on paint film resistance, R_{pf}, for SMP/ZINCALUME samples having 25,50,85% gloss level in SMP top coat, as indicated.

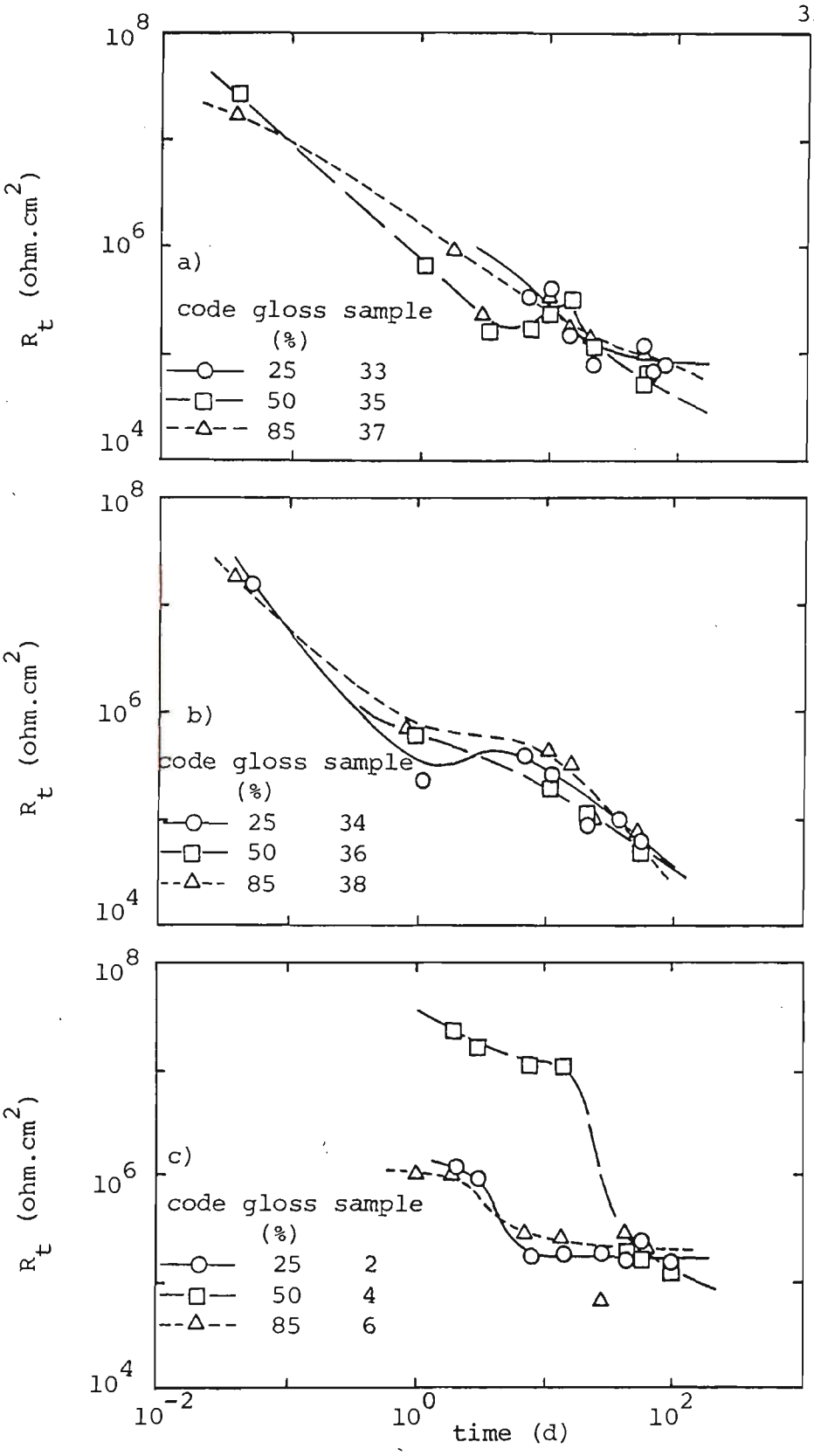

Figure R2/18. Effect of immersion time in 5% NaCl solution at 50°C on metal charge-transfer resistance, R_t, for SMP/ZINCALUME samples having 25,50,85% gloss level in SMP top coat, as indicated.

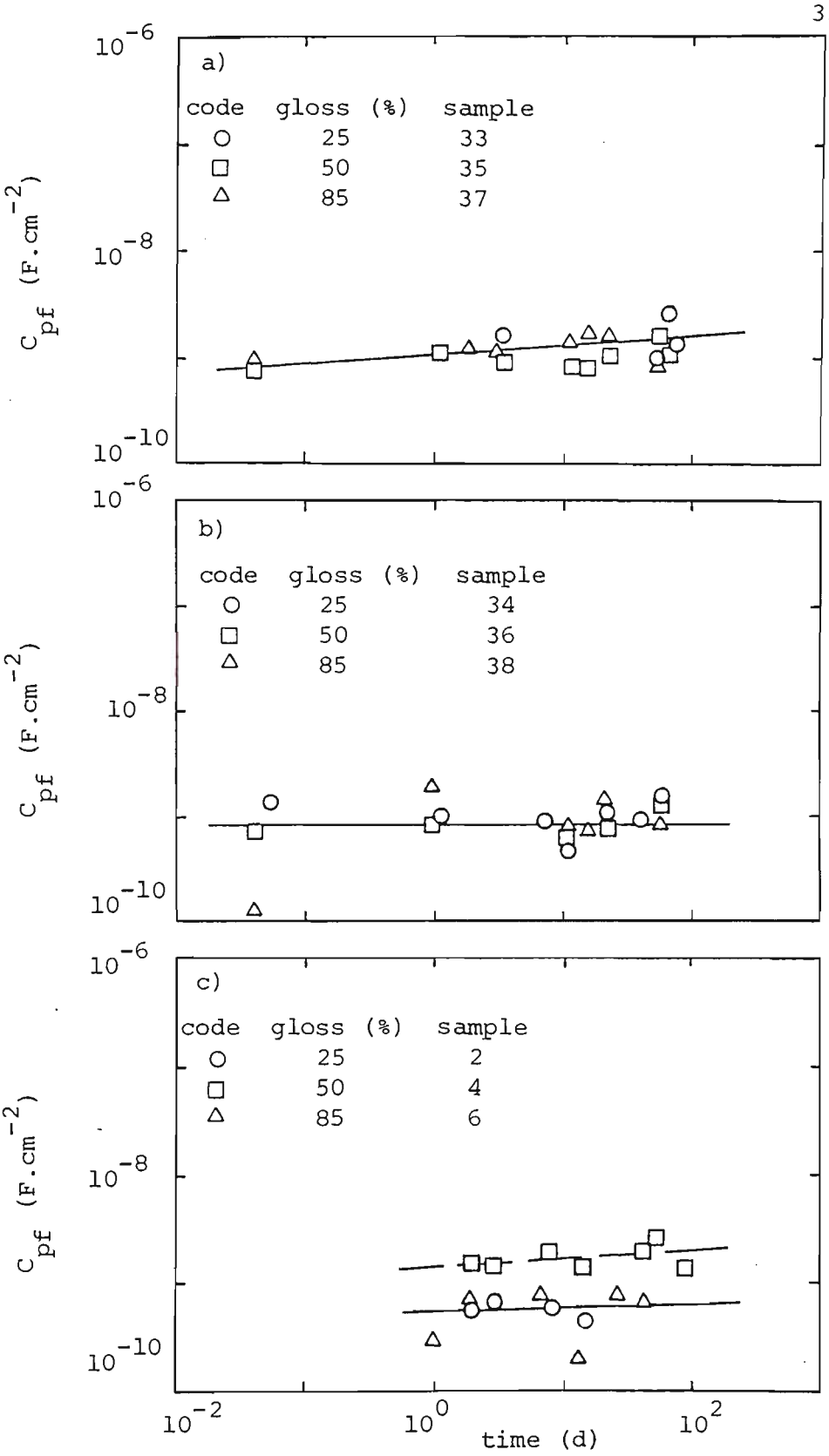

Figure R2/19. Effect of immersion time in 5% NaCl solution at 50°C on paint film capacitance, C_{pf}, for SMP/ZINCALUME samples having 25,50,85% gloss level in SMP top coat, as indicated.

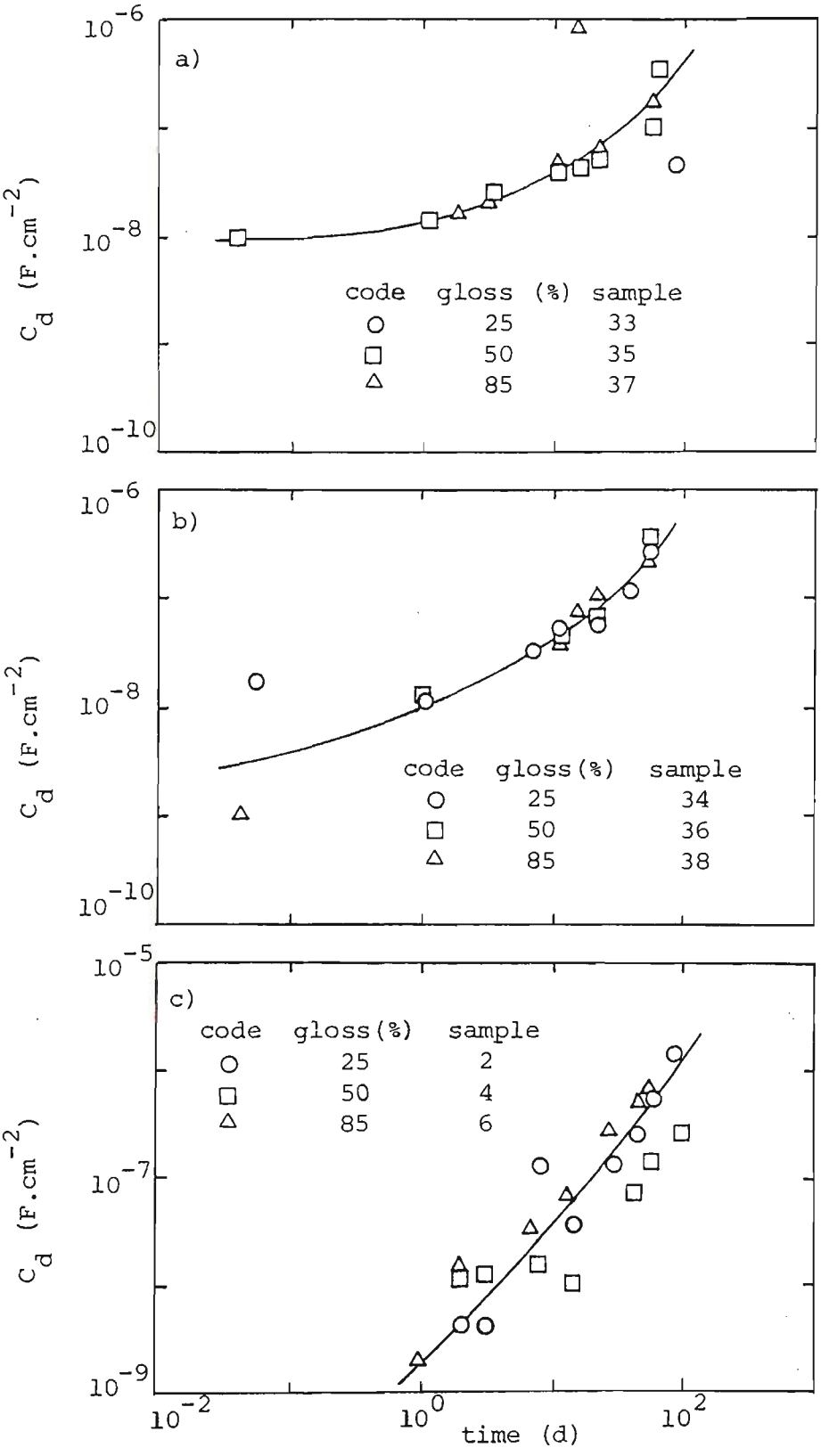

Figure R2/20. Effect of immersion time in 5% NaCl solution at 50°C on metal double layer capacitance, C_d, for SMP/ZINCALUME samples having 25,50,85% gloss level in SMP top coat, as indicated.

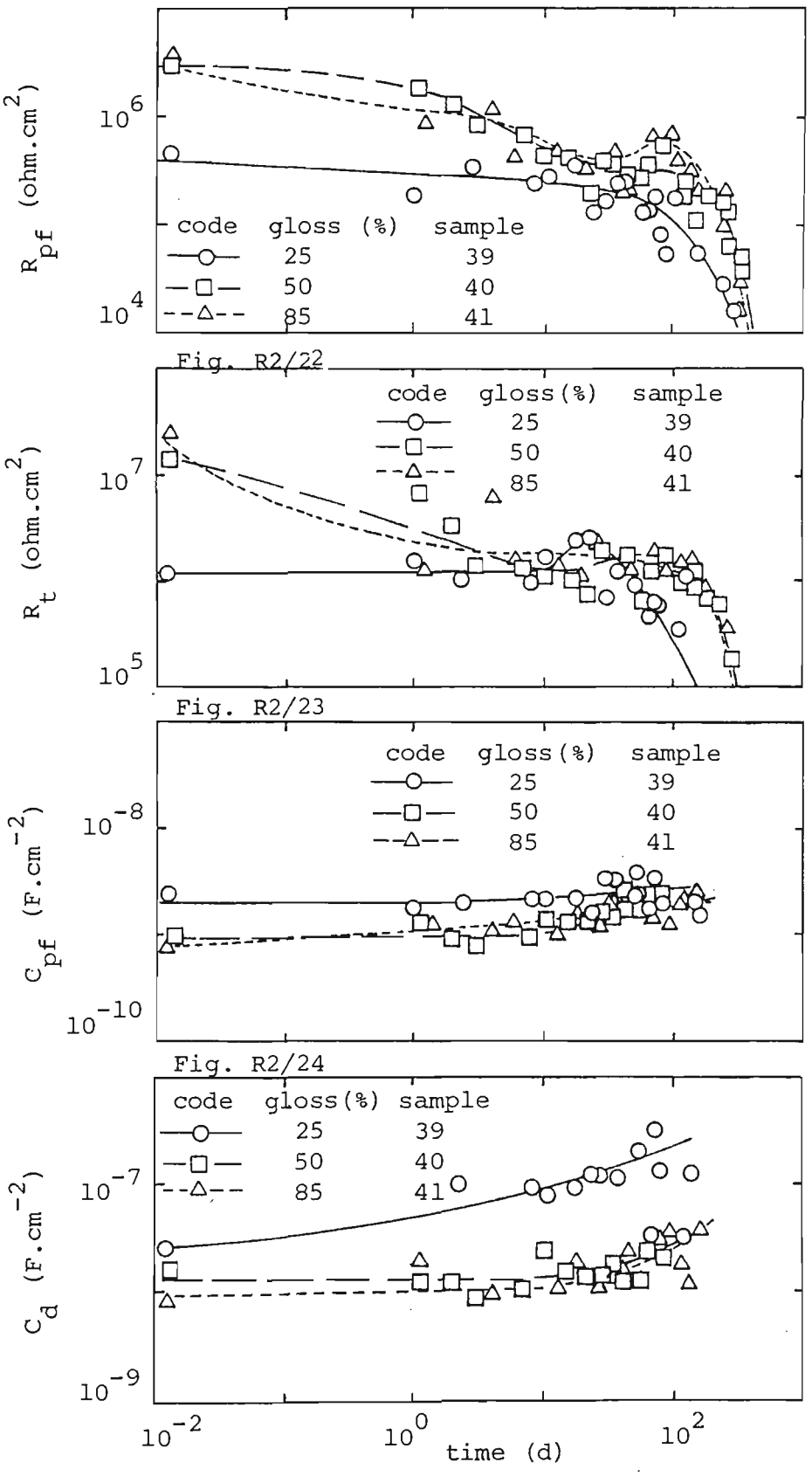

Figures R2/21-24. Effect of immersion time in 1000 mg.L^{-1} [Cl$^-$] (NaCl) solution at 50°C on paint film resistance, R_{pf}, (Fig. R2/21), metal charge-transfer resistance, R_t (Fig. R2/22), paint film capacitance, C_{pf}, (Fig. R2/23), and metal double layer capacitance, C_d, (Fig. R2/24), for SMP/ZINCALUME samples having 25,50,85% gloss level in SMP top coat, as indicated.

Fig. R2/25

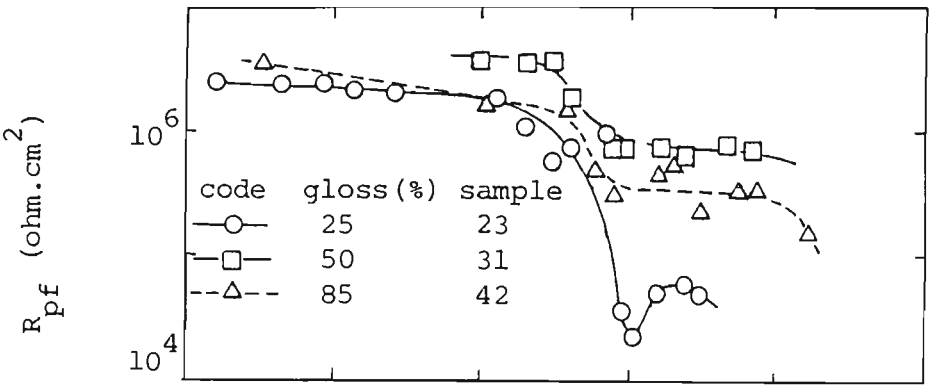

Fig. R2/26

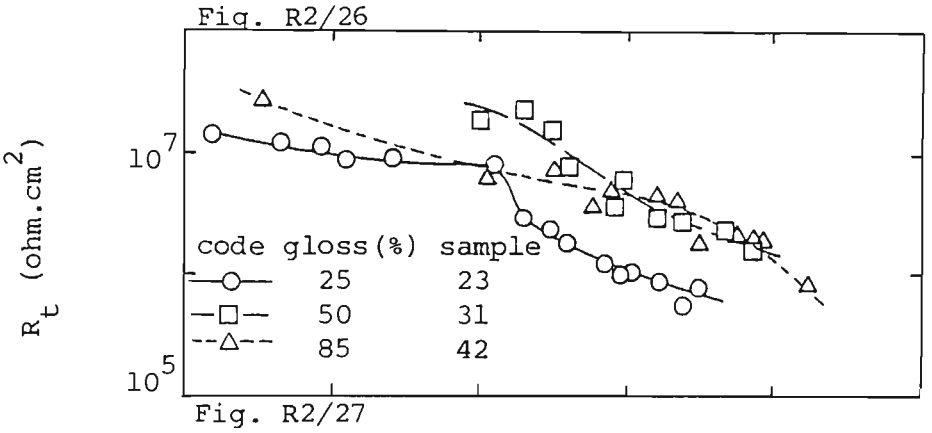

Fig. R2/27

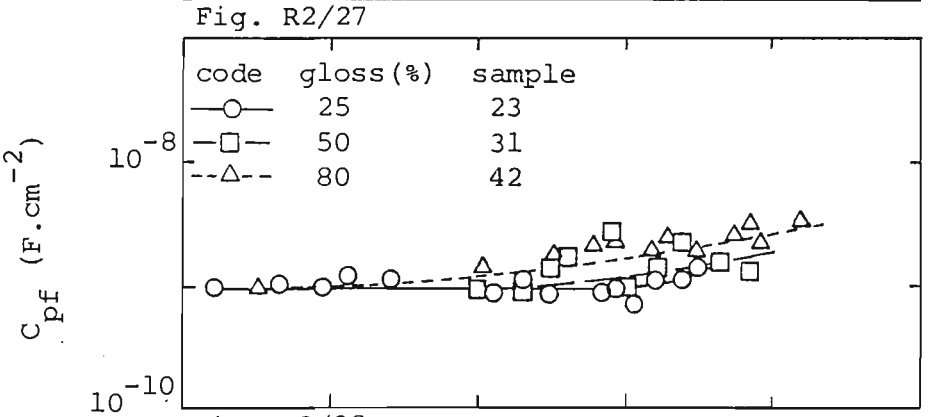

Fig. R2/28

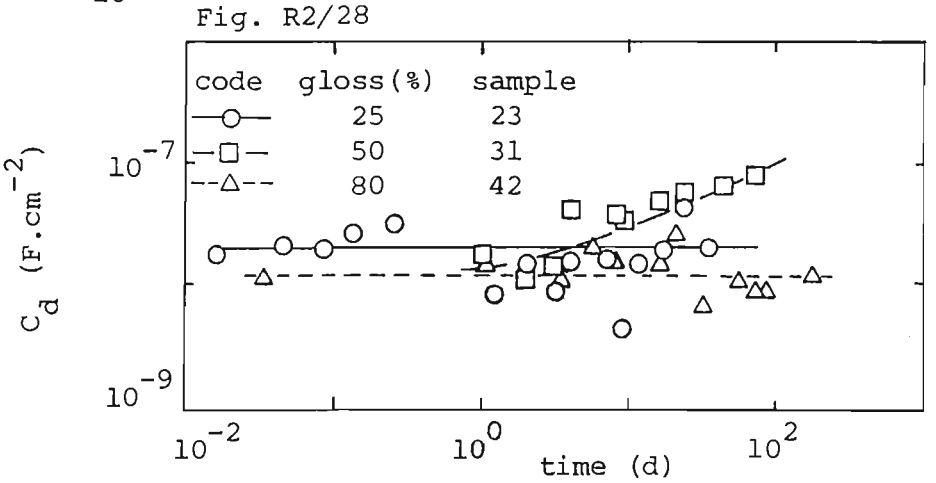

Figures R2/25-28. Effect of immersion time in 100 mg.L$^-$ [Cl$^-$] (NaCl) solution at 50°C on paint film resistance, R_{pf}, (Fig. R2/25), metal charge-transfer resistance, R_t, (Fig. R2/26), paint film capacitance, C_{pf}, (Fig. R2/27), and metal double layer capacitance, C_d, (Fig. R2/28), for SMP/ZINCALUME samples having 25,50,85% gloss level in SMP top coat, as indicated.

scale, on each of these parameters is shown in Figure R2/29 for the 5% NaCl solution, but which is reasonably typical of all three solutions, except that the trends occur at different times. Values of R_{pf}, R_t decrease markedly with immersion time, with R_{pf} values being lower than R_t. By comparison, values of C_{pf} are relatively more constant, but values of C_d show an increase with time. The marked drop off in R_{pf} values with time is characterized by a fast initial fall over the first five days or so, followed by a slower rate of decline. The rate of fall is related to the solution chloride ion concentration, with the largest drop occurring for the highest chloride solution, compare Figures R2/17,21,25. From the discussion in Section R2.1/2, it is believed that the value of R_{pf} at a given time is indicative of the state of degradation of the paint film caused by solution ingress via pathways through the film. The decrease in R_{pf} with time is then explained by more and more pathways opening up through the film with immersion time. The fact that the rate of fall of R_{pf} increases with solution concentration therefore indicates that paint degradation increases as solution chloride ion concentration is increased. The amount of flatting agent in the top coat is apparently much less important to painted metal degradation than solution concentration. These conclusions were also determined by the single frequency test results in Section R2.2/1.1.2. The slower rate of decline in R_{pf} values at times longer than about five days may be caused by the linking up of adjacent pathways to form a more conductive path through to the substrate, rather than just more pathways opening up, as is thought to be the case at lower times.

The decline in R_t values with time in Figure R2/29 is also characterized by a fast initial fall over the first few days, followed by a slower rate of decline in a similar manner to trends in R_{pf}. This suggests that the corrosion resistance of the substrate is controlled, at least in part, by the rate of degradation of

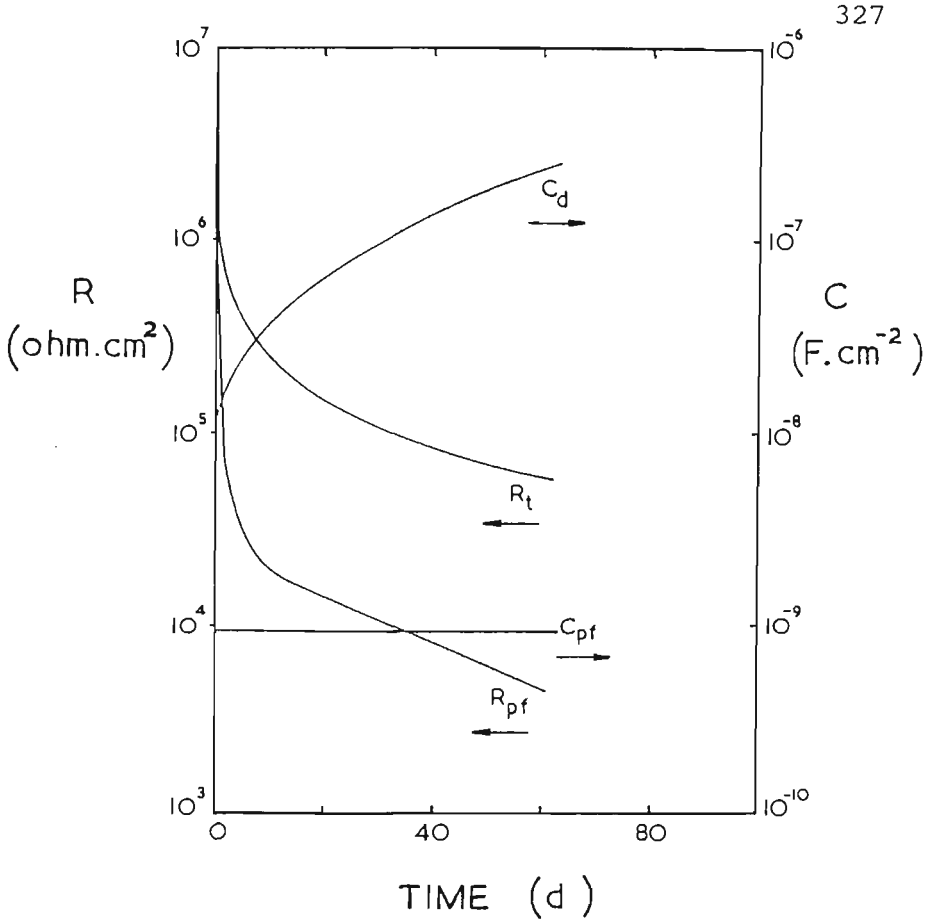

Figure R2/29. Summary graph (mean line estimated by eye from Figs. R2/17-20 up to 60 d) showing general trends with immersion time in 5% NaCl at 50C on paint film resistance, capacitance, R_{pf}, C_{pf} and metal charge-transfer resistance, double layer capacitance, R_t, C_d, for gloss series SMP/ZINCALUME samples. Note linear time axis in this case.

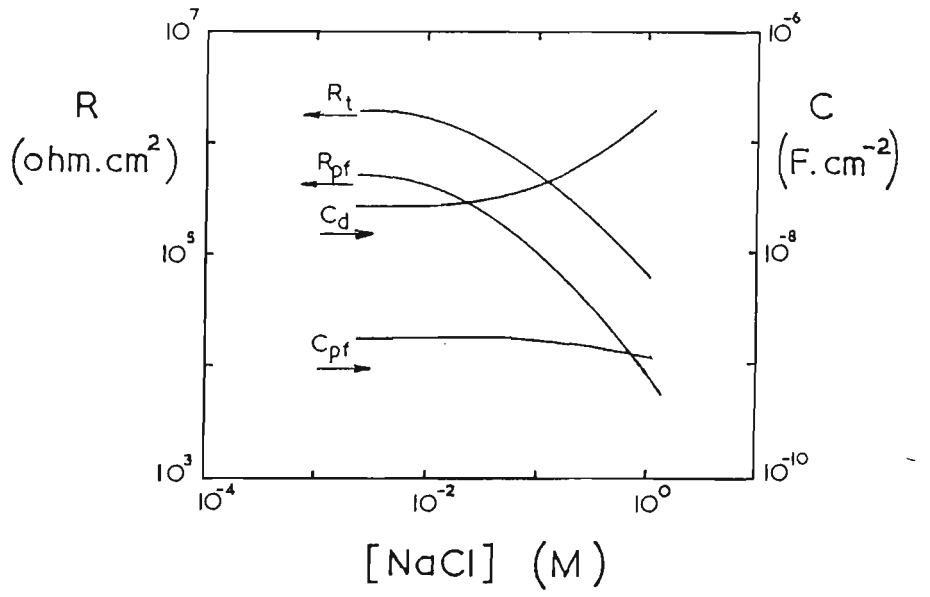

Figure R2/30. Summary graph (mean line estimated by eye from Figs. R2/17-28) showing general trend with NaCl concentration on painted metal parameter values after 40 d immersion. R_{pf}, C_{pf} paint film resistance, capacitance; R_t, C_d metal charge-transfer resistance, capacitance.

the paint film. The corrosion resistance drops from the moment of immersion, confirming previous comments re rapid solution uptake made in Sections R2.1/1. As stated in Section R2.1/4, the initial drop in R_t values with time is thought to be indicative of an increased corroding area, rather than an increasing corrosion rate. The value of R_t at any given time is thought to depend on the total summed area of the substrate exposed to the solution via the paint film pathways. The slower rate of decline of R_t values after about five days may be due to a combination of R_{pf} values slowing down and a more or less continuous film of solution forming adjacent to the substrate. This latter idea is consistent with the boundary or interfacial water layer theory, whereby a thin layer of water forms at the substrate/paint interface[8]. It is possible that further decreases in R_t with time would imply increasing corrosion rates.

The relatively constant values of C_{pf} with time in Figure R2/29 suggest that the paint film capacitance is determined solely by the characteristics of the paint film (dielectric constant, thickness, cross-sectional area) and not by the solution itself or the state of degradation of the film caused by solution uptake. In fact, the relatively constant C_{pf} values are explained by the capacitance of the small pathways being much less than the parallel capacitance of the remainder of the film which do not contribute significantly to the overall capacitance, even though the pathways control the performance of the paint film. These conclusions were drawn from the chloride equilibria studies in Section R2.1/5.

Values of C_d in Figure R2/29 are at least an order of magnitude higher than corresponding C_{pf} values. This is true for all chloride solutions, compare Figures R2/20,24,28 with R2/19,23,27. The values of C_d rise with time and

the rate of rise is faster in 5% NaCl solution. This is to be expected because C_d is thought to be directly related to the summed area of the exposed substrate, and will rise towards the double layer capacitance of the unpainted substrate as film degradation proceeds, see Section R2.1/6. This degradation is fastest in the 5% NaCl solution.

The fact that C_d values are about an order of magnitude higher than C_{pf} values and rise with time for all three chloride solutions is further supportive evidence (see also Section R2.1/7) that the high frequency Nyquist semicircle is due to the paint film and not the metal substrate. This is because the free film C_{pf} values in Sections R2.1/7, R2.2/3.2 are also about the same as C_{pf} values reported above, ie for attached films.

Figure R2/30 shows a summary graph (mean line estimated by eye from Figures R2/17-28) of R_{pf}, R_t, C_{pf} and C_d values obtained after 40 days immersion in the three chloride ion solutions. The values of R_{pf}, R_t fall, whilst C_d rises as solution chloride ion concentration increases, indicating greater rates of degradation of the paint film and increased areas and/or rates of substrate corrosion, confirming statements made above for R_{pf} and C_d. These results suggest that performance life (time to breakdown) decreases as chloride ion concentration increases, in agreement with both the results in Figure T6/4, Section T6/5, and outdoor exposure experience on the east coast of Australia, which shows that performance life decreases as distance from the ocean surf increases. Results for the single frequency test in Section R2.2/1.1.2 also support these conclusions. Values of C_{pf} are approximately constant with solution chloride ion concentration, with values slightly lower at 5% NaCl. This slight drop at higher concentrations was also noted for C_{pf} trends with solution chloride ion concentration in which the sample was

measured, as discussed in Section R2.1/5, and cannot be explained.

An estimate of sample failure for these attached films was obtained from R_{pf}/t plots in Figures R2/17,21,25 for the three chloride ion solutions. Sample failure was taken as the time, $t_{f,Rpf}$, for R_{pf} values to fall to 10^5 ohm.cm^2. Figure R2/31a is a plot of $t_{f,Rpf}$ versus $[Cl^-]$ which shows the data points and regression line. For a sample size, n, of 15, the Pearson correlation coefficient, r, is -0.746 which is statistically significant at the 99% level of confidence and shows that sample failure time, assessed by $t_{f,Rpf}$, is negatively correlated with solution chloride concentration. This trend agrees with similar trends for sample failure time, $t_{f,C}$, obtained from the single frequency test in Section R2.2/1.1.2 and shown in curve 1, Figure R2/47, Section R2.2/5.2.

An estimate of sample failure was also obtained from R_t/t trends in Figures R2/18,22,26 for the three chloride ion solutions. Sample failure was taken in this as the time, $t_{f,Rt}$, for R_t values to fall to 10^6 ohm.cm^2. This criterion is an order of magnitude higher than that used for $t_{f,Rpf}$ because R_t values were generally higher than R_{pf} values at a given time. Figure R2/31b is a plot of the $t_{f,Rt}$ versus $[Cl^-]$ which shows the data points and regression line. These data give a negative correlation (n=15, r=-0.776) between sample failure time and log $[Cl^-]$ which is statistically significant at the 99% level of confidence and is in agreement with similar conclusions for $t_{f,Rpf}$ above, and $t_{f,C}$, as mentioned above. All three fail time estimates, $t_{f,C}$, $t_{f,Rpf}$, $t_{f,Rt}$ are compared in Figure R2/47, Section R2.2/5.2.

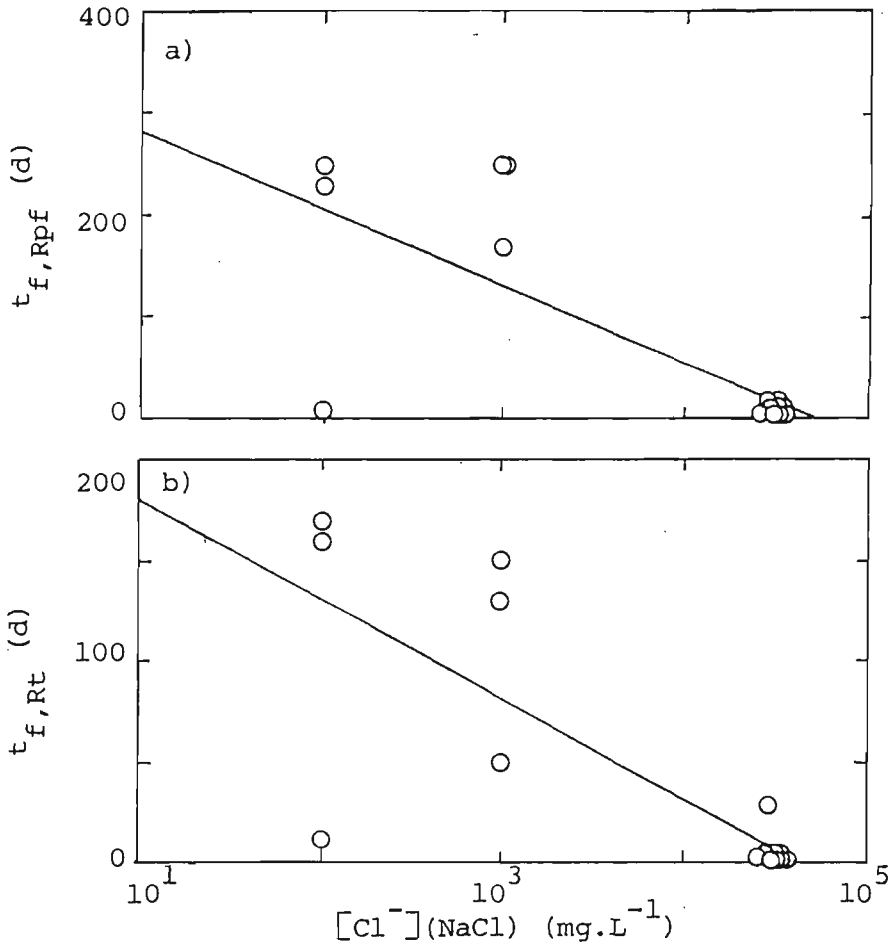

Figure R2/31. Effect of solution chloride ion concentration on sample failure time, taken as the time, $t_{f,Rpf}$, (Fig. R2/31a) for R_{pf} values to fall to 10^5 ohm.cm^2, or the time, $t_{f,Rt}$, (Fig. R2/31b), for R_t values to fall to 10^6 ohm.cm^2.

1.3 Single frequency/wide frequency range test comparisons

The resistive contribution, a_{flk}, of painted metal impedance at a frequency of 1 kHz is relatively constant at shorter times and declines markedly at longer times, for example, see Figure R2/15, Section R2.2/1.1. Just prior to the steep decline, values of a_{flk} can show a tendency to rise to a maximum value before declining. The rise to a maximum is more marked for some results than for others, it being barely detectable in Figure R2/15, but quite noticeable rises have previously been observed[9], for example Figure T1/1, Section T1/2. A discussion is given in Section T1/2, which also includes reasons for the sharp decline at longer times.

An inspection of many experimental Nyquist wide frequency range plots indicates that the 1 kHz point always occurs around the high frequency semicircle attributed to the paint film. It is reasonable to conclude that trends in a_{flk} plots versus time may be due to changes in the paint film parameters R_{pf} and C_{pf}. The changes in these parameters with time have been fully discussed in Section R2.2/1.2. Briefly, R_{pf} values decline markedly with time over about four decades, whilst C_{pf} values are relatively constant, approximately doubling over the same time interval. This implies that f_{bmax} ($=1/2\pi\ R_{pf}\ C_{pf}$) will increase with time, where f_{bmax} is the frequency at the top of the high frequency Nyquist semicircle. If f_{bmax} values increase with time, then the position of all other frequency points, including the 1 kHz point, must also change with time.

This effect can be demonstrated by producing Nyquist plots based on the single RC theoretical equivalent circuit model in Figure R2/32 for decreasing values of R_{pf} with C_{pf} remaining constant. This has been done using program

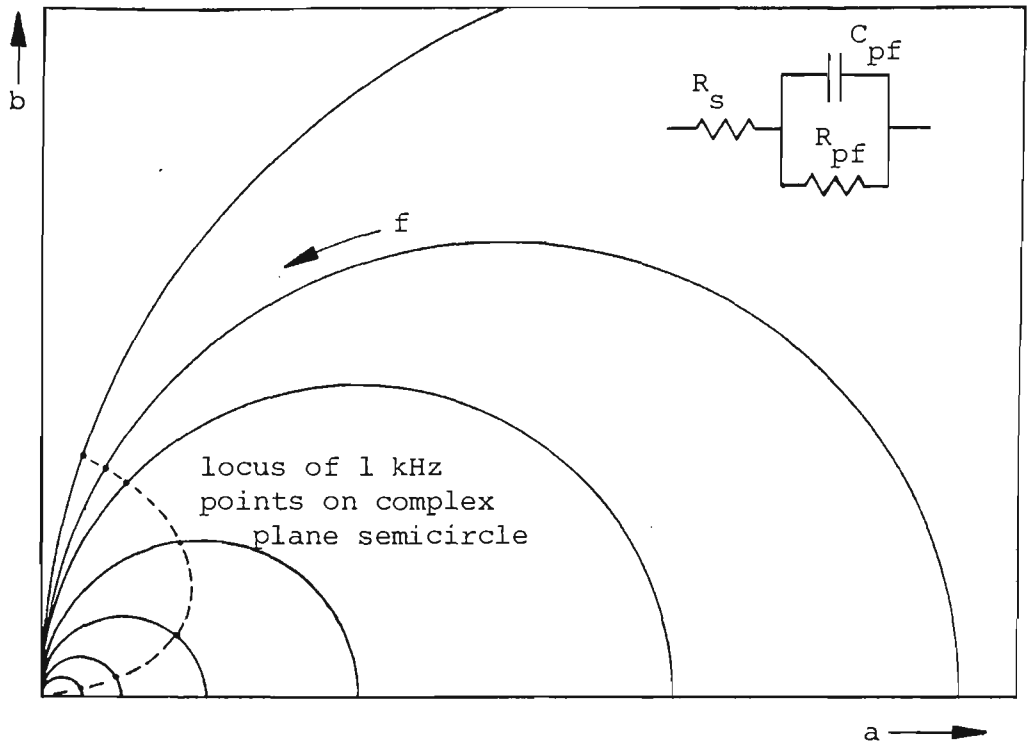

Figure R2/32. Schematic Nyquist plot of resistive, a, versus reactive, b, components of impedance for equivalent circuit shown, representing the painted metal/solution interface. The locus of 1 kHz points passes through a maximum value of a as the semicircle diameter, equal to R_{pf}, increases. R_s solution resistance; R_{pf}, C_{pf} paint film resistance, capacitance; f frequency.

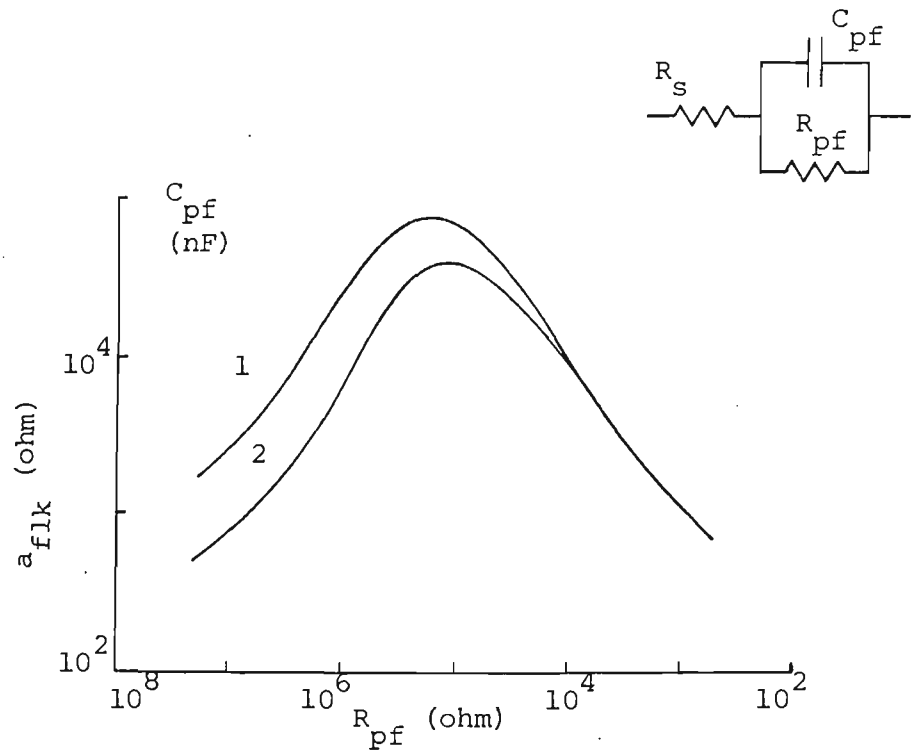

Figure R2/33. Effect of paint film resistance, R_{pf}, on the resistive component of impedance, a_{flk}, for two values of paint film capacitance, C_{pf}. Scale for R_{pf} decreases left to right corresponding to what happens with increasing immersion time.

equiv_crt, see Section A1/4.5. Figure R2/32 is a schematic diagram, showing that the position of the 1 kHz point starts off on the left hand, high frequency side of a large Nyquist plot at large R_{pf} values (equivalent to the semicircle diameter), but moves across the semicircle to the right hand, low frequency side as the value of R_{pf} decreases. The locus of the 1 kHz points on these semicircles is an arc (dashed line) which passes through a maximum a_{flk} value as R_{pf} decreases. Figure R2/33 is a plot of a_{flk} versus R_{pf} at two C_{pf} values. The values of R_{pf} and C_{pf} were read from a typical data set, Figures R2/17,19, Section R2.2/1.2, and the R_{pf} values in Figure R2/33 span the range of values for the time scale in Figure R2/17. Note that R_{pf} values are plotted decreasing from left to right in Figure R2/33, corresponding to what happens with increasing immersion time. Thus the plot shape, which shows a distinct maximum, of Figure R2/33 will be able to be compared with the a_{flk}/time plots. The maximum shown in some a_{flk}/time plots can therefore simply be explained by a decrease in the paint film resistance with immersion time, and implies nothing about the formation of protective corrosion products as previously stated[15]. This does not exclude the possibility of corrosion product formation at immersion times corresponding to the maximum, but it does indicate that the existence of a maximum is not necessarily an indication of corrosion product formation. The maximum a_{flk} value in Figure R2/33 occurs at R_{pf} values of around 100k-200k ohm.cm^2. It is obvious from Figure R2/17 that there is nothing significant recurring at times equivalent to these values, suggesting that the maximum in a_{flk} values does not indicate any specific change other than a decrease in R_{pf}.

A plot of a_{flk} versus decreasing R_{pf} values (corresponding to increasing immersion times) is shown in Figure R2/34b for the dual RC equivalent circuit model shown in Figure R2/34a. It is obvious that the values of a_{flk} rise to a

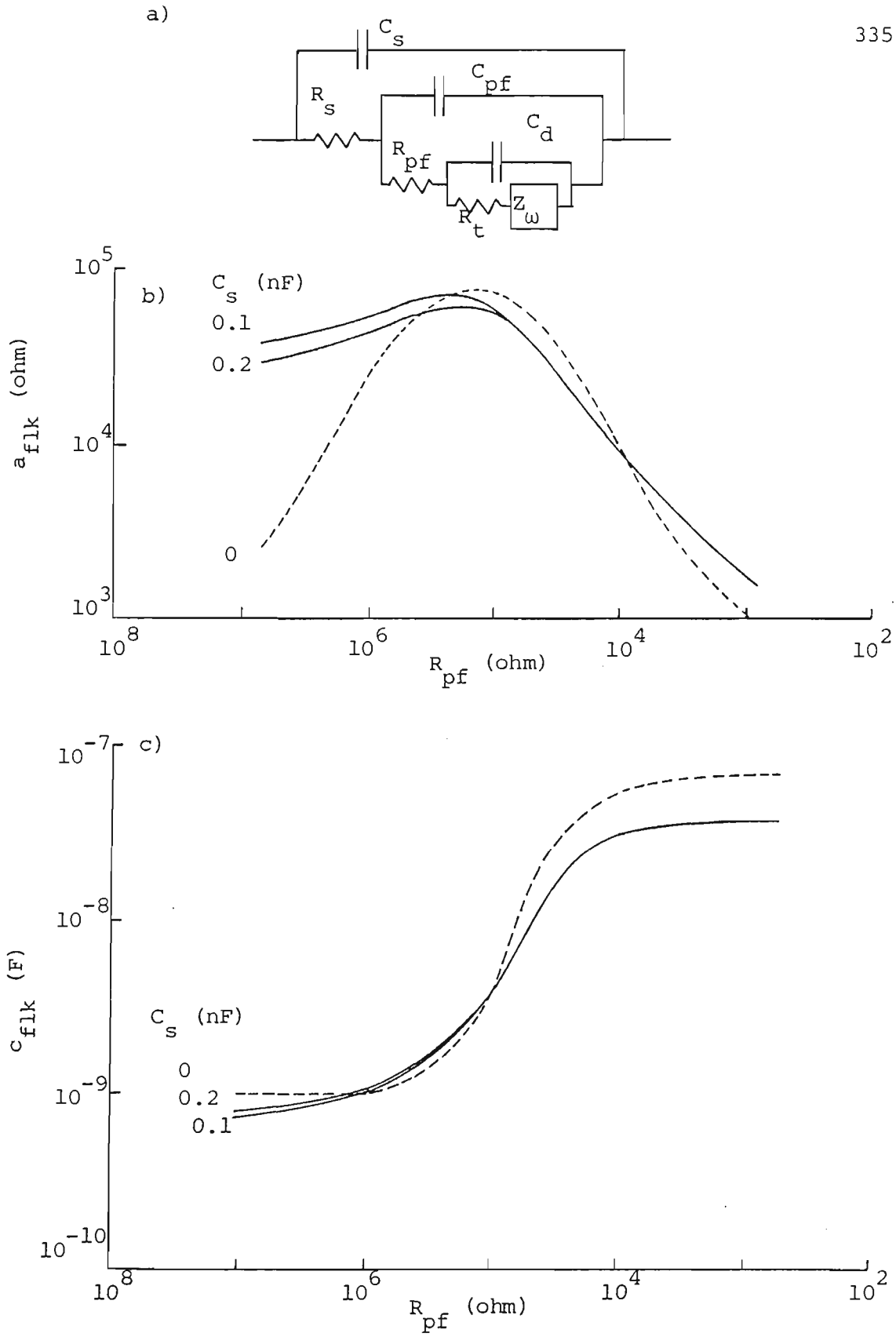

Figure R2/34. Effect of R_{pf} on resistive, a_{flk}, (Fig. R2/34b), and capacitive, c_{flk}, (Fig. R2/34c), components of impedance at different values of C_s, for the equivalent circuit model in Fig. R2/34a. R_s solution resistance; C_s stray capacitance; R_{pf}, C_{pf} paint film resistance, capacitance; R_t, C_d metal charge-transfer resistance, double layer capacitance; Z_ω Warburg diffusion impedance.

maximum and then decline as R_{pf} decreases for the curve with stray capacitance, C_s=0. However, the shape of this curve does not reproduce the shape obtained experimentally as a function of immersion time, for example, Figure R2/15. This is because the value of a_{flk} decreases at high R_{pf} values in the theoretical plot for C_s=0 in Figure R2/34b whereas it is seen to be constant at low immersion times (high R_{pf} values) in Figure R2/15. The likely reason is that R_{pf} values do not always decline as markedly at low times as they do at longer times, compare Figures R2/17,21,25. This can also be explained by the effect of stray capacitance, C_s, across the working electrode/solution interface, and this effect has been demonstrated for curves at C_s=0.1, 0.2 nF, Figure R2/34b. The values of a_{flk} at high R_{pf} increase for these values of C_s, so that the plot shape becomes more like the experimental plot shape of Figure R2/15. Values of a_{flk} are not markedly altered at low R_{pf} values by increasing C_s and neither is there much change on the corresponding plots of c_{flk} versus R_{pf} in Figure R2/34c.

The effect of other parameter values on the shape of a_{flk}/R_{pf} and c_{flk}/R_{pf} plots has also been investigated for the model in Figure R2/34a. Variation of solution resistance, R_s, from 10^2 to 10^3 ohm or C_{pf} from 1 to 2 nF has only a small effect on the curve shape for both a_{flk}/R_{pf} and c_{flk}/R_{pf} plots. Variation of R_t values over the range 100 k to 10 M ohm causes little change in plot shape for a_{flk}/R_{pf}, and a small decrease in c_{flk} only at low R_{pf} values. Variation in C_d over the range 7-700 nF causes a_{flk} values to fall a small amount, whilst c_{flk} values rise significantly at low R_{pf} values, see Figure R2/35b,c, respectively. However, changing values of C_d do not explain the shape of a_{flk}/t, c_{flk}/t plots obtained experimentally, eg Figure R2/15. Changing values of C_d changes the position where the a_{flk}/R_{pf}, c_{flk}/R_{pf},

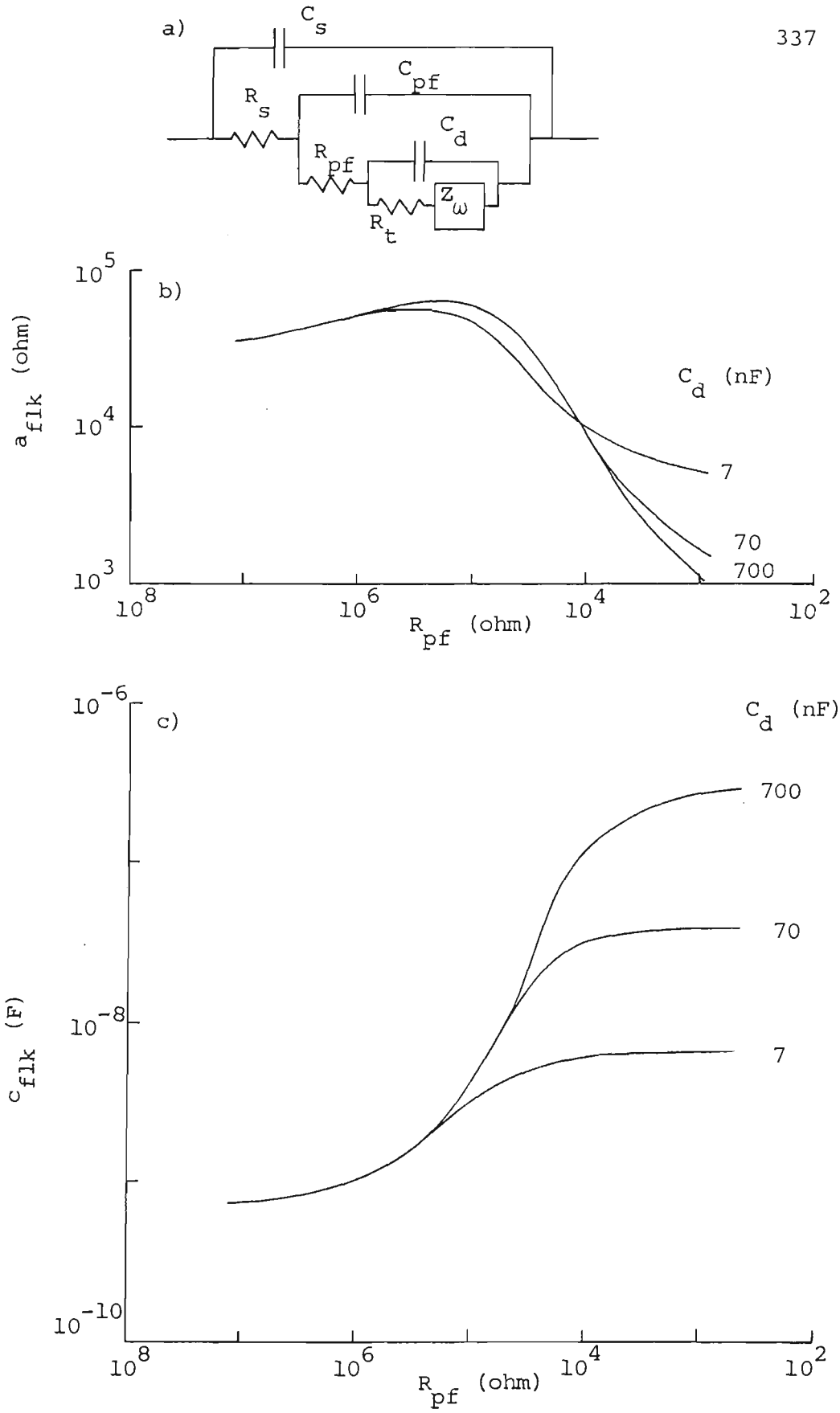

Figure R2/35. Effect of paint film resistance, R_{pf}, on resistive, a_{flk}, (Fig. R2/35b), and capacitive, c_{flk}, (Fig. R2/35c), components of impedance at different values of metal double layer capacitance, C_d, for the equivalent electrical circuit model in Fig. R2/35a. Other symbols have meanings as per Figure R2/34.

plots will bend away from the steeply falling, rising portion of the curve at low values of R_{pf}, respectively. This situation will also apply to experimental a_{flk}/t, c_{flk}/t plots when R_{pf} values decline with time and cause the same basic curve shape as those in Figure R2/35. It does not explain why the steeply falling, rising sections of the a_{flk}/R_{pf}, c_{flk}/R_{pf} curves start falling, rising at longer times as the solution becomes more dilute with respect to chloride ions, eg Figure R2/15.

This can, however, be simply explained by the change in R_{pf} values with time. The rate of fall of R_{pf} decreases, indicating a lower rate of paint film degradation as the solution chloride ion concentration decreases, see Figure R2/36a which is compiled from Figures R2/17,21,25.

Values of R_{pf} can be read from Figure R2/36a at given times (1, 10, 20, 30 ... 100 d) for each of the three solutions - 100, 1000, 30500 $mg.L^{-1}$ $[Cl^-]$. Using the a_{flk}/R_{pf} and c_{flk}/R_{pf} curves for C_d = 700 nF in Figure R2/35b,c respectively, values of a_{flk}, c_{flk} can be read off at these R_{pf} values. It is then possible to construct simulated plots of a_{flk}/t, c_{flk}/t, representing single frequency impedance behaviour in these three solutions, by plotting the a_{flk}, c_{flk} values at the above given times. This is shown in Figures R2/36b,c respectively. Although the painted metal sample in the 100, 1000 $mg.L^{-1}$ $[Cl^-]$ solutions had not degraded sufficiently at 100 d, Figure R2/36a, there is obviously a marked similarity between the simulated plots in Figures R2/36b,c and experimental a_{flk}/t, c_{flk}/t plots in Figure R2/15. These simulations demonstrate that the steeply rising, falling sections of a_{flk}/t, c_{flk}/t plots can be simply explained by the rate of decline of paint film resistance, R_{pf}. In the strongest chloride ion solution, 30500 $mg.L^{-1}$ $[Cl^-]$ (5% NaCl), the rate of decline of R_{pf} values in Figure R2/36a is steepest. This gives rise to the

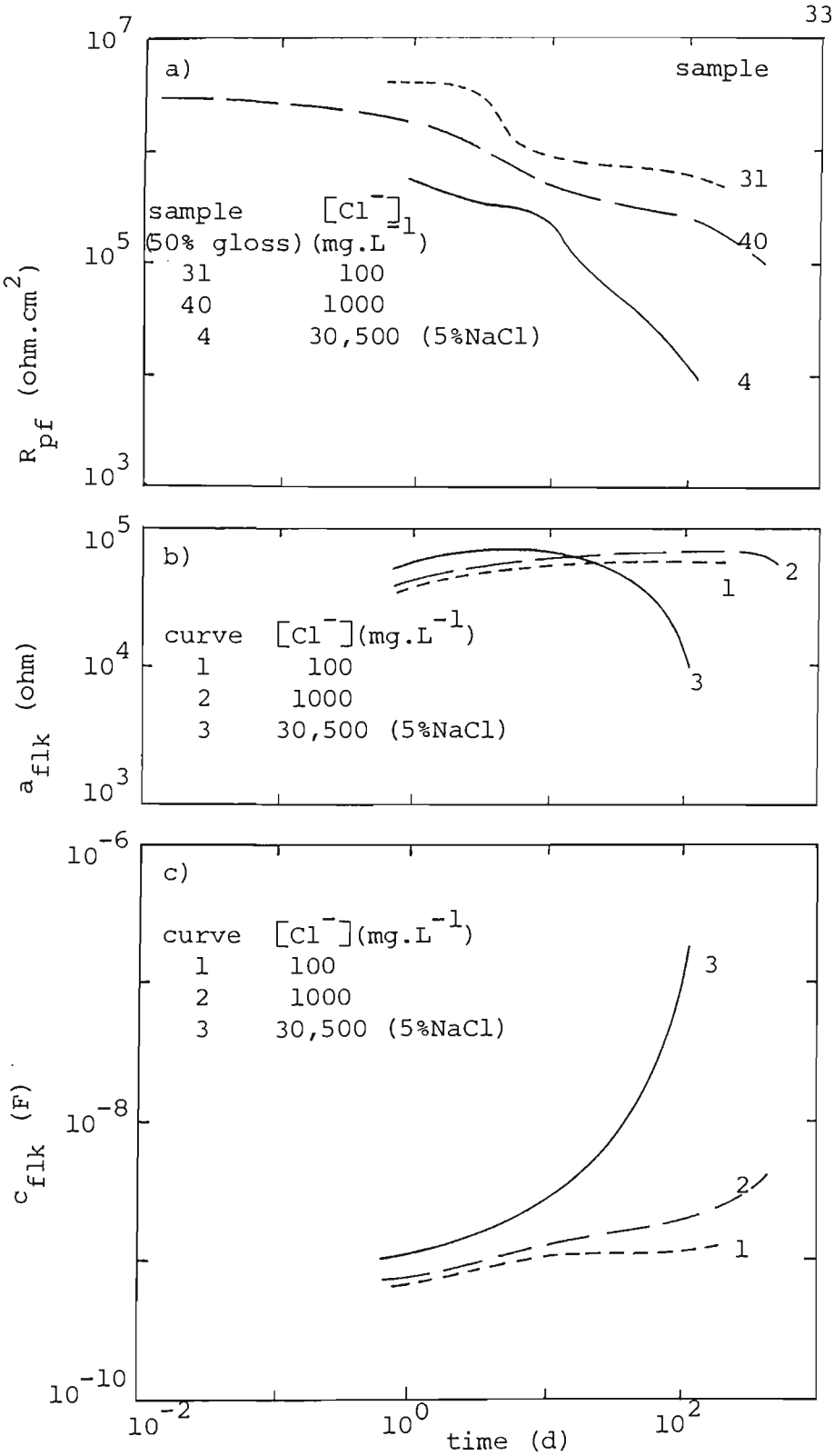

Figure R2/36. Effect of immersion time on a) paint film resistance, R_{pf}, b) resistive, a_{flk}, and c) capacitive, c_{flk}, components of impedance. Fig. R2/36a is experimental results; Figs. R2/36b,c are simulated curves using R_{pf} values from Fig. R2/36a and finding a_{flk}, c_{flk} values at C_d=700 nF from Fig. R2/35b,c using the R_{pf} values.

steepest fall in the simulated a_{flk}/t plot in Figure R2/36b, and the steepest rise in the simulated c_{flk}/t plot in Figure R2/36c.

A further comparison between the single frequency and wide frequency range test methods for attached film samples has been the comparison of sample failure times obtained by both these methods. This is described individually in Section R2.2/1.1.2 for the single frequency test and in Section R2.2/1.2 for the wide frequency range test. Both test methods are compared in Section R2.2/5.2.

2. Attached films - gravimetric results

Table R2/2 lists the gravimetrically determined mass gain results for attached films as described in Section E3.2/4.3. This table shows mass gain versus time for a series of samples at different gloss levels, immersed in solutions of differing chloride ion concentration.

The simple mass gain in column 6 is the difference between final sample mass (after the immersion period) and initial mass. No trends are evident from these results. This is probably because the overall mass change is a mass gain of water and a mass loss caused by soluble matter leaching from the paint film (organic silicates, diols or diacids from hydrolysis of the polymer) and corrosion of the substrate. Solution analysis, see Section E3.2/4.3, indicated that Zn, Al ions in solution from soluble corrosion products leaching through the paint film were less than 0.1 mg for all solutions, that is, less than the limit of reading of the balance. The solutions were not analyzed for organic soluble species. Therefore it cannot be proven from these results that there was a mass loss which complicated the overall mass gain trends.

Table R2/2 Gloss Series Attached Films - Gravimetric Results

(1) Sample number	(2) Gloss level (%)	(3) [Cl⁻](NaCl) solution (mg.L⁻¹)	(4) Initial mass (g)	(5) Final mass (g)	(6)=(5)-(4) Mass gain (mg)	(7) Desiccator 1 d reweigh (g)	(8)=(5)-(7) Water desorbed (mg)	(9) Water[2] uptake (% v/v)	(10) Immersion time (d)
21	25	30,500	6.7921	6.7931	1.0	6.7921	1.0	5.3	1
22		(5% NaCl)	6.5606	6.5626	2.0	6.5609	1.7	9.0	2
23			6.3372	6.3375	0.3	6.3364	1.1	5.8	3
24		1000	6.1820	6.1832	1.2	6.1819	1.3	6.9	1
25			6.7680	6.7689	0.9	6.7674	1.5	7.9	3
26			6.5285	- [1]					10
27		100	6.5399	6.5413	1.4	6.5399	1.4	7.4	1
28			6.6160	6.6177	1.7	6.6151	2.6	13.7	3
29			7.0651	- [1]					10
51	50	30,500	6.7260	6.7272	1.2	6.7260	1.2	6.3	1
52		(5% NaCl)	6.8210	6.8200	-1.0	6.8192	0.8	4.2	2
53			6.5456	6.5456	0.0	6.5441	1.5	7.9	3
54		1000	6.5139	6.5147	0.8	6.5138	0.7	3.7	1
55			6.6526	6.6543	1.7	6.6524	1.9	10.0	3
56			6.5883	- [1]					10
57		100	6.8910	6.8915	0.5	6.8902	1.3	6.9	1
58			6.6214	6.6223	0.9	6.6210	1.3	6.9	3
59			7.0480	- [1]					10
81	85	30,500	6.9165	6.9174	0.9	6.9169	0.5	2.6	1
82		(5% NaCl)	6.9808	6.9806	-0.2	6.9800	0.6	3.2	2
83			6.6361	6.6363	-0.2	6.6353	1.0	5.3	3
84		1000	6.6600	6.6608	0.8	6.6598	1.0	5.3	1
85			6.9093	6.9100	0.7	6.9089	1.0	5.3	3
86			6.6077	- [1]					10
87		100	6.7323	6.7325	0.2	6.7315	1.0	5.3	1
88			6.5306	- [1]					10
89			6.3168	6.3177	0.9	6.3160	1.7	9.0	3
blank	wax covered	30,500 5% NaCl	7.6392	7.6388	-0.4	6.6385	0.3	1.6	3

Notes:

1 wax coating lifted with solution under wax - sample not reweighed
2 water uptake (% v/v) = mass of water (column 8 x 100)/(volume of paint film x density of water)
= mass of water (mg) x 5.285

Table R2/3 Gloss Series Free Films - Gravimetric Results
25% gloss - 2 x 10 um SMP free films

(1) Sample number	(2) [Cl⁻](NaCl) solution (mg.L⁻¹)	(3) Initial mass (mg)	(4) Final mass (mg)	(5)=(4)-(3) Mass gain (mg)	(6) Desiccator 1 d reweigh (mg)	(7)=(4)-(6) Water desorbed (mg)	(8)=(3)-(6) Dissolved solids lost (mg)	(9) Water[1] uptake (% v/v)	(10) Immersion time (d)
1	30,500	33.0	31.8	-1.2	31.6	0.2	1.4	1.20	1
1[2]	(5% NaCl)	31.6	31.0	-0.6	31.0	0.0	0.6	0.00	+3
2		33.0	32.0	-1.0	31.9	0.1	1.1	0.60	2
3		32.9	30.8	-2.1	30.3	0.5	2.6	3.01	10
4		31.7	29.0	-2.7[3]	27.0	2.0	4.7	12.05[3]	38
5	1000	30.0	29.4	-0.6	28.8	0.6	1.2	3.61	1
5[2]		28.8	28.5	-0.3	28.0	0.5	0.8	3.01	+3
6		31.5	30.8	-0.7	30.1	0.7	1.4	4.22	2
7		30.7	28.8	-1.9	27.8	1.0	2.9	6.02	10
8		32.1	36.1	4.0[3]	25.6	10.5	6.5	63.25[3]	38
9	100	34.1	33.3	-0.8	32.9	0.4	1.2	2.41	1
9[2]		32.9	33.0	0.1	32.1	0.9	0.8	5.42	+3
10		34.0	33.3	-0.7	32.6	0.7	1.4	4.22	2
11		31.6	29.5	-2.1	28.6	0.9	3.0	5.42	10
12		33.9	34.3	0.4[3]	27.5	6.8	6.4	40.96[3]	38
13	30,500	32.6	32.0	-0.6	31.8	0.2	0.8	1.20	0.3
14	(5% NaCl)	32.4	31.4	-1.0	31.3	0.1	1.0	0.60	1
15		29.2	27.8	-1.4	27.8	0.0	1.4	0.00	2
16		32.4	30.9	-1.5	30.5	0.4	1.9	2.41	3
17	1000	28.8	28.5	-0.3	28.0	0.5	0.8	3.01	0.3
18		32.9	32.1	-0.8	31.8	0.3	1.1	1.81	1
19		32.8	31.7	-1.1	31.4	0.3	1.4	1.81	2
20		30.8	29.4	-1.4	28.9	0.5	1.9	3.01	3
21	100	32.5	32.2	-0.3	31.6	0.6	0.9	3.61	0.3
22		33.2	32.7	-0.5	32.2	0.5	1.0	3.01	1
23		31.9	31.2	-0.7	30.5	0.7	1.4	4.21	2
24		32.4	31.4	-1.0	30.5	0.9	1.9	5.42	3

Notes:

1 water uptake (% v/v) = (mass of water (column (7) x 100)/(volume of paint film x density of water)
= mass of water (mg) x 6.0241
2 desiccator samples re-immersed for a further 3 d
3 film had severely shrivelled up after 38 d immersion and results were not reliable

However, it was thought that a mass loss was probable, and that an alternative way of obtaining the mass of water absorbed during the immersion period was by weighing the samples again after one day in a desiccator which would presumably desorb any water absorbed during immersion. Column 8 shows the water desorbed for each sample. These mass changes are small and trends are not obvious from Table R2/2. It was considered at the outset that it would be difficult to find gravimetric water uptake trends on attached film samples because of the large mass of the substrate relative to the paint film, and the complicating effect caused by any corrosion of the substrate. Additionally, some samples showed the wax sealant lifting and solution under the wax.

The results in column 9 of Table R2/2 were treated statistically using a general linear model procedure, which is described along with the statistical results in Section A4/3.3. These results indicate that water uptake increases with time and with decreasing log chloride and gloss level according to Equation (A4/33), Section A4/3.3. Primer thickness was not considered because it was constant for all samples, see Section E3.2/4.3, at 5 µm.

$$X_V = 10.070 - 0.0471 \text{ gloss} - 1.028 \log [Cl^-] + 1.228 \text{ time} \qquad \text{(A4/33)}$$

where X_V = water uptake (% v/v)

This equation is shown plotted as water uptake at 1 day versus solution chloride ion concentration in curve 1 Figure R2/46, Section R2.2/5.1.2. The effect of all three independent variables (gloss, log chloride, time) on the dependent variable, water uptake, is approximately the same. The inverse relationship between water uptake and gloss level suggests that water uptake increases as the amount of flatting agent, added to the top coat formulation to suppress gloss, increases. This is the expected result because the large

flatting agent particles would encourage more water permeation, as discussed in Sections I4/1. The trend for water uptake to increase with decreasing chloride is in agreement with the conclusions of Brasher and Nurse[7] for a different painted metal/solution system; in agreement with the capacitance results on attached films in Section R2.2/1.1.1, and the gravimetric free film results in Section R2.2/4.

Equation (A4/33) represents a reasonable fit of the data, as discussed in Appendix A4/3.3, at times ≧1 d. Obviously, water uptake must be zero at zero time, so that the rate of water uptake between 0 and 1 d (data were not determined at times <1 d) must be more rapid than shown by Equation (A4/33) which gives a positive intercept at zero time. A similar situation was found for free films in Figure R2/42, Section R2.2/4. This subject is taken up further in Section R2.2/6.

3. Free films - impedance results

The samples referred to are described in Table E3/4, Section E3.2/2.2. These were free films (paint films only) made up of 2 x 10 μm SMP top coats having a gloss level of 25%. Impedance tests were performed in a U-cell, see Section E3.1/2 for a description of the U-cell, and Section E3.2/4.4 for a description of the impedance tests and the solutions used (30 500 (=5% NaCl), 1000, 100 $mg.L^{-1}$ $[Cl^-]$).

The aims of this section were:

1. to determine the water uptake of 25% gloss free films by the 1 kHz capacitance method so that comparisons can be made with free film

gravimetric results and also attached film 1 kHz capacitance and gravimetric results;

2. to determine the effect of immersion time on the impedance of free films so that comparisons can be made with attached film results.

Both single frequency and full frequency range tests are described. The comments made in Section R2.1/7 regarding the existence of pinholes in single coat free films also apply to this section. For these reasons 2 x 10 μm top coats were used rather than 1 x 20 μm top coat samples. Some of the samples would perform normally for some days, with impedance tests being performed at intervals, but they would suddenly give a low impedance and be deemed to have failed. Sometimes the cause could be identified as an over-stretched film resulting in a tear, but other times the cause was unexplained. In these cases, the test was repeated using a new sample.

3.1 Single frequency test

The capacitive, c_{flk} ($=1/2\pi f b_{flk}$), component of impedance, Z (=a + jb), was calculated from the reactive component, b_{flk}, at a frequency of 1 kHz over a range of immersion time, t, of the free films in the U-cell. Plots of c_{flk}/t were obtained, from which the following four parameters were calculated - sample failure time, $t_{f,C}$, based on the time for c_{flk} to rise to 10 $nF.cm^{-2}$; initial capacitance, $C_{m,0}$, extrapolated to zero time from the first 60 minutes of immersion; capacitance, $C_{m,2h}$, $C_{m,1d}$, after 2 h, 1 d immersion, respectively. The percentage volume of water taken up by the free films, $X_{v,2h}$, $X_{v,1d}$, was calculated at 2 h and 1 d respectively, using the Brasher and Kingsbury formula[153] described in Section T6/8.

Figure R2/37a shows typical examples of c_{flk}/t plots for free films in each of the three chloride ion solutions at 50°C. Figure R2/37b shows corresponding X_v/t plots. Only smoothed curves are shown so that the trends can be more readily compared. However, these curves accurately represent the large number of data points that were obtained.

3.1.1 Effect of $[Cl^-]$ on water uptake

Figure R2/37a shows a rapid increase in c_{flk} after only relatively short periods of immersion. The time at which this sharp rise occurs appears to be generally inversely related to solution chloride ion concentration, although exceptions occur. These rises are somewhat surprising because similar U-cell measurements at room temperature on different types of free films (SMP, vinyl, PVF_2, acrylic) immersed in 5% NaCl solution give paint film resistance, R_{pf}, and capacitance, C_{pf}, values (obtained from wide frequency range tests) that are relatively constant over an immersion period of days or even weeks. The difference here with these SMP free film tests must be attributed to the increase in temperature from room temperature to 50°C. The large increase in c_{flk} has been explained[7] by a reorientation in the mode of distribution of water within the paint film as discussed in Section R2.2/1.1.1. However, it is also likely that degradation of the paint film occurs which is brought about by hydrolysis of the silicone modified polyester, SMP, polymer.

In the hydrolysis reaction[188], oxygen-silicon bonds split to form hydroxyl and silanol polymers of lower molecular weight, and the silanols can then dimerize, as shown by the following reaction sequence, where P_c, P_{Si} represent carbon, siloxane polymer chains, respectively.

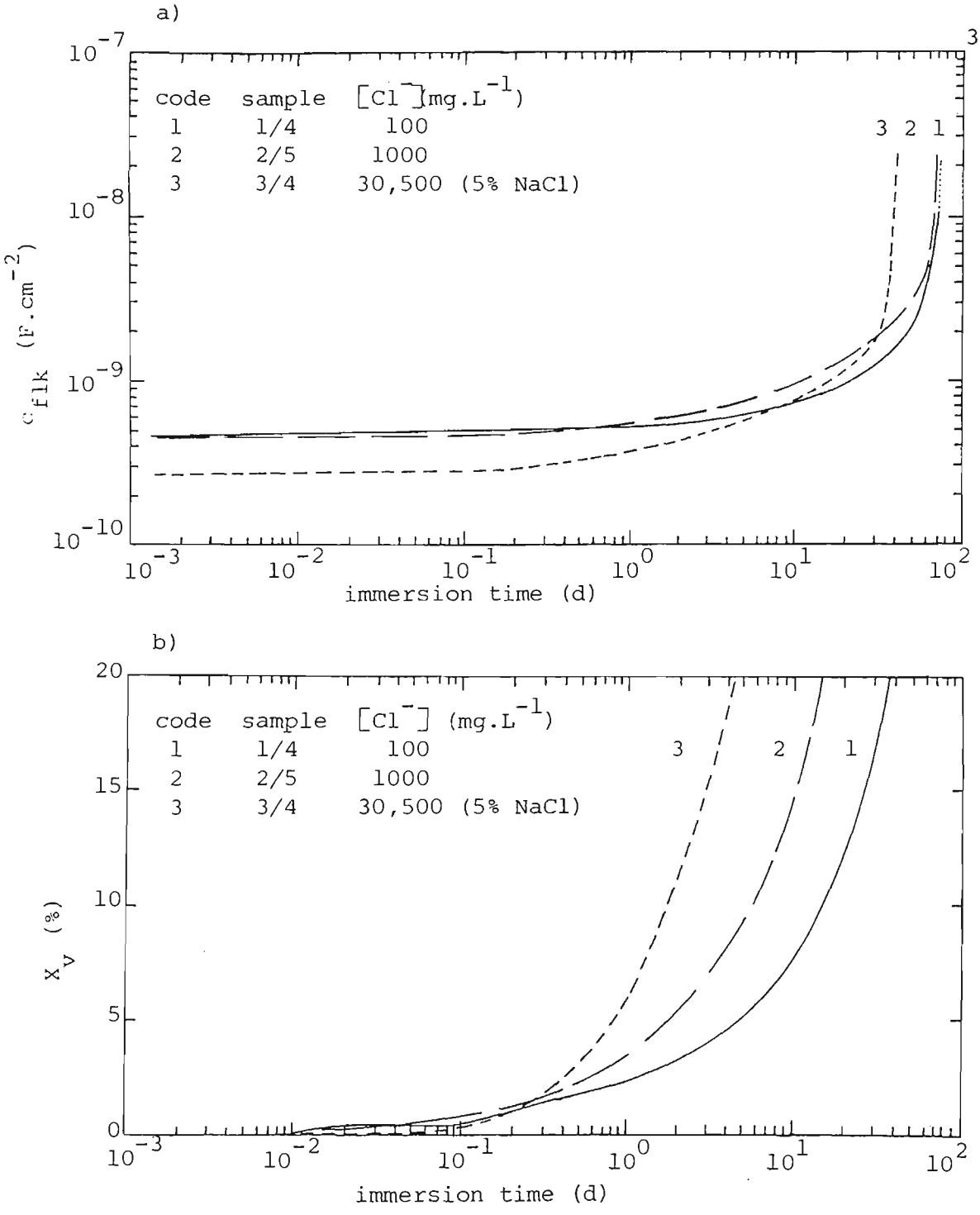

Figure R2/37. a) Capacitive component, c_{flk}, of impedance at a frequency of 1 kHz versus immersion time for 3 representative samples of 2 x 10 µm SMP free films in different chloride ion solutions at 50°C. b) corresponding calculated water uptake, X_v, at different solution chloride ion concentrations.

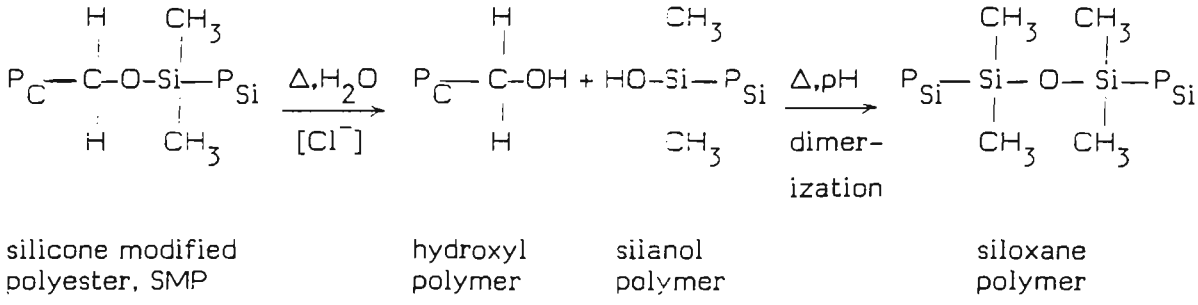

The hydrolysis reaction is expected to speed up with increase in temperature in probably an exponential manner according to the Arrhenius theory[189]. The solution chloride ion concentration apparently catalyses the hydrolysis reaction to some extent. Silicone modified polyesters are known to hydrolyze more than polyesters, fluorocarbons or vinyls[188].

The free films were considerably stretched, thinned and fragile at immersion times corresponding to the large rise in c_{flk}. The percentage water uptake, X_v, in the free films has been calculated on the assumption that the initial capacitance changes are indicative of water uptake[153]. Figure R2/37b shows large increases in X_v with time, closely following the trends in c_{flk}/t plots in Figure R2/37a. An inverse relationship generally holds between the time at which the sharp rise in X_v occurs and solution chloride ion concentration as was observed in c_{flk}/t plots, although exceptions occur.

Values of X_v, read at 2 hours and 1 day, from X_v/t plots like those in Figure R2/37b, are shown plotted as a function of solution chloride ion in Figure R2/38. There is a moderate degree of scatter in the points and regression lines are plotted through the data. The correlation is not significant at the 90% level of confidence between X_v and $[Cl^-]$ at 2 h immersion. However, there is a trend for X_v at 1 d to increase with $[Cl^-]$ which is significant at the

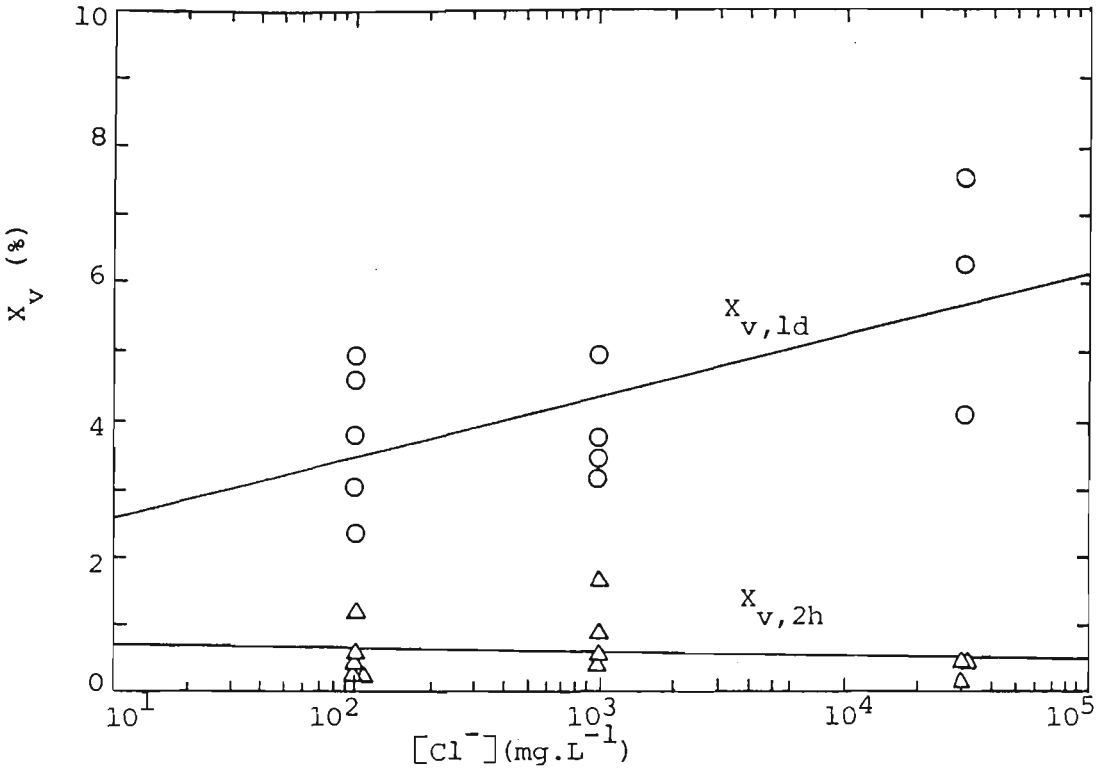

Figure R2/38. Water uptake, $X_{v,2h}$, $X_{v,1d}$, at 2 h, 1 d respectively, versus solution chloride ion concentration for 2 x 10 μm SMP free films at 50°C. Lines are regression lines but 2 h trend is not statistically significant at 90% level of confidence. X_v calculated from capacitance/time plots like those in Figure R2/37a.

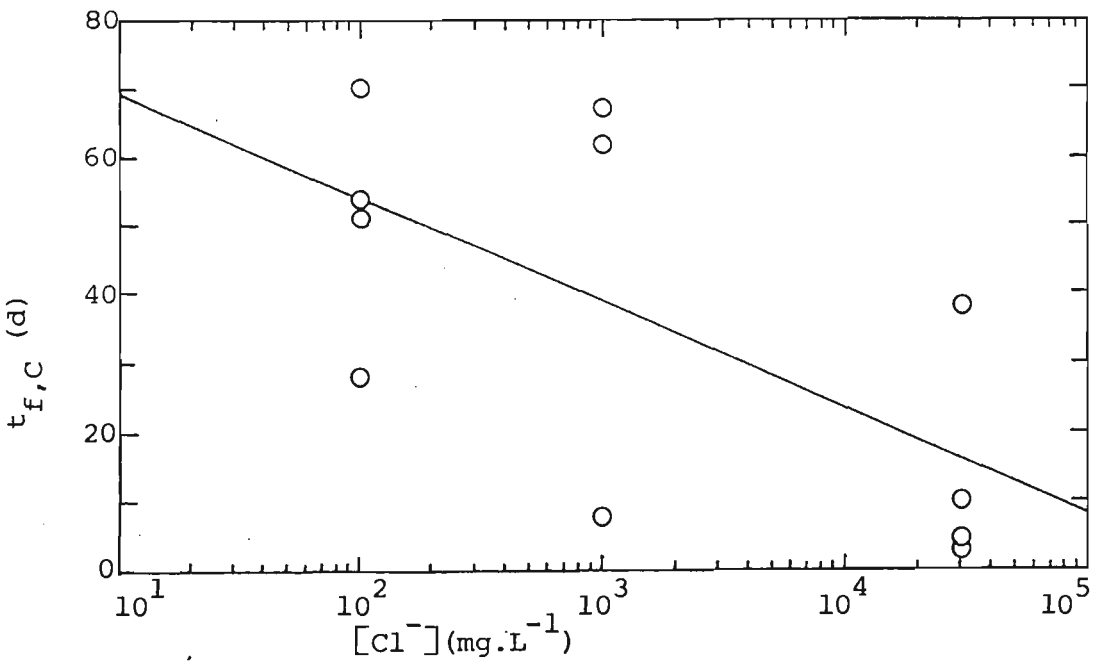

Figure R2/39. Sample fail time, $t_{f,C}$, versus solution chloride ion concentration for 2 x 10 μm SMP free films at 50°C. Line is regression line. Trend is statistically significant at 95% level of confidence. $t_{f,C}$ taken as time for c_{flk} to rise to 10 $nF.cm^{-2}$ in plots like those in Figure R2/37a.

95% level of confidence. A similar trend was found for attached film results in Section R2.2/1.1.1 and shown in curve 2, Figure R2/46, Section R2.2/5.1.2, where 1 d results gave a positive correlation with chloride ion but 2 h results in curve 2, Figure R2/45, gave a negative correlation. The subject of water uptake versus solution chloride ion concentration is discussed further in Section R2.2/6.

3.1.2 Effect of $[Cl^-]$ on sample failure

The shape of c_{flk}/t plots like those in Figure R2/37a for free films is similar to those like Figure R2/15b for attached films. After a period of steady values, c_{flk} rises steeply with immersion time. This has been discussed in Section R2.2/3.1.1.

An estimate of sample failure of U-cell free films was obtained from c_{flk}/t plots like those in Figure R2/37a as the time, $t_{f,C}$, taken for c_{flk} to rise to 10 $nF.cm^{-2}$. These times correspond to free films that were considerably stretched, thinned and fragile. A very large increase in c_{flk} usually was a sign of a visible tear in the film. Figure R2/39 is a plot of $t_{f,C}$ versus solution chloride ion concentration. The data points have a moderate amount of scatter. The regression line plotted through these points shows that sample failure occurs sooner in more concentrated solutions, and the $t_{f,C}/\log[Cl^-]$ trend is statistically significant at the 95% level of confidence. This subject is discussed further in Section R2.2/6.

3.2 Wide frequency range test

Both the paint film resistance, R_{pf}, and capacitance, C_{pf}, were calculated from Nyquist plots obtained at various time intervals in 100, 1000, 30 500 (=5%

NaCl) mg.L^{-1} [Cl^-] solutions at 50°C over the sample life of free films in the U-cell. The experimental method is detailed in Section E3.2/4.4. The method of calculation is indicated in Section T1/5.1 and described in a paper[17] written by the author.

The shape of Nyquist plots was always a well defined semicircle. The angle of depression, α, varied up to a maximum of 18°, which is greater than that observed in Section R2.1/7, and is possibly due to a greater degree of paint film heterogeneity for the present samples, as discussed in Section T1/5.3.

Values of R_{pf} decline markedly with time, as shown by several examples in Figure R2/40. An estimate of sample failure of U-cell free films was obtained from R_{pf}/t plots like those in Figure R2/40, as the time, $t_{f,Rpf}$, taken for R_{pf} to fall to 10^6 ohm.cm^2. Figure R2/41 is a plot of $t_{f,Rpf}$ versus solution chloride ion concentration. The data points show a large amount of scatter. The regression line plotted through these points suggests that sample failure occurs sooner in more concentrated solutions. However, the $t_{f,Rpf}$/log[Cl^-] trend is only statistically significant at the 90% level of confidence.

Values of C_{pf} are relatively constant with time, being around 1-2 nF.cm^{-2} (not shown). These values for free films are mentioned in Section R2.2/1.2 as being further supportive evidence that the Nyquist high frequency semicircle is due to the paint film.

3.3 Single frequency/wide frequency range test comparisons

Free film sample failure times as a function of solution chloride ion concentration are described individually for both the single frequency and wide

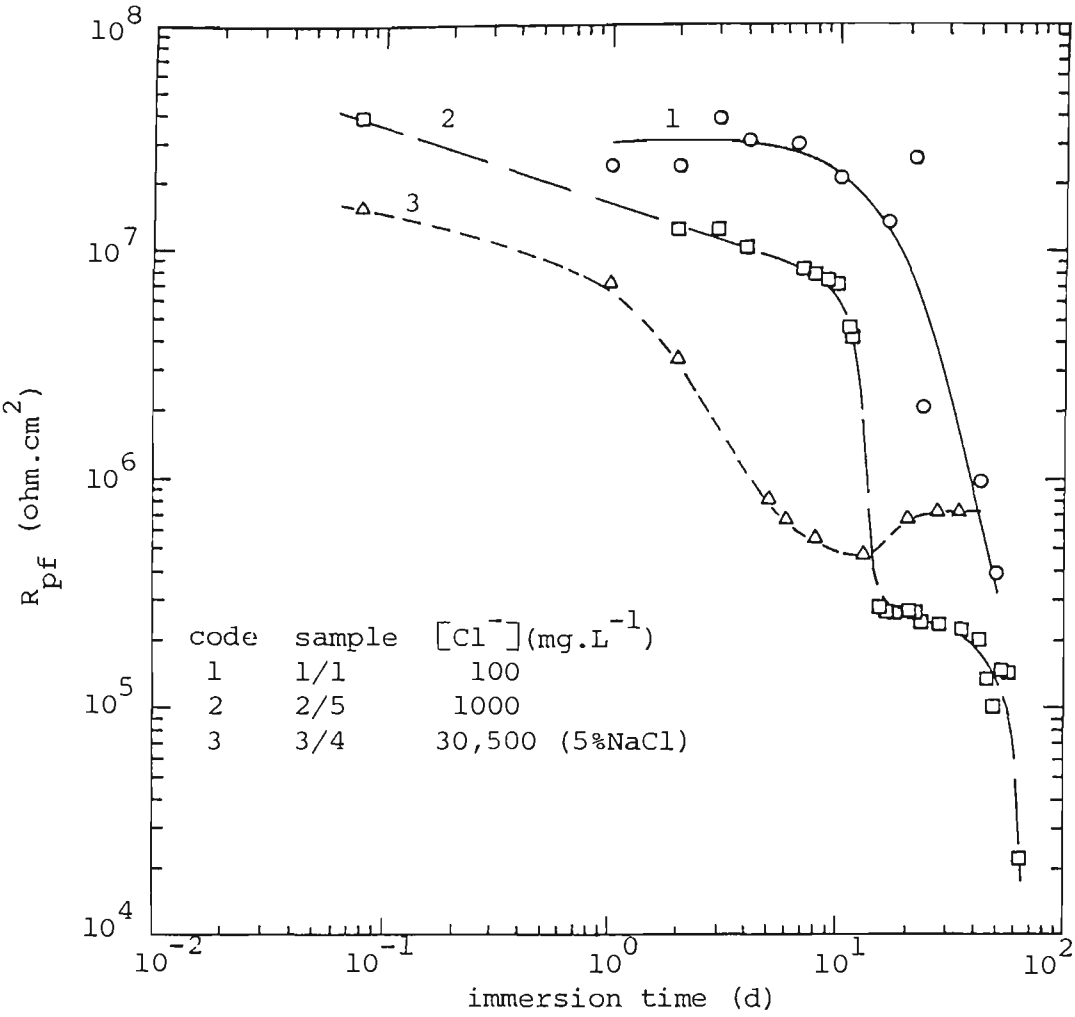

Figure R2/40. Paint film resistance, R_{pf}, versus immersion time for 3 representative samples of 2 x 10 µm SMP free films in different chloride ion solutions at 50°C.

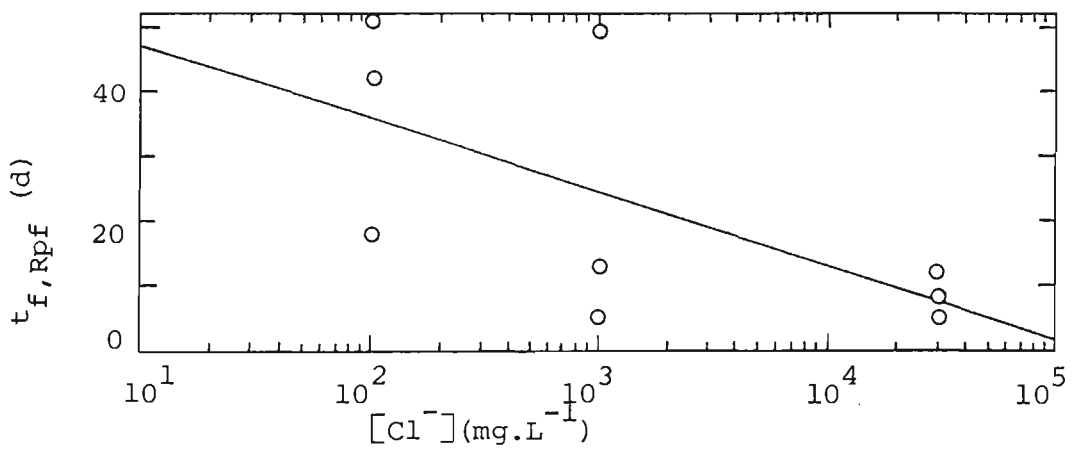

Figure R2/41. Sample fail time, $t_{f,Rpf}$, versus solution chloride ion concentration for 2 x 10 µm SMP free films at 50°C. Full line is regression line but trend is only statistically significant at 90% level of confidence. $t_{f,Rpf}$, time for R_{pf} to fall to 10^6 ohm.cm^2 in plots like those in Figure R2/40.

frequency range test methods in Sections R2.2/3.1.2 and R2.2/3.2, respectively. Both test methods are compared in Sections R2.2/5.2.

4. Free films - gravimetric results

Table R2/3 (in Section R2.2/2) lists gravimetrically determined mass gain results for free films as described in Section E3.2/4.5. This table shows mass gain versus time for 25% gloss 2 x 10 µm SMP free films (no primer), immersed in solutions of differing chloride ion concentration.

The simple mass gains in column 5 are nearly all negative, indicating an overall mass loss. As in Section R2.2/2, the overall mass gain is probably a mass gain of water and a mass loss by soluble matter. Weighings after one day in a desiccator were taken to indicate the amount of water desorbed. The difference between the initial mass in column 3 and the weigh after 1 d in a desiccator (column 6) was taken as the amount of dissolved solids lost during the immersion period. Three samples (coded 1,5,9) were re-immersed in their respective solutions for a further three days after the weighing following one day in a desiccator. It is seen that the water desorbed (column 7) following a second period in the desiccator is similar to the weighing after the first period in a desiccator. This suggests that the process of water absorption/desorption is a reversible one. There is also a suggestion that water desorbed (column 7) increases as solution chloride ion concentration decreases.

Water uptake was calculated from the water desorbed data in column 7, see note 1 in Table R2/3 for the method of calculation. The data in this table was statistically analyzed using a general linear model procedure, which is described along with the statistical results, in Section A4/3.4. These results

indicate that water uptake increases with time and with decreasing solution chloride ion concentration according to Equation (A4/34).

$$X_V = 5.80 - 1.18 \log [Cl^-] + 0.283 \text{ time} \qquad \text{(A4/34)}$$

where X_V = water uptake (% v/v)

This equation is shown plotted as water uptake at one day versus solution chloride ion concentration in curve 3 Figure R2/46, Section R2.2/5.1.2. The effect of the two independent variables (log chloride, time) on the dependent variable, water uptake, is about the same. The trend for water uptake to increase with decreasing chloride is in agreement with the conclusions of Brasher and Nurse[7] for a different painted metal/solution system; in agreement with the capacitance results on attached films in Section R2.2/1.1.1, and the gravimetric results on attached films in Section R2.2/2.

Equation (A4/34) is also plotted as water uptake versus time in Figure R2/42 along with the data points, which are scattered around three regression lines, one for each chloride solution. These lines also show that water uptake increases with decreasing chloride. They represent a reasonable fit of the data at times ≧0.3 d. Obviously, water uptake must be zero at zero time, so that the rate of water uptake between 0 and 0.3 d must be more rapid than shown by these regression lines. A similar situation was found for attached films in Section R2.2/2. This subject is taken up further in Section R2.2/6.

5. Attached/free film comparisons

The aim of this section is to compare the water uptake results in Sections R2.2/1-2 for attached films with those in Section R2.2/3-4 for free films.

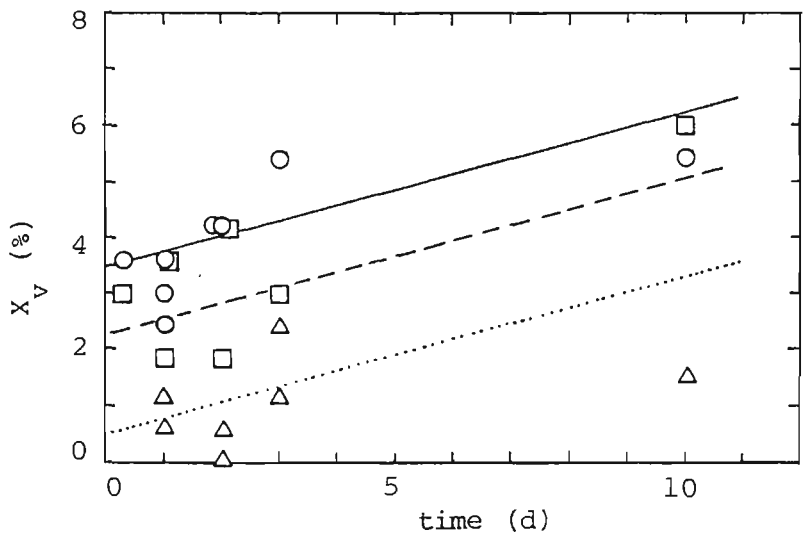

Figure R2/42. Effect of immersion time in various chloride ion solutions at 50°C on gravimetric water uptake, X_v, for 25% gloss free films. Lines shown are regression lines.

Code	$[Cl^-]$ $(mg.L^{-1})$
—○—	100
- - -□- - -	1000
·····△·····	30 500 (5% NaCl)

Failure times for attached films in Sections R2.2/1.1.2, 1.2 are also compared with failure times for free films in Sections R2.2/3.1.2, 3.2.

5.1 Water uptake

5.1.1 Effect of time

Figure R2/43 is a plot of water uptake calculated by the 1 kHz capacitance method as a function of immersion time comparing examples of attached and free films in each of the three chloride ion solutions. The free film sample results are replotted from Figure R2/37b, Section R2.2/3.1.1. This plot demonstrates that, for each solution, calculated water uptake for the attached films is greater than that for the free films.

Figure R2/44 is a plot of water uptake obtained gravimetrically as a function of immersion time comparing attached and free films in each of the three chloride ion solutions. Each line is a general linear model regression line, discussed in Appendix A4/3.3,3.4, using Equation (A4/33) for attached films and Equation (A4/34) for free films. These lines represent the best fit of the data that was obtainable. This plot also demonstrates that, for each solution, calculated water uptake for the attached films is greater than that for the free films. This fact has been noted previously in the literature by D'Alkaine et al[156] as shown in Figure T6/5, Section T6/6, for epoxy films either free or attached to a steel substrate. They concluded that such experiments introduce serious doubts about the extrapolation of free film results to films applied in actual practice. Funke[190] proposed that such results indicated water accumulation at the metal/film interface. Strictly, the water uptake data for the free films should be halved for comparison with attached film data

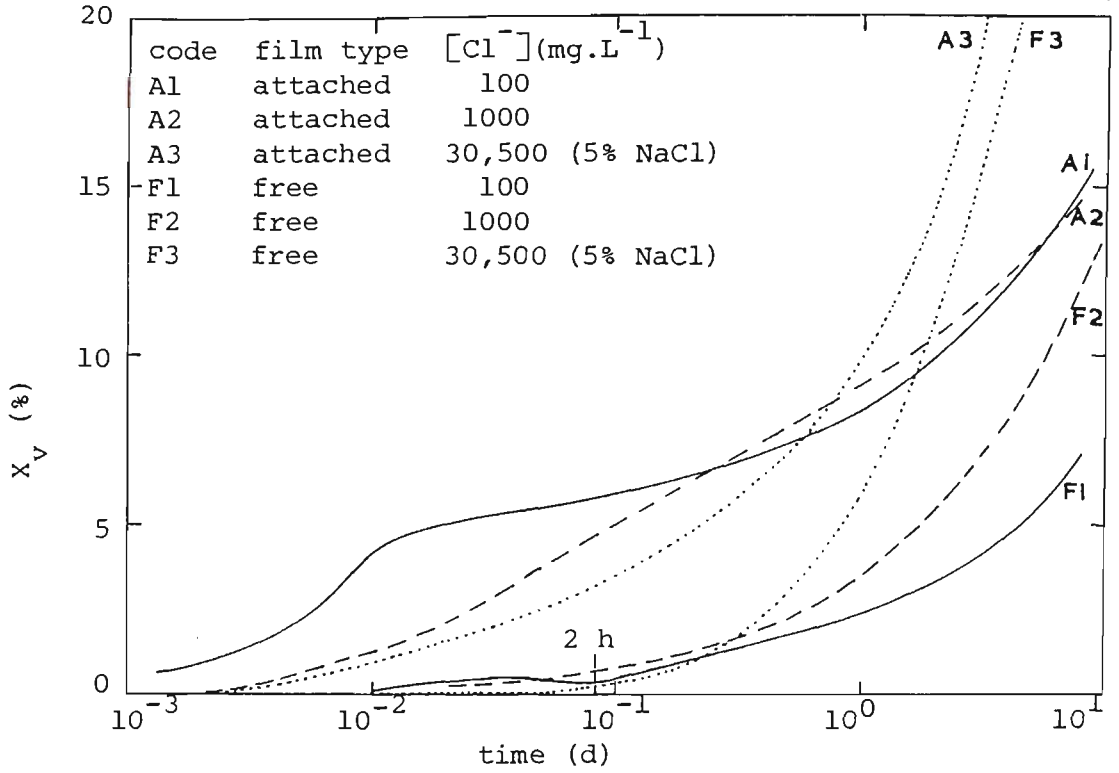

Figure R2/43. Effect of immersion time on water uptake calculated by the 1 kHz capacitance method for examples of free and attached films in three chloride ion solutions.

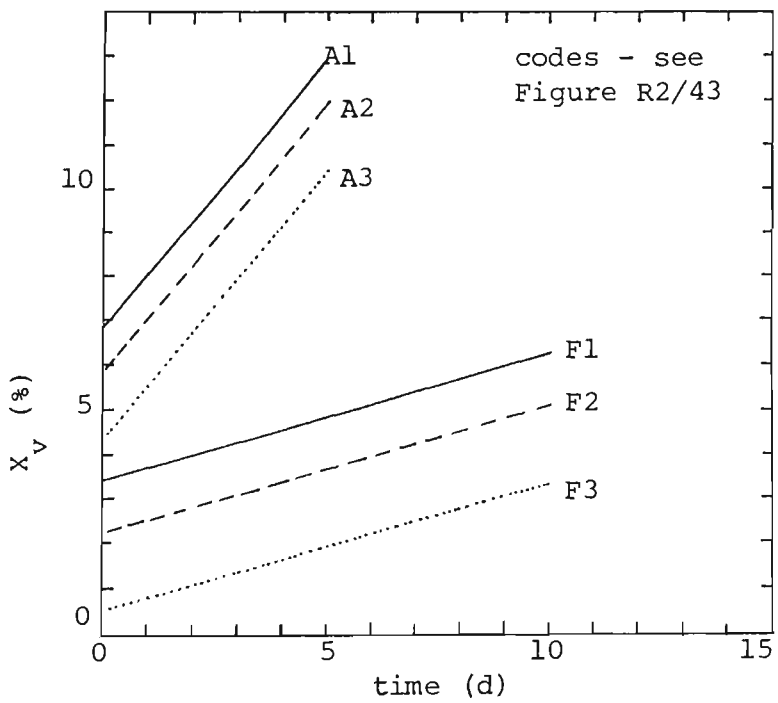

Figure R2/44. Effect of immersion time on gravimetric water uptake for free and attached films in three chloride ion solutions. Lines are regression lines using Equation (A4/33) for attached films and Equation (A4/34) for free films.

because free films have two sides exposed in the U-cell whereas attached films only have one. However, this only accentuates the difference.

With the present set of results, it is difficult to conclude that the higher water uptake on the attached films is due to the presence of the substrate because the attached film system comprised primer plus top coat whereas the free films were just top coat. However, the following two reasons suggest that the higher water uptake on the attached films may not be due to the primer. Firstly, free films have two surfaces exposed to the solution in U-cell tests whereas attached films have only one, which predicts that attached films should have a lower rate of water uptake than free films, but Figure R2/44 shows the opposite effect. Secondly, the discussion in partial correlation coefficients in Section A4/3.1 shows that water uptake decreases as primer thickness increases for the attached films. This suggests that the influence of the primer is to decrease water uptake, but again Figure R2/44 shows the opposite effect. It is therefore likely that the greater rate of water uptake on the attached films is due to the presence of the substrate.

5.1.2 Effect of $[Cl^-]$

Figures R2/45,46 are plots of water uptake versus solution chloride ion concentration for the free and the attached films. Water uptake, $X_{v,2h}$, $X_{v,1d}$, was obtained from capacitance and gravimetric calculation methods at 2 h and 1 d, respectively. The lines shown are general linear model equations that represent the best obtainable fit of the data using simple, linear models. In both Figures R2/45,46 for a given calculation method, the attached films, curves 1 and 2, show a greater amount of water uptake than the free films, curves 3 and 4, over the chloride range. This has been discussed in Section

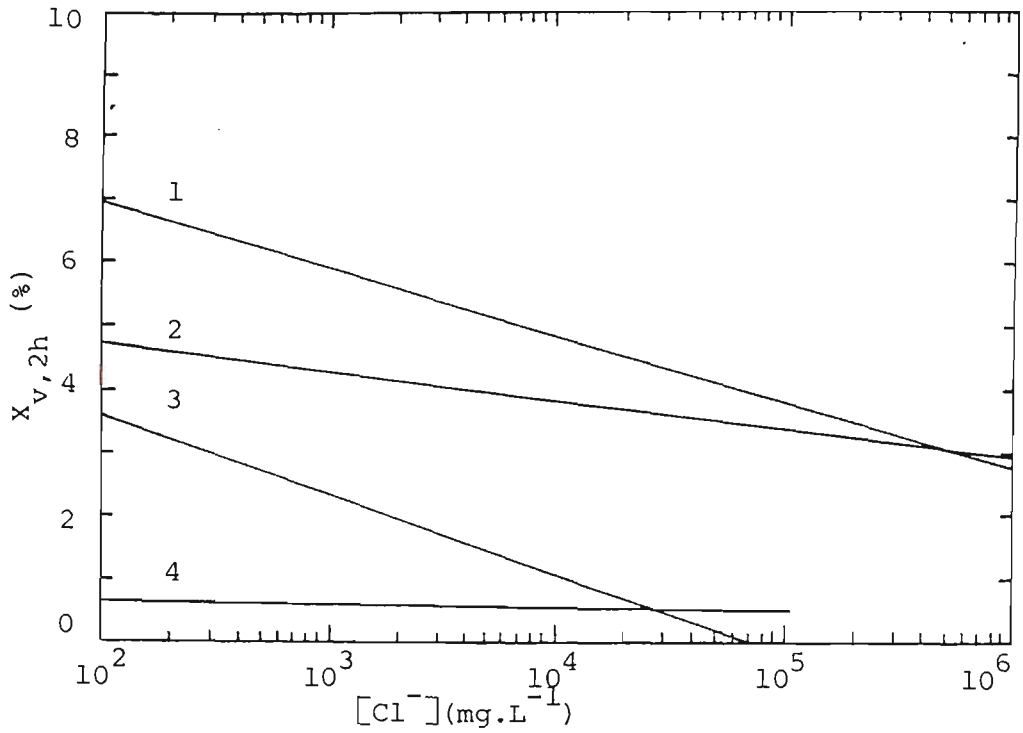

Figure R2/45. Regression lines for water uptake at 2 h, $X_{v,2h}$, versus solution chloride ion concentration at 50°C for free or attached paint films calculated by the gravimetric or capacitance method. 1. attached/gravimetric; 2. attached/capacitance; 3. free/gravimetric; 4. free/capacitance.

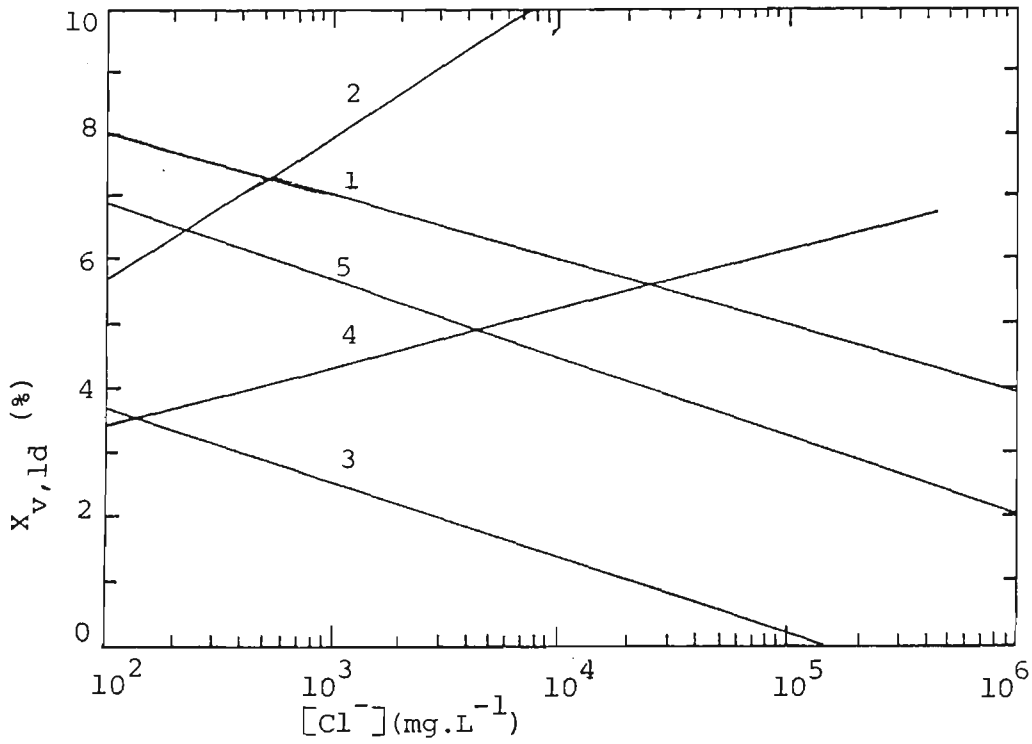

Figure R2/46. Regression lines for water uptake at 1 d, $X_{v,1d}$, versus solution chloride ion concentration at 50°C for free or attached paint films calculated by the gravimetric or capacitance method. 1. attached/gravimetric; 2. attached/capacitance; 3. free/gravimetric; 4. free/capacitance; 5. attached/capacitance (Brasher and Nurse[7]).

R2.2/5.1.1. The effect of $[Cl^-]$ is discussed further in Section R2.2/6. Curve 5 of Figure R2/46 is taken from results of Brasher and Nurse[7] for marine painted steel in sodium chloride solutions at room temperature, based on the capacitance method of calculating water uptake. This shows nearly the same slope as the present attached/gravimetric results, and the slightly lower water uptake results could be explained by the lower solution temperature.

5.2 Sample failure

Figure R2/47 is a plot of sample failure time versus solution chloride ion concentration for the free and the attached films. Sample failure time, $t_{f,C}$, was obtained from single frequency tests in Sections R2.2/1.1.2 (attached film), R2.2/3.1.2 (free film), whilst sample failure times, $t_{f,Rpf}$, $t_{f,Rt}$ were obtained from wide range frequency tests in Sections R2.2/1.2 (attached film), R2.2/3.2 (free film), respectively. The lines shown are regression lines to the data referred to in the above sections.

The most obvious feature in Figure R2/47 is the fact that fail times, $t_{f,C}$ and $t_{f,Rpf}$, are considerably less for the free films, curves 4 and 5, than for the attached films, curves 1-2. This is somewhat surprising because attached films have higher water uptake rates, see Section R2.2/5.1.1 and on this basis might be expected to fail earlier. Two reasons can be suggested for the difference in fail times between free and attached films. Firstly, the free films were composed of top coat only (2 x 10 μm thick) whereas the attached films were primer (5 μm) + top coat (1 x 20 μm). It is possible that a primer + top coat combination would give longer times to failure because epoxy primers do not hydrolyze to the same extent as silicone modified polyester, SMP, top coats[188]. As the primer is effectively in series with the top coat, the measured c_{flk}, value would be expected to

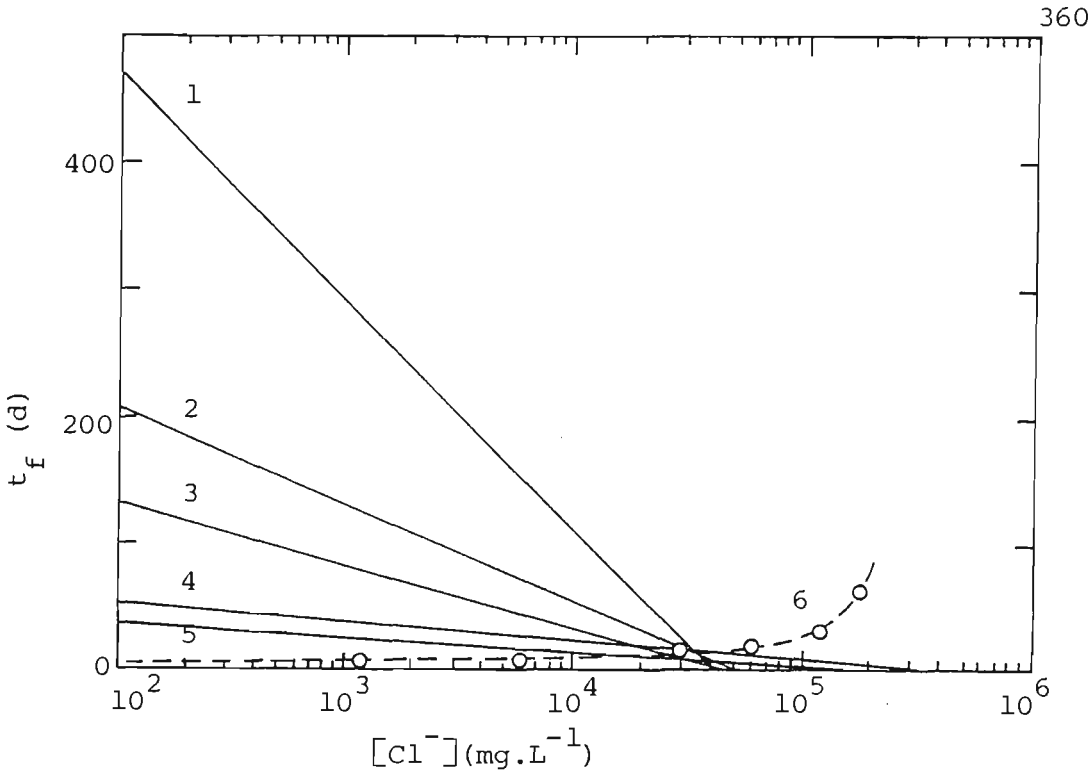

Figure R2/47. Sample fail time, t_f, based on failure criteria as indicated, versus solution chloride ion concentration at 50°C for free or attached paint films calculated by the 1 kHz capacitance, c_{flk}, paint film resistance, R_{pf}, or charge-transfer resistance, R_t, methods. Full lines are regression lines.

code	paint film	fail time	explanation and failure criteria
1	attached	$t_{f,C}$	time for c_{flk} to rise to 10 nF.cm^{-2}
2	attached	$t_{f,Rpf}$	time for R_{pf} to fall to 10^5 ohm.cm^2
3	attached	$t_{f,Rt}$	time for R_t to fall to 10^6 ohm.cm^2
4	free	$t_{f,C}$	time for c_{flk} to rise to 10 nF.cm^{-2}
5	free	$t_{f,Rpf}$	time for R_{pf} to fall to 10^6 ohm.cm^2
6	attached (Brasher/Nurse)	$t_{f,C}$	time for c_{flk} to rise to 20 nF

remain low for a longer time and follow the capacitance of the primer, even though the capacitance of the top coat may increase markedly due to hydrolysis. Additionally, the relatively non-hydrolyzable primer would be expected to act as a better rigid support for the more hydrolyzable top coat, thereby reducing stresses in the free film that give rise to tearing and early failure. Secondly, the attached films are physically attached to a rigid substrate. This may provide mechanical strength to the attached film, whereas stresses forming in free films as they degrade may distort them, for example, by stretching, which may eventually lead to a tear in the film and failure of the sample.

Curve 6 of Figure R2/47 shows the results of Brasher and Nurse[7] for marine painted steel at room temperature replotted from Figure T6/4, Section T6/5. Note that whilst the $t_{f,C}/[Cl^-]$ trends can be compared, a different failure criterion (time, $t_{f,C}$, for c_{flk} to rise to 0.02 μF) has been used. It is therefore not possible to compare the absolute values with other data sets in Figure R2/47. Whereas their results show failure time increasing with increasing $[Cl^-]$, the present results show the opposite trend for both the free, curves 4 and 5, and the attached films, curves 1-3. This supports the previous discussion in Section T6/5, where previous similar results by Walter[127] were compared with the Brasher/Nurse results. Although the two sets of results were obtained at different temperatures, the difference in trends is thought due to a difference in the mode of degradation. This subject is discussed further in Section R2.2/6.

For the free film results in curves 4 and 5, Figure R2/47, there is reasonable agreement between the $t_{f,C}/[Cl^-]$ regression line, curve 4, obtained from single frequency tests, and the $t_{f,Rpf}/[Cl^-]$ regression line, curve 5, obtained from wide frequency range tests. This indicates that the criteria for

sample failure (time, $t_{f,C}$, for c_{flk} to rise to 10 $nF.cm^{-2}$ and time, $t_{f,Rpf}$, for R_{pf} to fall to 10^6 $ohm.cm^2$) are approximately equivalent. It was not possible for $t_{f,Rpf}$ to have the same failure criterion (time for R_{pf} to fall to 10^5 $ohm.cm^2$, see below) as the attached films because R_{pf} had not fallen to that extent for all samples, eg sample 3/4 in Figure R2/40. However $t_{f,C}$ does have the same failure criterion as the attached films and is therefore strictly comparable.

For the attached film results in Figure R2/47, the $t_{f,C}/[Cl^-]$ regression line, curve 1, is substantially higher than either the $t_{f,Rpf}/[Cl^-]$ regression line, curve 2, or the $t_{f,Rt}/[Cl^-]$ regression line, curve 3. This simply indicates that the criteria for sample failure (time, $t_{f,C}$, for c_{flk} to rise to 10 $nF.cm^{-2}$; time, $t_{f,Rpf}$, for R_{pf} to fall to 10^5 $ohm.cm^2$; time, $t_{f,Rt}$, for R_t to fall to 10^6 $ohm.cm^2$) are not equivalent. It was not possible to choose a much lower criterion for $t_{f,Rpf}$ or $t_{f,Rt}$ (of say the time for R_{pf} or R_t to fall to 10^4 or 10^5 $ohm.cm^2$, respectively) because not all R_{pf}/time or R_t/time trends in Figures R2/21,22,25,26 for samples in 1000, 100 $mg.L^{-1}$ $[Cl^-]$ had fallen to this extent. Therefore it was not possible to increase $t_{f,Rpf}$ or $t_{f,Rt}$ values to match up better with $t_{f,C}$ values. The other alternative would be to change the criterion for $t_{f,C}$ (that is, the time for c_{flk} to rise to say 2 $nF.cm^{-2}$ instead of 10 $nF.cm^{-2}$). This was not attempted because columns 10, 11 of Table R2/1 in Section R2.2/1.1 show that the times $t_{f,C}$ and $t_{f,R}$ are roughly equivalent using the existing failure criteria.

It is believed that $t_{f,C}$ is a better measure of sample failure for these results than $t_{f,Rpf}$ for three reasons. Firstly, the single frequency test is much simpler to carry out experimentally, and does not require analysis of the impedance data. Secondly, the $t_{f,C}$ failure criterion is exactly the same for

free and attached films, so that comparisons can readily be made, whereas the $t_{f,Rpf}$ failure criterion is different for free and attached films, as discussed above, making comparisons more difficult. Thirdly, the $t_f/[Cl^-]$ trend for $t_{f,C}$ is statistically significant at a higher level of confidence than that for $t_{f,Rpf}$.

6. Gravimetric/capacitance comparisons

The aim of this section is to compare the gravimetric method, in Sections R2.2/2,4 with the capacitance method, in Sections R2.2/1,2, for calculating water uptake and sample failure on both free and attached films.

From an experimental point of view, the capacitance method of calculating water uptake appears far superior to the gravimetric method for both free and attached films. Water uptake can, in most cases, be readily and continuously calculated by the capacitance method. The main difficulty is with free films where stress in the film can lead to tears in the film and premature failure, but with attached films, the film is supported by the substrate and this is not a problem. The gravimetric method on attached films is difficult because the differences in sample mass before and after immersion are very small. With both attached and free film tests, gravimetric water uptake could not be calculated from a mass gain (due to soluble matter leaching from the film and, for attached films, corrosion of the substrate), but had to be calculated from water desorbed after storing in a desiccator. Short time measurements (<0.3 d) were not possible, and longer time measurements (>10 d) were complicated by solution penetrating under the wax sealed edges of the attached film samples.

Despite these experimental difficulties, water uptake calculated by the

gravimetric method is consistently negatively correlated with solution chloride for both free and attached films. This is shown by Equation (A4/34) in Section R2.2/4; curve 3 in Figures R2/45,46 for free films and by Equation (A4/33) in Section R2.2/2; curve 1 in Figures R2/45,46 for attached films, the latter in agreement with capacitance calculated trends in curve 5 for the results of Brasher and Nurse[7].

By comparison, water uptake calculated by the capacitance method gives inconsistent correlations with solution chloride. For free films, no significant correlation existed between 2 h water uptake and log [Cl^-], also 1 d water uptake was positively correlated with log [Cl^-], see Figure R2/38, Section R2.2/3.1.1 and curve 4 in Figures R2/45,46. For attached films, 2 h water uptake was negatively correlated with log [Cl^-], but 1 d water uptake was positively correlated, see curve 2 in Figures R2/45,46 respectively.

The following discussion attempts to explain these apparently contradictory results between gravimetric and capacitance methods. It was concluded from the discussion on Equations (A4/33,34) in Sections R2.2/2,4 that gravimetric water uptake for both free and attached films occurred at a higher rate in the initial period of immersion (the first few hours), followed by a slower rate at longer times. Referring to Figure R2/43, it is reasonable to assume that this higher rate in the initial period is indicated by the X_v/t trend up to, say, about 0.1 d. At longer times, the X_v/t trend for the capacitance method in Figure R2/43 bends upwards, suggesting higher water uptake rates. However, the X_v trend at longer times slows down for the gravimetric method, as indicated by the respective regression lines in Figure R2/44. If it is assumed that the gravimetric method must indicate water uptake within the paint film, then the capacitance method at the longer times must be indicative of something else superimposed on water uptake trends. It is suggested that this

'something else' is degradation of the paint film and uptake of solution chloride ions. Thus water may enter the paint film in the first few hours of immersion at a rate inversely related to the solution chloride ion concentration, as shown by the X_V/trends at 2 h in Figure R2/43 for attached films. This period would be equivalent to the Brasher/Nurse[7] explanation that water enters the film driven by the solution osmotic pressure, as discussed in Section T6/5. At longer times, the rate of water uptake decreases, but the rate of increase in the 1 kHz capacitance, from which water uptake is calculated, increases. This rapid capacitance increase has been attributed to reorientation of the mode of distribution of water within the film[7], and also to the much larger values of substrate capacitance exposed to the solution at pores in the paint film[6,7,187] as discussed in Section R2.2/1.1.1. This latter explanation would be possible for attached films and also feasible for free films, except that the substrate capacitance in this case would be the platinum auxiliary electrode capacitance in each arm of the U-cell.

The apparent (calculated) water uptake at longer times (eg 1 d), for attached films in Figure R2/43 alters its dependency on solution chloride to being directly related, rather than inversely related as it was in the first hour or so. If it is assumed that degradation of the paint film occurs due to hydrolysis, as discussed in Section R2.2/3.1.1, the rapid rise in capacitance (as seen, for example, in Figure R2/15) has still to be explained. It is hypothesized that chloride ions enter the film at these times, so that the rise in capacitance would be directly related to the concentration of chloride ions in the film. The chloride ions may, or may not, catalyse the paint film hydrolysis reaction, but they would certainly be expected to increase corrosion of the substrate in the case of attached films. It is interesting to note that, at these longer times, the dependency on solution chloride is the same as that for sample failure times.

Thus it seems that water initially enters the film, but after a few hours this rate slows down and paint film degradation becomes more and more significant. These explanations serve to explain why capacitance calculated water uptake at 1 d is positively correlated with solution chloride for both free and attached films in Figure R2/46. The capacitance method measures more than just water uptake at these longer times. Although more satisfactory experimentally, the capacitance method does not indicate water uptake correctly at immersion times longer than several hours under the conditions used. The gravimetric method gives estimates of water uptake up to relatively much longer times (but ≦10 d) even in the presence of paint film degradation.

Curve 6 in Figure R2/47 shows sample failure time increasing with solution chloride for marine painted steel tested by Brasher and Nurse[7]. Curves 1-5 show the opposite trend for the paint systems tested in this thesis, that is, sample failure time decreasing with solution chloride. It was suggested in Section R2.2/5.2 that these differences in trends could be due to a difference in the mode of degradation of the paint film. It is now apparent that both paint systems take up water in the initial stages of immersion. The paint systems tested in this thesis relatively quickly undergo degradation of the paint film and ingress of solution chloride, such that substrate corrosion and final breakdown (blistering) of the paint film occurs sooner, the higher the solution chloride concentration is. The Brasher/Nurse paint system continues to be controlled by the osmotic pressure of the solution at least right up until paint breakdown, such that sample failure occurs sooner, at lower solution chloride concentrations, as discussed in Section T6/5.

1. General

A brief description of the main programs and subprograms written for this thesis is contained in this appendix. Reference should also be made to the corresponding program flowchart diagram, eg for program CONTROL, refer to Figure A1/3.

A list of codes used in the program flowcharts is shown in Figure A1/1. Subroutines (rectangular boxes in the flowcharts) are generally accessed by the operator by selecting the appropriate program defined softkey.

Programs and data files were stored on hard disc using a directory structure. The main directory was termed ELCM for Electrochemistry. Other directories, containing programs and data, resided under ELCM. These sub-directories were:

directory code name	meaning	directory code name	meaning
contrl	control	plot	plot routines
ig	galvanic current	data	data files
z	impedance	util	utilities
ik	corrosion current	testprog	test programs
store	store/retrieve data		

A directory tree structure, containing programs that were written, is shown in Figure A1/2. Brief details and flowcharts are given only for the more important programs, and are described under each relevant directory heading.

2. Directory contrl (control)

2.1 Program CONTROL (refer Figure A1/3) 468 program lines

This was the main program controlling other subprograms selected by the operator, see Figure A1/3. Impedance experiments were carried out using subprogram FRA_EXPT. Polarization resistance experiments used subprogram RP_EXPT. However, galvanic current tests were carried out from CONTROL, rather than a separate subprogram, as dictated by programming considerations.

2.2 Galvanic current tests

Galvanic currents are measured by periodic calls to a subprogram ADC, which measures the voltage drop across a current measuring resistor, Rx, in the operational amplifier box, Figure E1/1, Section E1.1/1, switched to zero resistance ammeter mode. The measurements can be aborted at any time, or terminated normally when galvanic currents are sufficiently low. Galvanic current/time data, either collected directly from an experiment or retrieved from disc storage, can be converted into coulombs and mass loss in subprogram MASS_LOSS. This data can also be tabulated, plotted using subprogram PLOT8, or stored on disc via subprogram STORE_MNGR.

2.3 Subprogram scope 82 program lines

Subprogram scope dumps the VDU screen contents of the Tektronix Model 2430 oscilloscope to the HP Thinkjet Model 2225AK printer.

3. Directory ig (galvanic current)

3.1 Subprogram ADC (refer Figure A1/4) 106 program lines

Subprogram ADC controls the timing and measurements of voltages proportional to galvanic current on the analog-to-digital card (A/D card), Model HP 98640A, in the computer, refer to Figure E1/1, Section E1.1/1.

ADC first configures, initializes and calibrates the A/D card by making calls to a group of Pascal compiled CSUB programs called MEAS_LIB3 loaded to the main program CONTROL. These CSUBs are part of a commercially available software package called Measurement Library, part number HP 98645A.

Twenty readings are taken, and averaged, of the voltage drop, Vg, across Rx, the galvanic current sensing resistor in the operational amplifier box switched to zero resistance ammeter mode, see Figure E1/1. Galvanic current, Ig, is then calculated, along with the quantity of electricity, q (coulombs), since the last measurement interval, see Equations (A1/1,2).

$$Ig2 = Vg/Rx \qquad (A1/1)$$

$$q = q + (Ig2-Ig1)/2 \times (t2-t1) \qquad (A1/2)$$

where Ig1, Ig2 = previous/present galvanic current (A)

t1, t2 = previous/present time (s)

A new interrupt time interval is then calculated and set up. The new time is dependent on the number of readings already taken and the rate of change of Vg. The procedure of voltage measurement and setting the next interrupt

time continues until the value of Ig falls below a prescribed minimum (normally 15 μA), whereupon the measurements terminate.

The operations of ADC are a background process that allow other electrochemical tests or operations, such as plotting, to take place until the next interrupt time when they are momentarily interrupted whilst a measurement of Vg takes place.

3.2 Subprogram MASS LOSS (refer Figure A1/5) 589 program lines

Subprogram MASS_LOSS calculates mass loss from galvanic current, Ig, or polarization resistance, R_p, versus time, t, data passed from another program, eg CONTROL, or entered manually from the computer keyboard.

The program detects whether or not Ig or R_p data has been passed from another program. If not, then the data type (Ig or R_p) must be selected and the respective data entered manually, followed by a calculation of the quantity, q, of electricity passed, equal to the area under the Ig/t or R_p/t curve. If data has been passed from a previous program, this stage is skipped. The operator is then requested to enter the substrate type (Zn, galvanized, ZINCALUME coated steel, Al or Fe), which determines the anodic and cathodic Tafel constants b_a and b_c respectively, and the electrochemical equivalent, Eq. Mass loss, ΔM, can then be calculated according to Equations (A1/3,4)

$$B = [(1/b_a + 1/b_c) \times 2.303]^{-1} \quad \text{(A1/3)}$$

$$\Delta M(g.m^{-2}) = Eq \times Bxq \times 10^4/area \quad \text{(A1/4)}$$

After sample identification numbers have been entered by the operator, results can be tabulated, edited or stored on disc. Plotting is available by returning to the previous program.

4. Directory z (impedance)

4.1 Subprogram FRA EXPT (refer Figure A1/6) 2039 program lines

Subprogram FRA_EXPT controls the gathering of impedance data from experiments and subsequent operations of storing on disc or plotting.

Impedance data can be obtained in several different ways by selecting 'configure potentiostat' softkey. Firstly, the Frequency Response Analyser, FRA, can be used alone in 'FRA only compression mode', or it can be used in conjunction with the Electrochemical Interface, ECI, see Figure E1/1, Section E1.1/1, acting as a galvanostat. The ECI can also be configured as a potentiostat. Secondly, the operational amplifier box manually switched to galvanostat mode can be used in conjunction with the FRA instead of the ECI.

Both the FRA and the ECI can be set up remotely by program commands sent over the HPIB interface. A set of default commands are sent prior to an impedance test being performed, but any command can be separately altered by accessing softkeys 'alter FRA' or 'alter ECI'. Figure A1/6d shows a complete list of options available, eg 'bandwidth type' on the ECI or 'amplitude' on the FRA.

Two types of impedance tests can be carried out - a 1 kHz test or a wide frequency range test spanning the range 65 kHz to 0.1 Hz with lower

frequencies being also possible, see also Section E1.2/2.

Various plotting facilities are available. Firstly, the wide frequency range scan is automatically plotted on the VDU screen as a Nyquist impedance plot of b versus a. Axis size, frequency minimum and frequency scan rate can be altered both before and during a frequency scan. Secondly, data from disc and from a file in the FRA can be accessed and plotted with the aid of subprogram PLOT8. Three types of impedance plots are available - Nyquist b versus a, Bode log r versus log f and Bode Theta versus log f.

Impedance data can be stored on hard disc, see Figure E1/1, either as data previously stored in the FRA file, or directly as frequency scan data. Data stored on hard disc can be retrieved for analysis, tabulation or plotting.

4.2 Subprogram Rx 63 program lines

Subprogram Rx allows the operator to select by softkey choice the value of resistor, Rx, in the Solartron Model 1286 Electrochemical Interface, ECI, or in the operational amplifier box, see Figure E1/1. It resides under subprogram FRA_EXPT where it is used for impedance tests but it is also called from the main program CONTROL where it is used for galvanic current tests.

Depending on the mode of operation of the ECI and FRA, Rx is either the current select resistor (galvanostatic mode) or the current measuring resistor (potentiostatic and zero resistance ammeter modes). On selection of the Rx value, the ECI has its Rx value changed automatically, but when using the operational amplifier box Rx must be changed manually. The computer detects what type of test is being performed, and if an impedance test, then

the scale factor in the FRA is also changed automatically.

4.3 Subprogram FRA FILE (refer Figure A1/7) 58 program lines

Subprogram FRA_FILE transfers all data records of frequency, f, resistive, a, and reactive, b, components of impedance from the FRA file, a non-volatile memory in the Frequency Response Analyser, FRA, into the computer's memory. Values of f, a and b are tabulated as the transfer proceeds. If no data records are available for transfer the subprogram displays a message and terminates.

4.4 Subprogram FRA CHECK (refer Figure A1/8) 366 program lines

Subprogram FRA_CHECK performs a 1 kHz impedance check on the test cell to determine whether the sine wave current sent from the Frequency Response Analyser, FRA, to the test cell is optimized for subsequent impedance tests, either 1 kHz or wide frequency range.

Results of the FRA test (Ch 1, 2 r, θ, err) are analyzed by the computer in three ways. Firstly, integration errors in the FRA Ch2 analyzers are detected. The 1 kHz check is repeated or the check sequence terminates depending on the number of previous checks carried out, the maximum number allowed being 8. If the check is repeated, either the FRA's maximum integration time is lengthened; the maximum integration time lengthened plus a change to a less stringent integration requirement (short compared to long); or no alteration is made, depending on the number of previous checks. Secondly, the amplitude of the test cell's voltage response is detected. If too low (or too high), Ch1 voltage, which determines the cell current, see Figure

E1/5 in Section E1.2/2.2, is increased (or decreased), if it is less than (or greater than) prescribed limits, and the 1 kHz check repeated, if less than 8 previous checks have been carried out. Thirdly, if the amplitude of the test cell's voltage response is less than about one tenth of the voltage across the current control resistor, Rx (as measured on Ch1), or greater than about 10 times, the value of Rx is decreased or increased, respectively, and the check repeated if less than 8 previous checks have been carried out.

The final result is either conditions of FRA Ch1 voltage and Rx that are optimized for the test cell, or the 1 kHz check fails and no satisfactory conditions can be found. In the latter case, the operator may intervene and select conditions, as appropriate.

4.5 Subprogram equiv crt (refer Figure A1/9) 708 program lines

Subprogram equiv_crt plots an impedance curve in different formats for an equivalent electrical circuit model, representing the metal/solution or painted metal/solution interface, selected by the operator. The different plot formats are, at present, Nyquist b versus a, Bode log r versus log f, Bode Theta versus log f, and susceptance, s, versus radial frequency, ω. Values for parameters of the chosen equivalent circuit model can be changed by the operator, and an impedance curve replotted. This subprogram has two distinct uses. Firstly, it can aid in showing how the choice of model or particular parameter values of the model can affect the shape of the resulting impedance curve. Secondly, it allows comparison between the shape of an experimental impedance curve, and a theoretical one, obtained by appropriate choice of parameter values. This is a more efficient method of analysis of experimental impedance curves compared to manual analysis. An automatic curve fitting routine is at present

under development.

At present, the choice of equivalent circuits is a series resistance, R, capacitance, C, model; a parallel R, C model $C//R+Z_{\omega}$ where Z_{ω} is the Warburg diffusion impedance; $C//R+Z_{\omega}//R_{cp}$, where R_{cp} is corrosion product resistance; a dual parallel R, C model commonly used to represent the paint/metal/solution interface[17]; and the same dual parallel R, C model with a Warburg diffusion impedance, Z_{ω}, added to take into account the diffusion of reactants/products into/out of the paint film. After choosing an appropriate model, the operator may alter any of the default parameter values of the model, in order to see what effect it has on the resulting impedance plot shape, or to match a set of experimental impedance data points. Subprogram Enter is used to input the parameter values. A calculation routine then calculates the resistive, a, and reactive, b, components of impedance of this model over the frequency, f, range 80 kHz to 0.1 Hz, which covers the normal experimental range.

The calculations use a subprogram Parll, which calculates the impedance of two complex impedances, A + jB and C + jD, in parallel to produce one equivalent resistive, E, and one equivalent reactive, F, component. This subprogram can be called a number of times for complex equivalent circuit models. The operator may then select a plot format (Nyquist b/a, Bode log r/log f, Bode Theta/log f, s/ω). The list of plot requirements for the chosen plot format are then defined, see Section A1/7.1, and the calculated a, b, f impedance/frequency arrays for the model are converted into the required form for plotting. If, for example, a Bode log r/log f plot was selected, the X-axis plot array is set equal to the f array, whilst the Y-axis plot array is set equal to the square root of $a^2 + b^2$. The general purpose subprogram PLOT8 is

then called, and a curve of the calculated impedance array is plotted. If an experimental impedance array is present (if subprogram equiv_crt was itself called from subprogram FRA_EXPT, see Section A1/4.1), and if the plot format chosen was Nyquist b/a, then the X-axis plot array will be set equal to the experimental resistive impedance component, Xx, array and the Y-axis plot array will be set equal to the experimental reactive impedance component, -Yy, array. After redefining the plot requirements, subprogram PLOT8 is called a second time and the experimental data points will be plotted superimposed on the calculated impedance curve. This allows the operator to assess whether the parameter values of the chosen equivalent circuit model are correct for the experimental impedance data. If there is a mismatch between the experimental data points and the calculated impedance curve, the operator can alter any of the parameter values, or choose a different model and repeat the plotting process to improve upon the analysis of the experimental data.

4.6 Program sigma — 140 program lines

Program sigma calculates Warburg diffusion coefficients, σ, in the low frequency range from two resistive, a, or reactive, b, components of impedance at two frequencies. These calculated values are referred to as σ_a, σ_b respectively. The Warburg diffusion line at low frequencies does not have to be at 45° on a Nyquist plot of a versus b because sigma calculates an average σ value given by $\sigma_{av} = (\sigma_a + \sigma_b)/2$. This method is particularly useful when the Nyquist plot diffusion tails at low frequencies bend over towards the a-axis making normal calculation difficult, refer to Section T1/5.2.

5. Directory ik (corrosion current)

5.1 Subprogram RP_EXPT (refer Figure A1/10) 1587 program lines

Subprogram RP_EXPT sets up the Solartron Model 1250 Electrochemical Interface, ECI, so that the operator can initiate small rectangular anodic and cathodic dc current steps, I, which are sent through the test cell containing a working electrode whose corrosion current, I_k, is to be measured. Voltage response, E, of the working electrode is obtained for a series of these current steps at low polarizations and plotted. With the aid of an analysis routine, IK_CALC or IK_CALC8 and a curvefit routine, Curvefit, a curve of best fit is plotted through these data points to obtain corrosion current, I_k, corrosion potential, E_k, anodic Tafel slope for the metal, $b_{a,M}$, cathodic Tafel slope for the reduction reaction, $b_{c,X}$, and polarization resistance, R_p. Standard deviations for I_k, $b_{a,M}$ and $b_{c,X}$ are calculated using the analysis routine to give an estimate of the confidence limits for these values.

The operator sets up the X- and Y-axes of the VDU screen as time, t, and voltage response, E, axes and selects appropriate ranges using the 'enter parameter value' routine. The amplitude and polarity of current steps are also selected in this way. This routine consists of three softkeys for entering a multiply factor, multiply power and sign of a number. The routine can be selected before, or during, the application of current steps. Measurements of E_k are then initiated by selecting the 'start/stop Ek' softkey, which causes a trace of E_k to be plotted on the VDU screen. When the rate of change of E_k has slowed sufficiently, a current step can be applied to the test cell by selecting the 'start/stop I' softkey, and continues until this softkey is pressed again, which terminates the current. The voltage response then decays slowly

to the zero current value and may be switched off by again selecting the 'start/stop E_k' softkey. Both these softkeys have toggle functions which output instructions to the ECI. The voltage response to the current step is displayed on the computer screen. A number of such current steps, differing in magnitude and sign can be applied to the test cell in this manner, and the voltage responses all recorded on the screen. A hard copy of all the traces can be obtained by a graphics dump to the system printer, if desired. The last pulse obtained can be deleted, or the sequence of current steps can be restarted at any time. The top lines of the VDU screen give the set up values of I; volts and time ranges; status of E_k and I start/stop softkeys; and an update of measured values of current, voltage response and elapsed time since E_k start softkey was pressed.

After completing the sequence of current steps, this raw E/I data can either be plotted and analyzed or stored on disc. If the latter option is selected the voltage response arrays are trimmed of unnecessary readings at the start and end and passed to subprogram STORE_MNGR for storage. The analysis routine, see Figure E1/3 in Section E1.1/5, basically consists of entering the time, t_v, to read the voltage responses; calculations for each current step to find the voltage response, E, corresponding to time, t_v; determining a linear regression line for six readings of E_k before the current step and extrapolation to obtain the value of $[E_k]_{tv}$ at t_v and hence $\epsilon = E-[E_k]_{tv}$. Values of ϵ versus I are then plotted using subprogram Plot from THEO_IK, Section A1/5.3.

At this point, several options are available - the raw E/I data can be stored on disc as previously described; the raw E/I data can be recalculated and plotted using a different reading time, tv; tables of values can be printed both on the screen and the system printer; any I/ϵ data point can be deleted down to a

minimum of two anodic and two cathodic data points and restored again; a curve of best fit can be plotted through the I/ε data points using the selected IK_CALC subprogram, to arrive at values of corrosion rate parameters I_k, R_p, $b_{a,M}$ and $b_{c,X}$ and standard deviations Sig_ik, Sig_ba, and Sig_bc; or another sequence of current steps can be applied to the test cell.

The 'edit disc' softkey permits the operator to access raw I/E data stored on flexible discs. Any previous data set can be recalled from disc for plotting I/ε, curvefitting and analysis of corrosion rate parameters.

5.2 Subprograms IK CALC, IK CALC8, IK CALC9

Subprogram IK CALC (refer Figure A1/11) 569 program lines

Subprograms IK_CALC, IK_CALC8 and IK_CALC9 are iterative, non-linear analysis routines that calculate corrosion rate parameters - corrosion current, I_k, anodic Tafel slope for the metal, $b_{a,M}$, and cathodic Tafel slope for the reduction reaction, $b_{c,X}$, where X represents the reduction reaction, typically defined by Equations (A1/5, 6).

hydrogen evolution $2H^+ + 2e \Leftrightarrow H_2$ (A1/5)

oxygen reduction $\frac{1}{2}O_2 + 2H^+ + 2e \Leftrightarrow H_2O$ acid solutions (A1/6)

or $\frac{1}{2}O_2 + H_2O + 2e \Leftrightarrow 2OH^-$ neutral/alkaline solutions

All three subprograms are based on Equation (A1/7), which expresses the cell current, I, in terms of the voltage response ε.

$$I = I_k[\exp(2.303\varepsilon/b_{a,M}) - \exp(-2.303\varepsilon/b_{c,X})] \quad (A1/7)$$

where $\varepsilon = E-E_k$ = polarization value

E = corroding electrode's voltage response at applied current, I (galvanostatic experiment) or corroding electrode's control potential (potentiostatic experiment)

E_k = corroding electrode's corrosion potential

The conventional method of analyzing I/ε data obtained at low polarization, ε, values is to minimize the sum of squares, S, of the differences in cell current, according to Equation (A1/8).

$$S = \Sigma(I_i - I)^2 \qquad \text{(A1/8)}$$

where I = curve fitted value of cell current

I_i = individual data point value of cell current

This is a satisfactory method when errors are predominantly in cell currents, I, as they are for the potentiostatic (controlled potential) case. However, the galvanostatic (controlled current) method was used for this thesis, and errors are predominantly in the voltage response, E. It has been shown[53], both by theoretical prediction and comparison tests, that minimizing the sum of squares, S, of polarizations, ε, according to Equation (A1/9) will lead to significantly lower errors in estimating corrosion rate parameters I_k, $b_{a,M}$ and $b_{c,X}$ for the galvanostatic case, than by using Equation (A1/8).

$$S = \Sigma(\varepsilon_i - \varepsilon)^2 \qquad \text{(A1/9)}$$

where $\varepsilon = E - E_k$ = curve fitted value of polarization

$\varepsilon_i = E_i - E_k$ = individual data point value of polarization

E_i = individual data point value of voltage response

Subprogram IK_CALC was written as part of this thesis by the author, and uses Equation (A1/8) to calculate corrosion rate parameters. Subprograms IK_CALC8 and IK_CALC9 were subsequently written by M.A.D. Madurasinghe, in conjunction with the author, and are based on Equation (A1/9). Corrosion rate data presented in this thesis has been analyzed by a combination of all three subprograms, but mainly using IK_CALC8 which is based on the standard Newton iteration method. Subprogram IK_CALC9 is very similar to IK_CALC8 but is based on the method of repeated bi-section (to determine $b_{c,X}$) followed by successive Newton iterations to obtain $b_{a,M}$ and I_k. This produces similar results to IK_CALC8 but will return a maximum $b_{c,X}$ value of 10 000 mV/decade whereas IK_CALC8 will continue to minimize the sum of squares and will keep increasing the $b_{c,X}$ value until the program diverges.

Subprogram IK_CALC, refer to Figure A1/11, calls 3 subprograms - rp_guess, ba_guess and least_sq. Subprogram rp_guess estimates polarization resistance, R_p, as the slope of the line joining the smallest positive and negative I/ε data points. Subprogram ba_guess uses this R_p estimate and the largest positive I/ε data point to calculate estimates, A0, C0, of $b_{a,M}$ and I_k respectively. Subprogram least_sq uses estimates A0, C0 to calculate I_k, $b_{a,M}$ and $b_{c,X}$ by linear least squares method. Firstly, two starting values, B0, of $b_{c,X}$ are obtained at 4A0 and 8A0 respectively, and the corresponding sum of squares, S2, found for each B0 using a modification of Equation (A1/8). A third B0 value is found along with its S2 value, such that the second S2 value is lower than the other two. Using a parabola routine, parab, these three S2, B0 data pairs are used to calculate the equation for a parabola and the B0 corresponding to the parabola minimum is found. The S2 value corresponding to this B0 value is then calculated, to arrive at a total of 4S2,B0 data pairs. A better guess of A0, C0 is also obtained, The S2, B0 data pair with the highest

S2 value is discarded, the data pairs rearranged to make the second S2 value lower than the other two, and the parabola routine is repeated. This procedure continues until changes in S2 and B0 fall below prescribed limits and the final values of C0, A0, B0 (now the estimated values of I_k, $b_{a,M}$, $b_{c,X}$) are returned to the calling program.

5.3 Program THEO_IK (refer Figure 1/12) 1369 program lines

Program THEO_IK calculates estimates of corrosion rate parameters - corrosion current, I_k, anodic Tafel slope for the metal, $b_{a,M}$, cathodic Tafel slope, $b_{c,X}$, for the reduction reaction X according to Equations (A1/5,6), in Section A1/5.2 and their standard deviations Sig_ik, Sig_ba and Sig_bc, respectively. The calculations are based on theoretical (I/ε) data sets which are derived from known starting values of I_k, $b_{a,M}$ and $b_{c,X}$. This allows comparison between the estimates and the starting values to test the accuracy of the calculation method. A percentage error is deliberately added to either the voltage, ε, or current, I, data, depending on the calculation method, to test its ability to converge to the known starting values. A number of different calculation methods can be evaluated in this manner using THEO_IK. Additionally, experimental (I/ε) data can be entered manually and analyzed to obtain corrosion rate parameters I_k, $b_{a,M}$ and $b_{c,X}$.

After defining default values for variables including the corrosion rate parameters, an analysis method is selected. This can be either IK_CALC, IK_CALC8, IK_CALC9 as described in Section A1/5.2; or various routines, IK_CALC4-6 written by M.A.D. Madurasinghe in conjunction with the author, modelled on other author's methods; or other routines, IK_CALC3, IK_CALC7, written by M.A.D. Madurasinghe. Routine IK_CALC4 is used to test the

method of Mansfeld[47], based on the sum of squares of hyperbolic terms; IK_CALC5 is used to test the method of Feliu and Feliu[191], based on the sum of squares of weighted current, and depends on equally spaced voltages; and IK_CALC6 is used to test the method of Greene and Gandhi[192], based on three groups of current residuals. Routines IK_CALC3 (non weighted), and IK_CALC7 (weighted), are based on the sum of squares of currents. These routines are more fully described elsewhere[53]. Calculations of I/ε can be automatically calculated by the computer, or the operator can indicate that data will be entered manually by selecting a softkey.

The latter option uses the FNInput$ subprogram to input (I/ε) data which by-passes the entry stages for set up of corrosion rate parameters I_k, $b_{a,M}$, $b_{c,X}$; percentage error; whether the error is in voltages or currents; the voltage range and number of data points. Calculations and plotting of the (I/ε) data points are selected by softkey after corrosion rate parameters have been entered, or after manually entering (I/ε) data.

At this stage the (I/ε) data can be analyzed and corrosion rate parameters I_k, $b_{a,M}$, $b_{c,X}$ calculated, along with standard deviations Sig_ik, Sig_ba, Sig_bc respectively. This can be followed by a plot of the least squares curve through the (I/ε) data points. Analysis is accomplished by calls to the appropriate IK_CALC routine previously selected. Plotting is handled by subprograms Plot, which plots the (I/ε) data points, and Curvefit, which fits a curve through these points.

6. Directory Store

6.1 Subprogram STORE MNGR (refer Figure A1/13) 545 program lines

Subprogram STORE_MNGR manages the storage/retrieval of data to/from discs for the three experiments - impedance, galvanic current and corrosion current. As such, it is the software interface between experimental data and disc data. Sample numbers can be allotted to experimental data prior to storage for ease of identification, by calling subprogram SAMPLE_NUM. These sample numbers can also be viewed to identify data sets by calls to subprogram EDIT_DISC. The sample's initial immersion time can be entered, either automatically by press of a softkey or manually from the keyboard, and stored on disc along with the experimental data, or separately at another time. Finally, both disc and experimental data can be co-resident in memory and can be swapped so as to print out or pass back to another program either disc or experimental data.

6.2 Subprogram SAMPLE NUM (refer Figure A1/14) 912 program lines

Subprogram SAMPLE_NUM allocates numbers to a series of samples. The series is identified by a range of numbers and a series title, and these details are kept on disc in a data file named SERIESNAME, see Section A1/8.1. An example of a sample series title might be 'the effect of solution chloride ion concentration of the pitting of aluminium'. Each series can be subdivided into groups, with each group identified by a range of numbers and a group title. In the above example, a group title might be '100 mg.L^{-1} [Cl^-]'. Group details are kept on disc in a data file named GROUPNAME, see Section A1/8.2. Sample details such as sample area and initial immersion time are kept on disc

in a data file named SAMPLE_INFO, see Section A1/8.3.

All samples evaluated, whether by impedance, galvanic current or corrosion current tests, can be divided into two categories - painted and unpainted. Within the painted category are sub-categories for tests that relate to curing; inhibitors in the primer; free films; pretreatments; primers; solutions; substrate; top coat and other. The unpainted category is divided into sub-categories for aluminium; galvanized; mini-line; steel; zinc; Zn-5%Al coated steel; Zn-55%Al coated steel; atmospheric corrosion monitors and others. Each sub-category is allocated a range of sample numbers, generally 100. For example, aluminium samples have sample numbers ranging from 0 to 99. A two-digit number, representing the year, is attached to these numbers, so that a sample is identified by a number plus a year, eg aluminium would have numbers 0 87 to 99 87 in the year 1987. This method uniquely distinguishes samples of a sub-category allocated in one particular year from samples in the same category but allocated in a different year. The number and year codes are allocated automatically upon selecting a given sample sub-category.

After selection of the relevant sub-category, SERIESNAME data file is searched to locate the last sample number, if any, allocated to that sub-category, and hence identifies the next number to be allocated. A series title is entered from the keyboard, followed by the total number of samples in the series. A group title is entered, followed by the number of samples in the group. Sample area is then requested for each of these samples, and if any more groups remain, the procedure is repeated, starting with entering a new group title. The complete series is then listed on the VDU screen, and may be printed, stored on hard disc, or a limited amount of editing performed.

Series details (year, series low, series high, group record and series title) are stored by finding the end of the SERIESNAME data file and storing in the next record. A dummy value for group record is temporarily stored because it is as yet unknown. Likewise, group details are stored at the end of the GROUPNAME data file. This established the group record which can now be stored back in the same SERIESNAME record over the dummy group record where the series details were stored. The group details consist of year, series low, group low, group high, sample record (temporarily a dummy value) and group title. Sample details are then stored in SAMPLEINFO data file. These details are year, number, last run, last run record, first run record, two coded integers representing the initial immersion time and date, and sample area coded as an integer. The sample record, now known, can be written over the dummy value in GROUPNAME data file. Dummy values are temporarily stored for last run record and first run record which point to records in the RUNINFO data file, see Section A1/8.4, where the first and last experimental run information is stored. Subprogram SAMPLE_NUM does not deal with this data file. Having stored all series details the subprogram is terminated, and control passes back to subprogram STORE_MNGR, see Section A1/6.1.

Sample area is stored so that impedance, galvanic current or corrosion current data can be readily converted to unit area. Initial immersion time is used to automatically calculate the immersion time interval when experiments are performed.

6.3 Subprogram STORE DATA (refer Figure A1/15) 847 program lines

Subprogram STORE_DATA controls the storage of experimental data for impedance, galvanic current or corrosion current tests. In order to save space

on disc, most real numbers are coded and stored as integers. All data files listed in Section A1/8 are accessed by subprogram STORE_DATA. The next experimental run number is automatically allocated, and the sample's immersion time interval is calculated and stored along with the run information. These tasks assist the operator and minimize operator errors.

The subprogram first requests input of the sample number. Impedance data is stored on hard disc, whilst galvanic current and corrosion current data are stored on 3.5 inch flexible discs. The operator may ask the computer on which flexible disc the relevant sample number is, and this information is provided by two data files Ig_code or Ik_code residing on hard disc, depending on whether the data type is galvanic current or corrosion current. For all experiment types, the SERIESNAME data file is searched to find the relevant sample number and series information, including the group record. The GROUPNAME data file is random accessed at this group record to obtain information, see Section A1/6.2, including the sample record. The SAMPLEINFO data file is then random accessed at this sample record to locate sample information, including the last run, last and first run records. By this method, subprogram STORE_DATA has access to all relevant records in all of the data files, given only the sample number. The initial immersion time, if entered, and sample area is decoded, and the last run is listed for the selected sample number.

The subprogram at this point takes either of two paths, depending on whether an experimental data set is to be stored or just the initial immersion time.

If the former, then the next run number is determined by incrementing the last run number, and the immersion time interval, delta t, is calculated as the difference between the run time and the initial immersion time, if it had been

previously entered. If it had, then delta t is coded as an integer. The experimental data is also coded at this point. If an impedance test, then frequency, Freq, resistive, Xx, and reactive, Yy, components of impedance are coded. Error, Err, which indicates the reliability of the particular reading, is coded along with frequency, making the code for freq negative when an error is coded. If a galvanic current test, then galvanic current, I_g, at time, t, coulombs, Q, (area under Ig/t curve), and mass loss, delta M, are coded as integers. If a corrosion current test, then applied current, I, measured current, Im, and voltage, E, at t, are coded. The next data record in data file SAMPLEDATA is found at the end of this file, and the coded experimental data is stored. The next run record in data file RUNINFO is found at the end of this file, and the coded run information, together with the data record is stored. Run information consists of, for example, an impedance test - year, sample number, run number, data record, results record (as yet unused), number of data records, run time and date, time interval delta t, and offsets to aid the decoding of run time/date. The run record is then stored in data file SAMPLEINFO at the sample record which was previously determined.

If only initial immersion time is to be stored, then it is coded as 2 integers and stored in data file SAMPLEINFO at sample record previously determined. All run records in data file RUNINFO are then located and a coded delta t is stored at each run record. The delta t is calculated by decoding the initial immersion time at the relevant sample record in SAMPLEINFO data file and calculating delta t as the difference between run time/date and initial immersion time. Run time/date is obtained at run record in data file RUNINFO and decoded.

6.4 Subprogram EDIT_DISC (refer Figure A1/16) 1478 program lines

Subprogram EDIT_DISC controls the retrieval of experimental data and sample details from disc for impedance, galvanic current and corrosion current tests. The required data can be listed, printed or, in the case of experimental data, taken back to a calling program for plotting or analysis. No editing facility to change information stored on disc is available at present. Experimental data, which is coded as integers in subprogram STORE_DATA, see Section A1/6.3, is here decoded back into real numbers, with the loss of a small and insignificant degree of precision. All data files listed in Section A1/8 are accessed by subprogram EDIT_DISC. Series, group, sample and run details can be obtained for the complete data file; for all series of the same type; for a selected series of the same type; for a selected series (group, sample, run details) and for a selected sample (sample, run details). Experimental data can be retrieved from disc upon entry of the required sample and run numbers. Galvanic current, Ig, and corrosion current, Ik, information are stored on flexible discs, whereas impedance information is stored on hard disc. Two data files, Ig_code and Ik_code, reside on hard disc and can be accessed to tell the operator on which flexible disc the required information is.

Series information is located in SERIESNAME data file in one of two ways - complete listing, or a listing of selected sample type. A complete listing simply searches the complete SERIESNAME file from beginning to end and lists each record to the VDU screen. A selected type listing first requests input of the sample type to be selected, using subprogram SAMPLE_NUM, see Section A1/6.2. This also gets a sample number range from sample type minimum to maximum. The SERIESNAME file is then searched from beginning to end and if the particular record has a Series_high sample number that lies

within this range, the record is listed to the VDU screen.

Group information is located in GROUPNAME data file as a listing on the VDU screen in one of three ways - complete, selected type or selected series. A complete listing simply searches GROUPNAME file from beginning to end and lists each record. A selected type or a selected series listing first gets the selected sample type and range (sample type minimum to maximum) in the same manner as described above for selected type listing of series details. Group records are then listed to the VDU screen for records of the selected type. For a selected series listing, the operator is requested to enter the group record of the selected sample type and is prompted with a list of group records for each series of the selected type. The GROUPNAME file is accessed at this group record and group records listed for all groups in that series.

Sample information is located in SAMPLEINFO data file as a listing on the VDU screen in one of four ways - complete, selected type, selected series or selected sample. If a complete listing is requested, then all records in SAMPLEINFO are accessed from beginning to end of the file and listed. If either a selected type or selected series listing is requested, then subprogram SAMPLE_NUM is called so the operator can select the sample type, see Section A1/6.2. This also obtains the sample type minimum and maximum sample numbers. If a selected type listing has been requested, then all records are accessed in SAMPLEINFO, but only listed if the sample number of the particular record is within the range of sample type minimum to maximum. If a selected series listing is required, then series details for all series within the range sample type minimum to maximum are listed and the operator is requested to enter the group record displayed for the series selected, and is

prompted with a list of group records for each series of the selected type. As can be seen in Tables AI/1-3, this locates the relevant Sample_rec in GROUPNAME, and all sample records of this selected series can be listed from SAMPLEINFO by knowing the number of samples in the series, which was previously obtained from SERIESNAME. If sample information is required for a selected sample, then subprogram STORE_DATA is called and the operator requested to enter the required sample number. Sample_rec record is also obtained from GROUPNAME and control passes back to EDIT_DISC. SAMPLEINFO file is then accessed at Sample_rec and details for the required sample listed to the VDU screen.

Run information is located in RUNINFO data file as a listing on the VDU screen in one of four ways - complete, selected type, selected series or selected sample. A complete listing simply lists all records in RUNINFO from beginning to end of the file. A selected type or selected series listing first gets the selected sample type and range from subprogram SAMPLE_NUM as described above. If a selected type listing is requested, then only those records in RUNINFO whose sample number is within range of sample type minimum to maximum will be listed. If a selected series is requested, then a search of SERIESNAME locates and lists all series of the relevant sample type along with each group record, Group_rec. The operator is requested to select a Group_rec record for the selected series and this procedure automatically defines the relevant Series_low and Series_high sample numbers. Then only those records in RUNINFO whose sample number is within the range of Series_low to Series_high will be listed. If only run information for one sample is selected, then subprogram STORE_DATA is called and the operator is requested to enter the required sample number. Sample_rec record is also obtained from GROUPNAME which locates the first and last run records

(First_rec, Last_rec) for this sample. Control then passes back to EDIT_DISC and a search of RUNINFO from First_rec to Last_rec locates and lists all runs of the selected sample.

If experimental data is required then subprogram STORE_DATA is called and the operator is requested to enter the selected sample number, as above. This locates the last run record (Last_rec) for the selected sample, and control passes back to EDIT_DISC. The last run record indicates how many experimental runs have been stored on disc. The operator is requested to select a run number and RUNINFO is searched from First_rec to Last_rec to locate both the correct sample number and the selected run number. This also locates the number of data points (N, Kend0 or Count) and a pointer to the data record (Datarec or Data_rec) in SAMPLEDATA file which contains the first experimental data record. SAMPLEDATA is then accessed from this data record for the number of data points and after suitable decoding, the experimental data records are listed to the VDU screen.

7. Directory plot

7.1 Subprogram PLOT8 (refer Figure A1/17) 1672 program lines

Subprogram PLOT8 is a general purpose graphics plotting routine which gets 3 data arrays X, Y, Z from a calling program and plots the X-array versus the Y-array. The Z-array is used only for Nyquist impedance plots. The calling program can pass a list of requirements to subprogram PLOT8, and these are described below. These requirements can be overridden, or other requirements selected by the operator before or after a plot, and these are also described below. The plot device can be either the VDU screen, printer or plotter.

The list of requirements passed to PLOT8 are as follows - plot type (linear x/linear y; linear x/log y; log x/linear y; log x/log y); plot title; title position (left, right, centre justified at top of plot); axis labels; Y-scale negative; Y-scale tick marks (LHS, RHS, both sides); Y-scale equals X-scale; autoscaled or fixed (X or Y) or both axes; X-scale on/off; symbols choice (off/on); and pen choice (points, vectors, frame, scale, title).

Within subprogram PLOT8, the following parameters can be altered by the operator - axis range (X, Y-axis origin; minimum, maximum); pen choice (points, vectors, frame, scale, title); symbol choice (off/on); symbol type (circle, triangle, square, hexagon); symbol fill (open, closed); symbol size (small to large); graph extension (constrained, not constrained by axes); plot title (40 character maximum); output device (VDU screen, printer, plotter); axes or grid; scales (origin, position, height, width, exponent size/width if applicable) (incomplete). Future extensions partially complete are axis labels, line type, legends, plot page position.

Two special purpose applications are included. Firstly, a third data array (the Z-array) can be passed to PLOT8 containing information that will allow digits, rather than points, to print out on Nyquist a/b impedance plots at each frequency decade. Secondly, a flag can be set and passed to PLOT8 to indicate that control is to be automatically passed back to the calling program. This is used when impedance plots of data points are superimposed onto curves fitted through these points, which require two calls to PLOT8 to plot both data points and curve, see Section A1/4.5.

The subprogram is made up of the main portion where various parameters can be altered, and the plot subroutine. The main portion calls further

subprograms to select the symbol type (Symbol) and to enter parameter variables (Enter). The plot subroutine calls further subprograms to calculate axis tick mark spacing (Tkmark); to round down the minimum and round up the maximum axis values (Rnd_lin, Rnd_log); to print axis scales (Scle_lin, Scle_log); and to plot data points and draw curves (Points).

8. Directory data (experimental data files)

8.1 SERIESNAME data file (refer Tables A1/1-3)

The SERIESNAME data file contains records, each being 76 bytes long, that hold the following information - sample number details (Year, Series_low, Series_high), a pointer (Group_rec) that allows random access to group information contained at Group_rec record in data file GROUPNAME; and a string of length 68 characters (Seriesname$) that contains the title of the sample series, (eg 'effect of [Cl^-] on pitting of Al'), pertaining to the sample numbers ranging from Series_low to Series_high. Tables A1/1-3 lists these parameters for the three test types (impedance, galvanic current, corrosion current) along with their type (real, integer, string) and length (bytes), plus a pathname (@Series) which is programmatically assigned to this file when read from or written to. The contents of SERIESNAME is the same for all 3 test methods as can be seen in Tables A1/1-3. However, impedance data is stored on hard disc using an HP-UX file structure (record length = 1 byte), whilst galvanic current and corrosion current data are stored on 3.5 in flexible discs using a BDAT (binary data) structure (record length is defined when creating the file, for example, SERIESNAME for galvanic current data is created with a record length of 80 characters).

8.2 GROUPNAME data file (refer Tables A1/1-3)

The GROUPNAME data file contains records, each being 76 bytes long, that hold the following information - group number details (Gp_year, Group_low, Group_high); the first sample in the first group of the relevant series (Series_low); a pointer (Sample_rec) that allows random access to sample information contained at Sample_rec record in data file SAMPLEINFO; and a string of length 66 characters (Groupname$) that contains the title of the particular sample group (eg 100 $mg.L^{-1}$ $[Cl^-]$), pertaining to sample numbers ranging from Group_low to Group_high. The contents of GROUPNAME is the same for all 3 test methods, refer Tables A1/1-3. Further information of data file structure can be obtained from Section A1/8.1.

8.3 SAMPLEINFO data file (refer Tables A1/1-3)

The SAMPLEINFO data file contains records, each being 16 bytes long (18 bytes for galvanic current tests), that hold the following information - sample number details (Dyear, Sample/Sample_no); the last experiment carried out (Last_run); pointers (Last_rec, First_rec) that allow random access to experimental run information between First_rec and Last_rec records in data file RUNINFO; and coded sample details for initial immersion time (Datetime 1, Datetime_2) and sample area (Area1_c or Area1_c and Area2_c, depending on test type).

The contents of SAMPLEINFO are similar for all 3 test methods, refer Tables A1/1-3, except that galvanic current tests require storage of 2 coded numbers for areas of cathode and anode, whereas impedance and corrosion current tests only store a coded number for the working electrode (the sample under test).

Further information on data file structure can be obtained from Section A1/8.1.

8.4 RUNINFO data file (refer Tables A1/1-3)

The RUNINFO data file contains records that hold experimental run information for each sample. The record length and the information contained depends on the test type, although year, sample and run number (Ryear, Sample_no, Run-no) are common to all three test types. Other information contained is a pointer (Datarec for impedance, Data_rec for corrosion current and galvanic current test types) allows random access to experimental data at record Datarec or Data_rec; the number of data points (N-coord, which also contains coded information on the impedance co-ordinates, for impedance test, Kend0 for corrosion current test and Count for galvanic current test); coded numbers for run date/time (Datetime_1, Datetime_2), immersion time interval (Delta_time) for impedance and galvanic current tests, and special offset coded numbers (corrosion current test only) that allow maximum use of the integer range to store E, I, T as 2-byte integers rather than 8-byte real numbers with the minimum loss of precision. Further information on data file structure can be obtained from Section A1/8.1.

8.5 SAMPLEDATA data file (refer Tables A1/1-3)

The SAMPLEDATA data file contains records that hold the actual experimental data for each run of each sample. The record length and the information contained depends on the test type. For impedance tests, coded 2-byte integers for frequency, Freq_i (which also contains codes for whether the reading was suspect and returned an integration error), and two numbers,

Xx_i, Yy_i, which normally represent the resistive, a, and reactive, b, components of impedance, Z, are stored for N+1 records, where N is the number of data points. The first record contains a duplicate of the reading closest to a frequency of 1 kHz. Ths is done for ease of searching if only 1 kHz records are required, although this feature has not yet been implemented. For corrosion current tests, the first record for each current pulse contains the set value of current, I0, and the number of readings, Jtrm, of voltage, E, current, I, and time, T. Then follows the number of readings of E, I and T as 2-byte integer coded numbers E0_c, I0_c, T0_c. In the same manner, the remaining data pulse readings are stored, making a total of Kend0 data pulses. For galvanic current tests, a total of Count data records (galvanic current, Ig and Time) are stored. The first record stores coulombs of electricity, Q, and mass loss, Mass, as 2-byte coded integers Q_c, Mass_c respectively. Then follow Count records of 2-byte coded integers Ig_c, Time_c representing Ig and Time respectively. For each test type, the number of data points to be stored (N, Kend0, Count) is stored in RUNINFO data file.

8.6 Ik code, Ig code data files (refer Tables A1/2-3)

The Ik_code and Ig_code data files contains records that hold information to enable the operator to select the required flexible disc, Disc_no, for samples of a particular series. Ik_code is used for corrosion current test, whilst Ig_code is used for galvanic current tests. These files are accessed by subprogram EDIT_DISC if flexible disc information is required. Besides Disc_no, they contain sample series numbers (Series_year, Series_low, Series_high) and a pointer (Series_rec) to the record in SERIESNAME where the series information is located.

Table A1/1 Data File Information - Impedance[1]

file name	path name	record name	record length (bytes)	variable name	variable type[2]	variable length (bytes)
SERIESNAME	@Series	Series	76	Year	I	2
				Series_low	I	2
				Series_high	I	2
				Group_rec	I	2
				Seriesname$	S	68
GROUPNAME	@Group	Group_rec	76	Gp_year	I	2
				Series_low	I	2
				Group_low	I	2
				Group_high	I	2
				Sample_rec	I	2
				Groupname$	S	66
SAMPLEINFO	@Details	Sample_rec	16	Dyear	I	2
				Sample	I	2
				Last_run	I	2
				Last_rec	I	2
				First_rec	I	2
				Datetime_1	I	2
				Datetime_2	I	2
				Area1_c	I	2
RUNINFO	@Run	Run_rec	28	Ryear	I	2
				Sample_no	I	2
				Run_no	I	2
				Datarec	R	8
				Results_rec	I	2
				N_coord	I	2
				Datetime_1	I	2
				Datetime_2	I	2
				Delta_time	I	2
				Offset_x	I	2
				Offset_y	I	2
SAMPLEDATA	@Data	Datarec	6	Freq_i (includes Err code)	I	2
				Xx_i	I	2
				Yy_i	I	2

Notes:

1 Impedance data files are stored on hard disc and have an HP-UX file structure

2 I integer (2 bytes)
R real (8 bytes)
S string (1 byte/character + 1 null character

Table A1/2 Data File Information - Corrosion Current[1]

file name	path name	record name	record length (bytes)	variable name	variable type[2]	variable length (bytes)
SERIESNAME	@Series	Series	80	Year	I	2
				Series_low	I	2
				Series_high	I	2
				Group_rec	I	2
				Seriesname$	S	4+68[3]
GROUPNAME	@Group	Group_rec	80	Gp_year	I	2
				Series_low	I	2
				Group_low	I	2
				Group_high	I	2
				Sample_rec	I	2
				Groupname$	S	4+66[3]
SAMPLEINFO	@Details	Sample_rec	16	Dyear	I	2
				Sample	I	2
				Last_run	I	2
				Last_rec	I	2
				First_rec	I	2
				Datetime_1	I	2
				Datetime_2	I	2
				Area1_c	I	2
RUNINFO	@Run	Run_rec	24	Ryear	I	2
				Sample_no	I	2
				Run_no	I	2
				Data_rec	I	2
				Results_rec	I	2
				Kend0	I	2
				Datetime_1	I	2
				Datetime_2	I	2
				Delta_time	I	2
				Offset-e	I	2
				Offset_i	I	2
				Offset_t	I	2
SAMPLEDATA	@Data	Data_rec	6	Ix0[4]	I	2
				Jtrm[4]	I	2
				E0_c	I	2
				I0_c	I	2
				T0_c	I	2
Ik_code	@Code	Series	10	Series_year	I	2
				Series_low	I	2
				Series_high	I	2
				Disc_no	I	2
				Series_rec	I	2

Notes:

1 Corrosion current data files are stored on 3 1/2 in flexible discs and have a BDAT (binary data) structure

2 I integer (2 bytes)
S string (1 byte/character + 4 byte header)

3 string requires 4-byte header + 1 byte/character for BDAT files

4 stored as first record of each data set only

Table A1/3 Data File Information - Galvanic Current[1]

file name	path name	record name	record length (bytes)	variable name	variable type[2]	variable length (bytes)
SERIESNAME	@Series	Series	80	Year	I	2
				Series_low	I	2
				Series_high	I	2
				Group_rec	I	2
				Seriesname$	S	4+68[3]
GROUPNAME	@Group	Group_rec	80	Gp_year	I	2
				Series_low	I	2
				Group_low	I	2
				Group_high	I	2
				Sample_rec	I	2
				Groupname$	S	4+66[3]
SAMPLEINFO	@Details	Sample_rec	18	Dyear	I	2
				Sample	I	2
				Last_run	I	2
				Last_rec	I	2
				First_rec	I	2
				Datetime_1	I	2
				Datetime_2	I	2
				Area1_c	I	2
				Area2_c	I	2
RUNINFO	@Run	Run_rec	10	Ryear	I	2
				Sample_no	I	2
				Run_no	I	2
				Data_rec	I	2
				Count	I	2
SAMPLEDATA	@Data	Data_rec	4	Q_c[4]	I	2
				Mass_c[4]	I	2
				Ig_c	I	2
				Time_c	I	2
Ig_code	@Code	Series	10	Series_year	I	2
				Series_low	I	2
				Series_high	I	2
				Disc_no	I	2
				Series_rec	I	2

Notes:

1 Galvanic current data files are stored on 3 1/2 in flexible discs and have a BDAT (binary data) structure

2 I integer (2 bytes)
S string (1 byte/character + 4 byte header)

3 string requires 4-byte header + 1 byte/character for BDAT files

4 stored in first record of each data set only

Figure A1/1. Codes used for program flowcharts.

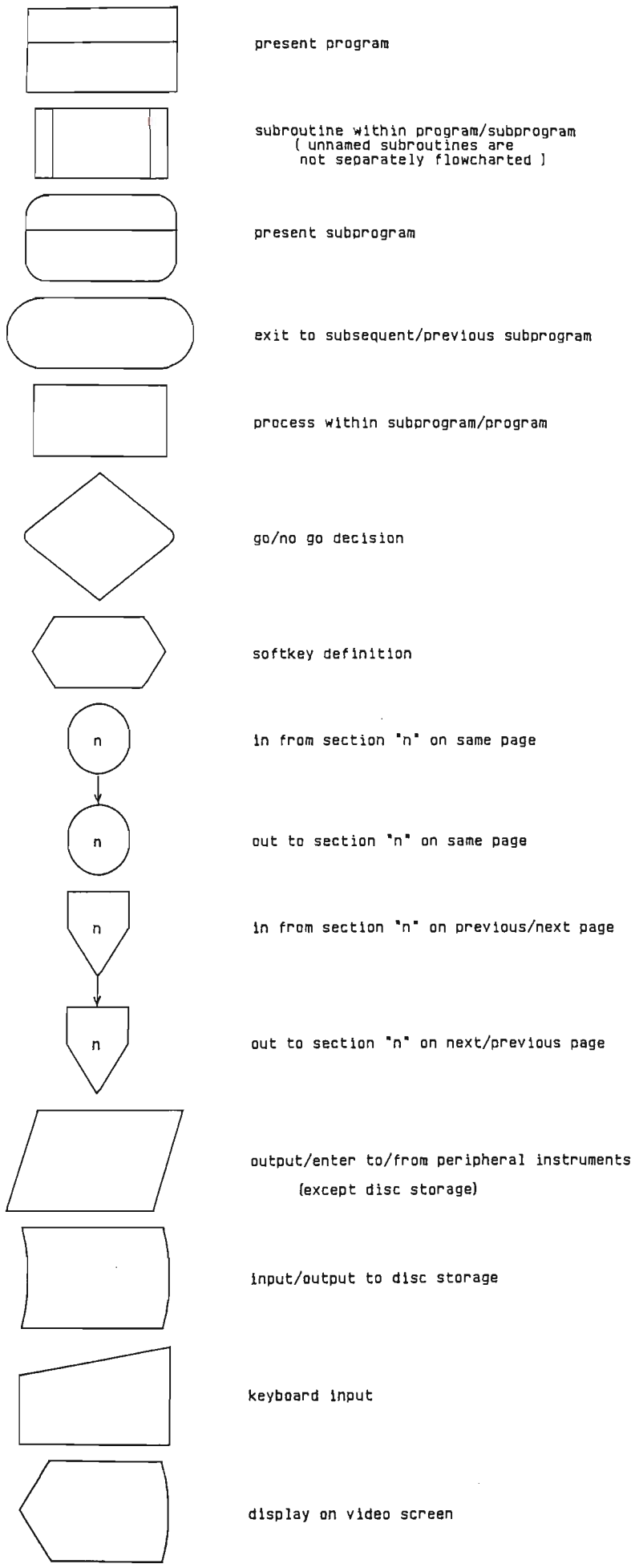

Figure A1/2. Program/data directory structure.

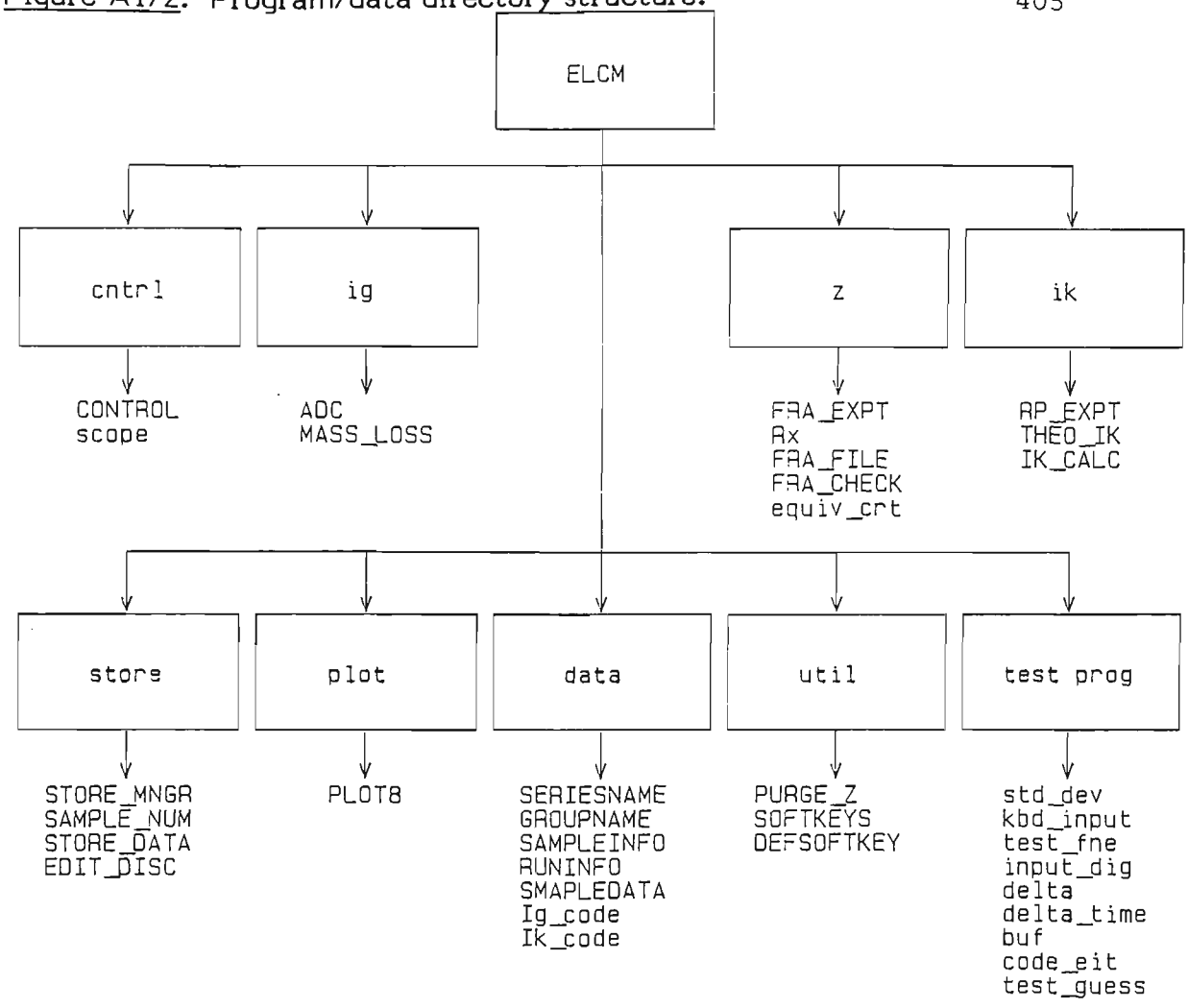

Figure A1/3. Program CONTROL flowchart.

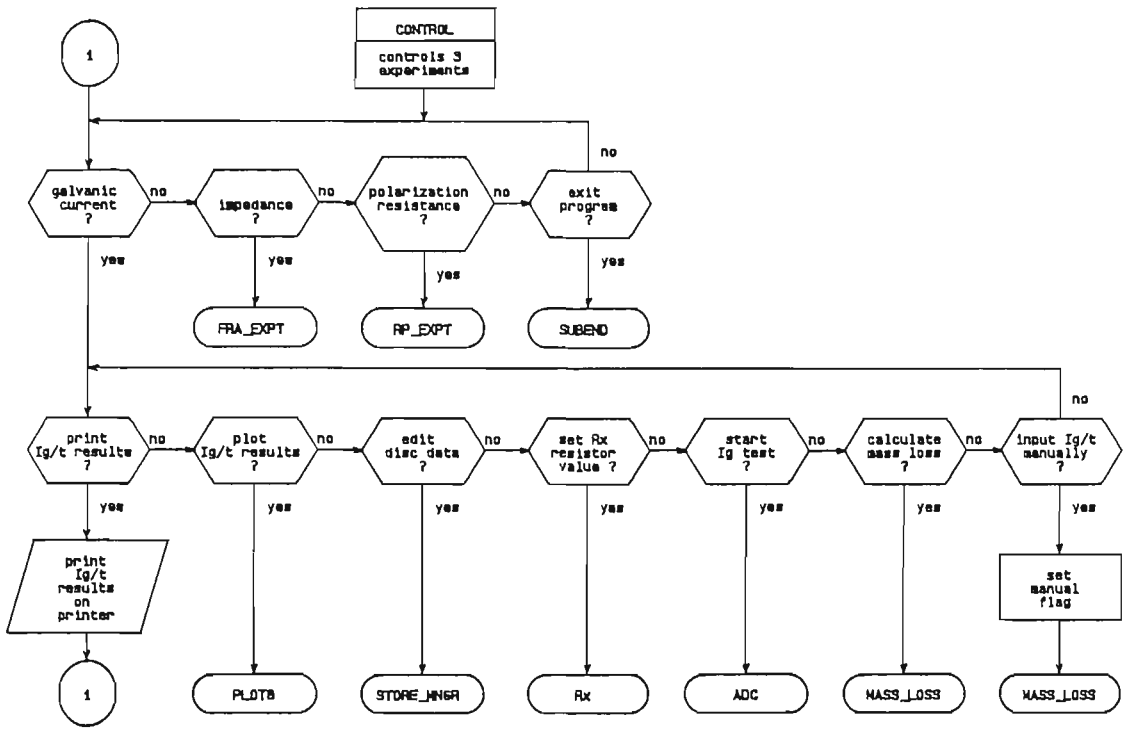

Figure A1/4. Subprogram ADC flowchart.

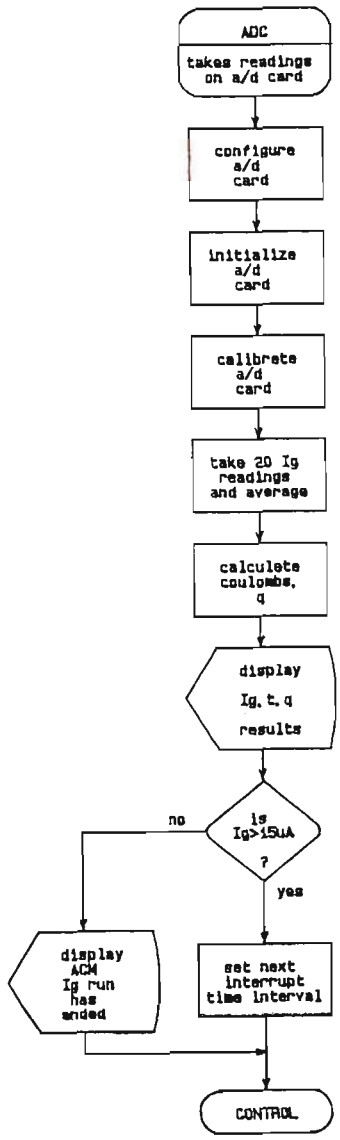

Figure A1/5. Subprogram MASS_LOSS flowchart.

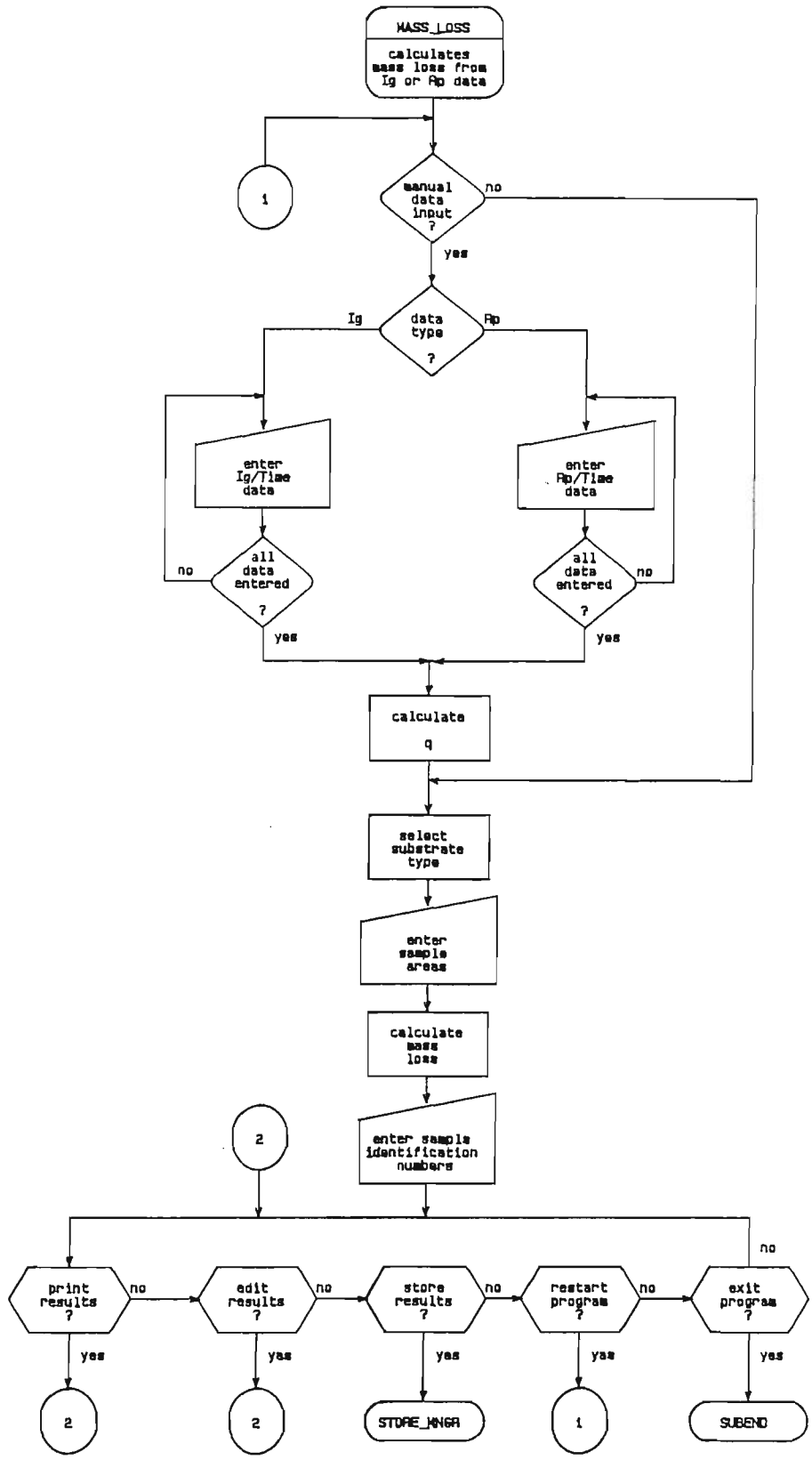

Figure A1/6a. Subprogram FRA_EXPT flowchart.

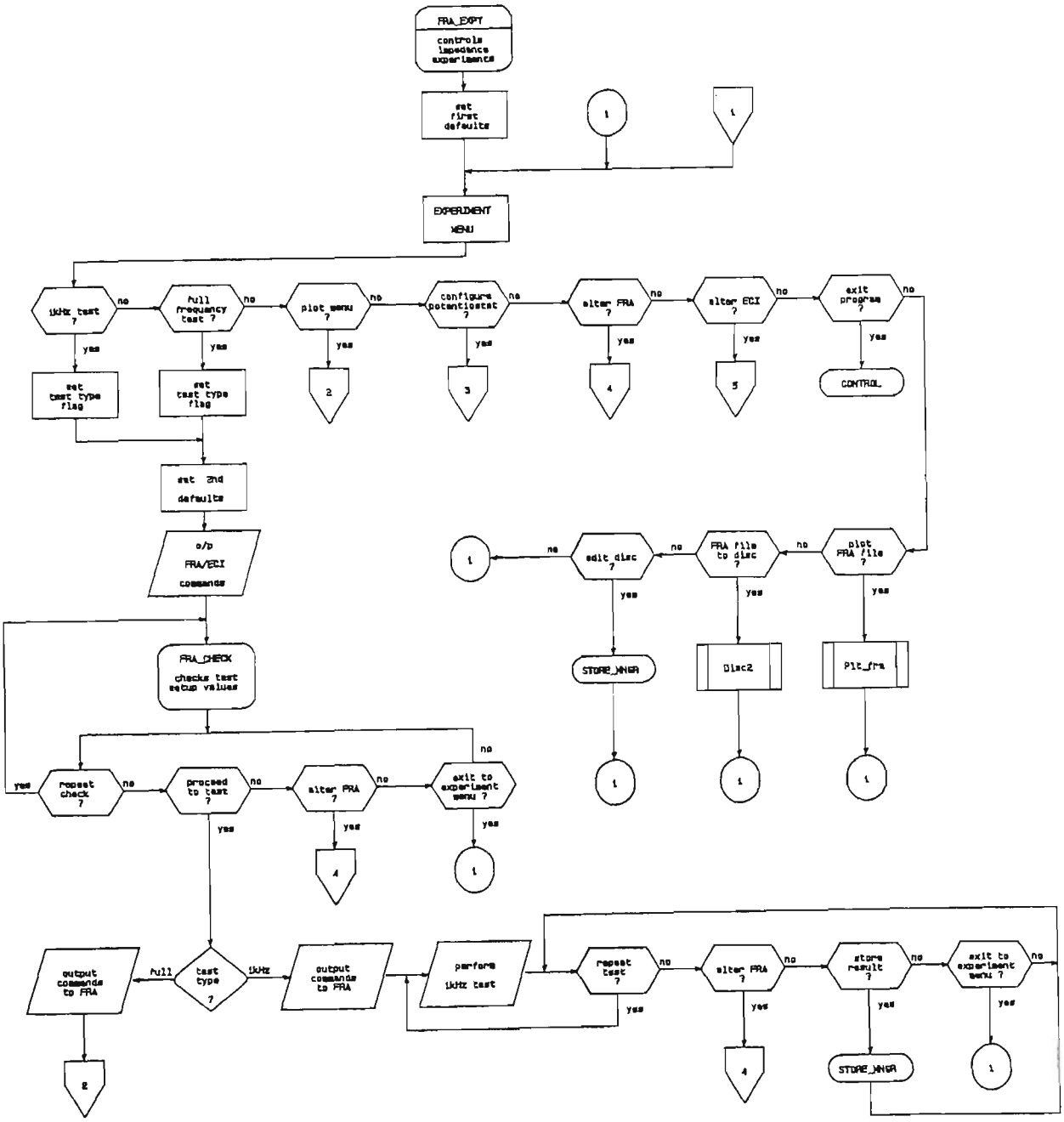

Figure A1/6b.

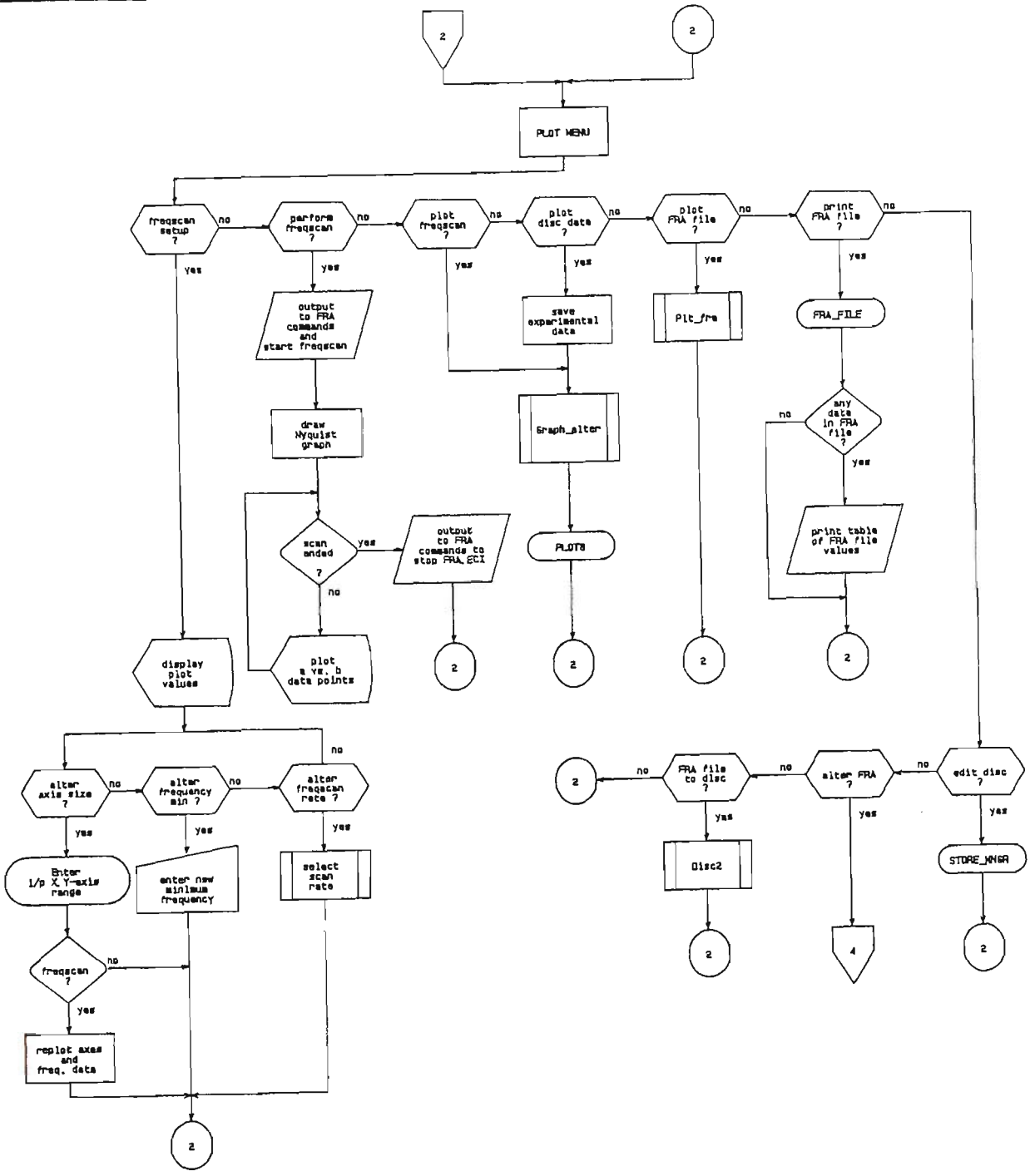
2
2
PLOT MENU
freqscan setup ?
no
perform freqscan ?
no
plot freqscan ?
no
plot disc data ?
no
plot FRA file ?
no
print FRA file ?
no
yes
yes
yes
yes
yes
yes
output to FRA commands and start freqscan
save experimental data
Plt_fra
FRA_FILE
draw Nyquist graph
Graph_alter
any data in FRA file ?
no
yes
scan ended ?
yes
no
output to FRA commands to stop FRA_ECI
PLOT8
print table of FRA file values
display plot values
plot a vs. b data points
2
2
2
2
no
alter axis size ?
no
alter frequency min ?
no
alter freqscan rate ?
yes
yes
yes
Enter L/p X,Y-axis range
enter new minimum frequency
select scan rate
freqscan ?
no
yes
replot axes and freq. data
2
2
no
FRA file to disc ?
no
alter FRA ?
no
edit disc ?
yes
yes
yes
Disc2
STORE_MNGR
2
4
2

Figure A1/6c.

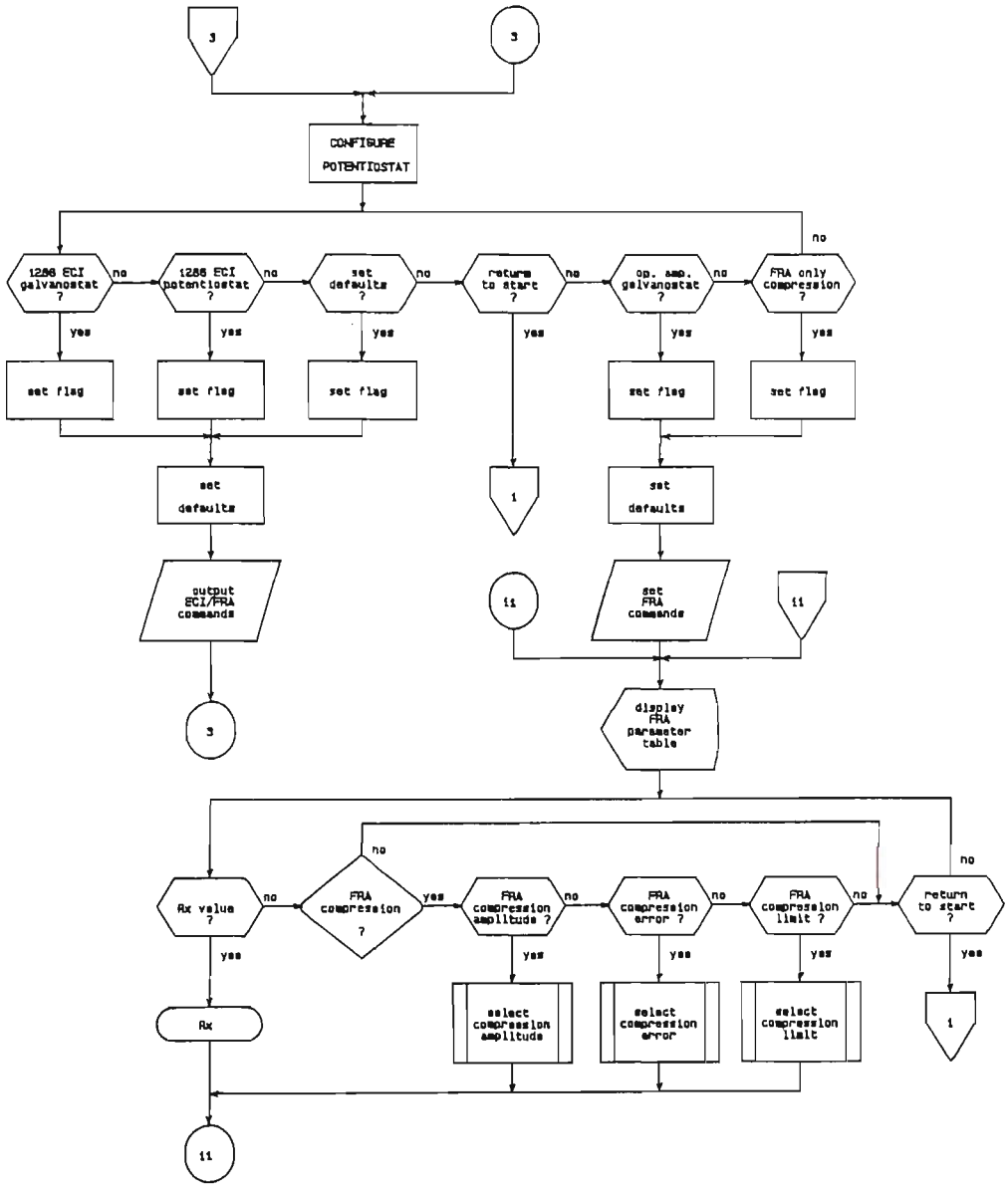
3
3
CONFIGURE POTENTIOSTAT
1286 ECI galvanostat ?
no
1286 ECI potentiostat ?
no
set defaults ?
no
return to start ?
no
op. amp. galvanostat ?
no
FRA only compression ?
no
yes
set flag
set flag
set flag
yes
set flag
set flag
set defaults
output ECI/FRA commands
3
1
set defaults
set FRA commands
11
11
display FRA parameter table
Rx value ?
no
FRA compression ?
no
yes
FRA compression amplitude ?
no
FRA compression error ?
no
FRA compression limit ?
no
return to start ?
no
yes
Rx
select compression amplitude
select compression error
select compression limit
1
11

Figure A1/6d.

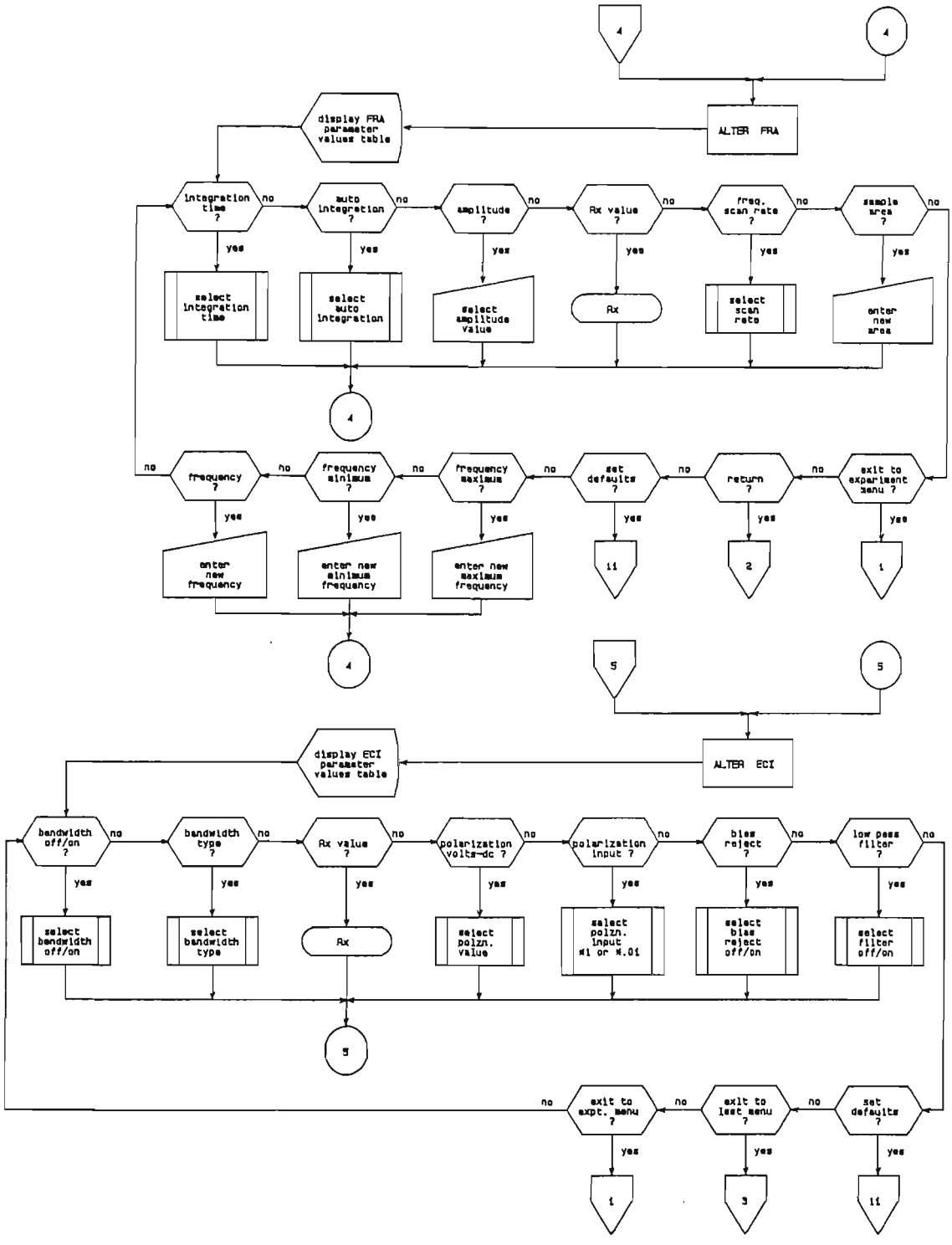
4
4
ALTER FRA
display FRA parameter values table
integration time ?
auto integration ?
amplitude ?
Rx value ?
freq. scan rate ?
sample area ?
yes
no
select integration time
select auto integration
select amplitude value
Rx
select scan rate
enter new area
4
frequency ?
frequency minimum ?
frequency maximum ?
set defaults ?
return ?
exit to experiment menu ?
enter new frequency
enter new minimum frequency
enter new maximum frequency
11
2
1
4
5
5
ALTER ECI
display ECI parameter values table
bandwidth off/on ?
bandwidth type ?
Rx value ?
polarization volts-dc ?
polarization input ?
bias reject ?
low pass filter ?
select bandwidth off/on
select bandwidth type
Rx
select polzn. value
select polzn. input #1 or #.01
select bias reject off/on
select filter off/on
3
exit to expt. menu ?
exit to test menu ?
set defaults ?
1
3
11

Figure A1/6e.

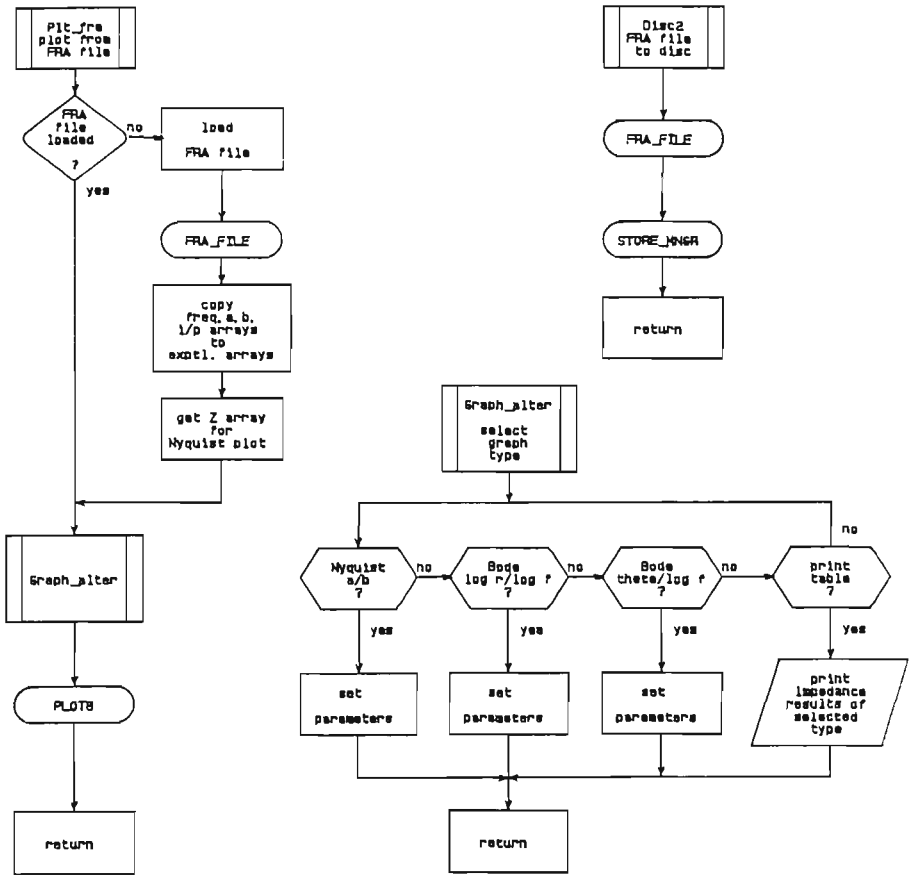
Plt_fra
plot from
FRA file
FRA
file
loaded
?
no
yes
load
FRA file
FRA_FILE
copy
freq. a, b,
i/p arrays
to
expt1. arrays
get Z array
for
Nyquist plot
Graph_alter
PLOT8
return
Disc2
FRA file
to disc
FRA_FILE
STORE_MNGR
return
Graph_alter
select
graph
type
Nyquist
a/b
?
Bode
log r/log f
?
Bode
theta/log f
?
print
table
?
set
parameters
print
impedance
results of
selected
type
return

Figure A1/7. Subprogram FRA_FILE flowchart.

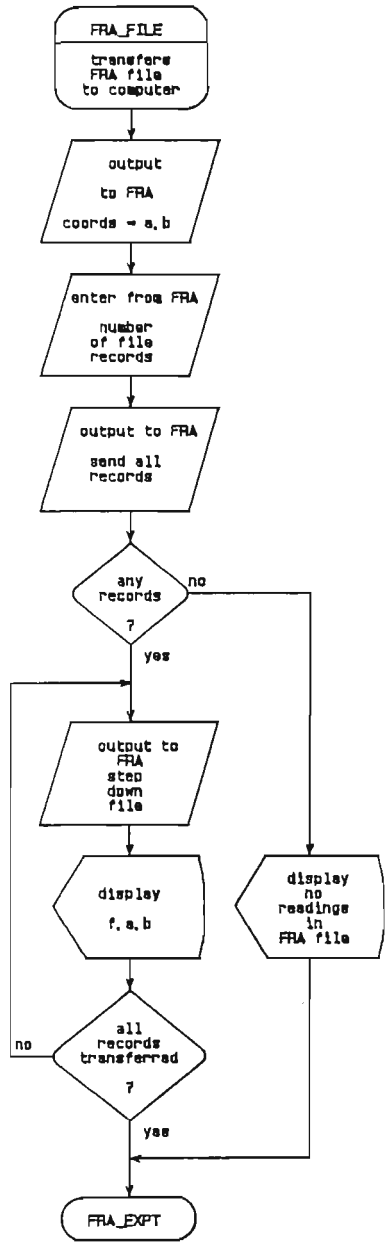

Figure A1/8a. Subprogram FRA_CHECK flowchart.

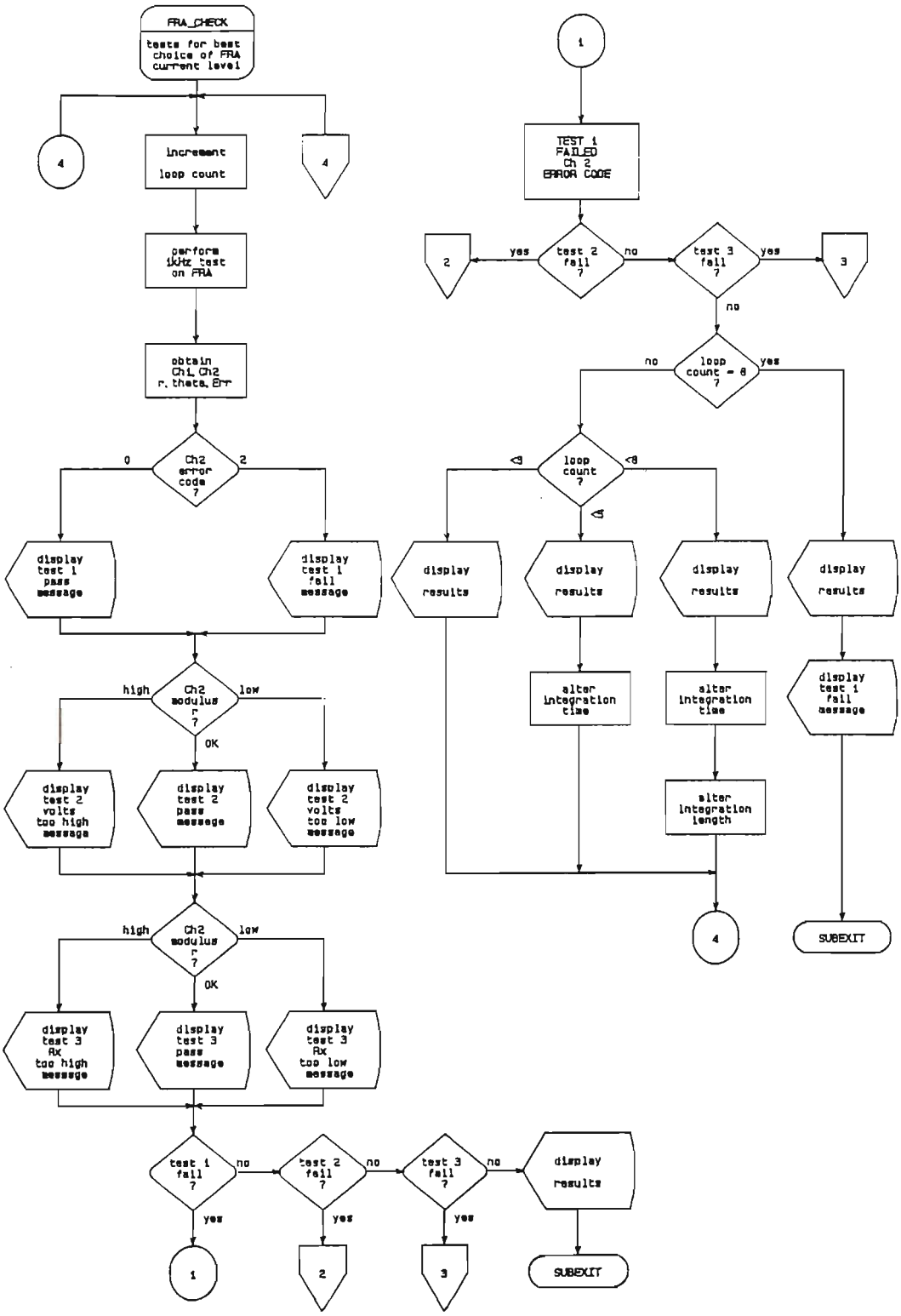

Figure A1/8b.

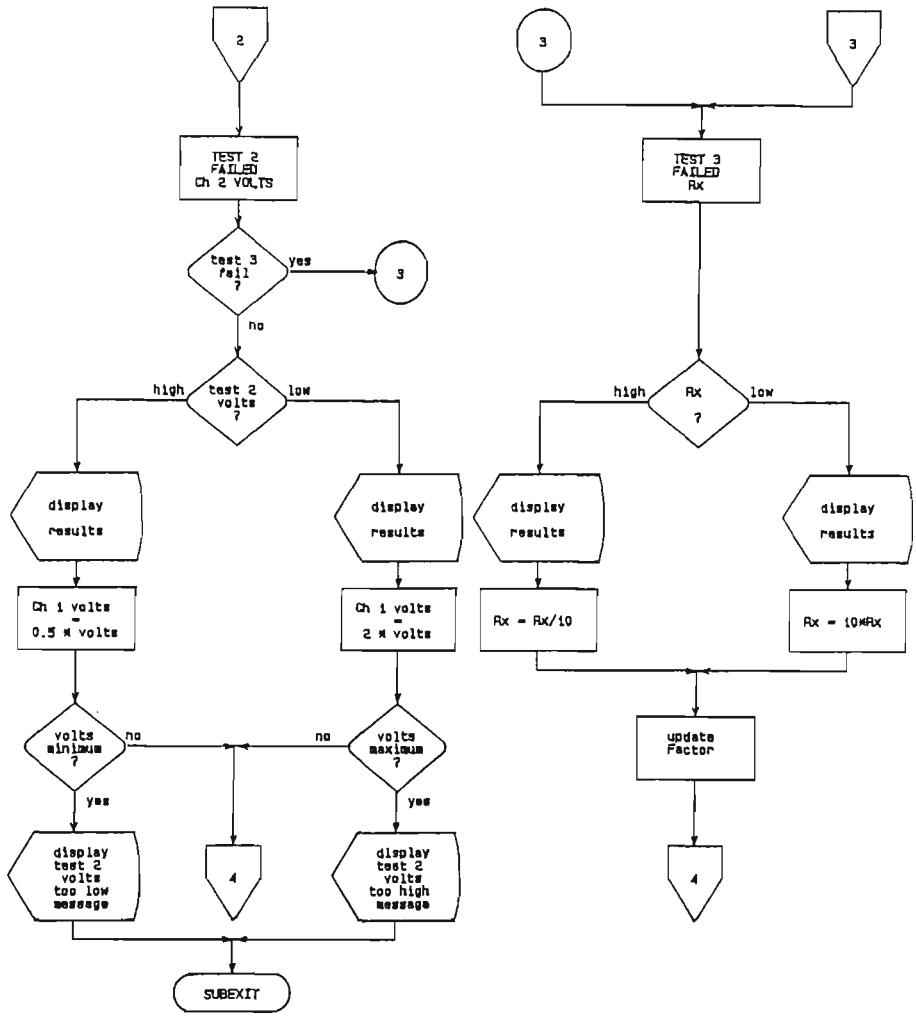
2
TEST 2
FAILED
Ch 2 VOLTS
test 3
fail
?
yes
3
no
high
test 2
volts
?
low
display
results
Ch 1 volts
=
0.5 * volts
volts
minimum
?
no
yes
display
test 2
volts
too low
message
4
display
results
Ch 1 volts
=
2 * volts
volts
maximum
?
no
yes
display
test 2
volts
too high
message
SUBEXIT
3
3
TEST 3
FAILED
Rx
high
Rx
?
low
display
results
Rx = Rx/10
display
results
Rx = 10*Rx
update
Factor
4

Figure A1/9a. Subprogram EUIQV_CRT flowchart.

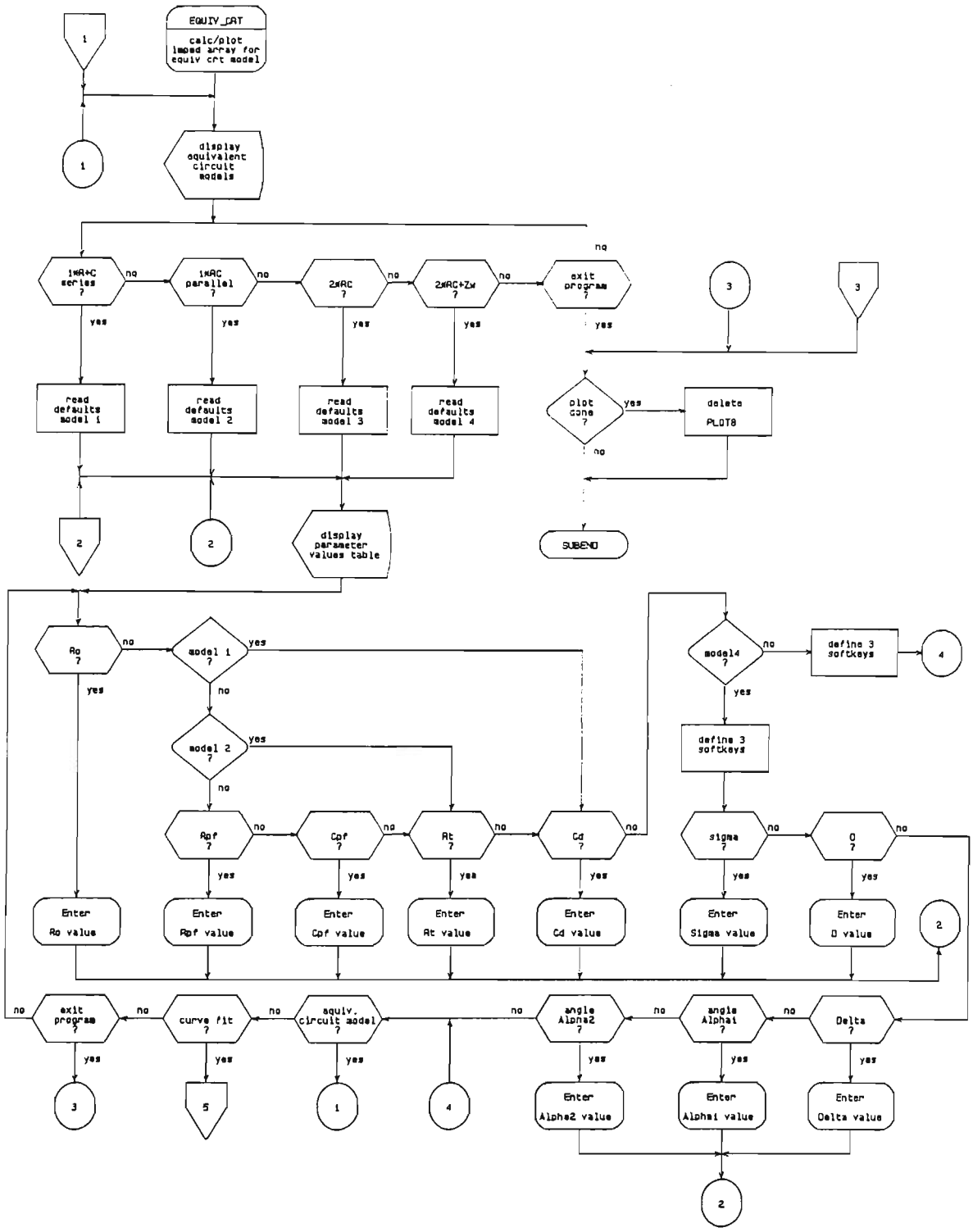

Figure A1/9b.

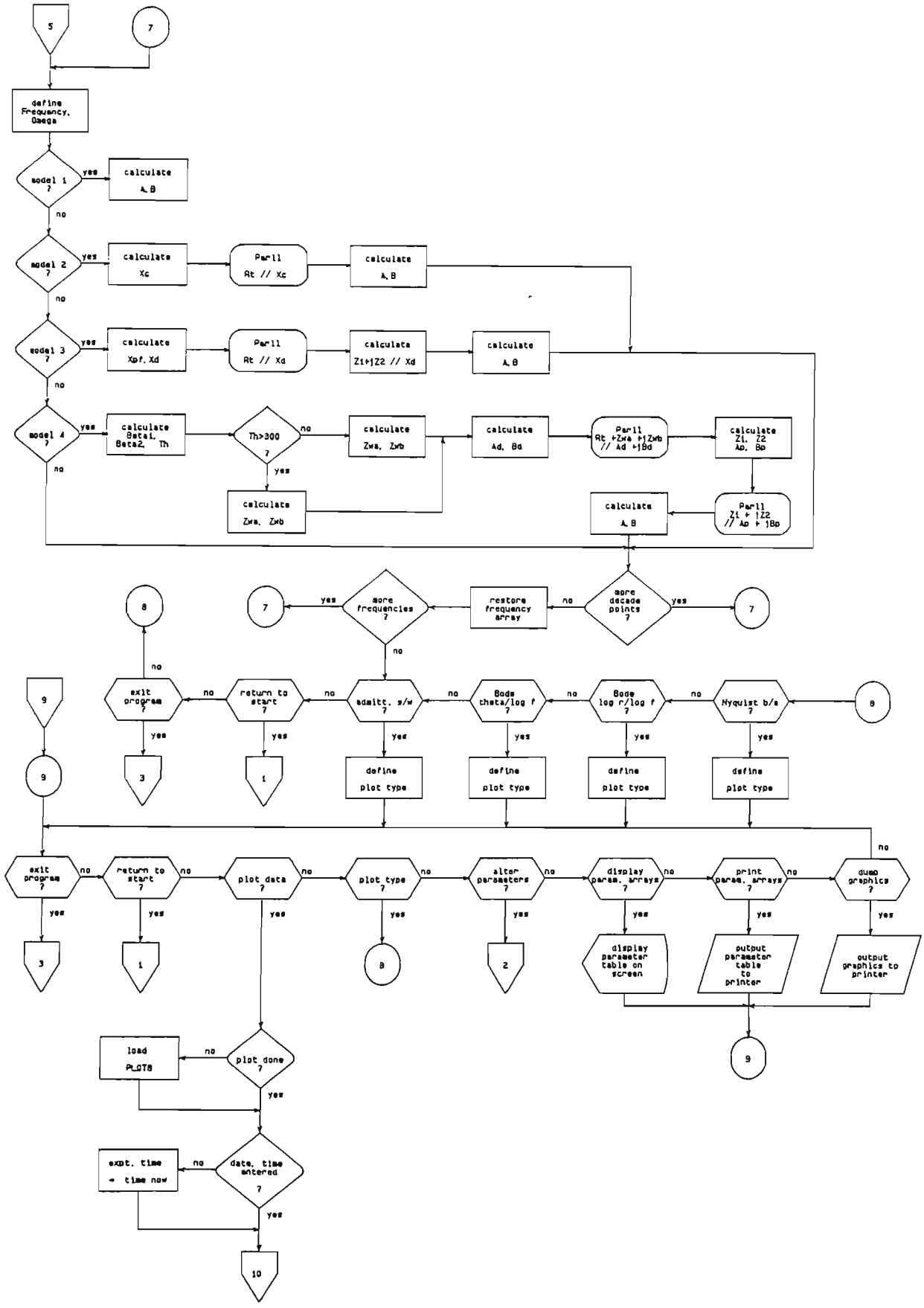
5
7
define Frequency, Omega
model 1 ?
yes
calculate A, B
no
model 2 ?
yes
calculate Xc
Parll Rt // Xc
calculate A, B
no
model 3 ?
yes
calculate Xbf, Xd
Parll Rt // Xd
calculate Zi+jZ2 // Xd
calculate A, B
no
model 4 ?
yes
calculate Beta1, Beta2, Th
Th>300 ?
no
calculate Zwa, Zwb
calculate Ad, Bd
Parll Rt +Zwa +jZwb // Ad +jBd
calculate Zi, Z2 Ad, Bd
yes
calculate Zwa, Zwb
calculate A, B
Parll Zi + jZ2 // Ad + jBd
no
more decade points ?
yes
7
restore frequency array
no
more frequencies ?
yes
7
no
8
9
exit program ?
no
return to start ?
no
admitt. s/w ?
no
Bode theta/log f ?
no
Bode log r/log f ?
no
Nyquist b/s ?
yes
8
yes
3
yes
1
yes
define plot type
yes
define plot type
yes
define plot type
yes
define plot type
9
exit program ?
no
return to start ?
no
plot data ?
no
plot type ?
no
alter parameters ?
no
display param. arrays ?
no
print param. arrays ?
no
dump graphics ?
yes
3
yes
1
yes
yes
8
yes
2
yes
display parameter table on screen
yes
output parameter table to printer
yes
output graphics to printer
load PLOTS
no
plot done ?
yes
9
expt. time = time now
no
date, time entered ?
yes
10

Figure A1/9c.

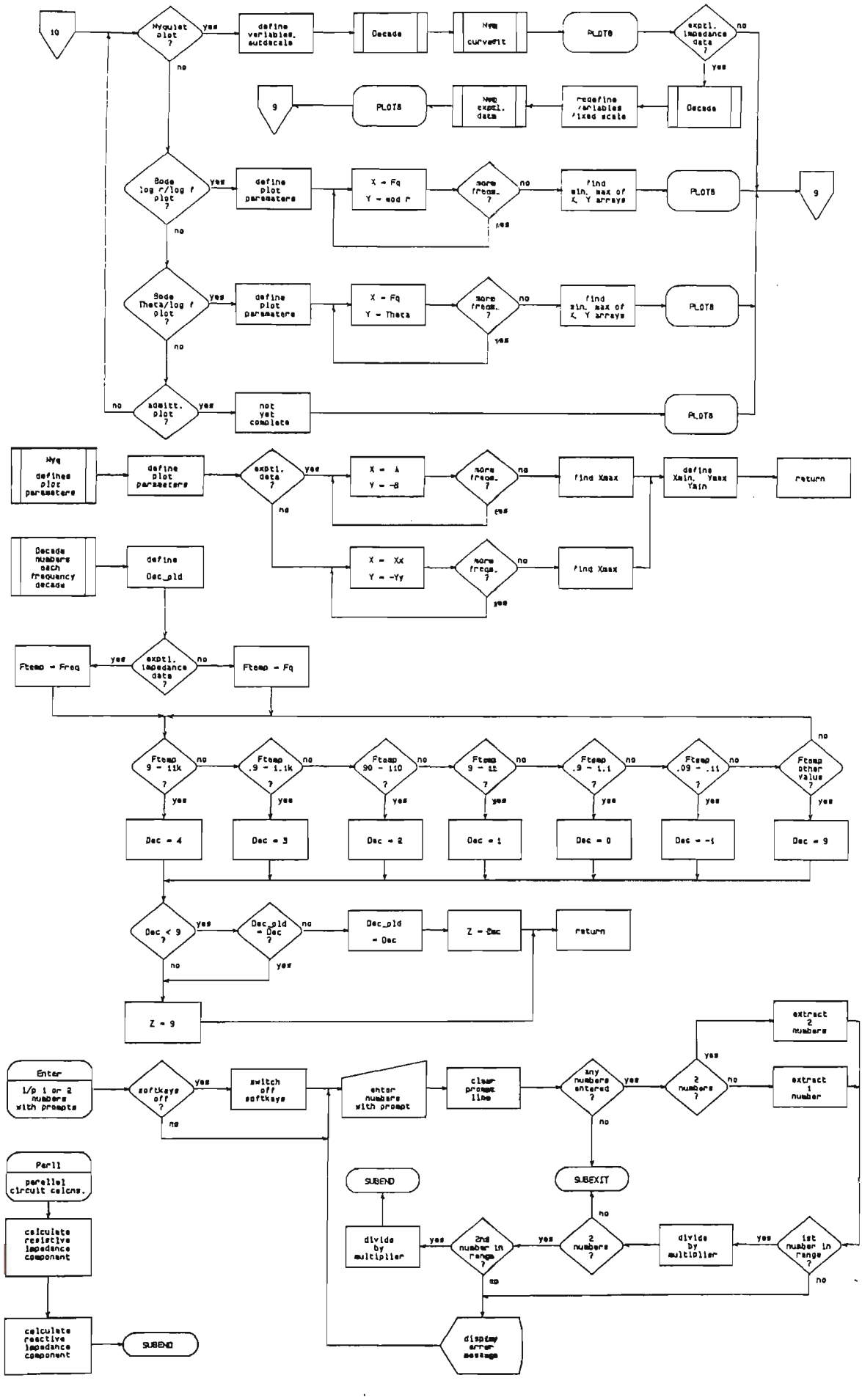
10
Hyquiet plot ?
yes
no
define variables, autoscale
Decade
Hyq curvefit
PLOT8
exptl. impedance data ?
yes
no
redefine variables fixed scale
Decade
Hyq exptl. data
PLOT8
9
Bode log r/log f plot ?
define plot parameters
X = Fq
Y = mod r
more freqs. ?
find min, max of X, Y arrays
Bode Theta/log f plot ?
define plot parameters
X = Fq
Y = Theta
more freqs. ?
find min, max of X, Y arrays
admitt. plot ?
not yet complete
Hyq defines plot parameters
define plot parameters
exptl. data ?
X = A
Y = -B
more freqs. ?
find Xmax
define Xmin, Ymax Ymin
return
Decade numbers each frequency decade
define Dec_old
X = Xx
Y = -Yy
more freqs. ?
find Xmax
Ftemp = Freq
exptl. impedance data ?
Ftemp = Fq
Ftemp 9 - 11k ?
Ftemp .9 - 1.1k ?
Ftemp 90 - 110 ?
Ftemp 9 - 11 ?
Ftemp .9 - 1.1 ?
Ftemp .09 - .11 ?
Ftemp other value ?
Dec = 4
Dec = 3
Dec = 2
Dec = 1
Dec = 0
Dec = -1
Dec = 9
Dec < 9 ?
Dec_old = Dec ?
Dec_old = Dec
Z = Dec
return
Z = 9
Enter l/p 1 or 2 numbers with prompts
softkeys off ?
switch off softkeys
enter numbers with prompt
clear prompt line
any numbers entered ?
2 numbers ?
extract 2 numbers
extract 1 number
Perll
parellel circuit calcns.
calculate resistive impedance component
calculate reactive impedance component
SUBEND
SUBEND
SUBEXIT
divide by multiplier
2nd number in range ?
2 numbers ?
divide by multiplier
1st number in range ?
display error message

Figure A1/10a. Subprogram RP_EXPT flowchart.

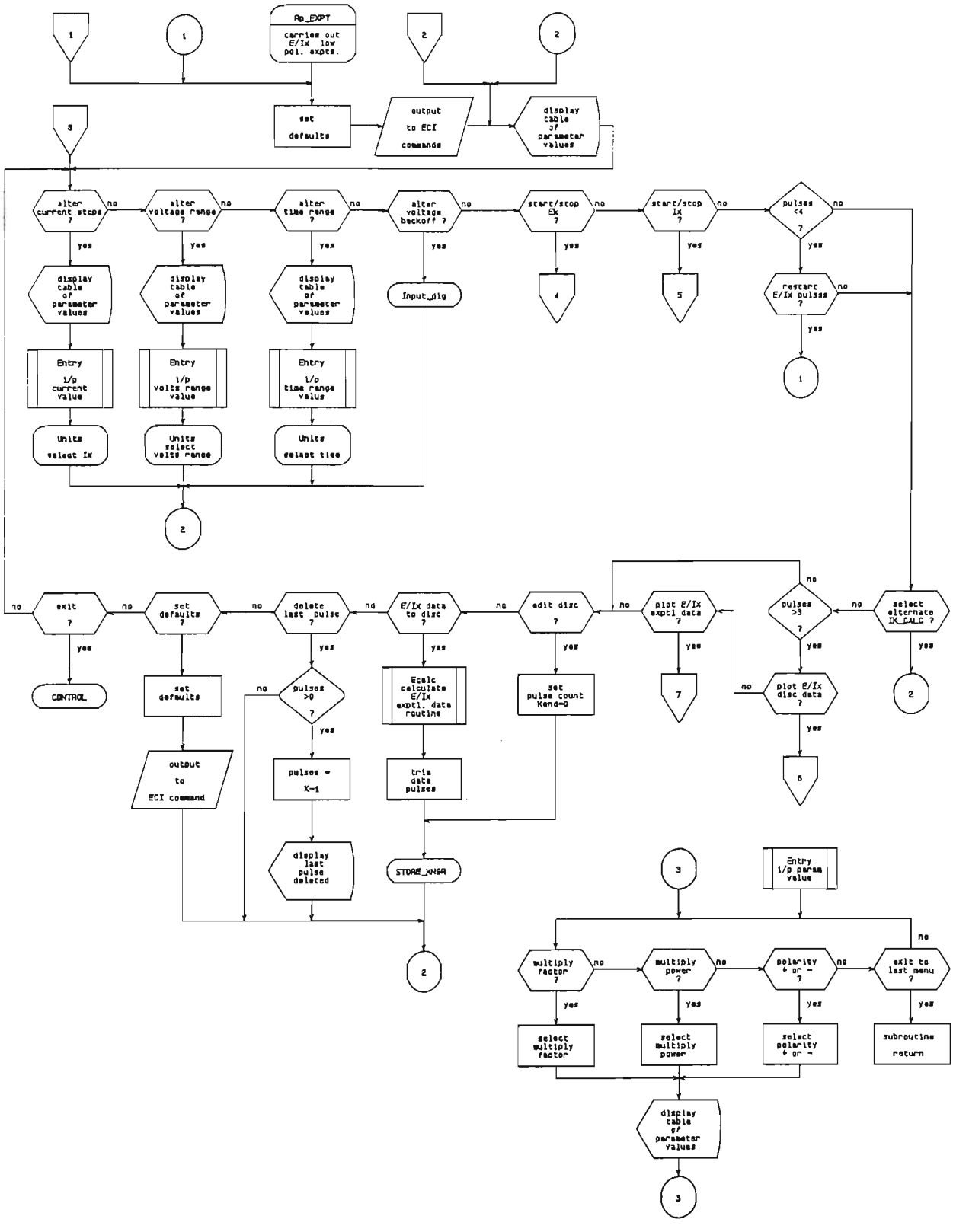

Figure A1/10b.

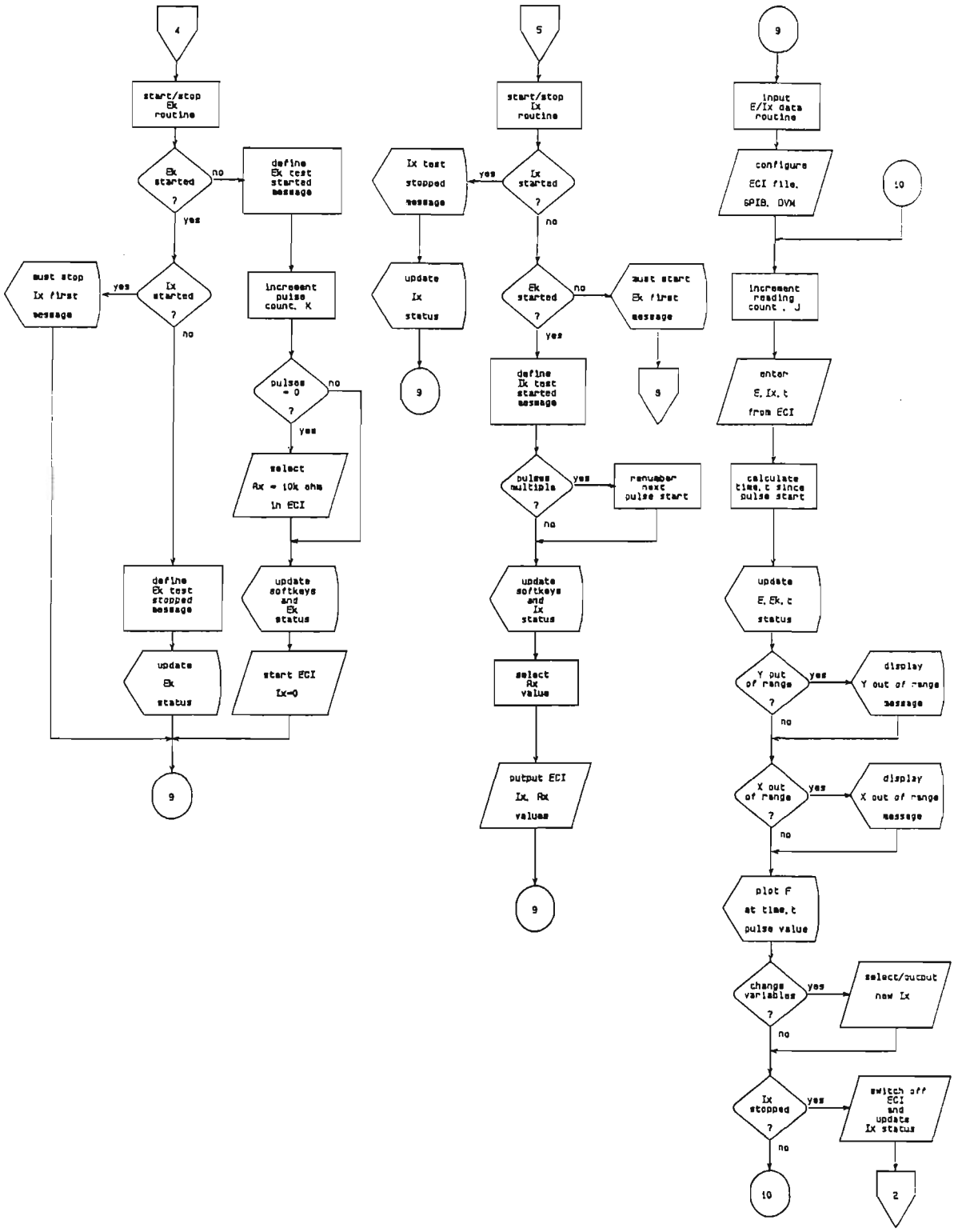

Figure A1/10c.

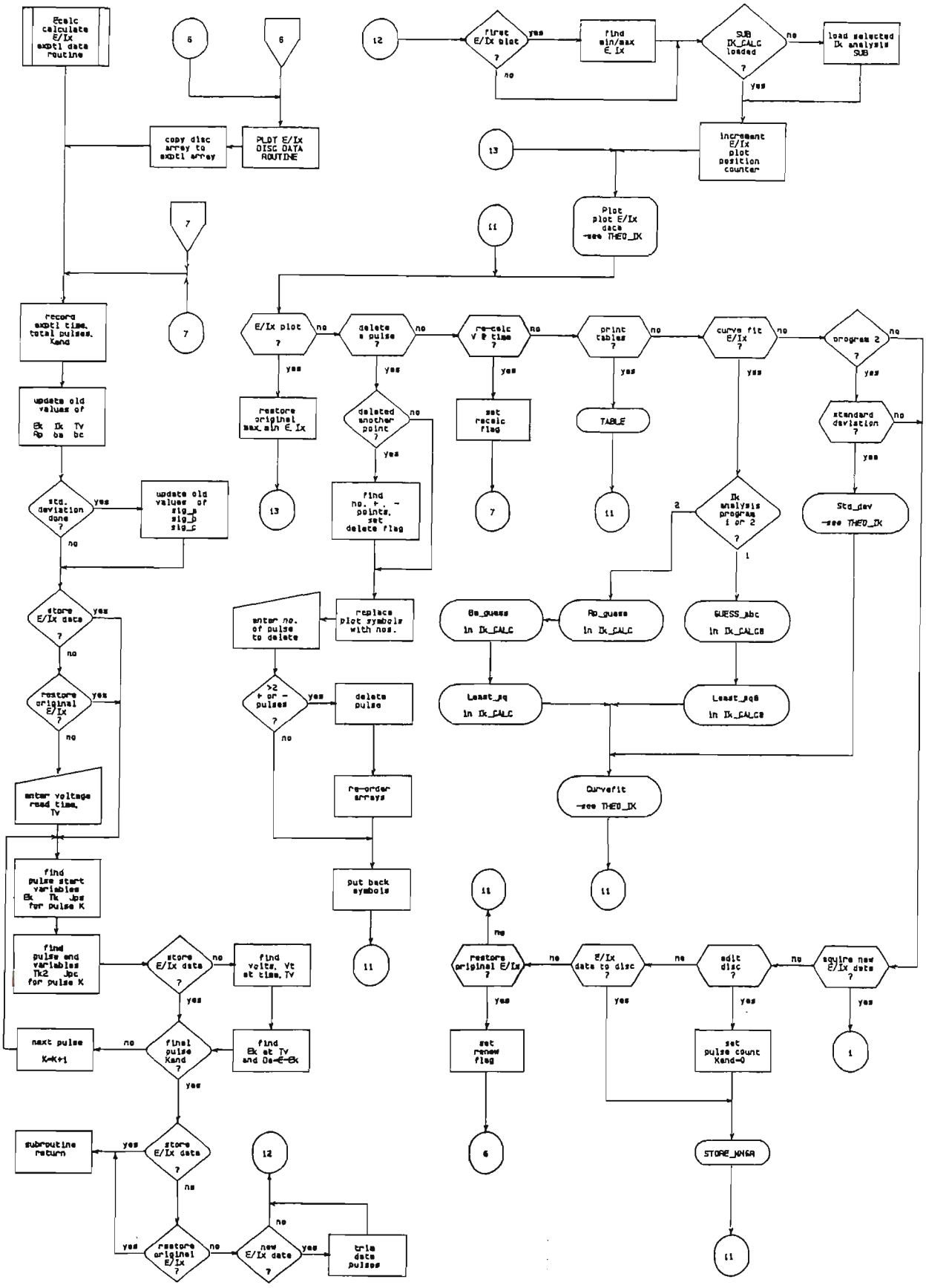

Figure A1/11. Subprogram IK_CALC flowchart.

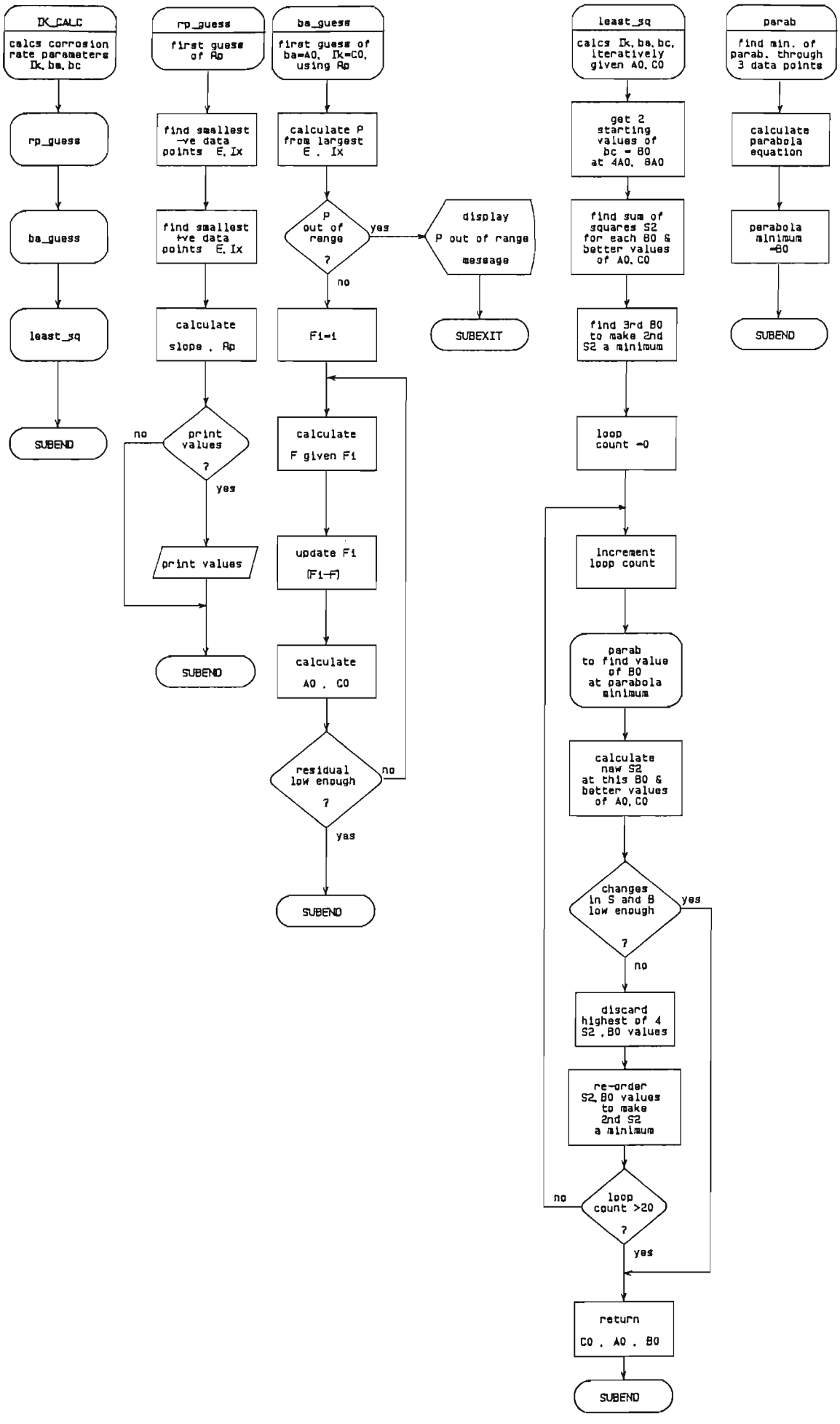

Figure A1/12a. Program THEO_IK flowchart.

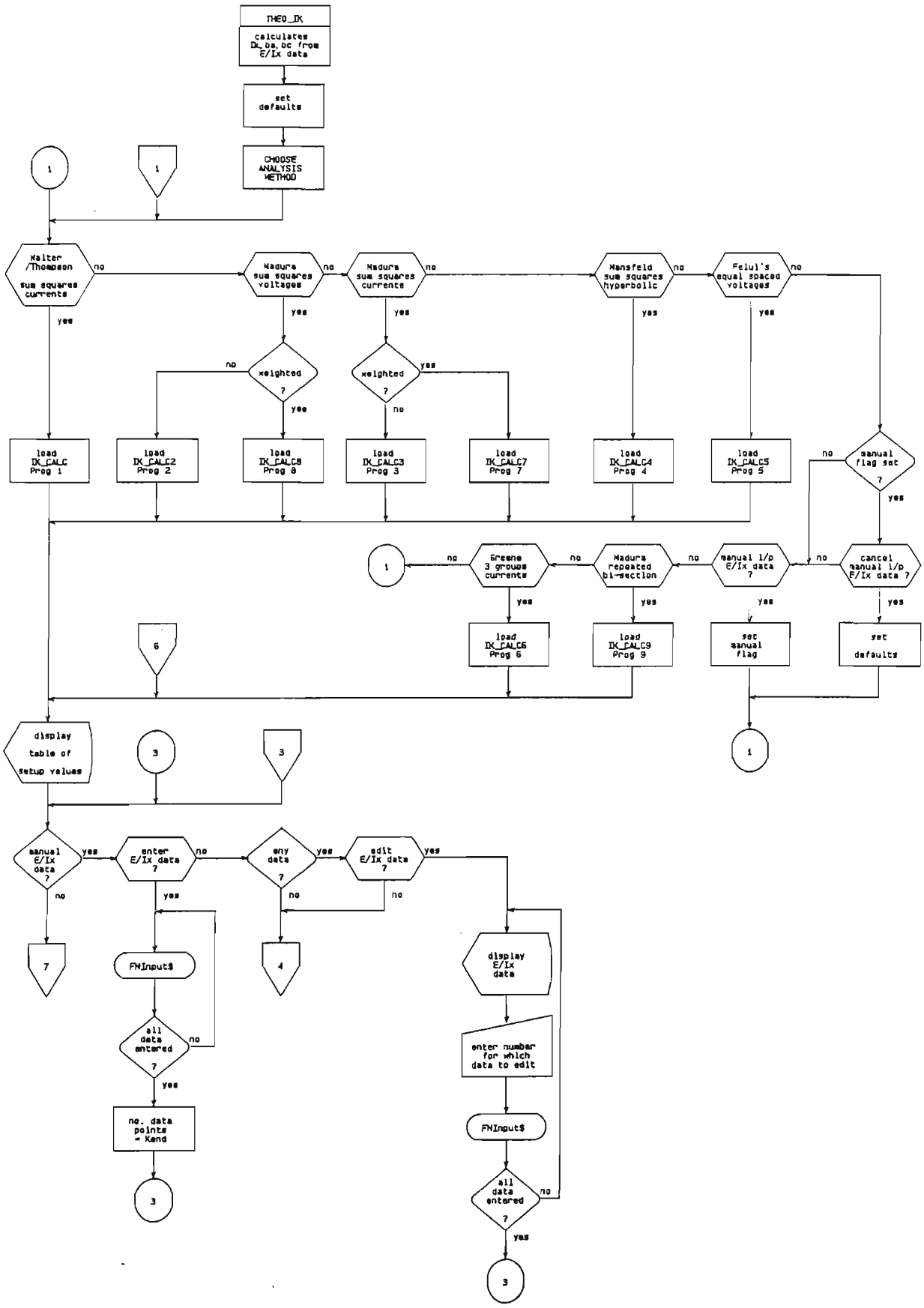

Figure A1/12b.

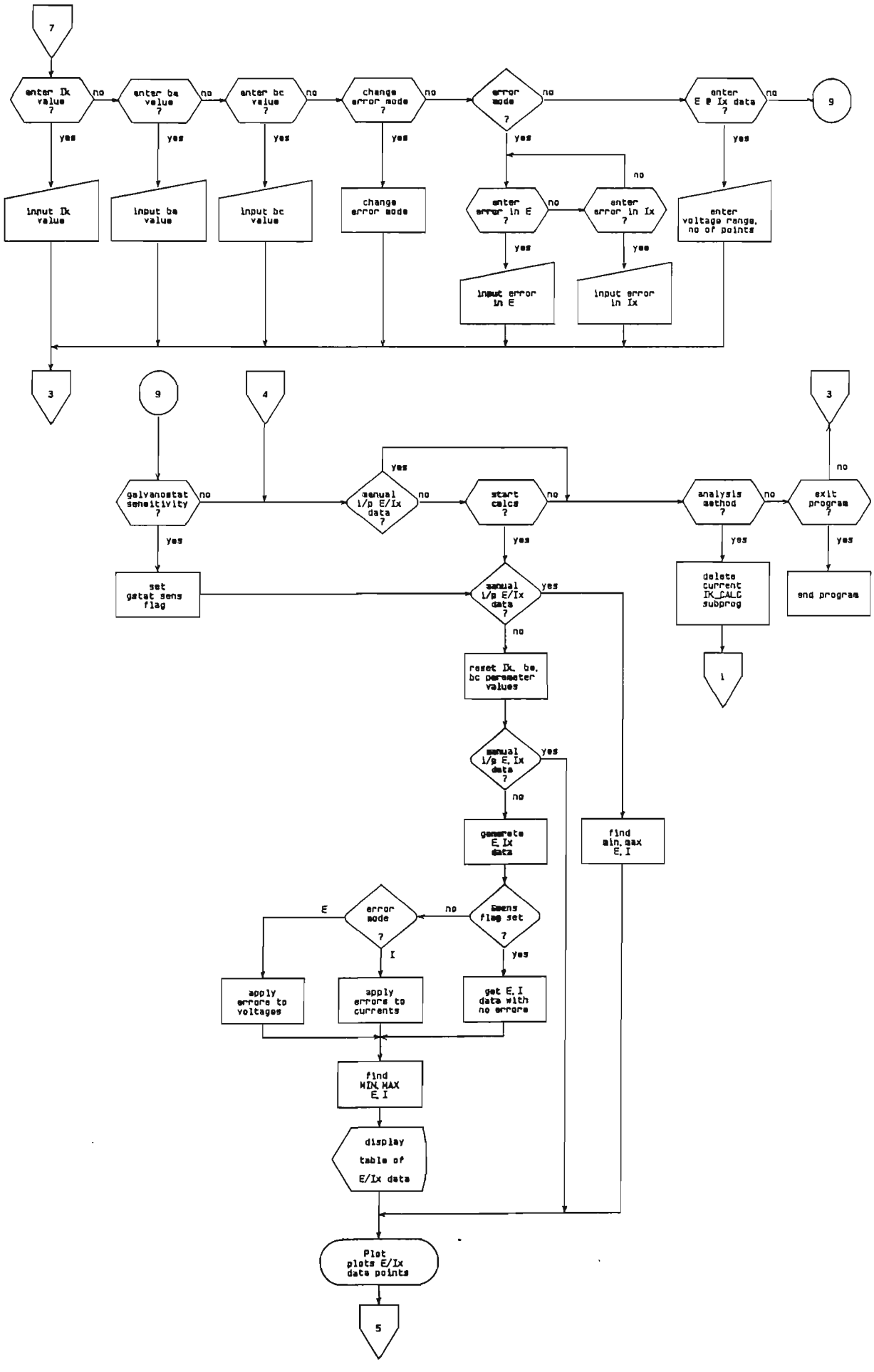

Figure A1/12c.

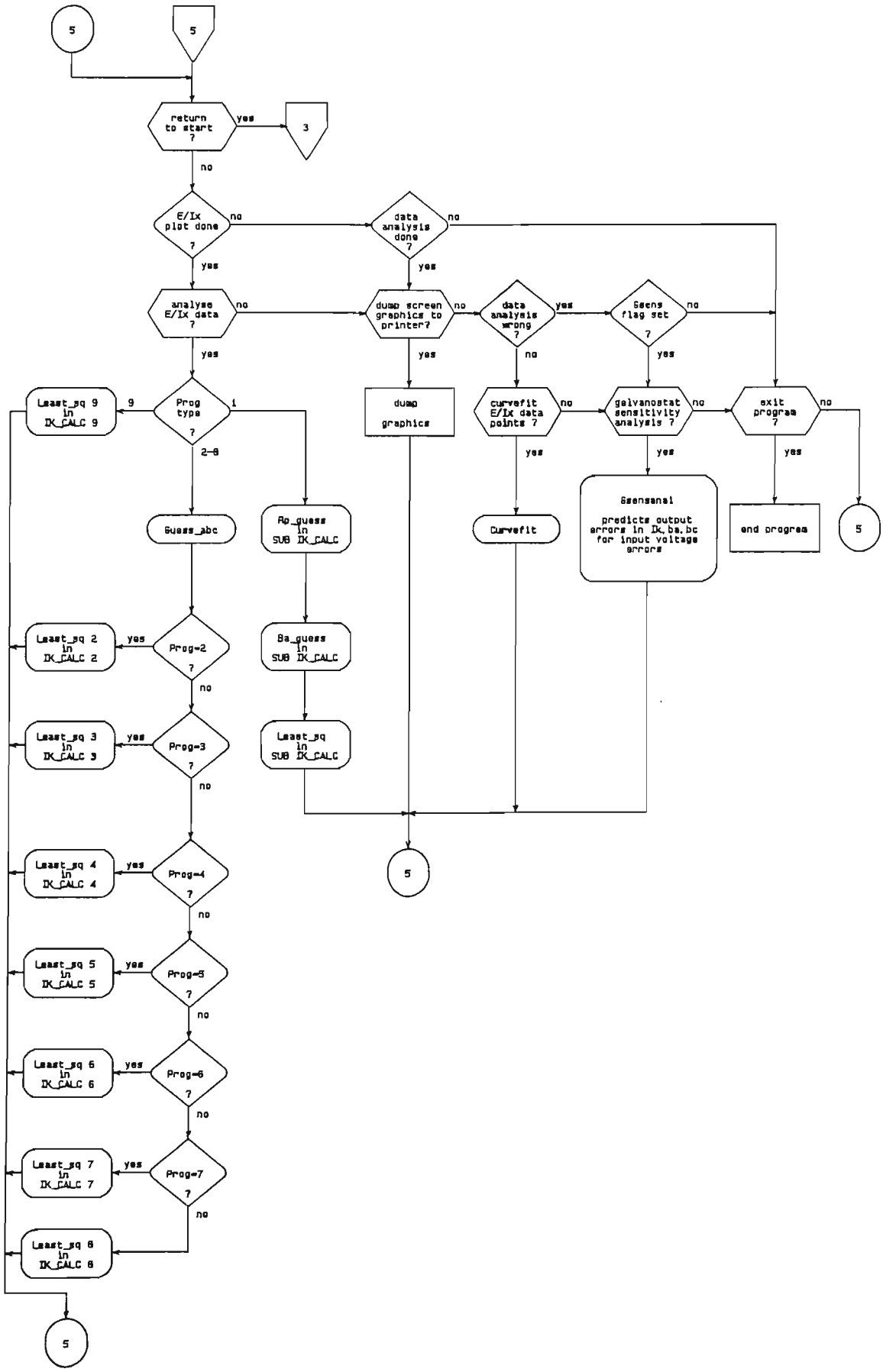

Figure A1/12d.

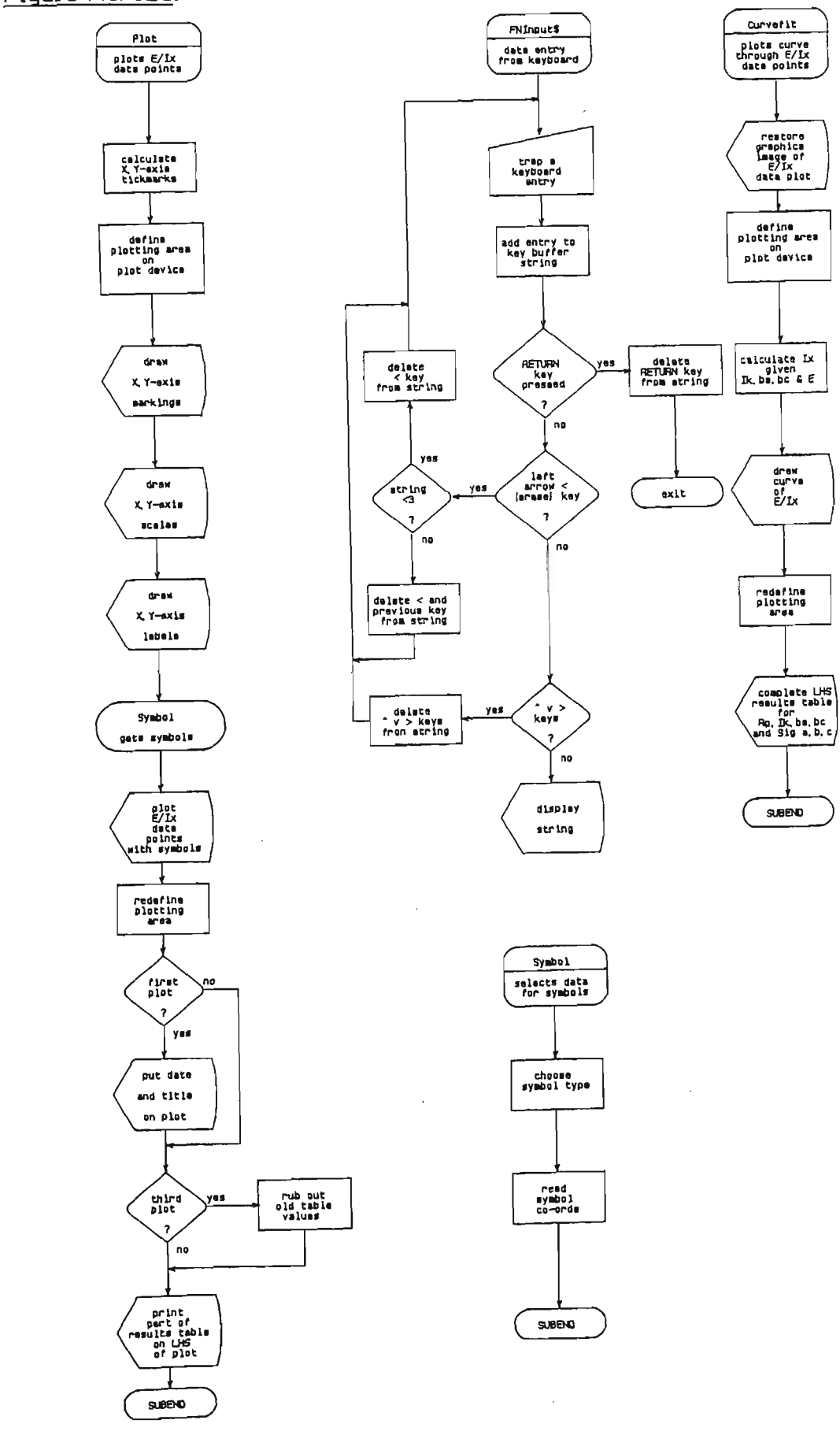

Figure A1/13. Subprogram STORE_MNGR flowchart.

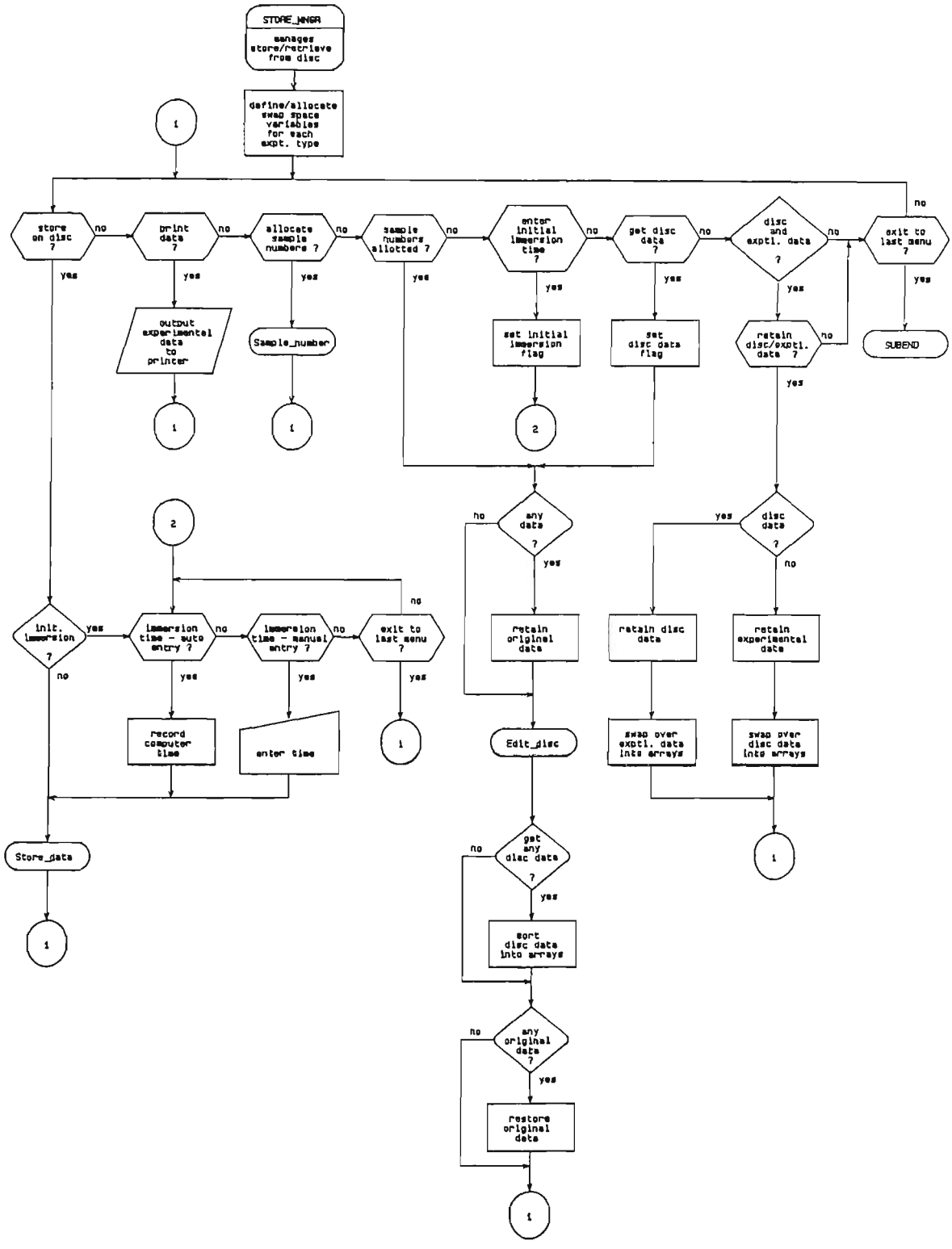

Figure A1/14. Subprogram SAMPLE_NUM flowchart.

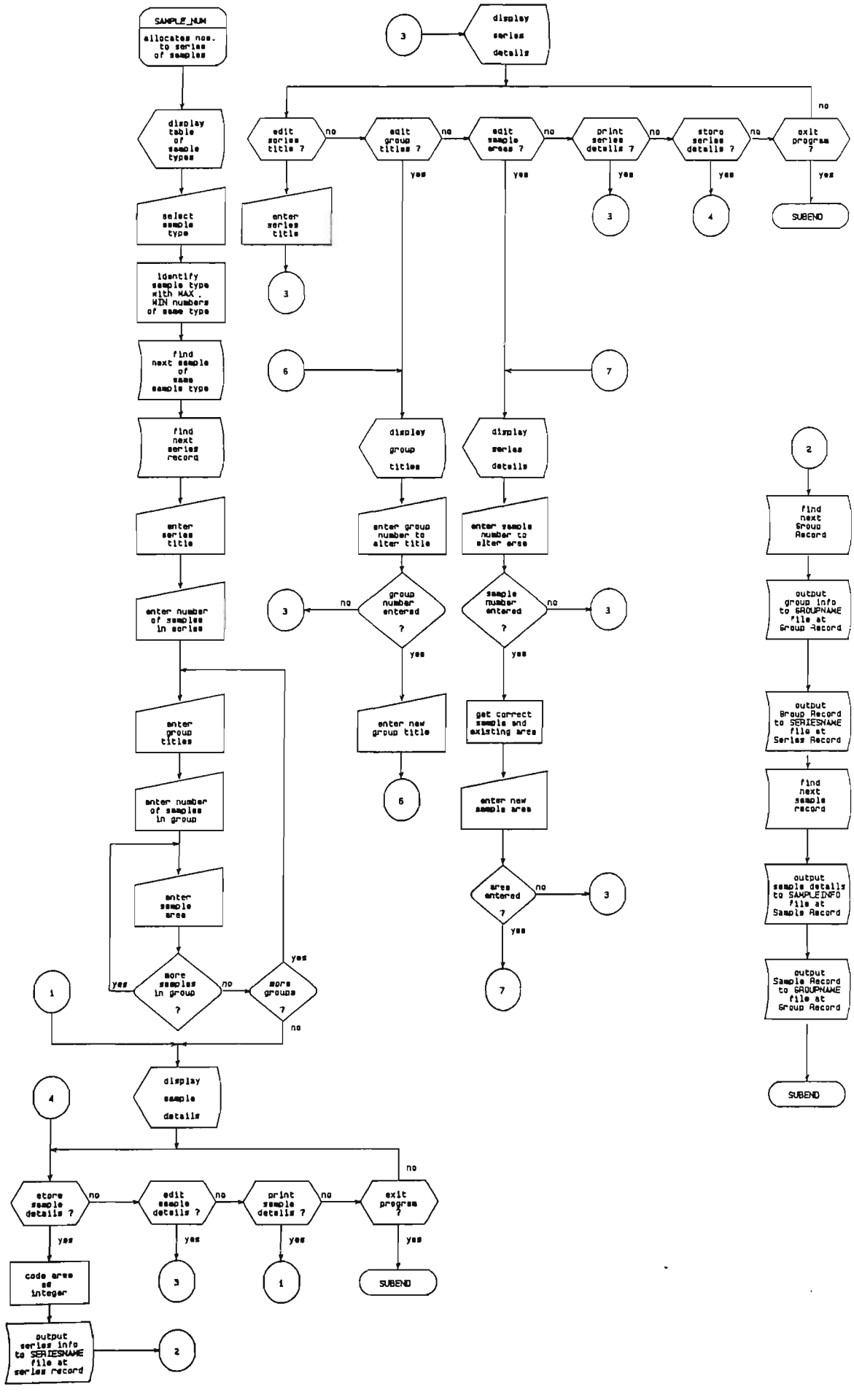

Figure A1/15. Subprogram STORE_DATA flowchart.

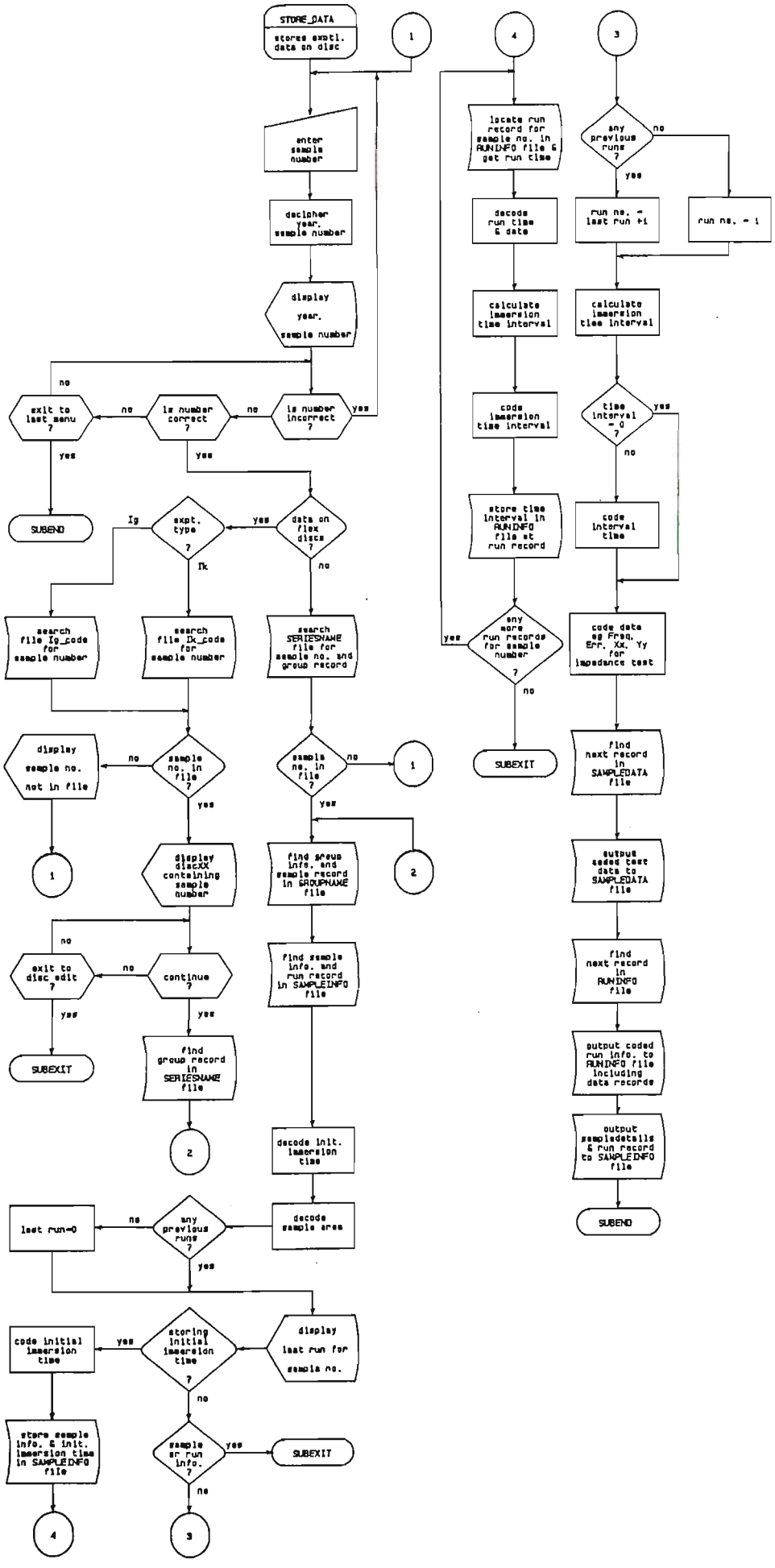

Figure A1/16a. Subprogram EDIT_DISC flowchart.

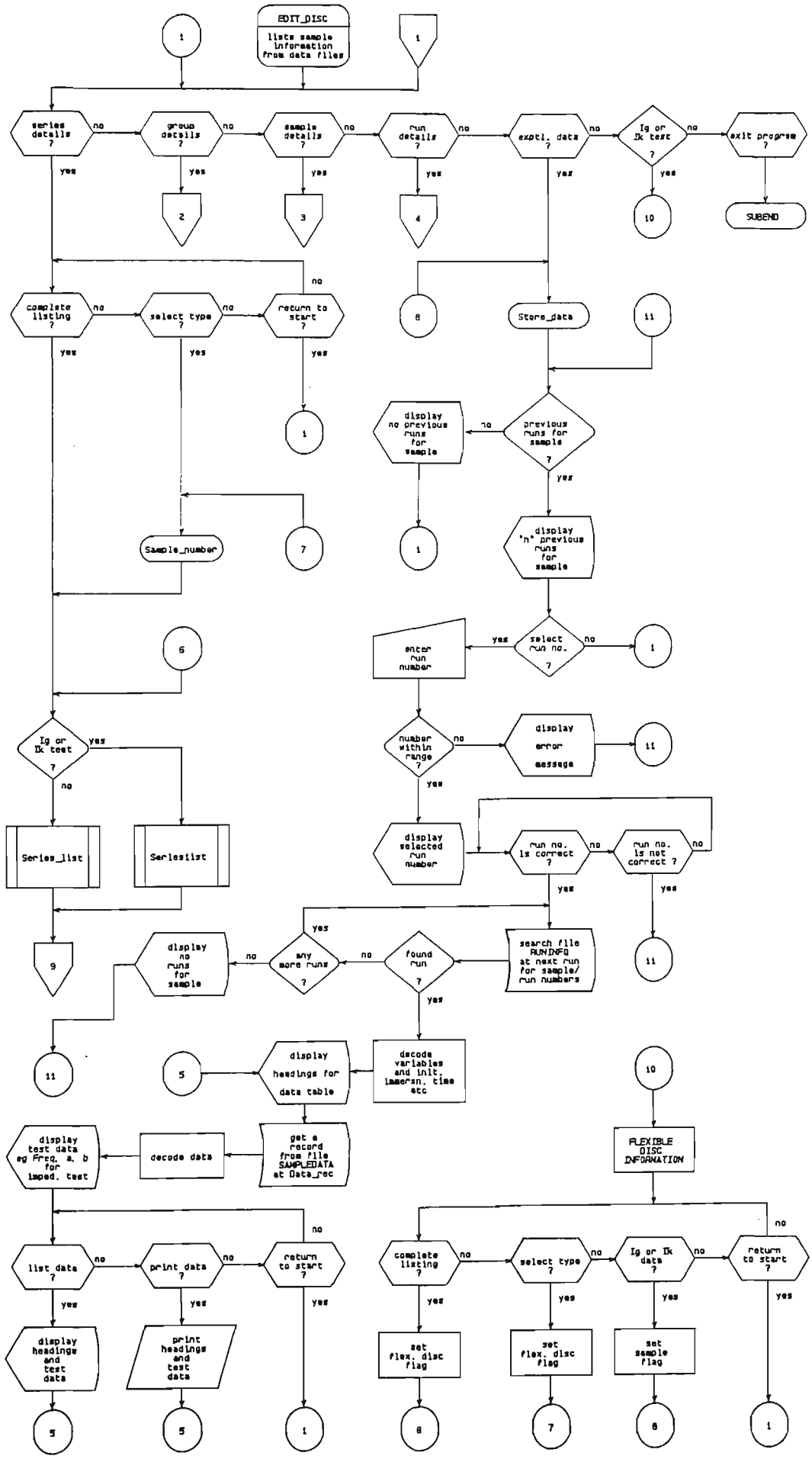

Figure A1/16b.

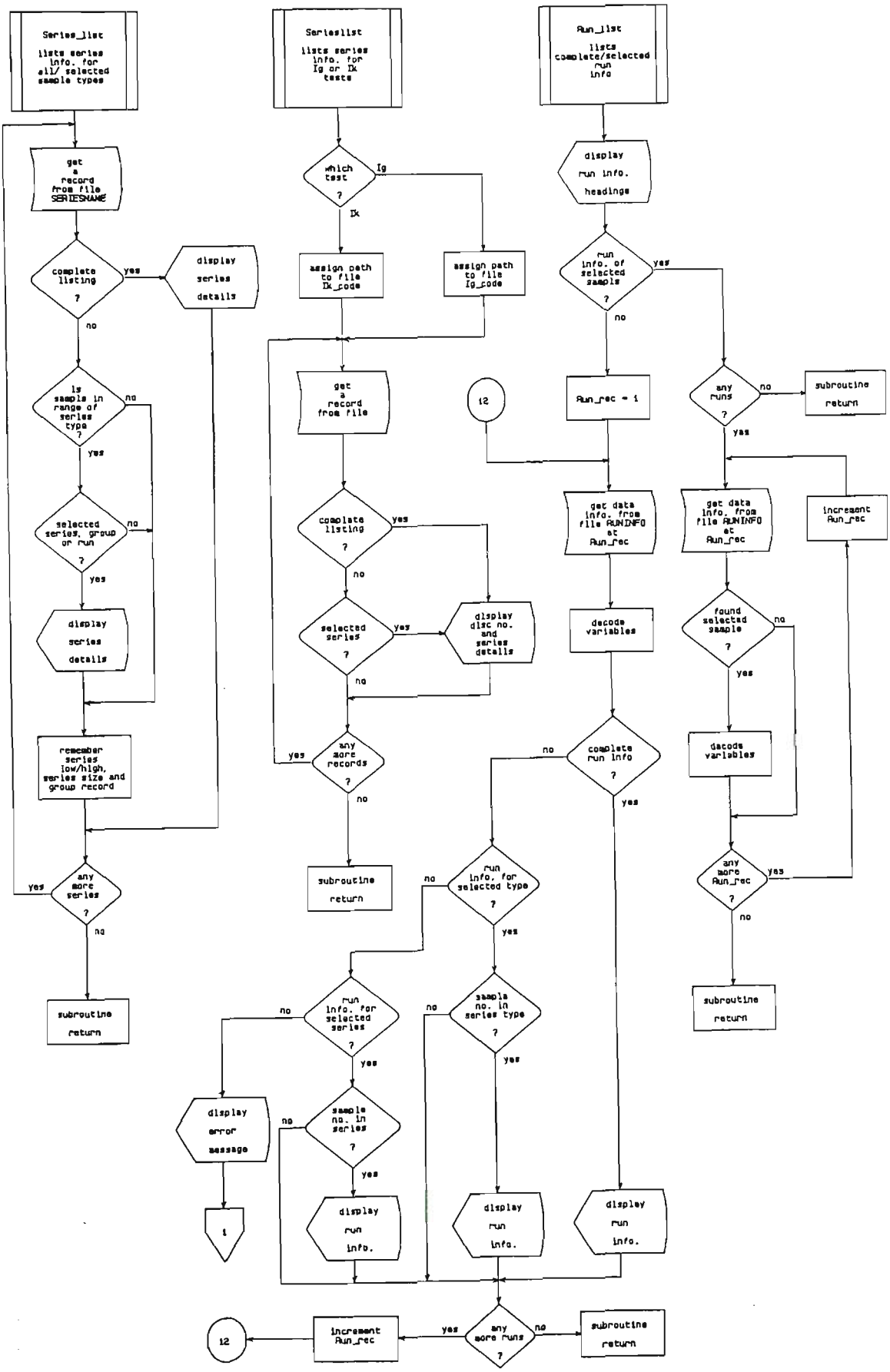

Figure A1/16c.

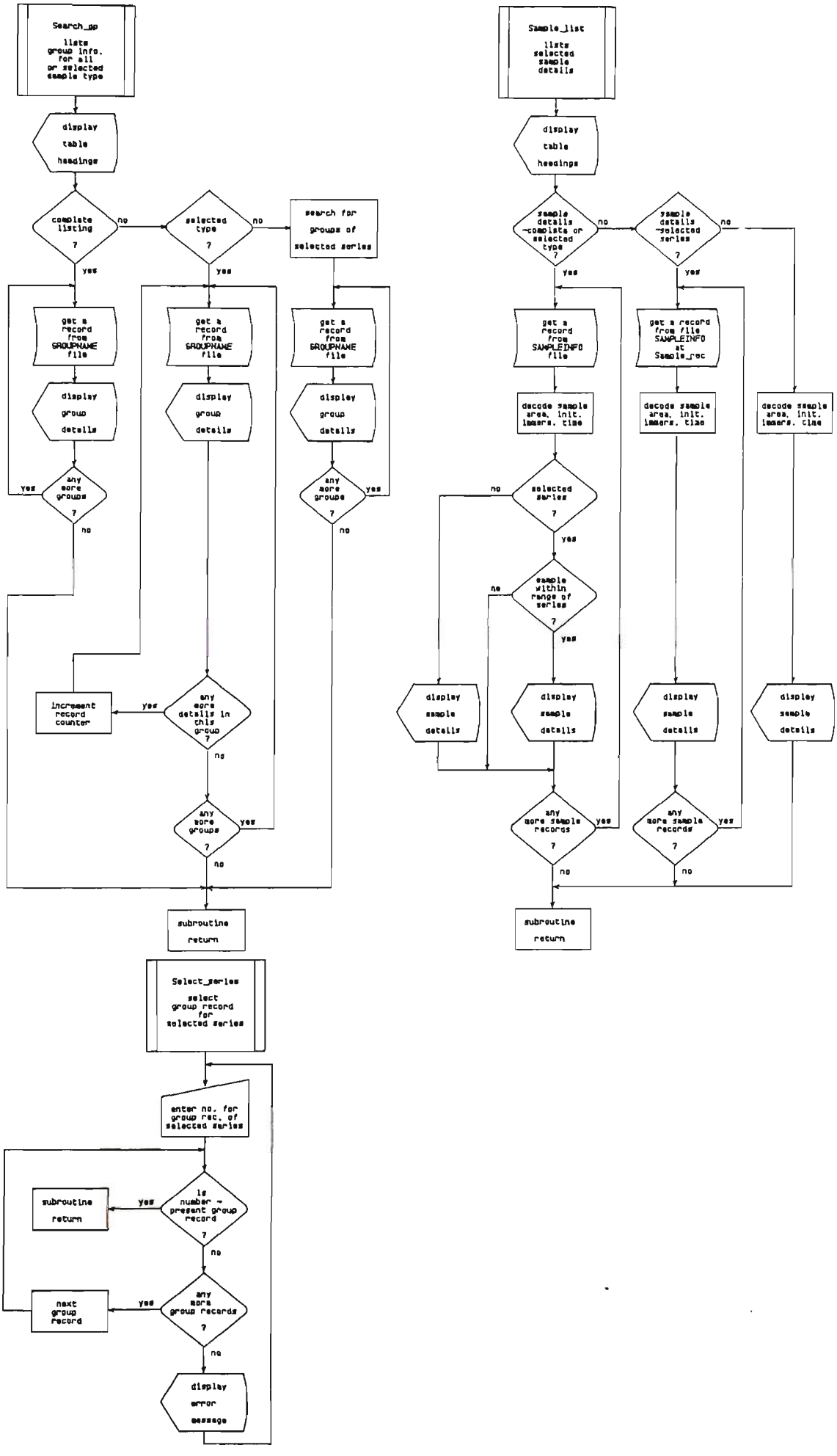

Figure A1/16d.

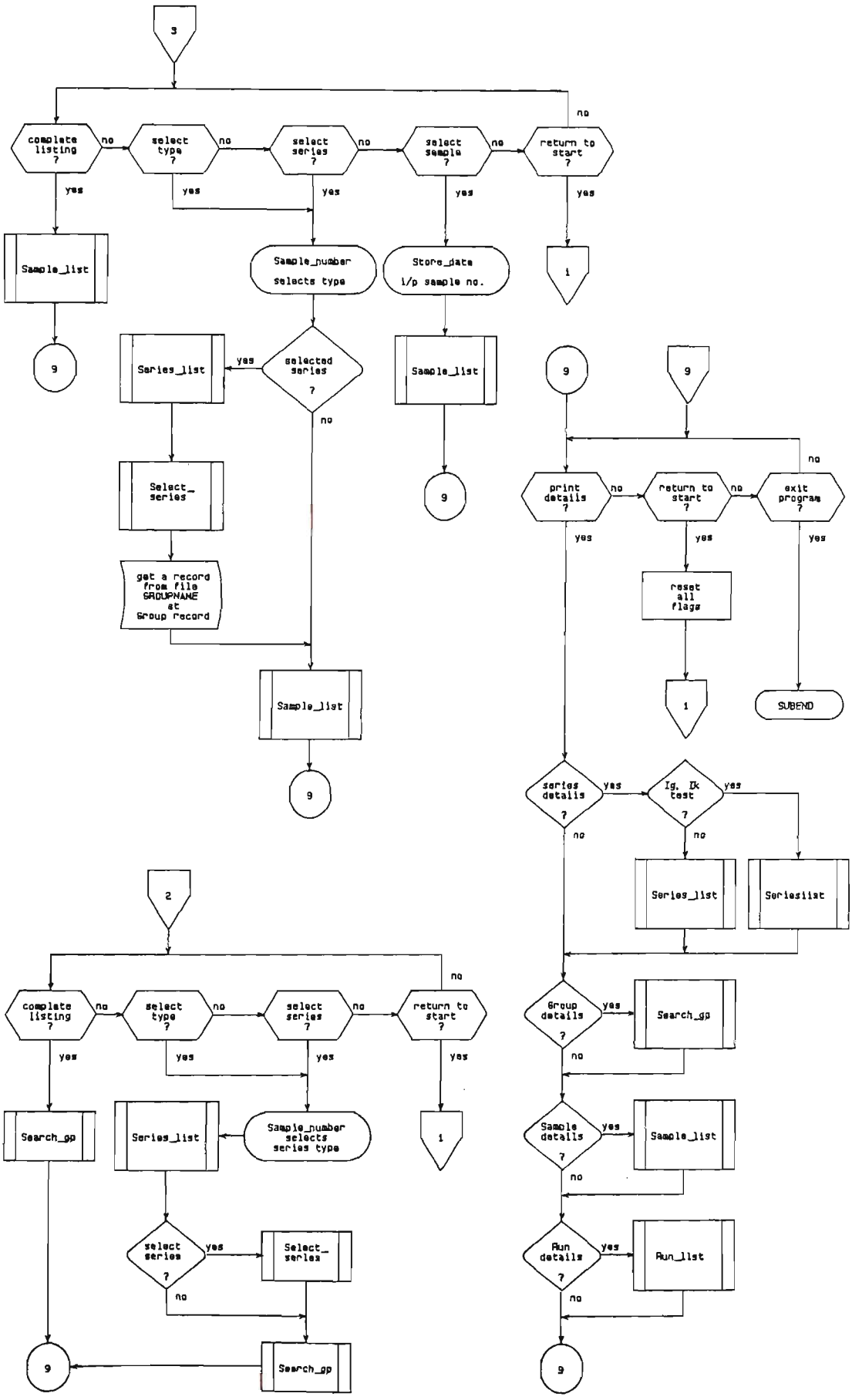

Figure A1/16e.

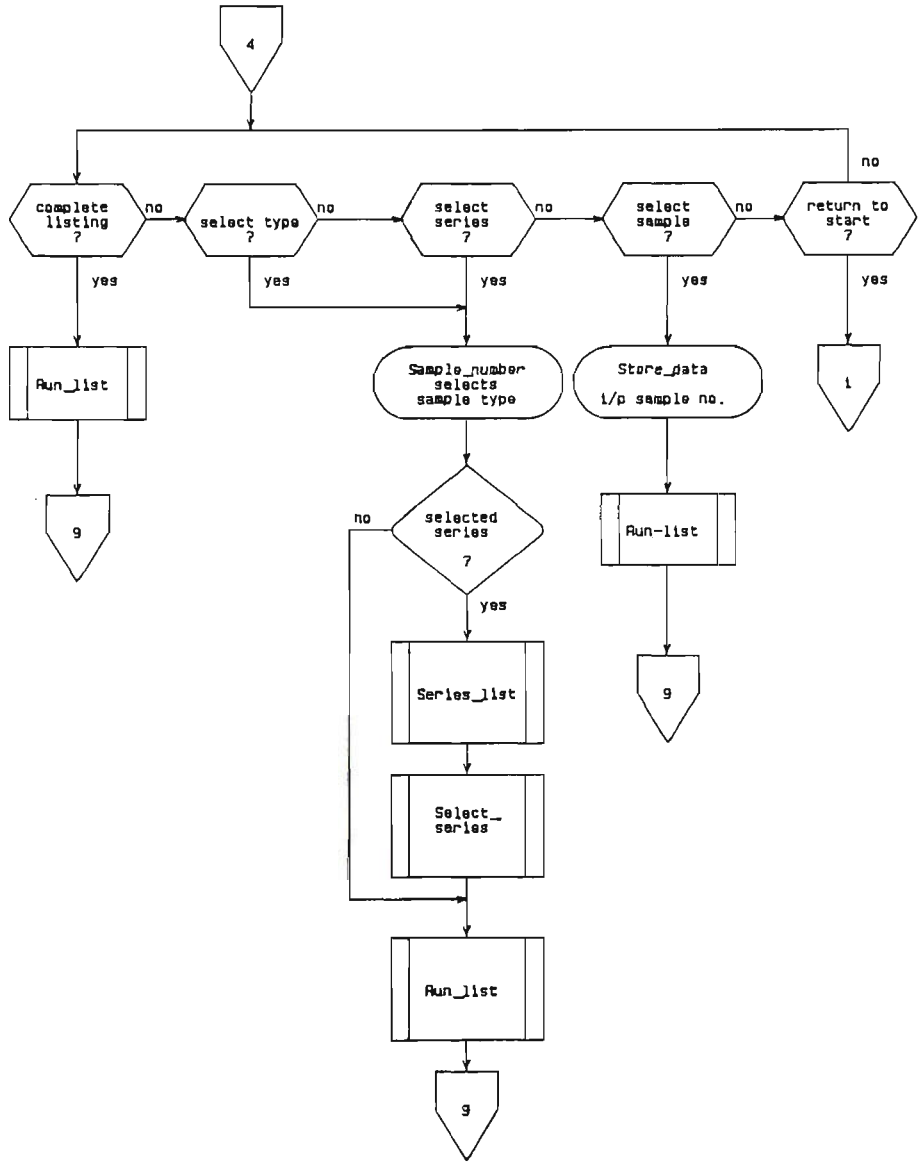

Figure A1/17a. Subprogram PLOT8 flowchart.

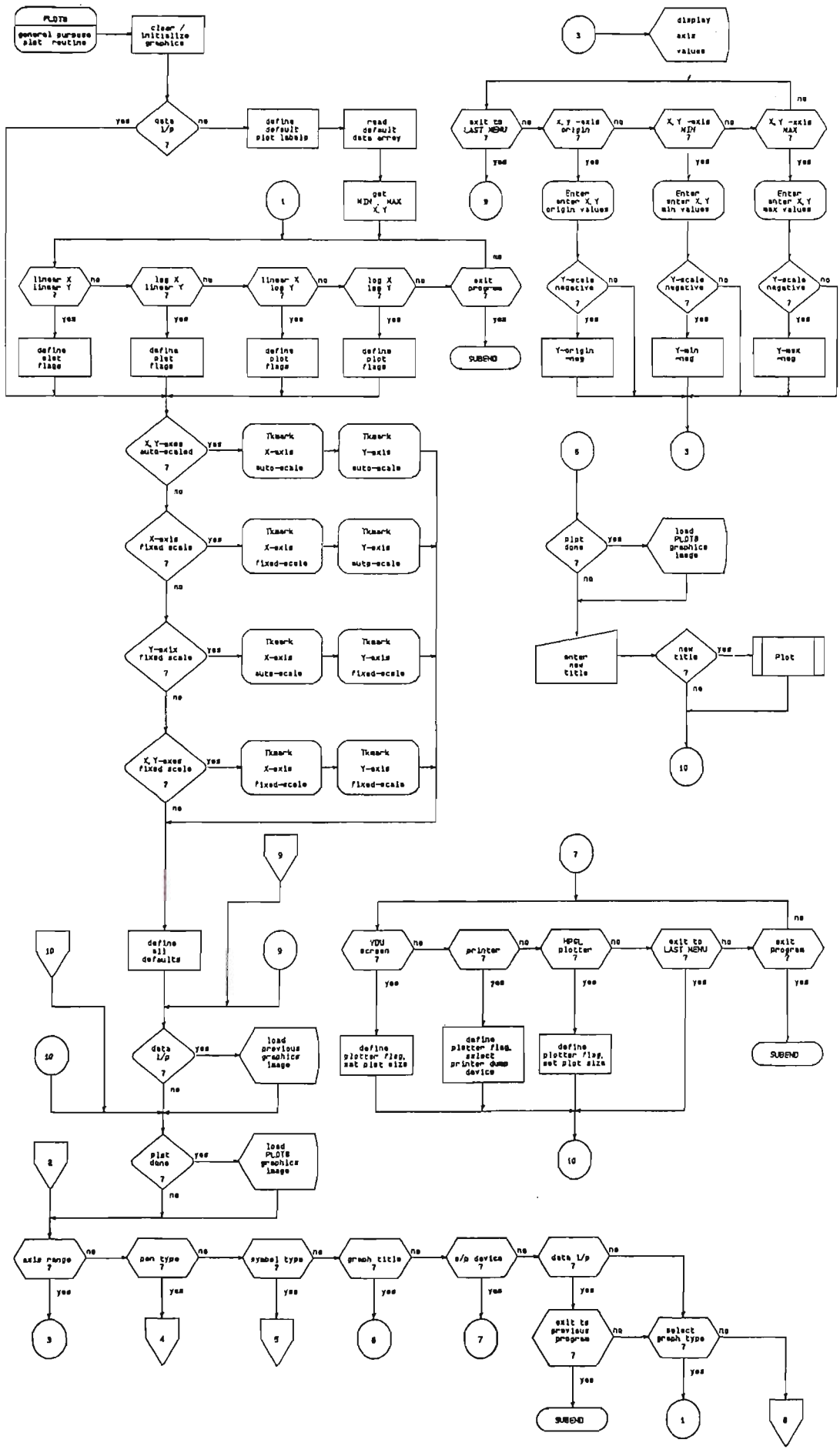

Figure A1/17b.

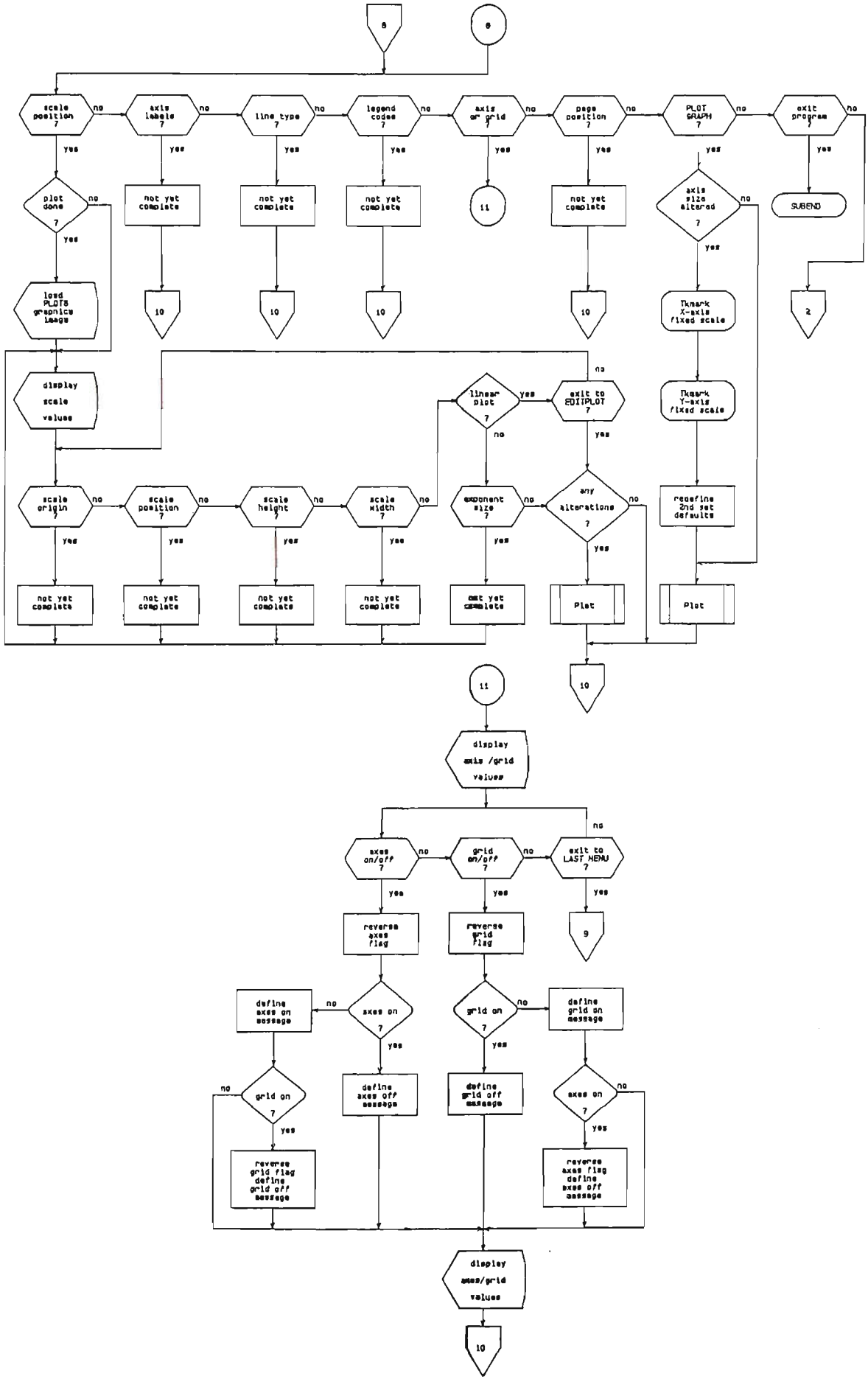

Figure A1/17c.

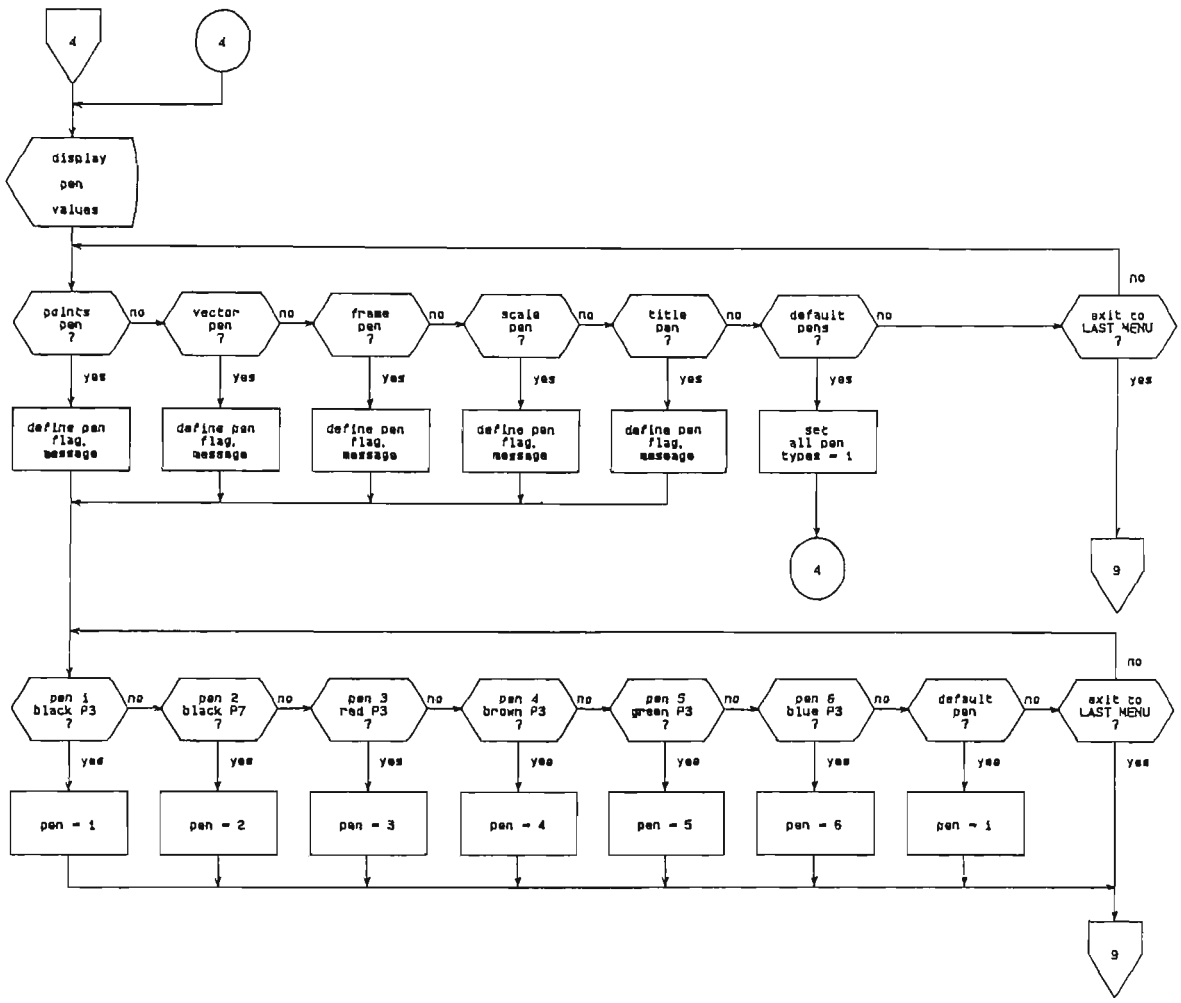

Figure A1/17d.

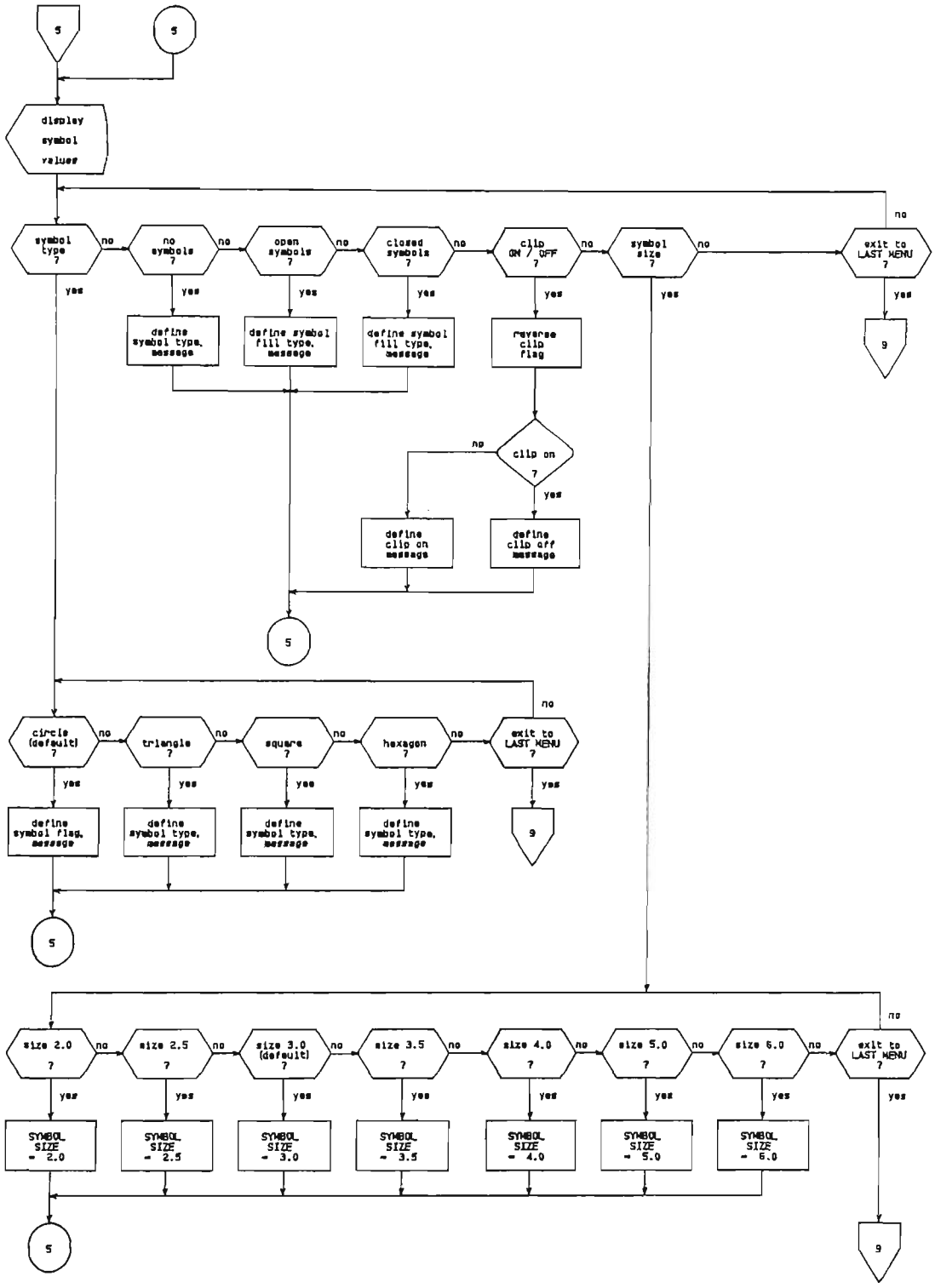

Figure A1/17e.

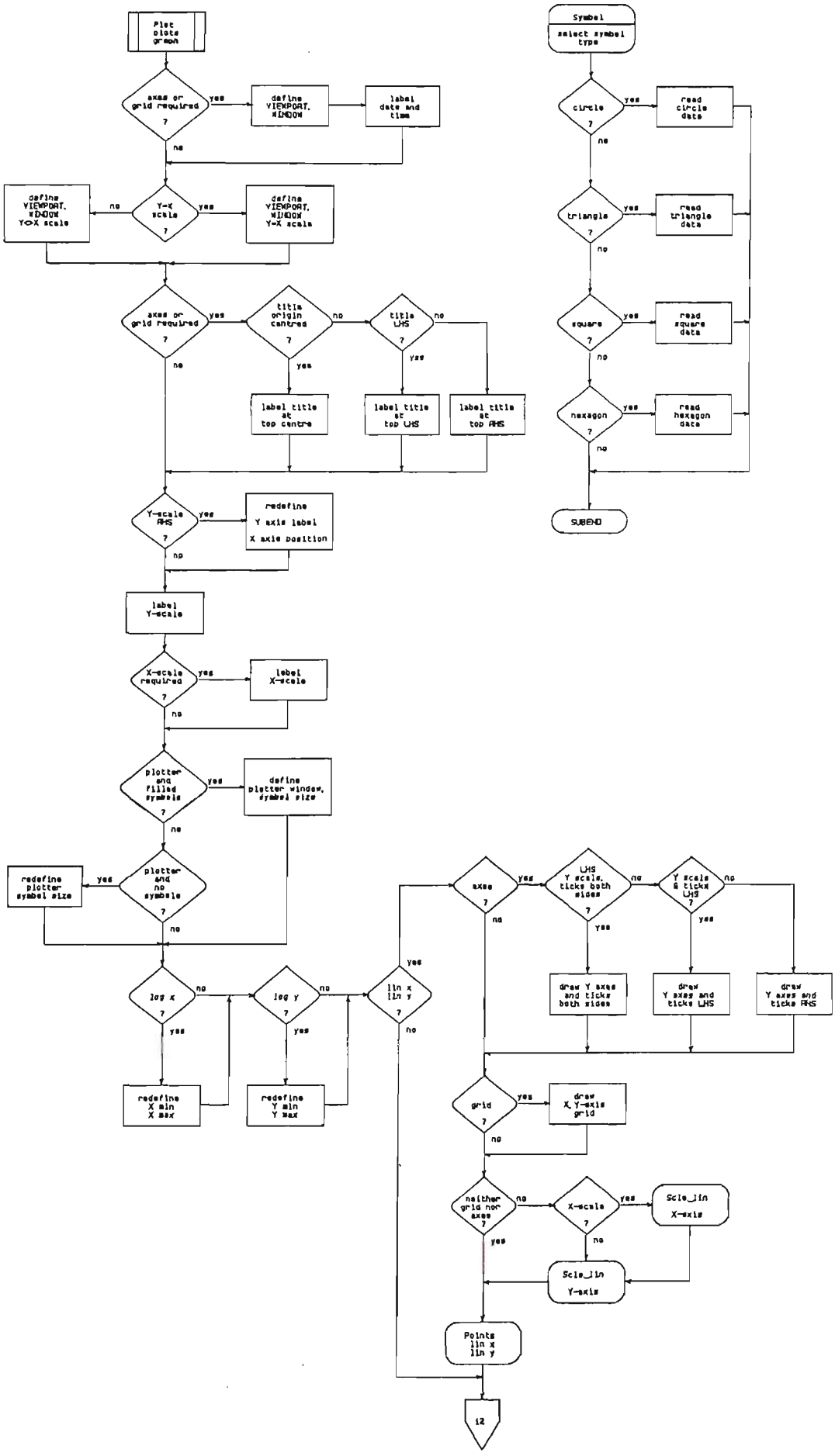

Figure A1/17f.

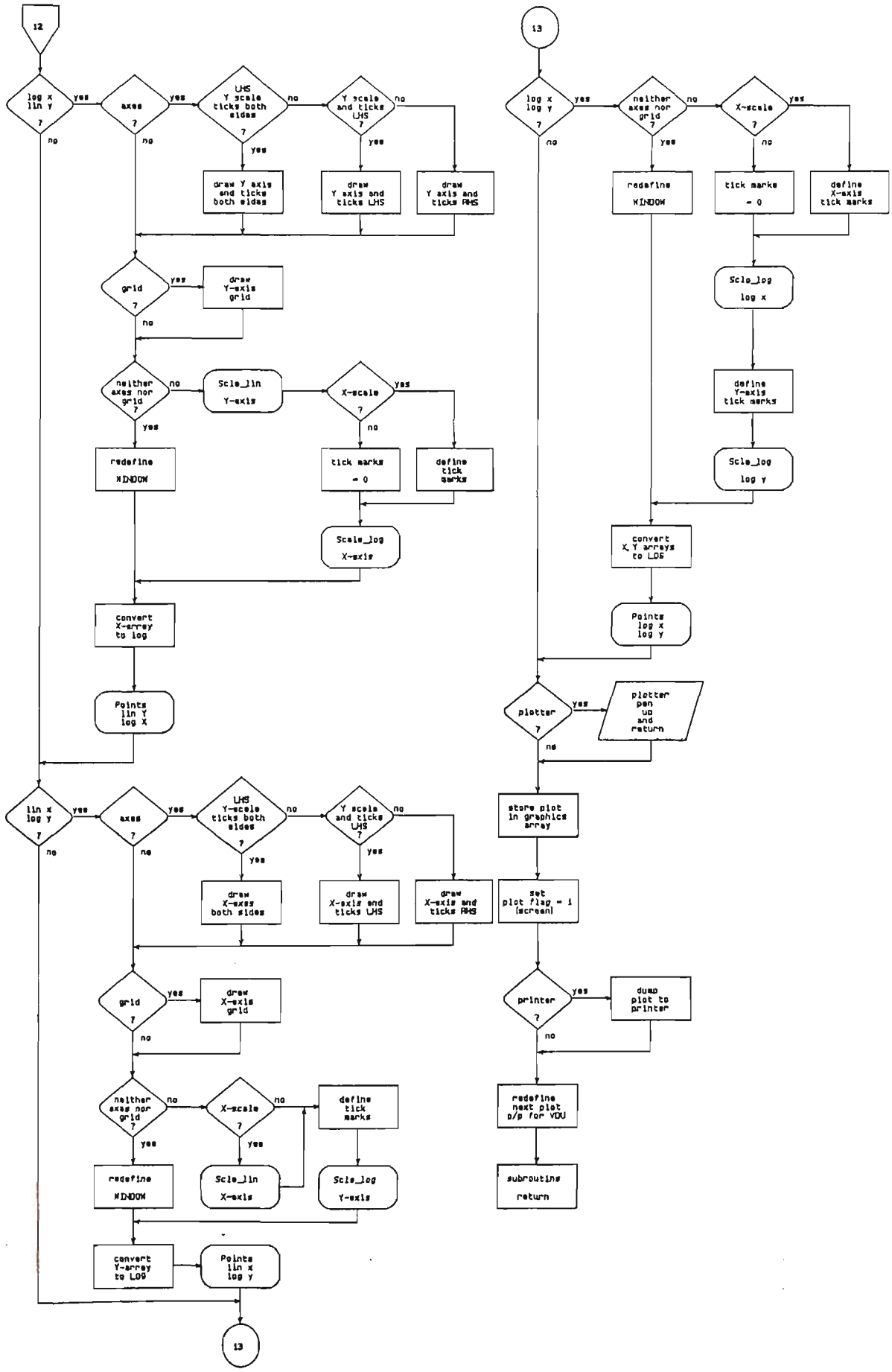

Figure A1/17g.

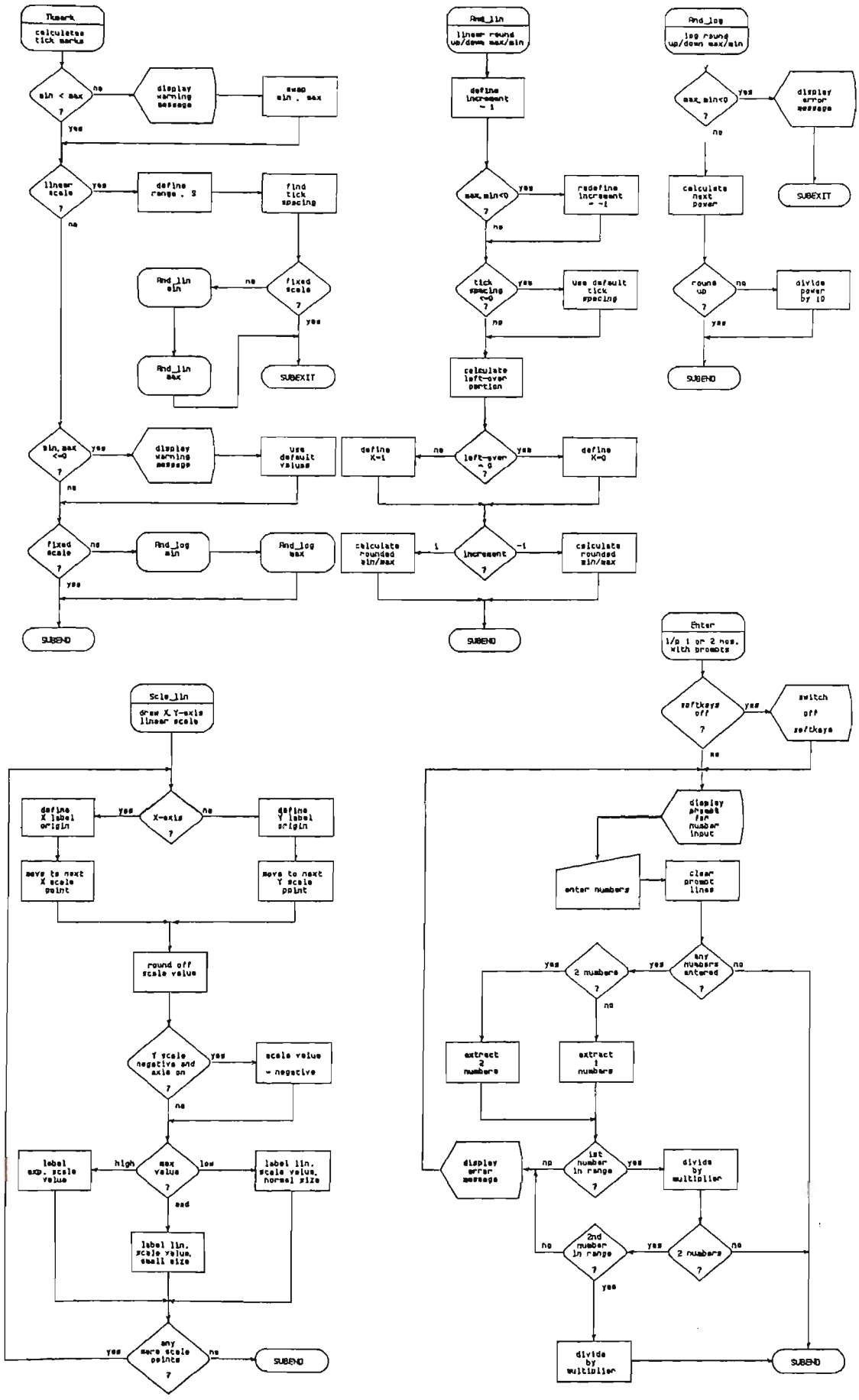

Figure A1/17h.

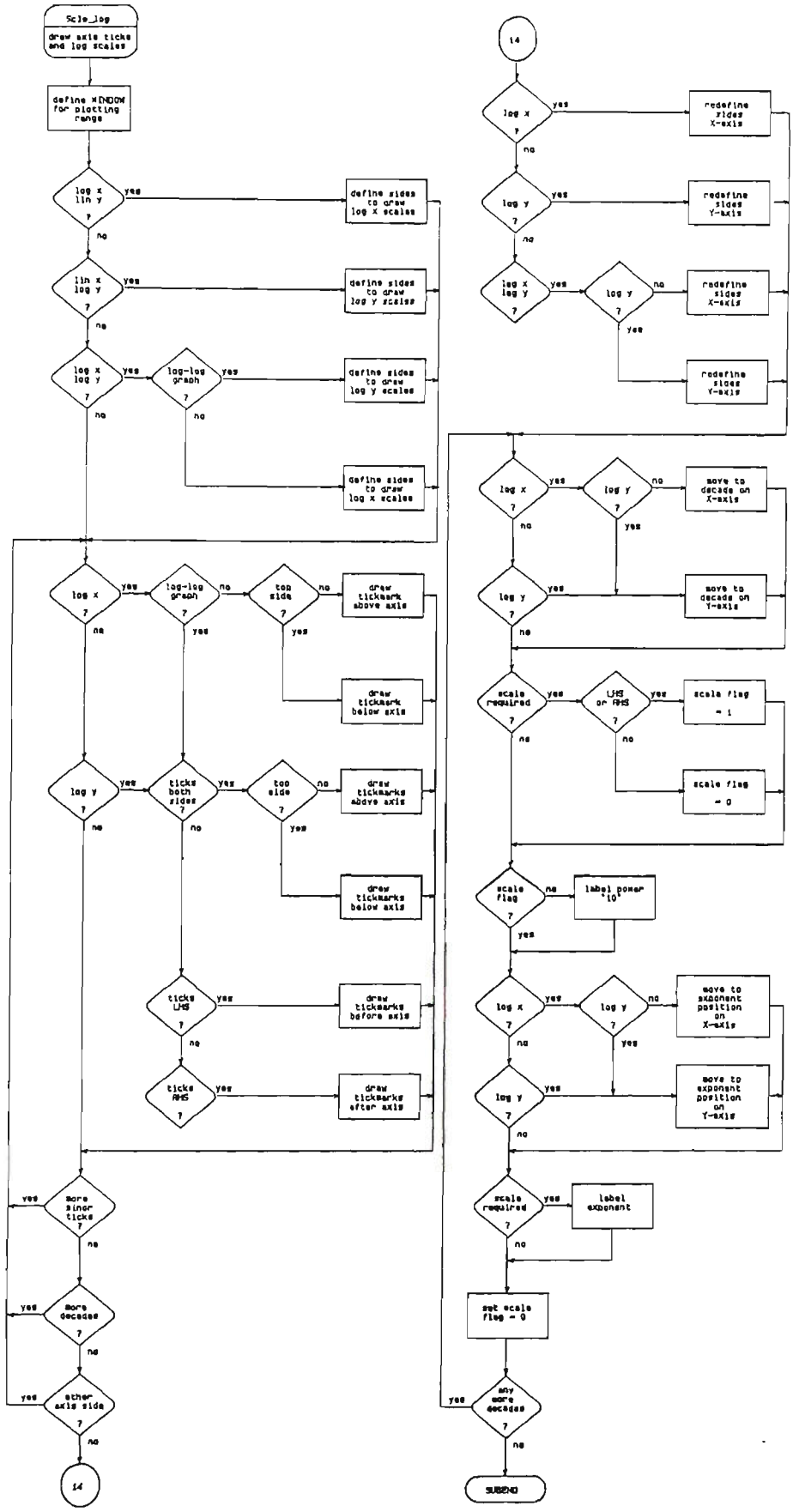

APPENDIX A2 - Relationship Between Total Summed Pathway Area of Paint Film and $[Cl^-]$ of Measurement Solution

Aim: To determine how the total summed area of pathways in the paint film are related to the chloride ion concentration of the measurement solution.

Table A2/1 shows values of solution conductivity as a function of the chloride ion concentration of the measurement solution.

Table A2/1 Solution Conductivity, k, Versus Chloride Ion Concentration, $[Cl^-]$, at Room Temperature (23°C)

$[Cl^-]$ (mg/L)	k (ohm cm)$^{-1}$
10^0	3.7×10^{-6}
10^1	3.5×10^{-5}
10^2	3.25×10^{-4}
10^3	3.05×10^{-3}
10^4	2.8×10^{-2}

This table suggests that conductivity is related to concentration by the approximate expression

$$k = k_o C \qquad (A2/1)$$

where k_o = constant

$\approx 3.2 \times 10^{-6}$ (ohm.L.mg^{-1} cm^{-1})

C = chloride ion concentration (mg.L^{-1})

Equation (A2/1) is of similar form to the more usual expression

$$k = \Lambda C \qquad (A2/2)$$

where Λ = equivalent conductance (ohm^{-1} cm^{2} equiv^{-1})

C = concentration (equiv.cm^{-3})

Equation (A2/2) is itself an approximate relationship between conductivity and concentration, which was subsequently modified to expressions like the Kohlrausch equation or the Debye-Huckel-Onsager equation[193]. The plot shown in Figure R2/2, and discussed in Section R2.1/2 is of the form, which is equivalent to Equation (A2/4)

$$\log R_{pf} = \log R^{o}_{pf} + m \log (C/C_o) \quad \text{(A2/3)}$$

$$R_{pf} = R^{o}_{pf} (C/C_o)^{m} \quad \text{(A2/4)}$$

where R^{o}_{pf} = value of R_{pf} at some concentration, C_o

m = slope of plot (and is negative)

Now if it is assumed that the paint film resistance, R_{pf}, is determined predominantly by D-type pathway areas in the paint film, and that the conductivity of these pathways is the bulk solution conductivity, k, then

$$R_{pf} = \ell/nAk \quad \text{(A2/5)}$$

where A = summed cross-sectional area of pathway (cm^{2})

ℓ = average length of pathway (cm)

k = conductivity of bulk solution (ohm.cm)$^{-1}$

n = number of pathways at given immersion time

Rearranging Equation (A2/5) gives

$$nA = \ell/kR_{pf} \quad \text{(A2/6)}$$

Substituting Equations (A2/1) and (A2/4) into (A2/6) gives

$$nA = \ell/\{[R^{o}_{pf}(C/C_o)^{m}]\,(k_o C)\}$$

$$= \ell/\{[R^{o}_{pf}\, k_o\, C_o^{-(1+m)}]\}C^{-(1+m)} \qquad \text{(A2/7)}$$

Equation (A2/7) predicts that nA will increase as concentration decreases only if $m > -1$. This condition is met because $m = -0.3$ for the 0.5-1.5 hour line in Figure R2/3.

Conclude: For the data presented in Figure R2/3, and making the assumptions discussed above, the total summed pathway area, nA, will increase as chloride ion concentration of the measurement solution decreases.

1. Impedance equations for depressed Nyquist semicircles

Aim: To derive from the general impedance equation of Equation (T1/1), Section T1/4, for an unpainted metal, equations that take into account depressed Nyquist semicircles caused by frequency dispersion.

Derivation: The general impedance equation of Equation (T1/1), Section T1/4 for an unpainted metal and represented by the equivalent circuit of Figure T1/2 can be rearranged to the form of Equation (A3/1).

$$Z = R_s + R_t/(1 + j\omega R_t C_d) \qquad (A3/1)$$

Following the idea of Kendig et al[26], the occurrence of a depressed semicircle requires replacing the frequency dependent term, $j\omega R_t C_d$ in Equation (A3/1) by the frequency dependent term $(j\omega R_t C_d)^{\beta}$ to give Equation (A3/2).

$$Z = R_s + R_t/[1 + (j\omega\tau)^{\beta}] \qquad (A3/2)$$

where $\tau = R_t C_d$

This approach fits experimental data to semicircles with centres below the a-axis to give solution resistance, R_s, and charge-transfer resistance, R_t, without requiring a physical model that explains the depressed semicircle[26]. Equation (A3/2) can be expressed in the form Z = a-jb to give Equations (A3/3) and (A3/4).

$$a = R_s + \frac{R_t\,[1 + (\omega\tau)^{\beta}\cos(\pi\beta/2)]}{[1 + (\omega\tau)^{\beta}\cos(\pi\beta/2)]^2 + (\omega\tau)^{2\beta}\sin^2(\pi\beta/2)} \qquad \text{(A3/3)}$$

$$b = \frac{R_t(\omega\tau)^{\beta}\sin(\pi\beta/2)}{[1 + (\omega\tau)^{\beta}\cos(\pi\beta/2)]^2 + (\omega\tau)^{2\beta}\sin^2(\pi\beta/2)} \qquad \text{(A3/4)}$$

Eliminating the ω from Equations (A3/3) and (A3/4) gives Equation (A3/5).

$$[a - R_s - R_t/2]^2 + [b + R_t/2\tan(\pi\beta/2)]^2 = [R_t/2\sin(\pi\beta/2)]^2 \qquad \text{(A3/5)}$$

This is the equation of a circle with centre at the point $[R_s + R_t/2, -R_t/2\tan(\pi\beta/2)]$ and diameter $R_t/\sin(\pi\beta/2)$, as shown in Figure A3/1. The point at which the semicircle cuts the a-axis can be found by setting b=0 in Equation (A3/5), giving Equation (A3/6).

$$[a - R_s - R_t/2]^2 = R_t^2/[4\tan^2(\pi\beta/2)] - R_t^2/[4\tan(\pi\beta/2)] \qquad \text{(A3/6)}$$

On rearrangement, this gives Equation (A3/7)

$$[a - R_s - R_t/2]^2 = [R_t/2]^2$$
$$a = R_s + R_t \qquad \text{(A3/7)}$$

Thus R_t is the chord of the semicircle on the a-axis instead of the diameter of the depressed semicircle. The angle of depression, α, is given in Figure A3/1.

The same procedure can be used for the more complicated painted metal equivalent circuit of Figure T1/4. The principle here is to split up the

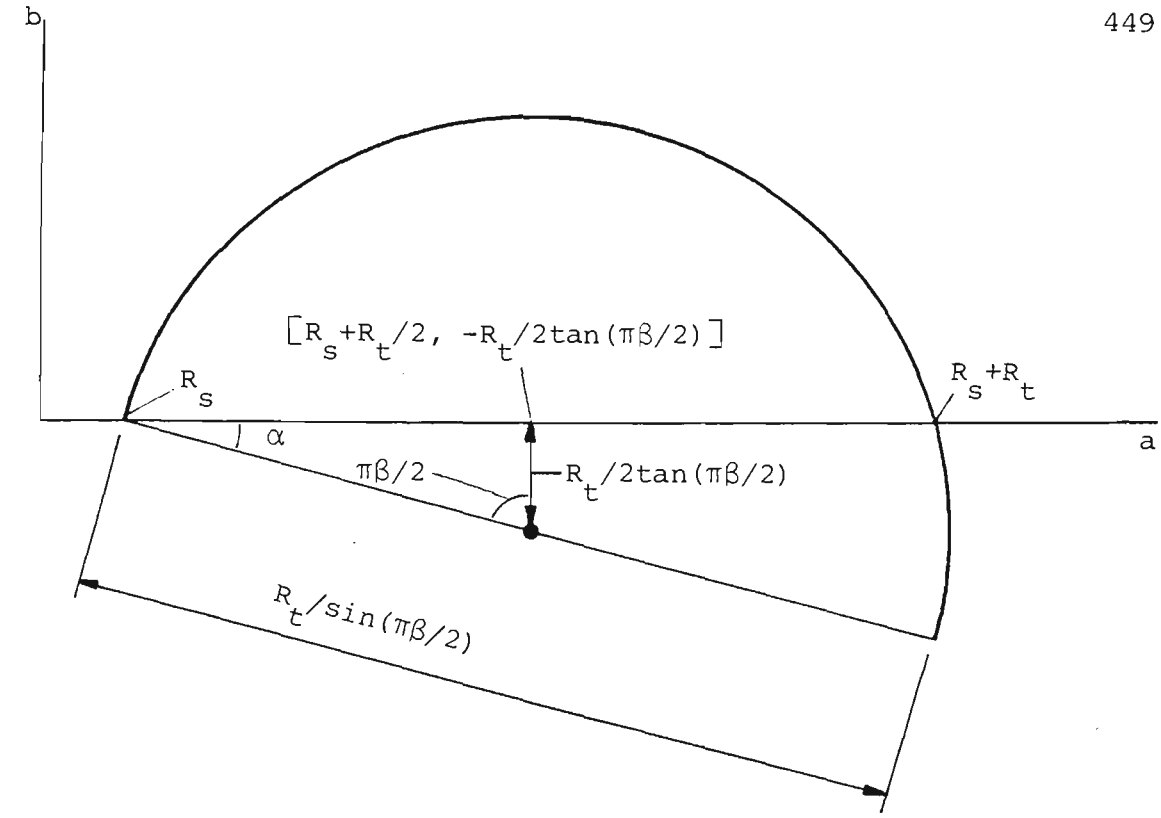

Figure A3/1. Nyquist plot of resistive, a, versus reactive, b, components of impedance for an unpainted metal showing a depressed semicircle caused by frequency dispersion. R_s solution resistance; R_t charge-transfer resistance; α [$=\pi/2(1-\beta)$] angle of depression.

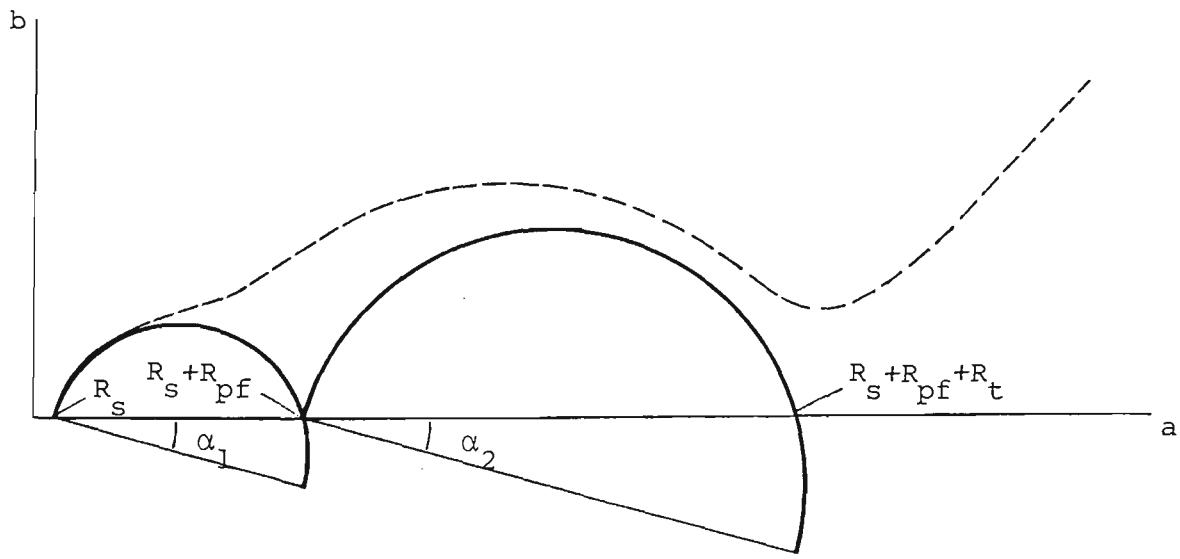

Figure A3/2. Nyquist plot for a painted metal showing depressed semicircles for metal and paint film caused by frequency dispersion. The chord of the paint film, metal semicircles is given by R_{pf}, R_t respectively. R_{pf} paint film resistance; α_1, α_2 angle of depression of paint film, metal semicircle, respectively; other symbols as per Figure A3/1.

frequency range into high, middle and low regions. In the high region, if $\tau_1 (=R_{pf}.C_{pf}) \ll \tau_2 (=R_t.C_d)$ is true, then there will be a region on the high frequency semicircle where the impedance contributions from the metal substrate semicircle (due to τ_2) will be negligible. The impedance within this region then becomes equivalent to that for the paint film (due to τ_1). The high frequency semicircle can be derived from this region of the impedance curve as an asymptote to the curve. This gives rise to a depressed semicircle with an angle of depression, α_1, and the chord of the semicircle equal to R_{pf}, as shown diagramatically in Figure A3/2. In the middle frequency region, if $\tau_1 \ll \tau_2$ and terms in $\omega^{-1/2}$ can be ignored, there will be a region on the impedance curve where the impedance contributions from the first, high frequency semicircle will be negligible, and contributions from the diffusion impedance can also be neglected. The second semicircle due to the metal substrate can be derived from this region of the impedance curve as an asymptote to the curve. This gives rise to a second depressed semicircle with an angle of depression, α_2, and the chord of the semicircle equal to R_t, as shown in Figure A3/2. At much lower frequencies, the substrate and paint film impedance contributions become negligible and the diffusion impedance (terms in $\omega^{-1/2}$) predominates.

2. Cell impedance corrections for identical working, auxiliary electrodes

Aim: To derive corrections for the cell impedance parameters (charge-transfer resistance, R_t, double layer capacitance, C_d, diffusion coefficient, σ) where the cell impedance consists of identical working and auxiliary electrodes. This is the case for impedance measurements on ACMs in Section R1.5. Refer also to Section T1/6.

Derivation: Figure A3/3a depicts an equivalent electrical circuit for one block (-AWRWA-) of a 3-electrode ACM used for impedance measurements. The working plates are wired together and connected to the working electrode input, W, of the potentiostat. Likewise, all auxiliary plates are connected to the auxiliary electrode input, A. Although the reference plates are connected together within the ACM, no connection, n/c, is made to the reference electrode input, R, of the potentiostat. When a thin water film is applied to the ACM surface, interfacial impedance will exist between one ACM plate and the next, except where two auxiliary plates are joined together. These interfacial impedances are represented for simplicity in Figure A3/3a as parallel combinations of R_t and C_d in series with solution resistance, R_s, although in actual fact these impedances will include the Warburg diffusion impedance, Z_ω, as described in Section T1/5.2 and Figure T1/4.

The diagram in Figure A3/3a can be simplified to that in Figure A3/3b for the working to auxiliary interfacial impedance of 1 block of the ACM. Here a_W, a_A are the exposed areas of an individual working, auxiliary plate, respectively. For n working electrode plates in the ACM, the total exposed working electrode is $A_W = na_W$. Areas of working, reference and auxiliary plates are given in Table E2/1, Section E2.4/3. For example, A_W for ACM3 (Zn) is 5.4 cm^2. Figure A3/3b shows two interfacial impedances between working and auxiliary lead out wires for two working and auxiliary ACM plates. Each half block is composed of two parallel R_t,C_d combinations for the interfacial impedance between one working plate and its adjacent auxiliary plate, separated by the solution resistance, R_s, of the water film.

The impedance, Z, of each half block can be derived as follows.

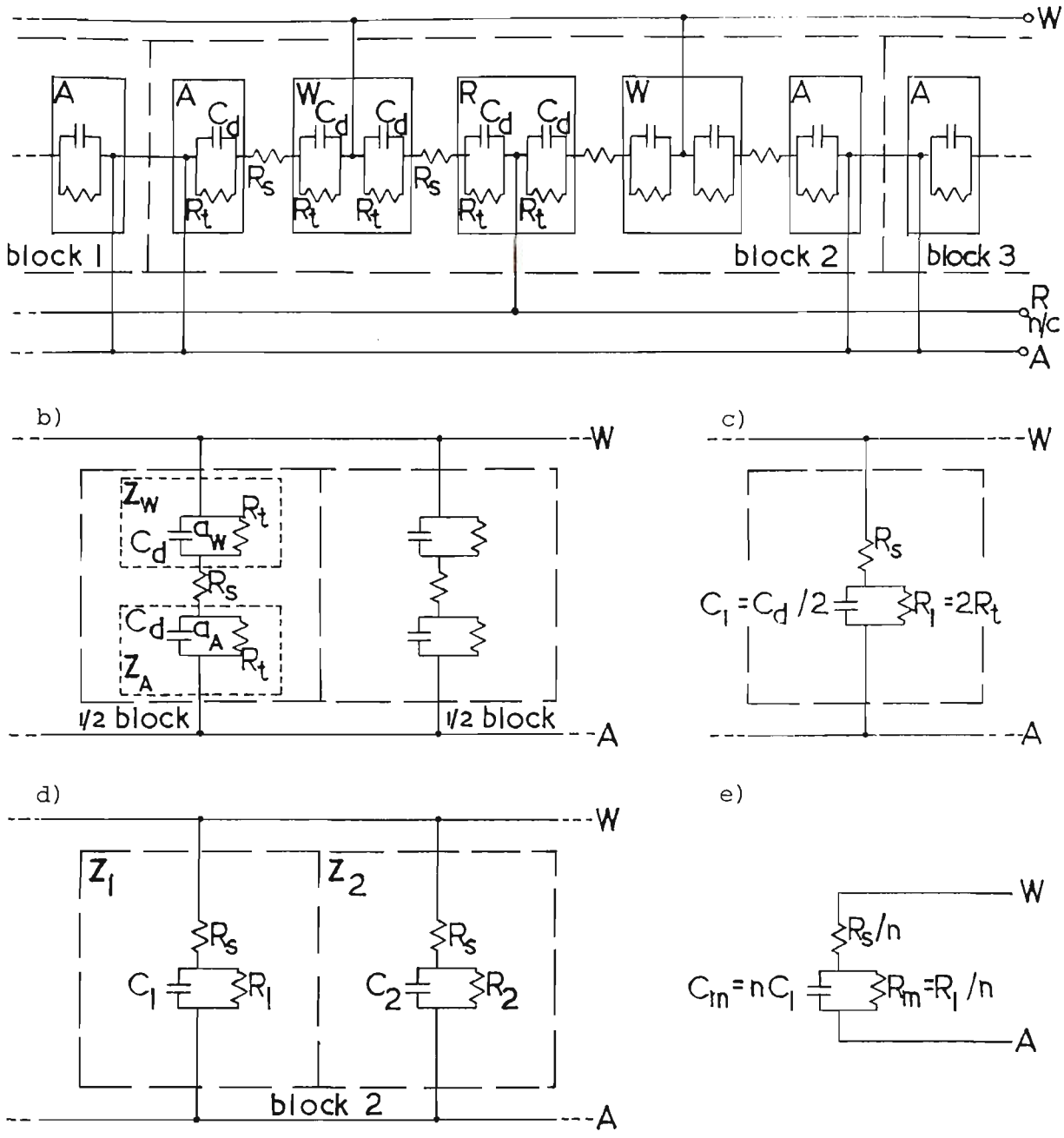

Figure A3/3. Various equivalent circuit models for a 3-electrode ACM used for impedance measurements. a) one block (-AWRWA-) with all W, all A, and all R plates separately wired together (no connection, n/c, is made to R plates for impedance tests); b) simplified version of a) for 1 W/A block shown as 2 half blocks; c) simplified version of b) for 1 half block; d) simplified version of b) using c); e) total impedance of circuit in a) represented by n W/A blocks. W,R,A working, auxiliary, reference plates and output terminals to a potentiostat; interfacial impedances for each plate R_t, C_d, R_s charge-transfer resistance, double layer capacitance, solution resistance; a_W, a_A exposed area for 1 working, auxiliary plate; Z_1, C_1, R_1 impedances for a half block; R_m, C_m, R_s/n measured R_t, C_d and R_s for n blocks in ACM.

$$Z = Z_W + R_s + Z_A \qquad \text{(A3/8)}$$

$$= (R_t jX)/(R_t+jX) + R_s + (R_t jX)/(R_t+jX)$$

where $X = -1/2\pi f C_d$ and is the reactance of capacitance, C_d,

j = imaginary number equal to $\sqrt{-1}$

Simplifying gives Equation (A3/9)

$$Z = R_s + (2R_t jX)/(R_t+jX) \qquad \text{(A3/9)}$$

$$= R_s + [j(2R_t)(2X)]/[(2R_t) + j(2X)]$$

$$= R_s + (jR_m X_m)/(R_m+jX_m) \qquad \text{(A3/10)}$$

where $R_1 = 2R_t \qquad \therefore R_t = R_1/2 \qquad \text{(A3/11)}$

$X_1 = 2X \qquad \therefore X = X_1/2$

$= -1/2\pi f C_1 \qquad$ or $C_d = 2C_1 \qquad \text{(A3/12)}$

Equations (A3/11-12) indicate that Figure A3/3c is equivalent to a half block in Figure A3/3b, so that the equivalent circuit of Figure A3/3b for one block reduces to Figure A3/3d. The impedance of Figure A3/3d can be derived as followed.

$$Z = Z_1 Z_2/(Z_1 + Z_2) \qquad \text{(A3/13)}$$

$$= Z_1/2 \qquad \text{(because } Z_1 = Z_2\text{)}$$

Total impedance of n such working/auxiliary blocks is given by Equation (A3/14).

$$Z = Z_1/n \qquad \text{(A3/14)}$$

$$= 1/n\,[R_s + (R_1 jX_1)]/[R_1+jX_1]$$

$$= R_s/n + [(R_1/n).j(X_1/n)]/[(R_1/n) + j(X_1/n)]$$

$$= R_s^m + (R_m.jX_m)/(R_m + jX_m) \quad (A3/15)$$

where m = measured value

$$R_s^m = R_s/n \qquad \therefore R_s = nR_s^m \quad (A3/16)$$

$$R_m = R_l/n \qquad \therefore R_l = nR_m \quad (A3/17)$$

$$X_m = X_l/n = 1/n\,(2\pi f C_l)$$

$$C_m = nC_l \qquad \therefore C_l = C_m/n \quad (A3/18)$$

Substituting Equations (A3/11-12) into (A3/17-18) gives Equations (A3/19-20)

$$R_t = nR_m/2 \quad (A3/19)$$

$$C_d = 2\,C_m/n \quad (A3/20)$$

Equations (A3/16), (A3/19-20) give the interfacial impedance parameter for one working plate of the ACM. These equations can readily be converted to unit area to give Equations (A3/21-23).

$$R_t\,(ohm.cm^2) = na_W R_m/2 = R_m A_W/2 = R_t^m A_W/2 \quad (A3/21)$$

$$C_d\,(F.cm^{-2}) = 2\,C_m/na_W = 2C_m/A_W = 2C_d^m/A_W \quad (A3/22)$$

$$R_s\,(ohm.cm^2) = na_W R_s^m = R_s^m A_W \quad (A3/23)$$

In these equations, R_m, C_m are shortened versions of R_t^m, C_d^n indicating measured values of charge-transfer resistance, double-layer capacitance for the ACM as obtained from Nyquist or Bode plots.

This theory can be extended to include a correction for the measured value of the Warburg diffusion coefficient, σ^m, where $\sigma = \sigma^m.A_W/2$ and m indicates measured value. This has been applied to correct measured σ^m values obtained from Nyquist plots in Section R1.5/3.

1. Glossary of terms

1.1 General Linear Model (GLM) The general linear model procedure performs a multiple regression on a chosen subset of the variables; attempts to fit a linear model equation to the data, for example, Equation (A4/1); gives Pearson's correlation coefficients for all variables and calculates a multiple correlation coefficient, R^2.

$$y = A + Bx_1 + Cx_2 + Dx_3 \qquad (A4/1)$$

1.2 Multiple correlation coefficient, R^2 is the proportion of the total variance explained by the model, and is a measure of the goodness of fit of the model equation to the data set.

1.3 Pearson's correlation coefficient, r The Pearson's correlation coefficient, r, (also known as the Product-Moment correlation coefficient) is given by Equation (A4/2).

$$r = [\sum(x-x)(y-y)]/[\sqrt{\sum(x-x)^2.\sum y-y)^2}] \qquad (A4/2)$$

where r = correlation coefficient between two variables x and y

x,y = mean values of x and y data sets, respectively.

Noting that $S_{xy} = [\sum(x-x)(y-y)]/N$, $S_x = \sqrt{[\sum(x-x)^2/N]}$, $S_y = \sqrt{[\sum(y-y)^2/N]}$ then Equation (A4/2) can be rewritten as Equation (A4/3).

$$r = S_{xy}/S_xS_y \qquad (A4/3)$$

where S_{xy} = covariance of variables x and y

S_x, S_y = standard deviations of variables x and y, respectively.

Values of r lie between -1 and +1. The signs, + and -, are used to indicate a positive and negative correlation, respectively. The quantity r is a dimensionless quantity, and is used to indicate the degree of correlation between variables x and y.

The calculated values of r can be compared to standard tables of r to indicate whether the correlation between x and y is significant. There are various levels of confidence, typically 90, 95 and 99%, and tabulated r values are given for a range of sample size, n, in the data set. Some tables give r values versus the number of degrees of freedom, f, in the data set, rather than versus n. If the absolute value of calculated r is equal to or greater than the tabulated r value, the correlation between x and y is said to be significant at the particular level of significance, otherwise the correlation is not significant. If a correlation is not significant at the 90% level of confidence it is either too scattered or the data set sample size, n, is too small.

A tabulated r value is quoted at a particular level of confidence and for a number of degrees of freedom, f. For example, $[r_{.05}]_{19}$ indicates the tabulated correlation coefficient at the 95% level of confidence for 19 degrees of freedom, where 0.05 is the probability of observing a value of r greater than or equal to $[r_{.05}]_{19}$ if the true value of r in the sample population is zero.

1.4 Degrees of freedom, f The number of degrees of freedom, f, of a statistic is the number, n, of independent observations in the sample (ie the sample size) minus the number, k, of population parameters which must be estimated from sample observations, where f = n-k. For simple cases, k is 2.

An example of the use of f is in looking up tabulated values of correlation coefficient, r, based on degrees of freedom.

1.5 Maximum effect of independent variables on dependent variable. To determine the maximum change in the dependent variable, y, due to changes in an independent variable, x, the sample range (= maximum value - minimum value) of the relevant independent variable, x, is multiplied by its regression coefficient of the linear model equation. This is employed when actual values of the independent variable are pre-chosen. For example, if the linear model is Equation (A4/1), then for max x_1, = 85, min x_1 = 25, then the maximum effect of x_1 on y is 508. Similar values calculated to find the maximum effect of other independent variables x2, x3 on y can be determined and the relative effect of x1, x2, x3 on y can be compared.

1.6 Confidence limits. The 99% confidence limits for a parameter estimate, A, in the linear model Equation (A4/1) are $A \pm C_b\sigma$ where C_b(=2.576) is the two-tailed 99% confidence band for a normal distribution and σ is the standard error of estimate.

1.7 Standard error of estimate, σ. The standard error of estimate of y on x, $S_{y.x}$, is a measure of the scatter in y values about the regression line of y as a function of x, and is defined by Equation (A4/4).

$$S_{y.x} = \sqrt{[\Sigma(y-y_{est})^2/N]} \qquad (A4/4)$$

where y_{est} = value of y for given values of x from the regression equation, eg Equation (A4/1).

The standard error of estimate has properties analogous to those of the standard deviation.

1.8 Student's t value is a measure of how many standard deviations the parameter (ie the regression coefficient) is away from zero. Because all t values are in standard measure, they can be directly compared for different regression coefficients. The t value essentially determines whether the effect of an independent variable is significant by testing to see if its regression coefficient is sufficiently different from zero. The Student t value for a regression coefficient is the value of the coefficient in standard measure, that is, the regression coefficient divided by its standard error. For example, a t value of 13.73 would indicate a very low probability of observing a t value this high if the true regression coefficient is zero. A t value of 0.34 would indicate a very high probability that the regression coefficient is zero.

1.9 Probability, p is the probability of calculating regression coefficients of the observed size if the true coefficent is zero. For example, a probability of 0.82 means that there is a high chance (82%) that the associated regression coefficient is zero, whereas a probability of 0.01 means that there is a low chance (1%) that the associated regression coefficient is zero.

1.10 Standard deviation, s is a measure of the spread or scatter in the data set, and is defined by Equation (A4/5)

$$s = \sqrt{[\sum (x_i - x)^2/(n-1)]} \qquad \text{(A4/5)}$$

where s = standard deviation

x_i = individual value of x

$(x_i - x)$ = deviation of x_i from the mean value, x

1.11 Partial correlation coefficient. It is often important to measure the correlation between a dependent variable and one particular independent variable when all other variables involved are kept constant, that is, the effects of all other variables are removed. This can be obtained from the partial correlation coefficient, defined by Equation (A4/6).

$$[r_{12}]_3 = (r_{12} - r_{13}\, r_{23})/\sqrt{[(1-r_{13}^2)(1-r_{23}^2)]} \qquad \text{(A4/6)}$$

where $[r_{12}]_3$ = partial correlation coefficient between variables 1 and 2, keeping variable 3 constant

r_{13}, r_{23}, r_{12} = correlation coefficients between variables 1 and 3, 2 and 3, 1 and 2, respectively.

1.12 Least squares linear regression. The linear model equation referred to in Section A4/1.1 is an equation for estimating a dependent variable, y, from other independent variables x_1, x_2, x_3 ..., and is called a regression equation of y on x_1, x_2, x_3 ... . In functional notation this can be written as $y = F(x_1, x_2, x_3 \ldots)$ to mean that y is a function of x_1, x_2, x_3 ... .

For a simple case of one dependent variable, y, and one independent variable, x, the least squares linear regression line that best fits through the set of points (x_1, y_1), (x_2, y_2) ... (x_n, y_n) has the form of Equation (A4/7).

$$y = A + Bx \qquad \text{(A4/7)}$$

The intercept, A, and slope, B, of the line y versus x are determined by, from Equations (A4/8), (A4/9), respectively.

$$A = \frac{(\Sigma y)(\Sigma x^2) - (\Sigma x)(\Sigma xy)}{n\,\Sigma x^2 - (\Sigma x)^2} \qquad (A4/8)$$

$$B = \frac{n\Sigma xy - (\Sigma x)(\Sigma y)}{n\Sigma x^2 - (\Sigma x)^2} \qquad (A4/9)$$

Linear regression lines for the above simple 2 variable (x and y) case were calculated using a Hewlett-Packard Model HP-15C calculator.

For the more complicated case of one dependent variable, y, and two independent variables, x_1 and x_2, the least squares linear regression equation has the form of Equation (A4/10).

$$y = A + Bx_1 + Cx_2 \qquad (A4/10)$$

If x_2 is held constant, then the graph of y versus x_1 is a straight line of slope B. If x_1 is held constant, then the graph of y versus x is a straight line of slope C. The constants B and C are called partial regression coefficients of y on x_1 keeping x_2 constant, and of y on x_2 keeping x_1 constant, respectively. Multiple regression equations of the form of Equations (A4/1) and (A4/10) were calculated using the General Linear Model, GLM, module of the Statistical Analysis System, SAS, statistical software package.

2. Unpainted metals

2.1 Weighed mass loss versus $[SO_2]$ (Section R1.3)

Table A4/1 Steel Abraded #600 Grade

PGB run	Nx area[1] (total area) (mm^2)	water[2] (mL)	mass loss ($g.m^{-2}$) at $[SO_2]$ (ppm) 0	0.03	0.05	0.1	0.2	0.4	0.5	0.6	0.8	1.0
113	4x750	0.375	2.53			18.80	23.3					
114	(3000)		1.07					36.4		37.90		
115			2.27								48.90	66.80
116			4.40				23.9				46.10	
118	2x750	0.375	2.27		14.5							
119	1x1500	0.75	1.73			16.67						
120	(3000)		5.87				24.93					
121			2.93					24.40				
122			4.27							40.67		
123			4.00								55.33	
124												50.13
125			3.33		19.6							
126			3.47			28.67						
127			4.80	22.13								
128			4.53		19.2							
129			3.60			17.30						
130			4.53				26.13					
131			2.67						40.27			
138			0.67									53.07
139			1.73								37.20	

Notes:

1 Nxarea number of samples, N, of exposed area as given; (total area) total exposed sample area per test chamber (=Nxarea)

2 water volume of water per sample

3 N number of samples
r Pearson's correlation coefficient
$[r_p]_f$ tabular correlation coefficient for f degrees of freedom (f=N-2) at (1-p)x100% level of confidence, eg $[r_{.01}]_4$ correlation coefficient for 6 samples at 99% level of confidence
A,B intercept, slope respectively for linear regression equation y = A+Bx where y is mass loss and x is $[SO_2]$

statistics[3]:

N	r	$[r_{.01}]_{41}$	A	B
43	0.94	0.389	7.68	52.12

A significant correlation exists at the 99% level of confidence between mass loss of steel and $[SO_2]$. The linear regression equation is

$$\text{mass loss} = 7.68 + 52.12\,[SO_2] \qquad \text{(A4/11)}$$

Table A4/2 Steel Abraded #600 Grade

PGB run	Nx area[1] (total area) (mm^2)	water[2] (mL)	mass loss ($g.m^{-2}$) at $[SO_2]$ (ppm) 0	0.03	0.05	0.1	0.2	0.4	0.5	0.6	0.8	1.0
145	4x338	0.17	2.66				15.09					
146	(1352)		0.89									30.42
147			0.59						20.68			

Notes:

1, 2, 3 see notes in Table A4/1.

statistics[3]:	N	r	$[r_{.01}]_4$	A	B
	6	0.96	0.917	3.36	29.51

A significant correlation exists at the 99% level of confidence between mass loss of steel and $[SO_2]$. The linear regression equation is

$$\text{mass loss} = 3.36 + 29.51\,[SO_2] \qquad \text{(A4/12)}$$

Table A4/3 Zinc Abraded $600 Grade

PGB run	Nx area[1] (total area) (mm^2)	water[2] (mL)	mass loss ($g.m^{-2}$) at $[SO_2]$ (ppm) 0	0.03	0.05	0.1	0.2	0.4	0.5	0.6	0.8	1.0
118	2x750	0.375	12.1		12.5							
119	1x1500	0.75	3.07			11.87						
120	(3000)		9.20				7.20					
121			7.60					8.27				
122			9.20							11.33		
123			10.0								13.30	
124												9.60
125			7.73		9.47							
126			7.87			11.33						
127			8.53	13.47								
128			9.60		8.93							

Notes:

1, 2, 3 see notes in Table A4/1.

statistics[3]:	N	r	$[r_{.1}]_{19}$	A	B
	21	0.25	0.369	9.29	2.09

A significant correlation does NOT exist even at the 90% level of confidence between mass loss of zinc and $[SO_2]$. The linear regression equation is

$$\text{mass loss} = 9.29 + 2.09\,[SO_2] \qquad \text{(A4/13)}$$

Table A4/4 Zinc Abraded #600 Grade

PGB run	Nx area[1] (total area) (mm^2)	water[2] (mL)	mass loss ($g.m^{-2}$) at $[SO_2]$ (ppm) 0	0.03	0.05	0.1	0.2	0.4	0.5	0.6	0.8	1.0
145	4x338	0.17	3.85				2.66					
146	(1352)		3.54									3.84
147			2.36						2.95			
200									3.54			
									3.84			
									4.43			
									3.54			
201							2.95					
							3.25					
							3.25					
							3.25					

Notes:
1, 2, 3 see notes in Table A4/1.

statistics[3]:	N	r	$[r_{.1}]_{12}$	A	B
	14	0.45	0.458	3.09	0.87

A significant correlation does NOT exist even at the 90% level of confidence between mass loss of zinc and $[SO_2]$. The linear regression equation is

$$\text{mass loss} = 3.09 + 0.87\,[SO_2] \qquad \text{(A4/14)}$$

Table A4/5 Cast Zn-55%Al Alloy Abraded #600 Grade

PGB run	Nx area[1] (total area) (mm^2)	water[2] (mL)	mass loss ($g.m^{-2}$) at $[SO_2]$ (ppm) 0	0.03	0.05	0.1	0.2	0.4	0.5	0.6	0.8	1.0
118	1x1500	0.75	1.20		1.47							
119	2x750	0.375	0.00			0.87						
120	(3000)		0.00				0.80					
121			-0.73					0.60				
122			1.00							0.80		
123			0.20								1.53	
124												0.73
125			-0.13		0.33							
126			1.20			1.53						
127			0.27	0.07								
128			0.60		0.67							

Notes:
1, 2, 3 see notes in Table A4/1.

statistics[3]:	N	r	$[r_{.1}]_{19}$	A	B
	21	0.32	0.369	0.51	0.66

A significant correlation does NOT exist even at the 90% level of confidence between mass loss of cast Zn-55%Al alloy and $[SO_2]$. The linear regression equation is

$$\text{mass loss} = 0.51 + 0.66\,[SO_2] \qquad \text{(A4/15)}$$

Table A4/6 Rolled Zn-55%Al Alloy Abraded #600 Grade

PGB run	Nx area[1] (total area) (mm^2)	water[2] (mL)	mass loss ($g.m^{-2}$) at $[SO_2]$ (ppm) 0	0.03	0.05	0.1	0.2	0.4	0.5	0.6	0.8	1.0
145	4x338	0.17	1.48				2.96					
146	(1352)		0.59									3.54
147			0.59						2.95			

Notes:

1, 2, 3 see notes in Table A4/1.

statistics[3]:	N	r	$[r_{.05}]_4$	A	B
	6	0.83	0.811	1.26	2.69

A significant correlation exists at the 95% level of confidence between mass loss of rolled Zn-55%Al alloy and $[SO_2]$. The linear regression equation is

$$\text{mass loss} = 1.26 + 2.69\,[SO_2] \qquad \text{(A4/16)}$$

Table A4/7 Aluminium Abraded #600 Grade

PGB run	Nx area[1] (total area) (mm^2)	water[2] (mL)	mass loss ($g.m^{-2}$) at $[SO_2]$ (ppm) 0	0.03	0.05	0.1	0.2	0.4	0.5	0.6	0.8	1.0
145	4x338	0.17	0.89				0.89					
146	(1352)		0.30									0.59
147			0.59						0.89			

Notes:

1, 2, 3 see notes in Table A4/1.

statistics[3]:	N	r	$[r_{.1}]_4$	A	B
	6	0.08	0.811	0.72	0.71

A significant correlation does NOT exist even at the 90% level of confidence between mass loss of aluminium and $[SO_2]$. The linear regression equation is

$$\text{mass loss} = 0.72 + 0.71\,[SO_2] \qquad \text{(A4/17)}$$

Table A4/8 Unpassivated ZINCALUME

PGB run	Nx area[1] (total area) (mm^2)	water[2] (mL)	mass loss ($g.m^{-2}$) at $[SO_2]$ (ppm) 0	0.03	0.05	0.1	0.2	0.4	0.5	0.6	0.8	1.0
129	2x750	0.375	0.53			1.73						
130	1x1500	0.75	0.67				2.27					
131	(3000)		0.53						1.73			
138			0.93									2.4
139			2.67								3.47	

Notes:

1, 2, 3 see notes in Table A4/1.

statistics[3]:	N	r	$[r_{.05}]_8$	A	B
	10	0.65	0.632	1.23	1.80

A significant correlation exists at the 95% level of confidence between mass loss of unpassivated ZINCALUME and $[SO_2]$. The linear regression equation is

$$\text{mass loss} = 1.23 + 1.80\,[SO_2] \qquad \text{(A4/18)}$$

Table A4/9 Passivated ZINCALUME

PGB run	Nx area[1] (total area) (mm^2)	water[2] (mL)	mass loss ($g.m^{-2}$) at $[SO_2]$ (ppm) 0	0.03	0.05	0.1	0.2	0.4	0.5	0.6	0.8	1.0
113	4x750	0.375	0.67			0.67	0.53					
114	(3000)		0.00					0.53		0.67		
115			1.33								1.47	1.73
116			1.07				1.07				0.40	

Notes:

1, 2, 3 see notes in Table A4/1.

statistics[3]:	N	r	$[r_{.1}]_{10}$	A	B
	12	0.38	0.497	0.67	0.51

A significant correlation does NOT exist even at the 90% level of confidence between mass loss of passivated ZINCALUME and $[SO_2]$. The linear regression equation is

$$\text{mass loss} = 0.67 + 0.51\,[SO_2] \qquad \text{(A4/19)}$$

Table A4/10 Unpassivated Galvanized

PGB run	Nx area[1] (total area) (mm^2)	water[2] (mL)	mass loss ($g.m^{-2}$) at $[SO_2]$ (ppm) 0	0.03	0.05	0.1	0.2	0.4	0.5	0.6	0.8	1.0
129	2x750	0.375	11.07			12.8						
130	1x1500	0.75	11.20				10.40					
131	(3000)		12.00						13.07			
138			10.40									8.53
139			9.53								10.67	

Notes:

1, 2, 3 see notes in Table A4/1.

statistics[3]:	N	r	$[r_{.1}]_8$	A	B
	10	-0.33	0.549	11.29	-1.27

A significant correlation does NOT exist even at the 90% level of confidence between mass loss of unpassivated galvanized and $[SO_2]$. The linear regression equation is

$$\text{mass loss} = 11.29 - 1.27\,[SO_2] \qquad \text{(A4/20)}$$

Table A4/11 passivated Galvanized

PGB run	Nx area[1] (total area) (mm^2)	water[2] (mL)	mass loss ($g.m^{-2}$) at $[SO_2]$ (ppm) 0	0.03	0.05	0.1	0.2	0.4	0.5	0.6	0.8	1.0
113	4x750	0.375	0.40			1.33	1.60					
114	(3000)		0.27					2.4		2.53		
115			0.80								6.00	8.27
116			2.53				2.00				3.20	

Notes:

1, 2, 3 see notes in Table A4/1.

statistics[3]:	N	r	$[r_{.01}]_{10}$	A	B
	12	0.91	0.708	0.39	6.00

A significant correlation exists at the 99% level of confidence between mass loss of passivated galvanized and $[SO_2]$. The linear regression equation is

$$\text{mass loss} = 0.39 + 6.00\,[SO_2] \qquad \text{(A4/21)}$$

2.2 ACM 2-electrode type mass loss vs $[SO_2]$ (Section R1.4)

Table A4/12 ACM1 Cast Zn-55%Al/Fe 4-Cycle Distilled Water PGB Tests

PGB run	A[5] (mm^2)	V[1] (mL)	ACM anode area (mm^2)	$[SO_2]$ (ppm)	q = area under Ig/t curve (C) cycle 1	cycle 2	cycle 3	cycle 4	∑q	mass[2] loss ($g.m^{-2}$)	red[3] rust (%)
118	1600	0.8	1270	0.05	1.19	0.75	0.57	1.11	3.62	4.23	
119				0.1	1.33	0.86	1.23	0.74	4.16	4.86	
120				0.2	1.01	0.60	0.77	0.48	2.86	3.34	
121				0.4	1.38	0.60	0.33	0.45	2.76	3.22	
122				0.6	1.49	0.51	0.21	0.16	2.37	2.77	
123				0.8	1.70	0.30	0.20	0.20	2.40	2.80	
124				1.0	0.94	0.26	0.20	0.21	1.61	1.88	
125				0.05	0.58	0.67	0.70	0.49	2.44	2.85	
126				0.1	1.20	1.39	0.73	1.14	4.46	5.21	
127				0.03	1.02	1.30	0.83	0.97	4.12	4.81	
128				0.05	0.91	1.31	1.17	0.81	4.20	4.91	
160				0	1.53	0.98	0.76	0.70	3.97	4.64	
161				0.5	1.23	1.07	0.90	0.68	3.88	4.53	
330				1.0	1.74	1.57	1.36	1.06	5.74	6.70	0.55
331				0.8	1.09	1.27	1.03	0.86	4.25	4.96	1.38
332				0.6	0.90	0.91	0.61	0.74	3.15	3.68	0.0
333				0.4	0.78	0.92	0.75	0.71	3.17	3.70	1.76
334				0.2	0.78	0.74	0.58	0.54	2.64	3.08	0.75
335				0.1	0.92	0.86	0.75	0.63	3.17	3.70	6.11
336				0.0	0.90	0.77	0.62	0.59	2.89	3.38	1.70
				∑q	22.62	16.50	14.3	13.27			

Notes:

1 V – water volume = quantity of water applied to ACM surface per cycle
2 mass loss – calculated, Sections R1.4/1, T2/4, using the electrochemical equivalent for Zn
3 red rust – percentage of red rust on steel plates of ACM
4 statistics symbols – see Note 3 in Table A4/1
5 A – exposed area

statistics[4]:	N	r	$[r_{.1}]_{18}$	A	B
	20	-0.08	0.378	4.05	-0.25

A significant negative correlation does NOT exist even at the 90% level of confidence between mass loss of cast Zn-55%Al alloy in ACM1 and $[SO_2]$. The linear regression equation is

$$\text{mass loss} = 4.05 - 0.25\,[SO_2] \qquad \text{(A4/22)}$$

Table A4/13 ACM2 Zn/Fe 4-Cycle Distilled Water PGB Tests

PGB run	A[5] (mm^2)	V[1] (mL)	ACM anode area (mm^2)	$[SO_2]$ (ppm)	q = area under Ig/t curve (C) cycle 1	cycle 2	cycle 3	cycle 4	$\sum q$	mass[2] loss ($g.m^{-2}$)	red[3] rust (%)
129	1590	0.80	7100	0.1	6.94	3.79	3.33	3.13	17.19	6.62	
130				0.2	8.67	5.62	5.21	4.80	24.30	9.35	
131				0.5	4.78	7.19	3.91	1.67	17.55	6.75	
138				1.0	4.79	0.78	0.59	0.68	6.84	2.63	
139				0.75	7.91	6.60	1.68	1.13	17.32	6.67	
140				0.5	6.61	8.64	1.37	1.12	17.74	6.83	
162				0.5	5.93	5.26	2.53	2.56	16.28	6.27	
163				0	3.34	4.59	3.90	2.90	14.73	5.67	
164				0	3.32	3.71	2.24	1.75	11.02	4.24	
				$\sum q$	52.29	46.18	24.76	19.74			

Notes:

1-5 see Notes in Table A4/12

3 slight red rust (less than 0.1% of steel area) occasionally seen after cycle with build-up of white corrosion products on steel plates

statistics[4]:	N	r	$[r_{.1}]_7$	A	B
	9	-0.31	0.582	6.78	-1.68

A significant correlation does NOT exist even at the 90% level of confidence between mass loss of Zn in ACM2 and $[SO_2]$. The linear regression equation is

$$\text{mass loss} = 6.78 - 1.68\,[SO_2] \qquad \text{(A4/23)}$$

Table A4/14 ACM9 Rolled Zn-55%Al/Fe 4-Cycle Distilled Water PGB Tests

PGB run	A[5] (mm^2)	V[1] (mL)	ACM anode area (mm^2)	$[SO_2]$ (ppm)	q = area under Ig/t curve (C) cycle 1	cycle 2	cycle 3	cycle 4	$\sum q$	mass[2] loss ($g.m^{-2}$)	red[3] rust (%)
236	1820	0.91	9200	0	3.83	3.21	2.20	2.32	11.56	5.84	32.8
238	1400	0.70	6800	0	2.03	1.77	1.55	1.62	6.97	3.52	28.4
240				0	1.95	1.72	1.17	1.47	6.31	3.19	28.9
242				0.1	2.02	1.04	1.59	1.65	6.30	3.18	15.0
245				0.1	1.60	1.16	0.734	1.07	4.56	2.31	13.9
248				0.05	1.27	1.19	1.20	1.29	4.95	2.50	21.8
249				0.05	1.71	0.936	0.724	1.04	4.41	2.23	17.9
251				0.2	1.60	0.962	0.445	0.665	3.67	1.86	4.3
253				0.2	1.50	0.994	0.864	0.992	4.35	2.20	9.0
255				0.5	2.78	2.16	3.04	2.97	10.95	5.54	1.1
257				0.5	2.63	1.98	2.14	1.67	8.42	4.26	1.8
259				1.0	2.83	2.56	1.34	1.03	7.76	3.92	0.5
261				1.0	3.76	3.29	1.68	1.41	10.14	5.13	1.9
263				0	1.71	0.925	0.753	0.805	4.19	2.12	12.4
265				0	1.33	0.771	0.858	0.803	3.76	1.90	12.1
278				0	1.64	1.89	1.49	0.710	5.73	2.90	7.0
291				0.4	4.75	3.46	2.68	2.37	13.26	6.70	0.8
293				0.4	4.06	2.75	1.90	1.83	10.54	5.33	2.0
295				0.2	2.89	1.75	2.14	1.73	8.51	4.30	17.1
296				0.2	3.04	1.87	2.25	1.95	9.11	4.61	6.7
297				0.2	2.83	1.65	2.18	1.78	8.44	4.27	17.9
298				0.1	1.99	1.15	3.05	1.09	7.28	3.68	22.8
299				0.1	2.20	1.30	2.88	1.29	7.67	3.88	11.9
300				0	1.20	0.637	0.444	0.490	2.77	1.40	11.4
301				0	1.36	0.662	0.412	0.411	2.85	1.44	2.0
302				0.5	3.74	3.13	1.99	1.89	10.75	5.43	0.3
303				0.5	3.29	2.42	1.72	1.50	8.93	4.51	1.9
304				1.0	2.97	2.07	1.31	1.25	7.6	3.84	0.7
				$\sum q$	68.51	49.41	44.72	39.10			

Notes:

1-5 see Notes in Table A4/12

statistics[4]:	N	r	$[r_{.01}]_{26}$	A	B
mass loss/$[SO_2]$	28	0.49	0.479	3.06	2.24
red rust/$[SO_2]$	28	-0.65	0.479	16.08	-19.99

A significant positive correlation exists at the 99% level of confidence between mass loss of rolled Zn-55%Al alloy in ACM9 and $[SO_2]$. The linear regression equation is

$$\text{mass loss} = 3.06 + 2.24\,[SO_2] \qquad \text{(A4/24)}$$

A significant negative correlation exists at the 99% level of confidence between % red rust on steel plates of ACM9 and $[SO_2]$. The linear regression equation is

$$\%\ \text{red rust} = 16.08 - 19.99\,[SO_2] \qquad \text{(A4/25)}$$

2.3 Corrosion Rate Control in ACMs (Section R1.6/8)

Table A4/15 Correlation Coefficients between $\log I_k$, $\log b_a$, $\log b_c$

source of data: Figures R1/31,33,34,36,38-45 Sections R1.6/3,5-7

	$\log I_k$ correlation coefficients, r, for		
	ACM3 (Zn)	ACM4 (RZA)[1]	ACM8 (Fe)
$\log b_a$	0.375	-0.566	-0.657
lob b_c	0.363	-0.354	-0.295
$\log R_p$	-0.502	-0.881	-0.966
N [2]	97	95	83
$[r_{.01}]_N$ [3]	0.262	0.265	0.283

Notes:

1 RZA rolled Zn-55%Al alloy
2 N number of samples
3 $[r_{.01}]_N$ tabular correlation coefficient for N samples at 99% level of confidence

All correlations are significant at the 99% level of confidence.
For all ACMs, a significant negative correlation exists between $\log I_k$ and $\log R_p$.
For ACM3 (Zn), significant positive correlations exist between $\log I_k$ and $\log b_a$, $\log b_c$.
For ACM4 (RZA), significant negative correlations exist between $\log I_k$ and $\log b_a$, $\log b_c$.
For ACM8 (Fe), a significant negative correlation exists between $\log I_k$ and $\log b_a$, $\log b_c$.
Correlations between $\log I_k$ and $\log R_p$ are better than correlations between $\log I_k$ and $\log b_a$ or $\log b_c$ for ACM4,8.

3. Painted metals

3.1 Water uptake by capacitance method on attached films

Pearson's correlation coefficients in Table A4/16 indicate that significant negative correlations exist between 2 h water uptake/log chloride and 2 h water uptake/primer thickness at the 99% level of confidence. No significant correlation exists between 2 h water uptake/gloss even at the 90% level of confidence. The strong correlation between independent variables log chloride/primer thickness and log chloride/gloss is an unfortunate bad experimental design by accident (no correlation should exist). This makes it difficult to resolve whether the correlation existing between 2 h water uptake/log chloride is real or simply due to a correlation between 2 h water uptake/primer thickness. Partial correlation coefficients can be calculated using Equation (A4/6) and the Pearson's correlation coefficients shown in Table A4/16.

$$[r\, X_v, Cl]pthk = \frac{-0.54 - (-0.59 \times 0.49)}{\sqrt{(1-0.59^2)(1-0.49^2)}} = -0.357 \qquad \text{(A4/26)}$$

$$[r\, X_v, pthk]Cl = \frac{-0.59 - (-0.54 \times 0.49)}{\sqrt{(1-0.54^2)(1-0.49^2)}} = -0.444 \qquad \text{(A4/27)}$$

where pthk = primer thickness

X_v = 2 h water uptake by capacitance method

Cl = log (solution chloride ion concentration)

tabulated $[r_{.05}]_{29}$ .432; $[r_{.01}]_{29}$ .522 (total of 3 variables)

Table A4/16 Correlation Coefficients

source: data from Table R2/1, Section R2.2/1.1.1

sample size 32

Pearson's correlation coefficients, r

2 h water uptake/gloss -0.214

2 h water uptake/log chloride -0.542

2 h water uptake/primer thickness -0.589

log chloride/primer thickness +0.487

log chloride/gloss +0.397

tabulated $[r_{.01}]_{30}$ .449; $[r_{.05}]_{30}$ .349; $[r_{.10}]_{30}$ .296 (2 variables)

R^2 0.473 (for Table A4/17).

Table A4/17 Dependent Variable: 2 h Water Uptake by Capacitance Method

parameter	range	regress coeff	99% conf limits	Student's t value	probability	std error of est	max effect on water uptake
intercept		7.53	±1.44	13.51	0.0001	0.558	
gloss	60	-0.012	±0.394	-1.47	0.153	0.008	0.72
log [Cl^-]	2.4843	-0.194	±0.551	-0.91	0.372	0.214	0.48
primer thick	3.0	-0.460	±0.384	-3.08	0.005	0.149	1.38

general linear model equation:

$$X_v = 7.53 - 0.012 \text{ gloss} - 0.194 \log [Cl^-] - 0.460 \text{ primer thickness} \quad \text{(A4/28)}$$

where X_v = 2 h water uptake (% v/v)

These calculations show that the partial negative correlation between 2 h water uptake and primer thickness is significant at the 95% level of confidence, but not the partial correlation betwen water uptake and log chloride. This indicates that, even allowing for the accidental correlation between log chloride/primer thickness, there is a significant negative correlation between water uptake and primer thickness (water uptake increases as primer thickness decreases), but that a correlation between water uptake/log chloride cannot be resolved.

The R^2 value in Table A4/16 indicates that only 47% of the total variance can be explained by the general linear model, as given by Equation (A4/28). The model is only a moderate fit to the data set. The 99% confidence limits for the regression coefficients are shown in column 4 of Table A4/17. It can be seen that the confidence limit for gloss and log chloride are substantially greater than their respective regression coefficient, of the same order for primer thickness and reasonably low for the intercept. Furthermore column 6 of Table A4/17 indicates that there is a 37.2% chance that the regression coefficient for water uptake/log chloride is zero, and 15.3% that the regression coefficient for water uptake/gloss is zero, which is also reflected in the low Student's t values for these parameters in column 5. Not much faith can be put in the general linear model Equation (A4/28) based on these conclusions.

As a further attempt to determine whether a correlation exists for 2 h water uptake/log [Cl^-] and 2 h water uptake/gloss, samples with primer thickness not equal to 2 µm were deleted from the 32 sample data set of Table R2/1, Section R2.2/1.1.1. This eliminated the effect of primer thickness. Statistical analysis indicated that there was now no significant correlations with water uptake, but only a nuisance correlation between log

chloride/gloss.

A further statistical analysis was run, using all the 32 sample data set once again, but eliminating gloss as a variable, ie all samples were treated as if they had the same gloss level. This was done to eliminate the nuisance correlation between log chloride/gloss, but the effect of gloss appears to be small in any case. The nuisance correlation between log chloride/primer thickness still existed. The results obtained appear below.

Table A4/18 Correlation Coefficients

source: data from Table R2/1, Section R2.2/1.1.1, with effect of gloss eliminated

sample size 32

Pearson's correlation coefficients, r

2 h water uptake/log chloride -0.542

2 h water uptake/primer thickness -0.589

log chloride/primer thickness +0.487

tabulated $[r_{.01}]_{30}$ .449;

R^2 0.432 (for Table A4/19).

Table A4/19 Dependent Variable: 2 h Water Uptake by Capacitance Method

parameter	range	regress coeff	99% conf limits	Student's t value	probability	std error of est	max effect on water uptake
intercept		7.24	±1.37	13.64	0.0001	0.531	
log $[Cl^-]$	2.4843	-0.374	±0.461	-2.09	0.045	0.179	0.93
primer thick	3.0	-0.355	±0.345	-2.65	0.013	0.134	1.07

general linear model equation:

$$X_v = 7.24 - 0.374 \log [Cl^-] - 0.355 \text{ primer thickness} \quad \text{(A4/29)}$$

where X_v = 2 h water uptake (% v/v)

The Pearson's correlation coefficients in Table A4/18 are unaltered compared to those in Table A4/16, so that the partial correlation coefficients will be calculated exactly the same as Equations (A4/26,27). The same conclusion will also apply, that is, even allowing for the accidental correlation between log chloride/primer thickness, there is a significant negative correlation between water uptake and primer thickness. The R^2 value of 0.432 still only indicates a moderate fit of the general linear model Equation (A4/29) to the data set. However, the Student's t values and probabilities in Table A4/19, columns 5 and 6, have substantially improved. There is now an acceptably low probability of 4.5 and 1.3% that the regression coefficients for water uptake/log chloride and water uptake/primer thickness are zero, respectively. The general linear model Equation (A4/29) is now more reliable as an indicator of the behaviour between water uptake, log chloride and primer thickness. However the nuisance correlation between log chloride/primer thickness still places some doubt on the use of this equation. It can be seen in column 4 of Table A4/19 that the 99% confidence limits for log chloride and primer thickness are of the same order as the regression coefficient itself, but that the intercept is somewhat more reliable. The two independent variables (log chloride, primer thickness) have about the same effect on the dependent variable, water uptake, as shown by column 8.

3.2 Sample failure times by capacitance method on attached films

Table A4/20 Pearson's correlation coefficients, r

source: data from Table R2/1, Section R2.2/1.1.1

sample size 31 (sample 32 failed prematurely, values not used)

parameter	log [Cl^-]	gloss	primer	$X_{v,2h}$
$t_{f,R}$	-.85	-.42	-.50	.72
$t_{f,C}$	-.97	-.40	-.54	.555
$\overline{t_f}$	-.94	-.42	-.54	.64
log [Cl^-]	1.00	.40	.49	-.54

tabulated $[r_{.01}]_{29}$ .456; $[r_{.05}]_{29}$ .355

R^2 values (for Table A4/21) for dependent variables as shown

$t_{f,R}$	0.716
$t_{f,C}$	0.943
$\overline{t_f}$	0.890

Tables A4/21 General Linear Model Results

parameter	range	regression coefficient	99% conf limits	Student's t value	probability	std error of estimate	max effect on dependent variable
dependent variable: sample fail time, $t_{f,R}$							
intercept		612.5	±115.8	13.62	0.0001	44.96	
log [Cl^-]	2.48	-115.1	±34.7	-8.54	0.0001	13.47	285
dependent variable: sample fail time, $t_{f,C}$							
intercept		827.8	±70.7	30.18	0.0001	27.43	
log [Cl^-]	2.48	-179.3	±21.2	-21.81	0.0001	8.22	445
dependent variable: sample fail time, t_f							
intercept		719.6	±82.4	22.50	0.0001	31.99	
log [Cl^-]	2.48	-147.1	±24.7	-15.35	0.0001	9.59	365

general linear model equations:

$$t_{f,R} = 612.5 - 115.1 \log \text{chloride} \quad \text{(A4/30)}$$

$$t_{f,C} = 827.8 - 179.3 \log \text{chloride} \quad \text{(A4/31)}$$

$$\overline{t_f} = 719.6 - 147.1 \log \text{chloride} \quad \text{(A4/32)}$$

The Pearson's correlation coefficients in Table A4/20 show very strong negative correlations between all thee sample failure time estimates, $t_{f,R}$, $t_{f,C}$, $\overline{t_f}$, and log solution chloride, suggesting that fail times increase as solution chloride decreases. However, a positive correlation also exists with 2 h water uptake, $X_{v,2h}$, and negative correlations with both gloss level and primer thickness that suggest fail times increase as 2 h water uptake increases but as gloss level and primer thickness decrease. Each of these latter correlations is the opposite of what is expected in practice and is caused by an accidental correlation between log chloride and each of these three variables, as seen in Table A4/20. It is necessary to calculate partial correlation coefficients to sort out which correlations are significant, see Table A4/22.

Table A4/22 indicates very strong negative partial correlations between all three fail times and log chloride, which are significant at the 99% level of confidence, and indicate that fail times increase as log chloride decreases. Negative partial correlations between all three fail times and both primer thickness and gloss level are not significant even at the 95% level of confidence, thus eliminating primer thickness and gloss level from further consideration.

Table A4/22 Partial Correlation Coefficients for Sample Fail Times

$t_{f,R}$ [r 1,2]3	value	$t_{f,C}$ [r 1,2]3	value	$\overline{t_f}$ [r 1,2]3	value
[r $t_{f,R}$, Cl] pthk	-0.80	[r $t_{f,C}$, Cl] pthk	-0.96	[r t_f, Cl] pthk	-0.92
[r $t_{f,R}$, pthk] Cl	-0.18	[r $t_{f,C}$, pthk] Cl	-0.31	[r t_f, pthk] Cl	-0.27
[r $t_{f,R}$, Cl] X_v	-0.79	[r $t_{f,C}$, Cl] X_v	-0.96	[r t_f, Cl] X_v	-0.92
[r $t_{f,R}$, X_v] Cl	+0.59	[r $t_{f,C}$, X_v] Cl	+0.15	[r t_f, X_v] Cl	+0.46
[r $t_{f,R}$, Cl] gloss	-0.82	[r $t_{f,C}$, Cl] gloss	-0.96	[r t_f, Cl] gloss	-0.93
[r $t_{f,R}$, gloss] Cl	-0.17	[r $t_{f,C}$, gloss] Cl	-0.05	[r t_f, gloss] Cl	-0.14

Notes:

tabulated $[r_{.01}]_{28}$ .530 $[r_{.05}]_{28}$ .439 (3 variables)

[r 1,2]3	partial correlation coefficient, r, between dependent variable 1 and independent variable 2, holding independent variable 3 constant.
$t_{f,R}$, $t_{f,C}$, $\overline{t_f}$	sample failure times based on resistive, capacitive contributions of impedance, and average, respectively, see Notes to Table R2/1, Section R2.2/1.1.1
Cl	log solution chloride ion concentration
pthk	primer thickness
X_v	2 h water uptake calculated by capacitance method
gloss	top coat gloss level, inversely related to amount of flatting agent

3.3 Water uptake by gravimetric method on attached films

Table A4/23 Correlation Coefficients

source: data from Table R2/2, Section R2.2/2
sample size 21
Pearson's correlation coefficients, r

water uptake/gloss	-0.469
water uptake/log chloride	-0.437
water uptake/time	0.460

tabulated $[r_{.05}]_{19}$ 0.433

R^2 0.621 (for Table A4/24)

Table A4/24 Dependent Variable: Gravimetric Water Uptake

parameter	range	regression coefficient	99% conf limits	Student's t value	probability	std error of estimate	max effect on dependent variable
intercept		10.070	±4.31	6.02	0.0001	1.672	
gloss	60	-0.047	±0.039	-3.14	0.0059	0.015	2.83
log [Cl^-]	2.48	-1.03	±0.904	-2.93	0.0094	0.351	2.55
time	2	1.23	±1.028	3.08	0.0068	0.399	2.46

general linear model equation:

$$X_v = 10.07 - 0.0471 \text{ gloss} - 1.03 \text{ log chloride} + 1.23 \text{ time} \qquad \text{(A4/33)}$$

where X_v = gravimetric water uptake (% v/v)

This form of equation gave just slightly better fit to the data than models of the form $X_v = A + \text{time}\,(B + C\ \text{gloss} + D \log [Cl^-])$ and is preferred for consistency with gravimetric/free films in Table A4/26, Section A4/3.4. However the form of Equation (A4/33) will not be correct at zero or very low times. Pearson correlation coefficients in Table A4/23 indicate significant negative correlations exist between water uptake/gloss level and water uptake/log chloride, and a significant positive correlation exists between water uptake/time at the 95% level of confidence. This means that water uptake increases with time, and with decreasing log chloride and gloss level. Cross-correlations between independent variables (eg chloride/time, chloride/gloss, gloss/time) were all zero, indicating that the coefficients obtained from the general linear model equation (A4/1) are meaningful. The R^2 value of 0.621 indicates a reasonably good fit of the data to the model equation. All three independent variables (gloss, log chloride, time) have about the same effect on the dependent variable, water uptake, as shown in column 8 of Table A4/24. All probabilities are close to zero in column 6, indicating that all estimates of the parameter coefficients are valid. This is also indicated by all the Student t values in column 5 being reasonably large. The 99% confidence limits for the regression coefficients are shown in column 4. It can be seen that the confidence limits are of the same order as the regression coefficient for gloss, log chloride and time, but are lower for the intercept, which is therefore more reliable.

3.4 Water uptake by gravimetric method on free films

Table A4/25 Correlation Coefficients

source: data from Table R2/3, Section R2.2/4 gives the following results:

sample size 21 (38 d sample results not included)

Pearson's correlation coefficients, r

water uptake/log chloride	-0.704
water uptake/time	0.481
log chloride/time	0.055
tabulated $[r_{.05}]_{19}$	0.433

R^2 0.767 (for Table A4/26)

Table A4/26 Dependent Variable: Gravimetric Water Uptake

parameter	range	regression coefficient	99% conf limits	Student's t value	probability	std error of estimate	max effect on dependent variable
intercept		5.80	±1.61	9.30	0.0001	0.624	
log $[Cl^-]$	2.48	-1.18	±0.471	-6.44	0.0001	0.183	2.93
time	9.7	0.283	±0.160	4.58	0.0002	0.062	2.75

general linear model equation:

$$X_v = 5.80 - 1.18 \log \text{chloride} + 0.283 \text{ time} \qquad \text{(A4/34)}$$

where X_v = gravimetric water uptake (% v/v)

This form of equation gave a better overall fit to the data compared with models of the form X_v = A + time (B log $[Cl^-]$ but will not be valid at zero or very low times.

Pearson's correlation coefficients in Table A4/25 indicate a significant negative correlation exists between water uptake and log chloride, and a significant positive correlation exists between water uptake and time at the 95% level of confidence. This means that water uptake increases with time and with decreasing solution chloride ion concentration. The fact that the Pearson's correlation coefficient for log chloride/time is only 0.055 (no correlation should exist), indicates that the regression coefficients of the general linear model equation are good estimates of the individual effects of log chloride and time. The R^2 value of 0.767 indicates that the data is a good fit to the model equation. The two independent variates (log chloride, time) have about the same effect on the dependent variable, water uptake, see column 8 Table A4/26. All probabilities are very close to zero, column 6, indicating that all estimates of the regression coefficients are valid. This is also indicated by all the Student's t values, column 5, which are reasonably large. The 99% confidence limits for the regression coefficients are shown in column 4. It can be seen that the confidence limits are reasonably low for all three parameters, indicating that the regression coefficients are reliable.

1. Calculation of error in R_t due to partial short circuits using the $R_{cp}/[R_t]_C$ method, Section R1.8/4 - ACM experimental data, impedance test

Table A5/1

Experimental details	cycle/ run	R_{WA} (ohm)	R_{cp} (ohm)	$[R_t]_C$ (ohm)	$R_{cp}/[R_t]_C$	$[R_t]_C/R_t \times 100$ (%)
PGB 354	1/4	1.10×10^{7}	3.75×10^{5}	144	2.60×10^{3}	>90
ACM3 (Zn)	2/3	1.89×10^{6}	6.44×10^{4}	65	9.91×10^{2}	>90
0.2 ppm $[SO_2]$	3/4	5.60×10^{5}	1.91×10^{4}	35	5.46×10^{2}	>90
	4/4	2.82×10^{5}	9.61×10^{3}	40	2.40×10^{2}	>90
PGB 352	1/4	-	-	84	-	-
ACM8 (Fe)	2/4	2090	70.2	33	2.13	48
0.5 ppm $[SO_2]$	3/4	1190	40.0	19	2.11	47
	4/4	416	14.0	10	1.40	23
PGB 357[1]	1/4	$>1.5\times10^{6}$	$>4.38\times10^{4}$			
ACM4 (rolled	2/4	$>0.8\times10^{6}$	$>2.34\times10^{4}$			
Zn-55%Al)	3/4	2.8×10^{6}	8.17×10^{4}			
0.5 ppm $[SO_2]$	4/4	1.8×10^{6}	5.25×10^{4}			

Notes:

1 Values of R_{cp} from impedance test not available for ACM4 (rolled Zn-55%Al) and values taken from corrosion current test.

Codes:

R_{WA}	multimeter resistance of nominally dry corrosion product bridging working, W, to auxiliary, A, plates of ACM
R_{cp}	corrosion product resistance due to partial shorts (calculated using Equation (R1/5), Section R1.8/4)
$[R_t]_C$	value of R_t calculated from experimental Nyquist plots in error due to effect of R_{cp}
R_t	true value of charge-transfer resistance
$[R_t]_C/R_t \times 100$	calculated value of R_t as a percentage of true value
C	calculated value

For PGB 354 using ACM3 (Zn), partial short circuits due to R_{cp} do not appear to be a problem as R_t is calculated to be greater than 90% of the true value. For PGB 352 using ACM8 (Fe), there is a gradual worsening of partial short circuits due to R_{cp} and R_t is calculated to be only 48, 47, 23% of the true values at the end of PGB cycles 2, 3, 4 respectively. No calculations of the error in R_t for ACM4 (rolled Zn-55%Al) are possible because impedance tests with measurements of R_{cp} were not made. A corrosion current test with R_{cp} measurements, PGB 357, shows that partial shorts are not likely to be a problem with ACM4 due to the high values of R_{WA}.

2. Calculation of error in R_t due to partial short circuits using the $[R_t/\sigma]_C$ method, Section R1.8/4 - ACM experimental data, impedance test

For ACM3 (Zn), Table A5/2, the $[R_t/\sigma]_C$ ratio for cycle 1 run 1 in column 6 is similar at all $[SO_2]$ values. The same ratio for ACM8 (Fe) in Table A5/3, column 6, has different values to ACM3 (Zn), but again the values are reasonably similar at all $[SO_2]$. This suggests that the ratios of charge transfer and diffusion remain approximately the same over the $[SO_2]$ range, at least for cycle 1 run 1, thus supporting the assumption made in Section R1.8/4. It appears reasonable that ratio $[R_t/\sigma]_C$ for cycle 1 run 1 can be taken as R_t/σ, that is, the true ratio in the absence of partial shorts. This enables the error in R_t to be calculated using Figure R1/56 in Section R1.8/4. However, the error in R_t is calculated to be >100% for some of the ACM8 (Fe) runs. This is attributed to the fact that R_t falls significantly from its first cycle value in later cycles, whereas σ remains more constant. This can be seen in Table A5/3 by comparing the R_t value for cycle 1 run 1 in column 6 with runs 3 or 4 in column 3. The assumption that ratio $[R_t/\sigma]_C$ for cycle 1

run 1 can be taken as R_t/σ is then not strictly correct for ACM8 (Fe) and some error will be introduced as a result. Therefore the errors in R_t in column 7 of Table A5/3 can only be taken as an approximate guide in this case.

Table A5/2 ACM3 (Zn)

$[SO_2]$ (ppm)	PGB[5] No/cycle/ run	$[R_t]_C$[4] (ohm)	$[\sigma]_C$[4] (ohm.$s^{1/2}$)	$[R_t/\sigma]_C$	$[R_t/\sigma]_C$ for[1,2] cycle 1 run 1	$[R_t]_C/R_t \times 100$[3] (%)
0.0	231/1/3	370	1470	0.252	450/5726	86
	231/2/4	215	1560	0.138	= 0.078	97
	231/3/3	300	867	0.346		76
	231/4/4	180	1450	0.124		97
0.05	235/1/4	1020	7760	0.131	360/5424	97
	235/2/4	700	6200	0.113	= 0.066	97
	235/3/4	68	128	0.531		60
	235/4/3	17.2	0.47	36.287		7
0.1	237/1/3	610	2700	0.226	530/6451	90
	237/2/3	520	2390	0.218	= 0.082	92
	237/3/3	320	965	0.332		77
	237/4/4	380	2030	0.187		95
0.1	239/1/3	510	2590	0.197	450/6881	90
	239/2/4	260	413	0.630	=0.065	54
	239/3/4	110	699	0.157		94
	239/4/3	98	465	0.211		89
0.2	233/1/5	365	3920	0.093	338/6421	98
	233/2/4	160	308	0.519	=0.053	60
	233/3/4	12.5	21.3	0.587		55
	233/4/3	2.8	0.55	5.138		12
0.2	354/1/4	144	5340	0.027	207/4890	>100
	354/2/3	65	486	0.134	=0.042	91
	354/3/4	35	1180	0.030		>100
	354/4/4	40	1130	0.035		>100
0.5	241/1/3	420	4190	0.100	330/5723	97
	241/2/4	70	1520	0.046	=0.058	>100
	241/3/2	26	665	0.039		>100
	241/4/4	26	155	0.168		92
1.0	289/1/4	365	2150	0.170	365/4753	95
	289/2/3	320	823	0.389	=0.077	72
	289/3/3	127	608	0.209		92
	289/4/4	180	448	0.402		71
1.0	290/1/4	440	1560	0.282	440/5873	81
	290/2/4	725	1530	0.474	=0.075	65
	290/3/4	415	164	2.530		20
	290/4/4	190	20.7	9.179		7

Notes:

1 ratio $[R_t/\sigma]_C$ for cycle 1 run 1 is assumed to be equal to ratio R_t/σ because shape of Nyquist plot shows either none or minimal signs of partial short circuits

2 ratio $[R_t/\sigma]_C$ for cycle 1 run 1 is assumed to hold for all cycles/runs at a given $[SO_2]$ even in the presence of partial shorts

3 ratio $[R_t]_C/R_t$ x100 is obtained from Figure R1/56, Section R1.8/4

4 calculated values of R_t, σ are not corrected for area

5 error in R_t can be calculated for all runs in each cycle by the $[R_t/\sigma]_C$ method, but has only been calculated for the last run of each cycle in this table.

Codes:

$[R_t]_C$, $[\sigma]_C$ values of R_t, σ, respectively, calculated from experimental Nyquist plots in error due to effect of partial short circuits

$[R_t]_C/R_t$ x100 calculated value of R_t as a percentage of true value

C calculated value

R_t charge-transfer resistance (true value) (ohm)

σ diffusion coefficient (ohm.$s^{1/2}$)

Table A5/3 ACM8 (Fe)

$[SO_2]$ (ppm)	PGB[5] No/cycle/ run	$[R_t]_C$ [4] (ohm)	$[\sigma]_C$ [4] (ohm.$s^{1/2}$)	$[R_t/\sigma]_C$	$[R_t/\sigma]_C$ for [1,2] cycle 1 run 1	$[R_t]_C/R_t \times 100$ [3] (%)
0.0	246/1/4	320	4410	0.073	1110/4070	>100
	246/2/4	200	3980	0.050	= 0.273	>100
	246/3/4	200	4520	0.044		>100
	246/4/4	200	5630	0.036		>100
0.0	247/1/3	400	4650	0.086	1160/4650	>100
	247/2/4	280	5030	0.056	= 0.249	>100
	247/3/4	375	8980	0.042		>100
	247/4/4	620	11200	0.055		>100
0.1	250/1/4	170	396	0.429	680/2050	89
	250/2/3	65	357	0.182	= 0.332	>100
	250/3/3	43	107	0.402		92
	250/4/3	36	29.0	1.241		26
0.1	252/1/4	210	422	0.498	380/1110	80
	252/2/4	82	407	0.201	= 0.342	>100
	252/3/4	50	90.6	0.552		74
	252/4/4	30	15.6	1.923		30
0.2	254/1/4	56	29.6	1.892	375/935	33
	254/2/4	32	76.1	0.420	= 0.401	97
	254/3/3	17.5	10.7	1.651		35
	254/4/3	12.5	3.93	3.181		23
0.2	256/1/4	155	324	0.478	365/1050	82
	256/2/4	48	93.9	0.511	= 0.348	80
	256/3/3	29	32.0	0.906		50
	256/4/3	20	11.9	1.681		33
0.5	258/1/4	140	361	0.388	230/552	>100
	258/2/4	52	319	0.163	= 0.417	>100
	258/3/4	19	32.9	0.578		80
	258/4/4	-	25.6	-		-
0.5	260/1/4	82	156	0.526	185/611	71
	260/2/4	29	365	0.079	= 0.303	>100
	260/3/4	19	97.7	0.194		>100
	260/4/4	17	60.6	0.281		>100
0.5	352/1/4	84	157	0.535	163/679	65
	352/2/4	33	54.7	0.603	= 0.240	60
	352/3/4	19	18.1	1.050		40
	352/4/4	10	6.39	1.565		31
1.0	262/1/4	130	294	0.442	155/474	85
	262/2/4	55	241	0.228	= 0.327	>100
	262/3/3	19	8.76	2.169		26
	262/4/4	13	10.2	1.275		37
1.0	264/1/4	95	221	0.430	145/462	85
	264/2/4	28	520	0.054	= 0.314	>100
	264/3/3	17.5	12.1	1.446		35
	264/4/4	11	10.9	1.009		41

Notes: see Table A5/2

Codes: see Table A5/2

Table A5/2 shows for ACM3 (Zn) that error in R_t due to partial short circuits are only likely to become substantial (that is, the calculated R_t value falls below, say, 50% of the 'true' value) in cycles 3, 4 and even then only at certain $[SO_2]$, namely 1.0 ppm (PGB 290) $[SO_2]$ for cycle 3 and 0.05 (PGB 235), 0.2 (PGB 233), 1.0 ppm (PGB 290) $[SO_2]$ for cycle 4. A further observation is that PGB 289 at 1.0 ppm $[SO_2]$ did not show substantial errors in R_t even in cycle 4, whereas a repeat test, PGB 290 at 1.0 ppm $[SO_2]$ did in cycles 3,4. This suggests firstly, that the formation of corrosion products that give rise to partial shorts can occur at random for apparently identical tests. Secondly, the partial shorts can be substantially minimized by stopping the test after 1 or 2 cycles, rather than 3 or 4.

Table A5/3 for ACM8 (Fe) also shows that errors in R_t due to partial shorts are only likely to become substantial in cycles 3, 4 and then only at certain $[SO_2]$, namely 0.2 (PGB 254), 0.5 (PGB 352), 1.0 ppm $[SO_2]$ for cycle 3 and 0.1, 0.2, 0.5 (PGB 352), 1.0 ppm $[SO_2]$ for cycle 4. This also demonstrates the randomness with which these partial shorts occur. However, some of the $[R_t]_C/R_t$ values in column 7 are >100% (or nearly 100%) and yet the corresponding Nyquist plot shape suggests that partial shorts are a problem, for example PGB 252/2/4 at 0.1 ppm $[SO_2]$, PGB 254/2/4 at 0.2 ppm $[SO_2]$, PGB 258, 260 at 0.5 ppm $[SO_2]$. This is attributed to the incorrect assumption that $[R_t/\sigma]_C$ for cycle 1 run 1 can be taken as the true ratio R_t/σ as discussed above, and illustrates a weakness of the calculation method for ACM8 (Fe).

A further observation from Tables A5/2,3 is that the ratio $[R_t/\sigma]_C$ in column 5 for cycle 1 run 1 is generally lower for ACM3 (Zn) than for ACM8 (Fe) but that 0 $[SO_2]$ is an exception for ACM8 (Fe). This indicates that diffusion is more rate determining than charge-transfer for ACM3 (Zn) than it is for ACM9 (Fe)

in these instances, a finding that supports the discussion in Section R1.5/3.2.

The uncorrected R_t/time plots for ACM3 (Zn), ACM8 (Fe) shown in Figures R1/20,21 respectively can be corrected using the error in R_t values tabulated in column 7 of Tables A5/2, 3.

For ACM3 (Zn), correction for the effect of partial shorts using Tables A5/2,3 moves cycle 3,4 R_t values up towards cycle 1,2 values but all four cycles do not come into line, suggesting that the R_t/time trends are real in the majority of cases. However, several problems are apparent. Firstly, PGB 241 at 0.5 ppm [SO_2] shows R_t values fall significantly from cycle to cycle, yet Table A5/2 column 7 shows only slight error in R_t. Inspection of the relevant Nyquist plots suggests (large semicircle, horizontal diffusion tail) that partial shorts become a problem in cycle 4, indicating errors in R_t in this cycle. Secondly, corrections to the R_t values for PGB 290 at 1.0 ppm [SO_2] appear to overcorrect the original trends, suggesting that the $[R_t/\sigma]_C$ method is incorrect in this case. This is thought to be because of the difficulty involved in calculating reliable σ values from small, horizontal diffusion tails like cycle 4 run 1 (curve 3) shown in Figure R1/14, Section R1.5/2. Such problems indicate weaknesses in the $[R_t/\sigma]_C$ method.

For ACM8 (Fe), correction of R_t moves values upwards but there is still a marked decrease in R_t from cycle to cycle, suggesting that this is a real effect. This is especially the case for cycles 1, 2 where R_t values are not significantly in error. Problems with some of the $[R_t/\sigma]_C$ values in column 7, Table A5/3 exceeding 100% have already been discussed above.

1 B.B. Damaskin, The Principles of Current Methods for the Study of Electrochemical Reactions, pp.61-85, McGraw-Hill, New York (1967).

2 G.W. Walter, Corros. Sci. 16, 573 (1976).

3 S. Barnartt, Corros. Sci. 9, 145 (1969).

4 M. Sluyters-Rehbach, J.H. Sluyters, Sine Wave Methods in the Study of Electrode Processes, Electroanal. Chem. Ed. A.J. Bard, p.110, Marcel Dekker, New york (1970).

5 D.D. Macdonald, M.C.H. McKubre, Electrochemical Corrosion Testing, Ed. F. Mansfeld, U. Bertocci, ASTM STP727, p.117, ASTM, Philadelphia (1981).

6 F. Wormwell, D.M. Brasher, J. Iron Steel Instit. 164, 141 (1950).

7 D.M. Brasher, J.T. Nurse, J. Appl. Chem. 9, 96 (1959).

8 H. Leidheiser, Jr., Corrosion 39, 189 (1983).

9 G.W. Walter, Preprints 21st. Australasian Corrosion Association Conference, Brisbane, Nov. (1981).

10 H. Leidheiser, Jr., Proc. Conf. Corrosion Control by Coatings, Lehigh University, p.143 (1978).

11 H. Leidheiser, Jr., M.W. Kendig, Corrosion 32, 69 (1976).

12 R.E. Touhsaent, H. Leidheiser, Jr., Corrosion 28, 435 (1972).

13 B.S. Smith, Australian Defence Scientific Service Materials Research Laboratories Report No. 630 (1975).

14 J.C. Padget, P.J. Moreland, J. Coatings Technol. 55, 39 (1983).

15 G.W. Walter, Proc. 7th International Congress Metallic Corrosion, Rio de Janeiro, Vol. 4, Section 10, p.1744 (1978).

16 G.W. Walter, J. Electroanal. Chem. 118, 259 (1981).

17 G.W. Walter, Corros. Sci. 26, 681 (1986).

18 J.E.B. Randles, Disc. Faraday Soc. 1, 11 (1947).

19 Yu. N. Mikhailovskii, V.V. Leonov, N.D. Tomashov, Korr. Met. and Spanov, British Lending Library Translation, p.202 (1965).

20 L. Beaunier, I. Epelboin, J.C. Lestrade, H. Takenouti, Surface Technol. 4, 237 (1976).

21 J.C. Scantlebury, K.K. Ho, JOCCA 62, 89 (1976).

22 F. Mansfeld, M.W. Kendig, S. Tsai, Corrosion 38, 378 (1982).

23 M. Kendig, F. Mansfeld, S. Tsai, Corros. Sci. 23, 317 (1983).

24 M. Piens, R. Verbist, Corrosion Control by Organic Coatings, Ed. H. Leidheiser, Jr., p.32, NACE, Houston (1981).

25 R.D. Armstrong, M.F. Bell, A.A. Metcalfe, Electrochem. 6, 98 (1976).

26 M.W. Kendig, E.M. Meyer, G. Lindberg, F. Mansfeld, Corros. Sci. 23, 1007 (1983).

27 L. Lemaitre, M. Moors, A.P. van Peteghem, J. Appl. Electrochem. 13, 803 (1983).

28 U. Rammelt, G. Reinard, K. Rammelt, J. Electroanal. Chem. Interfacial Electrochem. 180, 327 (1984).

29 B.D. Cahan, C. Chen, J. Electrochem. Soc. 129, 474 (1982).

30 M.G. Fontana, N.D. Greene, Corrosion Engineering, McGraw-Hill, New York (1967).

31 C. Wagner, W. Traud, Z. Elektrochem. 44, 391 (1938).

32 F. Mansfeld, Corrosion 27, 436 (1971).

33 F. Mansfeld, Corrosion 29, 403 (1973).

34 F. Mansfeld, J.V. Kenkel, Galvanic and Pitting Corrosion - Field and Laboratory Studies, Ed. R. Baboian, W.D. France, Jr., L.C. Rowe, J.F. Rynewicz, ASTM STP526 pp.20-47, ASTM, Philadelphia (1976).

35 F. Mansfeld, J.V. Kenkel, Corros. Sci. 15, 239 (1975).

36 F. Mansfeld, Corrosion Processes Ed. R.N. Parkins, Ch. 1, Applied Science, London (1982).

37 W.G. Whitman, R.P. Russell, Industr. Engng. Chem. 16, 276 (1924).

38 J. Devay, B. Lenyel, Jr., L. Meszaros, Acta. Chim. Hung. 62, 157 (1969).

39 G. Lauer, F. Mansfeld, Corrosion 26, 504 (1970).

40 J.A. Fraunhofer, C.H. Banks, Potentiostat and its Applications, pp.35-39, Butterworths, London (1972).

41 K.F. Bonhoeffer, W. Jena, Z. Elektrochem. 59, 151 (1951).

42 M. Stern, A.L. Geary, J. Electrochem. Soc. 104, 56 (1957).

43 M. Stern, E.D. Weisert, Proc. ASTM 59, 1280 (1959).

44 F. Mansfeld, Advances in Corrosion Science and Technology, Ed. M.G. Fontana, R.W. Staehle, Vol. 6, p.163 Plenum, New York (1976).

45 T.P. Hoar, Corros. Sci. 7, 455 (1967).

46 S. Barnartt, Electrochim. Acta 15, 1313 (1970).

47 F. Mansfeld, Corrosion 29, 397 (1973).

48 K.B. Oldham, F. Mansfeld, Corros. Sci. 13, 813 (1973).

49 J.C. Reeve, G. Bech-Nielsen, Corros. Sci. 13, 351 (1973).

50 A.C. Makrides, Corrosion 29, 148 (1973).

51 G.W. Walter, Corros. Sci. 17, 983 (1977).

52 G.W. Walter, Corros. Sci. 15, 47 (1975).

53 G.W. Walter, M.A.D. Madurasinghe, Corros. Sci. 27 (1989).

54 I.M. Callow, J.A. Richardson, J.L. Dawson, Br. Corros. J. 11, 132 (1976).

55 G.W. Walter, Corros. Sci. 18, 927 (1978).

56 D.A. Jones, N.D. Greene, Corrosion 22, 198 (1966).

57 D. Britz, P. Hougaard, Corros. Sci. 23, 987 (1983).

58 P. Hougaard, D. Britz, Corros. Sci. 23, 271 (1983).

59 M.L. Allen, B.W. Cherry, Proc. 27th Australasian Corrosion Association Conference, melbourne, Nov (1987).

60 M. Katoh, M. Koyama, Boshoku Gijutsu, 34, 215 (1985), BISI Translation No. 24452.

61 N. Azzerri, J. Appl. Electrochem. 6, 139 (1976).

62 N. Azzerri, R. Bruno, L. Spendorini, Corros. Sci. 21, 781 (1981).

63 J.A. Gonzalez, A. Molina, M.L. Eseudero, C. Andrade, Corros. Sci. 25, 917 (1985).

64 M. Stern, Corrosion 14, 440t (1958).

65 K.B. Oldham, F. Mansfeld, Corrosion 27, 434 (1971).

66 F. Mansfeld, K.B. Oldham, Corros. Sci. 11, 787 (1971).

67 F. Mansfeld, Corrosion 32, 143 (1976).

68 D.M. Drazic, M.D. Drazic, J. Serb. Chem. Soc. 51, 479 (1986).

69 L. Ferari, Chem. Aust. 401, Oct (1985).

70 Acid Rain, Environmental Resources Ltd., Graham and Trotman, London (1983).

71 A.G. Clarke, M. Radojevic, Atmospheric Environment 21, 1115 (1987).

72 D.F. Miller, D. Lamb, A.W. Gertler, Atmospheric Environment 21, 991 (1987).

73 T. Ibusuki, H.M. Barnes, Atmospheric Environment 18, 145 (1984).

74 B.J. Mason, Physics of Cloud, pp.70-78, Clarendon (1971).

75 T.C. Hudson, J.F. Stanners, J. Applied Chem. 3, 86 (1953).

76 Air Pollution Guide, Clean Air p.86, Nov (1984).

77 W. Funke, H. Haagen, Effects of Hostile Environments on Coatings and Plastics, ACS, Ed. D.P. Gainer, C.A.S. Stahl, p.309 (1983).

78 J.R. Duncan, D.J. Spedding, Corros. Sci. 13, 881 (1973).

79 R. Avery, Clean Air p.94, Nov (1984).

80 G.L. Holbrow, Trans. Inst. Met. Finishing 39, 183 (1962).

81 Ecos No. 34, p.21, Summer (1982/3).

82 G. Schikorr, Werkstoffe u. Korrosion 14, 69 (1963); 15, 457 (1964).

83 U.R. Evans, The Corrosion and Oxidation of Metals, 2nd Supplementary Volume, pp.246-275, Arnold, London (1976).

84 U.R. Evans, C.A.J. Taylor, Corros. Sci. 12, 227 (1972).

85 R. Ericsson, T. Sydberger, Werkstoffe u. Korrosion 31, 455 (1980).

86 J.R. Duncan, D.J. Spedding, E.E. Wheeler, Corros. Sci. 13, 69 (1973).

87 L.G. Johansson, N.G. Vannerberg, Werkstoffe u. Korrosion 32, 265 (1981).

88 J.R. Walton, J.B. Johnson, G.C. Wood, Br. Corros. J. 17, 59 (1982).

89 J.R. Walton, J.B. Johnson, G.C. Wood, Br. Corros. J. 17, 65 (1982).

90 W.H.J. Vernon, Trans. Far. Soc. 31, 1678 (1935).

91 G. Schikorr, Corrosion Behaviour of Zinc Vol. 1 Behaviour of Zinc in the Atmosphere, Metall-Verlag GmbH Berlin Grunewald (1964), p.72, English Edn., Amer. Zinc Instit/Zinc Development Association (1965).

92 K. Barton, E. Beranek, Werkstoffe u. Korrosion 10, 377 (1959).

93 F.H. Haynie, J.B. Upham, Materials Protection and Performance 9, 35 (1970).

94 E.O. Edney, D.C. Stiles, J.W. Spence, F.H. Haynie, W.E. Wilson, Materials Degradation Caused by Acid Rain, Ed. R. Baboian, p.172, ACS, Washington DC (1986).

95 E.O. Edney, D.C. Stiles, J.W. Spence, F.H. Haynie, W.E. Wilson, Atmospheric Environment 20, 541 (1986).

96 J.F.H. van Eijnsbergen, 2nd Sth. African Corrosion Conf, March (1972).

97 B.S. Skerry, J.B. Johnson, G.C. Wood, Corros. Sci. 28, 721 (1988).

98 G. Schikorr, Aluminium 43, 108 (1967).

99 D.J. Spedding, Br. Corros. J. 7, 281 (1972).

100 N.D. Tomashov, G.K. Berukshtis, A.A. Lokotilov, Zavodskaya Lab. 22, 345 (1956).

101 Yu. N. Mikhailovskii, N.D. Tomashov, Zavodskaya Lat. 23, 1462 (1957).

102 N.D. Tomashov, A.A. Lokotilov, Corrosion and Protection of Metals, pp.158-170, Moscow (1959).

103 G.K. Berukshtis, G.B. Klark, Corrosion of Metals and Alloys, Collection, translated from Russian by National Lending Library, Boston Spa, pp.379-400 (1964).

104 P.J. Sereda, ASTM Bulletin No. 246, p.47 (1960).

105 P.J. Sereda, Indust. Engng. Chem. 52, 157 (1965).

106 V. Kucera. E. Mattsson, Corrosion in Natural Environments, ASTM STP558, p.239, ASTM, Philadelphia (1974).

107 I.L. Rosenfeld, 1st International Congress on Metallic Corrosion, p.243, Butterworths, London (1962).

108 Yu. P. Gladkikh, Yu. N. Mikhailovskii, L.A. Shuvakhina, R.I. Nazarova, Protection of Metals 6, 456 (1970).

109 S.G. Fishman, C.R. Crowe, Corros. Sci. 17, 27 (1977).

110 N.D. Tomashov, Theory of Corrosion and Protection of Metals, Ch. 14, Macmillan, New York (1966).

111 F. Mansfeld, J.V. Kenkel, Corros. Sci. 16, 111 (1976).

112 J.A. Gonzalez, Werkstoffe u. Korrosion 29, 556 (1978).

113 F. Mansfeld, S. Tsai, Corros. Sci. 20, 853 (1980).

114 F. Mansfeld, S. Tsai, S. Jeanjaquet, E. Meyer, K. Fertig, C. Ogden, Atmospheric Corrosion of Metals, ASTM STP767, Eds. S.W. Dean, Jr., E.C. Rhea, p.309, ASTM, Philadelphia (1982).

115 S. Haagenrud, V. Kucera, J. Gullman, Atmospheric Corrosion, Ed. W.H. Ailor, Ch. 47, p.669, Wiley, New York (1982).

116 J.A. Gonzalez, E. Otero, C. Cabanas, J.M. Bastidas, Br. Corros. J. 19, 89 (1984).

117 S. Feliu, M. Morcillo, J.M. Bastidas, Pitture e Vernici 60, 29 (1984).

118 S. Feliu, J.M. Bastidas, M. Morcillo, JOCCA 68, 133 (1985).

119 F. Mansfeld, S.L. Jeanjaquet, M.W. Kendig, Corros. Sci. 26, 735 (1986).

120 M. Metikos-Hukovic, C. Zevnik, Werkstoffe u. Korrosion 35, 116 (1984).

121 P.J. Sereda, S.G. Croll, H.F. Slade, Atmospheric Corrosion of Metals, ASTM STP767, Eds. S.W. Dean, Jr., E.C. Rhea, p.267, ASTM Philadelphia (1982).

122 F. Mansfeld, S.L. Jeanjaquet, M.W. Kendig, Atmospheric Environment 20, 1179 (1986).

123 F. Mansfeld, J. Electrochem. Soc. 135, 1354 (1988).

124 S.E. Haagenrud, Werkstoffe u. Korrosion 31, 543 (1980).

125 F. Mansfeld, Proc. International Symp. Corrosion and Corrosion Protection, (H.H. Uhlig), Ed. Frankenthal, F. Mansfeld, vol. 81-8, p.266, Electrochem. Soc. (1981).

126 Corrosion of Metals and Alloys - Determination of Bimetallic Corrosion in Outdoor Exposure Corrosion Tests, International Standard, ISO 7441 (1984).

127 G.W. Walter, Corros. Sci. 26, 27 (1986).

128 N.D. Tomashov, Yu. N. Mikhailovskii, V.L. Leonov, Corrosion 20, 125t (1964).

129 J.E.O. Mayne, Official Digest 24, 127 (1952).

130 J.E.O. Mayne, Corros. Technol. 1, 286 (1954).

131 J.E.O. Mayne, U.R. Evans, J. Soc. Chem. Ind. Rev. 22, 109 (1944).

132 J.E.O. Mayne, JOCCA 32, 481 (1949).

133 J.D. Edwards, R.I. Wray, Ind. Engng. Chem. 28, 549 (1936).

134 S. Guruviah, JOCCA 53, 669 (1970).

135 F.L. Floyd, R.G. Groseclose, C.M. Frey, JOCCA 66, 329 (1983).

136 W. Funke, E. Machunsky, G. Handloser, Farbe Lacke 84, 493 (1978).

137 J.E.O. Mayne, Research 6, 278 (1952).

138 J.C. Hudson, T.A. Banfield, J. Iron Steel Inst. 154, 334 (1945).

139 K. Baumann, Plaste Kautsch. 19, 455 (1972).

140 J.E.O. Mayne, Anti-Corrosion, p.3 Oct (1973).

141 J.E.O. Mayne, JOCCA 40, 183 (1957).

142 R.C. Bacon, J.J. Smith, F.M. Rugg, Ind. Engng. Chem. 40, 161 (1948).

143 J.M. Sykes, U.K. Corrosion 87 Conf., Brighton, p.359 (1987).

144 J. Wolstenholme, Corros. Sci. 13, 521 (1973).

145 J.E.O. Mayne, Chem. Ind., 293 (1951).

146 W.W. Kittleberger, A.C. Elm. Ind. Engng. Chem. 44, 326 (1952).

147 C.C. Maitland, J.E.O. Mayne, Official Digest 34, 972 (1962).

148 R.S. Morrell, Varnishes and their Components, Ed. H. Frowde, p.267, Hodder and Stoughton, London (1923).

149 W.W. Kittleberger, A.C. Elm, Ind. Engng. Chem. (Ind. Edn) 38, 695 (1946).

150 New England Society for Coatings Technology Technical Committee, J. Coatings Technol. 53, 27 (1981).

151 B.W. Cherry, J.E.O. Mayne, Proc. 1st Internat. Congr. Metallic Corrosion, p.539, London (1961).

152 J.A. Von Fraunhofer, J. Boxall, Protective Paint Coatings for Metals, p.7, Portcullis, U.K. (1976).

153 D.M. Brasher, A.H. Kingsbury, J. Appl. Chem. 4, 62 (1954).

154 P. Walker, Official Digest 37, 1561 (1965).

155 G.E. Johnson, H.E. Bair, E.W. Anderson, Corrosion Control by Organic Coatings, Ed. H. Leidheiser, Jr., p.4, NACE, Houston (1981).

156 C.V. D'Alkaine, C. Garcia, H. Corti, D. Gomez, JOCCA 63, 23 (1980).

157 P. Kresse, Paint and Resin Technology, 21 Nov (1973).

158 D.J. Mills, J.E.O. Mayne, Corrosion Control by Organic Coatings, Ed. H. Leidheiser, Jr., p.12, NACE, Houston (1981).

159 J.E.O. Mayne, D.J. Mills, JOCCA 58, 155 (1975).

160 W. Funke, JOCCA 62, 63 (1979).

161 G.W. Walter, Corros. Sci. 26, 39 (1986).

162 S.A. Lindquist, Corrosion 41, 69 (1985).

163 S. Barnartt, J. Electrochem. Soc. 108, 102 (1961).

164 J.B. Horton, A.R. Borzillo, G.J. Harvey, J. Reynolds, 6th International Congress on Metallic Corrosion, Sydney, paper 5-7, (1975).

165 D.J. Spedding, Br. Corros. J. 7, 281 (1972).

166 K.E. Johnson, A.F. Bromley, Anti-Corrosion, 17 Nov (1973).

167 CRC Handbook of Chemistry and Physics, Ed. R.C. Weast, 56th Edn. (1975/6).

168 A.A. Presnyakov, Yu. A. Gorban, V.V. Chervyakova, Zhur. Fiz. Khim. 35, 1289 (1961).

169 G.J. Harvey, BHP Technical Bulletin 25, 63 (1981).

170 D.J. Willis, private communication.

171 J.R. Duncan, D.J. Spedding, Corros. Sci. 14, 241 (1974).

172 F. Mansfeld, Electrochemical Corrosion Testing, Ed. F. Mansfeld, U. Bertocci, ASTM STP727, pp.215-237, ASTM, Philadelphia (1981).

173 G.W. Walter, Proc. 6th Internat. Congress Metallic Corrosion, Sydney, Section 5, 859, Australasian Corrosion Association, Dec (1975).

174 J.O'M. Bockris, H. Kita, J. Electrochem. Soc. 108, 676 (1961).

175 F. Hilbert, Y. Miyoshi, G. Eichkorn, W.J. Lorenz, J. Electrochem. Soc. 118, 1919 (1971).

176 S. Barnartt, J. Electrochem. Soc. 119, 812 (1972).

177 G.J. Bignold, M. Fleischman, Electrochim. Acta 19, 363 (1974).

178 D.M. Drazic, S.K. Zecevic, Corros. Sci. 25, 209 (1985).

179 V. Kucera, E. Mattsson, Proc. 7th Scand. Congr. Metallic Corrosion, Royal Norwegian Council for Scientific and Industrial Research, p.202, Trondheim (1975).

180 V. Kucera, J. Gullman, Electrochemical Corrosion Testing, ASTM STP727, Eds. F. Mansfeld, U. Bertocci, p.238 (1981).

181 I. Epelboin, M. Keddam, H. Takenouti, J. Appl. Electrochem. 2, 71 (1972).

182 J.E.O. Mayne, J.D. Scantlebury, Br. Polymer J. 2, 240 (1970).

183 B.W. Cherry, P.H. Wright, A.T.R. 7, 1 (1973).

184 E.M. Kinsella, J.E.O. Mayne, Br. Polymer J. 1, 173 (1969).

185 CRC Handbook of Chemistry and Physics, 56th Edn., p.E-60 (1975).

186 J.O'M. Bockris, A.K.N. Reddy, Modern Electrochemistry, Vol. 1, p.157, Macdonald, London (1970).

187 D.M. Brasher, Electroplating and Metal Finishing 280, Sept (1956).

188 M. Binns, private communication.

189 G.M. Barrow, Physical Chemistry (2nd Edn), McGraw-Hill, New York (1966).

190 W. Funke, Werkstoffe u. Korrosion 20, 12 (1969).

191 B.W. Cherry, private communication.